

# The Two-Particle Self-Consistent approach and its application to real materials

DISSERTATION  
zur Erlangung des Doktorgrades  
der Naturwissenschaften

vorgelegt beim Fachbereich Physik  
der Johann Wolfgang Goethe-Universität  
in Frankfurt am Main

von  
Karim Zantout  
aus Beirut, Libanon

Frankfurt am Main, Dezember 2020  
(D30)



Vom Fachbereich Physik der  
Johann Wolfgang Goethe-Universität als Dissertation angenommen.

Dekan: Prof. Dr. Harald Appelshäuser

Gutachter: Prof. Dr. Roser Valentí

Prof. Dr. Eberhard Engel

Datum der Disputation: noch nicht bekannt



---

*dedicated to all  
that fight their way through the darkness of prejudice  
and to all those  
who shine their light upon them.*



## Zusammenfassung

Innerhalb des weiten Feldes der Festkörperphysik beschäftigt sich diese Arbeit mit dem Gebiet der sogenannten korrelierten Elektronensysteme. Um diesen Begriff genauer zu verstehen, starten wir von der empirischen Beobachtung, dass die Elemente einer großen Gruppe von Materialien bei hinreichend tiefen Temperaturen in Form von Kristallen auftreten. Diese periodische Anordnung von ladungsneutralen Elementarzellen findet auf einer Größenskala statt, welche die elektrostatische Wechselwirkung als einzig dominante Wechselwirkung auszeichnet. Außerdem folgert man aus dem Vergleich der auftretenden Längen- und Energieskalen, dass eine genaue Beschreibung des Systems im Rahmen der Quantenmechanik erfolgen muss. Bei einem Kristall handelt es sich offensichtlich um ein Vielteilchensystem, in dem Elektronen und Atomrümpfe über die langreichweitige Coulomb-Wechselwirkung miteinander wechselwirken. Ein solches System, das typischerweise eine Teilchenzahl von der Größenordnung  $10^{23}$  pro Quadratcentimeter aufweist, kann mit keiner bekannten numerischen oder analytischen Methode exakt beschrieben werden. Doch selbst wenn es möglich wäre das Energiespektrum des Hamiltonoperators des Kristalls zu bestimmen, würde die riesige Datenmenge zunächst wenig Aufschluss über die darin enthaltene Physik preisgeben.

Es ist daher ein zentrales Problem der theoretischen Festkörperphysik effektive Modelle herzuleiten, die einfach genug sind, um eine analytische oder numerische Lösung zuzulassen, aber gleichzeitig so komplex sind, dass die wesentliche Physik darin enthalten bleibt.

Eine fundamentale Näherung, auf die wir in dieser Arbeit zurückgreifen, ist die sogenannte Born-Oppenheimer-Approximation. Diese macht sich den großen Massenunterschied zwischen Elektronen und Atomrümpfen zunutze, um die elektronischen Freiheitsgrade von denen der schweren Atomrümpfe zu entkoppeln. Da wir uns in dieser Arbeit ausschließlich mit elektronischen Eigenschaften von Kristallen bei tiefen Temperaturen beschäftigen, wollen wir weiterhin annehmen, dass die Atomrümpfe auf ihren Gleichgewichtspositionen festgefroren sind.

Doch auch die drastische Vereinfachung, die uns die Born-Oppenheimer-Approximation ermöglicht, ist leider immer noch nicht ausreichend, um das verbleibende elektronische Vielteilchenproblem zu lösen. Um das Modell noch weiter zu vereinfachen, betrachten wir den thermodynamischen Grenzfall, indem das System als unendlich ausgeht angenommen wird, während die Teilchendichte konstant bleibt. Außerdem beschränken wir uns zunächst auf Grundzustandseigenschaften.

In dieser Situation stellt die Dichtefunktionaltheorie (DFT) einen prominenten und erfolgreichen Zugang zum elektronischen Vielteilchenproblem dar. Aufbauend auf den fundamentalen Theoremen von Hohenberg und Kohn erlaubt DFT Erwartungswerte von Observablen nicht nur über  $3N$ -Raumintegrale auszudrücken, sondern auch als Funktionale der Grundzustandsdichte. Obwohl diese Umformulierung des Problems bereits eine elegante Vereinfachung darstellt, erlaubt erst die Kohn-Sham Formulierung von

---

DFT die physikalischen Eigenschaften von Kristallen explizit zu berechnen. Der Kohn-Sham Ansatz postuliert, dass sich das elektronische Vielteilchensystem auch als effektives nicht-wechselwirkendes Elektronengas beschreiben lässt, das sich in einem effektiven externen Potential, erzeugt durch die Atomrümpfe und elektronische Austausch- und Korrelationseffekte, befindet.

Diese Reduktion des ursprünglichen Viel-Elektronensystems auf ein effektives nicht-wechselwirkendes System in einem externen Potential führt zu dem sogenannten Kohn-Sham Hamiltonoperator. Bei diesem Operator handelt es sich um einen Einteilchen-Hamiltonoperator, in einem externen periodischen Potential, sodass das Energiespektrum – vermöge des Bloch-Theorems – eine Bandstruktur aufweist, in der der Gitterimpuls  $k$  eine gute Quantenzahl ist. Die für DFT fundamentale Grundzustandsdichte erhält man als Summe von Betragsquadraten der Kohn-Sham Energieeigenzustände, nachdem man das Austausch- und Korrelationspotential beispielsweise mittels der lokalen Dichteapproximation festgelegt (LDA) hat.

Es ist unbestreitbar, dass die Kohn-Sham DFT in den Bereichen der Chemie und der Festkörperphysik besonders aufgrund der stetigen Verbesserung der Austausch- und Korrelationspotentiale große Erfolge gefeiert hat und auch aktuell ein aktives und grundlegendes Forschungsgebiet darstellt. In der Praxis interpretiert man das Spektrum des Kohn-Sham Hamiltonoperators als Näherung zum Energiespektrum des wechselwirkenden Elektronensystems.

Als Maß aller Dinge gilt hier das Experiment, wobei besonders die winkelaufgelöste Photoemissionsspektroskopie (ARPES) und die de-Haas-van-Alphen Spektroskopie (dHvA) Rückschlüsse auf bestimmte Teile des elektronischen Energiespektrums erlauben.

Jedoch trifft man auch auf Materialien, wo die Bandstruktur von DFT stark von der Gemessenen abweicht. So werden beispielsweise viele Übergangsmetalloxide im Rahmen von LDA als Metalle charakterisiert, während das Experiment klar einen Isolator vorfindet. Weitere typische Effekte betreffen die unterschätzte effektive Masse der Elektronen und fehlende inkohärente Zustände bei tieferen Bindungsenergien.

Diese Effekte sind charakteristisch für korrelierte Elektronensysteme, wobei sich der Begriff korreliert darauf bezieht, dass das Verhalten der Elektronen kollektiv beschrieben werden muss und die unabhängige Teilchenannahme, die in den Kohn-Sham Ansatz eingeht, nicht mehr gerechtfertigt ist.

In Kapitel 1 gehen wir genauer auf die Phänomenologie korrelierter Elektronensysteme ein und präsentieren zwei Materialklassen von unkonventionellen Supraleitern, deren Vielteilcheneigenschaften wir später genauer untersuchen wollen. Hierbei handelt es sich um die organischen  $\kappa$ -(ET)<sub>2</sub>X Ladungstransfersalze und den Eisenpniktid-Supraleiter LiFeAs.

Bei den organischen Supraleitern stellt man eine verblüffende Ähnlichkeit zwischen dem Phasendiagramm dieser Systeme und dem der Kupratsupraleiter fest, weshalb der Schluss nahe liegt, dass trotz der strukturellen und chemischen Verschiedenheit beider Systeme ein ähnlicher Mechanismus die Supraleitung steuert. Aus diesem Grund geht man davon aus, dass Spin-Fluktuationen sowohl bei den Kupraten als auch bei den organischen  $\kappa$ -(ET)<sub>2</sub>X-Supraleitern zur Bildung von Cooper-Paaren führen. Da die Einheitszelle in organischen Supraleitern typischerweise hunderte Atome beinhaltet, ist es für die gängigen Vielteilchenmethoden unmöglich die Korrelationseffekte aller Elektronen zu beschreiben. Aus diesem Grund bedient man sich effektiver Modelle, welche die langkettigen organischen Bestandteile auf verschiedene Weise beschreiben. Wir behandeln das Molekül-Modell und das sich daraus ergebende Dimer-Modell.

In ähnlicher Weise stellt man in den Phasendiagrammen der Eisenpniktid-Supraleiter

---

fest, dass die supraleitende Phase oft an eine Phase mit magnetischer Ordnung angrenzt, weshalb auch für LiFeAs vermutet wird, dass die Tieftemperatur-Eigenschaften durch Spinfluktuationen bestimmt werden.

Da das Kohn-Sham Energiespektrum in DFT trotz des fehlenden kollektiven Aspekts der Elektronendynamik in vielerlei Hinsicht einen guten nicht-wechselwirkenden Startpunkt für Vielteilchen-Rechnungen darstellt, befassen wir uns nach einer ausführlichen Behandlung der Dichtefunktionaltheorie in Kapitel 2 mit der projektiven Wannierfunktionsmethode. Ein besonderes Merkmal von DFT ist ihr sogenannter *ab-initio*-Charakter, was bedeutet, dass DFT nur die chemische Zusammensetzung und Kristallstruktur zu Beginn benötigt und auf keine zusätzlichen physikalischen Parameter außer Naturkonstanten angewiesen ist.

Man stellt nun im Vergleich mit dem Experiment fest, dass die Vielteilchennatur nicht bei allen Elektronen eines Systems gleichermaßen auftreten, sondern auf bestimmte Orbitale beschränkt ist. So sind es bei Verbindungen, die Übergangsmetalle beinhalten, oft die partiell gefüllten stark lokalisierten *d*-Orbitale, welche Korrelationseffekte aufweisen, während die Elektronen in anderen Orbitalen hinreichend genau mittels des Kohn-Sham Energiespektrums in DFT beschrieben werden.

Die projektive Wannierfunktionen-Methode erlaubt nun einen Basiswechsel derart durchzuführen, dass die Elektronen der lokalisierten und korrelierten Orbitale separat in einem effektiven Niedrig-Energie-Modell beschrieben werden können.

Nachdem wir diejenigen Orbitale aus DFT extrahiert haben, die durch Vielteilcheneffekte korrigiert werden müssen, folgt nun der nächste Schritt der Modellierung in Kapitel 3. Hierbei erfolgen zwei drastische Approximationen, die zu dem berühmten Hubbard-Modell führen.

Zum einen Vernachlässigen wir das Kontinuum, indem wir nur die Matrixelemente des Niedrig-Energie Modells in der Wannierbasis betrachten und die explizite Form der Wannierfunktionen nicht berücksichtigen und somit zu einem reinen Gittermodell gelangen. Zum anderen behalten wir nur den Anteil der Coulomb-Wechselwirkung zwischen Elektronen auf dem gleichen Gitterplatz, sodass Elektronen auf unterschiedlichen Gitterplätzen keine Abstoßung spüren. Dieses Vorgehen wirkt zunächst übermäßig vereinfachend, aber während die Information zu der Form der Orbitale in den effektiven Parametern des Hubbard-Modells eingebaut sind, lässt sich die Einschränkung der Coulomb-Abstoßung auf gleiche Gitterplätze durch starke Abschirmungseffekte begründen.

Letztlich ist es jedoch die große Vielfalt, die im einfach anmutenden Hubbard-Modell enthalten ist, und der Erfolg, der in realistischen Materialrechnungen erlangt werden konnte, welche das Hubbard-Modell so populär machen.

Um die *ab-initio*-Eigenschaft unserer Modellierung zu wahren, stellen wir in demselben Kapitel die eingeschränkte Random-Phase-Approximation vor, welche erlaubt, genährte effektive Coulomb-Wechselwirkungsparameter für das Hubbard-Modell zu einem jeweiligen Material zu bestimmen.

Bis zu diesem Punkt haben wir also ein effektives Gittermodell mit lokaler effektiver Coulomb-Wechselwirkung konstruiert, welches die Korrelationsphänomene der Elektronen in den lokalisierten Orbitalen nahe der Fermi-Kante beschreiben soll. Leider gibt es für das Hubbard-Modell nur in bestimmten Grenzfällen exakte Lösungen und so ist man darauf angewiesen, genährte Vielteilchen-Lösungen zu konstruieren. Eine gängige und elegante Methodologie, die sich in diesem Rahmen anbietet und in Kapitel 4 vorgestellt wird, ist die Verwendungen von Greenschen Funktionen. Diese Objekte erlauben es den Effekt von Elektron-Elektron-Wechselwirkung in Form der sogenannten Selbstenergie

---

zu bestimmen, welche die Einteilchen-Eigenschaften der nicht-wechselwirkenden Teilchen renormiert.

In den Fällen, in denen die Fermi-Flüssigkeitstheorie anwendbar ist, kann man aus der Selbstenergie beispielsweise die Lebenszeit oder effektive Masse der Quasiteilchen extrahieren.

Kapitel 5 bildet dann das Zentrum dieser Arbeit. In diesem Kapitel leiten wir ausführlich die sogenannte Two-Particle Self-Consistent Methode (TPSC) her, welche ursprünglich von Y.M. Vilk und A.-M.S. Tremblay für das Einband-Hubbard Modell entwickelt wurde.

Diese lässt sich in der Sprache von funktionalen Ableitungen nach Kadanoff-Baym herleiten und wir geben eine explizite Erweiterung für Viel-Orbital-Systeme an, in denen neben der Coulomb-Abstoßung auch die Hunds-Wechselwirkung Eingang findet.

Im Gegensatz zu der Einband-Formulierung treten hierbei einige Hindernisse auf, die entsprechend mit weiteren Approximationen umgangen werden können. Der fundamentale Gedanke der Methode ist jedoch der folgende und in allen TPSC-Varianten gleich: Der effektive Wechselwirkungsvertex wird als Impuls- und Energie-unabhängig angenommen, sodass sich die Gleichungen zur Bestimmung der Selbstenergie enorm vereinfachen. Weiterhin wird der Wert des effektiven Wechselwirkungsvertex durch Erzwingung des Pauli-Prinzips in Form sogenannter lokaler Summenregeln festgelegt. Die Selbstenergieeffekte, welche durch diese Art der Approximation behandelt werden, sind Spin- und Ladungsfluktuationen aus dem paramagnetischen Grundzustand, welche an die elektronischen Zustände koppeln.

Wir wenden in demselben Kapitel TPSC dann auch auf die organischen  $\kappa$ -(ET)<sub>2</sub>X Supraleiter an und studieren die supraleitenden Eigenschaften im Rahmen der linearisierten Eliashberg-Gleichung. Hierbei vergleichen wir das eingangs vorgestellte Molekül- und Dimer-Modell bezüglich supraleitender kritischer Temperaturen und der Symmetrie der supraleitenden Lückenfunktion. Dabei stellen wir fest, dass das komplexere Molekül-Modell eine exotische  $s+d_{x^2-y^2}$  Lückenfunktion stabilisiert, während das Dimer-Modell nur  $d_{xy}$ -Lösungen zulässt. Darüber hinaus finden wir im Dimer-Modell einen direkten Zusammenhang zwischen der supraleitenden kritischen Temperatur und dem Maß an geometrischer Frustration, welcher sich nicht mit den experimentell bestimmten kritischen Temperaturen deckt. Aus diesem Grund schließen wir, dass das Dimer-Modell zur Beschreibung der Supraleitung unzureichend ist und man auf komplexere Systeme wie das Molekül-Modell mit eventuell Nächster-Nachbar-Wechselwirkung angewiesen ist.

Die Erweiterung von TPSC auf Viel-Orbital-Systeme fand zum ersten Mal im Jahre 2013 statt und die Formulierung, die wir in dieser Arbeit vorstellen, basiert auf einer neu hergeleiteten Version aus dem letzten Jahr.

Aus diesem Grund ist Kapitel 6 dem Test dieser Methode und dem Vergleich mit der etablierten Dynamischen Molekularfeldnäherung (DMFT) gewidmet. In dieser weit verbreiteten Approximation wird die Selbstenergie als lokale Größe approximiert und die daraus gewonnene Lösung entspricht der exakten Lösung im unendlich-dimensionalen Grenzfall.

Bei diesem Vergleich der beiden Methoden, den wir für ein einfaches Zwei-Orbital Modell durchführen, stellen wir zunächst fest, dass die Viel-Orbital-Version von TPSC einige Probleme mit der Bestimmung des effektiven Wechselwirkungsvertex aufweist, da die gefundenen Lösungen zu unphysikalischen Signaturen in der Greenschen Funktion führen. Um solche Effekte zu verhindern, ist es notwendig die Erzwingung des Pauli-Prinzips auf physikalische Lösungen einzuschränken, was mit der Annahme eines konstanten effektiven Wechselwirkungsvertex nicht vereinbar ist, sodass wir statt einer

---

exakten Lösung nach einer optimalen Lösung suchen, die die lokalen Summenregeln unter Einhaltung der Physikalität möglichst genau erfüllt.

Im direkten Vergleich von TPSC und DMFT stellen wir weiterhin fest, dass beide Methoden die Renormierung der Quasiteilchen qualitativ sehr ähnlich beschreiben und auch quantitativ in einigen Bereichen große Übereinstimmung aufweisen. Nichtsdestotrotz sehen wir aber auch, dass bestimmte Effekte der Hunds-Wechselwirkung innerhalb von TPSC nicht wiedergegeben werden. Wir führen dies auf einen bestimmten Ansatz für den effektiven Wechselwirkungsvertex zurück, der zumindest für die Einband-Formulierung von TPSC sehr erfolgreich eingesetzt werden konnte.

Nachdem in Kapitel 6 die Viel-Orbital TPSC-Variante getestet wurde, wenden wir sie in Kapitel 7 auf den zu Beginn eingeführten eisenbasierten Supraleiter LiFeAs an. Wir sind hierbei an den elektronischen Eigenschaften in der normalleitenden paramagnetischen Phase interessiert. Dabei spielen zwei Aspekte eine besondere Rolle:

Zum einen wollen wir die Diskrepanz bezüglich der Größe der Elektronen- und Lochtaschen auf der Fermioberfläche im Vergleich von Experiment und der Kohn-Sham DFT-Bandstruktur auflösen. In der Literatur wird dieser Umstand bei den eisenbasierten Supraleitern als Rot-Blau-Verschiebung bezeichnet. Zum anderen wollen wir versuchen die energieabhängigen Quasiteilchen-Lebenszeiten aus Experimenten zu reproduzieren. Tatsächlich realisiert TPSC die Rot-Blau-Verschiebung in ausreichendem Maße, so dass die Übereinstimmung mit dem Experiment sichtlich zunimmt. Zusätzlich stellen wir fest, dass Elektron-Elektron-Wechselwirkung dazu führt, dass die elektronischen Zustände nahe des Ursprungs des reziproken Gitters inkohärent werden und eine blumenartige Form annehmen, was ebenfalls vom Experiment beobachtet wird.

Um zu unterstreichen, dass diese beiden Eigenschaften aus der Impulsabhängigkeit der Selbstenergie stammen, zeigen wir zudem Rechnungen, in denen die TPSC-Selbstenergie durch ihren Impulsmittelwert ersetzt wurde. In dieser lokalen Näherung verschwinden sowohl die blumenförmigen Zustände als auch die Rot-Blau-Verschiebung. Erstaunlicherweise stimmt dann aber die daraus resultierende Fermioberfläche in hohem Maße mit der aus DMFT-Rechnungen überein. Dies zeigt, dass die Impulsabhängigkeit in diesem System nicht zu vernachlässigen ist und eventuell auf Spinfluktuationen zurückgeführt werden kann.

Bezüglich der energieabhängigen Quasiteilchen-Lebenszeiten finden wir, dass diese ebenfalls starke impulsabhängigkeit aufweisen und qualitativ mit den experimentellen Befunden einer Forschungsgruppe übereinstimmen. Seitens der Experimentatoren gibt es keine endgültig übereinstimmenden Resultate diesbezüglich.

Im letzten Kapitel fassen wir die gesamte Arbeit zusammen und geben einen Ausblick für mögliche zukünftige Aktivitäten auf diesem Gebiet.

Im Vordergrund stehen hierbei potentielle Verbesserung der Viel-Orbital TPSC-Methode. Dazu bietet sich zunächst die Kombination mit anderen Methoden wie DMFT an, da diese viele präzise Bestandteile zur Gesamtlösung beitragen kann. Dies hätte den weiteren Vorteil, dass TPSC ohne einen Ansatz für den effektiven Wechselwirkungsvertex auskommt und somit die damit einhergehenden Probleme eventuell behoben wären.

Weitere Verbesserungen der Methode könnten darin bestehen die kürzlich publizierte "TPSC+"-Erweiterung auch auf die Viel-Orbital-Variante anzuwenden. Andererseits könnte man aber auch versuchen TPSC dahingehend zu erweitern, dass auch dynamische Abschirmeffekte eingebaut werden können.

Eine weitere mögliche Baustelle ist die Einbindung des sogenannten transversalen Teilchen-Loch-Kanals. Dieser kann in der hier vorgestellten Viel-Orbital-TPSC-Variante nicht eingebaut werden, da nicht genügend lokale Summenregeln existieren. Die Kombination von TPSC mit DMFT oder anderen Vielteilchenmethoden könnte dieses Problem

---

ebenfalls lösen.

Im Wesentlichen stellen wir also fest, dass TPSC durchaus das Potential hat nicht-lokale Selbstenergieeffekte aus Spinfuktuationen präzise zu beschreiben und dass die genannten Kinderkrankheiten im Laufe weiterer Forschung behoben werden können.

# Contents

Zusammenfassung . . . . .	i
Contents . . . . .	vii
Notation . . . . .	ix
CHAPTER 1. Introduction . . . . .	1
1.1. Non-interacting vs. interacting electrons in a solid . . . . .	1
1.2. Two classes of unconventional superconductors . . . . .	3
CHAPTER 2. Density Functional Theory . . . . .	5
2.1. Fundamentals of Density Functional Theory . . . . .	6
2.2. Kohn-Sham Density Functional Theory . . . . .	7
2.3. Exchange-correlation potential . . . . .	9
2.4. Many-body extensions to DFT . . . . .	10
2.5. Maximally localized Wannier functions . . . . .	12
CHAPTER 3. The Hubbard model . . . . .	14
3.1. Introduction . . . . .	14
3.2. Exactly solvable limits . . . . .	15
3.3. Rigorous results for the Hubbard model . . . . .	16
3.4. Multi-orbital Coulomb interaction . . . . .	17
3.5. Constrained Random Phase Approximation . . . . .	18
CHAPTER 4. Green's functions . . . . .	21
4.1. Mathematical motivation . . . . .	21
4.2. Single-particle Green's functions and propagators . . . . .	22
4.3. Single-particle Green's function and density of states . . . . .	23
4.4. Many-body Green's function . . . . .	24
4.5. Imaginary time Green's function . . . . .	25
4.6. Lehman representation and spectral weight . . . . .	31
4.7. Relation between retarded Green's function and Matsubara Green's function . . . . .	38
4.8. Non-interacting lattice Green's function . . . . .	42
4.9. Green's functions and observables . . . . .	45
4.10. Analytic continuation . . . . .	50
CHAPTER 5. Two-Particle Self-Consistent approach . . . . .	53
5.1. The Kadanoff-Baym formalism . . . . .	53
5.2. Conserving approximations . . . . .	80
5.3. Single-band TPSC . . . . .	82
5.4. Multi-site TPSC . . . . .	87
5.5. Multi-site TPSC application: Organic superconductors . . . . .	95
5.6. Multi-orbital TPSC . . . . .	103
5.7. Double counting . . . . .	120

---

CHAPTER 6. Benchmarking the multi-orbital TPSC . . . . .	122
6.1. Model Hamiltonian . . . . .	122
6.2. Double occupations and spin vertex . . . . .	122
6.3. Charge vertex . . . . .	125
6.4. Self-energy and quasi-particle properties . . . . .	129
CHAPTER 7. Nonlocal correlation effects in LiFeAs . . . . .	133
7.1. Introduction . . . . .	133
7.2. Experiment and Density Functional Theory . . . . .	134
7.3. TPSC results . . . . .	140
7.4. Comparison of “local TPSC” and DMFT . . . . .	145
7.5. Conclusions . . . . .	147
CHAPTER 8. Summary and Outlook . . . . .	148
Appendix A. Transversal particle-hole channel for multi-orbital TPSC . . . . .	151
A.1. Self-energy and susceptibilities: Transverse channel . . . . .	152
Appendix B. Computational details . . . . .	157
B.1. Matsubara functions . . . . .	157
B.2. Non-convolutional k-integration . . . . .	161
B.3. The cross correlation theorem . . . . .	163
B.4. Numerical instabilities at low temperatures . . . . .	164
Appendix C. Formal results . . . . .	166
C.1. Proof of internal accuracy check . . . . .	166
C.2. Multi-orbital Hamiltonian representation . . . . .	168
Appendix. References . . . . .	171
Appendix. Acknowledgements . . . . .	185
Appendix. Curriculum Vitae . . . . .	186

## Notation

Discrete Fourier transform	$f(k) = \sum_r e^{ik \cdot r} f(r)$
Inverse discrete Fourier transform	$f(r) = \frac{1}{N} \sum_k e^{-ik \cdot r} f(k)$
Heaviside function	$\theta(t) = \begin{cases} 1 & t \geq 0 \\ 0 & t < 0 \end{cases}$
Partial derivative with respect to $t$	$\partial_t = \frac{\partial}{\partial t}$
(Continuous) Fourier transformation	$\mathcal{F}$
Schwartz function space over $\mathbb{R}$	$S(\mathbb{R})$
Dirac delta distribution	$\delta(\cdot)$
retarded Green's function	$G^R$
imaginary time Green's function	$G(\tau)$
Matsubara Green's function	$G(i\omega_n)$
identity mapping	$\mathbb{I}$
density of states	$\rho(\cdot)$
anti-commutator of $A$ and $B$	$\{A, B\} = AB + BA$
commutator of $A$ and $B$	$[A, B] = AB - BA$
real part	$\text{Re}$
imaginary part	$\text{Im}$
imaginary time ordering operator	$T_\tau$
space-imaginary time pair	$(1) = (r_1, \tau_1)$
temperature	$T$
Boltzmann constant	$k_B$
inverse temperature	$\tilde{\beta} = \frac{1}{k_B T}$
Matsubara frequency	$\omega_n = \frac{(2n+1)\pi}{\tilde{\beta}}$
overline summation/integration convention	$f_{\bar{\alpha}, \bar{\sigma}}(\bar{1}) g_{\bar{\alpha}, \bar{\sigma}}(\bar{1}) = \int_0^{\tilde{\beta}} d\tau \sum_{r, \alpha, \sigma} f_{\alpha, \sigma}(r, \tau) g_{\alpha, \sigma}(r, \tau)$
self energy	$\Sigma$
spin/charge two-particle irreducible vertex	$\Gamma^{sp/ch}$
spin/charge susceptibility	$\chi^{sp/ch}$
particle-hole bubble	$\chi^0$

---

Hamiltonian	$H$
chemical potential	$\mu$
particle number operator	$\hat{N}$
Fermi-Dirac distribution function	$f_{FD}$
Spin Pauli matrices	$\sigma_x, \sigma_y, \sigma_z$

## CHAPTER 1

# Introduction

Condensed matter physics reveals a plethora of phases of matter and phenomena as a consequence of the large particle number in the systems studied. In order to understand the mechanisms that drive the rich physics of solids it is important to identify the energy scales and degrees of freedom that play a role.

In this thesis we want to concentrate on the special case where the electron-electron interaction plays an important role for describing the electronic properties of the material. It is common to call such systems *correlated electronic systems* because the expectation value of an operator  $A(1)B(2)$ , where  $A$  acts on particle 1 and  $B$  acts on particle 2, does not decompose into a product of expectation values of  $A(1)$  and  $B(2)$ . From a physical point of view this concept can be seen as a fingerprint of collective emergent behavior of electrons.

### 1.1. Non-interacting vs. interacting electrons in a solid

We know from elementary quantum mechanics that the energy spectrum of a free electron in space is given by all non-negative numbers and that the eigenfunctions are given by plane waves  $\{e^{ik \cdot x}\}_{k \in \mathbb{R}^n}$  where  $k$  is the wave vector quantum number. As a consequence we see that the eigen states describe a particle delocalized in space. Keeping this in mind we start now to move closer to our actual goal of describing electrons in a solid.

Experience tells us that many materials tend to form crystalline structures at sufficiently low temperatures<sup>1</sup>. Furthermore, a comparison of length and energy scales tells us that the Coulomb interaction will be the only dominant interaction to consider in this quantum mechanical system.

Within a crystal we find positively charged atomic cores and electrons which together constitute the atomic ingredients of the crystal. In order to decouple the electronic from the core degrees of freedom one traditionally makes use of the Born-Oppenheimer approximation. Still, we are left with a large number of the order  $10^{23}$  electrons that are coupled to each other by the long-range Coulomb repulsion.

A central topic in theoretical solid state theory is therefore the derivation of effective models that are simple enough to be treated analytically or numerically while at the same time containing the essential physics of the material.

In chap. 2 we present the famous Density Function Theory (DFT) which is in principle exact for ground state properties, where the electron equations of motion are decoupled from each other and replaced by free electrons in an effective self-consistent potential that is created from the atomic cores and all other electrons. The Bloch theorem gives us consequently a band structure of the energy spectrum, where the crystal momentum  $k$  is a good quantum number and the eigen states are so-called *Bloch waves*. A common point with the example of the free particle is that the electrons are again delocalized in space but there are many differences regarding the detailed form of the eigen states and the energy spectrum.

---

<sup>1</sup>A rigorous understanding of this observation is still not known and a famous problem in mathematical physics [1].

## 1.1. NON-INTERACTING VS. INTERACTING

---

In many case studies of real materials DFT has proven to be very successful in the description of material properties which supports the idea that in such materials the many-body character of the electrons is subdued because of efficient screening effects. Most importantly, those properties are calculated from *ab-initio* which signifies that the theory is based on fundamental principles, it has no adjustable parameters and takes only the crystal structure and chemical composition as input.

On the other hand, we find materials where the Kohn-Sham electronic structure in DFT is not able to properly describe the observed electronic structure. Among the class of such materials we find certain transition metal oxides which are predicted to be metals while experimental studies find them to be insulators. This is a very distinct discrepancy between DFT and experiment but one also finds examples where the predicted effective electron mass is underestimated or certain electronic states at lower binding energies are not resolved by the theory.

The previously mentioned features can be directly connected to electronic correlation effects where f.i. the enhanced effective electron mass is due to electron-electron scattering processes.

In order to take those many-body effects into account we restrict the Hilbert space to the orbital manifold where the electronic correlation effects are strongest. In the case of the previously mentioned transition metal oxides we are referring to the localized transition metal *d*-orbitals.

The famous Hubbard model that is described in chap. 3 will serve us as the effective model for describing electronic correlation effects. This lattice model where the Coulomb repulsion is approximated to be an effective local repulsive term can be motivated from the strong localization of the orbitals and the effective electronic screening. By means of the projective Wannier function method and the constrained Random Phase Approximation (cRPA) we are able to retain the *ab-initio* character of our material study. Both methods are introduced in chap. 2, 3 and take the DFT result as input to construct the Hubbard model for the correlated electronic states.

Albeit its simple shape in the single-band case a general solution of the Hubbard model is still unknown except for some limiting cases. For this reason we have to rely on approximative many-body schemes that are at the core of this thesis.

Those methods are often formulated in terms of Green's functions that are introduced in chap. 4. This formulation allows to express the effect of electron-electron interaction in terms of the so-called *self-energy* which is responsible for the effective mass increase and the finite quasi-particle lifetime of Bloch wave excitations. In the limit of very strong electron-electron coupling the Hubbard model predicts a transition from the delocalized Bloch wave picture to the multiplet atomic orbitals picture.

Chapter 5 is devoted to the explicit derivation and discussion of the Two-Particle Self-Consistent approach (TPSC) which is the many-body approximation that we are using throughout this work.

This method was originally developed by Y.M. Vilk and A.-M.S. Tremblay for the single-band Hubbard model. The derivation is expressed in the language of functional derivatives and follows the Kadanoff-Baym approach for deriving so-called *conserving approximations*.

We discuss all those concepts in detail and present a multi-site and multi-orbital version of TPSC, where in the latter additional interaction terms such as the Hund's coupling enter the Hamiltonian.

In contrast to the single-band TPSC we will encounter some pitfalls in the multi-orbital

version that we can circumvent by applying additional approximations.

The fundamental idea of all TPSC schemes is to approximate the interaction vertex to be an effective momentum- and frequency independent vertex function. By enforcing the Pauli principle one is able to determine the effective vertex function from so-called local spin and charge sum rules. This leads to a self-energy that is both frequency- and momentum-dependent due to the coupling of spin and charge fluctuations to the electronic propagator.

In order to benchmark this novel approach we devote chap. 6 to an extensive comparison of TPSC and the established dynamical mean field theory (DMFT). DMFT approximates the self-energy to be local but dynamical, which becomes exact for infinite lattice connectivity.

In chap. 7 we present a real material study of LiFeAs and compare the results also to DMFT while the last chapter 8 is devoted to a summary and an outlook regarding possible future extensions of the multi-orbital TPSC method.

## 1.2. Two classes of unconventional superconductors

In this thesis we are studying representatives of two classes of unconventional superconductors, namely the organic charge transfer salts  $\kappa$ -(ET)<sub>2</sub>X (chap. 5) and ironpnictide superconductors, more specifically LiFeAs (chap. 7).

Although those materials have not much in common when it comes to chemical composition or crystal structure one finds an interesting similarity in the phase diagrams (see fig. 1.1). Most notably, there is a proximity between a spin ordered phase and

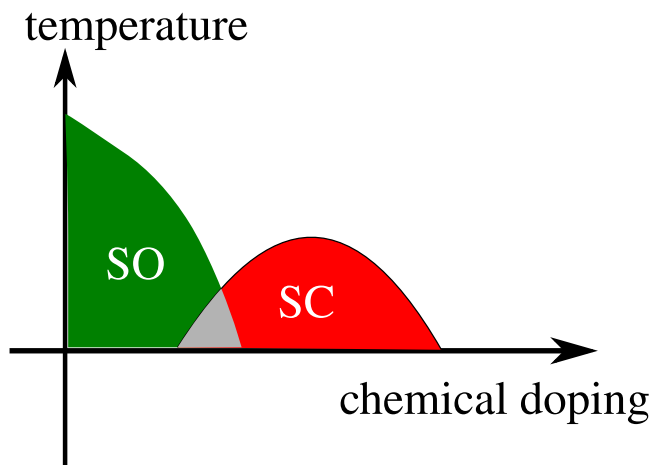


FIGURE 1.1. Schematic phase diagram of Cuprate, organic and ironpnictide superconductors [2–4]. The common point of all three material classes is the vicinity of the superconducting phase (SC) to some kind of spin ordered phase (SO). Notice that the gray shaded region is different for all three material families, f.i. in the cuprate superconductors there is no overlap of superconductivity and spin order [3]. Moreover, there are additional features that appear in different classes like Pseudogap phases or structural transitions.

the superconducting phase in organic  $\kappa$ -(ET)<sub>2</sub>X, ironpnictide and cuprate superconductors [2–5]. Since TPSC takes low energy spin and charge fluctuations into account we assume that it is a suitable method to treat the low temperature physics of all those three materials to some extent as will be discussed in chap. 5 and 7.

In LiFeAs we want to study the discrepancy between the energy spectrum obtained from Kohn-Sham DFT and the one measured in experiment and we want to find out in how far TPSC can reconcile those by means of non-local self-energy effects. The key features that discriminate the energy spectrum of DFT from experiment are the sizes of the electron and hole pockets on the Fermi surface and the incoherent flower-like spectral weight around  $\Gamma$ . The first feature cannot be explained in terms of a local self-energy because in order to reconcile DFT with experiment one needs a shrinking of both the electron and the hole pockets which means that the self-energy shifts have to be different at the different positions in the Brillouin zone, i.e. momentum-dependent. Indeed, published DMFT results [6–8] were not able to reproduce the two above mentioned experimental features and more advanced non-local many-body techniques such as GW+DMFT were suggested as possible resort [9, 10]. The advantage of TPSC in comparison to GW+DMFT consists of its cheap numerical implementation and the inclusion of spin fluctuations while it has the disadvantage of neglecting high-energy charge fluctuations and the exact summation of local diagrams that is included in DMFT.

Furthermore, we want to compute quasi-particle lifetimes and compare to the ones obtained from experiment. This is especially useful since there is a debate on whether those lifetimes are non-local or orbital-dependent objects [11, 12].

Our objective in the study of the  $\kappa$ -(ET)<sub>2</sub>X superconductors is twofold: There are two prominent models for these materials, namely the molecule model and the simpler dimer model. We want to study in how far those models are appropriate to obtain superconducting critical temperatures and what kind of superconducting gap symmetries are stabilized. While the first point is of general interest regarding material design and understanding the superconducting pairing mechanism, the second point is important to resolve the ongoing controversy on which superconducting symmetry is actually realized in those materials.

## Density Functional Theory

This chapter is based on the presentation of Density Functional Theory in Ref. [13–16]. Structural and electronic properties of crystalline materials are a key interest not only in many fields of solid state physics but also in quantum chemistry and material sciences in general. From a comparison of the energy scales and range of the fundamental interactions we can clearly state that the electrodynamic interaction between the constituent electrons and nuclei govern the physics of such quantum systems<sup>1</sup>. Thus, we can immediately write down the Hamiltonian of the system which is given by the sum of the respective kinetic energy and Coulomb interaction terms,

$$\begin{aligned}
 H = & \underbrace{\sum_{i=1}^{N_e} \frac{p_i^2}{2m} + \frac{1}{2} \sum_{\substack{i,j=1 \\ i \neq j}}^{N_e} V_{e,e}(x_i - x_j)}_{:=H_{e,e}} + \underbrace{\sum_{i=1}^{N_I} \frac{P_i^2}{2M_i} + \frac{1}{2} \sum_{\substack{i,j=1 \\ i \neq j}}^{N_k} V_{Ion}(X_i - X_j)}_{:=H_{I,I}} \\
 (2.1) \quad & + \underbrace{\sum_{i=1}^{N_e} \sum_{j=1}^{N_I} V_{e,Ion}(x_i - X_j)}_{:=H_{e,I}},
 \end{aligned}$$

where  $N_e$  is the number of electrons with mass  $m$  and  $N_I$  the number of ions with masses  $M_i$  in the system. The momentum operator  $p_i$  acts on the  $i$ -th electron while  $V_{e,e}$  describes the Coulomb repulsion between electrons  $i, j$  at position  $x_i$  and  $x_j$  respectively. Similarly, the momentum operator  $P_i$  acts on the  $i$ -th nucleus while  $V_{Ion}$  describes the nucleus-nucleus interaction between ions  $i, j$  at position  $X_i$  and  $X_j$  respectively. Finally, the potential  $V_{e,Ion}$  contains the electron-nucleus interaction at electron position  $x_i$  and nucleus position  $X_j$  with  $i = 1, \dots, N_e$  and  $j = 1, \dots, N_I$ .

The corresponding Schrödinger equation to the Hamilton operator  $H$  is a coupled partial differential equation in  $\sim 10^{23}$  coordinates due to the large particle number in macroscopic crystals. For this reason there is no way so far to solve this problem analytically or numerically exact in the general case. Obviously, the numerical treatment would be of limited use due to the memory constraints that arise from calculations in such large Hilbert spaces.

Therefore, the only way to obtain properties from the fundamental laws of quantum mechanics without adjustable parameters is by means of approximations.

One of the most famous and successful method that is able to obtain such *ab-initio* computed material properties is the combination of the Born-Oppenheimer approximation [17] and Density Functional Theory (DFT) which is based on the seminal theorems by Hohenberg and Kohn [18].

While this methodology is related to the Thomas-Fermi theory [19, 20] the DFT framework possesses much stronger predictive power [19, 21].

During the last decades a lot of effort has been spent to further improve on the method

---

<sup>1</sup>We also neglect relativistic effects since we are dealing with crystals composed of light atoms but we will discuss possible effects of spin-orbit coupling later for the specific materials.

by developing new energy functionals [22–25], inclusion of Hubbard correlations [26] or by extending to time-dependent DFT [27]. Note that this short list by far too short to comprise the plethora of developments on this vast field of theoretical physics and chemistry. For more detailed information on the history and recent progressions of DFT we refer to Ref. [13, 14, 16] and the references therein.

In this chapter we will only outline the principle of the DFT scheme that we will use for our real materials calculations in sec. 5.5 and chap. 7.

### 2.1. Fundamentals of Density Functional Theory

The first approximation that we apply to simplify the many-body problem with Hamiltonian  $H$  given in eq. (2.1) is the so-called Born-Oppenheimer approximation. It states that due to large difference between electron mass  $m$  and ion masses  $M_i$  one can decouple the electron dynamics from the nuclei dynamics, i.e. from the electron point of view the nuclei move so slow that they assume fixed positions in real space. Thus, the full Hamiltonian splits into two parts where the electronic part is given by

$$(2.2) \quad H_e = \sum_{i=1}^{N_e} \frac{p_i^2}{2m} + \sum_{\substack{i,j=1 \\ i \neq j}}^{N_e} V_{e,e}(x_i - x_j) + \sum_{i=1}^{N_e} \sum_{j=1}^{N_I} V_{e,Ion}(x_i - R_j) + \sum_{\substack{i,j=1 \\ i \neq j}}^{N_k} V_{Ion}(R_i - R_j),$$

where  $R_j$  is the equilibrium position of the nucleus  $j$ . Note that the nucleus position operator  $X_j$  is reduced to a mere parameter  $R_j$  and thus the overall effect from the ions is condensed into an effective local external potential

$$(2.3) \quad V_{ext} = \sum_{i=1}^{N_e} \sum_{j=1}^{N_I} V_{e,Ion}(x_i - R_j) + \sum_{\substack{i,j=1 \\ i \neq j}}^{N_k} V_{Ion}(R_i - R_j).$$

In our case the positions of the nuclei are given from experimental measurements but in principle one could also obtain those positions by minimizing the total energy of the system with the atomic positions as variational parameters.

We present now the two fundamental theorems by Hohenberg and Kohn which are needed for the next step in DFT.

**THEOREM 2.1.1.** *Given two external potentials  $V_{ext,1}$ ,  $V_{ext,2}$  (see eq. (2.3)) that enter the electronic Hamiltonian  $H_e$  in eq. (2.2) and produce different ground states  $\Psi_1$ ,  $\Psi_2$  respectively. Then the densities  $n_1(x)$ ,  $n_2(x)$  that correspond to those ground states are also different, where the single-particle densities  $n_1(x)$ ,  $n_2(x)$  are defined by*

$$(2.4) \quad n_{1,2}(x) := N_e \sum_{\sigma_i} \int \Psi_{1,2}^*(x, x_2, \dots, x_{N_e}) \Psi_{1,2}(x, x_2, \dots, x_{N_e}) dx_2 \cdots dx_{N_e}.$$

*In the case of non-degenerate ground state one can establish a bijection between external potentials and the corresponding ground state of the electronic Hamiltonian.*

**PROOF.** For a rigorous and formal proof of this result we refer to Ref. [28].  $\square$

Note that this theorem proves only the *existence* of a bijective map – every one-to-one map can be made bijective by restricting the codomain to the image of the map – between a not specified set of external potentials and a corresponding set of ground state densities but this is already enough to conclude that the ground state expectation value  $\langle \Psi | \cdot | \Psi \rangle$  of any observable  $O$  is a unique functional of the ground state density  $n(x)$ , i.e.

$$(2.5) \quad \langle \Psi | O | \Psi \rangle \equiv O[n(x)].$$

The second important theorem that is known as the *Hohenberg-Kohn variational principle* tells us how to determine the ground state energy.

**THEOREM 2.1.2.** *For a given external potential  $V_{ext}$  one determines the ground state energy of the Hamiltonian  $H_e$  by*

$$(2.6) \quad E[V_{ext}] = \min_{n(x)} \left\{ F_{HK}[n(x)] + \int n(x)V_{ext}(x)dx \right\},$$

where  $F_{HK}[n(x)]$  is the universal(!) so-called *Hohenberg-Kohn functional*.

**PROOF.** See [15] Thm. 37.4. □

There are a few mathematical issues about this theorem which have their roots in the problems that we already discussed in the context of the existence theorem 2.1.1: Neither the set of ground state densities nor the corresponding set of external potentials are known explicitly and therefore we have no explicit form of the Hohenberg-Kohn functional.

The importance and beauty of the theorems is less the usefulness in practical calculations but more the conceptual value they have. Namely, the theorems imply that ground state expectation values of the many-electron system can be calculated from the single-particle density  $n(x)$  instead of the direct computation by means of integrals over  $\sim 10^{23}$ -dimensional coordinate space.

Moreover, it is the universality of the Hohenberg-Kohn functional  $F_{KH}[n(x)]$  which is the same for all many-electron system. The two theorems also provide a foundation for approximations that do not aim at approximating the wave functions, e.g. variational Monte Carlo methods (see [29] for a general review), or the Hamilton operator itself, e.g. perturbation theory (see f.i. [30]), but on approximating the density functionals such as in Thomas-Fermi theory [19].

Finally, we point out that equation (2.6) also tells us that the ground state density is the minimum of the total energy functional

$$(2.7) \quad E[V_{ext}, n] := F_{HK}[n(x)] + \int n(x)V_{ext}(x)dx,$$

which leads to an Euler-Lagrange equation<sup>2</sup> where the chemical potential appears as a Lagrange multiplier to ensure the right particle number.

Notice that all the above stated relations of observables and the ground state density are only valid for the ground state. This means that we can only rewrite ground state expectation values as density functionals but the theorem makes no statement on excited states. In order to access the excitation spectrum within DFT one can use an analogue of the Hohenberg-Kohn theorem which is the so-called Runge-Gross theorem [31] in combination with the scheme presented in [27].

From the conceptual foundations of DFT we move now to a formulation that allows for real material calculations.

## 2.2. Kohn-Sham Density Functional Theory

The following DFT scheme is due to the work of Kohn and Sham [32]. The universality of the Hohenberg-Kohn functional  $F_{HK}[n(x)]$  also applies in the limit of vanishing interaction<sup>3</sup> and yields the functional  $F_{HK}[n(x)] \rightarrow T_0[n]$ , where  $T_0[n]$  denotes the non-interacting limit of the Hohenberg-Kohn functional.

The idea of Kohn and Sham was to reformulate the problem of interacting electrons by

<sup>2</sup>At this stage one needs to assume further regularity properties of the functionals.

<sup>3</sup>This is the limit of a non-interacting electron gas.

## 2.2. KOHN-SHAM DENSITY FUNCTIONAL THEORY

---

separating the Hohenberg-Kohn functional into kinetic energy, Hartree and correlation and exchange functionals,

$$\begin{aligned}
 (2.8) \quad F_{HK}[n(x)] &= T[n(x)] + V_{e,e}[n(x)] \\
 (2.9) \quad &= T_0[n(x)] + V_H[n(x)] + \underbrace{T[n(x)] - T_0[n(x)]}_{=:V_C[n(x)]} + \underbrace{V_{e,e}[n(x)] - V_H[n(x)]}_{=:V_X[n(x)]} \\
 (2.10) \quad &=: T_0[n(x)] + V_H[n(x)] + V_{XC}[n(x)],
 \end{aligned}$$

where  $T[n(x)]$ ,  $V_{e,e}[n(x)]$  are the exact kinetic and electron-electron interaction energy functionals respectively and  $V_H$  is the Hartree functional given by

$$(2.11) \quad V_H[n(x)] := \frac{e^2}{8\pi\epsilon_0} \int \int \frac{n(x')n(x)}{|x-x'|} dx' dx.$$

The functional  $V_C[n(x)]$  is called *correlation functional* and  $V_X[n(x)]$  is the *exchange functional*. More details on those two potentials will be provided in the next sections.

The total energy functional  $E[V_{ext}, n]$  (see eq. (2.7)) takes the form

$$(2.12) \quad E[V_{ext}, n] := T_0[n(x)] + V_H[n(x)] + V_{XC}[n(x)] + \int n(x)V_{ext}(x)dx.$$

So far, the previously described steps merely allowed us to separate the complicated total energy functional into tractable parts and an unknown exchange-correlation functional which accounts for the complicated many-body effects which go beyond the Hartree description.

The Kohn-Sham ansatz which results in an enormous simplification is the idea to assume that the total energy functional  $E[V_{ext}, n]$  in eq. (2.12) describes a non-interacting electron gas in an external potential that is due to exchange-correlation functional for the same density and the surrounding nuclei<sup>4</sup>.

This interpretation allows us write down the corresponding Hamiltonian of the electron gas,

$$(2.13) \quad H_{KS} := T_0 + \hat{V}_H + \hat{V}_{XC} + V_{ext}$$

$$(2.14) \quad = \sum_{i=1}^{N_e} \frac{p_i^2}{2m} + \frac{e^2}{4\pi\epsilon_0} \int \frac{n(x)}{|x-x'|} dx + \hat{V}_{XC} + V_{ext},$$

that is coined the *Kohn-Sham Hamiltonian*. The exchange-correlation potential is obtained by functional differentiation<sup>5</sup>,

$$(2.15) \quad \hat{V}_{XC} = \frac{\delta V_{XC}[n(x)]}{\delta n(x)}.$$

Thus, the Kohn-Sham ansatz reduces the second Hohenberg-Kohn theorem to the determination of the lowest  $N_e$  eigenfunctions  $\{\phi_i\}_{i \in \mathbb{N}}$  of the Kohn-Sham Hamiltonian  $H_{KS}$ . From the eigenfunctions  $\phi_1, \dots, \phi_{N_e}$  we can determine the ground state density

---

<sup>4</sup>This assumption leads to the question whether and how one can find such a suitable non-interacting system with the same ground state density as the ground state density of any interacting system. There are only a few rigorous statements on this question but due to the large success of Kohn-Sham DFT we assume that such a connection between the two systems is given. For a more detailed discussion we refer to [13] and the references therein.

<sup>5</sup>Differentiability of the exchange-correlation functional is assumed to be given at least for our practical purposes. A more detailed discussion of this and related mathematical issues can be found in [13, 15] and the references within.

$n(x)$  via

$$(2.16) \quad n(x) = \sum_{i=1}^{N_e} \phi_i^*(x) \phi_i(x)$$

because we have a system of non-interacting electrons in an effective potential.

This reduction of the coupled many-body differential equations to an effective single-particle Schrödinger-like equation

$$(2.17) \quad H_{KS} \phi_i = \epsilon_i \phi_i$$

that is called *Kohn-Sham equation* is a enormous simplification but one has to be cautious about the following point.

The Kohn-Sham eigenenergies and eigenfunctions allow *a priori* no physical interpretation as electron wave functions and single-particle energies. The only formally correct information that one can deduce from them is the ground state density and ground state energy.

Nevertheless, one can use the Slater determinant  $\Phi$  constructed from the first  $N_e$  eigenfunctions  $\phi_1, \dots, \phi_{N_e}$  of the Kohn-Sham Hamiltonian as an approximation to the true ground state wave functions  $\Psi$ . The justification of this approach is due to the fact that in the limit of no electron-electron interaction both many-body wave functions  $\Phi$  and  $\Psi$  will coincide.

Moreover, one can also use the Kohn-Sham eigenenergies as approximations to the true ionization potentials which is motivated in Ref. [33–35].

We further notice that the Kohn-Sham equation is a self-consistency equation since the external potential  $\hat{V}_H + \hat{V}_{XC} + V_{ext}$  that appears in the Kohn-Sham Hamiltonian (see eq. (2.14)) is a functional of the electron density  $n(x)$  which itself directly depends on the Kohn-Sham eigenfunctions  $\phi_1, \dots, \phi_{N_e}$ .

### 2.3. Exchange-correlation potential

We focus now our attention on the Kohn-Sham Hamiltonian and observe that all terms are known except for the exchange-correlation potential. This is the next step where approximations are needed in order to solve the many-body problem within the Kohn-Sham DFT framework.

The possibly simplest non-trivial ansatz that one can think of is

$$(2.18) \quad V_{XC} = \int n(x) \epsilon_{XC}(n(x)) dx,$$

which means that the exchange correlation potential is assumed to depend only on the local electron density [18]. Therefore, such approximations are called *local density approximations* (LDA).

More often, the LDAs are used synonymous with the specific LDA, where the exchange-correlation energy density  $\epsilon_{XC}(n(x)) = \epsilon_{XC}^{Hom}(n(x))$  is the one of the homogeneous electron gas with electron density  $n(x)$ .

The exchange energy density  $\epsilon_X$  for the homogenous electron gas in a cubic box of volume  $V$  can be calculated analytically [36] and is given by

$$(2.19) \quad \epsilon_X(n) = -\frac{e^2}{8\pi\epsilon_0 V} \sum_{i,j=1}^{\infty} \theta(\epsilon_F - \epsilon_i) \theta(\epsilon_F - \epsilon_j) \int \int \frac{\phi_i^*(x) \phi_j(x) \phi_j^*(x') \phi_i(x')}{|x - x'|} dx' dx$$

$$(2.20) \quad = -\frac{3(3\pi^2)^{1/3} e^2}{16\pi^2 \epsilon_0} n^{4/3},$$

where  $\epsilon_F$  is the Fermi energy.

Combining the LDA ansatz equation (2.18) with the exchange energy density result for the homogeneous electron gas we arrive at the exchange energy

$$(2.21) \quad V_X = -\frac{3(3\pi^2)^{1/3}e^2}{16\pi^2\epsilon_0} \int n(x)^{4/3} dx.$$

The physical interpretation to this reduction of the total energy is the following: If we neglect the quantum statistics of the electrons the interaction energy of the electron gas would be given by the Hartree term in eq. (2.11). But due to the Pauli principle we get an additional term in the two-body operator expectation value  $\langle \Phi | V_{e,e} | \Phi \rangle$  that has a minus sign due to the anti-symmetry of the electron wave function  $|\Phi\rangle$ . Thus, the electrons feel a kind of ‘‘Pauli repulsion’’ which screens the Coulomb repulsive potential.

In contrast, there is no analytic expression for the correlation potential  $V_C$  but only approximate formulas in special density limits (see discussion in [13]).

On the other hand, one can revert to numerically exact Quantum Monte Carlo data [37] and interpolation schemes that respects the above described limiting cases formulae (see discussion in [13]).

One can expect the LDA approximation to give accurate ground state properties if the system considered is close to a homogeneous electron gas such as simple metals. The electrons in many classes of materials cannot be regarded as close relatives of the homogeneous electron gas, where the electronic density varies only slowly as a function of position, and for this reason further improvements on top of the LDA were developed, e.g. the Generalized Gradient Approximation (GGA) [38–40]. Nevertheless, LDA and GGA can yield sufficiently accurate results in the case of crystals due to error cancellation effects between the long-range underestimated exchange and overestimated correlation potentials [13].

## 2.4. Many-body extensions to DFT

The Kohn-Sham DFT is obviously a mean-field-like theory where the full many-body system with electron-electron interaction  $V_{e,e}$  is mapped onto an effective single-particle problem with self-consistently determined exchange-correlation potential  $V_{XC}$  (see fig. 2.1). This description allows for the application of the Bloch theorem which roughly speaking states that electrons are delocalized over the whole crystal and that the energy spectrum of the Kohn-Sham Hamiltonian  $H_{KS}$  consists of energybands  $\epsilon_j(k)$ , where  $j$  is a band label and  $k$  is the crystal momentum. Thus, the original many-body interacting electron system is mapped onto an effective single-electron system with good quantum numbers  $n$ ,  $k$ .

For practical reasons one expands the eigenfunctions  $\{\phi_i\}_{i \in \mathbb{N}}$  of the Kohn-Sham Hamiltonian  $H_{KS}$  in terms of spherical harmonics and radial functions at positions close to a nucleus while the eigenfunctions are expanded in terms of plane waves at positions away from the nuclei. Such a position dependent expansion is more efficient since one can expect from a semi-classical picture that an electron close to a nucleus will feel a central-potential-like attraction while electrons further away will be quasi-free due to screening effects from the other electrons.

In this thesis we are mainly interested in low temperature properties and excitations of many-electron systems and therefore we focus on the energy spectrum in a small energy window around the Fermi energy  $\epsilon_F$ . Many classes of materials exhibit valence states that have mostly  $s$ - and  $p$ -orbital character. Those orbitals are more extended in space than  $d$ - and  $f$ -orbitals which results in efficient screening of the electron-electron interaction (compare to [41, 42]). Such systems are perfect candidates for an

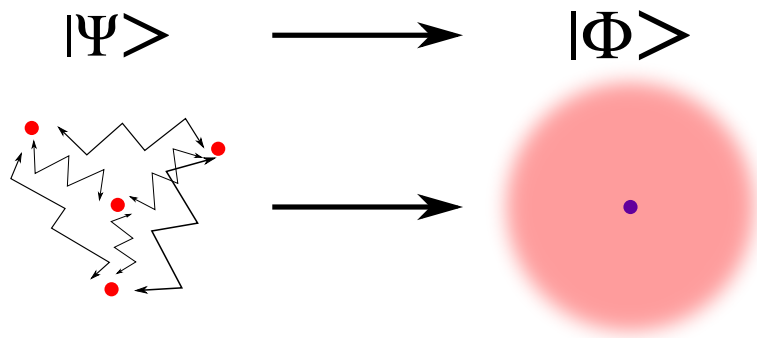


FIGURE 2.1. Figurative representation of the mean-field idea. Starting point is an interacting system of particles (red circles on the left-hand side) which are described by a many-body state  $|\Psi\rangle$ . The mean-field approach describes the effect of the many-body interaction in terms of an effective single-particle potential (blurred red circle on the right-hand side) acting on each particle. The resulting many-body state  $|\Phi\rangle$  is constructed as a Slater determinant formed by the single-particle states. In Kohn-Sham DFT the effective non-interacting particles are not the same electrons as from the interacting problem.

independent-particle treatment and this partly explains the large successes of Kohn-Sham DFT or mean-field theories. In those cases one can even take the Kohn-Sham energy spectrum and eigen states as good approximations.

On the other hand, we often encounter systems with partially filled  $d$ - and  $f$ -orbitals where the Kohn-Sham DFT energy spectrum is not even qualitatively close to the experimental observations, e.g. Mott insulators in the family of transition metal oxides [43, 44] or heavy-fermion materials in the family of Lanthanides and Actinides [45, 46].

Those examples are by definition [43, 47] true many-body effects that go beyond an independent particle description. Nevertheless, attempts to remedy this deficiency of the single-particle picture consist of introducing a local repulsion on those localized  $d$ - or  $f$ -orbitals. A common method is the so-called LDA+ $U$  approach [26], where  $U$  is the on-site Coulomb repulsion. Despite the fact that the  $U$ -term in the total energy functional can open a band gap in the Kohn-Sham energy spectrum that is of the order of  $U$  and gives rise to spin and orbital order as in the Mott insulating state, there are important differences on the mechanism of the gap opening [44, 47]; more specifically, the LDA+ $U$  approach remains in the single-particle picture while the Mott insulating state cannot be described therein.

For this reason we will need a many-body method on top of DFT that can account for the electron-electron interaction effects that go beyond the single-particle picture<sup>6</sup>. We will call those electronic *correlation* effects which should not be confused with the notion of correlation within the DFT framework. We use the expression of correlations in the broad sense that the behavior of the electrons is not independent of each other

<sup>6</sup>Obviously, this is not the only possible approach to tackle the many-body problem but in case where we see from experiment that the DFT predicted results are close to the measured results it can be a promising approach to correct the DFT results by including electron-electron interaction effects on top of DFT. This can be especially helpful when we observe that the difference between observed and calculated properties are “typical” many-body effects (see sec. 4.9) and not due to other sources such as couplings to the lattice, relativistic effects etc. Nevertheless, there are many different other approaches possible that do not rely on combining two methods but they also have their weak points. An interesting and extended discussion of those points can be found in Ref. [48]

but they influence each other. For example, two-body expectation values of operators  $A_1 B_2$ , where  $A_1$  acts on particle 1 and  $B_2$  acts on particle 2 will not factorize, i.e.

$$(2.22) \quad \langle A_1 B_2 \rangle - \langle A_1 \rangle \langle B_2 \rangle \neq 0.$$

Since many-body approximations rely on mathematical tools that are very involved one is usually forced to solve the interacting electron problem in terms of a model system instead of solving the Schrödinger equation of the full electronic Hamiltonian in eq. (2.2) directly. This step is called *downfolding* since the all-electron system is mapped down onto a specific low-energy Hamiltonian of correlated electrons [49–52]. Formally, downfolding is based on the idea of the renormalization group approach [53–55] where high-energy degrees of freedom are successively integrated out.

### 2.5. Maximally localized Wannier functions

As discussed in the previous section we need to construct a simple model for the correlated valence states of the Kohn-Sham DFT. A simple and successful model that is assumed to capture important effects of correlated electrons in partially filled *d*- and *f*-orbitals is the so-called *Hubbard model* that is described in more detail in chap. 3. This model is a lattice model where electrons are not moving in continuous space anymore but are constrained to localized orbitals that are centered at discrete lattice sites, where they can “hop” to different sites and feel a local repulsion when they happen to be on the same position.

In order to map the Kohn-Sham states  $\phi_{\alpha,k}$  to electronic states on the lattice we need a new localized basis representation. A possible candidate is the representation in terms of so-called *maximally localized Wannier functions*

$$(2.23) \quad w_{\alpha,r}(x) = \frac{V}{(2\pi)^3} \int_{BZ} e^{-ik \cdot r} \sum_{\alpha} U_{\alpha\beta}(k) \phi_{\alpha,k}(x) dk,$$

where  $r$  is a unit cell position and  $U_{\alpha\beta}(k)$  is a unitary transformation in the restricted orbital space that is chosen such that spread of the Wannier functions

$$(2.24) \quad \sum_{\beta} \langle w_{\beta,r} | x^2 | w_{\beta,r} \rangle - \langle w_{\beta,r} | x | w_{\beta,r} \rangle^2$$

is minimal. Notice that the sum in eq. (2.23) only runs over the bands that belong to the correlated orbitals. The details on how to determine the momentum-dependent transformations  $U_{\alpha\beta}(k)$  are explained in Refs. [56–59].

We consider the Hamiltonian  $H(k)$  expressed in the basis of Kohn-Sham orbitals,

$$(2.25) \quad H_{\alpha\beta}(k) = \epsilon_{\alpha}(k) \delta_{\alpha,\beta},$$

where  $\alpha, \beta$  are the indices of the bands close to the Fermi energy that have the most overlap with the localized orbitals that we consider as correlated. By means of the transformation  $U_{\alpha\beta}(k)$  we express  $H(k)$  in the basis of the maximally localized Wannier functions,

$$(2.26) \quad \tilde{H}(k) = U^{\dagger}(k) H(k) U(k),$$

and a simple Fourier transformation gives us the real space representation

$$(2.27) \quad H(r_i - r_j) = \frac{1}{N} \sum_k e^{-ik \cdot (r_i - r_j)} \tilde{H}(k),$$

where  $N$  is the number of unit cells. The real space Hamiltonian operator  $H(r)$  leads to the full lattice Hamiltonian of the correlated electrons  $H$  that is written in second

quantization as

$$(2.28) \quad H = \sum_{\alpha, \beta, i, j, \sigma} t_{\alpha, \beta}^{r_i - r_j} c_{\alpha, \sigma}^\dagger(r_i) c_{\beta, \sigma}(r_j),$$

where the matrix elements of  $H(r)$  are denoted by the hopping term  $t$  in order to emphasize that the contribution has the shape of a single-particle term such as the kinetic energy. The operator  $c_{\alpha, \sigma}(r_i)$  destroys an electron with spin  $\sigma$  at unit cell position  $r_i$  and Wannier orbital  $\alpha$  while the adjoint operator  $c_{\alpha, \sigma}^\dagger(r_i)$  creates an electron with spin  $\sigma$  at unit cell position  $r_i$  and Wannier orbital  $\alpha$ .

The lattice model contains no explicit information on the shape of the Wannier orbitals but only implicitly via the hopping term  $t$  which is an enormous simplification for many-body techniques.

Notice that the Wannier projected operator  $H$  in eq. (2.28) still incorporates some part of the full electron-electron interaction, namely in terms of a homogeneous electron gas (LDA) or beyond (GGA etc.). In that regard we have to keep in mind that the additional interaction correction that we are introducing to the correlated orbitals should not contain the contributions that are already present in DFT. Otherwise we are committing the so-called *double-counting* error. There is no general solution to the double counting problem due to the non-linear nature of the commonly used exchange-correlation potentials, the non-diagrammatic formulation of DFT and the self-consistency which makes it hard to assess the portion and orbital origin of exchange and correlation effects that entered the correlated orbitals [60] even though many different schemes – based on different assumptions or physical intuition – were proposed (see discussion and references in [52]).

For the moment we will assume that the Hamiltonian  $H$  in eq. (2.28) describes the non-interacting electrons in an effective potential as generated by the downfolding procedure and later come back to the double-counting problem.

Thus, the Hamiltonian  $H$  in eq. (2.28) constitutes the starting point of our treatment of correlations that is further discussed in the next chapter.

## CHAPTER 3

### The Hubbard model

The following presentation is based on [60–63].

One of the most famous and successful models that is assumed to capture correlation effects in many classes of materials is the Hubbard model [64–66]. In the following sections we will introduce the model in its original formulation and discuss the correlation phenomena that it hosts. Moreover, we will relate it to realistic material calculations via the low-energy model that we constructed in the previous chapter and present a scheme, called the constrained Random Phase Approximation (cRPA) [52, 57, 67–71], which can be used to calculate interaction parameters from *ab-initio*.

Since a detailed discussion of the Hubbard model and reported results on it are beyond the scope of this thesis we refer to Ref. [61, 62] for further reading.

#### 3.1. Introduction

The Hubbard model – in the simplest form – is a single-orbital lattice model described by the Hamiltonian

$$(3.1) \quad H = \sum_{i,j,\sigma} t^{r_i-r_j} c_\sigma^\dagger(r_i) c_\sigma(r_j) + \frac{1}{2} \sum_{i,\sigma} U n_\sigma(r_i) n_{-\sigma}(r_i),$$

where  $t^{r_i-r_j}$  are hopping elements between unit cell positions  $r_i$  and  $r_j$ . The on-site Hubbard interaction  $U$  is an effective local electron-electron repulsion. The operator  $c_\sigma(r_i)$  destroys an electron with spin  $\sigma$  at unit cell position  $r_i$  while the adjoint operator  $c_\sigma^\dagger(r_i)$  creates an electron with spin  $\sigma$  at unit cell position  $r_i$ . The density operator  $n_\sigma(r_i) := c_\sigma^\dagger(r_i) c_\sigma(r_i)$  measures the occupation of particles at  $r_i$  with spin  $\sigma$ . Thus, the Hubbard model contains only two ingredients, where the first is the kinetic part which favors delocalized electronic states while the second repulsive part penalizes double occupation and thus favors localized electrons.

This model can be interpreted as a further reduction of the downfolded Hamiltonian in eq. (2.28) to a single-orbital model and the additional approximation of the electron-electron interaction amplitude

$$(3.2) \quad U(\{r_i, \alpha_i\}) = \langle \omega_{\alpha_1, r_1} \omega_{\alpha_2, r_2} | V_{e,e} | \omega_{\alpha_3, r_3} \omega_{\alpha_4, r_4} \rangle$$

to a single-orbital local interaction, i.e.  $\alpha_i = \alpha_j$  and  $r_i = r_j$ , where the Wannier functions  $\omega_{\alpha_i, r_i}$  were defined in sec. 2.5.

The model was originally conceived in order to study the low electric conductivity in transition metal oxides and indeed even early approximate solutions<sup>1</sup> of the Hubbard model were able to observe the Mott-metal insulator transition [61, 65]. Notice that under the assumption of non-vanishing hopping  $t$  we can have a true insulating state only in the special case of half-filling, i.e. the number of electrons coincides with the number of lattice sites. The reason is that otherwise there are always empty or double occupied sites that can serve to minimize the total energy by hopping.

Before we give an overview on the properties of the Hubbard model we mention important perturbative limits of the Hubbard model, namely the  $t - J$  model (see

---

<sup>1</sup>The approximation we are referring to is the so-called Hubbard-I approximation [61, 65].

e.g. [72, 73]),

$$(3.3) \quad H = P \left( -t \sum_{\langle i,j \rangle, \sigma} c_{\sigma}^{\dagger}(r_i) c_{\sigma}(r_j) + J \sum_{\langle i,j \rangle} \left( \mathbf{S}(r_i) \cdot \mathbf{S}(r_j) - \frac{n(r_i)n(r_j)}{4} \right) \right) P$$

that is derived from perturbation in  $t/U$  and where  $J = 4t^2/U$  is the exchange parameter,  $P$  is the projector on states where at most one electron is located at each site and  $\mathbf{S}(r_i)$  is the spin operator acting on site  $r_i$ . The idea behind this approximation is to shrink the configuration space at each site by excluding doubly occupied sites due to their large energy cost. Inside the Mott insulating regime, where the electrons are localized to their respective sites one can further reduce the  $t - J$  model to the famous *antiferromagnetic Heisenberg model*,

$$(3.4) \quad H = J \sum_{\langle i,j \rangle} \mathbf{S}(r_i) \cdot \mathbf{S}(r_j),$$

where the electrons can only interact via spin exchange.

Only recently a connection between the Hubbard model and the lattice Kondo model was established in the strong coupling limit [74].

It is important to note that the restriction to on-site interaction may be too restrictive for some materials and thus the inclusion of further neighbor interaction becomes relevant. For example, nearest neighbor repulsion can create charge density instabilities [75, 76] but we will not consider such *extended Hubbard models* assuming that those are negligible due to efficient screening.

In the next section we will consider the limiting cases where the model is solvable and use those to get an intuition about what can be expected to happen in between.

### 3.2. Exactly solvable limits

So far, there is no analytical solution of the Hubbard model except for a few cases. Apart for the trivial cases, where  $U = 0$  and the system is perfectly described in terms of band theory (see eq. (2.25)) we also have the trivial case of  $t = 0$ . In this case one can easily diagonalize the Hamiltonian in real space since the problem reduces to a sum of single site with their specific multiplet energy spectrum (see fig. 3.1). For this reason one calls the  $t = 0$  case the *atomic limit*.

When starting from the non-interacting  $U = 0$  limit and adiabatically turning on the on-site interaction we observe the so-called *Brinkman-Rice effect* [77] which describes the shrinking bandwidth due to interactions. This phenomenon can be understood as the suppression of hopping processes due to energy cost  $U$  for double occupation. Alternatively, one can also stay in the quasi-particle picture and explain the effect as an enhancement of the *effective mass*  $m^*$  due to the electron-electron interaction. The spectral weight that is subtracted due to the band narrowing is shifted to the higher energy multiplet excitations that have some resemblance with the atomic limit<sup>2</sup>. Those emerging excitations are called *Hubbard excitations/bands* while the narrowing low-energy part of the spectrum consists of *quasi-particle excitations*. Those low energy excitations will have a finite *lifetime* since the momentum  $k$  is not a good quantum number anymore.

All the above mentioned concepts will be discussed in more rigor at the end of chap. 4 where the Green's function formalism allows for a precise definition.

The ground state of the Hubbard model in one dimension can be constructed from a generalized Bethe ansatz [78] and also the excitation spectrum [79–82]. For more

<sup>2</sup>Those higher energy excitations are different to the atomic multiplet spectrum due to the underlying lattice structure which results in a finite lifetime of those excitations in contrast to the atomic limit, where the corresponding excitations are true eigenstates.

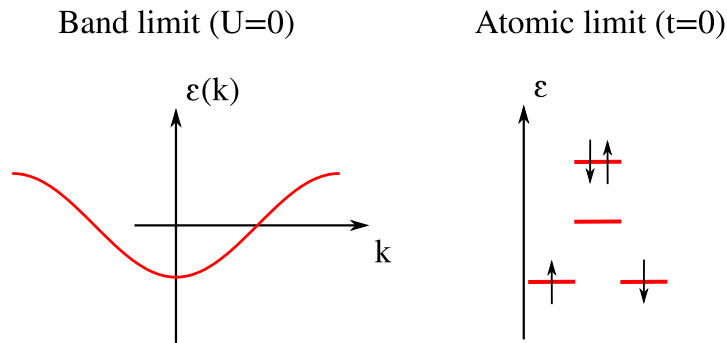


FIGURE 3.1. Sketch of the two extremes in the single-orbital Hubbard model. On the left-hand side we see the band limit, where the Hubbard interaction  $U = 0$  and  $k$  is a good quantum number. In this case the electrons are delocalized over the whole crystal. On the right-hand side we depict the atomic limit, where  $t = 0$  and every single site of the lattice behaves like an atom with multiplet states with four different configurations, namely the site is unoccupied, the site is occupied with one electron (either spin up or down) or the site is doubly occupied.

details and further results we refer to [83, 84] since we will be mainly interested in quasi two-dimensional materials and those behave indeed very different since in one dimension the ground state is insulating for any  $U > 0$  and therefore no Mott-metal insulator transition occurs [78].

But not only the one-dimensional limit is solvable but also the infinite dimension/lattice-connectivity limit [85–87]. The solution is then given by the dynamical mean field theory (DMFT) result [85, 87, 88], where the Mott-metal insulator transition is also part of the phase diagram. For this reason and due to the large successes of DMFT in applications to real materials, we will later use this method as a benchmark for the many-body approach studied in this thesis.

### 3.3. Rigorous results for the Hubbard model

Since the first appearance of the Hubbard model in 1963 a lot of research was done in order to obtain rigorous results. We will not be able to give an adequate overview on this field and can only refer to [61, 83, 89].

Under certain assumptions regarding the hopping elements one can proof the non-existence of ferromagnetic order for the ground state in the half-filled Hubbard model [89, 90]. This theorem by Lieb is important for assessing the quality of approximate methods when approaching zero temperature.

From the seminal Mermin-Wagner-Hohenberg theorem – that can be applied due to the continuous  $SU(2)$  spin rotation symmetry in the Hubbard model – we can deduce that in two dimensions and at finite temperature  $T > 0$  there is no superconductivity or spin long-range order [91–95] while Kosterlitz-Thouless phase transitions<sup>3</sup> [96–98] are not excluded [99].

---

<sup>3</sup>Such phase transitions are of topological nature and not accompanied by a spontaneous symmetry breaking. They are characterized by a change in the response to an external perturbation of the system, more specifically a divergence in the correlation length at the critical temperature which would correspond to an infinite order Ehrenfest phase transition.

### 3.4. Multi-orbital Coulomb interaction

In order to extend the Hubbard model to more orbitals we need to reconsider the general interaction term

$$(3.5) \quad U(\{r_i, \alpha_i\}, \sigma, \sigma') = \left\langle \omega_{\alpha_1, \sigma, r_1} \omega_{\alpha_2, \sigma', r_2} | V_{e,e} | \omega_{\alpha_3, \sigma, r_3} \omega_{\alpha_4, \sigma', r_4} \right\rangle,$$

where – in contrast to eq. (3.2) – we have written the spin dependence explicitly and took advantage of spin conservation.

From those matrix elements we can construct the on-site interaction part of the Hamiltonian in terms of

$$(3.6) \quad H_e = \frac{1}{2} \sum_{\alpha_i, \sigma, \sigma'} \left\langle \omega_{\alpha_1, \sigma, r} \omega_{\alpha_2, \sigma', r} | V_{e,e} | \omega_{\alpha_3, \sigma, r} \omega_{\alpha_4, \sigma', r} \right\rangle c_{\alpha_1, \sigma}^\dagger(r) c_{\alpha_2, \sigma'}^\dagger(r) c_{\alpha_4, \sigma}(r) c_{\alpha_3, \sigma'}(r).$$

An important difference that arises between orbitals of a single atoms and orbitals in a crystal is the crystal field splitting which occurs due to the static electric field of the surrounding ions.

In the application that we will be dealing with in chap. 7 the correlated electrons occupy Fe 3d orbitals in a tetrahedral environment. Thus, the five 3d orbitals will split into three  $t_{2g}$  and two  $e_g$  states, where the  $t_{2g}$  are energetically lower. The shape of the three  $t_{2g}$  orbitals calls for a multi-orbital Hubbard model where this symmetry is respected. By further ignoring matrix elements that involve more than two different interacting orbitals and assume same orbital overlap for all interacting orbitals we can simplify the general on-site interaction Hamiltonian in eq. (3.6) to the following rotational invariant *Kanamori-Hubbard Hamiltonian* [66],

$$(3.7) \quad \begin{aligned} H = & \sum_{\alpha, \beta, i, j, \sigma} t_{\alpha\beta}^{r_i - r_j} c_{\alpha, \sigma}^\dagger(r_i) c_{\beta, \sigma}(r_j) + \frac{1}{2} \sum_{\alpha, \beta, i, \sigma} U_{\alpha\beta} n_{\alpha, \sigma}(r_i) n_{\beta, -\sigma}(r_i) \\ & + \frac{1}{2} \sum_{\substack{\alpha, \beta, i, \sigma \\ \alpha \neq \beta}} (U_{\alpha\beta} - J_{\alpha\beta}) n_{\alpha, \sigma}(r_i) n_{\beta, \sigma}(r_i) \\ & - \frac{1}{2} \sum_{\substack{\alpha, \beta, i, \sigma \\ \alpha \neq \beta}} J_{\alpha\beta} \left( c_{\alpha, \sigma}^\dagger(r_i) c_{\alpha, -\sigma}(r_i) c_{\beta, -\sigma}^\dagger(r_i) c_{\beta, \sigma}(r_i) \right. \\ & \left. + c_{\alpha, \sigma}^\dagger(r_i) c_{\beta, -\sigma}(r_i) c_{\alpha, -\sigma}^\dagger(r_i) c_{\beta, \sigma}(r_i) \right), \end{aligned}$$

where the coupling constants are given by

$$(3.8) \quad U_{\alpha\beta} = \begin{cases} U & \alpha = \beta \\ U - 2J & \alpha \neq \beta \end{cases} \quad \text{and} \quad J_{\alpha\beta} = J(1 - \delta_{\alpha, \beta}).$$

Apart from the orbital rotational invariance, Hund's first rule is also taken account of<sup>4</sup> and the remaining orbital independent constants can be calculated via

$$(3.9) \quad U = \langle \omega_{\sigma, r} \omega_{-\sigma, r} | V_{e,e} | \omega_{\sigma, r} \omega_{-\sigma, r} \rangle,$$

$$(3.10) \quad J = \langle \omega_{\alpha, \sigma, r} \omega_{\beta, \sigma, r} | V_{e,e} | \omega_{\beta, \sigma, r} \omega_{\alpha, \sigma, r} \rangle, \quad \alpha \neq \beta,$$

where we dropped the orbital indices in the expression for  $U$  due to orbital symmetry. Apart from the density-density interaction we encounter the so-called *spin-flip term* which flips the spin of two electrons in different orbitals and the *pair-hopping term*

<sup>4</sup>In the case of density-density interactions in eq. (3.7) we observe for unequal orbitals that the equal spin state comes along with  $U_{\alpha\beta} - J_{\alpha\beta}$  while the opposite spin state is scaled with  $U_{\alpha\beta}$ . Therefore, the high spin state is favored which reflects Hund's first rule.

which describes the process of annihilating two electrons in one orbital and creating them in a different one.

In the case where the full  $d$ -shell is part of the correlated subspace, one can rely on so-called Slater-Koster integrals (see Ref. [26, 62] for more details) in order to restore rotational invariance.

For the real material calculation that we are going to perform in chap. 7 we will make use of the constrained Random Phase Approximation [67–69] that allows to calculate the interaction values  $U_{\alpha\beta}$ ,  $J_{\alpha\beta}$  from *ab-initio*.

### 3.5. Constrained Random Phase Approximation

Before we present the constrained Random Phase Approximation (cRPA) we mention a different approach to calculate the interaction values  $U_{\alpha\beta}$ ,  $J_{\alpha\beta}$  from *ab-initio*, namely the constrained LDA (cLDA) [69, 100–105]. In this approach the effective interaction is determined by total energy variations as functionals of the correlated electron densities in order to find the cost of double occupation at a specific site<sup>5</sup>.

We employ the cRPA scheme since it includes dynamical screening effects [69], i.e. frequency-dependent interaction values. We will explain this phenomenon in the following.

If we calculated the interaction values  $U$ ,  $J$  directly from (3.9), (3.10) we would get typically values of the order of 15eV [100]. Such large Coulomb strengths are closer to the interaction values of isolated atoms/ions rather than expected from electrons in a solid. The important feature that a “direct” calculation is missing are screening effects: If electrons feel the Coulomb repulsion of a specific electron they get repelled by it and effectively a screening hole is created around that electron which reduces the repulsion to an effective/screened Coulomb interaction. An important feature of that phenomenon is the dynamical aspect, namely the screening is less efficient at large energy scales, where the creation of an screening hole is energetically less favorable and the “bare” interaction is recovered [68, 69, 106].

The formal description of the dynamical screening can be expressed in the language of functional derivatives (see sec. 5.1.2) where the dynamical density fluctuation to an artificial external perturbation can be expressed in terms of functional derivatives [107, 108].

Within the Random Phase Approximation one restricts the response of the system to fluctuations in the Hartree potential. By this means one can express the density fluctuations  $\delta n$  due to the external field  $\phi$  as

$$(3.12) \quad \frac{\delta n}{\delta \phi} = (1 - PV_{e,e})^{-1} P,$$

where  $P$  is the polarization bubble (compare to eq. (5.92)),

$$(3.13) \quad \begin{aligned} & P(x, x', \omega) \\ &= - \lim_{\epsilon \searrow 0} \sum_{k,n} \sum_{\text{occ } k', m} \sum_{\text{unocc}} \phi_{n,k}(x) \phi_{n,k}^*(x') \phi_{m,k'}^*(x) \phi_{m,k'}(x'). \\ & \cdot \left( \frac{1}{\omega - \epsilon_m(k') + \epsilon_n(k) + i\epsilon} - \frac{1}{\omega + \epsilon_m(k') - \epsilon_n(k) - i\epsilon} \right). \end{aligned}$$

<sup>5</sup>The very first cLDA formula that was applied to determine the Hubbard interaction  $U$  was given by

$$(3.11) \quad E[n] = c_0 + c_1 n + \frac{U}{2} n(n-1),$$

where  $c_0, c_1$  are parameters to describe the minimum of the total energy functional [100].

From the polarization  $P$  one can calculate the screened electron-electron interaction  $W_{e,e}$  via

$$(3.14) \quad W_{e,e} = (1 - V_{e,e}P)^{-1} V_{e,e}.$$

The contributions to the polarization  $P$  (see eq. (3.13)) can be decomposed<sup>6</sup> into contributions that stem from the correlated states  $P_c$  and the remaining contributions  $P_r$ , i.e.  $P = P_c + P_r$ . This allows to rewrite the screened interaction  $W_{e,e}$  as

$$(3.15) \quad W_{e,e} = (1 - W_r P_d)^{-1} W_r,$$

where we defined a screened interaction that includes all screening contributions except for the ones of the correlated subspace (see fig. 3.2), i.e.

$$(3.16) \quad W_r = (1 - V_{e,e}P_r)^{-1} V_{e,e}.$$

The screened interaction  $W_r$  inherits its frequency-dependence from the polarization  $P_r$

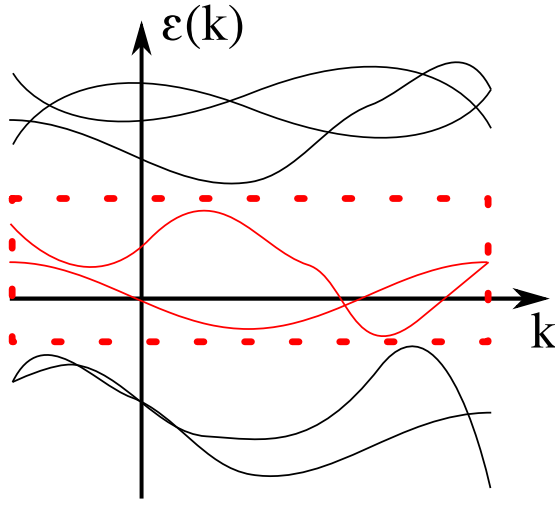


FIGURE 3.2. Schematic representation of the decomposition in correlated and rest subspace. While the correlated subspace consists of all states within the red box, all other states above and below this region belong to the high energy rest space. For the calculation of the polarization contribution  $P_r$  that is needed for the screened interaction  $W_r$  (see eq. (3.16)) one considers excitations that are not completely contained within the red box, i.e. within the low-energy subspace.

and – in analogy to eqs. (3.9), (3.10) – we can calculate the screened effective interaction values

$$(3.17) \quad U_{\alpha\beta} := U_{\alpha\beta}(\omega = 0) = \langle \omega_{\alpha,\sigma,r} \omega_{\beta,-\sigma,r} | W_r | \omega_{\alpha,\sigma,r} \omega_{\beta,-\sigma,r} \rangle,$$

$$(3.18) \quad J_{\alpha\beta} := J_{\alpha\beta}(\omega = 0) = \langle \omega_{\alpha,\sigma,r} \omega_{\beta,\sigma,r} | W_r | \omega_{\beta,\sigma,r} \omega_{\alpha,\sigma,r} \rangle, \quad \alpha \neq \beta.$$

Notice that the frequency-dependent interaction cannot be included into the standard Hamiltonian formalism and requires the functional-integral formalism [68]. As a first step we will therefore only take the static limit  $\omega = 0$  values of the effective screened interaction values but one has to keep in mind that dynamical screening can lead to additional features that effect the spectral properties over the whole energy range of the low-energy subspace [52, 68, 106].

A simple way to approximate the dynamical interaction in terms of an effective static

<sup>6</sup>The decomposition is done by simply restricting the sums in eq. (3.13) to bands  $n, m$  that belong to the correlated subspace in order to obtain  $P_c$ .

### 3.5. CONSTRAINED RANDOM PHASE APPROXIMATION

---

Hubbard repulsion is by means of the Lang-Firsov transformation [106, 109], where apart from the renormalization of  $U$ ,  $J$  a rescaling of the hopping parameters takes place.

In the end, we also mention that the cRPA computed values have their limitations since they depend directly on the accuracy of the DFT result and the RPA approximation that is built in. This might cause problems in the case of strongly correlated systems, where the correlation effects on the electronic structure outside of the correlated energy window are large and would also need to be included in the determination scheme of  $U$ ,  $J$ . For a more detailed discussion of this issue and other *ab-initio* methods for calculation of screened interaction parameters we refer to Ref. [52].

## CHAPTER 4

### Green's functions

In this section we lay the foundation for the Two-Particle Self-Consistent approach (TPSC) following the many-body physics script of A.-M. Tremblay [110] and the textbook of A. L. Fetter and J. D. Walecka [30] while the mathematical motivation for Green's function follows Ref. [15].

Apart from the basic notion of many-body theory where the Green's function formalism and linear response theory are important tools to describe single- and two-particle properties [30, 111–113] we will need to introduce the language of functional derivatives [114] to find approximate expressions for those two objects.

TPSC is derived within the framework of the so-called conserving approximations that are based on the Kadanoff-Baym scheme [113, 115, 116] and the Luttinger-Ward functional [117, 118].

We will present the derivation of the many-body equations for a multi-site system in order to use the expressions for both the single-band and multi-site TPSC later. In the case of multi-orbital systems we will get many different additional terms and –for clarity– present that case separately. All expressions are given in Planck units where  $\hbar = k_B = 1$ .

#### 4.1. Mathematical motivation

The concept of Green's functions has its roots in the question of whether a linear partial differential equation with constant coefficients and inhomogeneity  $g$ ,

$$(4.1) \quad Af := \left[ \sum_{\substack{\alpha=(\alpha_1, \dots, \alpha_d) \in \mathbb{N}^d \\ |\alpha_1| + \dots + |\alpha_d| \leq m}} a_\alpha \frac{\partial^\alpha}{\partial x_1^{\alpha_1} \dots \partial x_d^{\alpha_d}} \right] f = g, \quad a_\alpha \in \mathbb{C}, \quad m \in \mathbb{N},$$

has solutions  $f$  and if so, what kind of regularity properties do those solutions possess (see f.i. Refs. [15, 119]). This question crucially depends on the inhomogeneity term  $g$  and on what kind of properties of the solutions  $f$  are desired.

Obviously, in physics many equations of motion or equations of state fall into this category of partial differential equations, e.g. the Laplace equation, the Heat equation and the wave equation but also the Schrödinger equation for many different systems.

Central to the question mentioned above is the notion of *distributions* or *generalized functions* since – by duality (see Ref. [15]) – one can translate the original linear partial differential operator  $A$  (eq. (4.1)) into a linear and continuous operator acting on distributions. This allows to search for solutions in a larger space, namely for *distributional solutions*.

An important property of the distributional formulation of the problem in eq. (4.1) is that it always has a *fundamental solution*  $G$  that satisfies

$$(4.2) \quad AG = \delta,$$

where  $\delta$  is the Dirac distribution (see [15] Thm. 8.2). Once a fundamental solution  $G$  is found one can compute a special solution  $f$  of the distributional problem in eq. (4.1)

via the convolution  $f = G * g^1$ .

Moreover, we note that the same concept can be also used for discrete lattice problems where the domain is a lattice and the differential operators are discrete differential operators. The physical pictures that one can draw from this abstract mathematical concept of fundamental solutions are various and we will develop those from the point of view of theory and experiment in the following sections.

#### 4.2. Single-particle Green's functions and propagators

We consider a single particle with mass  $m$  in a time-independent potential  $V$  that moves in space. Therefore, the Hamiltonian  $H$  is given by

$$(4.3) \quad H = -\frac{1}{2m}\Delta + V$$

and the time-dependent Schrödinger equation is given by

$$(4.4) \quad \left(i\frac{\partial}{\partial t} - H\right)\psi = 0,$$

where  $\psi$  is a wave function solution. Assuming that the particle is prepared in some state  $|\psi(t_0)\rangle$  at  $t = t_0$  we can calculate the state of the particle at time  $t > t_0$  via the unitary time evolution operator

$$(4.5) \quad U(t, t_0) = e^{-iH(t-t_0)}$$

as

$$(4.6) \quad |\psi(t)\rangle = U(t, t_0) |\psi(t_0)\rangle.$$

In position space we can use the closure relation

$$(4.7) \quad \mathbb{I} = \int dx |x\rangle \langle x|$$

to obtain

$$(4.8) \quad \psi(x, t) = i \int dx_0 \underbrace{(-i \langle x | U(t, t_0) | x_0 \rangle)}_{=: G(x, t; x_0, t_0)} \psi(x_0, t_0)$$

from eq. (4.6).

We call the object  $G$  defined in eq. (4.8) *propagator* since it propagates the wave function of the particle from the wave function  $\psi(x_0, t_0)$  to the state  $\psi(x, t)$  by means of a convolution.

To emphasize the time ordering  $t > t_0$  (causality) we define

$$(4.9) \quad G^R(x, t; x_0, t_0) := \theta(t - t_0)G(x, t; x_0, t_0),$$

where  $\theta$  is the Heaviside function

$$(4.10) \quad \theta(t) = \begin{cases} 1 & t \geq 0 \\ 0 & t < 0 \end{cases}.$$

The superscript in  $G^R$  stands for *retarded* which expresses the causality that is built into the propagator, where the effect follows the cause and not the other way round.

The convolution in eq. (4.8) already suggests that  $G^R$  is indeed a Green's function<sup>2</sup> of the linear operator  $A = i\partial_t - H$  and one can easily verify that  $G^R$  fulfills

$$(4.11) \quad (i\partial_t - H)G^R(x, t; x_0, t_0) = \delta(t - t_0)\delta(x - x_0).$$

---

<sup>1</sup>Strictly speaking one would have to check that the pair  $(G, g)$  fulfills the so-called support condition in order for the convolution to be well-defined.

<sup>2</sup>In this case the Green's function is a fundamental solution that also fulfills the initial condition  $\lim_{t \searrow t'} G(x, t; x_0, t_0) = -i\delta(x - x_0)$  (see eq. (4.8)).

So far, it seems that the retarded Green's function  $G^R$  is merely a solution of the time-dependent Schrödinger equation with a singular source term at space-time  $(x_0, t_0)$  that can also serve as propagator between wave functions.

In the following we will cast a glance at the large amount of information that is contained in those elegant objects. It is already worthwhile to emphasize that the time evolution via the retarded Green's function  $G^R$  is in general simpler than time evolution with the unitary operator  $U$  since the convolution in eq. (4.8) is easier to perform than the operator action in eq. (4.6). Moreover, the time evolution via the Green's function  $G^R$  does not depend on the initial state  $|\psi(x_0, t_0)\rangle$ .

### 4.3. Single-particle Green's function and density of states

To be able to relate the retarded Green's function  $G^R$  (eqs. (4.8) and (4.9)) to the density of states one takes advantage of the time-translational invariance of  $G^R$  (see eq. (4.8)) and performs a Fourier transform  $\mathcal{F}$  to obtain

$$(4.12) \quad G^R(x, x_0, \omega) := [\mathcal{F}G^R(x, \cdot; x_0, 0)](\omega) = \lim_{\epsilon \searrow 0} \langle x | (\omega - H + i\epsilon)^{-1} | x_0 \rangle,$$

which is the resolvent operator in position representation and where  $\lim$  is the weak limit, namely

$$(4.13) \quad \lim_{\epsilon \searrow 0} f_\epsilon(x) = f(x) \quad :\iff \quad \lim_{\epsilon \searrow 0} \int_{\mathbb{R}} \phi(x) f_\epsilon(x) dx = \int_{\mathbb{R}} \phi(x) f(x) dx$$

for all test functions  $\phi \in C_c^\infty(\mathbb{R})$  from the space of smooth test functions with compact support. We are left to prove the second equality in eq. (4.12).

PROOF OF (4.12). We exploit the two identities of Fourier transforms of tempered distributions,

$$(4.14) \quad [\mathcal{F}\theta](\omega) = \frac{i}{\omega} + \pi\delta(\omega)$$

$$(4.15) \quad [\mathcal{F}e^{-i\omega_0 \cdot} f](\omega) = [\mathcal{F}f](\omega - \omega_0),$$

and calculate via the spectral decomposition of the Hamiltonian,  $H = \sum_n E_n |n\rangle \langle n|$ ,

where  $E_n$  are the energy eigenvalues and  $|n\rangle$  are the corresponding energy eigenstates,

$$(4.16) \quad [\mathcal{F}G^R(x, \cdot; x_0, 0)](\omega) = \mathcal{F}[-i\theta(\cdot) \langle x | U(\cdot, 0) | x_0 \rangle](\omega)$$

$$(4.17) \quad = \mathcal{F}[-i\theta(\cdot) \sum_n \langle x | n \rangle e^{-iE_n \cdot} \langle n | x_0 \rangle](\omega)$$

$$(4.18) \quad = \sum_n \langle x | n \rangle \left( \frac{1}{\omega - E_n} - i\pi\delta(\omega - E_n) \right) \langle n | x_0 \rangle.$$

At this stage we make use of the weak approximation of the  $\delta$ -Distribution in terms of the heat kernel

$$(4.19) \quad \eta(\epsilon, x) := \frac{1}{\pi} \frac{\epsilon}{\epsilon^2 + x^2},$$

which leads to the weak limit

$$(4.20) \quad \lim_{\epsilon \searrow 0} \eta(\epsilon, x) = \delta(x).$$

This yields the final expression

$$(4.21) \quad G^R(x, x_0, \omega) = \sum_n \langle x | n \rangle \left( \frac{1}{\omega - E_n} - i\pi\delta(\omega - E_n) \right) \langle n | x_0 \rangle$$

$$(4.22) \quad = \lim_{\epsilon \searrow 0} \sum_n \langle x | n \rangle \left( \frac{\omega - E_n}{(\omega - E_n)^2 + \epsilon^2} - i \frac{\epsilon}{(\omega - E_n)^2 + \epsilon^2} \right) \langle n | x_0 \rangle$$

#### 4.4. MANY-BODY GREEN'S FUNCTION

---

$$(4.23) \quad = \lim_{\epsilon \searrow 0} \sum_n \langle x|n\rangle \frac{1}{\omega - E_n + i\epsilon} \langle n|x_0\rangle$$

$$(4.24) \quad = \lim_{\epsilon \searrow 0} \langle x|(\omega\mathbb{I} - H + i\epsilon\mathbb{I})^{-1}|x_0\rangle,$$

where  $\mathbb{I}$  is the identity operator.  $\square$

We already see that the retarded Green's function in frequency space  $G^R(x, x_0, \omega)$  has poles at the eigenenergies of the Hamiltonian  $H$ .

If we consider the spectral decomposition of the single-particle Hamiltonian

$$(4.25) \quad H = \sum_n E_n |n\rangle \langle n|$$

we can deduce from eq. (4.21) the expression

$$(4.26) \quad \text{Im}G^R(x, x, \omega) = -\pi \sum_n \delta(\omega - E_n) |\langle n|x\rangle|^2.$$

This result can be used to express the single-particle density of states  $\rho(\omega)$  in terms of the retarded Green's function  $G^R$ , namely

$$(4.27) \quad \rho(\omega) = \sum_n \delta(\omega - E_n) = -\frac{1}{\pi} \int \text{Im}G^R(x, x, \omega) dx.$$

In the following sections we will encounter a similar relation between Green's functions and spectral properties in the many-body context.

#### 4.4. Many-body Green's function

So far, we introduced the Green's function as a mathematical object and showed its usefulness in the context of single-particle physics. In order to describe realistic models of materials we have to extend the previous definition to include finite temperature and many-body effects.

We start with the many-body extension at zero temperature and denote the expressions in second quantization. Motivated from the single-particle retarded Green's function  $G^R$  (eqs. (4.8) and (4.9)) we define the object

$$(4.28) \quad \tilde{G}^R(x, t; x_0, t_0) := -i\theta(t - t_0) \langle 0| \Psi(x) e^{-iH(t-t_0)} \Psi^\dagger(x_0) |0\rangle,$$

where  $|0\rangle$  is the many-body ground state wave function and  $\Psi(x)$  is the field operator that destroys a particle at position  $x$  while  $\Psi^\dagger(x_0)$  creates a particle at position  $x_0$ .

In the case where we choose an energy scale where the ground state energy is zero<sup>3</sup> we work in the Heisenberg picture and further simplify the expression:

$$(4.29) \quad \tilde{G}^R(x, t; x_0, t_0) = -i\theta(t - t_0) \langle 0| \mathbb{I} \Psi(x) e^{-iH(t-t_0)} \Psi^\dagger(x_0) \mathbb{I} |0\rangle$$

$$(4.30) \quad = -i\theta(t - t_0) \langle 0| e^{-iHt} e^{iHt_0} \Psi(x) e^{-iH(t-t_0)} \Psi^\dagger(x_0) e^{-iHt_0} e^{iHt_0} |0\rangle$$

$$(4.31) \quad = -i\theta(t - t_0) \langle 0| e^{-iHt} \Psi(x, t) \Psi^\dagger(x_0, t_0) e^{iHt_0} |0\rangle$$

$$(4.32) \quad = -i\theta(t - t_0) \langle 0| e^{-i0t} \Psi(x, t) \Psi^\dagger(x_0, t_0) e^{i0t_0} |0\rangle$$

$$(4.33) \quad = -i\theta(t - t_0) \langle 0| \Psi(x, t) \Psi^\dagger(x_0, t_0) |0\rangle.$$

Although it is very tempting to use  $\tilde{G}^R$  in eq. (4.33) as a definition for the zero temperature many-body retarded Green's function we have to reconsider eq. (4.8) in the limit  $t \searrow t_0$ , i.e.  $\lim_{t \searrow t_0} G(x, t; x_0, t_0) = -i\delta(x - x_0)$ . This boundary condition was important for the interpretation of the Green's function as a propagator and we want to retain this

<sup>3</sup>This can be always done by defining an energy unit that is shifted with respect to the ground state energy.

property in the many-body case. In order to do so we can do a minimal modification to eq. (4.33) and define the zero-temperature many-body retarded Green's function

$$(4.34) \quad G^R(x, t; x_0, t_0) := -i\theta(t - t_0) \langle 0 | \left\{ \Psi(x, t), \Psi^\dagger(x_0, t_0) \right\} | 0 \rangle,$$

where the anticommutator  $\{\cdot, \cdot\}$  enforces the equal time boundary condition.

The object  $G^R(x, t; x_0, t_0)$  can be interpreted as a measure for the time and position correlation of excitations<sup>4</sup> of the ground state. Additionally, we retain the meaning of  $G^R$  as a propagator but in the many-body context it is not only the particles that can propagate but also the holes due to the anti-commutator in the definition.

Finally, we can extend the definition of the many-body retarded Green's function to finite temperatures by taking account of the finite-temperature statistics of the particles. This is done by replacing the ground state average by a thermodynamic average in eq. (4.34).

Thus, we obtain the finite temperature many-body retarded Green's function

$$(4.35) \quad G^R(x, t; x_0, t_0) := -i\theta(t - t_0) \left\langle \left\{ \Psi(x, t), \Psi^\dagger(x_0, t_0) \right\} \right\rangle,$$

where we have chosen to work in the grand canonical ensemble, i.e.

$$(4.36) \quad \langle O \rangle := \frac{\text{tr} \left( e^{-\tilde{\beta}H} O \right)}{Z}, \quad Z := \text{tr} \left( e^{-\tilde{\beta}H} \right),$$

where  $\tilde{\beta}$  is the inverse temperature and  $H$  is the grand canonical Hamiltonian, i.e. it contains an additional term  $-\mu\hat{N}$ , where  $\mu$  is the chemical potential and  $\hat{N}$  is the particle number operator.

The definition of the retarded Green's function in eq. (4.35) is given in position representation which is due to the mathematical motivation that we started with. Nevertheless, one is free to define  $G^R$  in different representations which leads to

$$(4.37) \quad G^R(\alpha, t; \beta, t_0) := -i\theta(t - t_0) \left\langle \left\{ c_\alpha(t), c_\beta^\dagger(t_0) \right\} \right\rangle,$$

where  $\alpha, \beta$  are quantum numbers from a complete set of quantum numbers and  $c_\alpha(t)$  destroys a particle in the state  $\alpha$  at time  $t$  while  $c_\beta^\dagger(t_0)$  creates a particle in the state  $\beta$  at time  $t_0$ .

#### 4.5. Imaginary time Green's function

So far, we have only considered “physical times”  $t$  as arguments for the retarded many-body Green's function  $G^R$ , i.e.  $t \in \mathbb{R}$ , but in principle there is no problem to extend the definition to imaginary time. Like in classical electrodynamics we will see that this generalization from real to imaginary arguments can simplify many mathematical expressions as one can use the tools of complex analysis.

A simple example where the notion of complex time can be helpful is the evaluation of thermal averages like in equation (4.35) for the finite temperature retarded many-body Green's function  $G^R$ . In this equation we encounter the operator exponential  $\exp(-\tilde{\beta}H) = \exp(-i(-i\tilde{\beta})H)$  where we interpret  $-i\tilde{\beta}$  as some imaginary time point. From classical many-body theory we know that if we evaluate the time evolution in eq. (4.35) perturbatively in the Dirac picture we encounter time ordered contour integrals on the real line. In interpreting  $-i\tilde{\beta}$  as some imaginary time we can reformulate

$$(4.38) \quad e^{-\tilde{\beta}H} = U(-i\tilde{\beta}, 0) = e^{-\tilde{\beta}H_0} U_I(-i\tilde{\beta}, 0),$$

<sup>4</sup>It is both particle and hole excitations that are being probed in the retarded Green's function since we introduced the anti-commutator.

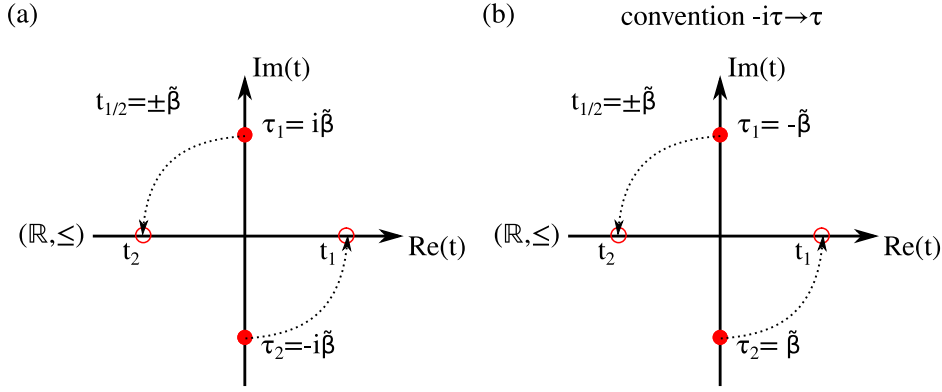


FIGURE 4.1. Definition of the imaginary time order. (a) Given the two exemplary imaginary times  $t_1 = \tilde{\beta}$  and  $t_2 = -\tilde{\beta}$  we calculate  $\tau_1 = i\tilde{\beta}$  and  $\tau_2 = -i\tilde{\beta}$ . We define the time order on the imaginary axis by first rotating the points by  $90^\circ$  counter clockwise in the complex plane and apply the canonical order on  $\mathbb{R}$ , denoted by  $(\mathbb{R}, \leq)$ , to those rotated points. For example,  $\tau_{1/2}$  is mapped to  $t_{2/1}$  respectively and since  $t_2 < t_1$  we conclude  $\tau_1 < \tau_2$ . (b) If we work in the convention where imaginary times  $\tau$  are denoted as their negative real counterparts  $-t = i\tau$  the previously defined order in (a) comes out naturally since in this convention  $\tau_1 = -\tilde{\beta} < \tilde{\beta} = \tau_2$ .

where  $H_0$  is the unperturbed grand canonical Hamiltonian and  $U_I$  is the time evolution operator in the Dirac picture. Thus, one can incorporate the contour from the imaginary time contour integral of  $U_I(-i\tilde{\beta}, 0)$  into the real time contour of the other operator in eq. (4.35) which leads to the so-called Kadanoff-Baym contour.

After this short motivation we formulate the transition to imaginary time formally: A complex time  $t \in \mathbb{C}$  is decomposed as  $t = \text{Re}(t) + i\text{Im}(t)$  and we define  $\tau := it$ . In the case of eq. (4.38) we see that for  $t = -\tilde{\beta} + i \cdot 0$  the object  $\tau$  appears naturally in the time evolution operator

$$(4.39) \quad e^{-\tilde{\beta}H} = U(\tau, 0) = e^{-iH\tau}.$$

Another important object that we will need in the following is the time ordering with respect to purely imaginary times  $\tau \in \{it \mid t \in \mathbb{R}\}$ . For this reason we define the fermionic imaginary time ordering operator

$$(4.40) \quad T_\tau A(\tau_1)B(\tau_2) := \begin{cases} A(\tau_1)B(\tau_2) & \tau_1 > \tau_2 \\ -B(\tau_2)A(\tau_1) & \tau_1 < \tau_2 \end{cases},$$

where we defined a total order  $(\{it \mid t \in \mathbb{R}\}, \leq)$  by applying the canonical total order  $(\mathbb{R}, \leq)$  to the imaginary part of the numbers in  $\{it \mid t \in \mathbb{R}\}$  (see fig. 4.1). Finally, we define the imaginary time Green's function  $G$  as

$$(4.41) \quad G(x, \tau; x_0, \tau_0) := -\left\langle T_\tau \Psi(x, \tau) \Psi^\dagger(x_0, \tau_0) \right\rangle,$$

where the time evolution of the field operators  $\Psi$ ,  $\Psi^\dagger$  is given by the imaginary time Heisenberg equation of motion

$$(4.42) \quad \frac{d}{dt}A = i[H, A] \Leftrightarrow \frac{d}{d\tau}A = [H, A]$$

which leads to

$$(4.43) \quad \Psi(x, \tau) := e^{\tau H} \Psi(x) e^{-\tau H}$$

$$(4.44) \quad \Psi^\dagger(x, \tau) := e^{\tau H} \Psi^\dagger(x) e^{-\tau H},$$

where a field operator without time argument is defined to be the corresponding field operator in the Schrödinger picture. Note that the time evolution in eqs. (4.43) and (4.44) seems inconsistent with eq. (4.39) which suggests  $-i\tau$  as imaginary time argument for the left-hand sides of equations (4.43) and (4.44). This abuse of notation in eq. (4.39) is a widely used convention to avoid the lengthy  $-i\tau$  imaginary time argument by replacing it with  $\tau$ , i.e. for a imaginary time function  $f$  we denote  $f(-i\tau)$  by  $f(\tau)$ . In this convention and for  $t \in \mathbb{R}$  we see that  $\Psi^\dagger$  is not the adjoint of  $\Psi$  since  $\tau \in \mathbb{R}$  but if we reinsert  $\tau = it$  we see that  $\Psi^\dagger(x, \tau) = \Psi^\dagger(x, t)$ .

Since we are dealing later with lattice models we choose a representation of the imaginary time Green's function, where the unit cell position is denoted separately from the other quantum numbers (like orbital and spin quantum numbers). This leads to the representation

$$(4.45) \quad G_{\alpha\beta,\sigma}(r, \tau; r_0, \tau_0) := - \left\langle T_\tau c_{\alpha,\sigma}(r, \tau) c_{\beta,\sigma}^\dagger(r_0, \tau_0) \right\rangle$$

where  $c_{\alpha,\sigma}(r, \tau)$  destroys a particle with quantum number  $\alpha$  and spin  $\sigma$  at unit cell position  $r$  while  $c_{\beta,\sigma}^\dagger(r_0, \tau_0)$  creates a particle with quantum number  $\beta$  and spin  $\sigma$  at unit cell position  $r_0$ . We denote the quantum numbers  $\alpha$  and  $\beta$  separated from  $\sigma$  by a comma to emphasize that the object  $G_\sigma(r, \tau; r_0, \tau_0)$  is a complex valued matrix in  $\mathbb{C}^{M \times M}$ , where  $M$  is the dimension of the vector space spanned from the quantum numbers  $\alpha$ . We restrict the imaginary time domain of the Green's function  $G$  to  $(-\tilde{\beta}, \tilde{\beta})$  because we see in eqs. (4.38) and (4.39) that only those imaginary times are needed to evaluate thermodynamic expectation values.

We summarize a few properties of the imaginary time Green's function  $G_{\alpha\beta,\sigma}(r, \tau; r_0, \tau_0)$ .

PROPOSITION 4.5.1. *(i) The imaginary time Green's function of a time-independent Hamiltonian is time translational invariant, i.e.*

$$(4.46) \quad G_{\alpha\beta,\sigma}(r, \tau; r_0, \tau_0) = G_{\alpha\beta,\sigma}(r, \tau - \tau_0; r_0, 0) =: G_{\alpha\beta,\sigma}(r, r_0, \tau - \tau_0).$$

*(ii) If the system is space translational invariant, then so is the imaginary time Green's function,*

$$(4.47) \quad G_{\alpha\beta,\sigma}(r, r_0, \tau) = G_{\alpha\beta,\sigma}(r - r_0, 0, \tau) =: G_{\alpha\beta,\sigma}(r - r_0, \tau)$$

*and we can identify the Fourier transformed Green's function with*

$$(4.48) \quad G_{\alpha\beta,\sigma}(k, \tau) = - \left\langle T_\tau c_{\alpha,\sigma}(k, \tau) c_{\beta,\sigma}^\dagger(k) \right\rangle.$$

*(iii) The adjoint of the Green's function is directly related to the Green's function via*

$$(4.49) \quad G_{\alpha\beta,\sigma}^*(r, \tau) = G_{\beta\alpha,\sigma}(r, \tau) \quad \text{and} \quad G_{\alpha\beta,\sigma}^*(k, \tau) = G_{\beta\alpha,\sigma}(k, \tau).$$

*(iv) The imaginary time Green's function  $G$  is anti-periodic in time in the case of  $\tau \in (0, \tilde{\beta})$ :*

$$(4.50) \quad G_{\alpha\beta,\sigma}(r, \tau) = -G_{\alpha\beta,\sigma}(r, \tau + \tilde{\beta}),$$

$$(4.51) \quad G_{\alpha\beta,\sigma}(k, \tau) = -G_{\alpha\beta,\sigma}(k, \tau + \tilde{\beta}), \quad \tau \in (-\tilde{\beta}, 0).$$

*Those relations tell us that it is sufficient to know the imaginary time Green's function  $G$  on the interval  $[0, \tilde{\beta})$  instead of  $(-\tilde{\beta}, \tilde{\beta})$ . The value at  $\tau = 0$  (where the imaginary time Green's function coincides with the retarded Green's function up to a factor  $i$ ) is considered separately.*

## 4.5. IMAGINARY TIME GREEN'S FUNCTION

(v) *The imaginary time Green's function is discontinuous at  $\tau = 0$  and shows a jump that is minus the Kronecker symbol,*

$$(4.52) \quad \lim_{\tau \searrow 0} (G_{\alpha\beta,\sigma}(k, \tau) - G_{\alpha\beta,\sigma}(k, -\tau)) = \lim_{\tau \searrow 0} (G_{\alpha\beta,\sigma}(r, \tau) - G_{\alpha\beta,\sigma}(r, -\tau)) = -\delta_{\alpha,\beta}.$$

PROOF. (i) We make use of the time-independence of the grand-canonical Hamiltonian  $H$  and evaluate the time ordering operator in the definition of the Green's function which leads to

$$(4.53) \quad G_{\alpha\beta,\sigma}(r, \tau; r_0, \tau_0) = -\frac{1}{Z} \text{tr} \left[ e^{-\tilde{\beta}H} T_\tau e^{\tau H} c_{\alpha,\sigma}(r) e^{-\tau H} e^{\tau_0 H} c_{\beta,\sigma}^\dagger(r_0) e^{-\tau_0 H} \right]$$

$$= -\frac{1}{Z} \text{tr} \left[ e^{-\tilde{\beta}H} e^{\tau H} c_{\alpha,\sigma}(r) e^{-(\tau-\tau_0)H} c_{\beta,\sigma}^\dagger(r_0) e^{-\tau_0 H} \right] \theta(\tau - \tau_0)$$

$$(4.54) \quad + \frac{1}{Z} \text{tr} \left[ e^{-\tilde{\beta}H} e^{\tau_0 H} c_{\beta,\sigma}^\dagger(r_0) e^{-(\tau_0-\tau)H} c_{\alpha,\sigma}(r) e^{-\tau H} \right] \theta(\tau_0 - \tau).$$

Now, one has to use the cyclic property of the trace and commute the operator exponentials ( $H$  is time independent) to get

$$(4.55) \quad G_{\alpha\beta,\sigma}(r, \tau; r_0, \tau_0) = -\frac{1}{Z} \text{tr} \left[ e^{-\tilde{\beta}H} e^{(\tau-\tau_0)H} c_{\alpha,\sigma}(r) e^{-(\tau-\tau_0)H} c_{\beta,\sigma}^\dagger(r_0) \right] \theta(\tau - \tau_0)$$

$$+ \frac{1}{Z} \text{tr} \left[ e^{-\tilde{\beta}H} e^{(\tau_0-\tau)H} c_{\beta,\sigma}^\dagger(r_0) e^{-(\tau_0-\tau)H} c_{\alpha,\sigma}(r) \right] \theta(\tau_0 - \tau).$$

$$(4.56) \quad = -\frac{1}{Z} \text{tr} \left[ e^{-\tilde{\beta}H} T_{\tau-\tau_0} e^{(\tau-\tau_0)H} c_{\alpha,\sigma}(r) e^{-(\tau-\tau_0)H} c_{\beta,\sigma}^\dagger(r_0) \right]$$

$$(4.57) \quad = G_{\alpha\beta,\sigma}(r, \tau - \tau_0; r_0, 0).$$

(ii) We present the proof for discrete lattice systems but the same steps can be easily generalized for continuous systems. The periodicity of the system implies space translation invariance of the grand-canonical Hamiltonian  $H$  which is mathematically expressed as

$$(4.58) \quad [\tilde{T}_s, H] = 0,$$

where  $\tilde{T}_s$  is the space translation operator that shifts a state by some lattice vector  $s \in S$  and  $S$  is a set of lattice vectors. The commutation relation in eq. (4.58) also applies to any power series of  $H$ . Therefore, we have

$$(4.59) \quad [\tilde{T}_s, e^{-\tilde{\beta}H}] = 0$$

and

$$(4.60) \quad G_{\alpha\beta,\sigma}(r, r_0, \tau) = -\frac{1}{Z} \text{tr} \left[ e^{-\tilde{\beta}H} T_\tau \tilde{T}_s \tilde{T}_{-s} c_{\alpha,\sigma}(r, \tau) \tilde{T}_s \tilde{T}_{-s} c_{\beta,\sigma}^\dagger(r_0) \right]$$

$$(4.61) \quad = -\frac{1}{Z} \text{tr} \left[ e^{-\tilde{\beta}H} T_\tau c_{\alpha,\sigma}(r+s, \tau) c_{\beta,\sigma}^\dagger(r_0+s) \right]$$

$$(4.62) \quad = G_{\alpha\beta,\sigma}(r+s, r_0+s, \tau).$$

For the special choice of  $s = -r_0$  we see that the Green's function only depends on the relative position coordinate  $r - r_0$  and we define

$$(4.63) \quad G_{\alpha\beta,\sigma}(r, r_0, \tau) = G_{\alpha\beta,\sigma}(r - r_0, \underbrace{r_0 - r_0}_{=0}, \tau) =: G_{\alpha\beta,\sigma}(r - r_0, \tau).$$

This result will be needed later but now one has to change from the real space to the reciprocal space representation of the creation and annihilation operators that appear in the Green's function  $G_{\alpha\beta,\sigma}(r, r_0, \tau)$  which leads to

$$(4.64) \quad G_{\alpha\beta,\sigma}(r, r_0, \tau) = - \left\langle T_\tau \sum_k \frac{1}{\sqrt{N}} e^{-ik \cdot r} c_{\alpha,\sigma}(k, \tau) \sum_{k'} \frac{1}{\sqrt{N}} e^{ik' \cdot r_0} c_{\beta,\sigma}^\dagger(k') \right\rangle$$

$$(4.65) \quad = -\frac{1}{N} \left\langle \sum_{k,k'} T_\tau c_{\alpha,\sigma}(k, \tau) e^{-i[(k-k') \cdot \frac{r+r_0}{2} + (r-r_0) \cdot \frac{k+k'}{2}]} c_{\beta,\sigma}^\dagger(k') \right\rangle,$$

where  $N$  is the number of unit cells in the system. Using the independence of the Green's function on the center of position coordinate (eq. (4.63)) we derive

$$(4.66) \quad 1 \cdot G_{\alpha\beta,\sigma}(r, r_0, \tau)$$

$$(4.67) \quad = -\frac{1}{N} \left\langle \sum_{k,k'} T_\tau c_{\alpha,\sigma}(k, \tau) \frac{1}{N} \sum_{(r+r_0)/2} e^{-i(k-k') \cdot \frac{r+r_0}{2}} e^{-i \frac{k+k'}{2} \cdot (r-r_0)} c_{\beta,\sigma}^\dagger(k') \right\rangle$$

$$(4.68) \quad = -\frac{1}{N} \left\langle \sum_{k,k'} T_\tau c_{\alpha,\sigma}(k, \tau) \delta_{k,k'} e^{-i \frac{k+k'}{2} (r-r_0)} c_{\beta,\sigma}^\dagger(k') \right\rangle$$

$$(4.69) \quad = -\frac{1}{N} \left\langle \sum_k T_\tau c_{\alpha,\sigma}(k, \tau) e^{-ik \cdot (r-r_0)} c_{\beta,\sigma}^\dagger(k) \right\rangle$$

$$(4.70) \quad = \frac{1}{N} \sum_k e^{-ik \cdot (r-r_0)} \left[ -\left\langle T_\tau c_{\alpha,\sigma}(k, \tau) c_{\beta,\sigma}^\dagger(k) \right\rangle \right]$$

$$(4.71) \quad = \frac{1}{N} \sum_k e^{-ik \cdot (r-r_0)} G_{\alpha\beta,\sigma}(k, \tau).$$

- (iii) We show the proof for the momentum space Green's function but the proof for the real space Green's function works analogously.

$$(4.72) \quad G_{\alpha\beta,\sigma}^*(k, \tau) = -\left\langle c_{\alpha,\sigma}(k, \tau) c_{\beta,\sigma}^\dagger(k) \right\rangle^*$$

$$(4.73) \quad = -\frac{1}{Z} \text{tr} \left[ T_\tau c_{\beta,\sigma}(k) e^{-\tau H} c_{\alpha,\sigma}^\dagger(k) e^{\tau H} e^{-\tilde{\beta} H} \right]$$

$$(4.74) \quad = -\frac{1}{Z} \text{tr} \left[ T_\tau e^{\tau H} e^{-\tilde{\beta} H} c_{\beta,\sigma}(k) e^{-\tau H} c_{\alpha,\sigma}^\dagger(k) \right]$$

$$(4.75) \quad = -\frac{1}{Z} \text{tr} \left[ T_\tau e^{-\tilde{\beta} H} c_{\beta,\sigma}(k, \tau) c_{\alpha,\sigma}^\dagger(k) \right]$$

$$(4.76) \quad = G_{\beta\alpha,\sigma}(k, \tau).$$

- (iv) Again, we present the proof only for the momentum space Green's function for the same reason as in the previous point.

We start with exploiting the condition  $\tau \in (-\tilde{\beta}, 0)$  and find

$$(4.77) \quad G_{\alpha\beta,\sigma}(k, \tau) = -\left\langle T_\tau c_{\alpha,\sigma}(k, \tau) c_{\beta,\sigma}^\dagger(k) \right\rangle$$

$$(4.78) \quad = \left\langle c_{\beta,\sigma}^\dagger(k) c_{\alpha,\sigma}(k, \tau) \right\rangle$$

$$(4.79) \quad = \frac{1}{Z} \text{tr} \left[ e^{-\tilde{\beta} H} c_{\beta,\sigma}^\dagger(k) e^{\tau H} c_{\alpha,\sigma}(k) e^{-\tau H} \right]$$

$$(4.80) \quad = \frac{1}{Z} \text{tr} \left[ e^{\tau H} c_{\alpha,\sigma}(k) e^{-\tau H} e^{-\tilde{\beta} H} c_{\beta,\sigma}^\dagger(k) \right]$$

$$(4.81) \quad = \frac{1}{Z} \text{tr} \left[ e^{-\tilde{\beta} H} e^{(\tilde{\beta}+\tau)H} c_{\alpha,\sigma}(k) e^{-(\tau+\tilde{\beta})H} c_{\beta,\sigma}^\dagger(k) \right]$$

$$(4.82) \quad = -G_{\alpha\beta,\sigma}(k, \tau + \tilde{\beta}).$$

Note that it was necessary to demand  $\tau > -\tilde{\beta}$  because otherwise we would not have been able to reintroduce the time ordering operator  $T_\tau$  in eq. (4.82).

## 4.5. IMAGINARY TIME GREEN'S FUNCTION

(v) The proof is independent of the basis choice and we use the momentum basis

$$(4.83) \quad \lim_{\tau \searrow 0} (G_{\alpha\beta,\sigma}(k, \tau) - G_{\alpha\beta,\sigma}(k, -\tau))$$

$$(4.84) \quad = \lim_{\tau \searrow 0} \left( - \left\langle c_{\alpha,\sigma}(k, \tau) c_{\beta,\sigma}^\dagger(k) \right\rangle - \left\langle c_{\beta,\sigma}^\dagger(k) c_{\alpha,\sigma}(k, -\tau) \right\rangle \right)$$

$$(4.85) \quad = - \left\langle \left\{ c_{\alpha,\sigma}(k), c_{\beta,\sigma}^\dagger(k) \right\} \right\rangle$$

$$(4.86) \quad = - \delta_{\alpha,\beta}.$$

□

In order to underline the difference between real and imaginary time Green's function we present the example of non-interacting particles.

EXAMPLE 4.5.2 (Non-interacting electrons). Consider electrons in a periodic lattice that are described by the Hamiltonian

$$(4.87) \quad H = \sum_k \underbrace{(\epsilon(k) - \mu)}_{=: \xi(k)} c^\dagger(k) c(k),$$

where  $\mu$  is the chemical potential and  $\epsilon$  is the dispersion relation. We find  $c(k, \tau)$  by solving the imaginary time Heisenberg equation of motion

$$(4.88) \quad \frac{d}{d\tau} c(k, \tau) = [H, c(k)] = \sum_{k'} \xi(k') \left[ c^\dagger(k') c(k'), c(k) \right] = - \sum_{k'} \xi(k') \delta_{k,k'} c(k)$$

$$(4.89) \quad = -\xi(k) c(k).$$

This differential equation can be easily solved considering the initial condition  $c(k, 0) = c(k)$ . The solution is given by

$$(4.90) \quad c(k, \tau) = e^{-\xi(k)\tau} c(k).$$

Inserting this equation into the definition of the imaginary time Green's function (eq. (4.48)) gives

$$(4.91) \quad G(k, \tau) = - \left\langle T_\tau c(k, \tau) c^\dagger(k) \right\rangle$$

$$(4.92) \quad = - e^{-\xi(k)\tau} \{ [1 - f_{FD}(\xi(k))] \theta(\tau) - f_{FD}(\xi(k)) \theta(-\tau) \},$$

where we used the Fermi-Dirac distribution function

$$(4.93) \quad f_{FD}(\xi(k)) = \left\langle c^\dagger(k) c(k) \right\rangle = \frac{1}{e^{\beta\xi(k)} + 1}.$$

For the real time retarded Green's function (eq. (4.37)) we can calculate  $c(k, t)$  in a similar fashion as the imaginary time counter part previously (eq. (4.89)). We find

$$(4.94) \quad c(k, t) = e^{-i\xi(k)t} c(k)$$

and inserting this result into the definition of the retarded Green's function  $G^R$  gives

$$(4.95) \quad G^R(k, t) = -i\theta(t) \left\langle \left\{ c(k, t), c^\dagger(k) \right\} \right\rangle$$

$$(4.96) \quad = -ie^{-i\xi(k)t} \theta(t) \left\langle \left\{ c(k), c^\dagger(k) \right\} \right\rangle$$

$$(4.97) \quad = -ie^{-i\xi(k)t} \theta(t).$$

We plot the imaginary time Green's functions  $G$  and the real-time Green's function  $G^R$  for this non-interacting system in fig. 4.2. For simplicity we assume flat bands, i.e.  $\xi(k) = \xi$  and consider the case of an unoccupied band ( $\xi = 1 > 0$ ), a band at the Fermi energy ( $\xi = 0$ ) and an occupied band ( $\xi = -1 < 0$ ). The definition of the real-time Green's function in equation (4.37) allows us to interpret  $G^R(t)$  as a measure

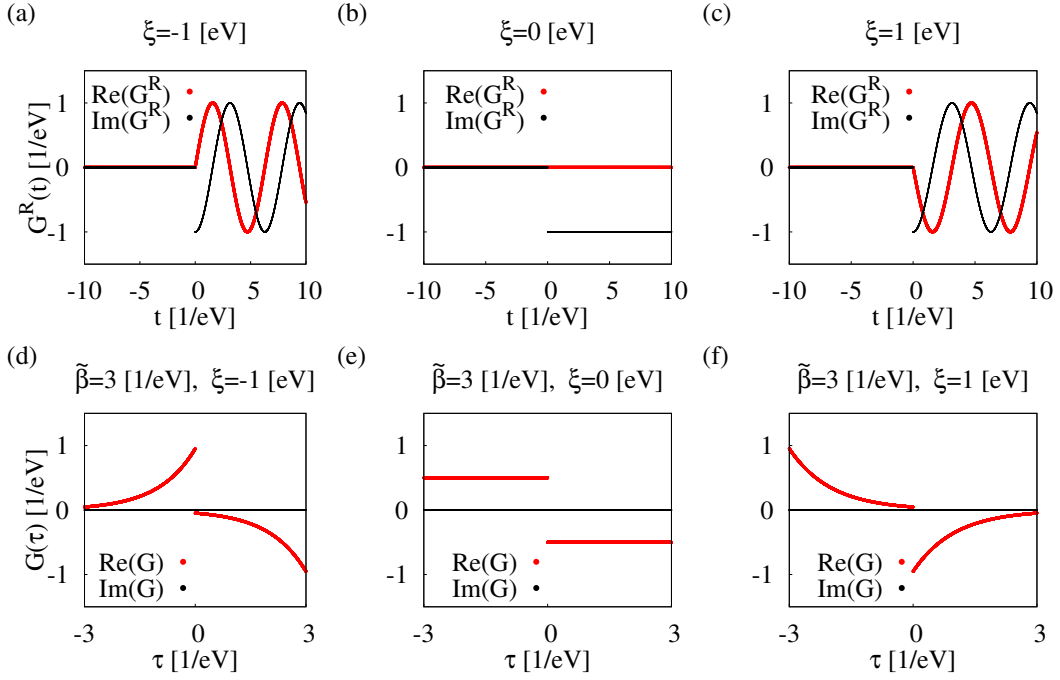


FIGURE 4.2. Real time retarded Green's function  $G^R$  and imaginary time Green's function  $G$  for non-interacting particle described by the grand canonical Hamiltonian  $H$  in eq. (4.87). (a)-(c) show  $G^R(t)$  in the case where  $\xi(k)$  is a constant  $\xi = -1, 0, 1\text{eV}$  respectively. We see that the retarded Green's function is basically given by an oscillating phase factor for  $t > 0$  if  $\xi \neq 0$ . This is the manifestation of the Green's function as a correlation function that measures how large the overlap between an excitation  $b_k^\dagger |0\rangle$  at  $t = 0$  and the time-propagated excitation  $e^{-iHt} b_k^\dagger |0\rangle$  for  $t > 0$  is (see main text). (d)-(f) show the imaginary time Green's function for inverse temperature  $\tilde{\beta} = 3(\text{eV})^{-1}$ . In contrast to the real-time Green's function we see that  $G$  shows exponential growth/decay and is indeed anti-symmetric in  $(-\tilde{\beta}, \tilde{\beta})$ . Finally, all Green's function exhibit a discontinuity at  $t = 0$  which has width 1. This is due to the fermionic anti-commutation relation.

for the overlap between an excitation  $b_k^\dagger |0\rangle$  to the ground state<sup>5</sup> at  $t = 0$  and the time-propagated excitation  $e^{-iHt} b_k^\dagger |0\rangle$  for  $t > 0$ . In the case of non-interacting electrons the time-propagation reduces to a simple phase factor (see eq. (4.94)) which leads in (a),(c) to an oscillation in the cases  $\xi \neq 0$  and else (b) to a constant prefactor for  $\xi = 0$ . In (d)-(f) we present the imaginary time Green's function  $G$  at inverse temperature  $\tilde{\beta} = 3(\text{eV})^{-1}$ . Apart from the exponential growth/decay from eq. (4.92) we observe the anti-periodicity (see eq.(4.51)) that will serve later to expand  $G$  in a Fourier series. Note that all Green's function in (a)-(f) show a characteristic jump of height 1 that is due to the fermionic commutation relation.

#### 4.6. Lehman representation and spectral weight

The retarded Green's function carries not only information on how to propagate some state in time but also information about the energy spectrum. In this section we

<sup>5</sup>We use the letter  $b$  instead of  $c$  because the anti-commutator in the definition of  $G^R$  takes care of both particle ( $\xi > 0$ ) and hole excitations ( $\xi \leq 0$ ).

study this relation. We start by performing a Fourier transform to bring the retarded Green's function from time space to frequency space but first one needs to manipulate the anti-commutator expectation value by the resolution of the identity

$$(4.98) \quad \mathbb{I} = \sum_n |n\rangle \langle n|,$$

where  $\{|n\rangle\}$  is the set of (many-body) eigenstates of  $H$  with corresponding eigenenergies

$$(4.99) \quad H|n\rangle = (E_n - \mu N_n) |n\rangle,$$

where we explicitly wrote the energy contribution from  $-\mu\hat{N}$ , namely  $-\mu N_n$ , in the grand canonical Hamiltonian  $H$ . Thus, we can evaluate

$$\begin{aligned} & \langle \{c_{\alpha,\sigma}(k, t), c_{\beta,\sigma}^\dagger(k)\} \rangle \\ &= \frac{1}{Z} \sum_{m,n} \left[ \langle n | e^{-\tilde{\beta}H} e^{iHt} c_{\alpha,\sigma}(k) e^{-iHt} |m\rangle \langle m | c_{\beta,\sigma}^\dagger(k) |n\rangle + \right. \\ (4.100) \quad & \left. + \langle n | e^{-\tilde{\beta}H} c_{\beta,\sigma}^\dagger(k) |m\rangle \langle m | e^{iHt} c_{\alpha,\sigma}(k) e^{-iHt} |n\rangle \right] \\ &= \frac{1}{Z} \sum_{m,n} \left[ e^{-\tilde{\beta}(E_n - \mu N_n)} \left( e^{-it(E_m - (N_n + 1)\mu - (E_n - N_n\mu))} \langle n | c_{\alpha,\sigma}(k) |m\rangle \langle m | c_{\beta,\sigma}^\dagger(k) |n\rangle + \right. \right. \\ (4.101) \quad & \left. \left. + e^{-it(E_n - N_n\mu - (E_m - (N_n - 1)\mu))} \langle n | c_{\beta,\sigma}^\dagger(k) |m\rangle \langle m | c_{\alpha,\sigma}(k) |n\rangle \right) \right]. \end{aligned}$$

This expression can be used to evaluate the Fourier transform of the retarded Green's function following the same steps as in eq. (4.14) to eq. (4.24). The result is the so-called *Lehmann representation* of the retarded Green's function

$$\begin{aligned} & G_{\alpha\beta,\sigma}^R(k, \omega) \\ (4.102) \quad &= \mathcal{F} [G_{\alpha\beta,\sigma}^R(k, \cdot)] (\omega) \\ &= \lim_{\epsilon \searrow 0} \frac{1}{Z} \sum_{m,n} \left[ \left( \frac{1}{\omega + i\epsilon - (E_m - E_n - \mu)} \langle n | c_{\alpha,\sigma}(k) |m\rangle \langle m | c_{\beta,\sigma}^\dagger(k) |n\rangle + \right. \right. \\ (4.103) \quad & \left. \left. + \frac{1}{\omega + i\epsilon - (E_n - E_m - \mu)} \langle n | c_{\beta,\sigma}^\dagger(k) |m\rangle \langle m | c_{\alpha,\sigma}(k) |n\rangle \right) e^{-\tilde{\beta}(E_n - \mu N_n)} \right]. \end{aligned}$$

Next, we can interchange the summation indices in the second line to obtain

$$(4.104) \quad G_{\alpha\beta,\sigma}^R(k, \omega) = \lim_{\epsilon \searrow 0} \frac{1}{Z} \sum_{m,n} \left( e^{-\tilde{\beta}(E_n - \mu N_n)} + e^{-\tilde{\beta}(E_m - \mu N_m)} \right) \left( \frac{\langle n | c_{\alpha,\sigma}(k) |m\rangle \langle m | c_{\beta,\sigma}^\dagger(k) |n\rangle}{\omega + i\epsilon - (E_m - E_n - \mu)} \right).$$

If we make use of the weak approximation for the Dirac distribution in eq. (4.20) we can identify the imaginary part of the retarded Green's function as

$$\begin{aligned} & \text{Im}(G_{\alpha\beta,\sigma}^R(k, \omega)) \\ (4.105) \quad &= \lim_{\epsilon \searrow 0} \frac{1}{Z} \sum_{m,n} \left( e^{-\tilde{\beta}(E_n - \mu N_n)} + e^{-\tilde{\beta}(E_m - \mu N_m)} \right) \left( \frac{-\epsilon \langle n | c_{\alpha,\sigma}(k) |m\rangle \langle m | c_{\beta,\sigma}^\dagger(k) |n\rangle}{(\omega - (E_m - E_n - \mu))^2 + \epsilon^2} \right) \\ &= -\frac{\pi}{Z} \sum_{m,n} \left[ \left( e^{-\tilde{\beta}(E_n - \mu N_n)} + e^{-\tilde{\beta}(E_m - \mu N_m)} \right) \times \right. \\ (4.106) \quad & \left. \times \langle n | c_{\alpha,\sigma}(k) |m\rangle \langle m | c_{\beta,\sigma}^\dagger(k) |n\rangle \delta(\omega - (E_m - E_n - \mu)) \right]. \end{aligned}$$

The matrix elements in eq. (4.106) tell us that

$$(4.107) \quad N_m = N_n + 1$$

while the Dirac distribution enforces

$$(4.108) \quad \omega = E_m - E_n - \mu.$$

Together, those two conservation laws can be used to simplify

$$(4.109) \quad \begin{aligned} & \text{Im}(G_{\alpha\beta,\sigma}^R(k, \omega)) \\ &= -\frac{\pi}{Z} \sum_{m,n} \left[ (1 + e^{-\tilde{\beta}\omega}) e^{-\tilde{\beta}(E_n - \mu N_n)} \times \right. \\ & \quad \left. \times \langle n | c_{\alpha,\sigma}(k) | m \rangle \langle m | c_{\beta,\sigma}^\dagger(k) | n \rangle \delta(\omega - (E_m - E_n - \mu)) \right]. \end{aligned}$$

At this point we are ready to define the *spectral function*

$$(4.110) \quad \begin{aligned} & A_{\alpha,\sigma}(k, \omega) \\ &:= \frac{2\pi}{Z} \sum_{m,n} (1 + e^{-\tilde{\beta}\omega}) e^{-\tilde{\beta}(E_n - \mu N_n)} |\langle n | c_{\alpha,\sigma}(k) | m \rangle|^2 \delta(\omega - (E_m - E_n - \mu)) \end{aligned}$$

$$(4.111) \quad = -2\text{Im}(G_{\alpha\alpha,\sigma}^R(k, \omega)).$$

In sec. 4.9 we will discuss the physical meaning and importance of this object but first we derive a relation between the spectral function in time space  $A_{\alpha,\sigma}(k, t)$  and the retarded Green's function  $G_{\alpha\alpha,\sigma}^R(k, t)$ . This relation is established via Fourier transformation,

$$(4.112) \quad \begin{aligned} & A_{\alpha,\sigma}(k, t) \\ &= \int_{-\infty}^{\infty} e^{-i\omega t} A_{\alpha,\sigma}(k, \omega) \frac{d\omega}{2\pi} \end{aligned}$$

$$(4.113) \quad = \frac{1}{Z} \sum_{m,n} e^{-i(E_m - E_n - \mu)t} \left[ e^{-\beta(E_n - \mu N_n)} + e^{-\beta(E_m - \mu N_m)} \right] |\langle n | c_{\alpha,\sigma}(k) | m \rangle|^2$$

$$(4.114) \quad = \frac{1}{Z} \sum_{m,n} \left[ e^{-\tilde{\beta}(E_n - \mu N_n)} + e^{-\tilde{\beta}(E_m - \mu N_m)} \right] \langle n | e^{iHt} c_{\alpha,\sigma}(k) e^{-iHt} | m \rangle \langle m | c_{\alpha,\sigma}^\dagger(k) | n \rangle$$

$$(4.115) \quad = \frac{1}{Z} \sum_n \langle n | e^{-\tilde{\beta}(E_n - \mu N_n)} \left\{ c_{\alpha,\sigma}(k, t), c_{\alpha,\sigma}^\dagger(k) \right\} | n \rangle$$

$$(4.116) \quad = \left\langle \left\{ c_{\alpha,\sigma}(k, t), c_{\alpha,\sigma}^\dagger(k) \right\} \right\rangle.$$

Therefore, we can write

$$(4.117) \quad G_{\alpha\alpha,\sigma}^R(k, t) = -iA_{\alpha,\sigma}(k, t)\theta(t).$$

Again, by the same steps as between eq. (4.14) and (4.24) we can relate the retarded Green's function  $G^R$  to the spectral function  $A(k, \omega)$  via

$$(4.118) \quad G_{\alpha\alpha,\sigma}^R(k, \omega) = \mathcal{F} [G_{\alpha\alpha,\sigma}^R(k, \cdot)] (\omega)$$

$$(4.119) \quad = -i\mathcal{F} [A_{\alpha,\sigma}(k, \cdot)\theta(\cdot)] (\omega)$$

$$(4.120) \quad = -i \int_{-\infty}^{\infty} A_{\alpha,\sigma}(k, \omega') \mathcal{F} [e^{-i\omega'\cdot}\theta(\cdot)] (\omega) \frac{d\omega'}{2\pi}$$

$$(4.121) \quad = \lim_{\epsilon \searrow 0} \int_{-\infty}^{\infty} \frac{A_{\alpha,\sigma}(k, \omega')}{\omega + i\epsilon - \omega'} \frac{d\omega'}{2\pi}$$

$$(4.122) \quad = -\lim_{\epsilon \searrow 0} \int_{-\infty}^{\infty} \frac{\text{Im}(G_{\alpha\alpha,\sigma}^R(k, \omega'))}{\omega + i\epsilon - \omega'} \frac{d\omega'}{\pi},$$

which is the so-called spectral representation of the retarded Green's function. Finally, we show that the spectral function  $A(k, \omega)$  is normalized:

$$(4.123) \quad \begin{aligned} & \int_{-\infty}^{\infty} \frac{d\omega}{2\pi} A_{\alpha, \sigma}(k, \omega) \\ &= \frac{1}{Z} \sum_{m, n} \left( e^{-\tilde{\beta}(E_n - \mu N_n)} + e^{-\tilde{\beta}(E_m - \mu N_m)} \right) \langle n | c_{\alpha, \sigma}(k) | m \rangle \langle m | c_{\alpha, \sigma}^\dagger(k) | n \rangle \end{aligned}$$

$$(4.124) \quad \begin{aligned} &= \frac{1}{Z} \sum_n e^{-\tilde{\beta}(E_n - \mu N_n)} \langle n | c_{\alpha, \sigma}(k) c_{\alpha, \sigma}^\dagger(k) | n \rangle \\ &+ \frac{1}{Z} \sum_m e^{-\tilde{\beta}(E_m - \mu N_m)} \langle m | c_{\alpha, \sigma}^\dagger(k) c_{\alpha, \sigma}(k) | m \rangle \end{aligned}$$

$$(4.125) \quad = \left\langle \left\{ c_{\alpha, \sigma}(k), c_{\alpha, \sigma}^\dagger(k) \right\} \right\rangle$$

$$(4.126) \quad = 1.$$

We will come back to the implications of this property.

**4.6.1. Matsubara Green's function.** Expanding periodic or anti-periodic functions in a Fourier series can be a useful tool to rewrite information about a function in terms of Fourier coefficients.

The definition of the Fourier series for the imaginary time Green's function  $G_{\alpha\beta, \sigma}$  defined on the domain  $(-\tilde{\beta}, \tilde{\beta})$  is

$$(4.127) \quad G_{\alpha\beta, \sigma}(k, i\tilde{\omega}_n) = \frac{1}{2} \int_{-\tilde{\beta}}^{\tilde{\beta}} e^{i\tilde{\omega}_n \tau} G_{\alpha\beta, \sigma}(k, \tau) d\tau$$

$$(4.128) \quad G_{\alpha\beta, \sigma}(k, \tau) = \frac{1}{\tilde{\beta}} \sum_{n=-\infty}^{\infty} e^{-i\tilde{\omega}_n \tau} G_{\alpha\beta, \sigma}(k, i\tilde{\omega}_n),$$

where  $\tilde{\omega}_n := \frac{2\pi n}{2\tilde{\beta}}$ .

The next step is simply imposing the anti-periodicity in imaginary time (eq. (4.51)) to obtain

$$(4.129) \quad G_{\alpha\beta, \sigma}(k, i\tilde{\omega}_n) = \frac{1}{2} \left[ \int_{-\tilde{\beta}}^0 e^{i\tilde{\omega}_n \tau} G_{\alpha\beta, \sigma}(k, \tau) d\tau + \int_0^{\tilde{\beta}} e^{i\tilde{\omega}_n \tau} G_{\alpha\beta, \sigma}(k, \tau) d\tau \right]$$

$$(4.130) \quad = \frac{1}{2} \left[ - \int_{-\tilde{\beta}}^0 e^{i\tilde{\omega}_n \tau} G_{\alpha\beta, \sigma}(k, \tau + \tilde{\beta}) d\tau + \int_0^{\tilde{\beta}} e^{i\tilde{\omega}_n \tau} G_{\alpha\beta, \sigma}(k, \tau) d\tau \right]$$

$$(4.131) \quad = \frac{1}{2} \left[ - \int_0^{\tilde{\beta}} e^{i\tilde{\omega}_n \tau} e^{i\tilde{\omega}_n \tilde{\beta}} G_{\alpha\beta, \sigma}(k, \tau) d\tau + \int_0^{\tilde{\beta}} e^{i\tilde{\omega}_n \tau} G_{\alpha\beta, \sigma}(k, \tau) d\tau \right]$$

$$(4.132) \quad = \frac{1}{2} (1 - (-1)^n) \left[ \int_0^{\tilde{\beta}} e^{i\tilde{\omega}_n \tau} G_{\alpha\beta, \sigma}(k, \tau) d\tau \right].$$

The prefactor of the integral is 1 if  $n$  is odd and 0 if  $n$  is even.

Skipping all even contributions is equivalent to restricting the frequency summations over  $\tilde{\omega}_n$  to a summation over the so-called Matsubara frequencies

$$(4.133) \quad \omega_n := \frac{(2n+1)\pi}{\tilde{\beta}}.$$

Thus, the final formulas for the Fourier series read

$$(4.134) \quad G_{\alpha\beta, \sigma}(k, i\omega_n) := \int_0^{\tilde{\beta}} e^{i\omega_n \tau} G_{\alpha\beta, \sigma}(k, \tau) d\tau,$$

$$(4.135) \quad G_{\alpha\beta,\sigma}(k, \tau) = \frac{1}{\tilde{\beta}} \sum_{n=-\infty}^{\infty} e^{-i\omega_n \tau} G_{\alpha\beta,\sigma}(k, i\omega_n),$$

where the Fourier coefficient  $G_{\alpha\beta,\sigma}(k, i\omega_n)$  is called Matsubara Green's function. Note that we write  $i\omega_n$  for the Matsubara frequencies which seems inconsistent to the imaginary time convention where the  $-i\tau$  is denoted by  $\tau$  in function arguments. This convention for the frequency domain is widely used and we also make use of it to make this thesis better comparable to the literature.

From the properties of the imaginary time Green's function  $G(\tau)$  we can easily deduce important properties of the Matsubara Green's function  $G(i\omega_n)$ .

PROPOSITION 4.6.1. *(i) The Matsubara Green's function  $G(i\omega_n)$  is related to its adjoint via*

$$(4.136) \quad G_{\alpha\beta,\sigma}(k, i\omega_n) = G_{\beta\alpha,\sigma}^*(k, -i\omega_n).$$

*(ii) The high-frequency behavior of the Matsubara Green's function  $G(i\omega_n)$  is given by*

$$(4.137) \quad G_{\alpha\beta,\sigma}(k, i\omega_n) = \frac{\delta_{\alpha,\beta}}{i\omega_n} + O\left(\left(\frac{1}{i\omega_n}\right)^2\right).$$

PROOF. (i) Since eq. (4.49) already shows the property in imaginary time  $\tau$  we only have to calculate

$$(4.138) \quad G_{\alpha\beta,\sigma}^*(k, i\omega_n) = \int_0^{\tilde{\beta}} e^{-i\omega_n \tau} G_{\alpha\beta,\sigma}^*(k, \tau) d\tau$$

$$(4.139) \quad = \int_0^{\tilde{\beta}} e^{-i\omega_n \tau} G_{\beta\alpha,\sigma}(k, \tau) d\tau$$

$$(4.140) \quad = G_{\beta\alpha,\sigma}(k, -i\omega_n).$$

(ii) To be able to expand  $G_{\alpha\beta,\sigma}(k, i\omega_n)$  in powers of  $\omega_n$  one has to start with the Fourier transformation to imaginary time and integrate by parts, i.e.

$$(4.141) \quad \begin{aligned} & G_{\alpha\beta,\sigma}(k, i\omega_n) \\ &= \int_{0^+}^{\beta+0^-} G_{\alpha\beta,\sigma}(k, \tau) e^{i\omega_n \tau} d\tau \end{aligned}$$

$$(4.142) \quad = \frac{-G_{\alpha\beta,\sigma}(k, \beta+0^-) - G_{\alpha\beta,\sigma}(k, 0^+)}{i\omega_n} - \int_{0^+}^{\beta+0^-} G'_{\alpha\beta,\sigma}(k, \tau) \frac{e^{i\omega_n \tau}}{i\omega_n} d\tau.$$

Iterating the integration by parts and taking advantage of the anti-periodicity of the Matsubara Green's function  $G$  (see eq. 4.51) gives

$$(4.143) \quad G_{\alpha\beta,\sigma}(k, i\omega_n) = \sum_{j \geq 0} (-1)^{j+1} \frac{G_{\alpha\beta,\sigma}^{(j)}(k, 0^+) - G_{\alpha\beta,\sigma}^{(j)}(k, 0^-)}{(i\omega_n)^{j+1}}.$$

In the case of  $\alpha = \beta$  the first term in this series is merely  $\frac{1}{\omega_n}$  since  $\{c_{\alpha,\sigma}^\dagger, c_{\beta,\sigma}\} = \delta_{\alpha,\beta}$  and hence

$$(4.144) \quad G_{\alpha\beta,\sigma}(k, i\omega_n) = \frac{\delta_{\alpha,\beta}}{i\omega_n} + O\left(\left(\frac{1}{i\omega_n}\right)^2\right).$$

□

EXAMPLE 4.6.2 (Non-interacting particles). We consider again the example 4.5.2 where we study non-interacting electrons on a lattice that are described by the Hamiltonian

$$(4.145) \quad H = \sum_k \underbrace{(\epsilon(k) - \mu)}_{=: \xi(k)} c^\dagger(k) c(k),$$

where  $\mu$  is the chemical potential and  $\epsilon$  is the dispersion relation. From the Heisenberg equation of motion we were able to find the time evolution of the annihilation operator

$$(4.146) \quad c(k, \tau) = e^{-\xi(k)\tau} c(k)$$

and the imaginary time Green's function

$$(4.147) \quad G(k, \tau) = -e^{-\xi(k)\tau} \{ [1 - f_{FD}(\xi(k))] \theta(\tau) - f_{FD}(\xi(k)) \theta(-\tau) \},$$

where we denote the Fermi-Dirac distribution function by

$$(4.148) \quad f_{FD}(\xi(k)) = \frac{1}{e^{\beta\xi(k)} + 1}.$$

In order to obtain the Matsubara Green's function we apply eq. (4.134) which yields

$$(4.149) \quad G(k, i\omega_n) = \int_0^{\tilde{\beta}} e^{i\omega_n\tau} G(k, \tau) d\tau$$

$$(4.150) \quad = - \int_0^{\tilde{\beta}} e^{i\omega_n\tau} \langle T_\tau (c(k, \tau) c^\dagger(k)) \rangle d\tau$$

$$(4.151) \quad = - \int_0^{\tilde{\beta}} e^{i\omega_n\tau} \langle c(k, \tau) c^\dagger(k) \rangle d\tau$$

$$(4.152) \quad = - \int_0^{\tilde{\beta}} e^{i\omega_n\tau} \langle e^{-\xi(k)\tau} c(k) c^\dagger(k) \rangle d\tau$$

$$(4.153) \quad = - \frac{1}{i\omega_n - \xi(k)} \left[ -e^{-\tilde{\beta}\xi(k)} - 1 \right] \langle c(k) c^\dagger(k) \rangle$$

$$(4.154) \quad = - \frac{1}{i\omega_n - \xi(k)} \left[ -e^{-\tilde{\beta}\xi(k)} - 1 \right] [1 - f_{FD}(\xi(k))]$$

$$(4.155) \quad = \frac{1}{i\omega_n - \xi(k)} \frac{e^{\tilde{\beta}\xi(k)} (e^{-\tilde{\beta}\xi(k)} + 1)}{1 + e^{\tilde{\beta}\xi(k)}}$$

$$(4.156) \quad = \frac{1}{i\omega_n - \xi(k)}.$$

Similarly, we obtain the retarded Green's function  $G^R(\omega)$  by Fourier transformation of the real-time Green's function

$$(4.157) \quad G^R(k, t) = -ie^{-i\xi(k)t} \theta(t)$$

from eq. (4.97). Using the same manipulations as in eqs. (4.14) to (4.24) we obtain

$$(4.158) \quad G^R(k, \omega) = \frac{1}{\omega - \xi(k)} - i\pi\delta(\omega - \xi(k)) = \lim_{\epsilon \searrow 0} \frac{1}{\omega + i\epsilon - \xi(k)}$$

via Fourier transformation.

We show a comparison of the real-frequency and imaginary frequency Green's function in fig. 4.3. For the purpose of illustration we choose dispersionless energies  $\xi(k) = \xi = -1, 0, 1$  eV. Moreover, we need to smooth the divergence of the Dirac distribution in eq. (4.158) and fix  $\epsilon = 0.1$  eV. This results in a broadening of the features in (a)-(c) but we can still recognize the peak of the imaginary part of the retarded Green's function at the energy eigenvalues. Moreover, we observe that the real part of  $G^R$  is

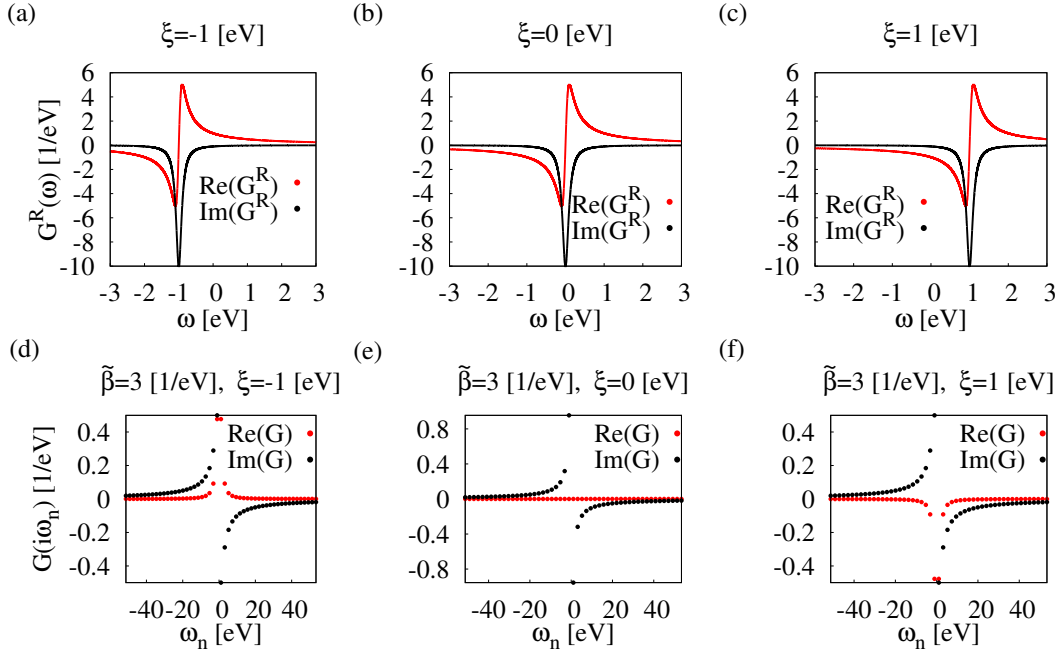


FIGURE 4.3. Real-frequency and imaginary frequency Green's function for the non-interacting system described by eq. (4.145) with constant energies  $\xi(k) = \xi$ . (a)-(c) show the retarded Green's function  $G^R(\omega)$  for  $\xi = -1, 0, 1\text{eV}$  respectively, where we introduce a smoothing term  $\epsilon = 0.1\text{eV}$  (see eq. (4.158)) to soften the divergence of the Dirac distribution  $\delta$ . Apart from the divergence of the imaginary part at the energy eigenvalues we see the symmetry/anti-symmetry of the imaginary/real part of  $G^R(\omega)$ . In (d)-(f) we present the retarded Green's function  $G(i\omega_n)$  at inverse temperature  $\tilde{\beta} = 3(\text{eV})^{-1}$  for  $\xi = -1, 0, 1\text{eV}$  respectively. In contrast to the real-frequency Green's function we see that the real part is symmetric while the imaginary part is anti-symmetric.

anti-symmetric while the imaginary part is symmetric around the energy eigenvalue. This is a special property of this simple model and not a general feature of the retarded Green's function.

For the Matsubara Green's function we have no divergences but we need to choose a temperature to evaluate the Matsubara frequencies. In (d)-(f) we show  $G(i\omega_n)$  at inverse temperature  $\tilde{\beta} = 3(\text{eV})^{-1}$  for the same energies as in (a)-(c). In contrast to the retarded Green's function, the symmetry properties of the Matsubara Green's function are always with respect to the origin and opposite to the ones of  $G^R$ : The imaginary part is anti-symmetric while the real part of  $G(i\omega_n)$  is symmetric. Finally, we observe that the imaginary part of the retarded Green's is directly connected to spectral properties of the system while those properties are hidden within the Matsubara Green's function. For this reason we will describe next the relation between those two Green's functions and why it makes sense to take the detour on the imaginary axis and calculate the spectral properties (on the real axis) afterwards.

## 4.7. RELATION BETWEEN RETARDED GREEN'S FUNCTION AND MATSUBARA GREEN'S FUNCTION

### 4.7. Relation between retarded Green's function and Matsubara Green's function

The central topic of this section is how to get from the Matsubara Green's function on the imaginary axis to the retarded Green's function on the real axis.

For an arbitrary function  $f$  this question has infinitely many answers since one can define any function piecewise and pick arbitrary functions for each axis. For example,

$$(4.159) \quad f(z) = \begin{cases} f_r(z) & z \in \mathbb{R} \\ f_i(\text{Im}(z)) & z \in i\mathbb{R} \setminus \{0\} \end{cases},$$

where  $f$  is a function with domain  $\mathbb{R} \cup i\mathbb{R}$  and  $f_r, f_i$  are arbitrary function on  $\mathbb{R}$ .

At this point it seems like there is no way to find the “right way” back to the real frequency axis but we have to remember how this whole idea of imaginary times and frequencies started. The first step was to extend the definition of the retarded Green's function to complex time arguments and this is where complex analysis is able to help resolve the problem of continuation from  $i\mathbb{R}$  to  $\mathbb{R}$ .

A fundamental theorem in complex analysis states that if we have an *analytic/holomorphic* function  $f$  defined on an open domain  $\emptyset \neq U \subset \mathbb{C}$  and if we have another analytic function  $g$  defined on a larger open connected domain  $V \supset U$  such that

$$(4.160) \quad g(z) = f(z) \quad \forall z \in U$$

then we know that  $g$  is uniquely determined by  $f$ .

Central to the whole argumentation is the property of analyticity and although Green's functions do not fall into the easy case of the above mentioned uniqueness theorem<sup>6</sup> we will still need the condition of analyticity. Starting point of this derivation is eq. (4.134) which relates the Matsubara Green's function with the imaginary time Green's function via

$$(4.161) \quad G_{\alpha\beta,\sigma}(k, i\omega_n) = \int_0^{\tilde{\beta}} e^{i\omega_n\tau} G_{\alpha\beta,\sigma}(k, \tau) d\tau$$

$$(4.162) \quad = - \int_0^{\tilde{\beta}} e^{i\omega_n\tau} \langle c_{\alpha,\sigma}(k, \tau) c_{\beta,\sigma}^\dagger(k) \rangle d\tau$$

$$(4.163) \quad = - \frac{1}{Z} \int_0^{\tilde{\beta}} e^{i\omega_n\tau} \text{tr} \left( e^{(\tau-\tilde{\beta})H} c_{\alpha,\sigma}(k) e^{-\tau H} c_{\beta,\sigma}^\dagger(k) \right) d\tau,$$

where we have used the explicit form of the Green's function (eq. (4.48)), the imaginary time evolution in eq. (4.44) and the thermal expectation value in eq. (4.36).

At this point we make use of the analyticity of the Green's function which is true as long as we stay away from the real axis. We rewrite the imaginary time integral as a contour integral in the complex time plane via  $\tau = it$ . This results in

$$(4.164) \quad G_{\alpha\beta,\sigma}(k, i\omega_n) = - \frac{i}{Z} \int_{\gamma_0} e^{-\omega_n t} \text{tr} \left( e^{(it-\tilde{\beta})H} c_{\alpha,\sigma}(k) e^{-itH} c_{\beta,\sigma}^\dagger(k) \right) dt,$$

where the contour  $\gamma_0$  is shown in fig. 4.4. In the case where the Matsubara frequencies are larger than zero,  $\omega_n > 0$ , we can deform  $\gamma_0$  all over the lower complex half-plane with non-negative real part  $\mathbb{H} := \{t \in \mathbb{C} \mid \text{Im}(t) \leq 0, \text{Re}(t) \geq 0\}$  –due to the exponentially decaying factors in eq. (4.164)– as long as we keep the end points of  $\gamma_0$  fixed<sup>7</sup>. We deform the contour  $\gamma_0$  into  $\gamma$  (see fig. 4.4) that is  $0 \rightarrow r - i0 \rightarrow r - i\tilde{\beta} \rightarrow -i\tilde{\beta}$  and where we take the limit  $r \rightarrow \infty$ . Thus,

$$G_{\alpha\beta,\sigma}(k, i\omega_n)$$

<sup>6</sup>This is because of the discontinuity of the Green's function on the real line (see prop. 4.5.1(v)).

<sup>7</sup>This is a special case of Cauchy's integral theorem.

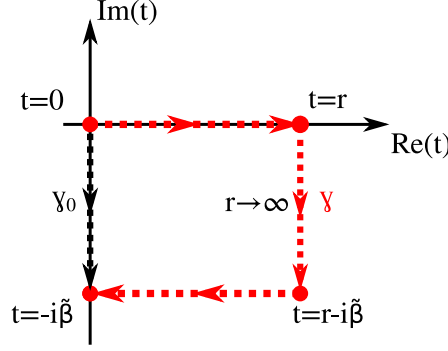


FIGURE 4.4. Integration contours  $\gamma_0$  and  $\gamma$  in the complex time plane that are considered in the evaluation of the Matsubara Green's function.

$$(4.165) \quad = -\frac{i}{Z} \int_{\gamma_0} e^{-\omega_n t} \text{tr} \left( e^{(it-\tilde{\beta})H} c_{\alpha,\sigma}(k) e^{-itH} c_{\beta,\sigma}^\dagger(k) \right) dt$$

$$(4.166) \quad = -i \int_{\gamma} e^{-\omega_n t} \left\langle e^{itH} c_{\alpha,\sigma}(k) e^{-itH} c_{\beta,\sigma}^\dagger(k) \right\rangle dt$$

$$(4.167) \quad = -i \lim_{r \rightarrow \infty} \int_0^r e^{-\omega_n x} \left\langle e^{ixH} c_{\alpha,\sigma}(k) e^{-ixH} c_{\beta,\sigma}^\dagger(k) \right\rangle dx$$

$$(4.168) \quad -i \lim_{r \rightarrow \infty} \int_0^{\tilde{\beta}} e^{-\omega_n(r-iy)} \left\langle e^{i(r-iy)H} c_{\alpha,\sigma}(k) e^{-i(r-iy)H} c_{\beta,\sigma}^\dagger(k) \right\rangle d(-iy)$$

$$(4.169) \quad -i \lim_{r \rightarrow \infty} \int_r^0 e^{-\omega_n(x-i\tilde{\beta})} \left\langle e^{i(x-i\tilde{\beta})H} c_{\alpha,\sigma}(k) e^{-i(x-i\tilde{\beta})H} c_{\beta,\sigma}^\dagger(k) \right\rangle dx.$$

While the term in line (4.168) vanishes because of the exponentially decaying term  $e^{-\omega_n r}$  we can use the definition of the Matsubara frequencies (see eq. (4.133)) and swap the integral boundaries to further simplify

$$(4.170) \quad G_{\alpha\beta,\sigma}(k, i\omega_n) = -i \int_0^\infty e^{-\omega_n x} \left\langle e^{ixH} c_{\alpha,\sigma}(k) e^{-ixH} c_{\beta,\sigma}^\dagger(k) \right\rangle dx \\ + i \int_0^\infty e^{-\omega_n x} \underbrace{e^{i(2n+1)\pi}}_{=-1} \left\langle e^{i(x-i\tilde{\beta})H} c_{\alpha,\sigma}(k) e^{-i(x-i\tilde{\beta})H} c_{\beta,\sigma}^\dagger(k) \right\rangle dx.$$

At this point we use the expression for the thermal average in the grand canonical ensemble (eq.(4.36)) and the cyclic property of the trace to get

$$(4.171) \quad G_{\alpha\beta,\sigma}(k, i\omega_n) = -i \int_0^\infty e^{-\omega_n x} \left\langle e^{ixH} c_{\alpha,\sigma}(k) e^{-ixH} c_{\beta,\sigma}^\dagger(k) \right\rangle dx \\ -i \frac{1}{Z} \int_0^\infty e^{-\omega_n x} \text{tr} \left( e^{-\tilde{\beta}H} e^{i(x-i\tilde{\beta})H} c_{\alpha,\sigma}(k) e^{-i(x-i\tilde{\beta})H} c_{\beta,\sigma}^\dagger(k) \right) dx$$

$$(4.172) \quad = -i \int_0^\infty e^{-\omega_n x} \left\langle e^{ixH} c_{\alpha,\sigma}(k) e^{-ixH} c_{\beta,\sigma}^\dagger(k) \right\rangle dx \\ -i \frac{1}{Z} \int_0^\infty e^{-\omega_n x} \text{tr} \left( e^{-\tilde{\beta}H} e^{-ixH} c_{\beta,\sigma}^\dagger(k) e^{ixH} c_{\alpha,\sigma}(k) \right) dx$$

$$(4.173) \quad = -i \int_0^\infty e^{-\omega_n x} \left\langle e^{ixH} c_{\alpha,\sigma}(k) e^{-ixH} c_{\beta,\sigma}^\dagger(k) \right\rangle dx \\ -i \int_0^\infty e^{-\omega_n x} \left\langle c_{\beta,\sigma}^\dagger(k) e^{ixH} c_{\alpha,\sigma}(k) e^{-ixH} \right\rangle dx$$

$$(4.174) \quad = -i \int_0^\infty e^{-\omega_n t} \left( \left\langle c_{\alpha,\sigma}(k, t) c_{\beta,\sigma}^\dagger(k) \right\rangle + \left\langle c_{\beta,\sigma}^\dagger(k) c_{\alpha,\sigma}(k, t) \right\rangle \right) dt$$

#### 4.7. RELATION BETWEEN RETARDED GREEN'S FUNCTION AND MATSUBARA GREEN'S FUNCTION

---

$$(4.175) \quad = \int_{-\infty}^{\infty} e^{i(i\omega_n)t} G_{\alpha\beta,\sigma}^R(k, t) dt$$

$$(4.176) \quad = G_{\alpha\beta,\sigma}^R(k, \omega) \Big|_{\omega \rightarrow i\omega_n}.$$

This results tells us that we can obtain the Matsubara Green's function  $G(i\omega_n)$  from the retarded Green's function  $G^R(\omega)$  via analytic continuation.

In applications we are usually interested in the opposite direction: Is it possible to construct the retarded Green's function from the Matsubara Green's function?

A simple example seems to provide a negative answer since given a Matsubara Green's function  $G(i\omega_n)$  we can multiply it by one in the form  $1 = 1 + 0 = 1 + e^{i\omega_n \tilde{\beta}} + 1$ . Therefore,  $G(i\omega_n)$  and  $G(i\omega_n)(1 + e^{i\omega_n \tilde{\beta}} + 1)$  are identical but they are not equal if interpret the functions as functions of complex numbers  $G(z)$  and  $G(z)(1 + e^{\tilde{\beta}z} + 1)$  in the case  $z \neq i\omega_n$ .

Fortunately, one can use a result from mathematical physics [120] which states that if (a)  $G(z)$  is analytic in the upper half-plane<sup>8</sup> and if (b)  $G(z)$  equals the Matsubara Green's function at  $z = i\omega_n$  and if (c)  $G(z)$  decays like

$$(4.177) \quad \lim_{|z(t)| \rightarrow \infty} G(z(t)) = 0,$$

where  $z(t)$  is the parameterization of a general straight line in the complex plane, then the analytic continuation in  $\mathbb{H}$  is unique and we have

$$(4.178) \quad G_{\alpha\beta,\sigma}^R(k, \omega) = \lim_{i\omega_n \rightarrow \omega + i0^+} G_{\alpha\beta,\sigma}(k, i\omega_n).$$

We are left to prove that the last condition (c) applies to the Green's function  $G(z)$ : First, we make use of the analyticity of  $G$  in the upper complex plane  $\mathbb{H}$  which allows us to make use of Cauchy's integral formula,

$$(4.179) \quad G_{\alpha\beta,\sigma}(k, z_0) = \frac{1}{2\pi i} \oint_{\gamma} \frac{G_{\alpha\beta,\sigma}(k, z)}{z - z_0} dz,$$

where  $\gamma$  is a counterclockwise oriented closed path and  $z_0 \in \mathbb{H}$  is in the interior of  $\gamma$ . We choose the contour as depicted in fig. 4.5, where  $\gamma$  follows a semicircle of radius  $r$  in the upper complex half-plane  $\mathbb{H}$  that encloses the imaginary time point  $z_0$ . In order

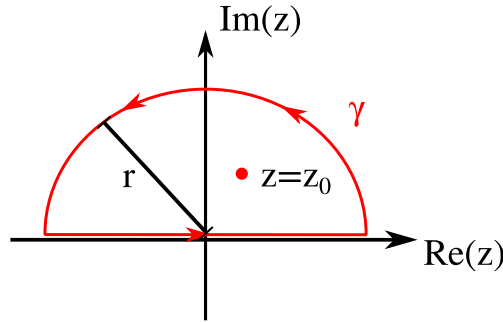


FIGURE 4.5. Integration contours  $\gamma$  in the complex frequency plane that is used in the calculation of Cauchy's integral formula (eq. (4.179)).

to stay in the analytic domain of  $G$  we shift the semicircle slightly above the real axis which leads to the expression

$$G_{\alpha\beta,\sigma}(k, z_0)$$

---

<sup>8</sup>We have already seen from eq. (4.164) and eq. (4.52) that the Green's function  $G(z)$  is anywhere analytic except for the real axis where it is discontinuous.

$$(4.180) \quad = \frac{1}{2\pi i} \lim_{\epsilon \searrow 0} \left( \int_{-r}^r \frac{G_{\alpha\beta,\sigma}(k, x + i\epsilon)}{x + i\epsilon - z_0} dx + \int_0^\pi \frac{G_{\alpha\beta,\sigma}(k, re^{i\phi} + i\epsilon)}{re^{i\phi} + i\epsilon - z_0} ire^{i\phi} d\phi \right).$$

From eq. (4.143) we see that  $G(z)$  decays like  $O\left(\frac{1}{z}\right)$  which allows us to neglect the second term in equation (4.180) in the limit  $r \rightarrow \infty$ .

Thus, we can evaluate the weak limit and identify the retarded Green's function in the integral kernel,

$$(4.181) \quad G_{\alpha\beta,\sigma}(k, z_0) = \frac{1}{2\pi i} \int_{-\infty}^{\infty} \frac{G_{\alpha\beta,\sigma}^R(k, \omega)}{\omega - z_0} d\omega.$$

This expression already reminds us of the spectral representation of the retarded Green's function in eq. (4.122). The remaining step to obtain the analogous representation for the Green's function  $G$  is to use the Kramers-Kronig relations

$$(4.182) \quad \operatorname{Re} [G(\omega + i0^+)] = \frac{1}{\pi} \text{p.v.} \int_{-\infty}^{\infty} \frac{\operatorname{Im} [G(\omega' + i0^+)]}{\omega' - \omega} d\omega'$$

$$(4.183) \quad \operatorname{Im} [G(\omega + i0^+)] = \frac{1}{\pi} \text{p.v.} \int_{-\infty}^{\infty} \frac{\operatorname{Re} [G(\omega' + i0^+)]}{\omega - \omega'} d\omega',$$

where p.v. is Cauchy's principle value. The shift into the upper complex plane  $\mathbb{H}$  with  $+i0^+$  is necessary to guarantee the analyticity of  $G$ . This leads to

$$(4.184) \quad G_{\alpha\beta,\sigma}(k, z_0) = \frac{1}{2\pi i} \int_{-\infty}^{\infty} \frac{G_{\alpha\beta,\sigma}^R(k, \omega)}{\omega - z_0} d\omega$$

$$(4.185) \quad = \frac{1}{2\pi i} \int_{-\infty}^{\infty} \frac{\operatorname{Re} [G_{\alpha\beta,\sigma}^R(k, \omega)]}{\omega - z_0} d\omega + \frac{1}{2\pi} \int_{-\infty}^{\infty} \frac{\operatorname{Im} [G_{\alpha\beta,\sigma}^R(k, \omega)]}{\omega - z_0} d\omega$$

$$(4.186) \quad = \frac{1}{2\pi^2 i} \int_{-\infty}^{\infty} \text{p.v.} \int_{-\infty}^{\infty} \frac{\operatorname{Im} [G_{\alpha\beta,\sigma}^R(k, \omega')]}{(\omega' - \omega)(\omega - z_0)} d\omega' d\omega +$$

$$+ \frac{1}{2\pi} \int_{-\infty}^{\infty} \frac{\operatorname{Im} [G_{\alpha\beta,\sigma}^R(k, \omega)]}{\omega - z_0} d\omega.$$

Now, we use contour integrals to obtain

$$(4.187) \quad \text{p.v.} \int_{-\infty}^{\infty} \frac{1}{(\omega' - \omega)(\omega - z_0)} d\omega = \lim_{\epsilon \searrow 0} \left( \int_{-\infty}^{\omega - \epsilon} \frac{1}{(\omega' - \omega)(\omega - z_0)} d\omega + \int_{\omega + \epsilon}^{\infty} \frac{1}{(\omega' - \omega)(\omega - z_0)} d\omega \right)$$

$$(4.188) \quad = \lim_{\epsilon \searrow 0} \left( \int_{-\infty}^{\omega - \epsilon} \frac{f(\omega)}{\omega - \omega'} d\omega + \int_{\omega + \epsilon}^{\infty} \frac{f(\omega)}{\omega - \omega'} d\omega \right)$$

$$(4.189) \quad = \lim_{\epsilon \searrow 0} \int_{\gamma_{r,\epsilon}} \frac{f(z)}{z - \omega'} dz - \lim_{\epsilon \searrow 0} \int_{\pi}^0 \frac{f(\omega' + \epsilon e^{i\phi})}{\epsilon e^{i\phi}} i\epsilon e^{i\phi} d\phi,$$

where we defined the function  $f(z) = \frac{1}{z_0 - z}$  and the contour  $\gamma_{r,\epsilon}$  is shown in fig. 4.6. The equality in line (4.189) holds because the half-circle segment of radius  $r$  does not contribute in the limit  $r \rightarrow \infty$ . By means of the residue theorem we obtain

$$(4.190) \quad \text{p.v.} \int_{-\infty}^{\infty} \frac{1}{(\omega' - \omega)(\omega - z_0)} d\omega = 2\pi i \operatorname{Res} \left( \frac{f(z)}{z - \omega'}, z_0 \right) + i\pi f(\omega')$$

$$(4.191) \quad = i\pi \frac{1}{z_0 - \omega'} + 2\pi i \frac{1}{\omega' - z_0}$$

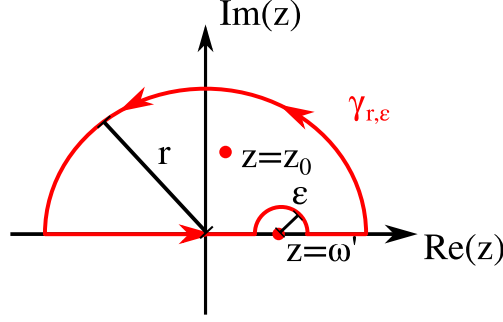


FIGURE 4.6. Contour that is needed to evaluate eq. (4.189).

$$(4.192) \quad = \frac{i\pi}{\omega' - z_0}.$$

With this result we can go back to eq. (4.186) and further calculate

$$(4.193) \quad G_{\alpha\alpha,\sigma}(k, z_0) = \frac{1}{2\pi} \int_{-\infty}^{\infty} \frac{\text{Im} [G_{\alpha\alpha,\sigma}^R(k, \omega')]}{\omega' - z_0} d\omega' + \frac{1}{2\pi} \int_{-\infty}^{\infty} \frac{\text{Im} [G_{\alpha\alpha,\sigma}^R(k, \omega)]}{\omega - z_0} d\omega$$

$$(4.194) \quad = -\frac{1}{2\pi} \int_{-\infty}^{\infty} \frac{A_{\alpha,\sigma}(k, \omega')}{\omega' - z_0} d\omega',$$

where we expressed the imaginary part of the retarded Green's function  $G^R$  by the spectral function  $A(k, \omega)$  (see eq. (4.111)).

Finally, we can deduce the limit behavior of  $G(z)$  from the generalized spectral representation in eq. (4.194) since the spectral function  $A(k, \omega)$  is normalized (see eq. (4.126)) and therefore

$$(4.195) \quad G(z) \sim \frac{1}{z} \xrightarrow{|z| \rightarrow \infty} 0.$$

In summary, we find a unique analytic continuation that relates the Matsubara Green's function  $G(i\omega_n)$  on the imaginary frequency axis to the retarded Green's function  $G^R(\omega)$  on the real frequency axis. This allows us to work in the Green's function representation on the imaginary axis and afterwards analytically continue onto the real axis via eq. (4.178) to obtain information about spectral properties.

In practice, we get the Matsubara Green's function only for a finite number of frequencies and we do not know the explicit dependence  $G = G(i\omega_n)$ . For this reason one has to make use of approximations that we explain in sec. 4.10.

#### 4.8. Non-interacting lattice Green's function

Before we tackle the problem of calculating the Green's function for interacting electrons we consider the important case of non-interacting electrons on a lattice in a paramagnetic state with time reversal and spin rotational symmetry. Such a system is described by the Hamiltonian

$$(4.196) \quad H^{kin} = \sum_{\alpha,\beta,\sigma,r_i,r_j} \left( t_{\alpha\beta}^{r_i-r_j} - \mu \delta_{r_i,r_j} \delta_{\alpha,\beta} \right) c_{\alpha,\sigma}^\dagger(r_i) c_{\beta,\sigma}(r_j)$$

$$(4.197) \quad = \frac{1}{N} \sum_{k,k',\alpha,\beta,\sigma,r_i,r_j} \left( t_{\alpha\beta}^{r_i-r_j} - \mu \delta_{r_i,r_j} \delta_{\alpha,\beta} \right) e^{ik \cdot r_i} c_{\alpha,\sigma}^\dagger(k) e^{-ik' \cdot r_j} c_{\beta,\sigma}(k'),$$

where  $t_{\alpha\beta}^{r_i-r_j}$  are all hoppings concerning the orbitals  $\alpha$  and  $\beta$  that are connected by lattice vectors  $r_i - r_j$ .

Now, we rewrite the expression in terms of center of position and relative position coordinates  $(r_i, r_j) \rightarrow (r_i - r_j, (r_i + r_j)/2) =: (r_{rel}, r_{cen})$  and get

$$(4.198) \quad H^{kin} = \frac{1}{N} \sum_{k, k', \alpha, \beta, \sigma, r_i, r_j} \left( t_{\alpha\beta}^{r_i - r_j} - \mu \delta_{r_i, r_j} \delta_{\alpha, \beta} \right) e^{ik \cdot r_i} c_{\alpha, \sigma}^\dagger(k) e^{-ik' \cdot r_j} c_{\beta, \sigma}(k')$$

$$(4.199) \quad = \frac{1}{N} \sum_{k', \alpha, \beta, \sigma, r_{rel}} \left( t_{\alpha\beta}^{r_{rel}} - \mu \delta_{r_{rel}, 0} \delta_{\alpha, \beta} \right) e^{ir_{rel} \cdot \frac{k+k'}{2}} \sum_{r_{cen}} e^{ir_{cen} \cdot (k'-k)} c_{\alpha, \sigma}^\dagger(k) c_{\beta, \sigma}(k')$$

$$(4.200) \quad = \sum_{k', \alpha, \beta, \sigma, r_{rel}} \left( t_{\alpha\beta}^{r_{rel}} - \mu \delta_{r_{rel}, 0} \delta_{\alpha, \beta} \right) \delta_{k, k'} e^{ir_{rel} \cdot (k+k')/2} c_{\alpha, \sigma}^\dagger(k) c_{\beta, \sigma}(k')$$

$$(4.201) \quad = \sum_{\alpha, \beta, \sigma, r_{rel}} \left( t_{\alpha\beta}^{r_{rel}} - \mu \delta_{r_{rel}, 0} \delta_{\alpha, \beta} \right) e^{ir_{rel} \cdot k} c_{\alpha, \sigma}^\dagger(k) c_{\beta, \sigma}(k).$$

We identify

$$(4.202) \quad H_{\alpha\beta, \sigma}^{kin}(k) := c_{\alpha, \sigma}^\dagger(k) \underbrace{\left( \sum_r t_{\alpha\beta}^r e^{ik \cdot r} - \mu \delta_{\alpha, \beta} \right)}_{=: h_{\alpha\beta}^{kin}(k)} c_{\beta, \sigma}(k).$$

Since the Hamiltonian is hermitian one finds a set of eigenvectors  $\{a_b(k)\}_{1 \leq b \leq N_{orb}}$  and corresponding eigenvalues  $\{\xi_b(k)\}_{1 \leq b \leq N_{orb}}$ , where  $b$  is the so-called band index and  $N_{orb}$  is the number of orbitals (or sites), that serve as a new basis, i.e.

$$(4.203) \quad h_{\sigma}^{kin}(k) := [a_1(k), \dots, a_{N_{orb}}(k)] \cdot \begin{bmatrix} \xi_1(k) & & \\ & \ddots & \\ & & \xi_{N_{orb}}(k) \end{bmatrix} \cdot [a_1(k), \dots, a_{N_{orb}}(k)]^\dagger.$$

Therefore, the eigenvectors  $\{a_b(k)\}_{1 \leq b \leq N_{orb}}$  are the ingredients for the transformation matrix from orbital- (or site-) to band-space and back.

We see an important property under inversion that is due to time-reversal symmetry, namely

$$(4.204) \quad a_b(-k) = a_b^*(k),$$

which can be seen from eq. (4.202) for the Hamiltonian since  $h_{\alpha\beta}^{kin}(-k) = h_{\alpha\beta}^{kin}(k)^*$ . Taking this together with the eigenspace decomposition (eq. (4.203)) we see that the eigenvectors  $\{a_b(k)\}_{1 \leq b \leq N_{orb}}$  get complex conjugated while the energy eigenvalues stay the same since they are real.

A similar calculation to the one performed in example 4.6.2 provides

$$(4.205) \quad c_{b, \sigma}(k, \tau) = e^{-\xi_b(k)\tau} c_{b, \sigma}(k),$$

which can be used to determine  $c_{\alpha, \sigma}(k, \tau)$  via

$$(4.206) \quad \partial_\tau c_{\alpha, \sigma}(k, \tau) = [H^{kin}(\tau), c_{\alpha, \sigma}(k, \tau)]$$

$$(4.207) \quad = \sum_{k', b', \sigma'} \xi_{b'}(k') \left[ c_{b', \sigma'}^\dagger(k', \tau) c_{b', \sigma'}(k', \tau), c_{\alpha, \sigma}(k, \tau) \right]$$

$$(4.208) \quad = \sum_{k', b', \sigma'} \xi_{b'}(k') \left[ c_{b', \sigma'}^\dagger(k', \tau) \{c_{b', \sigma'}(k', \tau), c_{\alpha, \sigma}(k, \tau)\} \right]$$

#### 4.8. NON-INTERACTING LATTICE GREEN'S FUNCTION

$$(4.209) \quad = - \sum_{k', b', \sigma'} \xi_{b'}(k') \{c_{b', \sigma'}^\dagger(k', \tau), \sum_b a_b^\alpha(k) c_{b, \sigma}(k, \tau)\} c_{b', \sigma'}(k', \tau)$$

$$(4.210) \quad = - \sum_b \xi_b(k) a_b^\alpha(k) c_{b, \sigma}(k, \tau)$$

$$(4.211) \quad \Rightarrow c_{\alpha, \sigma}(k, \tau) = \sum_b e^{-\xi_b(k)\tau} a_b^\alpha(k) c_{b, \sigma}(k)$$

$$(4.212) \quad = \sum_b a_b^\alpha(k) c_{b, \sigma}(k, \tau),$$

where we used the time-independence of the Hamiltonian  $H = H(\tau)$ . Now, we use this result (eq. (4.211)) and obtain the Matsubara Green's function

$$(4.213) \quad G_{\alpha\beta, \sigma}(k, i\omega_n) = \int_0^{\tilde{\beta}} e^{i\omega_n \tau} G_{\alpha\beta, \sigma}(k, \tau) d\tau$$

$$(4.214) \quad = - \int_0^{\tilde{\beta}} e^{i\omega_n \tau} \langle T_\tau c_{\alpha, \sigma}(k, \tau) c_{\beta, \sigma}^\dagger(k) \rangle d\tau$$

$$(4.215) \quad = - \int_0^{\tilde{\beta}} e^{i\omega_n \tau} \langle c_{\alpha, \sigma}(k, \tau) c_{\beta, \sigma}^\dagger(k) \rangle d\tau$$

$$(4.216) \quad = - \int_0^{\tilde{\beta}} e^{i\omega_n \tau} \left\langle \sum_b e^{-\xi_b(k)\tau} a_b^\alpha(k) c_{b, \sigma}(k) \sum_{b'} a_{b'}^\beta(k)^* c_{b', \sigma}^\dagger(k) \right\rangle d\tau$$

$$(4.217) \quad = - \sum_{b, b'} \frac{a_b^\alpha(k) a_{b'}^\beta(k)^*}{i\omega_n - \xi_b(k)} \left[ -e^{-\tilde{\beta}\xi_b(k)} - 1 \right] \langle c_{b, \sigma}(k) c_{b', \sigma}^\dagger(k) \rangle$$

$$(4.218) \quad = - \sum_{b, b'} \frac{a_b^\alpha(k) a_{b'}^\beta(k)^*}{i\omega_n - \xi_b(k)} \left[ -e^{-\tilde{\beta}\xi_b(k)} - 1 \right] [1 - f_{FD}(k)] \delta_{b, b'}$$

$$(4.219) \quad = \sum_b \frac{a_b^\alpha(k) a_b^\beta(k)^* e^{\tilde{\beta}\xi_b(k)} (e^{-\tilde{\beta}\xi_b(k)} + 1)}{i\omega_n - \xi_b(k) (1 + e^{\tilde{\beta}\xi_b(k)})}$$

$$(4.220) \quad = \sum_b \frac{a_b^\alpha(k) a_b^\beta(k)^*}{i\omega_n - \xi_b(k)}.$$

Clearly, we also see the property from the transformation of the set of eigenvectors  $\{a_b(k)\}_{1 \leq b \leq N_{\text{orb}}}$  (eq. (4.203)) under the constraint of time-reversal symmetry and paramagnetism, i.e.

$$(4.221) \quad G_{\alpha\beta, \sigma}(-k, i\omega_n) = G_{\beta\alpha, \sigma}(k, i\omega_n).$$

For completeness we present a different approach to determine the Matsubara Green's function by means of the equation of motion.

We start by explicit calculation the imaginary time derivative

$$(4.222) \quad - \frac{d}{d\tau} G_{\alpha\beta, \sigma}(k, \tau) \\ = \frac{d}{d\tau} \left[ \langle c_{\alpha, \sigma}(k, \tau) c_{\beta, \sigma}^\dagger(k) \rangle \theta(\tau) - \langle c_{\beta, \sigma}^\dagger(k) c_{\alpha, \sigma}(k, \tau) \rangle \theta(-\tau) \right] \\ = \delta(\tau) \langle c_{\alpha, \sigma}(k, \tau) c_{\beta, \sigma}^\dagger(k) + c_{\beta, \sigma}^\dagger(k) c_{\alpha, \sigma}(k, \tau) \rangle$$

$$(4.223) \quad + \left[ \left\langle \frac{d}{d\tau} c_{\alpha, \sigma}(k, \tau) c_{\beta, \sigma}^\dagger(k) \right\rangle \theta(\tau) - \left\langle c_{\beta, \sigma}^\dagger(k) \frac{d}{d\tau} c_{\alpha, \sigma}(k, \tau) \right\rangle \theta(-\tau) \right]$$

$$(4.224) \quad = \delta(\tau) \delta_{\alpha,\beta} + \left[ \left\langle [H, c_{\alpha,\sigma}(k, \tau)] c_{\beta,\sigma}^\dagger(k) \right\rangle \theta(\tau) - \left\langle c_{\beta,\sigma}^\dagger(k) [H, c_{\alpha,\sigma}(k, \tau)] \right\rangle \theta(-\tau) \right]$$

$$(4.225) \quad = \delta(\tau) \delta_{\alpha,\beta} + \left\langle T_\tau \left( [H, c_{\alpha,\sigma}(k, \tau)] c_{\beta,\sigma}^\dagger(k) \right) \right\rangle.$$

This time we express the time evolution of the annihilation operator in terms of the Hamiltonian matrix elements  $h_{\alpha\beta}^{kin}$  (eq. (4.201)) in orbital (site) space. Namely,

$$(4.226) \quad [H, c_{\alpha,\sigma}(k, \tau)] = \sum_{k', \nu, \beta, r, \sigma'} \left( t_{\nu\beta}^r e^{ik' \cdot r} - \mu \delta_{\nu,\beta} \right) \left[ c_{\nu,\sigma'}^\dagger(k', \tau) c_{\beta,\sigma'}(k', \tau), c_{\alpha,\sigma}(k, \tau) \right]$$

$$(4.227) \quad = \sum_{k', \nu, \beta, r, \sigma'} \left( t_{\nu\beta}^r e^{ik' \cdot r} - \mu \delta_{\nu,\beta} \right) \left( -c_{\beta}(k', \tau) \delta_{k,k'} \delta_{\alpha,\nu} \delta_{\sigma,\sigma'} \right)$$

$$(4.228) \quad = - \left( \sum_{\beta, r} t_{\alpha\beta}^r e^{ik' \cdot r} - \mu \delta_{\alpha,\beta} \right) c_{\beta,\sigma}(k, \tau)$$

$$(4.229) \quad = - \sum_{\beta} h_{\alpha\beta}^{kin}(k) c_{\beta,\sigma}(k, \tau).$$

Now, we use the equation of motion for the Green's function (eq. (4.225)) and calculate

$$(4.230) \quad - \frac{d}{d\tau} G_{\alpha\beta}(k, \tau) = \delta(\tau) \delta_{\alpha,\beta} - \sum_{\nu} h_{\alpha\nu}^{kin}(k) \left\langle T_\tau c_{\nu,\sigma}(k, \tau) c_{\beta,\sigma}^\dagger(k) \right\rangle$$

$$(4.231) \quad - \frac{d}{d\tau} G_{\alpha\beta,\sigma}(k, \tau) = \delta(\tau) \delta_{\alpha,\beta} + \sum_{\nu} h_{\alpha\nu}^{kin}(k) G_{\nu\beta,\sigma}(k, \tau).$$

Multiplying both sides with  $e^{i\omega_n \tau}$  and integrating afterwards over  $\tau$  in the interval  $(0, \beta)$  – which amounts to calculating the respective Fourier coefficients – yields

$$(4.232) \quad - \left[ e^{i\omega_n \tau} G_{\alpha\beta,\sigma}(k, \tau) \right]_{-0^+}^{\beta-0^+} + i\omega_n \int_0^\beta e^{i\omega_n \tau} G_{\alpha\beta,\sigma}(k, \tau) \\ = \delta_{\alpha,\beta} + \sum_{\nu} h_{\alpha\nu}^{kin}(k) G_{\nu\beta,\sigma}(k, i\omega_n),$$

where we used partial integration on the left-hand side. While the anti-periodicity of the imaginary time Green's function and the definition of the Matsubara frequencies are sufficient to treat the first term on the left-hand side, we identify the Matsubara Green's function in the remaining integral. Therefore, we obtain the final result

$$(4.233) \quad i\omega_n G_{\alpha\beta,\sigma}(k, i\omega_n) - \sum_{\nu} h_{\alpha\nu}^{kin}(k) G_{\nu\beta,\sigma}(k, i\omega_n) = \delta_{\alpha,\beta}$$

$$(4.234) \quad \left( i\omega_n \mathbb{I} - h^{kin}(k) \right) G(k, i\omega_n) = \mathbb{I}$$

$$(4.235) \quad G_{\alpha\beta,\sigma}(k, i\omega_n) = \left[ \left( i\omega_n \mathbb{I} - h^{kin}(k) \right)^{-1} \right]_{\alpha\beta,\sigma}.$$

#### 4.9. Green's functions and observables

In this section we show how to deduce physical observables from the Green's functions. While in some cases it is more convenient to express the observable in terms of the Matsubara Green's function, we will see cases where the retarded Green's function is more handy to use.

**4.9.1. Single-particle properties.** The easiest object that one can extract from the Green's function is the number of electrons per unit cell and orbital  $\langle n \rangle$  (filling) in the system and the respective spin-resolved orbital occupations  $\langle n_{\alpha,\sigma} \rangle$ ,

$$(4.236) \quad \langle n_{\alpha,\sigma} \rangle = \frac{1}{N} \sum_k \langle n_{\alpha,\sigma}(k) \rangle$$

$$(4.237) \quad = \frac{1}{N} \sum_k \langle c_{\alpha,\sigma}^\dagger(k) c_{\alpha,\sigma}(k) \rangle$$

$$(4.238) \quad = - \lim_{\tau \rightarrow 0^-} \frac{1}{N} \sum_k \langle T_\tau c_{\alpha,\sigma}(k, \tau) c_{\alpha,\sigma}^\dagger(k) \rangle$$

$$(4.239) \quad = \lim_{\tau \rightarrow 0^-} \frac{1}{N} \sum_k G_{\alpha\alpha,\sigma}(k, \tau)$$

$$(4.240) \quad = \frac{1}{\beta N} \lim_{\tau \rightarrow 0^-} \sum_k \sum_{n=-\infty}^{\infty} e^{-i\omega_n \tau} G_{\alpha\alpha,\sigma}(k, i\omega_n).$$

Note that the order of summation and limit are crucial here due to the  $O(1/\omega_n)$  slow decay of the Matsubara Green's function (see appendix B.1.1). From the orbital occupations one obtains the filling  $\langle n \rangle$  via

$$(4.241) \quad \langle n \rangle = \frac{1}{N_{\text{orb}}} \sum_{\alpha,\sigma} \langle n_{\alpha,\sigma} \rangle,$$

where  $N_{\text{orb}}$  is the number of orbitals.

In sec. 4.6 we defined the spectral weight  $A_{\alpha,\sigma}(k, \omega)$ , which was directly related to the imaginary part of the Green's function  $G^R$ .

A very successful and widely used technique that probes the electronic structure of a solid and more explicitly the spectral weight is the *angle-resolved photo-emission spectroscopy* (ARPES); for introductory literature see Refs. [121–125]. We remind here the basic principles following the previously cited references. Fundamental to ARPES measurements is the photoelectric effect that describes the emission of electrons due to absorption of photons by a crystal (see fig. 4.7). Measuring the momentum and

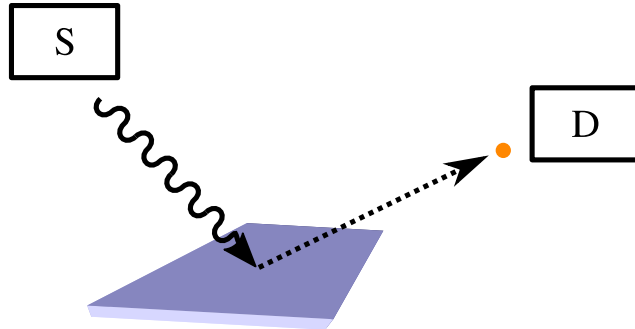


FIGURE 4.7. Basic setup of ARPES. Monochromatic light is emitted from a source  $S$  and hits the surface of a sample (purple). A photoelectron (orange) is emitted due to the photoelectric effect. By measuring the energy and momentum of the electron in the detector  $D$  one can reconstruct the spectral function  $A(k, \omega)$  of the sample.

energy of the free emitted photo-electrons and combining this with the photon wavelength of the light irradiating the sample one probes the spectral function  $A(k, \omega)$  (see

eq. (4.111)) which is the probability that excitations with momentum  $k$  and energy  $\omega$  are connected to eigenstates of the many-body system:

By taking advantage of momentum conservation<sup>9</sup> and energy conservation in this process one can use Fermi's golden rule among other approximations<sup>10</sup> to derive the photo-current

$$(4.242) \quad I(k, \omega) = C_k \int \int_{k-\delta k}^{k+\delta k} A(k', \omega') f_{FD}(\omega') R(\omega - \omega') dk' d\omega' + B,$$

where  $C_k$  is an intensity factor that is related to the dipole matrix element,  $R$  is a Gaussian energy resolution function of the photon monochromator and the electron detector. The small width  $\delta k$  accounts for the resolution in  $k$ -space and  $B$  is the so-called background which is due to extrinsic effects and deviations to the applied approximations. Thus, the measurement of the photo-current in eq.(4.242) allows<sup>11</sup> to extract the spectral function  $A(k, \omega)$ .

From the theoretical side one accesses the spectral function via the imaginary part of the retarded Green's function  $G^R$  (see eq. (4.111)). In numerical implementations of many-body methods it can be helpful to work on the Matsubara axis since a countable set of Matsubara Green's functions that decay as  $1/i\omega_n$  are easier to store and to sum than the continuous real axis Green's function. But working with Matsubara Green's function eventually necessitates analytic continuation to obtain the real axis Green's function  $G^R$  (see sec. 4.7 and analytic continuation 4.10).

In the case of independent electrons we already identified the spectral function  $A(\omega)$  with the density of states (see sec. 4.3). Introducing the Hubbard interaction between electrons the system cannot be diagonalized in terms Bloch waves anymore –  $k$  is not a good quantum number – and the lifetime of Bloch states becomes finite due to scattering processes between the electrons. This leads to the notion of *quasi-particles* where the original eigenstates represent renormalized (“interaction-weighted”) single-particle excitations with finite lifetime. Such quasi-particles have properties such as lifetimes, amplitudes and effective masses in addition to their unchanged spin, charge and momentum that appear naturally in the description of Fermi-liquid theory.

Note that the quasi-particle scattering rate close to the Fermi surface increases  $O(T^2)$  (see f.i. [126]), i.e. Fermi liquid theory is only applicable at sufficiently low temperatures because else it will impossible to identify quasi-particle states in the spectral function due to those thermal broadening effects.

All the above mentioned properties of quasi-particles are encoded in the spectral function  $A(k, \omega)$ .

The effect of the quasi-particle renormalization enters the Green's function in terms of the so-called *self-energy*  $\Sigma$ . Within sec. 5.1 we will formally introduce the self-energy and discuss its properties but for the moment will treat it as a complex (!) energy function that appears in the expression of the real axis Green's function as

$$(4.243) \quad G^R(k, \omega) = \left[ \omega - h^{kin}(k) - \Sigma(k, \omega) \right]^{-1},$$

which is why the self-energy can be interpreted as a correction to the kinetic part of the Hamiltonian  $h^{kin}$ .

For simplicity we will first restrict ourselves to the single-orbital case, where the matrix

<sup>9</sup>Only the momentum projection parallel to the sample surface is conserved because there is no translation invariance otherwise.

<sup>10</sup>F.i. the “sudden” approximation neglects interactions between the photo-hole and the emitted photo-electron, the independent particle-picture and the three-step model, where one assumes that the excitation of the photo-electron, its travel through the sample and the transmission into the vacuum are independent steps.

<sup>11</sup>For the details of this procedure we refer to literature cited at the beginning of this section.

inversion in eq. (4.243) reduces to a multiplicative inversion.

Thus, we can express the spectral function as

$$(4.244) \quad A(k, \omega) = -2\text{Im}G^R(k, \omega)$$

$$(4.245) \quad = \frac{-2\text{Im}\Sigma(k, \omega)}{(\omega - \xi(k) - \text{Re}\Sigma(k, \omega))^2 + (\text{Im}\Sigma(k, \omega))^2}.$$

Comparing this expression to the non-interacting result (momentum space version of eq. (4.24)),

$$(4.246) \quad A(k, \omega) = \delta(\xi(k) - \omega),$$

we observe that the self-energy introduces a broadening to the  $\delta$ -peak via the imaginary part of the self-energy  $\text{Im}\Sigma(k, \omega)$  and additional shifts to the Bloch eigenvalues  $\xi(k)$  via the real part of the self-energy  $\text{Re}\Sigma(k, \omega)$ .

The maxima/peaks<sup>12</sup> of the spectral function at fixed  $k$  are determined by solutions of the equation

$$(4.247) \quad f(k, \omega) := \omega - \xi(k) - \text{Re}\Sigma(k, \omega) = 0,$$

where the so-called *quasi-particle energies*  $\Xi(k)$  are the corresponding extremal points and thus fulfill the equation

$$(4.248) \quad \Xi(k) = \xi(k) + \text{Re}\Sigma(k, \Xi(k)).$$

The *quasi-particle weight*  $Z(k)$  is then defined as the inverse of the linear coefficient in the expansion of eq. 4.247 around  $\Xi(k)$ ,

$$(4.249) \quad \begin{aligned} & \omega - \xi(k) - \text{Re}\Sigma(k, \omega) \\ & = f(\Xi(k)) + \left. \frac{\partial f(k, \omega)}{\partial \omega} \right|_{\omega=\Xi(k)} (\omega - \Xi(k)) + O((\omega - \Xi(k))^2) \end{aligned}$$

$$(4.250) \quad = 0 + \underbrace{\left( 1 - \left. \frac{\partial \text{Re}\Sigma(k, \omega)}{\partial \omega} \right|_{\omega=\Xi(k)} \right)}_{=: Z(k)^{-1}} (\omega - \Xi(k)) + O((\omega - \Xi(k))^2).$$

Inserting this expansion into the expression for the spectral weight  $A(k, \omega)$  from eq. (4.245) we obtain

$$(4.251) \quad A(k, \omega) = \frac{-2\text{Im}\Sigma(k, \omega)}{Z(k)^{-2} (\omega - \Xi(k))^2 + (\text{Im}\Sigma(k, \omega))^2} + A^{inc}(k, \omega)$$

$$(4.252) \quad = 2 \frac{-Z(k)^2 \text{Im}\Sigma(k, \omega)}{(\omega - \Xi(k))^2 + (Z(k) \text{Im}\Sigma(k, \omega))^2} + A^{inc}(k, \omega),$$

where we absorb all contributions that go beyond the expansion around the quasi-particle peak into the term  $A^{inc}(k, \omega)$ . Before we discuss the meaning of each individual term we introduce the *quasi-particle scattering rate*<sup>13</sup>

$$(4.253) \quad \Gamma(k, \omega) := -Z(k) \text{Im}\Sigma(k, \omega),$$

which allows to rewrite the spectral function as

$$(4.254) \quad A(k, \omega) = 2\pi Z(k) \left[ \frac{1}{\pi} \frac{\Gamma(k, \omega)}{(\omega - \Xi(k))^2 + (\Gamma(k, \omega))^2} \right] + A^{inc}(k, \omega).$$

---

<sup>12</sup>We assumed here that such a solution exists and that the imaginary part is a smooth function of  $\omega$  and not too large.

<sup>13</sup>Within the real time Green's function  $G^R(k, t)$  the scattering rate appears as the factor in the exponential damping of the quasi-particle excitations,  $\exp(-\Gamma(k, \epsilon_k)t)$ ; see [30].

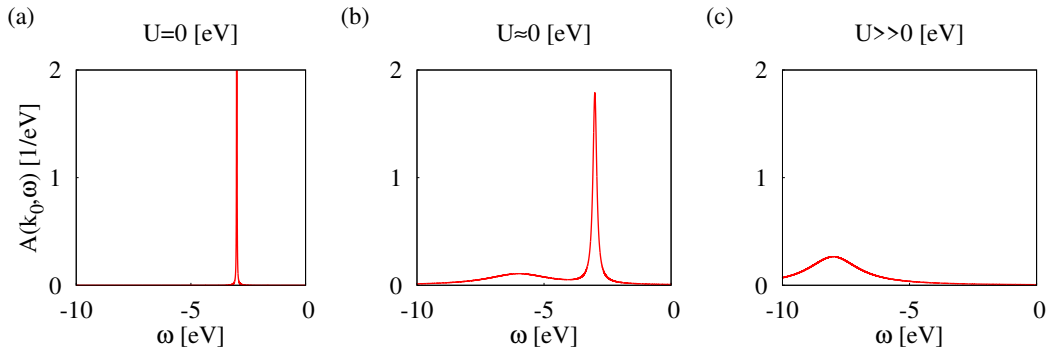


FIGURE 4.8. Spectral function  $A(k_0, \omega)$  at a fixed value of  $k = k_0$ . In the non-interacting case (a) we observe a true eigenstate at  $\omega = -3\text{eV}$  that is indicated by the  $\delta$ -peak at this energy. By turning on the interaction  $U$  the quasi-particle peak gets a finite height and broadens and a small amount of spectral weight is shifted to larger binding energies ( $\omega \lesssim -5\text{eV}$ ). At very large interaction strength (c) one observes the disappearance of the quasi-particle peak and all spectral weight is shifted into the satellite at  $\omega \lesssim -8\text{eV}$ .

We notice that the term in square brackets can be identified with the heat kernel (eq. (4.19)) if one assumes  $\Gamma(k, \omega) = \Gamma(k)$  and uses the fact<sup>14</sup> that the imaginary part of the self-energy is negative definite,  $\text{Im}\Sigma(k, \omega) < 0$ . This peak is centered around the quasi-particle energy  $\Xi(k)$  with a width of  $\Gamma(k, \omega)$  and a height of  $2Z(k)\Gamma(k, \omega)^{-1}$ . This motivates the naming *incoherent spectral weight*  $A^{inc}$  since the contributions can not be attributed to quasi-particle peak coherent excitations.

Due to the positivity and normalization of the heat kernel and the spectral weight (eq. (4.126)) to One and  $2\pi$  respectively we conclude

$$(4.255) \quad 0 \leq Z(k) \leq 1.$$

In fig. 4.8 we show schematically how the quasi-particle peak evolves with increasing Hubbard interaction  $U$ . In (a) we present the case where  $U = 0$  and the quasi-particle excitation corresponds to a true eigenstate of the system. Thus, we observe a  $\delta$ -peak at a given  $k$ -point. With increasing  $U$  we observe in (b) that the quasi-particle peak shrinks in height and gets broader while some spectral weight is shifted into a satellite feature at larger binding energies. Finally, at very large  $U$  (c) the quasi-particle peak disappears completely and the spectral weight is shifted into the incoherent spectral weight. Alternatively, one can interpret the diminishing quasi-particle weight  $Z(k)$  as a divergence of the so-called *effective mass*

$$(4.256) \quad m^* := m^0 Z(k)^{-1},$$

where  $m^0$  is the particle-mass in the non-interacting system.

We generalize the above results to multi-site/multi-orbital systems by restricting ourselves to low temperatures where we are basically interested in quasi-particle features on the Fermi surface. Under this assumption we define the quasi-particle energies  $\Xi_\alpha(k)$  as solutions of

$$(4.257) \quad \left| \omega - h^{kin}(k) - \text{Re}\Sigma(k, \omega) \right| = 0,$$

<sup>14</sup>This can be derived from the Lehmann representation of  $G^R$  and the Dyson equation by means of a linear algebra (see f.i. [110] Chap. 24.2). In the single-orbital case this is a consequence of the positivity of the spectral function  $A(k, \omega)$  (see eq. (4.245)).

#### 4.10. ANALYTIC CONTINUATION

---

where  $h^{kin}$  is the kinetic part of the Hamiltonian (see eq. (4.202)). Moreover, we define the *quasi-particle weight*

$$(4.258) \quad Z_\alpha(k) := \left( 1 - \frac{\partial \text{Re} \Sigma_{\alpha\alpha}(k, \omega)}{\partial \omega} \Big|_{\omega=0} \right)^{-1},$$

the *quasi-particle scattering rate*

$$(4.259) \quad \Gamma_\alpha(k, \omega) := -Z_\alpha(k) \text{Im} \Sigma_{\alpha\alpha}(k, \omega)$$

and the *quasi-particle effective mass (renormalization)*

$$(4.260) \quad \frac{m_\alpha^*}{m_\alpha^0} := 1 - \frac{\partial \text{Re} \Sigma_{\alpha\alpha}(k, \omega)}{\partial \omega} \Big|_{\omega=0}.$$

Since we are interested in evaluating derivatives of holomorphic functions (in the upper complex plane) we can make use of the Cauchy-Riemann differential equations

$$(4.261) \quad \frac{\partial \text{Re} f}{\partial x} = \frac{\partial \text{Im} f}{\partial y} \quad \text{and} \quad \frac{\partial \text{Re} f}{\partial y} = -\frac{\partial \text{Im} f}{\partial x},$$

where  $f$  is a holomorphic function in  $z = x + iy \in \mathbb{H}$ .

Thus, we can approximate

$$(4.262) \quad Z_\alpha(k) = \left( 1 - \frac{\partial \text{Im} \Sigma_{\alpha\alpha}(k, i\omega_n)}{\partial \omega_n} \Big|_{i\omega_n=0^+} \right)^{-1},$$

$$(4.263) \quad \Gamma_\alpha(k, 0) = -Z_\alpha(k) \text{Im} \Sigma_{\alpha\alpha}(k, i\omega_n \rightarrow 0),$$

where the limit  $i\omega_n \rightarrow 0$  corresponds to the limit of zero temperature. Note that the above appearing limits allow us to avoid analytic continuation of the Matsubara functions by means of extrapolation procedures. Those extrapolations in terms of polynomial fits to the Matsubara functions are discussed in the appendix B.1.3.

#### 4.10. Analytic continuation

Working in Matsubara space due to the numerical efficiency we are faced with the problem of analytic continuation to obtain the retarded Green's function from which we can extract physical observables (see sec. 4.7 and 4.9). Only a few properties can be directly accessed from the Matsubara Green's function if certain conditions are fulfilled (see appendix. B.1.3).

In sec. 4.7 we found out that we can uniquely and analytically continue the Matsubara Green's function from upper complex half-plane  $\mathbb{H}$  onto the real axis via

$$(4.264) \quad G_{\alpha\beta,\sigma}^R(k, \omega) = \lim_{i\omega_n \rightarrow \omega + i0^+} G_{\alpha\beta,\sigma}(k, i\omega_n).$$

A simple example for the non-interacting Green's function was provided in 4.6.2, where the analytic continuation is indeed the simple expression in eq. (4.264).

We remind ourselves of two important issues regarding the Green's function as function in the complex plane: First, the Green's function is analytic in the complex upper half-plane  $\mathbb{H}$  but discontinuous at the real axis. Second, by Cauchy's integral formula we were able to find a relation between the spectral function  $A_{\alpha,\sigma}(k, \omega)$  and the Green's function on  $\mathbb{H}$ ,

$$(4.265) \quad G_{\alpha\alpha,\sigma}(k, z_0) = -\frac{1}{2\pi} \int_{-\infty}^{\infty} \frac{A_{\alpha,\sigma}(k, \omega')}{\omega' - z_0} d\omega'.$$

The problem that we are facing in numerical analytic continuation consists of two issues.

The first and more severe problem is that our numerical procedure does not yield a closed analytic expression of the Green's function  $G_{\alpha\beta,\sigma}(k, i\omega_n)$  but a finite amount

of data points, namely the Matsubara Green's function for the first  $N_{mats}$  Matsubara frequencies. Thus, we cannot use the simple analytic continuation expression of eq. (4.264) but have to find approximate analytic continuation schemes.

The other issue that we are facing is the underlying numerical error in our data. In many applications one cannot guarantee full convergence of the calculations due to memory or computation time limitations. For this reason one needs an approximate analytic continuation methods that is stable against small errors in the input data.

Over the last decades a large set of tools was developed to deal with this problem, among which we find the Padé approximation [127, 128], the maximum entropy method [129–133], deconvolution procedures [134], singular value decomposition based algorithms [135], machine learning methods [136], sparse modeling approaches [137], and stochastic sampling techniques [138–143].

All the above methods have their advantages and drawbacks but in this section we will concentrate only on the Padé approximation because we expect the noise in our data to be negligible since the only constraint we have is sufficient resolution of the numerical objects which we can assure by increasing the number of  $k$ -points  $N$  and Matsubara frequencies  $N_{mats}$ . Therefore we can assume that the Padé approximation yields sufficiently accurate results.

**4.10.1. Padé approximation.** The fundamental idea of the Padé approximation is to approximate the complex analytic Green's function in terms of a finite continued fraction

$$(4.266) \quad \tilde{G}(z) := \frac{a_1}{1 + \frac{a_2(z - i\omega_1)}{1 + \dots + a_{N_{mats}}(z - i\omega_{N_{mats}-1})}},$$

where the coefficients  $a_1, \dots, a_{N_{mats}} \in \mathbb{C}$  are determined such that  $\tilde{G}(i\omega_n) = G(i\omega_n)$  for all  $n \in \{1, \dots, N_{mats}\}$ .

The coefficients can be computed recursively [144] which makes this analytic continuation technique very efficient.

On the other hand we have no way to control positivity of the imaginary part of the Green's function on the real axis and there is also no possibility to enforce normalization of the imaginary part of the Green's function.

In fig. 4.9 we show an example to demonstrate typical features that occur from Padé analytic continuation. While the qualitative agreement with the exact result (red curve) is convincing for both choices of numbers of Matsubara frequencies we observe that in the case where the number of Matsubara frequencies is large that not only the particle-hole symmetry is broken but also unphysical peaks appear at  $\omega \approx \pm 3\text{eV}$  (see (a)). Those features which remind us of typical overfitting errors disappear at a smaller number of Matsubara frequencies but the small wiggles around in the range  $1 < |\omega| < 3$  remain (see (b)).

In summary, we see that one has to be careful in interpreting peak structures in Padé data but the overall shape of the data can be reliable if the input data is not subject to large error sources.

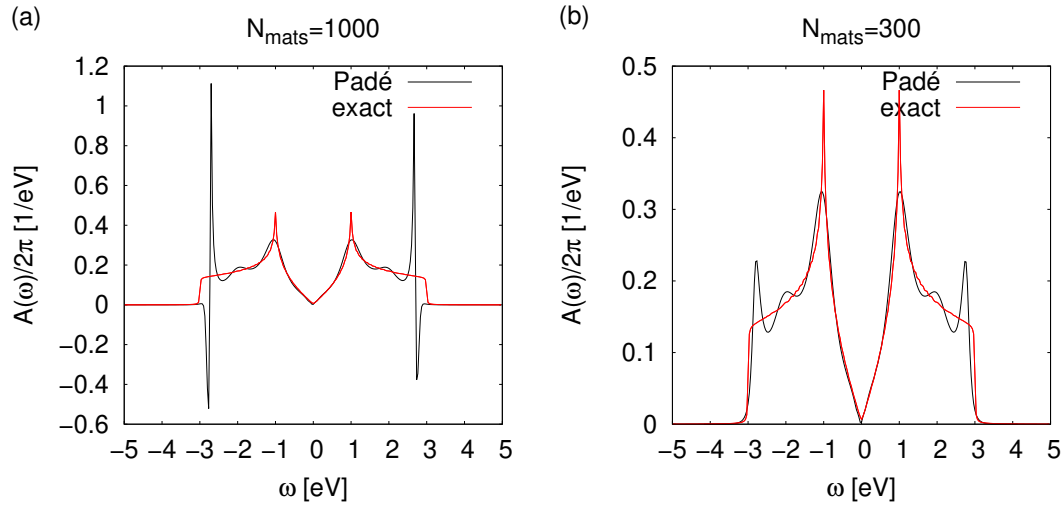


FIGURE 4.9. Analytical continuation of a Green's function via Padé approximation. We only present the spectral function obtained from the analytically continued Green's function. The red line represents the exact spectral function in this example. (a) When using a large number of Matsubara frequencies such as  $N_{mats} = 1000$  we observe peaks at  $\pm 3\text{eV}$  which are unphysical. (b) Such effects are not observed if one takes a smaller number of Matsubara frequencies,  $N_{mats} = 300$ , but the additional wiggles which are not present in the exact solution remain.

## Two-Particle Self-Consistent approach

In this chapter we develop a multi-orbital many-body approach for the Hubbard lattice model that we introduced earlier in chap. 3. The formalism is applied in the thermodynamic limit and to finite temperatures  $T$ .

The energy spectrum of the Hubbard model [64–66, 145] cannot be determined exactly in the general case. Therefore, a lot of effort has been invested to obtain good approximate solutions and many different approaches have been developed in the last six decades [88, 111, 112, 146–148].

The first approximate solutions of the Hubbard model were obtained from the Hartree-Fock approximation, the Hubbard-I approximation and the Gutzwiller variational wavefunction ansatz [64, 65, 149–151]. The Hartree-Fock approximation applied to the Hubbard model cannot account for non-local<sup>1</sup> and dynamical many-body effects such as finite quasi-particle lifetimes and mass renormalizations and provides accurate results only in the weak coupling limit (see Refs. [62] and [30]). The main issue is that the Hartree-Fock approximation for the Hubbard model is a static and local mean-field approximation. Therefore, its effect on the electronic band structure are restricted to orbital-dependent rigid shifts and it cannot account for electronic screening effects and non-local dynamical fluctuations that arise from electron-electron scattering processes (see also sec. 3.5).

It is obvious that for a good description of correlated materials within the Hubbard model the coupling between electrons and collective excitations – that is neglected both in the Hubbard-I and the Gutzwiller approach (see Ref. [61]) – must be taken account of.

In the following we will present an approach to the Hubbard model that takes both non-local and dynamical fluctuations into account while enforcing physical constraints such as the Mermin-Wagner theorem (see sec. 3.3) and certain local spin and charge sum rules. After introducing the Kadanoff-Baym formalism which is the framework of the Two-Particle Self-Consistent method (TPSC) we give an overview on related methods (sec. 5.2) and point out similarities and differences to TPSC. Finally, we present TPSC for the single-band (sec. 5.3), multi-site (sec. 5.4) and multi-orbital Hubbard model (sec. 5.6). In the case of the multi-site TPSC we present an application to organic superconductors in sec. 5.5 while the multi-orbital TPSC is studied in more detail chap. 6 and 7.

### 5.1. The Kadanoff-Baym formalism

This section is based on the script of A.-M. Tremblay [110] while we generalize the notation to multi-site problems similar to Ref. [152].

Starting point of our considerations is a lattice Hubbard model with multiple sites in the unit cell,

$$(5.1) \quad H = \sum_{\alpha,\beta,i,j,\sigma} \left( t_{\alpha,\beta}^{r_i-r_j} - \mu \delta_{\alpha,\beta} \delta_{i,j} \right) c_{\alpha,\sigma}^\dagger(r_i) c_{\beta,\sigma}(r_j) + \frac{1}{2} \sum_{\alpha,i,\sigma} U_\alpha n_{\alpha,\sigma}(r_i) n_{\alpha,-\sigma}(r_i),$$

<sup>1</sup>This statement is only true for local interactions on a lattice but otherwise the Hartree-Fock approximation is indeed a non-local approach.

## 5.1. THE KADANOFF-BAYM FORMALISM

---

where  $t_{\alpha,\beta}^{r_i-r_j}$  are the hopping amplitudes from site  $\alpha$  in the unit at position  $r_i$  and site  $\beta$  at unit cell  $r_j$ . Since we are interested in paramagnetic states only, we drop the spin index in the hopping elements  $t_{\alpha,\beta}^{r_i-r_j}$  due to time reversal and spin rotational invariance. The on-site Hubbard interaction is site-dependent and denoted by  $U_\alpha$ . The operator  $c_{\alpha,\sigma}(r_i)$  destroys an electron with spin  $\sigma$  at unit cell position  $r_i$  and site  $\alpha$  while the adjoint operator  $c_{\alpha,\sigma}^\dagger(r_i)$  creates an electron with spin  $\sigma$  at unit cell position  $r_i$  and site  $\alpha$ . The density operator  $n_{\alpha,\sigma}(r_i) := c_{\alpha,\sigma}^\dagger(r_i)c_{\alpha,\sigma}(r_i)$  measures the occupation of electrons at  $r_i$  and site  $\alpha$  with spin  $\sigma$ . We drop the implicit time-dependence of the Hamiltonian  $H$  in the notation.

As we discussed in sec. 3.2 the spectrum of this operator is known only in a few special cases and there is no general method that can be successfully applied over all temperature, filling, and interaction scales simultaneously. For this reason it is important to develop approximate methods which give accurate results in specific regions of the phase space.

In this thesis we are interested in approximate expressions for the Green's functions since we can deduce spectral properties (see sec. 4.9) from them and approximation schemes are easy to develop as we will see in this section.

**5.1.1. Motivation from statistical mechanics.** The Kadanoff-Baym approach [107, 113, 115, 116] that we are going to use in order to derive the Two-Particle Self-Consistent approach can be motivated from quantum statistical mechanics; more specifically, we consider the prototypical example from quantum statistical mechanics, where the magnetization in a system is determined in the presence of an external magnetic field.

We start from the grand canonical partition function

$$(5.2) \quad Z(h) = \text{tr} \left( e^{\tilde{\beta}H - hM} \right),$$

where  $H$  is the grand canonical Hamiltonian of the system and  $h$  is an external magnetic field that couples to the magnetization  $M$ .

The standard trick to obtain the thermal expectation value  $\langle M \rangle(h)$  as a function of the magnetic field  $h$  is via partial differentiation,

$$(5.3) \quad \frac{1}{\tilde{\beta}} \frac{\partial}{\partial h} \ln Z(h) = \frac{1}{Z(h)} \text{tr} \left( e^{-\tilde{\beta}(H-hM)} M \right) = \langle M \rangle(h).$$

One can even calculate higher order correlation function by taking higher order derivatives of the free energy, e.g.

$$(5.4) \quad \frac{1}{\tilde{\beta}^2} \frac{\partial^2}{\partial h^2} \ln Z(h) = \langle M^2 \rangle(h) - \langle M \rangle^2(h).$$

The above reminders on statistical mechanics suggest a similar approach to obtain the Green's function and higher order correlation functions because the Green's function is a thermal average of a special combination of a creation and an annihilation operator. The only difference that we will need to consider is that the magnetic field has to be replaced by some artificial field that couples to creation and annihilation operators.

**5.1.2. The functional derivative approach.** We introduce an artificial field  $\phi_{\alpha\beta,\sigma}(1,2)$  that depends on the sites  $\alpha, \beta$ , the coordinates  $1 := (r_1, \tau_1)$  and  $2 := (r_2, \tau_2)$ , and the spin  $\sigma$ .

This field is supposed to couple to the field operators and describes a perturbation to the Hamiltonian  $H$  in eq. (5.1).

We first consider the so-called *longitudinal particle-hole* channel where  $\phi$  couples equal spin creation and annihilation operators. Later, we will discuss the meaning of the

different channels in more detail and also include contributions from the *transversal particle-hole* channel where  $\phi$  couples opposite spin creation and annihilation operators (see sec. 5.1.9). In principle, there are also the so-called *particle-particle channel* and the *fully two-particle irreducible channel* but the fluctuations that are generated in those channel are usually negligible compared to the ones from the particle-hole channels except in the case where the Hubbard interaction  $U$  is attractive [153–155]. Thus, we will restrict ourselves to the particle-hole channels and start in the following with the longitudinal particle-hole channel.

The generalized partition function takes the form

$$(5.5) \quad Z[\phi] = \text{tr} \left[ e^{-\tilde{\beta}H} T_\tau e^{-\sum_{\alpha,\beta,\sigma} \int d(1) \int d(2) c_{\alpha,\sigma}^\dagger(1) \phi_{\alpha\beta,\sigma}(1,2) c_{\beta,\sigma}(2)} \right]$$

$$(5.6) \quad = \text{tr} \left[ e^{-\tilde{\beta}H} T_\tau e^{-c_{\bar{\alpha},\bar{\sigma}}^\dagger(\bar{1}) \phi_{\bar{\alpha}\bar{\beta},\bar{\sigma}}(\bar{1},\bar{2}) c_{\bar{\beta},\bar{\sigma}}(\bar{2})} \right]$$

$$(5.7) \quad = \text{tr} \left[ e^{-\tilde{\beta}H} T_\tau S[\phi] \right],$$

where we have introduced a short-hand notation for integrations and summation, i.e. bared symbols are summed or integrated over. Moreover, we defined the action

$$(5.8) \quad S[\phi] := e^{-c_{\bar{\alpha},\bar{\sigma}}^\dagger(\bar{1}) \phi_{\bar{\alpha}\bar{\beta},\bar{\sigma}}(\bar{1},\bar{2}) c_{\bar{\beta},\bar{\sigma}}(\bar{2})},$$

that stems from the artificial field  $\phi$ .

Obviously, one can recover the physics of the original system by setting the field  $\phi$  to zero but the advantages of such an artificial field become visible in the following steps. Within a time-ordered product of operators we can neglect possible  $\delta$ -functions from fermionic commutation relations. This helps us to evaluate the functional derivative of the form

$$(5.9) \quad T_\tau \frac{\delta \left( c_{\bar{\alpha},\bar{\sigma}}^\dagger(\bar{1}) \phi_{\bar{\alpha}\bar{\beta},\bar{\sigma}}(\bar{1},\bar{2}) c_{\bar{\beta},\bar{\sigma}}(\bar{2}) \right)^2}{\delta \phi_{\beta\alpha,\sigma'}(3,4)} = T_\tau c_{\beta,\sigma'}^\dagger(3) c_{\alpha,\sigma'}(4) \left( c_{\bar{\alpha},\bar{\sigma}}^\dagger(\bar{1}) \phi_{\bar{\alpha}\bar{\beta},\bar{\sigma}}(\bar{1}) c_{\bar{\beta},\bar{\sigma}}(\bar{1}) \right) \\ + T_\tau \left( c_{\bar{\alpha},\bar{\sigma}}^\dagger(\bar{1}) \phi_{\bar{\alpha}\bar{\beta},\bar{\sigma}}(\bar{1}) c_{\bar{\beta},\bar{\sigma}}(\bar{1}) \right) c_{\beta,\sigma'}^\dagger(3) c_{\alpha,\sigma'}(4)$$

$$(5.10) \quad = 2T_\tau \left( c_{\bar{\alpha},\bar{\sigma}}^\dagger(\bar{1}) \phi_{\bar{\alpha}\bar{\beta},\bar{\sigma}}(\bar{1}) c_{\bar{\beta},\bar{\sigma}}(\bar{1}) \right) c_{\beta,\sigma'}^\dagger(3) c_{\alpha,\sigma'}(4)$$

because we are always moving a pair of a creation and an annihilation operators which cancels the two appearing minus signs from the commutation relations. By induction we can generalize the above argument to arbitrary powers and get

$$(5.11) \quad T_\tau \frac{\delta S[\phi]}{\delta \phi_{\beta\alpha,\sigma'}(3,4)} = T_\tau \sum_{n=0}^{\infty} \frac{1}{n!} \frac{\delta}{\delta \phi_{\beta\alpha,\sigma'}(3,4)} \left( -c_{\bar{\alpha},\bar{\sigma}}^\dagger(\bar{1}) \phi_{\bar{\alpha}\bar{\beta},\bar{\sigma}}(\bar{1}) c_{\bar{\beta},\bar{\sigma}}(\bar{1}) \right)^n$$

$$(5.12) \quad = -T_\tau \sum_{n=1}^{\infty} \frac{1}{(n-1)!} \left( -c_{\bar{\alpha},\bar{\sigma}}^\dagger(\bar{1}) \phi_{\bar{\alpha}\bar{\beta},\bar{\sigma}}(\bar{1}) c_{\bar{\beta},\bar{\sigma}}(\bar{1}) \right)^{n-1} c_{\beta,\sigma'}^\dagger(3) c_{\alpha,\sigma'}(4)$$

$$(5.13) \quad = -T_\tau \sum_{n=0}^{\infty} \frac{1}{n!} \left( -c_{\bar{\alpha},\bar{\sigma}}^\dagger(\bar{1}) \phi_{\bar{\alpha}\bar{\beta},\bar{\sigma}}(\bar{1}) c_{\bar{\beta},\bar{\sigma}}(\bar{1}) \right)^n c_{\beta,\sigma'}^\dagger(3) c_{\alpha,\sigma'}(4)$$

$$(5.14) \quad = -S[\phi] c_{\beta,\sigma'}^\dagger(3) c_{\alpha,\sigma'}(4).$$

## 5.1. THE KADANOFF-BAYM FORMALISM

From this small exercise we can first define a generalized Green's function  $G(1, 2; [\phi]) =: G(1, 2)_\phi$  that appears naturally by functional derivation of  $\ln(Z)$  with respect to  $\phi$ ,

$$(5.15) \quad -\frac{\delta \ln(Z[\phi])}{\delta \phi_{\beta\alpha,\sigma}(2, 1)} = -\frac{1}{Z[\phi]} \frac{\delta Z[\phi]}{\delta \phi_{\beta\alpha,\sigma}(2, 1)}$$

$$(5.16) \quad = \frac{\left\langle T_\tau S[\phi] \frac{\delta(c_{\alpha,\sigma}^\dagger(\bar{1})\phi_{\alpha\bar{\beta},\bar{\sigma}}(\bar{1},\bar{2})c_{\bar{\beta},\bar{\sigma}}(\bar{2}))}{\delta \phi_{\beta\alpha,\sigma}(2,1)} \right\rangle}{\langle T_\tau S[\phi] \rangle}$$

$$(5.17) \quad = \frac{\left\langle T_\tau S[\phi] c_{\alpha,\sigma}^\dagger(\bar{1}) \delta_{\alpha,\beta} \delta_{\bar{\beta},\alpha} \delta_{\bar{\sigma},\sigma} \delta(\bar{1}-2) \delta(\bar{2}-1) c_{\bar{\beta},\bar{\sigma}}(\bar{2}) \right\rangle}{\langle T_\tau S[\phi] \rangle}$$

$$(5.18) \quad = \frac{\left\langle T_\tau S[\phi] c_{\beta,\sigma}^\dagger(2) c_{\alpha,\sigma}(1) \right\rangle}{\langle T_\tau S[\phi] \rangle}$$

$$(5.19) \quad = -\frac{\left\langle T_\tau S[\phi] c_{\alpha,\sigma}(1) c_{\beta,\sigma}^\dagger(2) \right\rangle}{\langle T_\tau S[\phi] \rangle}$$

$$(5.20) \quad =: G_{\alpha\beta,\sigma}(1, 2)_\phi,$$

where the Dirac delta function  $\delta(\bar{1}-2)$  is defined as  $\delta(\bar{r}_1 - r_2) \delta(\bar{\tau}_1 - \tau_2)$  which is consistent with the above described notation.

Later, we will also need higher order correlation functions like

$$(5.21) \quad \frac{\delta G_{\alpha\beta,\sigma}(1, 2)_\phi}{\delta \phi_{\gamma\epsilon,\sigma'}(3, 4)} = -\frac{\delta}{\delta \phi_{\gamma\epsilon,\sigma'}(3, 4)} \frac{\left\langle T_\tau S[\phi] c_{\alpha,\sigma}(1) c_{\beta,\sigma}^\dagger(2) \right\rangle}{\langle T_\tau S[\phi] \rangle}$$

$$(5.22) \quad = \frac{\left\langle T_\tau S[\phi] \frac{\delta(c_{\alpha,\sigma}^\dagger(\bar{1})\phi_{\alpha\bar{\beta},\bar{\sigma}}(\bar{1},\bar{2})c_{\bar{\beta},\bar{\sigma}}(\bar{2}))}{\delta \phi_{\gamma\epsilon,\sigma'}(3,4)} c_{\alpha,\sigma}(1) c_{\beta,\sigma}^\dagger(2) \right\rangle}{\langle T_\tau S[\phi] \rangle}$$

$$= \frac{\left\langle T_\tau S[\phi] c_{\alpha,\sigma}(1) c_{\beta,\sigma}^\dagger(2) \right\rangle \left\langle T_\tau S[\phi] \frac{\delta(c_{\alpha,\sigma}^\dagger(\bar{1})\phi_{\alpha\bar{\beta},\bar{\sigma}}(\bar{1},\bar{2})c_{\bar{\beta},\bar{\sigma}}(\bar{2}))}{\delta \phi_{\gamma\epsilon,\sigma'}(3,4)} \right\rangle}{\langle T_\tau S[\phi] \rangle^2}$$

$$(5.23) \quad = \frac{\left\langle T_\tau S[\phi] c_{\alpha,\sigma}(1) c_{\beta,\sigma}^\dagger(2) c_{\gamma,\sigma'}^\dagger(3) c_{\epsilon,\sigma'}(4) \right\rangle}{\langle T_\tau S[\phi] \rangle}$$

$$(5.24) \quad = \frac{\left\langle T_\tau S[\phi] c_{\alpha,\sigma}(1) c_{\beta,\sigma}^\dagger(2) \right\rangle \left\langle T_\tau S[\phi] c_{\gamma,\sigma'}^\dagger(3) c_{\epsilon,\sigma'}(4) \right\rangle}{\langle T_\tau S[\phi] \rangle^2}$$

$$(5.24) \quad = \left\langle c_{\alpha,\sigma}(1) c_{\beta,\sigma}^\dagger(2) c_{\gamma,\sigma'}^\dagger(3) c_{\epsilon,\sigma'}(4) \right\rangle_\phi + G_{\alpha\beta,\sigma}(1, 2)_\phi G_{\epsilon\gamma,\sigma'}(4, 3)_\phi,$$

where the subscript  $\langle \dots \rangle_\phi$  reminds us that the thermal average is taken with respect to the perturbed system.

**5.1.3. The Dyson equation.** To derive the Dyson equation which relates the Green's function of the non-interacting system  $G^0$  with the Green's function of the full interacting system  $G$  one has to start with the equation of motion for the annihilation operator  $c_{\nu,\sigma}(r_i, \tau)$ , i.e.

$$(5.25) \quad \frac{\partial c_{\nu,\sigma}(r_i, \tau)}{\partial \tau} = [H, c_{\nu,\sigma}(r_i, \tau)].$$



## 5.1. THE KADANOFF-BAYM FORMALISM

where we have used the product rule and the fact that  $T_\tau e^A e^B = T_\tau e^{A+B}$  that is valid only in special cases like

$$(5.36) \quad A = - \sum_{r_3} \int_{\tau_1}^{\beta} d\tau_3 c_{\alpha, \bar{\sigma}}^\dagger(3) \phi_{\alpha \bar{\beta}, \bar{\sigma}}(3, \bar{4}) c_{\bar{\beta}, \bar{\sigma}}(\bar{4}),$$

$$(5.37) \quad B = - \sum_{r'_3} \int_0^{\tau_1} d\tau'_3 c_{\alpha', \bar{\sigma}'}^\dagger(3') \phi_{\alpha' \bar{\beta}', \bar{\sigma}'}(3', \bar{4}') c_{\bar{\beta}', \bar{\sigma}'}(\bar{4}'),$$

because  $A$  commutes with  $B$ .

The time ordering in the last equation (eq. (5.35)) is still not complete since we have not ordered with respect to  $\tau_4$ ,  $\tau_2$  and for that reason we also keep the time ordering operator in the expectation values.

The reason why we performed this partial time ordering is that we can now commute  $T_\tau$  with  $\frac{\partial}{\partial \tau_1}$  since the expected ordering from  $\tau_4$  will have the same effect when commuted with  $c_{\nu, \sigma}(1)$  as if commuting without the time ordering operator because all operators that depend on  $\tau_4$  are also annihilation operators. Moreover, the time ordering with respect to  $\tau_2$  will obviously not effect the partial derivative  $\frac{\partial}{\partial \tau_1}$ . Thus, we further evaluate

$$(5.38) \quad \begin{aligned} \frac{\partial G_{\nu \xi, \sigma}(1, 2)_\phi}{\partial \tau_1} = & - \frac{1}{Z[\phi]} \left[ \left\langle T_\tau \frac{\partial}{\partial \tau_1} \left( e^{-\sum_{r_3} \int_{\tau_1}^{\beta} d\tau_3 c_{\alpha, \bar{\sigma}}^\dagger(3) \phi_{\alpha \bar{\beta}, \bar{\sigma}}(3, \bar{4}) c_{\bar{\beta}, \bar{\sigma}}(\bar{4})} c_{\nu, \sigma}(1) \times \right. \right. \right. \\ & \left. \left. \left. \times e^{-\sum_{r'_3} \int_0^{\tau_1} d\tau'_3 c_{\alpha', \bar{\sigma}'}^\dagger(3') \phi_{\alpha' \bar{\beta}', \bar{\sigma}'}(3', \bar{4}') c_{\bar{\beta}', \bar{\sigma}'}(\bar{4}')} \right) c_{\xi, \sigma}^\dagger(2) \right\rangle \Theta(\tau_1 - \tau_2) \right. \\ & - \left\langle T_\tau c_{\xi, \sigma}^\dagger(2) \frac{\partial}{\partial \tau_1} \left( e^{-\sum_{r_3} \int_{\tau_1}^{\beta} d\tau_3 c_{\alpha, \bar{\sigma}}^\dagger(3) \phi_{\alpha \bar{\beta}, \bar{\sigma}}(3, \bar{4}) c_{\bar{\beta}, \bar{\sigma}}(\bar{4})} \times \right. \right. \\ & \left. \left. \left. \times c_{\nu, \sigma}(1) e^{-\sum_{r'_3} \int_0^{\tau_1} d\tau'_3 c_{\alpha', \bar{\sigma}'}^\dagger(3') \phi_{\alpha' \bar{\beta}', \bar{\sigma}'}(3', \bar{4}') c_{\bar{\beta}', \bar{\sigma}'}(\bar{4}')} \right) \right\rangle \Theta(\tau_2 - \tau_1) \right] \\ & - \delta_{\nu, \xi} \delta(1 - 2). \end{aligned}$$

Within each of the two expectation values in the above equation that contain a partial time derivative  $\frac{\partial}{\partial \tau_1}$  we will get three contributions, namely two from the exponential functions and one from  $\frac{\partial c}{\partial \tau_1}$  (see eq. (5.28)). We evaluate the partial derivatives of the exponential functions in the following way:

$$(5.39) \quad \begin{aligned} & T_\tau \frac{\partial}{\partial \tau_1} e^{-\sum_{r_3} \int_{\tau_1}^{\beta} d\tau_3 c_{\alpha, \bar{\sigma}}^\dagger(3) \phi_{\alpha \bar{\beta}, \bar{\sigma}}(3, \bar{4}) c_{\bar{\beta}, \bar{\sigma}}(\bar{4})} \\ & = T_\tau \sum_{n=0}^{\infty} \frac{1}{n!} \frac{\partial}{\partial \tau_1} \left( - \sum_{r_3} \int_{\tau_1}^{\beta} d\tau_3 c_{\alpha, \bar{\sigma}}^\dagger(3) \phi_{\alpha \bar{\beta}, \bar{\sigma}}(3, \bar{4}) c_{\bar{\beta}, \bar{\sigma}}(\bar{4}) \right)^n \end{aligned}$$

$$(5.40) \quad \begin{aligned} & = T_\tau e^{-\sum_{r_3} \int_{\tau_1}^{\beta} d\tau_3 c_{\alpha, \bar{\sigma}}^\dagger(3) \phi_{\alpha \bar{\beta}, \bar{\sigma}}(3, \bar{4}) c_{\bar{\beta}, \bar{\sigma}}(\bar{4})} \times \\ & \times c_{\alpha'', \bar{\sigma}''}^\dagger(r''_3, \tau_1) \phi_{\alpha'' \bar{\beta}'', \bar{\sigma}''}(r''_3, \tau_1, \bar{4}'') c_{\bar{\beta}'', \bar{\sigma}''}(\bar{4}'') \end{aligned}$$

and analogously

$$\begin{aligned}
 & T_\tau \frac{\partial}{\partial \tau_1} e^{-\sum_{r'_3}^{\tau_1} \int_0^{\tau_1} d\tau'_3 c_{\alpha',\sigma'}^\dagger(3') \phi_{\alpha'\beta',\sigma'}(3',\bar{4}') c_{\beta',\sigma'}(\bar{4}')} \\
 &= -T_\tau e^{-\sum_{r'_3}^{\tau_1} \int_0^{\tau_1} d\tau'_3 c_{\alpha',\sigma'}^\dagger(3') \phi_{\alpha'\beta',\sigma'}(3',\bar{4}') c_{\beta',\sigma'}(\bar{4}')} \times \\
 (5.41) \quad & \times c_{\alpha'',\sigma''}^\dagger(\bar{r}_3'', \tau_1) \phi_{\alpha''\beta'',\sigma''}(\bar{r}_3'', \tau_1, \bar{4}'') c_{\beta'',\sigma''}(\bar{4}'').
 \end{aligned}$$

Putting all terms together we get

$$\begin{aligned}
 & \frac{\partial G_{\nu\xi,\sigma}(1,2)_\phi}{\partial \tau_1} \\
 &= -\frac{1}{Z[\phi]} \left[ \left\langle T_\tau e^{-\sum_{r_3}^{\beta} \int_{\tau_1}^{\beta} d\tau_3 c_{\alpha,\sigma}^\dagger(3) \phi_{\alpha\bar{\beta},\sigma}(3,\bar{4}) c_{\bar{\beta},\sigma}(\bar{4})} \times \right. \right. \\
 & \quad \times \left[ c_{\alpha'',\sigma''}^\dagger(\bar{r}_3'', \tau_1) \phi_{\alpha''\beta'',\sigma''}(\bar{r}_3'', \tau_1, \bar{4}'') c_{\beta'',\sigma''}(\bar{4}'') , c_{\nu,\sigma}(1) \right] \times \\
 & \quad \times e^{-\sum_{r'_3}^{\tau_1} \int_0^{\tau_1} d\tau'_3 c_{\alpha',\sigma'}^\dagger(3') \phi_{\alpha'\beta',\sigma'}(3',\bar{4}') c_{\beta',\sigma'}(\bar{4}')} c_{\xi,\sigma}^\dagger(2) \left. \right\rangle \Theta(\tau_1 - \tau_2) - \\
 & \quad - \left\langle T_\tau c_{\xi,\sigma}^\dagger(2) e^{-\sum_{r_3}^{\beta} \int_{\tau_1}^{\beta} d\tau_3 c_{\alpha,\sigma}^\dagger(3) \phi_{\alpha\bar{\beta},\sigma}(3,\bar{4}) c_{\bar{\beta},\sigma}(\bar{4})} \times \right. \\
 & \quad \times \left[ c_{\alpha'',\sigma''}^\dagger(\bar{r}_3'', \tau_1) \phi_{\alpha''\beta'',\sigma''}(\bar{r}_3'', \tau_1, \bar{4}'') c_{\beta'',\sigma''}(\bar{4}'') , c_{\nu,\sigma}(1) \right] \times \\
 & \quad \times e^{-\sum_{r'_3}^{\tau_1} \int_0^{\tau_1} d\tau'_3 c_{\alpha',\sigma'}^\dagger(3') \phi_{\alpha'\beta',\sigma'}(3',\bar{4}') c_{\beta',\sigma'}(\bar{4}')} \left. \right\rangle \Theta(\tau_2 - \tau_1) \Big] \\
 & - \frac{1}{Z[\phi]} \left[ \left\langle T_\tau \frac{\partial c_{\nu,\sigma}(1)}{\partial \tau_1} c_{\xi,\sigma}^\dagger(2) S[\phi] \right\rangle \Theta(\tau_1 - \tau_2) \right. \\
 & \quad \left. - \left\langle T_\tau c_{\xi,\sigma}^\dagger(2) \frac{\partial c_{\nu,\sigma}(1)}{\partial \tau_1} S[\phi] \right\rangle \Theta(\tau_2 - \tau_1) \right] \\
 (5.42) \quad & - \delta_{\nu,\xi} \delta(1-2) \\
 &= \frac{1}{Z[\phi]} \left[ \left\langle T_\tau e^{-\sum_{r_3}^{\beta} \int_{\tau_1}^{\beta} d\tau_3 c_{\alpha,\sigma}^\dagger(3) \phi_{\alpha\bar{\beta},\sigma}(3,\bar{4}) c_{\bar{\beta},\sigma}(\bar{4})} \phi_{\nu\beta'',\sigma}(1, \bar{4}'') c_{\beta'',\sigma}(\bar{4}'') \times \right. \right. \\
 & \quad \times e^{-\sum_{r'_3}^{\tau_1} \int_0^{\tau_1} d\tau'_3 c_{\alpha',\sigma'}^\dagger(3') \phi_{\alpha'\beta',\sigma'}(3',\bar{4}') c_{\beta',\sigma'}(\bar{4}')} c_{\xi,\sigma}^\dagger(2) \left. \right\rangle \Theta(\tau_1 - \tau_2) \\
 & \quad - \left\langle T_\tau c_{\xi,\sigma}^\dagger(2) e^{-\sum_{r_3}^{\beta} \int_{\tau_1}^{\beta} d\tau_3 c_{\alpha,\sigma}^\dagger(3) \phi_{\alpha\bar{\beta},\sigma}(3,\bar{4}) c_{\bar{\beta},\sigma}(\bar{4})} \phi_{\nu\beta'',\sigma}(1, \bar{4}'') c_{\beta'',\sigma}(\bar{4}'') \times \right. \\
 & \quad \times e^{-\sum_{r'_3}^{\tau_1} \int_0^{\tau_1} d\tau'_3 c_{\alpha',\sigma'}^\dagger(3') \phi_{\alpha'\beta',\sigma'}(3',\bar{4}') c_{\beta',\sigma'}(\bar{4}')} \left. \right\rangle \Theta(\tau_2 - \tau_1) \Big]
 \end{aligned}$$

$$(5.43) \quad - \left\langle \frac{\partial c_{\nu,\sigma}(1)}{\partial \tau_1} c_{\xi,\sigma}^\dagger(2) \right\rangle_\phi - \delta_{\nu,\xi} \delta(1-2),$$

where we have used the commutation relation in equation (5.32). Recombining the exponential functions and inserting the equation of motion of the annihilation operator  $c_{\nu,\sigma}(1)$  (eq. (5.28)) gives the final result

$$(5.44) \quad \begin{aligned} \frac{\partial G_{\nu\xi,\sigma}(1,2)_\phi}{\partial \tau_1} &= - \phi_{\nu\bar{\beta},\sigma}(1,\bar{3}) G_{\bar{\beta}\xi,\sigma}(\bar{3},2)_\phi \\ &+ \sum_{\beta} \left( t_{\nu\beta}^{r_1-\bar{r}_3} - \mu \delta_{r_1,\bar{r}_3} \delta_{\nu,\beta} \right) \delta(\tau_1 - \bar{\tau}_3) G_{\beta\xi,\sigma}(\bar{3},2)_\phi \\ &+ U_\nu \left\langle T_\tau c_{\nu,-\sigma}^\dagger(1^+) c_{\nu,-\sigma}(1) c_{\nu,\sigma}(1) c_{\xi,\sigma}^\dagger(2) \right\rangle \\ &- \delta(1-2) \delta_{\nu,\xi}. \end{aligned}$$

Rewriting the equation of motion for the Green's function (eq. (5.44)) such that the kinetic term and partial time derivative are on one side we get

$$(5.45) \quad \begin{aligned} &\left[ -\delta'(\tau_1 - \bar{\tau}_3) \delta_{r_1,\bar{r}_3} \delta_{\nu,\beta} - \left( t_{\nu\beta}^{r_1-\bar{r}_3} - \mu \delta_{r_1,\bar{r}_3} \delta_{\nu,\beta} \right) \delta(\tau_1 - \bar{\tau}_3) \right] G_{\bar{\beta}\xi,\sigma}(\bar{3},2)_\phi \\ &= U_\nu \left\langle T_\tau c_{\nu,-\sigma}^\dagger(1^+) c_{\nu,-\sigma}(1) c_{\nu,\sigma}(1) c_{\xi,\sigma}^\dagger(2) \right\rangle \\ &- \delta(1-2) \delta_{\nu,\xi} - \phi_{\nu\bar{\beta},\sigma}(1,\bar{3}) G_{\bar{\beta}\xi,\sigma}(\bar{3},2)_\phi. \end{aligned}$$

In the limit of no interaction and no external field  $\phi$  we can identify the inverse non-interacting Green's function

$$(5.46) \quad [(G^0)^{-1}]_{\nu\beta}(1,2) = \delta'(\tau_1 - \tau_2) \delta_{r_1,r_2} \delta_{\nu,\beta} + \left( t_{\nu\beta}^{r_1-r_2} - \mu \delta_{r_1,r_2} \delta_{\nu,\beta} \right) \delta(\tau_1 - \tau_2),$$

where the spin index naturally disappears due to our assumption of spin rotational invariance and the system being in a paramagnetic state. This step allows us now to write the equation of motion for the Green's function as

$$(5.47) \quad \left\{ [(G^0)^{-1}]_{\nu\bar{\beta}}(1,\bar{3}) - \phi_{\nu\bar{\beta},\sigma}(1,\bar{3}) - \Sigma_{\nu\bar{\beta},\sigma}(1,\bar{3})_\phi \right\} G_{\bar{\beta}\xi,\sigma}(\bar{3},2)_\phi = \delta(1-2) \delta_{\nu,\xi},$$

where we have implicitly defined the so-called *self-energy*

$$(5.48) \quad \Sigma_{\nu\bar{\beta},\sigma}(1,\bar{3})_\phi G_{\bar{\beta}\xi,\sigma}(\bar{3},2)_\phi = -U_\nu \left\langle T_\tau c_{\nu,-\sigma}^\dagger(1^+) c_{\nu,-\sigma}(1) c_{\nu,\sigma}(1) c_{\xi,\sigma}^\dagger(2) \right\rangle_\phi,$$

which absorbs all interaction effects that make the difference between the non-interacting Green's function  $G^0$  and the interacting Green's function  $G$ .

In the end, this allows us to rewrite the equation of motion in the form of the Dyson equation

$$(5.49) \quad [G^{-1}]_{\nu\xi,\sigma}(1,2)_\phi = [(G^0)^{-1}]_{\nu\xi}(1,2) - \phi_{\nu\xi,\sigma}(1,2) - \Sigma_{\nu\xi,\sigma}(1,2)_\phi,$$

which can be obtained by multiplying eq. (5.48) with  $[G^{-1}]_{\bar{\xi}\xi,\sigma}(\bar{2},2)_\phi$  that involves an integration of all internal degrees of freedom by the overline convention.

From now on, we are interested in finding an accurate approximation for the self-energy since by the Dyson equation we can obtain the full Green's function from this object.

**5.1.4. A self-consistent equation for the generalized susceptibility.** So far, we only have an implicit equation for the self-energy (eq. (5.48)) but the right-hand side of the equation is already known from the higher order derivative (eq. (5.24)) and therefore we can rewrite

$$\Sigma_{\alpha\bar{\beta},\sigma}(1,\bar{4})_\phi G_{\bar{\beta}\gamma,\sigma}(\bar{4},2)_\phi$$

$$(5.50) \quad = -U_\alpha \left\langle T_\tau c_{\alpha,-\sigma}^\dagger(1^+) c_{\alpha,-\sigma}(1) c_{\alpha,\sigma}(1) c_{\gamma,\sigma}^\dagger(2) \right\rangle_\phi$$

$$(5.51) \quad = U_\alpha \left( -\frac{\delta G_{\alpha\gamma,\sigma}(1,2)}{\delta \phi_{\alpha\alpha,-\sigma}(1^+,1)} + G_{\alpha\alpha,-\sigma}(1,1^+)_\phi G_{\alpha\gamma,\sigma}(1,2)_\phi \right).$$

The functional derivative that appears on the right-hand side of eq. (5.51) is a so-called *generalized susceptibility*

$$(5.52) \quad \chi := -\frac{\delta G}{\delta \phi}$$

and we will see later how it connects to ordinary spin and charge susceptibilities. Before we do that we derive the Bethe-Salpeter equation which is a self-consistent equation for generalized susceptibilities. The Bethe-Salpeter equation allows later us to determine the generalized susceptibility and thus to evaluate the self-energy by means of the implicit equation (5.51).

We start with the identity

$$(5.53) \quad \delta(1-2)\delta_{\alpha,\gamma} = G_{\alpha\bar{\beta},\sigma}(1,\bar{3})_\phi G_{\bar{\beta}\gamma,\sigma}^{-1}(\bar{3},2)_\phi$$

and perform a functional differentiation with respect to  $\phi$  on both sides which yields

$$(5.54) \quad 0 = \frac{\delta G_{\alpha\bar{\beta},\sigma}(1,\bar{3})_\phi}{\delta \phi_{\nu\epsilon,\sigma'}(4,5)} G_{\bar{\beta}\gamma,\sigma}^{-1}(\bar{3},2)_\phi + G_{\alpha\bar{\beta},\sigma}(1,\bar{3})_\phi \frac{\delta G_{\bar{\beta}\gamma,\sigma}^{-1}(\bar{3},2)_\phi}{\delta \phi_{\nu\epsilon,\sigma'}(4,5)}.$$

Multiplying by  $G_{\bar{\gamma}\zeta,\sigma}(\bar{2},6)$  and integrating over the internal degrees of freedom gives

$$(5.55) \quad \frac{\delta G_{\alpha\bar{\beta},\sigma}(1,\bar{3})_\phi}{\delta \phi_{\nu\epsilon,\sigma'}(4,5)} \delta_{\bar{\beta},\zeta} \delta(\bar{3}-6) = -G_{\alpha\bar{\beta},\sigma}(1,\bar{3})_\phi \frac{\delta G_{\bar{\beta}\gamma,\sigma}^{-1}(\bar{3},\bar{2})_\phi}{\delta \phi_{\nu\epsilon,\sigma'}(4,5)} G_{\bar{\gamma}\zeta,\sigma}(\bar{2},6)$$

Now, we use the Dyson equation (eq. 5.49) to simplify the functional derivative on the right-hand to obtain

$$(5.56) \quad \begin{aligned} \frac{\delta G_{\alpha\zeta,\sigma}(1,6)_\phi}{\delta \phi_{\nu\epsilon,\sigma'}(4,5)} &= -G_{\alpha\bar{\beta},\sigma}(1,\bar{3})_\phi \frac{\delta [(G^0)^{-1}]_{\bar{\beta}\bar{\gamma},\sigma}(\bar{3},\bar{2})}{\delta \phi_{\nu\epsilon,\sigma'}(4,5)} G_{\bar{\gamma}\zeta,\sigma}(\bar{2},6) \\ &\quad + G_{\alpha\bar{\beta},\sigma}(1,\bar{3})_\phi \frac{\delta \phi_{\bar{\beta}\bar{\gamma},\sigma}(\bar{3},\bar{2})_\phi}{\delta \phi_{\nu\epsilon,\sigma'}(4,5)} G_{\bar{\gamma}\zeta,\sigma}(\bar{2},6) \\ &\quad + G_{\alpha\bar{\beta},\sigma}(1,\bar{3})_\phi \frac{\delta \Sigma_{\bar{\beta}\bar{\gamma},\sigma}(\bar{3},\bar{2})_\phi}{\delta \phi_{\nu\epsilon,\sigma'}(4,5)} G_{\bar{\gamma}\zeta,\sigma}(\bar{2},6) \\ &= -0 \\ &\quad + G_{\alpha\bar{\beta},\sigma}(1,\bar{3})_\phi \delta(\bar{2}-5) \delta(\bar{3}-4) \delta_{\bar{\beta},\nu} \delta_{\epsilon,\bar{\gamma}} \delta_{\sigma,\sigma'} G_{\bar{\gamma}\zeta,\sigma}(\bar{2},6) \\ &\quad + G_{\alpha\bar{\beta},\sigma}(1,\bar{3})_\phi \frac{\delta \Sigma_{\bar{\beta}\bar{\gamma},\sigma}(\bar{3},\bar{2})_\phi}{\delta \phi_{\nu\epsilon,\sigma'}(4,5)} G_{\bar{\gamma}\zeta,\sigma}(\bar{2},6), \end{aligned}$$

where we used the fact that the non-interacting Green's function  $G^0$  does not depend on the artificial field  $\phi$  (see eq. (5.46)). Next, we make use of the chain rule and apply it to  $G_\phi$  which is a functional of  $\phi$ . This leads to the *Bethe-Salpeter equation*

$$(5.58) \quad \begin{aligned} \frac{\delta G_{\alpha\zeta,\sigma}(1,6)_\phi}{\delta \phi_{\nu\epsilon,\sigma'}(4,5)} &= G_{\alpha\nu,\sigma}(1,4)_\phi G_{\epsilon\zeta,\sigma}(5,6) \delta_{\sigma,\sigma'} \\ &\quad + G_{\alpha\bar{\beta},\sigma}(1,\bar{3})_\phi \frac{\delta \Sigma_{\bar{\beta}\bar{\gamma},\sigma}(\bar{3},\bar{2})_\phi}{\delta G_{\bar{\rho}\bar{\lambda},\sigma''}(\bar{7},\bar{8})_\phi} \frac{\delta G_{\bar{\rho}\bar{\lambda},\sigma''}(\bar{7},\bar{8})_\phi}{\delta \phi_{\nu\epsilon,\sigma'}(4,5)} G_{\bar{\gamma}\zeta,\sigma}(\bar{2},6)_\phi. \end{aligned}$$

## 5.1. THE KADANOFF-BAYM FORMALISM

In fig. 5.1 we show a diagrammatic representation of the Bethe-Salpeter equation (5.58). Note that the formulation of the Bethe-Salpeter equation (5.58) relies on the transition

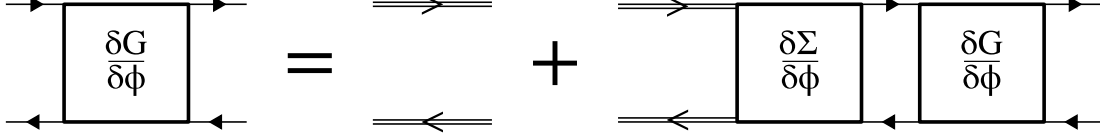


FIGURE 5.1. Diagrammatic representation of the Bethe-Salpeter equation (5.58). The double lines represent the full propagator  $G$  while single lines only encode the functional dependence of the respective object. We see that the Bethe-Salpeter equation is a self-consistent equation for  $\frac{\delta G}{\delta \phi}$  which again is directly related to the spin and charge susceptibilities as we show later.

from a functional dependence of the artificial source  $\phi$  to a functional dependence of the interacting Green's function  $G$ . Formally, this procedure is done by a Legendre transformation that we will discuss in the next section. In addition, the next section will also be important since it presents a generating functional for the Green's function that is crucial for the so-called *conserving approximations*.

**5.1.5. Luttinger-Ward functional.** We remind ourselves (see eqs. (5.7), (5.20)) that the free energy in the presence of the source field  $\phi$  is given by

$$(5.59) \quad F[\phi] = -\frac{1}{\tilde{\beta}} \ln Z[\phi] = -\frac{1}{\tilde{\beta}} \ln \text{tr} \left[ e^{-\tilde{\beta} H} T_{\tau} e^{-c_{\bar{\alpha}, \bar{\sigma}}^{\dagger}(\bar{1}) \phi_{\bar{\alpha} \bar{\beta}, \bar{\sigma}}(\bar{1}, \bar{2}) c_{\bar{\beta}, \bar{\sigma}}(\bar{2})} \right]$$

and that we obtain the Green's function  $G$  via functional differentiation

$$(5.60) \quad G_{\alpha \beta, \sigma}(1, 2)_{\phi} = -\frac{\delta \ln(Z[\phi])}{\delta \phi_{\beta \alpha, \sigma}(2, 1)} = \tilde{\beta} \frac{\delta F[\phi]}{\delta \phi_{\beta \alpha, \sigma}(2, 1)}.$$

The two above equations (5.59), (5.60) are sufficient to define the Legendre transform for the free energy  $F$  via

$$(5.61) \quad \Omega[G] = F[\phi] - \frac{1}{\tilde{\beta}} \text{tr}(\phi G),$$

where  $\Omega$  is coined the *Kadanoff-Baym functional*<sup>2</sup>. A common property of Legendre transformations is

$$(5.62) \quad \begin{aligned} & \tilde{\beta} \frac{\delta \Omega[G]}{\delta G_{\beta \alpha, \sigma}(2, 1)} \\ &= \tilde{\beta} \frac{\delta F[\phi]}{\delta G_{\beta \alpha, \sigma}(2, 1)} - \frac{\delta \text{tr}(\phi G)}{\delta G_{\beta \alpha, \sigma}(2, 1)} \end{aligned}$$

$$(5.63) \quad = \tilde{\beta} \frac{\delta F[\phi]}{\delta \phi_{\bar{\gamma} \bar{\epsilon}, \bar{\sigma}}(\bar{3}, \bar{4})} \frac{\delta \phi_{\bar{\gamma} \bar{\epsilon}, \bar{\sigma}}(\bar{3}, \bar{4})}{\delta G_{\beta \alpha, \sigma}(2, 1)} - \frac{\delta \phi_{\bar{\gamma} \bar{\epsilon}, \bar{\sigma}}(\bar{3}, \bar{4}) G_{\bar{\epsilon} \bar{\gamma}, \bar{\sigma}}(\bar{4}, \bar{3})}{\delta G_{\beta \alpha, \sigma}(2, 1)}$$

$$(5.64) \quad = G_{\bar{\epsilon} \bar{\gamma}, \bar{\sigma}}(\bar{4}, \bar{3}) \frac{\delta \phi_{\bar{\gamma} \bar{\epsilon}, \bar{\sigma}}(\bar{3}, \bar{4})}{\delta G_{\beta \alpha, \sigma}(2, 1)} - \frac{\delta \phi_{\bar{\gamma} \bar{\epsilon}, \bar{\sigma}}(\bar{3}, \bar{4})}{\delta G_{\beta \alpha, \sigma}(2, 1)} G_{\bar{\epsilon} \bar{\gamma}, \bar{\sigma}}(\bar{4}, \bar{3}) - \frac{\delta G_{\bar{\epsilon} \bar{\gamma}, \bar{\sigma}}(\bar{4}, \bar{3})}{\delta G_{\beta \alpha, \sigma}(2, 1)} \phi_{\bar{\gamma} \bar{\epsilon}, \bar{\sigma}}(\bar{3}, \bar{4})$$

$$(5.65) \quad = -\phi_{\alpha \beta, \sigma}(1, 2).$$

<sup>2</sup>Note that the definition of the Legendre transformation necessitates certain regularity properties that we assume to be fulfilled without proof. Moreover, depending on the different common conventions one might find the definition with an overall minus sign.

We notice that the above property in eq. (5.65) and the Dyson equation (5.49) help to deduce

$$(5.66) \quad \tilde{\beta} \frac{\delta \Omega[G]}{\delta G_{\beta\alpha,\sigma}(2,1)} = -\phi_{\alpha\beta,\sigma}(1,2)$$

$$(5.67) \quad = (G^{-1})_{\alpha\beta,\sigma}(1,2) - (G_0^{-1})_{\alpha\beta,\sigma}(1,2) + \Sigma_{\alpha\beta,\sigma}(1,2),$$

which reduces to the Dyson equation of our original system in the case where

$$(5.68) \quad \tilde{\beta} \frac{\delta \Omega[G]}{\delta G_{\beta\alpha,\sigma}(2,1)} = -\phi_{\alpha\beta,\sigma}(1,2) = 0.$$

With this set of equations at hand we can guess<sup>3</sup> the Kadanoff-Baym functional explicitly,

$$(5.69) \quad \Omega[G] = \Phi[G] - T \text{tr} [G (G_0^{-1} - G^{-1})] - T \text{tr} [\ln |-G|],$$

where  $\Phi[G]$  is the so-called *Luttinger-Ward functional* which is defined as the sum of all closed two-particle irreducible skeleton diagrams that can be constructed from  $G$  and the Hubbard interaction  $U$ . The term *two-particle irreducible* means that by cutting two Green's function lines the resulting diagram does not decompose into two disconnected diagrams while the term *skeleton diagram* signifies the absence of explicit self-energy lines in the diagrams.

Since the self-energy  $\Sigma$  is the sum of all one-particle irreducible skeleton diagrams (this is discussed in sec. 5.1.8) we find

$$(5.70) \quad \frac{\delta \Phi[G]}{\delta G_{\beta\alpha,\sigma}(2,1)} = \Sigma_{\alpha\beta,\sigma}(1,2).$$

The importance of the Luttinger-Ward functional for constructing so-called *conserving approximations* is discussed in sec. 5.2.

For the moment we use the construction of the Luttinger-Ward functional only to see that we can define a Legendre transformation that allows us to express the functional dependence in terms of the Green's function  $G$  instead of the artificial source field  $\phi$ .

**5.1.6. Susceptibilities.** To be able to further evaluate the generalized susceptibility  $\frac{\delta G}{\delta \phi}$  we have to treat the terms in the Bethe-Salpeter equation (5.58) separately. The first term corresponds to the *irreducible susceptibility*

$$(5.71) \quad \chi_{\lambda\zeta\nu\eta}^0(1,2) = -G_{\zeta\eta,\sigma}(1,2)G_{\nu\lambda,\sigma}(2,1),$$

which is a 4-tensor, where we have dropped the spin index due to spin-rotational invariance and the restriction to paramagnetic states.

First, we transform both time and space arguments to Fourier space and get

$$(5.72) \quad \chi_{\lambda\zeta\nu\eta}^0(q, iq_m) := -\frac{1}{\tilde{\beta}N} \lim_{\tau \nearrow 0} \sum_{k, i\omega_n} e^{-i\omega_n \tau} G_{\nu\lambda,\sigma}(k, i\omega_n) G_{\zeta\eta,\sigma}(k+q, i\omega_{n+m}),$$

where we defined the *bosonic Matsubara frequencies*

$$(5.73) \quad iq_n \equiv \frac{2\pi i n}{\tilde{\beta}}, \quad n \in \mathbb{Z}.$$

PROOF OF (5.72). By exploiting the translational invariances in space and imaginary time we find

$$(5.74) \quad \chi_{\lambda\zeta\nu\eta}^0(r_1 - r_2, \tau_1 - \tau_2) = -G_{\nu\lambda,\sigma}(-(r_1 - r_2), -(\tau_1 - \tau_2)) G_{\zeta\eta,\sigma}(r_1 - r_2, \tau_1 - \tau_2).$$

<sup>3</sup>Luttinger and Ward derive this expression in [118] by the technique of coupling constant integration. A more extensive derivation can be found in Ref. [156].

## 5.1. THE KADANOFF-BAYM FORMALISM

We can now perform a Fourier transform in both space and imaginary time argument to obtain

$$(5.75) \quad \chi_{\lambda\zeta\nu\eta}^0(q, iq_m) = - \int_{0+}^{\tilde{\beta}^-} d(\tau_1 - \tau_2) \sum_{r_1 - r_2} e^{iq_m(\tau_1 - \tau_2)} e^{iq \cdot (r_1 - r_2)} \times \\ \times G_{\nu\lambda,\sigma}(-r_1 - r_2, -(\tau_1 - \tau_2)) G_{\zeta\eta,\sigma}(r_1 - r_2, \tau_1 - \tau_2)$$

$$(5.76) \quad = - \int_{0+}^{\tilde{\beta}^-} d\tau \sum_r e^{iq_m\tau} e^{iq \cdot r} G_{\nu\lambda,\sigma}(-r, -\tau) G_{\zeta\eta,\sigma}(r, \tau)$$

$$(5.77) \quad = - \frac{1}{\tilde{\beta}^2 N^2} \sum_{k, k', i\omega_n, i\omega_{n'}, r} \int_{0+}^{\tilde{\beta}^-} d\tau \left[ e^{-i(-\omega_n + \omega_{n'} - q_m)\tau} e^{-i(-k + k' - q) \cdot r} \times \right. \\ \left. \times G_{\nu\lambda,\sigma}(k, i\omega_n) G_{\zeta\eta,\sigma}(k', i\omega_{n'}) \right]$$

$$(5.78) \quad = - \frac{1}{\tilde{\beta} N} \lim_{\tau \nearrow 0} \sum_{k, k', i\omega_n, i\omega_{n'}} e^{-i\omega_n\tau} \delta_{k', k+q} \delta_{\omega_{n'}, \omega_n + q_m} G_{\nu\lambda,\sigma}(k, i\omega_n) G_{\zeta\eta,\sigma}(k', i\omega_{n'})$$

$$(5.79) \quad = - \frac{1}{\tilde{\beta} N} \lim_{\tau \nearrow 0} \sum_{k, i\omega_n} e^{-i\omega_n\tau} G_{\nu\lambda,\sigma}(k, i\omega_n) G_{\zeta\eta,\sigma}(k + q, i\omega_{n+m}).$$

□

In the special case where  $G$  is the non-interacting Green's function (eq. (4.220)) one can perform the Matsubara sum explicitly. We derive an explicit expression in the following because the non-interacting case is needed later.

The Matsubara sum that arises is of the form

$$(5.80) \quad \lim_{\epsilon \searrow 0} \frac{1}{\tilde{\beta}} \sum_{i\omega_n} \frac{e^{i\omega_n \epsilon}}{i\omega_n - \xi}.$$

This sum is included in the contour integral

$$(5.81) \quad \lim_{\epsilon \searrow 0} \oint_{\partial B_R(0)} \frac{e^{\epsilon z}}{z - \xi} \frac{1}{e^{\tilde{\beta} z} + 1} \frac{dz}{2\pi i},$$

where  $\partial B_R(0) \subset \mathbb{C}$  is the circle centered around the origin of the complex plane with radius  $R$ . Obviously, the integral kernel goes to zero in all limits  $\text{Re}(z), \text{Im}(z) \rightarrow \pm\infty$  except along the imaginary axis due to the strong decay of the denominator and reduces thus to the divergences at the Matsubara frequencies that are treated in terms of the residual theorem. Thus, we find

$$(5.82) \quad I := \lim_{R \rightarrow \infty} \lim_{\epsilon \searrow 0} \oint_{\partial B_R(0)} \frac{e^{\epsilon z}}{z - \xi} \frac{1}{e^{\tilde{\beta} z} + 1} \frac{dz}{2\pi i}$$

$$(5.83) \quad = \lim_{R \rightarrow \infty} \lim_{\epsilon \searrow 0} \oint_{\partial B_R(0)} g_\epsilon(z) \frac{dz}{2\pi i}$$

$$(5.84) \quad = 0,$$

where we defined

$$(5.85) \quad g_\epsilon(z) := \frac{e^{\epsilon z}}{z - \xi} \frac{1}{e^{\tilde{\beta} z} + 1}.$$

On the other hand, the integral can be evaluated via the residue theorem with residues at  $z = i\omega_n, \xi$ :

$$(5.86) \quad 0 = I = \lim_{\epsilon \searrow 0} \sum_{i\omega_n} \text{Res}(g_\epsilon(z), i\omega_n) + \text{Res}(g_\epsilon(z), \xi)$$

$$(5.87) \quad = \lim_{\epsilon \searrow 0} \sum_{i\omega_n} \frac{e^{i\omega_n \epsilon}}{-\tilde{\beta}(i\omega_n - \xi)} + \frac{e^{\xi \epsilon}}{e^{\tilde{\beta}\xi} + 1},$$

which can be rearranged into

$$(5.88) \quad \lim_{\epsilon \searrow 0} \frac{1}{\tilde{\beta}} \sum_{i\omega_n} \frac{e^{i\omega_n \epsilon}}{i\omega_n - \xi} = \frac{1}{e^{\tilde{\beta}\xi} + 1} = f_{FD}(\xi).$$

With those preparations done we can proceed with the Matsubara sum that appears in the definition of the non-interacting irreducible susceptibility  $\chi^0$  (eq. (5.72)) which relies on the form of the non-interacting Green's function  $G^0$  in eq. (4.220). Combining both equations yields

$$(5.89) \quad \begin{aligned} \chi_{\eta\nu\zeta\lambda}^0(q, iq_m) &= -\frac{1}{\tilde{\beta}N} \sum_{k,b,c} a_b^\nu(k+q) a_b^{\lambda*}(k+q) a_c^\zeta(k) a_c^{\eta*}(k) \times \\ &\times \sum_{i\omega_n} \frac{1}{(i\omega_{n+m} - \xi_b(k+q))(i\omega_n - \xi_c(k))}. \end{aligned}$$

A closer look at the Matsubara sum reveals

$$(5.90) \quad \begin{aligned} &\sum_{i\omega_n} \frac{1}{(i\omega_{n+m} - \xi_b(k+q))(i\omega_n - \xi_c(k))} \\ &= \sum_{i\omega_n} \left( \frac{1}{i\omega_{n+m} - \xi_b(k+q)} - \frac{1}{i\omega_n - \xi_c(k)} \right) \frac{1}{-iq_m - \xi_c(k) + \xi_b(k+q)}. \end{aligned}$$

The denominator in eq. (5.90) is  $O\left(\left(\frac{1}{i\omega_n}\right)^2\right)$  and therefore the sum converges. Nevertheless, the additional factor  $\lim_{\epsilon \searrow 0} e^{i\omega_n \epsilon}$  will not change the result but allows us to use eq. (5.88) which leads to

$$(5.91) \quad \lim_{\epsilon \searrow 0} \sum_{i\omega_n} \left( \frac{e^{i\omega_n \epsilon}}{i\omega_{n+m} - \xi_b(k+q)} - \frac{e^{i\omega_n \epsilon}}{i\omega_n - \xi_c(k)} \right) = \tilde{\beta}[f_{FD}(\xi_b(k+q)) - f_{FD}(\xi_c(k))].$$

Reinserting this result into eq. (5.89) gives the final result

$$(5.92) \quad \begin{aligned} &\chi_{\eta\nu\zeta\lambda}^0(q, iq_m) \\ &= -\frac{1}{N} \sum_{k,b,c} a_b^\nu(k+q) a_b^{\lambda*}(k+q) a_c^\zeta(k) a_c^{\eta*}(k) \frac{f_{FD}(\xi_b(k+q)) - f_{FD}(\xi_c(k))}{-iq_m + \xi_b(k+q) - \xi_c(k)}. \end{aligned}$$

At this stage, we also derive important properties of the irreducible susceptibility  $\chi^0$  which follow directly from the properties of the Green's functions  $G$  (see prop. 4.6.1):

$$(5.93) \quad \chi_{\eta\nu\zeta\lambda}^0(q, -iq_m) = (\chi^0)_{\zeta\lambda\eta\nu}^*(q, iq_m).$$

PROOF OF (5.93). We simply calculate the left-hand side and use prop. 4.6.1 to obtain

$$(5.94) \quad \begin{aligned} &\chi_{\eta\nu\zeta\lambda}^0(q, -iq_m) \\ &= -\frac{1}{\tilde{\beta}N} \lim_{\tau \nearrow 0} \sum_{k, i\omega_n} e^{-i\omega_n \tau} G_{\nu\lambda, \sigma}(k+q, i\omega_{n-m}) G_{\zeta\eta, \sigma}(k, i\omega_n) \end{aligned}$$

$$(5.95) \quad = -\frac{1}{\tilde{\beta}N} \lim_{\tau \nearrow 0} \sum_{k, i\omega_n} e^{-i\omega_n \tau} G_{\lambda\nu, \sigma}^*(k+q, i\omega_{-(n-m)-1}) G_{\eta\zeta, \sigma}^*(k, i\omega_{-n-1}).$$

## 5.1. THE KADANOFF-BAYM FORMALISM

We can now change the summation order  $-n - 1 \rightarrow n$  which leads to

$$(5.96) \quad \chi_{\eta\nu\zeta\lambda}^0(q, -iq_m) = -\frac{1}{\tilde{\beta}N} \lim_{\tau \nearrow 0} \sum_{k, i\omega_n} e^{i\omega_n\tau} G_{\lambda\nu, \sigma}^*(k+q, i\omega_{n+m}) G_{\eta\zeta, \sigma}^*(k, i\omega_n)$$

$$(5.97) \quad = (\chi^0)_{\zeta\lambda\eta\nu}^*(q, iq_m).$$

□

Similarly, one finds

$$(5.98) \quad \chi_{\lambda\zeta\nu\eta}^0(-q, iq_m) = \chi_{\nu\eta\lambda\zeta}^0(q, iq_m).$$

PROOF OF (5.98). To prove the claim it is sufficient to change the order of  $k$ -summation, namely

$$(5.99) \quad \chi_{\lambda\zeta\nu\eta}^0(-q, iq_m) = -\frac{1}{\tilde{\beta}N} \lim_{\tau \nearrow 0} \sum_{-k, i\omega_n} e^{-i\omega_n\tau} G_{\nu\lambda, \sigma}(-k, i\omega_n) G_{\zeta\eta, \sigma}(-k-q, i\omega_{n+m})$$

$$(5.100) \quad = -\frac{1}{\tilde{\beta}N} \lim_{\tau \nearrow 0} \sum_{k, i\omega_n} e^{-i\omega_n\tau} G_{\lambda\nu, \sigma}(k, i\omega_n) G_{\eta\zeta, \sigma}(k+q, i\omega_{n+m})$$

$$(5.101) \quad = \chi_{\nu\eta\lambda\zeta}^0(q, iq_m).$$

□

The last useful relation regarding the irreducible susceptibility  $\chi^0$  is

$$(5.102) \quad \chi_{\lambda\zeta\nu\eta}^0(-q, -iq_m) = \chi_{\eta\nu\zeta\lambda}^0(q, iq_m).$$

PROOF OF (5.102). We obtain the desired result by simply shifting the summation indices,  $k \rightarrow k+q$  and  $n \rightarrow n+m$ ,

$$(5.103) \quad \chi_{\lambda\zeta\nu\eta}^0(-q, -iq_m) = -\frac{1}{\tilde{\beta}N} \lim_{\tau \nearrow 0} \sum_{k, i\omega_n} e^{-i\omega_n\tau} G_{\nu\lambda, \sigma}(k, i\omega_n) G_{\zeta\eta, \sigma}(k-q, i\omega_{n-m})$$

$$(5.104) \quad = -\frac{1}{\tilde{\beta}N} \lim_{\tau \nearrow 0} \sum_{k, i\omega_n} e^{-i\omega_n\tau} G_{\nu\lambda, \sigma}(k+q, i\omega_{n+m}) G_{\zeta\eta, \sigma}(k, i\omega_n)$$

$$(5.105) \quad = \chi_{\eta\nu\zeta\lambda}^0(q, iq_m).$$

□

Finally, we notice that the vector space isomorphism

$$(5.106) \quad \mathbb{C}^n \otimes \mathbb{C}^n \simeq \mathbb{C}^{n^2}$$

can be generalized to

$$(5.107) \quad \mathbb{C}^n \otimes \mathbb{C}^n \otimes \mathbb{C}^n \otimes \mathbb{C}^n \simeq \mathbb{C}^{n^2} \otimes \mathbb{C}^{n^2}.$$

Therefore, we can interpret the 4-tensor  $\chi^0$  as a matrix

$$(5.108) \quad \chi_{\eta\nu\zeta\lambda}^0 = \chi_{(\eta\nu), (\zeta\lambda)}^0.$$

Next, we define the *charge susceptibility* as the charge density correlation function that appears in linear response theory by means of the fluctuation-dissipation theorem<sup>4</sup>,

$$(5.109) \quad \chi_{\lambda\zeta\nu\eta}^{ch}(1, 2) := \langle T_\tau n_{\zeta\lambda}(1) n_{\nu\eta}(2) \rangle - \langle n_{\zeta\lambda}(1) \rangle \langle n_{\nu\eta}(2) \rangle,$$

<sup>4</sup>Note that linear response theory is traditionally formulated with density fluctuations for real times while we use an extended definition to complex times. Nevertheless, very similar steps as the ones that we presented for the Green's function are sufficient to relate this generalized object to the original charge susceptibility on the real axis (see [110]).

where we have defined a generalized density

$$(5.110) \quad n_{\alpha\beta,\sigma}(1) := c_{\beta,\sigma}^\dagger(1)c_{\alpha,\sigma}(1),$$

$$(5.111) \quad n_{\alpha,\sigma}(1) := c_{\alpha,\sigma}^\dagger(1)c_{\alpha,\sigma}(1),$$

$$(5.112) \quad n_{\alpha\beta}(1) := \sum_{\sigma} n_{\alpha\beta,\sigma}(1),$$

$$(5.113) \quad \langle n_{\alpha\beta,\sigma}(1) \rangle = G_{\alpha\beta,\sigma}(1, 1^+).$$

One obtains the so-called *local charge sum rule* by application of the local Pauli principle to the equal time and equal position charge susceptibility  $\chi^{ch}$ ,

$$(5.114) \quad \chi_{\nu\nu\nu\nu}^{ch}(0, 0^+) = \langle (n_{\nu,\uparrow} + n_{\nu,\downarrow})^2 \rangle - \langle n_{\nu} \rangle^2$$

$$(5.115) \quad \frac{1}{N} \sum_q e^{iq \cdot 0} \chi_{\nu\nu\nu\nu}^{ch}(q, 0^+) = \langle n_{\nu,\uparrow}^2 + 2n_{\nu,\uparrow}n_{\nu,\downarrow} + n_{\nu,\downarrow}^2 \rangle - \langle n_{\nu} \rangle^2$$

$$(5.116) \quad \frac{1}{\tilde{\beta}N} \sum_{q, iq_m} e^{iq_m \cdot 0^+} \chi_{\nu\nu\nu\nu}^{ch}(q, iq_m) = \langle n_{\nu,\uparrow}^2 \rangle + \langle n_{\nu,\downarrow}^2 \rangle + 2\langle n_{\nu,\uparrow}n_{\nu,\downarrow} \rangle - \langle n_{\nu} \rangle^2$$

$$(5.117) \quad \frac{1}{\tilde{\beta}N} \sum_{q, iq_m} \chi_{\nu\nu\nu\nu}^{ch}(q, iq_m) = \langle n_{\nu} \rangle + 2\langle n_{\nu,\uparrow}n_{\nu,\downarrow} \rangle - \langle n_{\nu} \rangle^2,$$

where we dropped the space-time dependence on the right-hand side due to translation invariance.

Taking a closer look at the second functional derivative of  $G$  in eq. (5.24) we can relate the charge susceptibility  $\chi^{ch}$  to the generalized susceptibility  $-\frac{\delta G}{\delta \phi}$  via

$$(5.118) \quad - \sum_{\sigma, \sigma'} \left. \frac{\delta G_{\zeta\lambda,\sigma}(1, 1^+)_{\phi}}{\delta \phi_{\nu\eta,\sigma'}(2^+, 2)} \right|_{\phi=0} = - \sum_{\sigma, \sigma'} \left[ \langle T_{\tau} c_{\zeta,\sigma}(1) c_{\lambda,\sigma}^\dagger(1^+) c_{\nu,\sigma'}^\dagger(2^+) c_{\eta,\sigma'}(2) \rangle + G_{\zeta\lambda,\sigma}(1, 1^+) G_{\eta\nu,\sigma'}(2, 2^+) \right]$$

$$(5.119) \quad = \sum_{\sigma, \sigma'} \langle T_{\tau} n_{\zeta\lambda,\sigma}(1) n_{\eta\nu,\sigma'}(2) \rangle - \langle n_{\zeta\lambda,\sigma}(1) \rangle \langle n_{\eta\nu,\sigma'}(2) \rangle$$

$$(5.120) \quad = \chi_{\lambda\zeta\eta\nu}^{ch}(1, 2)$$

and we define a generalized *three-point charge susceptibility*

$$(5.121) \quad \chi_{\lambda\zeta\eta\nu}^{ch}(1, 3; 2) := - \sum_{\sigma\sigma'} \left. \frac{\delta G_{\zeta\lambda,\sigma}(1, 3)_{\phi}}{\delta \phi_{\nu\eta,\sigma'}(2^+, 2)} \right|_{\phi=0}$$

that reproduces the previously defined charge susceptibility (eq. (5.109)) in the limit  $3 \rightarrow 1^+$ . The meaning of the local charge sum rule and the three-point charge susceptibility will be discussed later when we derive an explicit expression for the self-energy. Similar to the self-consistent equation for the generalized susceptibility  $-\frac{\delta G}{\delta \phi}$  (eq. (5.58) and fig. 5.1) we can find a self-consistent equation for the generalized three-point charge susceptibility  $\chi^{ch}(1, 3; 2)$ . Key ingredient is equation (5.58) which enters the definition of  $\chi^{ch}(1, 3; 2)$  (eq. (5.121)). We start by combining both equations which gives

$$(5.122) \quad \chi_{\lambda\zeta\eta\nu}^{ch}(1, 3; 2) = - \sum_{\sigma\sigma'} \left. \frac{\delta G_{\zeta\lambda,\sigma}(1, 3)_{\phi}}{\delta \phi_{\nu\eta,\sigma'}(2^+, 2)} \right|_{\phi=0} \\ = - \sum_{\sigma\sigma'} [G_{\zeta\nu,\sigma}(1, 2^+) G_{\eta\lambda,\sigma}(2, 3) \delta_{\sigma,\sigma'}]$$

## 5.1. THE KADANOFF-BAYM FORMALISM

$$(5.123) \quad + G_{\zeta\bar{\beta},\sigma}(1, \bar{3}) \left. \frac{\delta\Sigma_{\bar{\beta}\bar{\gamma},\sigma}(\bar{3}, \bar{2})_\phi}{\delta G_{\bar{\rho}\bar{\lambda},\sigma''}(\bar{7}, \bar{8})_\phi} \frac{\delta G_{\bar{\rho}\bar{\lambda},\sigma''}(\bar{7}, \bar{8})_\phi}{\delta\phi_{\nu\eta,\sigma'}(2^+, 2)} \right|_{\phi=0} G_{\bar{\gamma}\lambda,\sigma}(\bar{2}, 3) \Bigg]$$

$$(5.124) \quad = -G_{\zeta\nu,\bar{\sigma}}(1, 2^+)G_{\eta\lambda,\bar{\sigma}}(2, 3) - G_{\zeta\bar{\beta},\bar{\sigma}}(1, \bar{3}) \left. \frac{\delta\Sigma_{\bar{\beta}\bar{\gamma},\bar{\sigma}}(\bar{3}, \bar{2})_\phi}{\delta G_{\bar{\rho}\bar{\lambda},\bar{\sigma}''}(\bar{7}, \bar{8})_\phi} \frac{\delta G_{\bar{\rho}\bar{\lambda},\bar{\sigma}''}(\bar{7}, \bar{8})_\phi}{\delta\phi_{\nu\eta,\bar{\sigma}'}(2^+, 2)} \right|_{\phi=0} G_{\bar{\gamma}\lambda,\bar{\sigma}}(\bar{2}, 3).$$

Due to spin rotational invariance and paramagnetism we can assume  $G_\sigma = G_{-\sigma} = G$  which allows us to care only for the relative spin alignment in functional derivatives, i.e.

$$(5.125) \quad \frac{\delta\Sigma_\uparrow}{\delta G_\uparrow} = \frac{\delta\Sigma_\downarrow}{\delta G_\downarrow} \neq \frac{\delta\Sigma_\uparrow}{\delta G_\downarrow} = \frac{\delta\Sigma_\downarrow}{\delta G_\uparrow}$$

and similarly for  $\frac{\delta G_\sigma}{\delta\phi_{\sigma'}}$ . Thus, we can conclude

$$(5.126) \quad \begin{aligned} & \chi_{\lambda\zeta\eta\nu}^{ch}(1, 3; 2) \\ &= -2G_{\zeta\nu}(1, 2^+)G_{\eta\lambda}(2, 3) \\ & - G_{\zeta\bar{\beta}}(1, \bar{3}) \sum_\sigma \left. \frac{\delta\Sigma_{\bar{\beta}\bar{\gamma},\sigma}(\bar{3}, \bar{2})_\phi}{\delta G_{\bar{\rho},\bar{\lambda},\sigma''}(\bar{7}, \bar{8})_\phi} \right|_{\phi=0} \sum_{\sigma'} \left. \frac{\delta G_{\bar{\rho}\bar{\lambda},\sigma''}(\bar{7}, \bar{8})_\phi}{\delta\phi_{\nu\eta,\sigma'}(2^+, 2)} \right|_{\phi=0} G_{\bar{\gamma}\lambda}(\bar{2}, 3) \end{aligned}$$

$$(5.127) \quad \begin{aligned} & - G_{\zeta\bar{\beta}}(1, \bar{3}) \sum_\sigma \left. \frac{\delta\Sigma_{\bar{\beta}\bar{\gamma},\sigma}(\bar{3}, \bar{2})_\phi}{\delta G_{\bar{\rho},\bar{\lambda},\uparrow}(\bar{7}, \bar{8})_\phi} \right|_{\phi=0} \sum_{\sigma',\sigma''} \left. \frac{\delta G_{\bar{\rho}\bar{\lambda},\sigma''}(\bar{7}, \bar{8})_\phi}{\delta\phi_{\nu\eta,\sigma'}(2^+, 2)} \right|_{\phi=0} G_{\bar{\gamma}\lambda}(\bar{2}, 3) \\ &= -2G_{\zeta\nu}(1, 2^+)G_{\eta\lambda}(2, 3) \end{aligned}$$

$$(5.128) \quad + G_{\zeta\bar{\beta}}(1, \bar{3}) \sum_\sigma \left. \frac{\delta\Sigma_{\bar{\beta}\bar{\gamma},\sigma}(\bar{3}, \bar{2})_\phi}{\delta G_{\bar{\rho},\bar{\lambda},\uparrow}(\bar{7}, \bar{8})_\phi} \right|_{\phi=0} \chi_{\lambda\bar{\rho}\eta\nu}^{ch}(\bar{7}, \bar{8}; 2)G_{\bar{\gamma}\lambda}(\bar{2}, 3)$$

$$(5.129) \quad = -2G_{\zeta\nu}(1, 2^+)G_{\eta\lambda}(2, 3) + G_{\zeta\bar{\beta}}(1, \bar{3})\Gamma_{\bar{\gamma}\bar{\beta}\bar{\lambda}\bar{\rho}}^{ch}(\bar{3}, \bar{2}; \bar{7}, \bar{8})\chi_{\lambda\bar{\rho}\eta\nu}^{ch}(\bar{7}, \bar{8}; 2)G_{\bar{\gamma}\lambda}(\bar{2}, 3),$$

where we have defined the *irreducible charge vertex*

$$(5.130) \quad \Gamma_{\gamma\beta\lambda\rho}^{ch}(3, 2; 7, 8) := \sum_\sigma \left. \frac{\delta\Sigma_{\beta\gamma,\sigma}(3, 2)_\phi}{\delta G_{\rho\lambda,\uparrow}(7, 8)_\phi} \right|_{\phi=0}.$$

Equation (5.129) is the famous *Bethe-Salpeter equation* for the charge susceptibility and will be of great value in the next sections.

We turn now our attention to the *spin susceptibility*  $\chi^{sp}$  that is defined analogously to the charge susceptibility (eq. (5.109)),

$$(5.131) \quad \chi_{\lambda\zeta\eta\nu}^{sp}(1, 2) := 4\langle T_\tau S_{\lambda\zeta}^z(1) S_{\nu\eta}^z(2) \rangle - 4\langle S_{\lambda\zeta}^z(1) \rangle \langle S_{\nu\eta}^z(2) \rangle,$$

where we defined the generalized spin matrices

$$(5.132) \quad S_{\alpha\beta}(1) = \left( c_{\alpha,\uparrow}^\dagger(1) \quad c_{\alpha,\downarrow}^\dagger(1) \right) \cdot \tilde{\sigma} \cdot \left( c_{\beta,\uparrow}(1) \quad c_{\beta,\downarrow}(1) \right)^T$$

and  $\tilde{\sigma}$  is the three-dimensional vector consisting of the Pauli spin matrices

$$(5.133) \quad \tilde{\sigma} := (\sigma_x, \sigma_y, \sigma_z)^T$$

$$(5.134) \quad \sigma_x = \frac{1}{2} \begin{pmatrix} 0 & 1 \\ 1 & 0 \end{pmatrix}, \quad \sigma_y = \frac{1}{2} \begin{pmatrix} 0 & -i \\ i & 0 \end{pmatrix}, \quad \sigma_z = \frac{1}{2} \begin{pmatrix} 1 & 0 \\ 0 & -1 \end{pmatrix}.$$

Thus, we can express the spin susceptibility in terms of generalized densities,

$$\begin{aligned}
 & \chi_{\lambda\zeta\eta\nu}^{sp}(1, 2) \\
 &= 4 \left\langle T_\tau \left[ \left( c_{\lambda,\uparrow}^\dagger(1) \ c_{\lambda,\downarrow}^\dagger(1) \right) \cdot \sigma_z \cdot \left( c_{\zeta,\uparrow}(1) \ c_{\zeta,\downarrow}(1) \right)^T \right] \times \right. \\
 & \quad \times \left. \left[ \left( c_{\nu,\uparrow}^\dagger(1) \ c_{\nu,\downarrow}^\dagger(1) \right) \cdot \sigma_z \cdot \left( c_{\eta,\uparrow}(1) \ c_{\eta,\downarrow}(1) \right)^T \right] \right\rangle \\
 & \quad - 4 \left\langle \left( c_{\lambda,\uparrow}^\dagger(1) \ c_{\lambda,\downarrow}^\dagger(1) \right) \cdot \sigma_z \cdot \left( c_{\zeta,\uparrow}(1) \ c_{\zeta,\downarrow}(1) \right)^T \right\rangle \times \\
 (5.135) \quad & \quad \times \left\langle \left( c_{\nu,\uparrow}^\dagger(1) \ c_{\nu,\downarrow}^\dagger(1) \right) \cdot \sigma_z \cdot \left( c_{\eta,\uparrow}(1) \ c_{\eta,\downarrow}(1) \right)^T \right\rangle \\
 &= \left\langle T_\tau \left[ c_{\lambda,\uparrow}^\dagger(1)c_{\zeta,\uparrow}(1) - c_{\lambda,\downarrow}^\dagger(1)c_{\zeta,\downarrow}(1) \right] \left[ c_{\nu,\uparrow}^\dagger(1)c_{\eta,\uparrow}(1) - c_{\nu,\downarrow}^\dagger(1)c_{\eta,\downarrow}(1) \right] \right\rangle \\
 (5.136) \quad & - \left\langle c_{\lambda,\uparrow}^\dagger(1)c_{\zeta,\uparrow}(1) - c_{\lambda,\downarrow}^\dagger(1)c_{\zeta,\downarrow}(1) \right\rangle \left\langle c_{\nu,\uparrow}^\dagger(1)c_{\eta,\uparrow}(1) - c_{\nu,\downarrow}^\dagger(1)c_{\eta,\downarrow}(1) \right\rangle \\
 &= \left\langle T_\tau \left[ n_{\zeta\lambda,\uparrow}(1) - n_{\zeta\lambda,\downarrow}(1) \right] \left[ n_{\eta\nu,\uparrow}(2) - n_{\eta\nu,\downarrow}(2) \right] \right\rangle \\
 (5.137) \quad & - \left\langle n_{\zeta\lambda,\uparrow}(1) - n_{\zeta\lambda,\downarrow}(1) \right\rangle \left\langle n_{\eta\nu,\uparrow}(2) - n_{\eta\nu,\downarrow}(2) \right\rangle \\
 &= 2 \left\langle T_\tau c_{\lambda,\uparrow}^\dagger(1)c_{\zeta,\uparrow}(1)c_{\nu,\uparrow}^\dagger(2)c_{\eta,\uparrow}(2) \right\rangle - 2 \left\langle T_\tau c_{\lambda,\uparrow}^\dagger(1)c_{\zeta,\uparrow}(1)c_{\nu,\downarrow}^\dagger(2)c_{\eta,\downarrow}(2) \right\rangle \\
 (5.138) \quad & - \left\langle n_{\zeta\lambda,\uparrow}(1) - n_{\zeta\lambda,\downarrow}(1) \right\rangle \left\langle n_{\eta\nu,\uparrow}(2) - n_{\eta\nu,\downarrow}(2) \right\rangle.
 \end{aligned}$$

Similar to the derivation of the local charge sum rule (eq. (5.117)) we can derive the so-called *local spin sum rule*

$$(5.139) \quad \chi_{\nu\nu\nu\nu}^{sp}(0, 0^+) = \langle (n_{\nu,\uparrow} - n_{\nu,\downarrow})^2 \rangle - \langle n_{\nu,\uparrow} - n_{\nu,\downarrow} \rangle^2$$

$$(5.140) \quad \frac{1}{N} \sum_q e^{iq \cdot 0} \chi_{\nu\nu\nu\nu}^{sp}(q, 0^+) = \langle (n_{\nu,\uparrow} - n_{\nu,\downarrow})^2 \rangle - 0^2$$

$$(5.141) \quad \frac{1}{\beta N} \sum_{q, iq_m} e^{iq_n \cdot 0^+} \chi_{\nu\nu\nu\nu}^{sp}(q, iq_m) = \langle n_{\nu,\uparrow}^2 \rangle + \langle n_{\nu,\downarrow}^2 \rangle - 2\langle n_{\nu,\uparrow} n_{\nu,\downarrow} \rangle$$

$$(5.142) \quad \frac{1}{\beta N} \sum_{q, iq_m} \chi_{\nu\nu\nu\nu}^{sp}(q, iq_m) = \langle n_\nu \rangle - 2\langle n_{\nu,\uparrow} n_{\nu,\downarrow} \rangle,$$

where we took advantage of paramagnetism in eq. (5.140) and the local Pauli principle in eq. (5.142). Again, we dropped the lattice position and imaginary time dependence on the right-hand side due to translation invariance. We define the generalized *three-point spin susceptibility*  $\chi^{sp}(1, 3; 2)$  in analogy to the three-point charge susceptibility  $\chi^{ch}(1, 3; 2)$  (see eqs. (5.120), (5.121)) via

$$(5.143) \quad \chi_{\lambda\zeta\eta\nu}^{sp}(1, 3; 2) := - \sum_{\sigma\sigma'} \sigma\sigma' \frac{\delta G_{\zeta\lambda,\sigma}(1, 3)_\phi}{\delta \phi_{\nu\eta,\sigma'}(2^+, 2)} \Big|_{\phi=0},$$

where we introduce the convention  $\uparrow \equiv 1$  and  $\downarrow \equiv -1$  which allows us to account for sign changes in the definition of  $\chi^{sp}(1, 3; 2)$ . Analogous to the charge susceptibility we can reproduce the spin susceptibility  $\chi^{sp}$  in the limit  $3 \rightarrow 1^+$  as can be seen from the following simple calculation via eq. (5.58),

$$\begin{aligned}
 & - \sum_{\sigma,\sigma'} \sigma\sigma' \frac{\delta G_{\zeta\lambda,\sigma}(1, 1^+)_\phi}{\delta \phi_{\nu\eta,\sigma'}(2^+, 2)} \Big|_{\phi=0} \\
 (5.144) \quad &= - \sum_{\sigma,\sigma'} \sigma\sigma' \left[ \left\langle T_\tau c_{\zeta,\sigma}(1) c_{\lambda,\sigma}^\dagger(1^+) c_{\nu,\sigma'}^\dagger(2^+) c_{\eta,\sigma'}(2) \right\rangle + G_{\zeta\lambda,\sigma}(1, 1^+) G_{\eta\nu,\sigma'}(2, 2^+) \right]
 \end{aligned}$$

## 5.1. THE KADANOFF-BAYM FORMALISM

$$(5.145) = \sum_{\sigma, \sigma'} \sigma \sigma' \langle T_{\tau} n_{\zeta\lambda, \sigma}(1) n_{\eta\nu, \sigma'}(2) \rangle - \langle n_{\zeta\lambda, \sigma}(1) \rangle \langle n_{\eta\nu, \sigma'}(2) \rangle$$

$$= \langle T_{\tau} [n_{\zeta\lambda, \uparrow}(1) - n_{\zeta\lambda, \downarrow}(1)] [n_{\eta\nu, \uparrow}(2) - n_{\eta\nu, \downarrow}(2)] \rangle$$

$$(5.146) - \langle n_{\zeta\lambda, \uparrow}(1) - n_{\zeta\lambda, \downarrow}(1) \rangle \langle n_{\eta\nu, \uparrow}(2) - n_{\eta\nu, \downarrow}(2) \rangle$$

$$(5.147) = \chi_{\lambda\zeta\eta\nu}^{sp}(1, 2).$$

From eq. (5.58) we can also define a self-consistent equation for the three-point spin susceptibility which is called the *Bethe-Salpeter equation* for the spin susceptibility,

$$(5.148) \begin{aligned} & \chi_{\lambda\zeta\eta\nu}^{sp}(1, 3; 2) \\ &= - \sum_{\sigma\sigma'} \sigma\sigma' \left( G_{\zeta\nu, \sigma}(1, 2^+) G_{\eta\lambda, \sigma}(2, 3) \delta_{\sigma, \sigma'} \right. \\ & \quad \left. + G_{\zeta\bar{\beta}, \sigma}(1, \bar{3}) \frac{\delta\Sigma_{\bar{\beta}\bar{\gamma}, \sigma}(\bar{3}, \bar{2})_{\phi}}{\delta G_{\bar{\rho}\bar{\lambda}, \sigma''}(\bar{7}, \bar{8})_{\phi}} \frac{\delta G_{\bar{\rho}\bar{\lambda}, \sigma''}(\bar{7}, \bar{8})_{\phi}}{\delta\phi_{\nu\eta, \sigma'}(2^+, 2)} \Bigg|_{\phi=0} G_{\bar{\gamma}\lambda, \sigma}(\bar{2}, 3) \right) \end{aligned}$$

$$= - 2G_{\zeta\nu}(1, 2^+)_{\phi} G_{\eta\lambda}(2, 3)$$

$$(5.149) - G_{\zeta\bar{\beta}}(1, \bar{3}) \sum_{\sigma, \sigma', \sigma''} \sigma\sigma'(\sigma'')^2 \frac{\delta\Sigma_{\bar{\beta}\bar{\gamma}, \sigma}(\bar{3}, \bar{2})_{\phi}}{\delta G_{\bar{\rho}\bar{\lambda}, \sigma''}(\bar{7}, \bar{8})_{\phi}} \frac{\delta G_{\bar{\rho}\bar{\lambda}, \sigma''}(\bar{7}, \bar{8})_{\phi}}{\delta\phi_{\nu\eta, \sigma'}(2^+, 2)} \Bigg|_{\phi=0} G_{\bar{\gamma}\lambda}(\bar{2}, 3),$$

where we again dropped the spin index in the Green's function  $G$  due to time-reversal symmetry and spin rotation invariance. By the same argument we can again use eq. (5.125) which states the functional derivatives only depend on the relative spin alignment of the functional and the function it is differentiated by. This leads to

$$(5.150) \begin{aligned} & \chi_{\lambda\zeta\eta\nu}^{sp}(1, 3; 2) \\ &= - 2G_{\zeta\nu}(1, 2^+) G_{\eta\lambda}(2, 3) \\ & \quad + G_{\zeta\bar{\beta}}(1, \bar{3}) \sum_{\sigma} \sigma \frac{\delta\Sigma_{\bar{\beta}\bar{\gamma}, \sigma}(\bar{3}, \bar{2})_{\phi}}{\delta G_{\bar{\rho}\bar{\lambda}, \downarrow}(\bar{7}, \bar{8})_{\phi}} \Bigg|_{\phi=0} \sum_{\sigma', \sigma''} \sigma' \sigma'' \frac{\delta G_{\bar{\rho}\bar{\lambda}, \sigma''}(\bar{7}, \bar{8})_{\phi}}{\delta\phi_{\nu\eta, \sigma'}(2^+, 2)} \Bigg|_{\phi=0} G_{\bar{\gamma}\lambda}(\bar{2}, 3) \end{aligned}$$

$$= - 2G_{\zeta\nu}(1, 2^+) G_{\eta\lambda}(2, 3)$$

$$(5.151) - G_{\zeta\bar{\beta}}(1, \bar{3}) \sum_{\sigma} \sigma \frac{\delta\Sigma_{\bar{\beta}\bar{\gamma}, \sigma}(\bar{3}, \bar{2})_{\phi}}{\delta G_{\bar{\rho}\bar{\lambda}, \downarrow}(\bar{7}, \bar{8})_{\phi}} \Bigg|_{\phi=0} \chi_{\bar{\lambda}\bar{\rho}\eta\nu}^{sp}(\bar{7}, \bar{8}; 2) G_{\bar{\gamma}\lambda}(\bar{2}, 3)$$

$$(5.152) = - 2G_{\zeta\nu}(1, 2^+) G_{\eta\lambda}(2, 3) - G_{\zeta\bar{\beta}}(1, \bar{3}) \Gamma_{\bar{\gamma}\bar{\beta}\bar{\lambda}\bar{\rho}}^{sp}(\bar{3}, \bar{2}; \bar{7}, \bar{8}) \chi_{\bar{\lambda}\bar{\rho}\eta\nu}^{sp}(\bar{7}, \bar{8}; 2) G_{\bar{\gamma}\lambda}(\bar{2}, 3),$$

where we have defined the *irreducible spin vertex*

$$(5.153) \quad \Gamma_{\bar{\gamma}\bar{\beta}\bar{\lambda}\bar{\rho}}^{sp}(3, 2; 7, 8) = \sum_{\sigma} \sigma \frac{\delta\Sigma_{\bar{\beta}\bar{\gamma}, \sigma}(3, 2)_{\phi}}{\delta G_{\bar{\rho}\bar{\lambda}, \downarrow}(7, 8)_{\phi}} \Bigg|_{\phi=0}.$$

**5.1.7. Self-energy equation of motion.** We are now prepared to relate the spin and charge susceptibilities  $\chi^{sp/ch}$  to the self-energy  $\Sigma$ . Starting point is the implicit self-energy equation (5.51),

$$(5.154) \quad \begin{aligned} & \Sigma_{\alpha\bar{\beta}, \sigma}(1, \bar{4})_{\phi} G_{\bar{\beta}\bar{\gamma}, \sigma}(\bar{4}, 2)_{\phi} \\ &= U_{\alpha} \left( - \frac{\delta G_{\alpha\bar{\gamma}, \sigma}(1, 2)}{\delta\phi_{\alpha\alpha, -\sigma}(1^+, 1)} + G_{\alpha\alpha, -\sigma}(1, 1^+)_{\phi} G_{\alpha\bar{\gamma}, \sigma}(1, 2)_{\phi} \right). \end{aligned}$$

We can first decompose the generalized susceptibility  $-\frac{\delta G}{\delta \phi}$  into spin and charge channel via eqs. (5.121), (5.143),

$$(5.155) \quad -\frac{\delta G_\sigma}{\delta \phi_{-\sigma}} \Big|_{\phi=0} = -\frac{1}{4} 4 \frac{\delta G_\sigma}{\delta \phi_{-\sigma}} \Big|_{\phi=0} = \frac{1}{4} \left( \sum_{\sigma, \sigma'} \sigma \sigma' \frac{\delta G_\sigma}{\delta \phi_{\sigma'}} - \sum_{\sigma, \sigma'} \frac{\delta G_\sigma}{\delta \phi_{\sigma'}} \right) \Big|_{\phi=0}$$

$$(5.156) \quad = -\frac{1}{4} (\chi^{sp} - \chi^{ch}),$$

where we made use of spin-rotational invariance and time-reversal symmetry. Thus, we can identify in the limit  $\phi = 0$

$$(5.157) \quad \Sigma_{\alpha\bar{\beta},\sigma}(1,\bar{4})G_{\bar{\beta}\gamma,\sigma}(\bar{4},2) = U_\alpha \left[ \frac{1}{4} (\chi_{\gamma\alpha\alpha\alpha}^{ch}(1,2;1) - \chi_{\gamma\alpha\alpha\alpha}^{sp}(1,2;1)) + n_{\alpha,-\sigma}(1)G_{\alpha\gamma,\sigma}(1,2) \right].$$

Iterating once the Bethe-Salpeter equation for the spin and charge susceptibility  $\chi^{sp/ch}$  (eqs. (5.129), (5.152)) we get

$$(5.158) \quad \Sigma_{\alpha\bar{\beta},\sigma}(1,\bar{4})G_{\bar{\beta}\gamma,\sigma}(\bar{4},2) = U_\alpha \left[ \frac{1}{4} \left( G_{\alpha\bar{\beta}}(1,\bar{3})\Gamma_{\bar{\epsilon}\beta\lambda\bar{\rho}}^{ch}(\bar{3},\bar{4};\bar{7},\bar{8})\chi_{\lambda\bar{\rho}\alpha\alpha}^{ch}(\bar{7},\bar{8};1)G_{\bar{\epsilon}\gamma}(\bar{4},2) + G_{\alpha\bar{\beta}}(1,\bar{3})\Gamma_{\bar{\epsilon}\beta\lambda\bar{\rho}}^{sp}(\bar{3},\bar{4};\bar{7},\bar{8})\chi_{\lambda\bar{\rho}\alpha\alpha}^{sp}(\bar{7},\bar{8};1)G_{\bar{\epsilon}\gamma}(\bar{4},2) \right) + n_{\alpha,-\sigma}(1)G_{\alpha\gamma,\sigma}(1,2) \right].$$

Multiplying with  $G_{\bar{\gamma}\nu,\sigma}(\bar{2},5)$  and integrating over the internal degrees of freedom we obtain the *equation of motion for the self-energy*

$$(5.159) \quad \Sigma_{\alpha\nu,\sigma}(1,5) = U_\alpha n_{\alpha,-\sigma}(1)\delta_{\alpha,\nu}\delta(1-5) + \frac{U_\alpha}{4} \left[ \Gamma_{\nu\bar{\beta}\lambda\bar{\rho}}^{ch}(\bar{3},5;\bar{7},\bar{8})\chi_{\lambda\bar{\rho}\alpha\alpha}^{ch}(\bar{7},\bar{8};1) + \Gamma_{\nu\bar{\beta}\lambda\bar{\rho}}^{sp}(\bar{3},5;\bar{7},\bar{8})\chi_{\lambda\bar{\rho}\alpha\alpha}^{sp}(\bar{7},\bar{8};1) \right] G_{\alpha\bar{\beta}}(1,\bar{3}).$$

A diagrammatic representation of the equation of motion for the self-energy is shown in fig. 5.2. We can interpret the self-energy equation (5.159) as the Hartree contri-

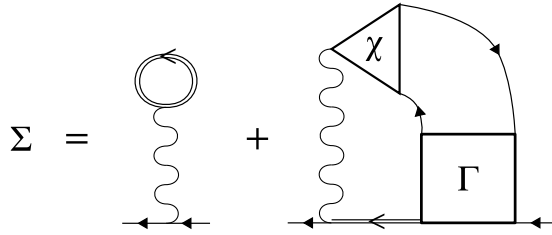


FIGURE 5.2. Diagrammatic representation of the self-energy equation of motion (5.159). The double lines represent interacting Green's functions while the wiggled single lines are Hubbard interactions  $U$ . For simplicity we dropped the spin and charge decomposition here.

bution<sup>5</sup> and an additional contribution that contains collective excitations from the paramagnetic state via susceptibilities  $\chi^{sp/ch}$  and effective interaction vertices  $\Gamma^{sp/ch}$ .

In summary, we have an equation that relates the self-energy to the spin and charge susceptibility and those susceptibilities themselves are determined by self-consistent equations, namely the Bethe-Salpeter equations. The remaining parts that enter both

<sup>5</sup>In the single-orbital case the Fock contribution cancels with the same spin-part of the Hartree term.

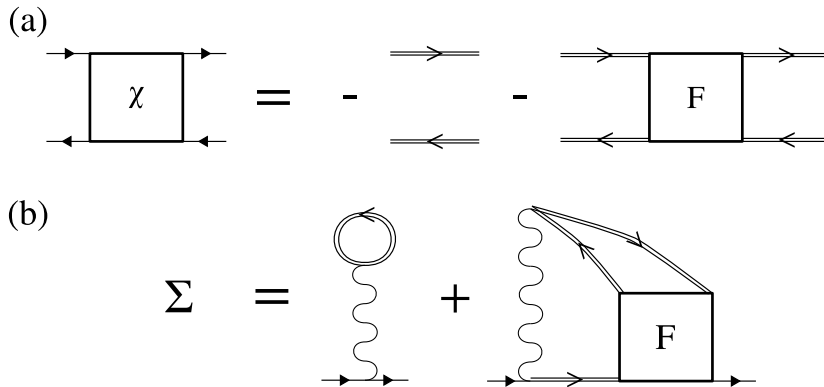


FIGURE 5.3. Diagrammatic representation of the equation of motion for (a) the generalized susceptibility  $\chi$  and (b) the self-energy  $\Sigma$ . Double lines represent the interacting Green's function  $G$  while  $F$  is the full vertex function. Although the diagram shows some similarity to fig. 5.1 and 5.2 they do not represent a particular choice of channel.

above mentioned equations are the irreducible vertices that are only given as functional derivatives  $\frac{\delta \Sigma}{\delta G}$  so far. This will be discussed in more details in sec. 5.2.

**5.1.8. Diagrammatics and channel decomposition.** Before we continue the derivation of the Bethe-Salpeter equations for the different susceptibilities and the equation of motion for the self-energy in the transversal particle-hole channel we go into more detail regarding the channel decomposition. We follow here the presentation in [110, 155, 157–160].

Similar to the derivations in the previous sections one can derive an equation of motion for the self-energy  $\Sigma$  and the generalized susceptibility  $\chi$  without any particular choice of channel. The resulting equations are shown diagrammatically in fig. 5.3 In contrast to the equations that we derived previously for  $\chi$  and  $\Sigma$  (eqs. (5.58) and (5.159)) we observe that the collective mode contribution  $\chi$  and the respective irreducible vertex  $\Gamma$  are replaced by the so-called *full vertex*  $F$  and interacting Green's function lines  $G$ . To see the connection between both formulations we repeat important aspects of diagrammatic quantum field theory.

The concept of *one-particle irreducibility*<sup>6</sup> is crucial in the diagrammatic description of the self-energy as a sum of all connected topologically distinct one-particle irreducible non-interacting Green's function diagrams where the external legs are amputated.

Such a diagrammatic series in terms of the non-interacting Green's function can be reformulated in terms of the full Green's function when restricting the diagrams to so-called *skeleton diagrams*, i.e. diagrams without the appearance of explicit self-energy lines. This restriction of diagrams is important to avoid double-counting since the full Green's function already contains all many-body corrections from the self-energy.

Similarly, one obtains for the generalized susceptibility the expression in fig. 5.3(a) where the full two-particle vertex  $F$  contains information about to quasi-particle scattering processes<sup>7</sup>. Due to particle number conservation one can prove that all contributions to  $F$  are one-particle irreducible.

For this reason one needs a different classification of the diagrams that enter  $F$  and here we introduce the notion of *two-particle irreducibility*. The basic idea is to distinguish between diagrams by cutting two internal Green's function lines. If the diagram

<sup>6</sup>This means that a Feynman diagram for the Green's function cannot be divided into two subdiagrams by cutting one internal non-interacting Green's function line.

<sup>7</sup>Obviously, this interpretation is only valid in the Fermi liquid regime.

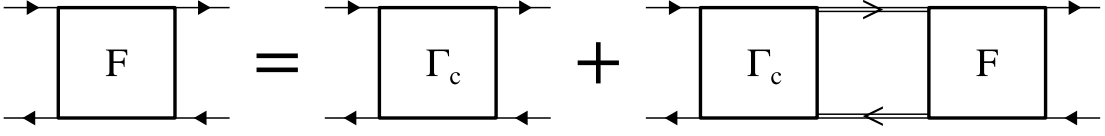


FIGURE 5.4. Diagrammatic representation of the Bethe-Salpeter equation that decomposes the full two-particle vertex  $F$  into the three different two-particle reducible channels  $c \in \{pp, ph, \overline{ph}\}$ , where  $\Gamma_c$  is the two-particle irreducible vertex in the channel  $c$  and double solid lines are full Green's functions.

decomposes into two subdiagrams we call the diagram *two-particle reducible* and else *two-particle irreducible*. A finer classification can be made in the case of two-particle reducible diagrams, namely in terms of *channels*: Assume that a two-particle reducible diagram has four outer legs labeled with 1, 2, 3 and 4, where 1 and 3 label outgoing particles while 2 and 4 denote incoming particles.

The case where 1 and 3 are separated from 2 and 4 are called *particle-particle (pp) reducible*. If 1 and 2 are separated from 3 and 4 we call the diagram *longitudinal particle-hole (ph) reducible*. The last remaining case is if one can separate 1 and 4 from 2 and 3, where such a diagram is called *transversal particle-hole ( $\overline{ph}$ ) reducible*.

Note that a connected two-particle diagram in  $F$  is either irreducible or reducible in exactly one of the three above mentioned channels. Thus, one can decompose the full two-particle vertex

$$(5.160) \quad F = \Lambda_c + \Gamma_c,$$

where  $c \in \{pp, ph, \overline{ph}\}$  and  $\Gamma_c$  contains all diagrams of  $F$  that are irreducible in the channel  $c$  while  $\Lambda_c$  contains the ones that are reducible in the channel  $c$ . Moreover, one can decompose  $F$  in each of the three channels via the Bethe-Salpeter equation in fig. 5.4. Combining the Bethe-Salpeter equation for  $F$  (fig. 5.4) with the equations for the generalized susceptibility  $\chi$  and the self-energy  $\Sigma$  we find a decomposition of the self-energy

$$(5.161) \quad \Sigma = \Sigma_{irr} + \Sigma_{pp} + \Sigma_{ph} + \Sigma_{\overline{ph}},$$

where  $\Sigma_{irr}$  contains the contributions from fully two-particle irreducible diagrams while the other three terms correspond to the three above mentioned channels  $pp, ph$  and  $\overline{ph}$ . In the same spirit one defines generalized susceptibilities for each channel as in fig. 5.1, where the two-particle irreducible vertex has to be replaced with the one from the respective channel. Furthermore, the particle-hole channels allow to make use of the spin-rotational invariance and time-reversal symmetry and to further decompose the generalized susceptibilities  $\chi$  and the vertices  $\Gamma$  into spin and charge components which finally leads to the representation in fig. (5.2) for each channel.

After this small journey into the diagrammatic formulation of quantum field theory we need to make a connection to our formulation in term of artificial source fields  $\phi$  and functional derivatives.

When reconsidering the equation that implicitly defines the self-energy (eq. (5.48)),

$$(5.162) \quad \Sigma_{\nu\overline{\beta},\sigma}(1,\overline{3})_{\phi} G_{\overline{\beta\xi},\sigma}(\overline{3},2)_{\phi} = -U_{\nu} \left\langle T_{\tau} c_{\nu,-\sigma}^{\dagger}(1^{+}) c_{\nu,-\sigma}(1) c_{\nu,\sigma}(1) c_{\xi,\sigma}^{\dagger}(2) \right\rangle_{\phi},$$

we recall that we introduced the artificial field  $\phi$  to express the right-hand side in terms of a functional derivative  $\frac{\delta G}{\delta \phi}$  (eq. (5.51)),

$$\Sigma_{\nu\overline{\beta},\sigma}(1,\overline{3})_{\phi} G_{\overline{\beta\xi},\sigma}(\overline{3},2)_{\phi}$$

$$(5.163) \quad = U_\nu \left( -\frac{\delta G_{\nu\xi,\sigma}(1,2)}{\delta \phi_{\nu\nu,-\sigma}(1^+,1)} + G_{\nu\nu,-\sigma}(1,1^+) \phi G_{\nu\xi,\sigma}(1,2) \phi \right),$$

which means that we defined  $\phi$  such that the functional derivative generates the thermodynamic average of

$$c_{\nu,-\sigma}^\dagger(1^+) c_{\nu,-\sigma}(1) (ph)$$

in the right-hand side of eq. (5.162) but one could also think of defining  $\phi$  such that it generates the average of

$$c_{\nu,-\sigma}^\dagger(1^+) c_{\nu,\sigma}(1) (\overline{ph})$$

or other combinations.

In choosing a specific form for  $\phi$  we determine in the Bethe-Salpeter equation (eq. (5.58)) a specific channel and thus a specific self-energy contribution (see eq. (5.161) and (5.163)).

As mentioned previously, we will constrain ourselves to the particle-hole channels since those will have the largest contributions to the self-energy in the repulsive Hubbard model [153–155].

Apart from the weight that both particle-hole channels contribute to the self-energy there is another important reason why we treat both and not only the longitudinal particle-hole channel.

By the Pauli principle – that is implemented in the imaginary time ordering operator – we know that by interchanging the two annihilation operators or the two creation operators in eq. (5.162) we collect a minus sign in front of the thermal average. As discussed earlier such an exchange of operators corresponds to a change in the particle-hole channel, i.e. one moves from the transversal to the longitudinal particle-hole channel and vice versa. This transition between the two channels has its manifestation in the relations

$$(5.164) \quad \Gamma_{ph}(1,2;3,4) = -\Gamma_{\overline{ph}}(1,4;3,2),$$

$$(5.165) \quad F(1,2;3,4) = -F(1,4;3,2),$$

which is the *crossing symmetry*<sup>8</sup> of the full vertex  $F$  and the irreducible particle-hole vertices  $\Gamma_{ph,\overline{ph}}$ .

We can enforce crossing symmetry on the self-energy from the longitudinal particle hole channel (see eq. (5.159)) by averaging with the self-energy from the transversal particle-hole channel (see sec. 5.4.2) because then we have only those two channel contributions in equal parts.

**5.1.9. Transversal particle-hole channel.** The derivation follows [154, 161, 162] but we extend the notation to multi-site problems.

To access fluctuations in the transversal particle-hole channel we define the artificial field

$$(5.166) \quad \Phi_{\alpha\beta}(1,2) = \begin{pmatrix} 0 & \phi_{\alpha\beta}^-(1,2) \\ \phi_{\alpha\beta}^+(1,2) & 0 \end{pmatrix}$$

that couples to different spins in the grand canonical partition function

$$(5.167) \quad Z[\Phi] = \left\langle T_\tau e^{-c_{\alpha,\uparrow}^\dagger(\overline{1}) \phi_{\alpha\overline{\beta}}^-(\overline{1},\overline{2}) c_{\overline{\beta},\downarrow}(\overline{2}) - c_{\alpha,\downarrow}^\dagger(\overline{1}) \phi_{\alpha\overline{\beta}}^+(\overline{1},\overline{2}) c_{\overline{\beta},\uparrow}(\overline{2})} \right\rangle$$

$$(5.168) \quad = \left\langle T_\tau e^{-\mathbf{c}_{\alpha}^\dagger(\overline{1}) \Phi_{\alpha\overline{\beta}}(\overline{1},\overline{2}) \mathbf{c}_{\overline{\beta}}(\overline{2})} \right\rangle.$$

---

<sup>8</sup>The terms crossing stems from the fact that the interchange of creation and annihilation operators within eq. (5.162) is visualized diagrammatically by swapping the opposite corners of the four-point diagram.

where we defined (spin-vector-valued) fields

$$(5.169) \quad \mathbf{c}_\alpha(1) := \begin{pmatrix} c_{\alpha,\uparrow}(1) \\ c_{\alpha,\downarrow}(1) \end{pmatrix}, \quad \mathbf{c}_\alpha^\dagger(1) := \begin{pmatrix} c_{\alpha,\uparrow}^\dagger(1) & c_{\alpha,\downarrow}^\dagger(1) \end{pmatrix}.$$

Analogously to the steps in the longitudinal channel (sec. 5.1.2), we define the generalized spin-space Green's function

$$(5.170) \quad \mathbf{G}_{\alpha\beta}^{\sigma\sigma'}(1, 2)_\Phi := - \left\langle T_\tau c_{\alpha,\sigma}(1) c_{\beta,\sigma'}^\dagger(2) \right\rangle_\Phi,$$

$$(5.171) \quad \mathbf{G}_{\alpha\beta}(1, 2)_\Phi := - \begin{pmatrix} \left\langle T_\tau c_{\alpha,\uparrow}(1) c_{\beta,\uparrow}^\dagger(2) \right\rangle_\Phi & \left\langle T_\tau c_{\alpha,\uparrow}(1) c_{\beta,\downarrow}^\dagger(2) \right\rangle_\Phi \\ \left\langle T_\tau c_{\alpha,\downarrow}(1) c_{\beta,\uparrow}^\dagger(2) \right\rangle_\Phi & \left\langle T_\tau c_{\alpha,\downarrow}(1) c_{\beta,\downarrow}^\dagger(2) \right\rangle_\Phi \end{pmatrix}.$$

Notice that we can only generate off-diagonal Green's function elements via functional differentiation

$$(5.172) \quad - \frac{\delta \ln Z[\Phi]}{\delta \Phi_{\beta\alpha}(2, 1)} = \begin{pmatrix} 0 & \mathbf{G}_{\alpha\beta}^{\uparrow\downarrow}(1, 2)_\Phi \\ \mathbf{G}_{\alpha\beta}^{\downarrow\uparrow}(1, 2)_\Phi & 0 \end{pmatrix},$$

where we defined the functional derivative<sup>9</sup>

$$(5.173) \quad \frac{\delta}{\delta \Phi_{\nu\epsilon}(4, 5)} := \begin{pmatrix} 0 & \frac{\delta}{\delta \phi_{\nu\epsilon}^+(4, 5)} \\ \frac{\delta}{\delta \phi_{\nu\epsilon}^-(4, 5)} & 0 \end{pmatrix}.$$

Following the same steps as in Section 5.1.3 we find the matrix Dyson equation

$$(5.174) \quad \mathbf{G}^{-1}(1, 2)_\Phi = (\mathbf{G}^0)^{-1}(1, 2) - \Sigma(1, 2)_\Phi - \Phi,$$

where the inverse is taken in the orbital-spin space with the implicitly defined self-energy equation

$$(5.175) \quad \begin{aligned} & \Sigma_{\alpha\bar{\lambda}}(1, \bar{3})_\Phi \mathbf{G}_{\bar{\lambda}\gamma}(\bar{3}, 2)_\Phi \\ &= -U_\alpha \begin{pmatrix} \left\langle T_\tau n_{\alpha,\downarrow}(1) c_{\alpha,\uparrow}(1) c_{\gamma,\uparrow}^\dagger(2) \right\rangle_\Phi & \left\langle T_\tau n_{\alpha,\downarrow}(1) c_{\alpha,\uparrow}(1) c_{\gamma,\downarrow}^\dagger(2) \right\rangle_\Phi \\ \left\langle T_\tau n_{\alpha,\uparrow}(1) c_{\alpha,\downarrow}(1) c_{\gamma,\uparrow}^\dagger(2) \right\rangle_\Phi & \left\langle T_\tau n_{\alpha,\uparrow}(1) c_{\alpha,\downarrow}(1) c_{\gamma,\downarrow}^\dagger(2) \right\rangle_\Phi \end{pmatrix}. \end{aligned}$$

As before we derive the Bethe-Salpeter equation for the generalized susceptibility from the matrix equation

$$(5.176) \quad \mathbf{G}_{\alpha\bar{\beta}}(1, \bar{3})_\Phi (\mathbf{G}^{-1})_{\bar{\beta}\gamma}(\bar{3}, 2)_\Phi = \mathbf{I} \delta(1-2) \delta_{\alpha,\gamma},$$

where  $\mathbf{I}$  is the identity matrix in spin space. By taking the functional derivative with respect to  $\Phi$  of eq. (5.176) we obtain the expression

$$(5.177) \quad 0 = \frac{\delta}{\delta \Phi_{\nu\epsilon}(4, 5)} \left[ \mathbf{G}_{\alpha\bar{\beta}}(1, \bar{3})_\Phi (\mathbf{G}^{-1})_{\bar{\beta}\gamma}(\bar{3}, 2)_\Phi \right]$$

$$(5.178) \quad = \left[ \begin{pmatrix} 0 & 1 \\ 0 & 0 \end{pmatrix} \frac{\delta}{\delta \phi_{\nu\epsilon}^+(4, 5)} + \begin{pmatrix} 0 & 0 \\ 1 & 0 \end{pmatrix} \frac{\delta}{\delta \phi_{\nu\epsilon}^-(4, 5)} \right] \left[ \mathbf{G}_{\alpha\bar{\beta}}(1, \bar{3})_\Phi (\mathbf{G}^{-1})_{\bar{\beta}\gamma}(\bar{3}, 2)_\Phi \right]$$

$$= \frac{\delta \mathbf{G}_{\alpha\bar{\beta}}(1, \bar{3})_\Phi}{\delta \Phi_{\nu\epsilon}(4, 5)} (\mathbf{G}^{-1})_{\bar{\beta}\gamma}(\bar{3}, 2)_\Phi + \begin{pmatrix} 0 & 1 \\ 0 & 0 \end{pmatrix} \mathbf{G}_{\alpha\bar{\beta}}(1, \bar{3})_\Phi \frac{\delta (\mathbf{G}^{-1})_{\bar{\beta}\gamma}(\bar{3}, 2)_\Phi}{\delta \phi_{\nu\epsilon}^+(4, 5)}$$

$$(5.179) \quad + \begin{pmatrix} 0 & 0 \\ 1 & 0 \end{pmatrix} \mathbf{G}_{\alpha\bar{\beta}}(1, \bar{3})_\Phi \frac{\delta (\mathbf{G}^{-1})_{\bar{\beta}\gamma}(\bar{3}, 2)_\Phi}{\delta \phi_{\nu\epsilon}^-(4, 5)}.$$

<sup>9</sup>One can easily check  $\mathbf{I} \delta(1-3) \delta(2-4) = \frac{\delta \Phi(1, 2)}{\delta \Phi(3, 4)}$ .

## 5.1. THE KADANOFF-BAYM FORMALISM

Multiplying both sides by  $\mathbf{G}_{\bar{\gamma}\zeta}(\bar{2}, 6)$  while integration over all internal degrees of freedom we obtain

$$(5.180) \quad 0 = \frac{\delta \mathbf{G}_{\alpha\zeta}(1, 6)_{\Phi}}{\delta \Phi_{\nu\epsilon}(4, 5)} + \begin{pmatrix} 0 & 1 \\ 0 & 0 \end{pmatrix} \mathbf{G}_{\alpha\bar{\beta}}(1, \bar{3})_{\Phi} \frac{\delta (\mathbf{G}^{-1})_{\bar{\beta}\bar{\gamma}}(\bar{3}, \bar{2})_{\Phi}}{\delta \phi_{\nu\epsilon}^+(4, 5)} \mathbf{G}_{\bar{\gamma}\zeta}(\bar{2}, 6) \\ + \begin{pmatrix} 0 & 0 \\ 1 & 0 \end{pmatrix} \mathbf{G}_{\alpha\bar{\beta}}(1, \bar{3})_{\Phi} \frac{\delta (\mathbf{G}^{-1})_{\bar{\beta}\bar{\gamma}}(\bar{3}, \bar{2})_{\Phi}}{\delta \phi_{\nu\epsilon}^-(4, 5)} \mathbf{G}_{\bar{\gamma}\zeta}(\bar{2}, 6).$$

We can now use the Dyson equation (5.174) to further simplify

$$(5.181) \quad \left. \frac{\delta \mathbf{G}_{\alpha\zeta}(1, 6)_{\Phi}}{\delta \Phi_{\nu\epsilon}(4, 5)} \right|_{\Phi=0} = \begin{pmatrix} 0 & 1 \\ 0 & 0 \end{pmatrix} \mathbf{G}_{\alpha\nu}(1, 4) \begin{pmatrix} 0 & 0 \\ 1 & 0 \end{pmatrix} \mathbf{G}_{\epsilon\zeta}(5, 6) \\ + \begin{pmatrix} 0 & 0 \\ 1 & 0 \end{pmatrix} \mathbf{G}_{\alpha\nu}(1, 4) \begin{pmatrix} 0 & 1 \\ 0 & 0 \end{pmatrix} \mathbf{G}_{\epsilon\zeta}(5, 6) \\ + \begin{pmatrix} 0 & 1 \\ 0 & 0 \end{pmatrix} \mathbf{G}_{\alpha\bar{\beta}}(1, \bar{3}) \left. \frac{\delta \Sigma_{\bar{\beta}\bar{\gamma}}(\bar{3}, \bar{2})_{\Phi}}{\delta \phi_{\nu\epsilon}^+(4, 5)} \right|_{\Phi=0} \mathbf{G}_{\bar{\gamma}\zeta}(\bar{2}, 6) \\ + \begin{pmatrix} 0 & 0 \\ 1 & 0 \end{pmatrix} \mathbf{G}_{\alpha\bar{\beta}}(1, \bar{3}) \left. \frac{\delta \Sigma_{\bar{\beta}\bar{\gamma}}(\bar{3}, \bar{2})_{\Phi}}{\delta \phi_{\nu\epsilon}^-(4, 5)} \right|_{\Phi=0} \mathbf{G}_{\bar{\gamma}\zeta}(\bar{2}, 6) \\ = \begin{pmatrix} \mathbf{G}_{\alpha\nu}^{\downarrow\downarrow}(1, 4) \mathbf{G}_{\epsilon\zeta}^{\uparrow\uparrow}(5, 6) & \mathbf{G}_{\alpha\nu}^{\downarrow\downarrow}(1, 4) \mathbf{G}_{\epsilon\zeta}^{\uparrow\downarrow}(5, 6) \\ \mathbf{G}_{\alpha\nu}^{\uparrow\uparrow}(1, 4) \mathbf{G}_{\epsilon\zeta}^{\downarrow\uparrow}(5, 6) & \mathbf{G}_{\alpha\nu}^{\uparrow\uparrow}(1, 4) \mathbf{G}_{\epsilon\zeta}^{\downarrow\downarrow}(5, 6) \end{pmatrix} \\ + \begin{pmatrix} 0 & 1 \\ 0 & 0 \end{pmatrix} \mathbf{G}_{\alpha\bar{\beta}}(1, \bar{3}) \left. \frac{\delta \Sigma_{\bar{\beta}\bar{\gamma}}(\bar{3}, \bar{2})_{\Phi}}{\delta \mathbf{G}_{\bar{\rho}\lambda}^{\bar{\sigma}\bar{\sigma}'}}(\bar{7}, \bar{8})_{\Phi}}{\delta \phi_{\nu\epsilon}^+(4, 5)} \right|_{\Phi=0} \mathbf{G}_{\bar{\gamma}\zeta}(\bar{2}, 6) \\ (5.182) \quad + \begin{pmatrix} 0 & 0 \\ 1 & 0 \end{pmatrix} \mathbf{G}_{\alpha\bar{\beta}}(1, \bar{3}) \left. \frac{\delta \Sigma_{\bar{\beta}\bar{\gamma}}(\bar{3}, \bar{2})_{\Phi}}{\delta \mathbf{G}_{\bar{\rho}\lambda}^{\bar{\sigma}\bar{\sigma}'}}(\bar{7}, \bar{8})_{\Phi}}{\delta \phi_{\nu\epsilon}^-(4, 5)} \right|_{\Phi=0} \mathbf{G}_{\bar{\gamma}\zeta}(\bar{2}, 6).$$

Things become much easier when we consider that the Hamiltonian without external field  $\Phi$  preserves the spin. Therefore, in the limit  $\Phi = 0$  that we are considering in eq. (5.182) we can neglect all terms that involve surplus or deficiency of spin in the thermal expectation values, namely

$$(5.183) \quad \mathbf{G}^{-\sigma\sigma} = \left. \frac{\delta \mathbf{G}^{\sigma\sigma}}{\delta \phi^{\pm}} \right|_{\phi^{\pm}=0} = \left. \frac{\delta \mathbf{G}^{\uparrow\downarrow}}{\delta \phi^+} \right|_{\phi^{\pm}=0} = \left. \frac{\delta \mathbf{G}^{\downarrow\uparrow}}{\delta \phi^-} \right|_{\phi^{\pm}=0} = 0.$$

This simplifies eq. (5.182) and we end up with

$$(5.184) \quad \begin{pmatrix} \left. \frac{\delta \mathbf{G}_{\alpha\zeta}^{\downarrow\uparrow}(1, 6)_{\Phi}}{\delta \phi_{\nu\epsilon}^+(4, 5)} \right|_{\phi^+=0} & 0 \\ 0 & \left. \frac{\delta \mathbf{G}_{\alpha\zeta}^{\uparrow\downarrow}(1, 6)_{\Phi}}{\delta \phi_{\nu\epsilon}^-(4, 5)} \right|_{\phi^-=0} \end{pmatrix} \\ = \begin{pmatrix} G_{\alpha\nu}(1, 4) G_{\epsilon\zeta}(5, 6) & 0 \\ 0 & G_{\alpha\nu}(1, 4) G_{\epsilon\zeta}(5, 6) \end{pmatrix} \\ + \begin{pmatrix} 0 & G_{\alpha\bar{\beta}}(1, \bar{3}) G_{\bar{\gamma}\zeta}(\bar{2}, 6) \\ 0 & 0 \end{pmatrix} \left. \frac{\delta \Sigma_{\bar{\beta}\bar{\gamma}}(\bar{3}, \bar{2})_{\Phi}}{\delta \mathbf{G}_{\bar{\rho}\lambda}^{\downarrow\uparrow}(\bar{7}, \bar{8})_{\Phi}} \frac{\delta \mathbf{G}_{\bar{\rho}\lambda}^{\downarrow\uparrow}(\bar{7}, \bar{8})_{\Phi}}{\delta \phi_{\nu\epsilon}^+(4, 5)} \right|_{\Phi=0} \\ (5.184) \quad + \begin{pmatrix} 0 & 0 \\ G_{\alpha\bar{\beta}}(1, \bar{3}) G_{\bar{\gamma}\zeta}(\bar{2}, 6) & 0 \end{pmatrix} \left. \frac{\delta \Sigma_{\bar{\beta}\bar{\gamma}}(\bar{3}, \bar{2})_{\Phi}}{\delta \mathbf{G}_{\bar{\rho}\lambda}^{\uparrow\downarrow}(\bar{7}, \bar{8})_{\Phi}} \frac{\delta \mathbf{G}_{\bar{\rho}\lambda}^{\uparrow\downarrow}(\bar{7}, \bar{8})_{\Phi}}{\delta \phi_{\nu\epsilon}^-(4, 5)} \right|_{\Phi=0}$$

$$\begin{aligned}
 &= \begin{pmatrix} G_{\alpha\nu}(1,4)G_{\epsilon\zeta}(5,6) & 0 \\ 0 & G_{\alpha\nu}(1,4)G_{\epsilon\zeta}(5,6) \end{pmatrix} \\
 &+ \begin{pmatrix} 0 & G_{\alpha\bar{\beta}}(1,\bar{3})G_{\bar{\gamma}\zeta}(\bar{2},6) \\ 0 & 0 \end{pmatrix} \begin{pmatrix} 0 & 0 \\ 1 & 0 \end{pmatrix} \frac{\delta\Sigma_{\bar{\beta}\bar{\gamma}}^{\uparrow\downarrow}(\bar{3},\bar{2})_{\Phi}}{\delta\mathbf{G}_{\bar{\rho}\bar{\lambda}}^{\uparrow\downarrow}(\bar{7},\bar{8})_{\Phi}} \frac{\delta\mathbf{G}_{\bar{\rho}\bar{\lambda}}^{\uparrow\downarrow}(\bar{7},\bar{8})_{\Phi}}{\delta\phi_{\nu\epsilon}^+(4,5)} \Bigg|_{\Phi=0} \\
 (5.185) \quad &+ \begin{pmatrix} 0 & 0 \\ G_{\alpha\bar{\beta}}(1,\bar{3})G_{\bar{\gamma}\zeta}(\bar{2},6) & 0 \end{pmatrix} \begin{pmatrix} 0 & 1 \\ 0 & 0 \end{pmatrix} \frac{\delta\Sigma_{\bar{\beta}\bar{\gamma}}^{\uparrow\downarrow}(\bar{3},\bar{2})_{\Phi}}{\delta\mathbf{G}_{\bar{\rho}\bar{\lambda}}^{\uparrow\downarrow}(\bar{7},\bar{8})_{\Phi}} \frac{\delta\mathbf{G}_{\bar{\rho}\bar{\lambda}}^{\uparrow\downarrow}(\bar{7},\bar{8})_{\Phi}}{\delta\phi_{\nu\epsilon}^-(4,5)} \Bigg|_{\Phi=0},
 \end{aligned}$$

where we identified  $G := G_{\sigma} = \mathbf{G}^{\uparrow\uparrow} = \mathbf{G}^{\downarrow\downarrow}$  due to paramagnetism and spin rotational invariance. Therefore, the only non-vanishing matrix elements are

$$\begin{aligned}
 \frac{\delta\mathbf{G}_{\alpha\zeta}^{\uparrow\downarrow}(1,6)_{\Phi}}{\delta\phi_{\nu\epsilon}^+(4,5)} \Bigg|_{\Phi=0} &= G_{\alpha\nu}(1,4)G_{\epsilon\zeta}(5,6) + G_{\alpha\bar{\beta}}(1,\bar{3}) \frac{\delta\Sigma_{\bar{\beta}\bar{\gamma}}^{\uparrow\downarrow}(\bar{3},\bar{2})_{\Phi}}{\delta\mathbf{G}_{\bar{\rho}\bar{\lambda}}^{\uparrow\downarrow}(\bar{7},\bar{8})_{\Phi}} \frac{\delta\mathbf{G}_{\bar{\rho}\bar{\lambda}}^{\uparrow\downarrow}(\bar{7},\bar{8})_{\Phi}}{\delta\phi_{\nu\epsilon}^+(4,5)} \Bigg|_{\Phi=0} G_{\bar{\gamma}\zeta}(\bar{2},6) \\
 (5.186) \quad &= - \left\langle T_{\tau} c_{\zeta,\uparrow}^{\dagger}(6) c_{\alpha,\downarrow}(1) c_{\nu,\downarrow}^{\dagger}(4) c_{\epsilon,\uparrow}(5) \right\rangle
 \end{aligned}$$

$$\begin{aligned}
 \frac{\delta\mathbf{G}_{\alpha\zeta}^{\uparrow\downarrow}(1,6)_{\Phi}}{\delta\phi_{\nu\epsilon}^-(4,5)} \Bigg|_{\Phi=0} &= G_{\alpha\nu}(1,4)G_{\epsilon\zeta}(5,6) + G_{\alpha\bar{\beta}}(1,\bar{3}) \frac{\delta\Sigma_{\bar{\beta}\bar{\gamma}}^{\uparrow\downarrow}(\bar{3},\bar{2})_{\Phi}}{\delta\mathbf{G}_{\bar{\rho}\bar{\lambda}}^{\uparrow\downarrow}(\bar{7},\bar{8})_{\Phi}} \frac{\delta\mathbf{G}_{\bar{\rho}\bar{\lambda}}^{\uparrow\downarrow}(\bar{7},\bar{8})_{\Phi}}{\delta\phi_{\nu\epsilon}^-(4,5)} \Bigg|_{\Phi=0} G_{\bar{\gamma}\zeta}(\bar{2},6) \\
 (5.187) \quad &= - \left\langle T_{\tau} c_{\zeta,\downarrow}^{\dagger}(6) c_{\alpha,\uparrow}(1) c_{\nu,\uparrow}^{\dagger}(4) c_{\epsilon,\downarrow}(5) \right\rangle,
 \end{aligned}$$

where the second equality comes from performing the functional derivative on the Green's function directly (eq. (5.168) and (5.171)). Finally, we arrive at the Bethe-Salpeter equations for the generalized susceptibilities in the transversal particle-hole channel. Notice that both expressions are closely related due to spin rotational invariance.

Before we continue with the derivation of the equation of motion for the self-energy in the transversal particle-hole channel we present again a few arguments why it is possible to go from functional derivatives with respect to  $\Phi$  to derivatives with respect to  $\mathbf{G}$ . Starting point is again the free energy  $F$  in the presence of the source field  $\Phi$  (see eqs. (5.168), (5.172)) that is given by

$$(5.188) \quad F[\Phi] = -\frac{1}{\beta} \ln Z[\Phi] = -\frac{1}{\beta} \ln \text{tr} \left( e^{-\tilde{\beta}H} T_{\tau} e^{-\mathbf{c}_{\alpha}^{\dagger}(1)\Phi_{\bar{\alpha}\bar{\beta}}(\bar{1},\bar{2})\mathbf{c}_{\bar{\beta}}(\bar{2})} \right).$$

We obtain the off-diagonal Green's function  $\mathbf{G}^{\sigma-\sigma}$  via functional differentiation

$$(5.189) \quad \tilde{\beta} \frac{\delta F[\Phi]}{\delta\Phi_{\beta\alpha}(2,1)} = \begin{pmatrix} 0 & \mathbf{G}_{\alpha\beta}^{\uparrow\downarrow}(1,2)_{\Phi} \\ \mathbf{G}_{\alpha\beta}^{\downarrow\uparrow}(1,2)_{\Phi} & 0 \end{pmatrix} =: \tilde{\mathbf{G}}_{\alpha\beta}(1,2).$$

The two above equations (5.188), (5.189) are sufficient to define the Legendre transform for the free energy  $F$  via

$$(5.190) \quad \Omega[\tilde{\mathbf{G}}] = F[\Phi] - \frac{1}{\tilde{\beta}} \text{tr} \left( \tilde{\mathbf{G}}\Phi \right),$$

where  $\Omega$  is coined the *Kadanoff-Baym functional* for the off-diagonal Green's function. We find the property

$$(5.191) \quad \tilde{\beta} \frac{\delta}{\delta\tilde{\mathbf{G}}_{\beta\alpha,\sigma}(2,1)} \Omega[\tilde{\mathbf{G}}] := \tilde{\beta} \begin{pmatrix} 0 & \frac{\delta}{\delta\mathbf{G}_{\beta\alpha,\sigma}^{\uparrow\downarrow}(2,1)} \\ \frac{\delta}{\delta\mathbf{G}_{\beta\alpha,\sigma}^{\downarrow\uparrow}(2,1)} & 0 \end{pmatrix} \Omega[\tilde{\mathbf{G}}]$$

$$(5.192) = \tilde{\beta} \frac{\delta F[\Phi]}{\delta \tilde{\mathbf{G}}_{\beta\alpha,\sigma}(2,1)} - \frac{\delta \text{tr}(\tilde{\mathbf{G}}\Phi)}{\delta \tilde{\mathbf{G}}_{\beta\alpha,\sigma}(2,1)}$$

$$(5.193) = \tilde{\beta} \frac{\delta \Phi_{\bar{\gamma}\bar{\epsilon},\bar{\sigma}}(\bar{3},\bar{4})}{\delta \tilde{\mathbf{G}}_{\beta\alpha,\sigma}(2,1)} \frac{\delta F[\Phi]}{\delta \Phi_{\bar{\gamma}\bar{\epsilon},\bar{\sigma}}(\bar{3},\bar{4})} - \frac{\delta \left( \mathbf{G}_{\bar{\epsilon}\bar{\gamma},\bar{\sigma}}^{\uparrow\downarrow}(\bar{4},\bar{3}) \phi_{\bar{\gamma}\bar{\epsilon},\bar{\sigma}}^+(\bar{3},\bar{4}) + \mathbf{G}_{\bar{\epsilon}\bar{\gamma},\bar{\sigma}}^{\downarrow\uparrow}(\bar{4},\bar{3}) \phi_{\bar{\gamma}\bar{\epsilon},\bar{\sigma}}^-(\bar{3},\bar{4}) \right)}{\delta \tilde{\mathbf{G}}_{\beta\alpha,\sigma}(2,1)}$$

$$(5.194) = \frac{\delta \Phi_{\bar{\gamma}\bar{\epsilon},\bar{\sigma}}(\bar{3},\bar{4})}{\delta \tilde{\mathbf{G}}_{\beta\alpha,\sigma}(2,1)} \tilde{\mathbf{G}}_{\bar{\epsilon}\bar{\gamma},\bar{\sigma}}(\bar{4},\bar{3}) - \frac{\delta \Phi_{\bar{\gamma}\bar{\epsilon},\bar{\sigma}}(\bar{3},\bar{4})}{\delta \tilde{\mathbf{G}}_{\beta\alpha,\sigma}(2,1)} \tilde{\mathbf{G}}_{\bar{\epsilon}\bar{\gamma},\bar{\sigma}}(\bar{4},\bar{3}) - \frac{\delta \tilde{\mathbf{G}}_{\bar{\epsilon}\bar{\gamma},\bar{\sigma}}(\bar{4},\bar{3})}{\delta \tilde{\mathbf{G}}_{\beta\alpha,\sigma}(2,1)} \Phi_{\bar{\gamma}\bar{\epsilon},\bar{\sigma}}(\bar{3},\bar{4})$$

$$(5.195) = -\Phi_{\alpha\beta,\sigma}(1,2).$$

Again, the above property (5.195) and the Dyson equation (5.174) help to deduce

$$(5.196) \quad \frac{1}{T} \frac{\delta \Omega[\tilde{\mathbf{G}}]}{\delta \tilde{\mathbf{G}}_{\beta\alpha,\sigma}(2,1)} = -\Phi_{\alpha\beta,\sigma}(1,2)$$

$$(5.197) \quad = (\mathbf{G}^{-1})_{\alpha\beta,\sigma}(1,2) - \left[ (\mathbf{G}^0)^{-1} \right]_{\alpha\beta,\sigma}(1,2) + \Sigma_{\alpha\beta,\sigma}(1,2),$$

which reduces to the Dyson equation of our original system in the case where

$$(5.198) \quad \frac{1}{T} \frac{\delta \Omega[\tilde{\mathbf{G}}]}{\delta \tilde{\mathbf{G}}_{\beta\alpha,\sigma}(2,1)} = -\Phi_{\alpha\beta,\sigma}(1,2) = 0.$$

In contrast to the longitudinal particle-hole channel we will stop at this point since the construction of a Luttinger-Ward functional for the off-diagonal Green's function is not very useful to us. The only important point that we wanted to stress in this small excursion was the transition from the functional dependence of  $\Phi$  to  $\tilde{\mathbf{G}}$  that we used earlier to derive the Bethe-Salpeter equations (5.187), (5.186).

At this point we will relate the generalized susceptibilities to the spin susceptibility. This can be done via spin ladder operators

$$(5.199) \quad \begin{aligned} S_{\alpha\beta}^{\pm}(1) &:= S_{\alpha\beta}^x(1) \pm i S_{\alpha\beta}^y(1) \\ &= \frac{1}{2} \left( c_{\alpha,\uparrow}^{\dagger}(1) c_{\beta,\downarrow}(1) + c_{\alpha,\downarrow}^{\dagger}(1) c_{\beta,\uparrow}(1) \pm (c_{\alpha,\uparrow}^{\dagger}(1) c_{\beta,\downarrow}(1) - c_{\alpha,\uparrow}^{\dagger}(1) c_{\beta,\downarrow}(1)) \right) \\ &= \begin{cases} c_{\alpha,\uparrow}^{\dagger}(1) c_{\beta,\downarrow}(1) & , + \\ c_{\alpha,\downarrow}^{\dagger}(1) c_{\beta,\uparrow}(1) & , - \end{cases} \end{aligned}$$

where we used the definition of the spin vector in eq. (5.132). As we did for the spin fluctuations in  $z$ -direction we can define the linear response to spin perturbations with respect to the  $S^{\pm}$  operators. We define

$$(5.200) \quad \chi_{\lambda\zeta\nu\eta}^{sp,\pm}(1,2) := 4 \left\langle T_{\tau} S_{\lambda\zeta}^+(1) S_{\eta\nu}^-(2) \right\rangle = 4 \left\langle T_{\tau} c_{\lambda,\uparrow}^{\dagger}(1) c_{\zeta,\downarrow}(1) c_{\eta,\downarrow}^{\dagger}(2) c_{\nu,\uparrow}(2) \right\rangle$$

$$(5.201) \quad = 4 \left\langle T_{\tau} S_{\lambda\zeta}^x(1) S_{\eta\nu}^x(2) \right\rangle + 4 \left\langle T_{\tau} S_{\lambda\zeta}^y(1) S_{\eta\nu}^y(2) \right\rangle$$

$$(5.202) \quad - 4i \left\langle T_{\tau} S_{\lambda\zeta}^x(1) S_{\eta\nu}^y(2) - S_{\lambda\zeta}^y(1) S_{\eta\nu}^x(2) \right\rangle$$

$$(5.203) \quad = 4 \left\langle T_{\tau} S_{\lambda\zeta}^x(1) S_{\eta\nu}^x(2) \right\rangle + 4 \left\langle T_{\tau} S_{\lambda\zeta}^y(1) S_{\eta\nu}^y(2) \right\rangle$$

$$(5.204) \quad - \left\langle T_{\tau} c_{\lambda,\uparrow}^{\dagger}(1) c_{\zeta,\downarrow}(1) c_{\eta,\downarrow}^{\dagger}(2) c_{\nu,\uparrow}(2) - c_{\lambda,\downarrow}^{\dagger}(1) c_{\zeta,\uparrow}(1) c_{\eta,\uparrow}^{\dagger}(2) c_{\nu,\downarrow}(2) \right\rangle$$

$$(5.205) \quad = 8 \left\langle T_{\tau} S_{\lambda\zeta}^z(1) S_{\eta\nu}^z(2) \right\rangle = 2 \chi_{\lambda\zeta\nu\eta}^{sp}(1,2) + 8 \left\langle S_{\lambda\zeta}^z(1) \right\rangle \left\langle S_{\eta\nu}^z(2) \right\rangle,$$

where we used spin rotational invariance and the definition of the spin susceptibility  $\chi^{sp}$  (eq. (5.131)) in the last equation.

We draw now the connection between the susceptibility  $\chi^{sp,\pm}$  and the self-energy. Similar to the longitudinal particle-hole channel we start from the implicit equation for the self-energy (eq. (5.51)),

$$(5.204) \quad \begin{aligned} & \Sigma_{\alpha\bar{\beta}}(1, \bar{3})_{\Phi} \mathbf{G}_{\bar{\beta}\gamma}(\bar{3}, 2)_{\Phi} \\ &= -U_{\alpha} \left( \begin{array}{cc} \left\langle T_{\tau} n_{\alpha,\downarrow}(1) c_{\alpha,\uparrow}(1) c_{\gamma,\uparrow}^{\dagger}(2) \right\rangle_{\Phi} & \left\langle T_{\tau} n_{\alpha,\downarrow}(1) c_{\alpha,\uparrow}(1) c_{\gamma,\downarrow}^{\dagger}(2) \right\rangle_{\Phi} \\ \left\langle T_{\tau} n_{\alpha,\uparrow}(1) c_{\alpha,\downarrow}(1) c_{\gamma,\uparrow}^{\dagger}(2) \right\rangle_{\Phi} & \left\langle T_{\tau} n_{\alpha,\uparrow}(1) c_{\alpha,\downarrow}(1) c_{\gamma,\downarrow}^{\dagger}(2) \right\rangle_{\Phi} \end{array} \right). \end{aligned}$$

Since the Hamiltonian is spin conserving, we obtain in the limit  $\Phi = 0$  the equation

$$(5.205) \quad \begin{aligned} & \Sigma_{\alpha\bar{\beta}}(1, \bar{3})_{\Phi} \mathbf{G}_{\bar{\beta}\gamma}(\bar{3}, 2) \\ &= -U_{\alpha} \left( \begin{array}{cc} \left\langle T_{\tau} n_{\alpha,\downarrow}(1) c_{\alpha,\uparrow}(1) c_{\gamma,\uparrow}^{\dagger}(2) \right\rangle & 0 \\ 0 & \left\langle T_{\tau} n_{\alpha,\uparrow}(1) c_{\alpha,\downarrow}(1) c_{\gamma,\downarrow}^{\dagger}(2) \right\rangle \end{array} \right). \end{aligned}$$

Multiplying with the inverse Green's function  $\mathbf{G}_{\bar{\gamma}\nu}(\bar{2}, 4)$  and integrating over all internal degrees of freedom yields

$$(5.206) \quad \Sigma_{\alpha\nu}(1, 4) = U_{\alpha} \left( \begin{array}{cc} \left. \frac{\delta \mathbf{G}_{\alpha\bar{\gamma}}^{\uparrow\downarrow}(1, \bar{3})_{\Phi}}{\delta \phi_{\alpha\alpha}^{\uparrow}(1^+, 1)} \right|_{\Phi=0} & 0 \\ 0 & \left. \frac{\delta \mathbf{G}_{\alpha\bar{\gamma}}^{\uparrow\downarrow}(1, \bar{3})_{\Phi}}{\delta \phi_{\alpha\alpha}^{\downarrow}(1^+, 1)} \right|_{\Phi=0} \end{array} \right) (\mathbf{G}^{-1})_{\bar{\gamma}\nu}(\bar{3}, 4).$$

Next, one can use the Bethe-Salpeter equations for the generalized susceptibilities (eq. (5.187)) to further evaluate

$$(5.207) \quad \begin{aligned} & \Sigma_{\alpha\nu}^{\uparrow\uparrow}(1, 2) = U_{\alpha} G_{\alpha\alpha}(1, 1^+) G_{\alpha\bar{\gamma}}(1, \bar{3}) G_{\bar{\gamma}\nu}^{-1}(\bar{3}, 4) \\ & + U_{\alpha} G_{\alpha\bar{\beta}}(1, \bar{9}) \left. \frac{\delta \Sigma_{\bar{\beta}\bar{\epsilon}}^{\uparrow\downarrow}(\bar{9}, \bar{5})_{\Phi}}{\delta \mathbf{G}_{\bar{\rho}\bar{\lambda}}^{\uparrow\downarrow}(\bar{7}, \bar{8})_{\Phi}} \frac{\delta \mathbf{G}_{\bar{\rho}\bar{\lambda}}^{\uparrow\downarrow}(\bar{7}, \bar{8})_{\Phi}}{\delta \phi_{\alpha\alpha}^{\uparrow}(1^+, 1)} \right|_{\Phi=0} G_{\bar{\epsilon}\bar{\gamma}}(\bar{5}, \bar{3}) G_{\bar{\epsilon}\nu}^{-1}(\bar{3}, 4) \end{aligned}$$

$$(5.208) \quad = U_{\alpha} G_{\alpha\alpha}(1, 1^+) \delta_{\alpha,\nu} \delta(1-4) + U_{\alpha} G_{\alpha\bar{\beta}}(1, \bar{9}) \left. \frac{\delta \Sigma_{\bar{\beta}\nu}^{\uparrow\downarrow}(\bar{9}, 4)_{\Phi}}{\delta \mathbf{G}_{\bar{\rho}\bar{\lambda}}^{\uparrow\downarrow}(\bar{7}, \bar{8})_{\Phi}} \frac{\delta \mathbf{G}_{\bar{\rho}\bar{\lambda}}^{\uparrow\downarrow}(\bar{7}, \bar{8})_{\Phi}}{\delta \phi_{\alpha\alpha}^{\uparrow}(1^+, 1)} \right|_{\Phi=0},$$

$$(5.209) \quad \begin{aligned} & \Sigma_{\alpha\nu}^{\downarrow\downarrow}(1, 2) = U_{\alpha} G_{\alpha\alpha}(1, 1^+) G_{\alpha\bar{\gamma}}(1, \bar{3}) G_{\bar{\gamma}\nu}^{-1}(\bar{3}, 4) \\ & + U_{\alpha} G_{\alpha\bar{\beta}}(1, \bar{9}) \left. \frac{\delta \Sigma_{\bar{\beta}\bar{\epsilon}}^{\downarrow\uparrow}(\bar{9}, \bar{5})_{\Phi}}{\delta \mathbf{G}_{\bar{\rho}\bar{\lambda}}^{\downarrow\uparrow}(\bar{7}, \bar{8})_{\Phi}} \frac{\delta \mathbf{G}_{\bar{\rho}\bar{\lambda}}^{\downarrow\uparrow}(\bar{7}, \bar{8})_{\Phi}}{\delta \phi_{\alpha\alpha}^{\downarrow}(1^+, 1)} \right|_{\Phi=0} G_{\bar{\epsilon}\bar{\gamma}}(\bar{5}, \bar{3}) G_{\bar{\epsilon}\nu}^{-1}(\bar{3}, 4) \end{aligned}$$

$$(5.210) \quad = U_{\alpha} G_{\alpha\alpha}(1, 1^+) \delta_{\alpha,\nu} \delta(1-4) + U_{\alpha} G_{\alpha\bar{\beta}}(1, \bar{9}) \left. \frac{\delta \Sigma_{\bar{\beta}\nu}^{\downarrow\uparrow}(\bar{9}, 4)_{\Phi}}{\delta \mathbf{G}_{\bar{\rho}\bar{\lambda}}^{\downarrow\uparrow}(\bar{7}, \bar{8})_{\Phi}} \frac{\delta \mathbf{G}_{\bar{\rho}\bar{\lambda}}^{\downarrow\uparrow}(\bar{7}, \bar{8})_{\Phi}}{\delta \phi_{\alpha\alpha}^{\downarrow}(1^+, 1)} \right|_{\Phi=0}.$$

We see now that the equation can be related to the spin susceptibilities via eq. (5.203) and we get

$$(5.211) \quad \begin{aligned} & \Sigma_{\alpha\nu,\sigma}(1, 4) \\ &= U_{\alpha} n_{\alpha,-\sigma}(1) \delta_{\alpha,\nu} \delta(1-4) + \frac{U_{\alpha}}{2} G_{\alpha\bar{\beta}}(1, \bar{9}) \Gamma_{\nu\bar{\beta}\bar{\lambda}\bar{\rho}}^{sp,tr}(\bar{9}, 4; \bar{7}, \bar{8}) \chi_{\bar{\lambda}\bar{\rho}\alpha}^{sp}(\bar{7}, \bar{8}; 1), \end{aligned}$$

where we defined the irreducible spin vertex in the transversal channel

$$(5.212) \quad \Gamma_{\nu\bar{\beta}\bar{\lambda}\bar{\rho}}^{sp,tr}(9, 4; 7, 8) := -\frac{\delta \Sigma_{\bar{\beta}\nu}^{\uparrow\downarrow}(9, 4)_{\Phi}}{\delta \mathbf{G}_{\bar{\rho}\bar{\lambda}}^{\uparrow\downarrow}(7, 8)_{\Phi}} = -\frac{\delta \Sigma_{\bar{\beta}\nu}^{\downarrow\uparrow}(9, 4)_{\Phi}}{\delta \mathbf{G}_{\bar{\rho}\bar{\lambda}}^{\downarrow\uparrow}(7, 8)_{\Phi}}.$$

## 5.2. CONSERVING APPROXIMATIONS

As expected we recover the Hartree-Fock term as in the longitudinal particle-hole channel but a different fluctuations part with transverse spin fluctuations only. Nevertheless, the diagrammatic representation follows the one from the longitudinal particle-hole channel (see fig. 5.2).

### 5.2. Conserving approximations

This short overview is based on Refs. [163, 164].

At the core of the *Kadanoff-Baym conserving approximations* we find the so-called Luttinger-Ward functional  $\Phi[G]$  [117, 118] that we introduced earlier in sec. 5.1.5. We repeat the basic facts that we introduced before: First, the Luttinger-Ward functional is defined as the sum of all closed two-particle irreducible skeleton diagrams that can be constructed from the full Green's function  $G$  and the Hubbard interaction  $U$  (see fig. 5.5). We also found that  $\Phi[G]$  is the generating functional for the self-energy

$$\Phi[G] = \begin{array}{c} \circ \\ | \\ \text{wiggled line} \\ | \\ \circ \end{array} + \begin{array}{c} \circ \\ \text{wiggled line} \\ \circ \end{array} + \dots$$

FIGURE 5.5. The exact Luttinger-Ward functional  $\Phi[G]$  is the sum of all closed two-particle irreducible skeleton diagrams constructed from the full Green's function  $G$  (lines with arrows) and the bare interaction vertex  $U$  (single-wiggled lines). Adapted from [164].

$$(5.213) \quad \Sigma_{\alpha\beta,\sigma}(1,2) = \frac{\delta\Phi[G]}{\delta G_{\beta\alpha,\sigma}(2,1)}$$

and on the two-particle level it also generates the particle-hole irreducible vertex

$$(5.214) \quad \Gamma_{\alpha\beta\gamma\epsilon}^{\sigma\sigma'}(1,2;3,4) := \frac{\delta\Phi[G]}{\delta G_{\alpha\beta,\sigma}(2,1)\delta G_{\epsilon\gamma,\sigma'}(3,4)}$$

from which the spin and charge irreducible vertices  $\Gamma^{sp/ch}$  can be derived by spin and charge channel decomposition (see eqs. (5.130), (5.153))<sup>10</sup>,

$$(5.215) \quad \Gamma^{ch} = \Gamma^{\sigma-\sigma} + \Gamma^{\sigma\sigma},$$

$$(5.216) \quad \Gamma^{sp} = \Gamma^{\sigma-\sigma} - \Gamma^{\sigma\uparrow}.$$

Working with the Luttinger-Ward functional can bear some dangers due to the infinite sum of diagrams: It was shown that even at small interaction strengths  $U/W$ ,  $W$  being the bandwidth of the Hubbard model, one encounters divergences in the charge vertex  $\Gamma^{ch}$  which lead to a branching of the self-energy  $\Sigma$  into a physical and a unphysical branch [165, 166] or just lead to worse results than second order perturbation theory [167].

The important advantage –avoiding the unphysical branches of solutions– of deriving approximations to the Hubbard model within the Luttinger-Ward framework consists of conservation laws that are fulfilled automatically. Notably, such approximations are thermodynamically consistent, which means that thermodynamic expectation

<sup>10</sup>We defined those expressions as they appeared naturally in the Bethe-Salpeter equations (5.129), (5.152) but one can motivate the spin and charge channel decomposition more formally by taking advantage of the spin rotation invariance and the crossing symmetry of the two-particle irreducible vertices [158, 159]. The final result are four independent irreducible vertices  $\Gamma^{sp/ch}$  and  $\Gamma^{s/t}$ , where the singlet and triplet vertex  $\Gamma^{s/t}$  stem from the particle-particle irreducible channel.

values can be expressed as derivatives of the free energy. Additionally, they preserve important physical constraints like the Ward identities for fluctuations and single-particle conservation laws [115, 117].

The simplest conserving approximation that can be thought of is the self-consistent Hartree-Fock approximation. In this approach, one assumes the Luttinger-Ward functional  $\Phi[G]$  to consist only of the first order terms which are the ones shown in fig. 5.5. Performing the functional derivatives in eqs. (5.213) and eq. (5.214) one obtains for local Hubbard interaction  $U_\alpha$

$$(5.217) \quad \Sigma_{\alpha\beta,\sigma}(1, 2) = U_\alpha n_{\alpha,-\sigma} \delta_{\alpha,\beta} \delta(1 - 2),$$

$$(5.218) \quad \Gamma_{\alpha\beta\gamma\epsilon}^{sp}(1, 2; 3, 4) = \Gamma_{\alpha\beta\gamma\epsilon}^{ch}(1, 2; 3, 4) = U_\alpha \delta(3 - 4) \delta(2 - 3) \delta(1 - 3^+) \delta_{\alpha,\beta} \delta_{\beta,\gamma} \delta_{\gamma,\epsilon}.$$

Inserting those expressions into the Bethe-Salpeter equations (5.129), (5.152) we obtain the random phase approximation result

$$(5.219) \quad \chi^{sp} = [\mathbb{I} - \chi^0 \Gamma^{sp}]^{-1} 2\chi^0,$$

$$(5.220) \quad \chi^{ch} = [\mathbb{I} + \chi^0 \Gamma^{ch}]^{-1} 2\chi^0,$$

where  $\chi^0$  is the irreducible susceptibility (see eq. (5.71)).

Among the class of more advanced techniques we find the ones that sum infinitely many diagrams of a certain topology. For example, in the fluctuation-exchange approximation (FLEX) one sums only bubble and ladder diagrams that can be rearranged in terms of geometric series [168–173]. This yields a self-energy that is frequency- and momentum dependent in contrast to the Hartree-Fock result for the Hubbard model. Another prominent conserving approximation is the GW approximation where only so-called ring diagrams appear in the Luttinger-Ward functional [108, 174–176]. This method can be also understood in terms of a perturbation theory in the screened interaction  $W$ .

The dynamical mean field theory (DMFT) can be formulated with a Luttinger-Ward functional that only contains diagrams from local propagators [85, 87, 88, 177, 178]. This approach is exact in the limit of infinite dimensions/ lattice connectivity, where the self-energy is local but dynamic, i.e.  $\Sigma = \Sigma(\omega)$ . For real material applications it is also possible to formulate a conserving approximation where the starting point is a density functional theory calculation and where correlation effects are treated within DMFT; this approach is coined DFT+DMFT [179–181]. Similarly, one can also combine GW and DMFT to treat non-local correlation effects within GW and local ones within DMFT [182, 183]. Moreover, the diagrammatic and cluster extensions to DMFT also fall into the category of conserving approximations, e.g. the cluster DMFT method (CDMFT) [61, 88, 184–187], the dynamical cluster approximation (DCA) [185, 186, 188–193], the dynamical vertex approximation (DVA) [147, 194, 195], TRILEX [196, 197], QUADRILEX [198], dual boson [199] and dual fermion techniques [200].

In summary, conserving approximations play a prominent role in modern developments of many-body methods due to their inherent enforcement of physical constraints. Although TPSC is not a conserving approximation we will see in section 5.3 in how far both many-body approaches are closely related.

**5.2.1. Two-particle properties.** Since the functional derivative formalism also determines two-particle objects it is also possible to access higher order correlation functions. In this work we will mainly focus on single-particle properties which is why we only mention a few observables that can be extracted.

Most prominently, one obtains spin and charge susceptibilities which reveal important insights into charge and spin order instabilities. Moreover, they allow to understand how nesting properties change due to interaction and temperature. For a more detailed listing and explicit examples that were calculated within the Two-Particle Self-Consistent approach we refer to Refs. [155, 163].

### 5.3. Single-band TPSC

In this section we sketch the Two-Particle Self-Consistent approach in its original formulation for the single-band repulsive Hubbard model [155, 163, 186, 201–204].

In chapter 3 we have constructed a lattice model for our material where the original long-range Coulomb interaction is reduced to closest neighbor interactions  $V_{ij}$  or even to local interactions  $U$ ,  $J$  only.

The simplest non-trivial representative of this class of lattice models is the single-band Hubbard model [64–66, 145] and is described by the Hubbard Hamiltonian

$$(5.221) \quad H = \sum_{i,j,\sigma} t^{r_i-r_j} c_\sigma^\dagger(r_i) c_\sigma(r_j) + \frac{U}{2} \sum_{i,\sigma} n_\sigma(r_i) n_{-\sigma}(r_i),$$

where  $t^{r_i-r_j}$  are the hopping amplitudes between lattice sites  $r_i$  and  $r_j$ . Since we are interested in paramagnetic states, spin rotational invariant and time-reversal symmetric systems only, we drop the spin index in the hopping elements  $t^{r_i-r_j}$ . The on-site Hubbard interaction is denoted by  $U$ . The operator  $c_\sigma(r_i)$  destroys an electron with spin  $\sigma$  at lattice site  $r_i$  while the adjoint operator  $c_\sigma^\dagger(r_i)$  creates an electron with spin  $\sigma$  at lattice site  $r_i$ . The density operator  $n_\sigma(r_i) := c_\sigma^\dagger(r_i) c_\sigma(r_i)$  measures the occupation of particles at  $r_i$  with spin  $\sigma$ . Although the operators are time-dependent we did not denote the time dependence explicitly in the Hamiltonian  $H$  because  $H$  itself is not explicitly time-dependent.

The Two-Particle Self-Consistent approach (TPSC) is a many-body method that was originally formulated to find approximate expression for the spin and charge fluctuations and the renormalization of single-particle properties within the repulsive single-band Hubbard model [155, 163]. Although TPSC itself is not a conserving approximation<sup>11</sup> in the sense of Kadanoff and Baym [113, 115, 116] it can be derived within this framework. The starting point of this class of methods is an approximation of the Luttinger-Ward functional  $\Phi[G]$  [117, 118]. In the case of TPSC one approximates the Luttinger-Ward functional as

$$(5.222) \quad \Phi[G] \approx \frac{1}{2} G_{\bar{\sigma}}(\bar{1}, \bar{1}^+) \Gamma^{\bar{\sigma}\bar{\sigma}'} G_{\bar{\sigma}'}(\bar{1}, \bar{1}^+),$$

where  $\Gamma^{\sigma\sigma'}$  is a local and static effective two-particle irreducible vertex that is assumed to contain the contribution of all diagrams in  $\Phi[G]$ . This assumption can be expected to give accurate results in the regions of weak and intermediate interaction strength where the four-point vertex  $\Gamma^{\sigma\sigma'}(1, 2; 3, 4)$  is not singular. However, recent studies have shown that the two-particle irreducible vertex  $\Gamma^{\sigma\sigma'}(1, 2; 3, 4)$  has non-trivial or even diverging momentum and frequency dependence in the regime of intermediate and strong coupling [158, 160, 165, 205, 206]. The diagrammatic representation of the Luttinger-Ward functional  $\Phi[G]$  in the TPSC approximation is shown in fig. 5.6.

As discussed for the Hartree-Fock approximation (see sec. 5.2) this kind of Luttinger-Ward functional leads to a static and local self-energy  $\Sigma_\sigma = \Gamma^{\sigma\sigma'} n_{\bar{\sigma}'}$  in the single-band case that can be absorbed into the chemical potential to ensure conservation of the particle number. At this step TPSC is still a conserving approximation but it recovers effectively the non-interacting Green's function in the paramagnetic case. As a result

<sup>11</sup>This is argued in the following derivation.

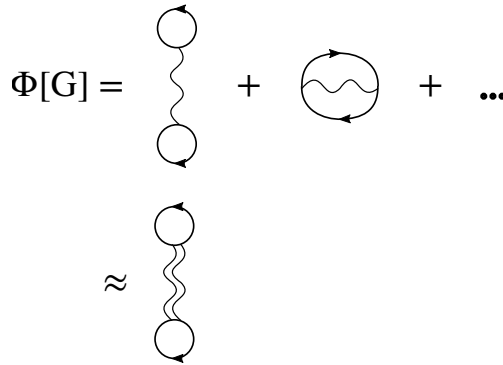


FIGURE 5.6. The exact Luttinger-Ward functional  $\Phi[G]$  is the sum of all closed two-particle irreducible skeleton diagrams constructed from the dressed Green's function  $G$  (lines with arrows) and the bare interaction vertex  $U$  (single-wiggled lines). Within TPSC one assumes that the sum of all diagrams can be condensed into a single diagram of first order where the bare interaction vertex becomes an effective two-particle irreducible vertex  $\Gamma^{\sigma\sigma'}$  (double-wiggled line). Figure reprinted from Ref. [164].

there is no single-particle renormalization at this first step of TPSC. We will consider now two-particle functions and come back to the effect on single-particle functions afterwards.

The next step in TPSC is to determine the value of the effective four-point vertex  $\Gamma^{\sigma\sigma'}$  or more specifically its value in the spin and charge channel, namely  $\Gamma^{sp}$  and  $\Gamma^{ch}$ . But how does one determine the effective value of a complicated two-particle function at minimal computational cost, i.e. without solving complicated parquet equations [147]? In TPSC one considers equations of  $\Gamma^{sp/ch}$  that encode the local Pauli principle ( $\langle n_\sigma^2(r_i) \rangle = \langle n_\sigma(r_i) \rangle$ ) by means of the local spin and charge sum rule (see eq. (5.117) and (5.142)),

$$(5.223) \quad \chi^{sp}(r=0, t=0) = n - 2\langle n_\uparrow n_\downarrow \rangle,$$

$$(5.224) \quad \chi^{ch}(r=0, t=0) = n + 2\langle n_\uparrow n_\downarrow \rangle - n^2,$$

where we dropped the dependence on the site position on the right-hand side due to the lattice periodicity. Those equations are the so-called local spin and charge sum rules that are direct results of the fluctuation-dissipation theorem and the local Pauli principle [163]. The Bethe-Salpeter equations for the spin and charge susceptibilities  $\chi^{sp/ch}$  ((5.129), (5.152)) reduce within TPSC to the following simple expressions:

$$(5.225) \quad \chi^{sp} = \frac{2\chi^0}{1 - \chi^0\Gamma^{sp}},$$

$$(5.226) \quad \chi^{ch} = \frac{2\chi^0}{1 + \chi^0\Gamma^{ch}},$$

where  $\chi^0$  is the particle-hole bubble diagram  $-G^0 * G^0$  computed from the bare Green's function  $G^0$  (see eq. (5.71)).

Note that we have only two sum rules (eqs. (5.223), (5.224)) but three unknowns:  $\Gamma^{sp}$ ,  $\Gamma^{ch}$  and  $\langle n_\uparrow n_\downarrow \rangle$ . One way of dealing with this set of under-determined equations is to take the double occupation  $\langle n_\uparrow n_\downarrow \rangle$  as an input from a different many-body method [207]. Another way to complete the set of equations for calculating  $\Gamma^{sp}$ ,  $\Gamma^{ch}$

### 5.3. SINGLE-BAND TPSC

and  $\langle n_\uparrow n_\downarrow \rangle$  is to make an ansatz for  $\Gamma^{sp}$  that is motivated from the local field approximation [202, 208, 209], namely

$$(5.227) \quad \Gamma^{sp} = U \frac{\langle n_\uparrow n_\downarrow \rangle}{\langle n_\uparrow \rangle \langle n_\downarrow \rangle}.$$

This ansatz gives accurate results when spin fluctuations are small and –albeit its simple form– is able to capture the physics of Kanamori-Brueckner screening [163, 202, 207] which describes the reduction of the bare interaction in the spin channel [66, 210].

Obviously, this ansatz breaks particle-hole symmetry which is a problem if the system considered exhibits particle-hole symmetry and the expression in eq. (5.227) breaks it artificially. To avoid such kind of effect one usually performs a particle-hole transformation when crossing the boundary of equal particle and hole concentration,

$$(5.228) \quad \Gamma^{sp} = U \begin{cases} \frac{\langle n_\uparrow n_\downarrow \rangle}{\langle n_\uparrow \rangle \langle n_\downarrow \rangle} & n \leq 1 \\ \frac{1 - n + \langle n_\uparrow n_\downarrow \rangle}{1 - n + \langle n_\uparrow \rangle \langle n_\downarrow \rangle} & n > 1 \end{cases}.$$

The first approach that takes the double occupation  $\langle n_\uparrow n_\downarrow \rangle$  as an input from a different many-body method and does not need eq. (5.228) should be considered when the interaction strength is large enough to cause diverging antiferromagnetic fluctuations in the system since in this regime the TPSC-internal ansatz fails (see fig. 5.7) [146, 211–213]: While TPSC predicts a decreasing double occupation over the whole temperature range in the two-dimensional Hubbard model on a square lattice at half filling and for weak to intermediate coupling strengths, it is well known that there exists a *crossover temperature*  $T_X$ <sup>12</sup> where antiferromagnetic fluctuations grow exponentially and Pseudogap physics can set in [146, 211–213]. If  $U/t$  is not too large –otherwise the Mott scale would dominate and the effect of increasing double occupation would disappear– one can understand the counter-intuitive increase of the double occupancy at  $T \lesssim T_X$  from quantum fluctuations in the Fermi liquid phase where particle localization is reduced [177, 214–216]. On the other hand, at large temperatures where thermal fluctuations dominate in the system the double occupation tends to increase to the non-interacting value  $\langle n_\uparrow n_\downarrow \rangle \rightarrow \langle n_\uparrow \rangle \langle n_\downarrow \rangle = 1/4$  at half-filling.

Now that the spin and charge collective modes are calculated one can use the equation of motion for the self-energy in the longitudinal particle-hole channel (see eq. (5.159)) to feed those fluctuation effects back to the single-particle properties [113, 163]. Note that this gives an improved self-energy formula that goes beyond the previously mentioned Hartree-Fock like expression,

$$(5.229) \quad \Sigma_\sigma^{(l)} = U n_{-\sigma} + \frac{U}{4} \left[ \Gamma^{sp} \chi^{sp} + \Gamma^{ch} \chi^{ch} \right] * G_\sigma^0.$$

The drawback of this procedure is that TPSC is not a conserving approximation in the Kadanoff-Baym sense anymore because the self-energy is not calculated from the functional derivative of the approximate Luttinger-Ward functional  $\frac{\delta \Phi[G]}{\delta G}$ . Nevertheless, many properties of conserving approximations and physical constraints are still obeyed to a high degree if not fulfilled exactly in the regime of weak to intermediate coupling strength [163], e.g. particle number<sup>13</sup> and spin conservation, Luttinger’s theorem, the Mermin-Wagner theorem, Ward identities, the f-sum rule and the consistency relation

<sup>12</sup>In this case of a two-dimensional Hubbard model the Mermin-Wagner theorem states that thermal fluctuations destroy a finite-temperature phase transition to the antiferromagnetic ground state which breaks  $SU(2)$  symmetry.

<sup>13</sup>In order to keep the number of particles one has to adjust the chemical potential according to the improved self-energy.

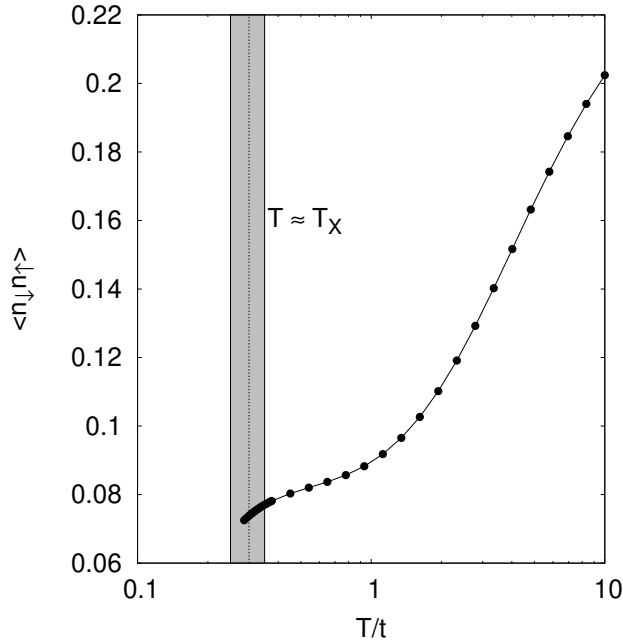


FIGURE 5.7. The double occupation  $\langle n_{\uparrow}n_{\downarrow} \rangle$  calculated from the TPSC ansatz eq. (5.228) for the nearest neighbor hopping Hubbard model on a square lattice at  $U/t = 8$  and half filling. While the double occupation is in good agreement with various many-body methods [146, 211–213] at temperatures above the crossover temperature  $T_X/t \approx 0.3$  [211] (gray shaded area) it starts a steep decrease at  $T \lesssim T_X$  where the above cited many-body methods see a small increase (see main text).

between one- and two-particle properties

$$(5.230) \quad \Sigma_{\sigma}(1, \bar{1})G_{\sigma}(\bar{1}, 1^{+}) = U\langle n_{\uparrow}n_{\downarrow} \rangle.$$

This stands in contrast to many approaches like the Random Phase Approximation, the Fluctuation Exchange Approximation [168, 169] and the Pseudopotential Parquet Approach [170, 171] where some of the above mentioned constraints are significantly violated [163].

Finally, one can improve on the self-energy formula (5.229) by considering also the transversal particle-hole channel (see sec. 5.1.8 and eq. (5.211)) and thus enforcing crossing symmetry of the two-particle irreducible vertex [112, 153, 158]. The final formula for the TPSC self-energy is then an average of the self-energy expressions in the longitudinal and transversal particle-hole channel,

$$(5.231) \quad \Sigma_{\sigma} = Un_{-\sigma} + \frac{U}{8} \left[ 3\Gamma^{sp}\chi^{sp} + \Gamma^{ch}\chi^{ch} \right] * G_{\sigma}^0.$$

Application of the Schwinger-Dyson equation

$$(5.232) \quad G^{-1} = (G^0)^{-1} + \mu - \Sigma$$

yields to the full TPSC Green's function  $G$  and the renormalized quasi-particle properties, where the chemical potential  $\mu$  has to be adjusted such that the particle number is conserved.

**5.3.1. Flowchart of the single-band TPSC.** For a better overview on the single-band TPSC approach we show a flowchart of the method in fig. 5.8.

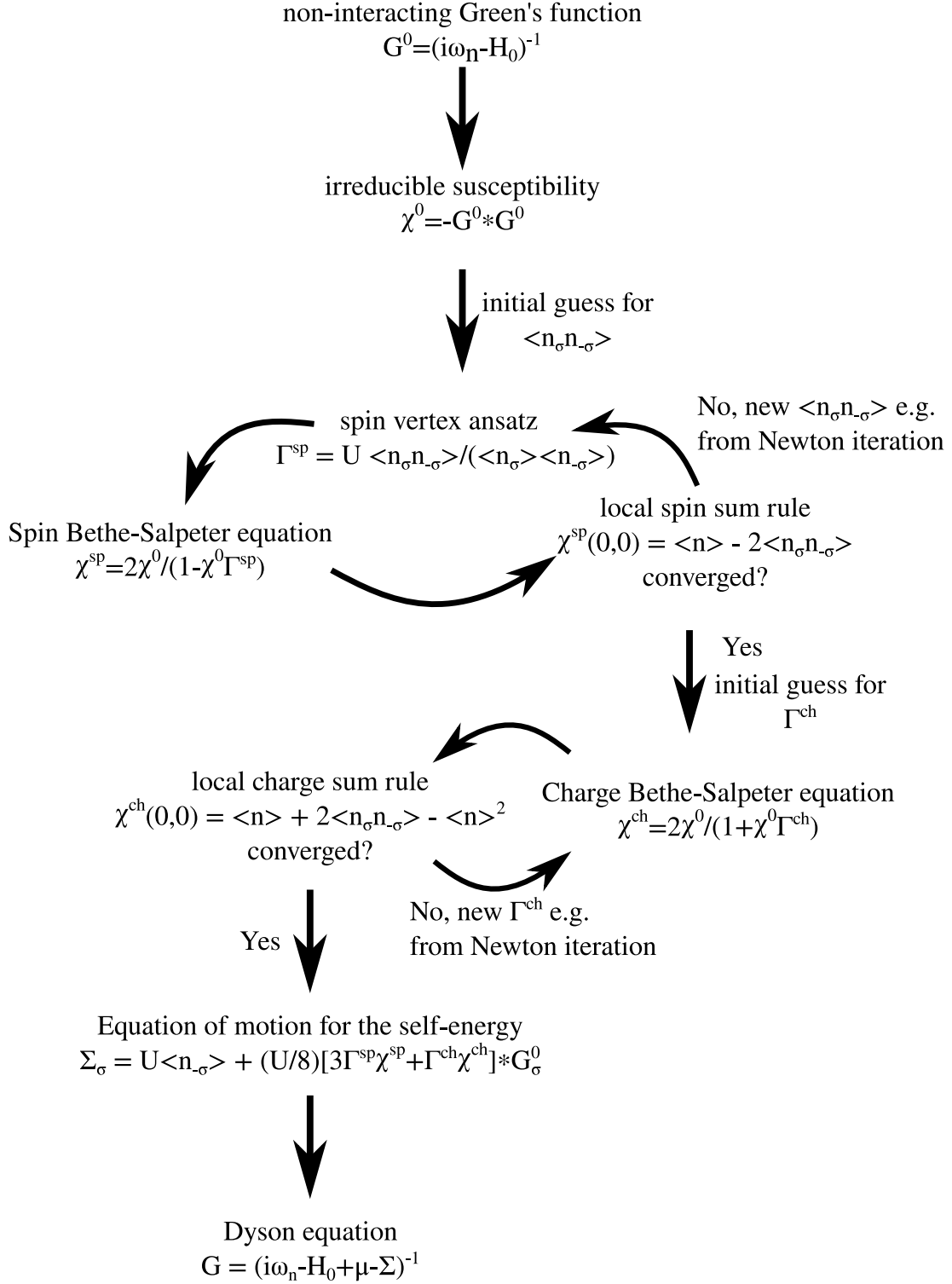


FIGURE 5.8. Single-band TPSC flow chart as described in sec. 5.3. After calculating the non-interacting Green's function and the irreducible susceptibility one has to converge the spin and charge with respect to the local spin and charge sum rule and the Bethe-Salpeter equations. From those one is able to evaluate the self-energy and thus interacting Green's function via the Dyson equation. Figure adapted from [164].

**5.3.2. Short summary on the applications of single-band TPSC.** Before we continue with the extensions of TPSC it is worthwhile to mention to which classes of materials and models this method was successfully applied.

A large amount of studies with single-band TPSC were performed for the Hubbard model on the square lattice<sup>14</sup> to analyze spin and charge fluctuations [201, 202, 217, 218], single-particle properties [163, 204, 219–221], universal critical behavior [222–224], the optical and dc conductivity [225] and unconventional superconductivity [207, 226–228]. Moreover, TPSC was also applied to analyze magnetic properties of the three-dimensional Hubbard model [229]. In order to classify TPSC among different many-body approaches detailed comparisons were performed in Ref. [148, 163, 230–232]. A slight modification of the above described single-band TPSC was developed to study the attractive Hubbard model, where the derivation is performed in the particle-particle channel [112, 161, 233–235]. But TPSC is not only restricted to on-site interaction  $U$  only and can also be extended to deal with nearest-neighbor repulsion  $V$  [236–238].

### 5.4. Multi-site TPSC

The presentation of this section is based on [154, 161, 164].

Going from single-band TPSC to a multi-site formulation is basically a change in the notation without additional new terms [152, 239, 240]. Nevertheless, we present the important equations and steps with all details since we presented only the basic ideas in the single-band case in sec. 5.3. We consider the multi-site<sup>15</sup> Hubbard Hamiltonian  $H$  (eq. (5.1)) given by

$$(5.233) \quad H = \sum_{\alpha, \beta, i, j, \sigma} t_{\alpha, \beta}^{r_i - r_j} c_{\alpha, \sigma}^\dagger(r_i) c_{\beta, \sigma}(r_j) + \frac{1}{2} \sum_{\alpha, i, \sigma} U_\alpha n_{\alpha, \sigma}(r_i) n_{\alpha, -\sigma}(r_i).$$

Similar, to the single-band case the multi-site TPSC Luttinger-Ward functional is given by

$$(5.234) \quad \Phi[G] \approx \frac{1}{2} G_{\overline{\alpha\alpha}, \overline{\sigma}}(\overline{1}, \overline{1}^+) \Gamma_{\overline{\alpha}}^{\overline{\sigma\sigma'}} G_{\overline{\alpha\alpha}, \overline{\sigma'}}(\overline{1}, \overline{1}^+),$$

where the effective two-particle irreducible vertex  $\Gamma_{\overline{\alpha}}^{\overline{\sigma\sigma'}}$  carries now a single site index  $\alpha$  since the Hamiltonian  $H$  has no inter-site interaction. Again, from functional differentiation this ansatz for the Luttinger-Ward functional  $\Phi[G]$  gives a static, local and diagonal self-energy

$$(5.235) \quad \Sigma_{\alpha\beta, \sigma}(1, 2) = \frac{\delta\Phi[G]}{\delta G_{\beta\alpha, \sigma}(2, 1)}$$

$$(5.236) \quad = \frac{\delta_{\alpha, \beta}}{2} [\Gamma_{\alpha}^{\sigma\sigma} G_{\alpha, \sigma}(1, 1^+) \delta(1-2) + G_{\alpha, \sigma}(1, 1^+) \Gamma_{\alpha}^{\sigma\sigma} \beta(1-2) \\ + \Gamma_{\alpha}^{\sigma-\sigma} G_{\alpha, -\sigma}(1, 1^+) \delta(1-2) + G_{\alpha, -\sigma}(1, 1^+) \delta(1-2) \Gamma_{\alpha}^{\sigma-\sigma}]$$

$$(5.237) \quad = (\Gamma_{\alpha}^{\sigma\sigma} n_{\alpha, \sigma}(1) + \Gamma_{\alpha}^{\sigma-\sigma} n_{\alpha, -\sigma}(1)) \delta_{\alpha, \beta} \delta(1-2)$$

$$(5.238) \quad = \Gamma_{\alpha}^{ch} n_{\alpha, -\sigma} \delta_{\alpha, \beta} \delta(1-2),$$

where we again took advantage of paramagnetism and the channel decomposition in eq. (5.216).

In case of unequally filled lattice sites, i.e. there are two distinct lattice indices  $\alpha, \beta$  where  $n_{\alpha} \neq n_{\beta}$ , one has to be careful about this first-step TPSC self-energy.

<sup>14</sup>The mentioned studies were often model calculations for Cuprate superconductors.

<sup>15</sup>By multi-site we mean multiple sites in the unit cell, where the interaction is still restricted to on-site repulsion.

#### 5.4. MULTI-SITE TPSC

Fortunately, the study of organic superconductors that is presented in sec. 5.5 does not fall into this category and we have equally occupied lattice sites. Therefore, the first-step TPSC self-energy can be absorbed into the chemical potential as was done in the single-band case. In the general case one would have to argue in how far those site-dependent energy shifts are already included in the kinetic term of the Hamiltonian  $H$  (see DFT+TPSC in chap. 7) or proceed in the following with a non-interacting Green's function  $G^0$  modified by those shifts. Alternatively, one can ignore the first-step TPSC self-energy as an additional approximation. In the following derivation we will assume that those self-energy shifts are accounted for either by the chemical potential or by the kinetic term in the Hamiltonian  $H$ .

The second functional derivative  $\frac{\delta\Phi[G]}{\delta G\delta G}$  leads again to site-dependent spin and charge vertices  $\Gamma_\alpha^{sp/ch}$  (eqs. (5.130), (5.153)) that are constants,

$$(5.239) \quad \Gamma_{\gamma\beta\lambda\rho}^{ch}(1, 2; 3, 4) = \sum_{\sigma} \frac{\delta\Sigma_{\beta\gamma,\sigma}(1, 2)_{\phi}}{\delta G_{\rho\lambda,\uparrow}(3, 4)_{\phi}} \Big|_{\phi=0}$$

$$(5.240) \quad = \sum_{\sigma} \frac{\delta\Phi[G]}{\delta G_{\gamma\beta,\sigma}(2, 1)\delta G_{\rho\lambda,\uparrow}(3, 4)}$$

$$= \frac{1}{2} \sum_{\sigma} \frac{\delta}{\delta G_{\gamma\beta,\sigma}(2, 1)}$$

$$(5.241) \quad \left[ \frac{\delta G_{\bar{\alpha}\bar{\alpha},\bar{\sigma}}(\bar{1}, \bar{1}^+)}{\delta G_{\rho\lambda,\uparrow}(3, 4)} \Gamma_{\bar{\alpha}}^{\bar{\sigma}\bar{\sigma}} G_{\bar{\alpha}\bar{\alpha},\bar{\sigma}}(\bar{1}, \bar{1}^+) + G_{\bar{\alpha}\bar{\alpha},\bar{\sigma}}(\bar{1}, \bar{1}^+) \Gamma_{\bar{\alpha}}^{\bar{\sigma}\bar{\sigma}} \frac{\delta G_{\bar{\alpha}\bar{\alpha},\bar{\sigma}}(\bar{1}, \bar{1}^+)}{\delta G_{\rho\lambda,\uparrow}(3, 4)} \right. \\ \left. + \frac{\delta G_{\bar{\alpha}\bar{\alpha},\bar{\sigma}}(\bar{1}, \bar{1}^+)}{\delta G_{\rho\lambda,\uparrow}(3, 4)} \Gamma_{\bar{\alpha}}^{\bar{\sigma}-\bar{\sigma}} G_{\bar{\alpha}\bar{\alpha},-\bar{\sigma}}(\bar{1}, \bar{1}^+) + G_{\bar{\alpha}\bar{\alpha},\bar{\sigma}}(\bar{1}, \bar{1}^+) \Gamma_{\bar{\alpha}}^{\bar{\sigma}-\bar{\sigma}} \frac{\delta G_{\bar{\alpha}\bar{\alpha},-\bar{\sigma}}(\bar{1}, \bar{1}^+)}{\delta G_{\rho\lambda,\uparrow}(3, 4)} \right]$$

$$(5.242) \quad = \sum_{\sigma} \delta_{\rho,\lambda} \frac{\delta}{\delta G_{\gamma\beta,\sigma}(2, 1)} \left[ G_{\lambda\lambda,\uparrow}(3, 3^+) \Gamma_{\lambda}^{\uparrow\uparrow} \delta(3-4) + \Gamma_{\lambda}^{\downarrow\uparrow} G_{\lambda\lambda,\downarrow}(3, 3^+) \delta(3-4) \right]$$

$$(5.243) \quad = \delta_{\rho,\lambda} \delta_{\lambda,\beta} \delta_{\gamma,\lambda} \delta_{\sigma,\downarrow} \delta(3-4) \delta(2-3) \delta(1-3^+) \left[ \Gamma_{\lambda}^{\uparrow\uparrow} + \Gamma_{\lambda}^{\downarrow\uparrow} \right]$$

$$(5.244) \quad = \delta_{\rho,\lambda} \delta_{\lambda,\beta} \delta_{\gamma,\lambda} \delta_{\sigma,\downarrow} \delta(3-4) \delta(2-3) \delta(1-3^+) \Gamma_{\lambda}^{ch}$$

and

$$(5.245) \quad \Gamma_{\gamma\beta\lambda\rho}^{sp}(1, 2; 3, 4) = \sum_{\sigma} \sigma \frac{\delta\Sigma_{\beta\gamma,\sigma}(3, 2)_{\phi}}{\delta G_{\rho\lambda,\downarrow}(7, 8)_{\phi}} \Big|_{\phi=0}$$

$$(5.246) \quad = \sum_{\sigma} \sigma \frac{\delta\Phi[G]}{\delta G_{\gamma\beta,\sigma}(2, 1)\delta G_{\rho\lambda,\downarrow}(3, 4)}$$

$$= \frac{1}{2} \sum_{\sigma} \sigma \frac{\delta}{\delta G_{\gamma\beta,\sigma}(2, 1)}$$

$$(5.247) \quad \left[ \frac{\delta G_{\bar{\alpha}\bar{\alpha},\bar{\sigma}}(\bar{1}, \bar{1}^+)}{\delta G_{\rho\lambda,\downarrow}(3, 4)} \Gamma_{\bar{\alpha}}^{\bar{\sigma}\bar{\sigma}} G_{\bar{\alpha}\bar{\alpha},\bar{\sigma}}(\bar{1}, \bar{1}^+) + G_{\bar{\alpha}\bar{\alpha},\bar{\sigma}}(\bar{1}, \bar{1}^+) \Gamma_{\bar{\alpha}}^{\bar{\sigma}\bar{\sigma}} \frac{\delta G_{\bar{\alpha}\bar{\alpha},\bar{\sigma}}(\bar{1}, \bar{1}^+)}{\delta G_{\rho\lambda,\downarrow}(3, 4)} \right. \\ \left. + \frac{\delta G_{\bar{\alpha}\bar{\alpha},\bar{\sigma}}(\bar{1}, \bar{1}^+)}{\delta G_{\rho\lambda,\downarrow}(3, 4)} \Gamma_{\bar{\alpha}}^{\bar{\sigma}-\bar{\sigma}} G_{\bar{\alpha}\bar{\alpha},-\bar{\sigma}}(\bar{1}, \bar{1}^+) + G_{\bar{\alpha}\bar{\alpha},\bar{\sigma}}(\bar{1}, \bar{1}^+) \Gamma_{\bar{\alpha}}^{\bar{\sigma}-\bar{\sigma}} \frac{\delta G_{\bar{\alpha}\bar{\alpha},-\bar{\sigma}}(\bar{1}, \bar{1}^+)}{\delta G_{\rho\lambda,\downarrow}(3, 4)} \right]$$

$$(5.248) \quad = \sum_{\sigma} \sigma \delta_{\rho,\lambda} \frac{\delta}{\delta G_{\gamma\beta,\sigma}(2,1)} \left[ G_{\lambda\lambda,\downarrow}(3,3^+) \Gamma_{\lambda}^{\uparrow\downarrow} \delta(3-4) + \Gamma_{\lambda}^{\uparrow\downarrow} G_{\lambda\lambda,\uparrow}(3,3^+) \delta(3-4) \right]$$

$$(5.249) \quad = \delta_{\rho,\lambda} \delta_{\lambda,\beta} \delta_{\gamma,\lambda} \delta_{\sigma,\downarrow} \delta(3-4) \delta(2-3) \delta(1-3^+) \left[ \Gamma_{\lambda}^{\uparrow\downarrow} - \Gamma_{\lambda}^{\downarrow\uparrow} \right]$$

$$(5.250) \quad = \delta_{\rho,\lambda} \delta_{\lambda,\beta} \delta_{\gamma,\lambda} \delta_{\sigma,\downarrow} \delta(3-4) \delta(2-3) \delta(1-3^+) \Gamma_{\lambda}^{sp}.$$

We remind of the local spin and charge sum rules (eqs. (5.117), (5.142)),

$$(5.251) \quad \frac{T}{N} \sum_q \chi_{\alpha\alpha\alpha\alpha}^{sp}(q) = \langle n_{\alpha} \rangle - 2\langle n_{\alpha,\uparrow} n_{\alpha,\downarrow} \rangle,$$

$$(5.252) \quad \frac{T}{N} \sum_q \chi_{\alpha\alpha\alpha\alpha}^{ch}(q) = \langle n_{\alpha} \rangle + 2\langle n_{\alpha,\uparrow} n_{\alpha,\downarrow} \rangle - \langle n_{\alpha} \rangle^2.$$

**5.4.1. Ansatz for the irreducible spin vertex.** As in the single-band case one can use the derivation in Ref. [163] to get an ansatz equation for the spin vertex  $\Gamma_{\alpha}^{sp}$ . We start with the implicit definition of the self-energy in eq. (5.48),

$$(5.253) \quad \Sigma_{\alpha\bar{\beta},\sigma}(1,\bar{3}) G_{\bar{\beta}\gamma,\sigma}(\bar{3},2) = -U_{\alpha} \left\langle T_{\tau} c_{\alpha,-\sigma}^{\dagger}(1^+) c_{\alpha,-\sigma}(1) c_{\alpha,\sigma}(1) c_{\gamma,\sigma}^{\dagger}(2) \right\rangle,$$

A simple ansatz can be obtained by performing a Hartree-Fock decoupling for the right-hand side of the equation and to write a prefactor  $A$  in front of the decoupled expectation values in order to restore the result for equal time/position evaluation, i.e.  $2 \rightarrow 1$ . This yields

$$(5.254) \quad \Sigma_{\alpha\bar{\beta},\sigma}(1,\bar{3}) G_{\bar{\beta}\gamma,\sigma}(\bar{3},2) = -U_{\alpha} \left\langle n_{\alpha,-\sigma}(1^+) c_{\alpha,\sigma}(1) c_{\gamma,\sigma}^{\dagger}(2) \right\rangle$$

$$(5.255) \quad \approx A_{\alpha} \langle n_{\alpha,-\sigma} \rangle G_{\alpha\gamma,\sigma}(1,2),$$

where we took advantage of imaginary time and space translational invariance of the system. To recover now the result for equal imaginary time and position we determine

$$(5.256) \quad A_{\alpha} = U_{\alpha} \frac{\langle n_{\alpha,\sigma} n_{\alpha,-\sigma} \rangle}{\langle n_{\alpha,\sigma} \rangle \langle n_{\alpha,-\sigma} \rangle}.$$

In principle, one would have to determine the occupations  $\langle n_{\alpha,\sigma} \rangle$  from the interacting system but we use the occupations of the non-interacting system and assume that those are close to the occupations of the interacting system after determining the chemical potential such that the particle number is conserved. In the case of the organic superconductors (see sec. 5.5) we know that this is indeed true and not an approximation. In the general case one can expect that this is a rather good approximation because single-particle renormalizations have usually smaller effect on the two-particle objects than the other way round: This scheme is consistent with the idea of single-band TPSC that spin and charge fluctuations are effectively calculated from the bare Green's function [163].

It was shown in the original single-band TPSC that such an ansatz can be also motivated from the local-field approach for the electron gas and reproduces Kanamori-Brueckner screening [201].

Substituting  $A$  back into the ansatz equation (eq. (5.253)) and multiplying with  $(G^{-1})_{\bar{\gamma}\nu}(\bar{2},2)$  where we again integrate over all internal degrees of freedom we find

$$(5.257) \quad \Sigma_{\alpha\nu,\sigma}(1,2) \approx A_{\alpha} \langle n_{\alpha,-\sigma}(1) \rangle \delta_{\alpha,\nu} \delta(1-2).$$

To obtain the renormalized vertex  $\Gamma^{sp}$  we perform the functional derivatives from eq. (5.153) with the approximated self-energy expression from eq. (5.257). This leads

to the ansatz

$$(5.258) \quad \Gamma_{\gamma\beta\lambda\rho}^{sp}(1, 2; 3, 4) = \sum_{\sigma} \sigma \frac{\delta \Sigma_{\beta\gamma,\sigma}(1, 2)}{\delta G_{\rho\lambda,\downarrow}(3, 4)}$$

$$(5.259) \quad = \delta_{\beta,\gamma} \delta(1-2) \sum_{\sigma} \sigma \left( \frac{\delta A_{\beta}}{\delta G_{\rho\lambda,\downarrow}(3, 4)} n_{\beta,-\sigma}(2) + A_{\beta} \frac{\delta n_{\beta,-\sigma}(2)}{\delta G_{\rho\lambda,\downarrow}(3, 4)} \right)$$

$$(5.260) \quad = A_{\beta} \delta_{\beta,\rho} \delta_{\beta,\lambda} \delta_{\beta,\gamma} \delta(2-3) \delta(2^+ - 4) \delta(1-2),$$

where the contribution of  $\frac{\delta A}{\delta G}$  in eq. (5.259) cancels due to spin rotational invariance. Thus, equation (5.260) together with the local spin sum rules (eq. (5.142)) give us a set of equations to uniquely determine the irreducible spin vertex

$$(5.261) \quad \Gamma_{\alpha}^{sp} = A_{\alpha} = U_{\alpha} \frac{\langle n_{\alpha,\uparrow} n_{\alpha,\downarrow} \rangle}{\langle n_{\alpha,\uparrow} \rangle \langle n_{\alpha,\downarrow} \rangle}.$$

**5.4.2. TPSC self-energy and susceptibilities.** Inserting the spin and charge vertices  $\Gamma^{ch/sp}$  obtained from the sum rules (eqs. (5.251),(5.252)) and the ansatz eq. (5.260) into the equation of motion for the self-energy (eq. (5.159)) gives

$$(5.262) \quad \Sigma_{\alpha\beta,\sigma}(1, 2) = U_{\alpha} \langle n_{\alpha,-\sigma} \rangle \delta_{\alpha,\beta} \delta(1-2) + \frac{U_{\alpha}}{4} G_{\alpha\beta}^0(1, 2) \left[ \Gamma_{\beta}^{sp} \chi_{\beta\beta\alpha\alpha}^{sp}(2, 1) + \Gamma_{\beta}^{ch} \chi_{\beta\beta\alpha\alpha}^{ch}(2, 1) \right],$$

where the spin susceptibility  $\chi^{sp}$  can be calculated via the Bethe-Salpeter eq. (5.152),

$$(5.263) \quad \chi_{\lambda\gamma\xi\nu}^{sp}(1, 2) = 2\chi_{\lambda\gamma\xi\nu}^0(1, 2) - G_{\gamma\bar{\alpha}}^0(1, \bar{3}) G_{\bar{\alpha}\lambda}^0(\bar{3}, 1) \Gamma_{\bar{\alpha}}^{sp} \chi_{\bar{\alpha}\bar{\alpha}\xi\nu}^{sp}(\bar{3}, 2)$$

$$(5.264) \quad = 2\chi_{\lambda\gamma\xi\nu}^0(1, 2) + \chi_{\lambda\gamma\bar{\alpha}\bar{\alpha}}^0(1, \bar{3}) \Gamma_{\bar{\alpha}}^{sp} \chi_{\bar{\alpha}\bar{\alpha}\xi\nu}^{sp}(\bar{3}, 2).$$

From this expression one can read that if we are interested in matrix elements  $\beta\beta\alpha\alpha$  (left-hand side) we only need to know matrix elements of the same form (right-hand side), namely  $\bar{\alpha}\bar{\alpha}\alpha\alpha$ . This observation allows us to save memory and numerical calculations by restricting all susceptibility calculations to matrix elements  $\chi_{\alpha\alpha\beta\beta}^{0/ch/sp}$ . The same idea enables us to rewrite eq. (5.264) in terms of a matrix multiplication,

$$(5.265) \quad 2\chi_{\alpha\alpha\beta\beta}^0(1, 2) = (\mathbb{I}_{\alpha,\bar{\alpha}} \delta(1-\bar{3}) - \chi_{\alpha\alpha\bar{\alpha}\bar{\alpha}}^0(1, \bar{3}) \Gamma_{\bar{\alpha}}^{sp}) \chi_{\bar{\alpha}\bar{\alpha}\beta\beta}^{sp}(\bar{3}, 2),$$

where  $\mathbb{I}$  denotes the identity in the matrix site-space  $\mathbb{R}^{N_{\text{orb}} \times N_{\text{orb}}}$ .

Analogously, one can derive from the Bethe-Salpeter equation (eq. (5.129)) for the charge susceptibility  $\chi^{ch}$  the expression

$$(5.266) \quad 2\chi_{\alpha\alpha\beta\beta}^0(1, 2) = (\mathbb{I}_{\alpha,\bar{\alpha}} \delta(1-\bar{3}) + \chi_{\alpha\alpha\bar{\alpha}\bar{\alpha}}^0(1, \bar{3}) \Gamma_{\bar{\alpha}}^{ch}) \chi_{\bar{\alpha}\bar{\alpha}\beta\beta}^{ch}(\bar{3}, 2).$$

Note that the spin and charge fluctuation assume the same shape as in RPA (see eqs. (5.219), (5.220)). Nevertheless, the important difference between RPA and TPSC is the vertex that is used in the expressions. While RPA takes no vertex corrections into account and the irreducible vertices  $\Gamma^{ch/sp}$  equal the bare interaction  $U$ , TPSC considers such effects that enter via the local spin and charge sum rules.

The above expressions for the self-energy  $\Sigma$  and the spin and charge susceptibility  $\chi^{sp/ch}$  (eqs. (5.262), (5.265) and (5.266)) are functions in real space and imaginary time. Due to efficient implementation schemes (see app. B) for reciprocal space and Matsubara functions we Fourier transform the above expressions and get

$$(5.267) \quad \chi^{sp}(q, iq_m) = [\mathbb{I} - \chi^0(q, iq_m) \Gamma^{sp}]^{-1} 2\chi^0(q, iq_m),$$

$$(5.268) \quad \chi^{ch}(q, iq_m) = [\mathbb{I} + \chi^0(q, iq_m) \Gamma^{ch}]^{-1} 2\chi^0(q, iq_m)$$

and

$$\begin{aligned} \Sigma_{\alpha\beta,\sigma}(k, i\omega_n) &= U_\alpha \langle n_{\alpha,-\sigma} \rangle \delta_{\alpha,\beta} + \frac{U_\alpha}{4} \sum_r \int_0^{\tilde{\beta}} e^{irk} e^{i\omega_n \tau} \times \\ (5.269) \quad &\times \left[ \Gamma_\beta^{sp} \chi_{\beta\beta\alpha\alpha}^{sp}(-r, -\tau) + \Gamma_\beta^{ch} \chi_{\beta\beta\alpha\alpha}^{ch}(-r, -\tau) \right] G_{\alpha\beta}^0(r, \tau) d\tau \end{aligned}$$

$$\begin{aligned} &= U_\alpha \langle n_{\alpha,-\sigma} \rangle \delta_{\alpha,\beta} + \frac{U_\alpha}{4N^2 \tilde{\beta}^2} \sum_{q, iq_m} \sum_{k', i\omega_{n'}} \sum_r \int_0^{\tilde{\beta}} e^{ir(k-k'+q)} e^{i(\omega_n - \omega_{n'} + q_m)\tau} \times \\ (5.270) \quad &\times \left[ \Gamma_\beta^{sp} \chi_{\beta\beta\alpha\alpha}^{sp}(q, iq_m) + \Gamma_\beta^{ch} \chi_{\beta\beta\alpha\alpha}^{ch}(q, iq_m) \right] G_{\alpha\beta}^0(k', i\omega_{n'}) d\tau \end{aligned}$$

$$\begin{aligned} &= U_\alpha \langle n_{\alpha,-\sigma} \rangle \delta_{\alpha,\beta} + \frac{U_\alpha T}{4N} \times \\ (5.271) \quad &\times \sum_{q, iq_m} \left[ \Gamma_\beta^{sp} \chi_{\beta\beta\alpha\alpha}^{sp}(q, iq_m) + \Gamma_\beta^{ch} \chi_{\beta\beta\alpha\alpha}^{ch}(q, iq_m) \right] G_{\alpha\beta}^0(k+q, i\omega_{n+m}). \end{aligned}$$

Alternatively, one can use the inversion property of the susceptibilities (see eq. (5.102)) to obtain

$$\begin{aligned} \Sigma_{\alpha\beta,\sigma}(k, i\omega_n) &= U_\alpha \langle n_{\alpha,-\sigma} \rangle \delta_{\alpha,\beta} + \frac{U_\alpha T}{4N} \times \\ (5.272) \quad &\times \sum_{q, iq_m} \left[ \chi_{\alpha\alpha\beta\beta}^{sp}(q, iq_m) \Gamma_\beta^{sp} + \chi_{\alpha\alpha\beta\beta}^{ch}(q, iq_m) \Gamma_\beta^{ch} \right] G_{\alpha\beta}^0(k-q, i\omega_{n-m}). \end{aligned}$$

Next, we include the effects from the transversal particle-hole channel (see sec. 5.1.9). Similarly to the longitudinal channel one start with eq. (5.204),

$$\begin{aligned} &\Sigma_{\alpha\bar{\beta}}(1, \bar{3})_{\Phi} \mathbf{G}_{\bar{\beta}\gamma}(\bar{3}, 2)_{\Phi} \\ (5.273) \quad &= -U_\alpha \left( \begin{array}{cc} \left\langle T_\tau n_{\alpha,\downarrow}(1) c_{\alpha,\uparrow}(1) c_{\gamma,\uparrow}^\dagger(2) \right\rangle_{\Phi} & \left\langle T_\tau n_{\alpha,\downarrow}(1) c_{\alpha,\uparrow}(1) c_{\gamma,\downarrow}^\dagger(2) \right\rangle_{\Phi} \\ \left\langle T_\tau n_{\alpha,\uparrow}(1) c_{\alpha,\downarrow}(1) c_{\gamma,\uparrow}^\dagger(2) \right\rangle_{\Phi} & \left\langle T_\tau n_{\alpha,\uparrow}(1) c_{\alpha,\downarrow}(1) c_{\gamma,\downarrow}^\dagger(2) \right\rangle_{\Phi} \end{array} \right) \end{aligned}$$

and factorizes this expression in a similar way as in eq. (5.255) which results in the ansatz

$$(5.274) \quad \Sigma_{\alpha\bar{\beta}}(1, \bar{3})_{\Phi} \mathbf{G}_{\bar{\beta}\gamma}(\bar{3}, 2)_{\Phi} = A_\alpha \begin{pmatrix} \mathbf{G}_{\alpha\alpha}^{\downarrow\downarrow}(1, 1^+)_{\Phi} & -\mathbf{G}_{\alpha\alpha}^{\uparrow\downarrow}(1, 1^+)_{\Phi} \\ -\mathbf{G}_{\alpha\alpha}^{\downarrow\uparrow}(1, 1^+)_{\Phi} & \mathbf{G}_{\alpha\alpha}^{\uparrow\uparrow}(1, 1^+)_{\Phi} \end{pmatrix} \mathbf{G}_{\alpha\gamma}(1, 2),$$

where  $A_\alpha$  is chosen such that the equal time and position limit is fulfilled, i.e. find again

$$(5.275) \quad A_\alpha = U_\alpha \frac{\langle n_{\alpha,\sigma} n_{\alpha,-\sigma} \rangle}{\langle n_{\alpha,\sigma} \rangle \langle n_{\alpha,-\sigma} \rangle}$$

because the spin off-diagonal Green's function elements will vanish due to spin conservation.

To obtain an expression for the irreducible transversal spin vertex  $\Gamma^{sp,tr}$  (eq. (5.212)) we multiply eq. (5.274) with the inverse Green's function  $(\mathbf{G}^{-1})_{\bar{\gamma},\epsilon}(\bar{2}, 4)$  from the right and integrate out all internal degrees of freedom which yields

$$(5.276) \quad \Sigma_{\alpha\epsilon}(1, 4)_{\Phi} = A_\alpha \begin{pmatrix} \mathbf{G}_{\alpha\alpha}^{\downarrow\downarrow}(1, 1^+)_{\Phi} & -\mathbf{G}_{\alpha\alpha}^{\uparrow\downarrow}(1, 1^+)_{\Phi} \\ -\mathbf{G}_{\alpha\alpha}^{\downarrow\uparrow}(1, 1^+)_{\Phi} & \mathbf{G}_{\alpha\alpha}^{\uparrow\uparrow}(1, 1^+)_{\Phi} \end{pmatrix} \delta(1-4) \delta_{\alpha,\epsilon}.$$

Thus, we obtain the space irreducible spin vertex

$$\Gamma_{\epsilon\alpha\lambda\rho}^{sp,tr}(1, 4; 7, 8) = - \frac{\delta \Sigma_{\alpha\epsilon}^{\uparrow\downarrow}(1, 4)_{\Phi}}{\delta \mathbf{G}_{\rho\lambda}^{\uparrow\downarrow}(7, 8)_{\Phi}}$$

$$(5.277) \quad = U_\alpha \frac{\langle n_{\alpha,\sigma} n_{\alpha,-\sigma} \rangle}{\langle n_{\alpha,\sigma} \rangle \langle n_{\alpha,-\sigma} \rangle} \delta_{\alpha,\rho} \delta_{\lambda,\epsilon} \delta_{\alpha,\epsilon} \delta(1-4) \delta(1-7) \delta(4-8)$$

as in the longitudinal channel and therefore we will have the same spin susceptibility  $\chi^{sp}$  (see eq. (5.203) and (5.187)). Finally, we can simplify the transversal self-energy expression (eq. (5.211)) and obtain

$$(5.278) \quad \Sigma_{\alpha\nu,\sigma}(1,4) = U_\alpha n_{\alpha,-\sigma}(1) \delta_{\alpha,\nu} \delta(1-4) + \frac{U_\alpha}{2} \Gamma_\nu^{sp} \chi_{\nu\alpha\alpha}^{sp}(4,1) G_{\alpha\nu}(1,4).$$

As discussed in sec. 5.1.8 we average over the transversal and longitudinal self-energy expressions (eq. (5.271) and (5.278)) to obtain the final result

$$(5.279) \quad \Sigma_{\alpha\beta,\sigma}(k, i\omega_n) = U_\alpha \langle n_{\alpha,-\sigma} \rangle \delta_{\alpha,\beta} + \frac{U_\alpha T}{8N} \times \sum_{q, iq_m} \left[ 3\Gamma_\beta^{sp} \chi_{\beta\beta\alpha\alpha}^{sp}(q, iq_m) + \Gamma_\beta^{ch} \chi_{\beta\beta\alpha\alpha}^{ch}(q, iq_m) \right] G_{\alpha\beta}^0(k+q, i\omega_{n+m}).$$

In the end one obtains the single-particle properties via the full Green's function  $G$  from the multi-site version of the Dyson equation

$$(5.280) \quad G = [(G^0)^{-1} + \mu - \Sigma]^{-1},$$

where the chemical potential  $\mu$  is used to fix the number of particles after introducing the improved self-energy expression from eq. (5.279).

#### 5.4.3. Internal accuracy check. We remind ourselves of the identity

$$(5.281) \quad \Sigma_{\alpha\bar{\beta},\sigma}(1, \bar{3}) G_{\bar{\beta}\gamma,\sigma}(\bar{3}, 2) = -U_\alpha \left\langle T_\tau n_{\alpha,-\sigma}(1^+) c_{\alpha,\sigma}(1) c_{\gamma,\sigma}^\dagger(2) \right\rangle$$

that we derived both in the longitudinal particle-hole channel (see eq. (5.48)) and the transversal particle-hole channel (see eq. (5.205)). Evaluating this equation at equal space-time variable and site index,  $2 \rightarrow 1^+$  and  $\gamma \rightarrow \alpha$ , gives

$$(5.282) \quad \Sigma_{\alpha\bar{\beta},\sigma}(1, \bar{3}) G_{\bar{\beta}\alpha,\sigma}(\bar{3}, 1^+) = U_\alpha \langle n_{\alpha,-\sigma} n_{\alpha,\sigma} \rangle,$$

which can be Fourier transformed into

$$(5.283) \quad \lim_{\tau \nearrow 0} \frac{T}{N} \sum_{k, i\omega_n} e^{-i\omega_n \tau} \Sigma_{\alpha\bar{\beta},\sigma}(k, i\omega_n) G_{\bar{\beta}\alpha,\sigma}(k, i\omega_n) = U_\alpha \langle n_{\alpha,-\sigma} n_{\alpha,\sigma} \rangle.$$

Note that the limit cannot be exchange with the infinite sum due to the constant Hartree-Fock term in the self-energy  $\Sigma$  (see eq. (5.279)) and the  $O\left(\frac{1}{i\omega_n}\right)$ -high frequency behavior of the Green's function  $G$ .

Inserting the explicit expression for the self-energy  $\Sigma$  (eq. (5.279)) into the above equation with  $G$  replaced with the non-interacting Green's function  $G^0$  gives

$$(5.284) \quad \begin{aligned} & \lim_{\tau \nearrow 0} \frac{T}{N} \sum_{k, i\omega_n} e^{-i\omega_n \tau} \Sigma_{\alpha\bar{\beta},\sigma}(k, i\omega_n) G_{\bar{\beta}\alpha,\sigma}^0(k, i\omega_n) \\ & = U_\alpha \langle n_{\alpha,-\sigma} \rangle \langle n_{\alpha,\sigma} \rangle + \\ & \quad + \frac{U_\alpha T}{8N} \sum_{q, iq_m} \left[ 3\Gamma_\beta^{sp} \chi_{\beta\beta\alpha\alpha}^{sp}(q, iq_m) + \Gamma_\beta^{ch} \chi_{\beta\beta\alpha\alpha}^{ch}(q, iq_m) \right] \times \\ & \quad \times \lim_{\tau \nearrow 0} \sum_{k, i\omega_n} e^{-i\omega_n \tau} G_{\alpha\bar{\beta}}^0(k+q, i\omega_{n+m}) G_{\bar{\beta}\alpha,\sigma}^0(k, i\omega_n), \end{aligned}$$

where we used that the off-diagonal of the non-interacting Green's function  $G^0$  decays faster than  $n \mapsto 1/(i\omega_n)$  (see eq. (4.235)) whence only the diagonal elements  $\Sigma_{\alpha\alpha}$  and

$G_{\alpha\alpha}^0$  contribute to the first term on the right-hand side of eq. (5.284). Moreover, we can identify the irreducible susceptibility  $\chi^0$  (eq. (5.72))

$$\begin{aligned}
 & \lim_{\tau \nearrow 0} \frac{T}{N} \sum_{k, i\omega_n} e^{-i\omega_n \tau \Sigma_{\alpha\bar{\beta},\sigma}}(k, i\omega_n) G_{\beta\alpha,\sigma}^0(k, i\omega_n) \\
 & = U_\alpha \langle n_{\alpha,-\sigma} \rangle^2 + \\
 (5.285) \quad & - \frac{U_\alpha T}{8N} \sum_{q, iq_m} \left[ 3\Gamma_{\beta}^{sp} \chi_{\beta\beta\alpha\alpha}^{sp}(q, iq_m) + \Gamma_{\beta}^{ch} \chi_{\beta\beta\alpha\alpha}^{ch}(q, iq_m) \right] \chi_{\alpha\alpha\bar{\beta}\bar{\beta}}^0(q, iq_m).
 \end{aligned}$$

We can now use the Bethe-Salpeter equations (5.129) and (5.264) to identify

$$\begin{aligned}
 & \lim_{\tau \nearrow 0} \frac{T}{N} \sum_{k, i\omega_n} e^{-i\omega_n \tau \Sigma_{\alpha\bar{\beta},\sigma}}(k, i\omega_n) G_{\beta\alpha,\sigma}^0(k, i\omega_n) \\
 (5.286) \quad & = U_\alpha \langle n_{\alpha,-\sigma} \rangle^2 - \frac{U_\alpha T}{8N} \sum_{q, iq_m} \left[ 3\chi_{\alpha\alpha\alpha\alpha}^{sp}(q, iq_m) - 4\chi_{\alpha\alpha\alpha\alpha}^0(q, iq_m) - \chi_{\alpha\alpha\alpha\alpha}^{ch}(q, iq_m) \right].
 \end{aligned}$$

From the local spin and charge sum rules (eqs. (5.251), (5.252)) for the spin and charge susceptibilities  $\chi^{sp/ch}$  and the same ones in the limit  $U = 0$  – this gives us a sum rule for  $\chi^0$  – we obtain

$$\begin{aligned}
 & \lim_{\tau \nearrow 0} \frac{T}{N} \sum_{k, i\omega_n} e^{-i\omega_n \tau \Sigma_{\alpha\bar{\beta},\sigma}}(k, i\omega_n) G_{\beta\alpha,\sigma}^0(k, i\omega_n) \\
 & = U_\alpha \langle n_{\alpha,-\sigma} \rangle^2 - \frac{U_\alpha}{8} \left[ 3(\langle n_\alpha \rangle - 2\langle n_{\alpha,\downarrow} n_{\alpha,\uparrow} \rangle) - 2(\langle n_\alpha \rangle - 2\langle n_{\alpha,\downarrow} \rangle \langle n_{\alpha,\uparrow} \rangle) - \right. \\
 (5.287) \quad & \left. - (\langle n_\alpha \rangle + 2\langle n_{\alpha,\downarrow} n_{\alpha,\uparrow} \rangle - \langle n_\alpha \rangle^2) \right]
 \end{aligned}$$

$$(5.288) \quad = U_\alpha \langle n_{\alpha,-\sigma} n_{\alpha,\sigma} \rangle.$$

We conclude that the sum rule

$$(5.289) \quad \lim_{\tau \nearrow 0} \frac{T}{N} \sum_{k, i\omega_n} e^{-i\omega_n \tau \Sigma_{\alpha\bar{\beta},\sigma}}(k, i\omega_n) G_{\beta\alpha,\sigma}^0(k, i\omega_n) = U_\alpha \langle n_{\alpha,-\sigma} n_{\alpha,\sigma} \rangle$$

is indeed fulfilled for the TPSC self-energy. For this reason we can use this sum rule as a benchmark for numerical convergence and more importantly the deviation between eq. 5.289 and the same equation with  $G^0$  replace by the full Green's function  $G$  gives us a measure for the applicability of the TPSC approximation.

**5.4.4. Flowchart of the multi-site TPSC.** For a better overview on the multi-site TPSC approach we give a flowchart of the method in fig. 5.9.

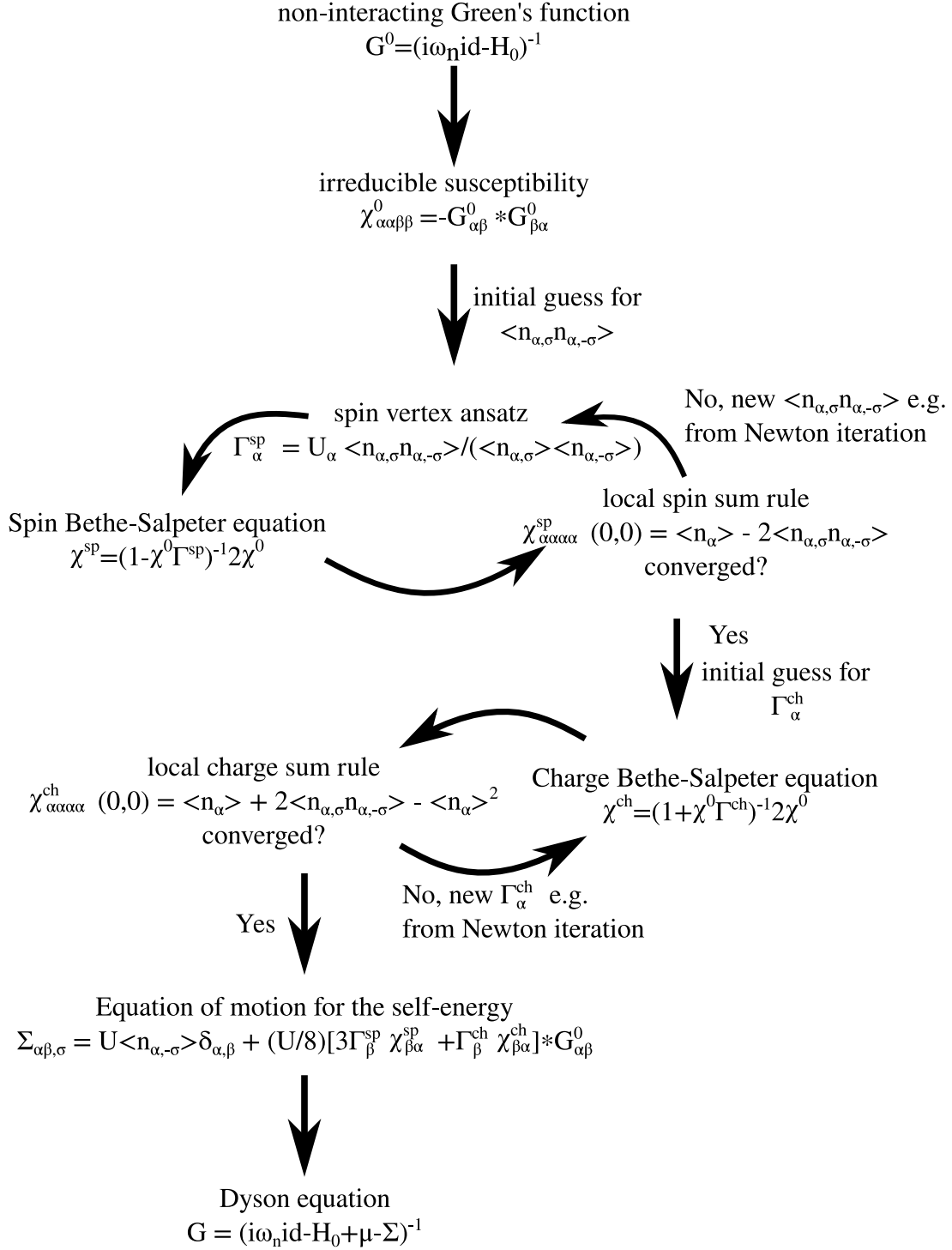


FIGURE 5.9. Multi-site TPSC flow chart as described in sec. 5.4. After calculating the non-interacting Green's function in site-space and the irreducible susceptibility components  $\alpha\alpha\beta\beta$  one has to converge the spin and charge with respect to the local spin and charge sum rule and the Bethe-Salpeter equations. From those one is able to evaluate the self-energy and thus interacting Green's function via the Dyson equation. Note that  $\text{id}$  is the identity map in site-space which is equivalent to  $\mathbb{I}$ . Figure adapted from Ref. [164].

**5.4.5. Short summary on the applications of multi-site TPSC.** The multi-site version of TPSC was applied to the Hubbard model on a honeycomb lattice where antiferromagnetic instabilities were studied [152]. Further investigations dealt not only with superconductivity in organic superconductors [239, 241, 242] and Cuprate superconductors [240, 243, 244] but also with correlation effects in layered transition metal dichalcogenides [245]. The approach was also used to define a measure for the strength of  $k$ -dependence of the self-energy [246].

### 5.5. Multi-site TPSC application: Organic superconductors

**K. Zantout, M. Altmeyer, S. Backes, R. Valenti**

Superconductivity in correlated BEDT-TTF molecular conductors: Critical temperatures and gap symmetries, Phys. Rev. B **97**, 014530 (2018) [241]

In this section we study the superconducting properties of a class of quasi two-dimensional organic charge transfer salts, the so-called  $\kappa$ -(BEDT-TTF)<sub>2</sub>X compounds, where BEDT-TTF stands for the organic molecule bis(ethylenedithio)tetrathiafulvalene and  $\kappa$  refers to a specific alignment of those molecules (see fig. 5.10) and  $X$  is a molecule complex that we will specify later. Those materials are also abbreviated  $\kappa$ -ET<sub>2</sub>X.

The research interest for this family of superconductors is due to the rich phase diagram of these crystals that contain anti-ferromagnetic Mott insulating, superconducting and possibly spin liquid phases [247–249]. More specifically, it is possible to move these systems to different phases by means of chemical substitution of the anion  $X^-$ , physical pressure or the so-called endgroup disorder freezing [2, 249–252].

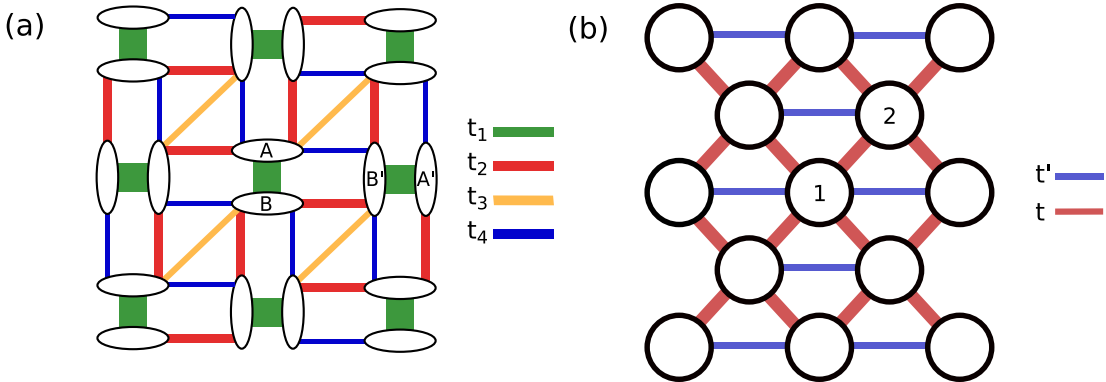


FIGURE 5.10. Model systems for  $\kappa$ -(BEDT-TTF)<sub>2</sub>X superconductors. (a) The ellipses represent the (BEDT-TTF) molecule, where A, A', B and B' represent the four molecules within one unit cell. The parameters  $t_1, \dots, t_4$  denote the major hopping matrix elements while the thickness of the corresponding line encodes the size of the hopping. The dimer model in (b) is obtained by integrating out the  $t_1$  hopping and averaging between  $t_2$  and  $t_4$  which results in the hopping  $t$  whereas  $t'$  is equal to  $|t_3|/2$ . Figure reprinted from Ref. [241].

Those materials consist of anionic layers  $X^-$  that separate the extended organic (BEDT-TTF)<sub>2</sub><sup>+</sup> molecules from each other (see fig. 5.11). Due to the insulating anion layers the electronic structure is highly anisotropic and quasi two-dimensional. At low temperatures of  $\sim 10$ K many representatives of this material class become superconducting [253–256]. Although many different experiments have been conducted to determine the symmetry of the superconducting gap function there is no final answer

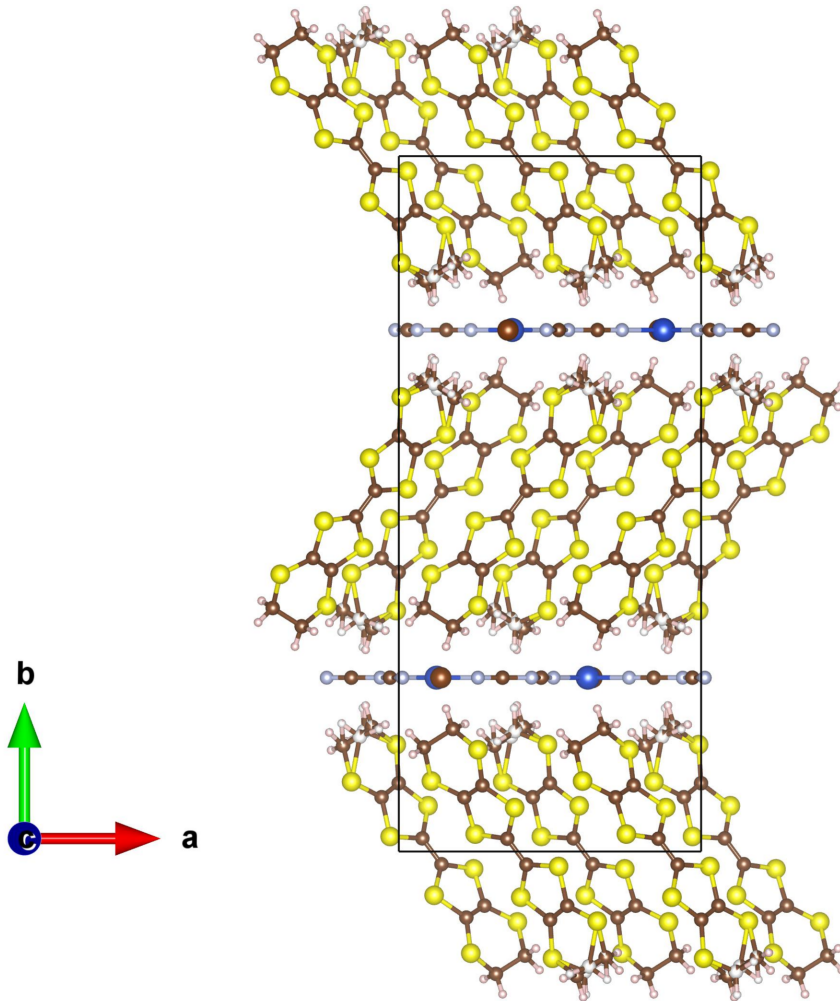


FIGURE 5.11. Schematic unit cell (back rectangle) of a  $\kappa$ -(BEDT-TTF) $_2$ X crystal. We recognize the two important constituents of those crystals, namely the extended organic molecules (BEDT-TTF) $_2^+$  (tilted aromatic compound) and the flat anion layers  $X^-$  separating them. The organic compound consists of carbon (brown), sulfur (yellow) and hydrogen (pink).

and published proposals range from  $s$ -wave [257–259] to  $d$ -wave [260–268] symmetry but even within the party that agrees on  $d$ -wave symmetry there are different claims regarding the local of the superconducting nodal lines [261, 266, 269, 270].

Due to the similarity of the organics phase diagram with the one of Cuprate superconductors one can assume that the same underlying pairing mechanism based on anti-ferromagnetic spin fluctuations drives superconductivity in  $\kappa$ -(BEDT-TTF) $_2$ X materials with the additional degree of freedom that comes from geometrical frustration [271, 272]. For this reason we will start with the DFT based kinetic Hamiltonian where we include an additional local Hubbard interaction for the correlated electronic states at the Fermi energy.

*Ab-initio* bandstructure calculations suggest two different effective low-energy Hubbard models for these materials [273]. The first model, that is coined *molecule model* in this section, is based on the four BEDT-TTF molecules that appear in one layer of the unit cell (see fig. 5.10(a)). This four-band model can be further simplified by taking advantage of the large hopping  $t_1$  (see figure) that is due to strong dimerization of two

parallel aligned BEDT-TTF molecules. Thus, one can integrate out the  $t_1$  degree of freedom, average between  $t_2$  and  $t_4$  and divide  $t_3$  by two in order to obtain the *dimer model* (see fig. 5.10(b)).

Studies that compared both models to each other found out that the averaging of the internal degrees of freedom within the dimer model can lead to qualitatively different results due to the neglect of the high in-plane anisotropy observed in  $\kappa$ -(BEDT-TTF)<sub>2</sub>X organic superconductors [269, 273]. More specifically, the mentioned calculations on the more accurate molecule model that takes account of these anisotropies predict an eight-node  $s+d_{x^2-y^2}$  superconducting gap symmetry while the calculations for the dimer model lead to a  $d_{xy}$  superconducting gap symmetry. The exotic eight-node superconducting gap function seems more promising in view of scanning tunneling spectroscopy measurements performed for  $\kappa$ -(BEDT-TTF)<sub>2</sub>Cu[N(CN)<sub>2</sub>]Br that are less compatible with the simple  $d_{xy}$  solution [269]. One should however note that those measurements are not phase sensitive and thus the issue is not settled from the experimental side although those results are already indications for the inadequacy of the dimer model to describe the superconductivity in  $\kappa$ -(BEDT-TTF)<sub>2</sub>Cu[N(CN)<sub>2</sub>]Br.

In contrast to the mentioned studies in Refs. [269, 273] which are based on weak-coupling random phase approximation calculations without finite-temperature effects we study here the dimer and molecule model within TPSC where we expect additional effects due to vertex renormalizations and finite-temperature effects. The superconducting critical temperature and gap symmetry is obtained by means of the linearized Eliashberg equation [274–276]

$$(5.290) \quad \lambda \Delta_{\mu\nu}(k, i\omega_n) = \frac{T}{N} \sum_{k', i\omega_{n'}} V_{\mu\nu}(k - k', iq_{n-n'}) \sum_{\alpha, \beta} G_{\mu\alpha}(k', i\omega_{n'}) \Delta_{\alpha\beta}(k', i\omega_{n'}) G_{\nu\beta}^*(k', i\omega_{n'}),$$

where the superconducting gap  $\Delta_{\mu\nu}(k, i\omega_n)$  is restricted to singlet states and even-frequency and -orbital solutions, i.e.

$$(5.291) \quad \Delta_{\nu\mu}(k, i\omega_n) = \Delta_{\mu\nu}(k, i\omega_n) = \Delta_{\mu\nu}(-k, i\omega_n) = \Delta_{\mu\nu}(k, -i\omega_n),$$

by symmetrizing

$$(5.292) \quad (G\Delta G)_{\mu\nu}(k, i\omega_n) \rightarrow \frac{1}{2} [(G\Delta G)_{\mu\nu}(k, i\omega_n) + (G\Delta G)_{\nu\mu}(-k, -i\omega_n)].$$

The largest positive eigenvalue of the linearized Eliashberg equation (5.290) is numerically obtained by the power method [277] and determines the superconducting critical temperature when it becomes unity. We use the pairing vertex

$$V(q, iq_m) = -\frac{3}{4} U^{\text{sp}} \chi^{\text{sp}}(q, iq_m) U + \frac{1}{4} U^{\text{ch}} \chi^{\text{ch}}(q, iq_m) U - \frac{1}{2} U$$

that is based on the random phase approximation in the particle-particle channel [168, 278].

As described previously the dimer model consists of a lattice model where the lattice sites are constructed from averaging between two parallel oriented BEDT-TTF molecules. This construction results in a half-filled anisotropic triangular lattice, where two dimers are located within the crystallographic unit cell [273] because we know that one electron is transferred from the (ET)<sub>2</sub> layer to the X layer. In the molecule model one takes each molecule as a lattice site which leads to a three-quarter filled four-band model [273]. The hopping parameters that are calculated from the projective Wannier function method are here restricted to four largest hopping amplitudes  $t_1, \dots, t_4$  (see fig. 5.10(a)). We take the hopping parameters from [273] which lead in the molecule

model to the kinetic Hamiltonian

$$(5.293a) \quad \langle 0|H_{\text{kin}}|1\rangle(k) = t_1 + t_3 e^{ik_x a},$$

$$(5.293b) \quad \langle 0|H_{\text{kin}}|2\rangle(k) = t_4 \left(1 + e^{-ik_y b}\right),$$

$$(5.293c) \quad \langle 0|H_{\text{kin}}|3\rangle(k) = t_2 \left(1 + e^{-ik_x a}\right),$$

$$(5.293d) \quad \langle 1|H_{\text{kin}}|2\rangle(k) = t_2 e^{-ik_y b} \left(1 + e^{-ik_x a}\right),$$

$$(5.293e) \quad \langle 1|H_{\text{kin}}|3\rangle(k) = t_4 e^{-ik_x a} \left(1 + e^{-ik_y b}\right),$$

$$(5.293f) \quad \langle 2|H_{\text{kin}}|3\rangle(k) = t_1 + t_3 e^{-ik_x a},$$

$$(5.293g) \quad \langle \alpha|H_{\text{kin}}|\alpha\rangle(k) = -\mu,$$

where  $a$  and  $b$  are the lattice constants of the two-dimensional ET plane,  $|\alpha\rangle$  is the Wannier state localized at the molecule position  $\alpha$ . The remaining matrix elements are obtained from  $H = H^\dagger$ . Note that the chemical potential was determined numerically to ensure the correct particle number in both models.

The hopping elements of the dimer model are obtained via

$$(5.294) \quad t = (|t_2| + |t_4|)/2,$$

$$(5.295) \quad t' = |t_3|/2$$

and lead to the kinetic Hamiltonian

$$(5.296a) \quad \langle 0|H_{\text{kin}}|0\rangle(k) = \langle 1|H_{\text{kin}}|1\rangle(k) = 2t' \cos(k_x a) - \mu$$

$$(5.296b) \quad \langle 0|H_{\text{kin}}|1\rangle(k) = t \left( e^{ik_x a/2 + ik_y b/2} + e^{-ik_x a/2 + ik_y b/2} + \right. \\ \left. + e^{ik_x a/2 - ik_y b/2} + e^{-ik_x a/2 - ik_y b/2} \right)$$

$$(5.296c) \quad = \langle 1|H_{\text{kin}}|0\rangle^*(k),$$

where  $|\alpha\rangle$  denotes the Wannier state localized at the dimer position  $\alpha$ . Note that the on-site Hubbard interaction in the dimer model  $U_{\text{dim}}$  can be approximated by  $U_{\text{dim}} \approx 2t_1$  [248, 279], while we denote the Coulomb interaction in the molecule by  $U_{\text{mol}}$ .

**5.5.1. Computational details.** The non-interacting susceptibility  $\chi^0$  was calculated by means of the adaptive cubature method (see appendix B) based on a three-point formula for triangles with an integration tolerance of  $10^{-6}$ . All susceptibilities were stored on  $200 \times 200$   $k$ -grids at  $iq_n = 0$  for the molecule model and else we employed an adaptive grid (see appendix B). In the case of the dimer model we used a  $300 \times 300$   $k$ -grid. All other quantities are well-converged on  $70 \times 70$   $k$ -grids. The summation over Matsubara frequencies was performed for  $N_{\text{Mats}} = 40 \cdot (0.025/T)$  frequencies and we included high-frequency corrections up to the order of  $1/\omega^2$  by extrapolation (see appendix B).

**5.5.2. Dimer model results.** In fig. 5.12 we show the superconducting gap function that we observed for all dimer model calculations of the organic superconductors in [273]. We observe a  $d_{xy}$  gap symmetry for both bands, where additional nodes occur at the boundary of the first Brillouin zone due to  $2\pi$  periodicity of the gap functions. Those additional nodes that are also relevant on the Fermi surface (black lines in fig. 5.12) have been already observed in previous calculations and attributed to strong inter-band coupling [280]. The  $d_{xy}$  symmetry itself can be understood from

the Hubbard model on a square lattice<sup>16</sup>, where we know that antiferromagnetic spin fluctuations yield a pairing vertex that is peaked at  $(\pi, \pi)$  due to the perfect nesting condition in the Hubbard square lattice at half-filling. Such a pairing favors  $d_{x^2-y^2}$  gap solutions [207] which has to be translated into the two-site Brillouin zone of the organic dimer model by rotation of  $45^\circ$  and additional folding of the corners of the Brillouin zone to the center. This transforms the original  $d_{x^2-y^2}$  gap solution of the

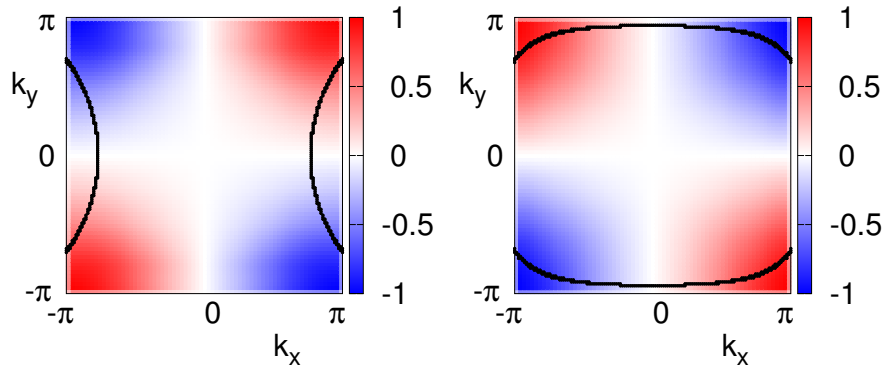


FIGURE 5.12. Superconducting gap  $\Delta(\vec{k}, i\omega_0)$  of the dimer model in the first physical Brillouin zone (see main text). The dominant  $d_{xy}$  character shows nodes along the boundaries, since it has to be  $2\pi$  periodic, and a sign change between (a) the first band and (b) the second band that has been previously assigned to strong inter-band coupling [280]. Figure reprinted from Ref. [241].

single-site unit cell into a  $d_{xy}$  solution of the dimer unit cell and we can understand the anisotropic hopping  $t'$  as a small perturbation that introduces geometric frustration (see fig. 5.10) and thus reduces spin fluctuations without changing the gap symmetry.

In order to understand the effect of  $t'/t$  in more detail we plot the largest eigenvalue of the linearized Eliashberg equation for  $T=0.003$  eV as a function of the Hubbard interaction  $U_{\text{dim}}/t$  and the frustration  $t'/t$  in fig. 5.13.

First, we remind that a large eigenvalue implies close proximity to the superconducting phase and  $\lambda = 1$  signifies the superconducting transition temperature  $T_c$ .

We observe that too large geometric frustration  $t'/t$  suppresses superconductivity since the key ingredient to the pairing vertex are antiferromagnetic fluctuations. Those fluctuations can be induced by the local on-site repulsion  $U_{\text{dim}}/t$  which leads to an enhancement of the largest Eliashberg eigenvalue as long as this value is not too large. In the case where  $U_{\text{dim}}/t \gtrsim 1.5$  and low geometric frustration we find that superconductivity is also suppressed. The reason here is that the strong interaction leads to pseudogap physics where sections of the Fermi surface states are gapped out and thus one reduces the essential states that are needed for forming Cooper pairs.

To avoid those antiferromagnetic ordering tendencies from strong interactions one can introduce geometric frustration  $t'/t$  which yields a good balance between strong pairing interaction and sufficient electronic states at the Fermi energy. For this reason we observe a maximum of the largest Eliashberg eigenvalue around the values  $t'/t \approx 0.25$  and  $U_{\text{dim}}/t > 3.4$ .

After having understood qualitatively the pairing mechanism in the dimer Hubbard model we move to the eight representative materials that were studied in Ref. [273].

<sup>16</sup>This corresponds to the limit of  $t' = 0$ .

We take the hopping amplitudes given in the reference and fix the Hubbard interaction to  $U_{\text{dim}} \approx 2t_1$  as mentioned earlier. With those parameters fixed we reduce the temperature until the largest eigenvalue of the linearized Eliashberg equation reaches unity. The results of this analysis are shown in table 5.1. Most remarkably, we find that the superconducting critical temperatures are not only far away from the experimentally measured but also they do not follow the same trend. If we want to understand

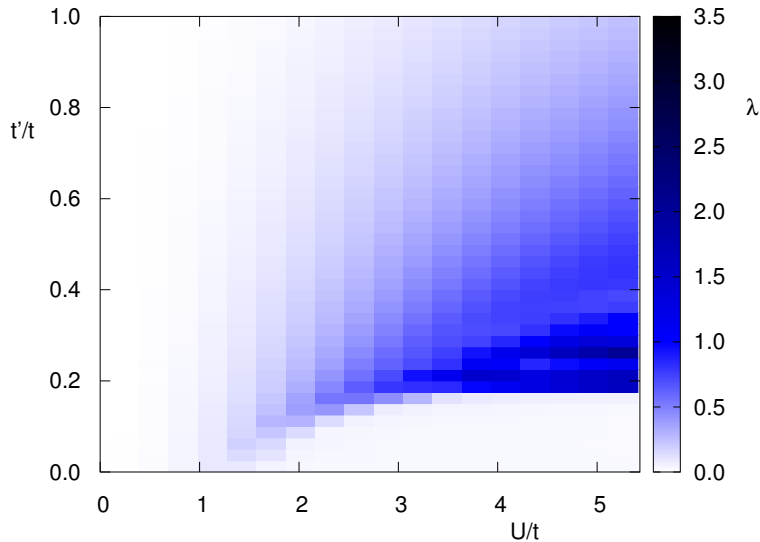


FIGURE 5.13. Largest positive eigenvalue of the linearized Eliashberg equation at fixed temperature  $T=0.003$  eV within the dimer model. While moderate on-site interactions  $U_{\text{dim}}/t$  are crucial to obtain superconductivity, we see that too strong correlations ( $U_{\text{dim}}/t \gtrsim 1.5$ ) result in the opening of a pseudogap and thus a suppression of quasiparticle states at the Fermi surface that are needed to form Cooper pairs. Too large antiferromagnetic fluctuations that lead to Mott insulating tendencies can be reduced by anisotropic next nearest neighbor hoppings and the implied geometric frustration. A combination of both ( $t'/t \approx 0.25$  and  $U_{\text{dim}}/t > 3.4$ ) is most favorable for superconductivity. Figure reprinted from Ref. [241].

those results by means of the analysis shown in fig. 5.13 we plot the calculated critical temperatures of the eight organic superconductors in dependence of their respective frustration  $t'/t$  in fig. 5.14.

In agreement to the analysis that we performed for fig. 5.13 we find that the critical temperatures  $T_c$  decreases quasi-linearly with frustration  $t'/t$ . This means that the critical temperatures of the organic superconductors are not determined by the interplay of the dimer Hubbard interaction  $U_{\text{dim}}$  and the geometric frustration  $t'/t$  but we need to consider more degrees of freedom within the materials. This leads us to the molecule model where each ET molecule is treated as a single site.

**5.5.3. Molecule model results.** We consider now the 4-band Hamiltonian from eq. (5.293), where each site corresponds to the center of one ET molecule (see fig. 5.10(b)). Due to the charge transfer of one electron from  $(\text{ET})_2$  to the anion layer X we have a filling of  $3/4$ .

For this more elaborate model of  $\kappa$ - $(\text{ET})_2\text{X}$  superconductors the spin-fluctuation random phase approximation study showed that an exotic  $s+d_{x^2-y^2}$  superconducting gap

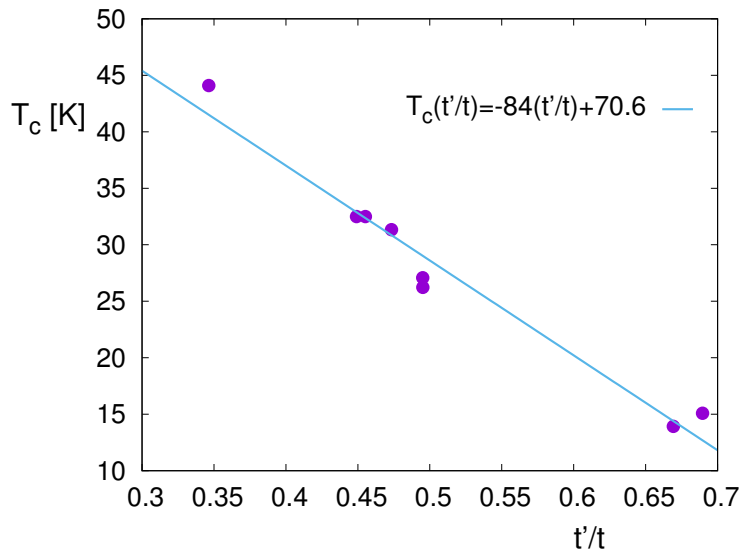


FIGURE 5.14. Critical temperature  $T_c$  calculated within the combined multi-site TPSC + linearized Eliashberg equation as a function of frustration  $t'/t$  for the eight  $\kappa$ -(ET) $_2$ X materials listed in table 5.1. We observe a quasi-linear drop of  $T_c$  as a function of increasing  $t'/t$  which can be understood from the analysis we performed for fig. 5.13, where too strong frustration reduces the pairing interaction due to suppression of antiferromagnetic fluctuations. As a guide to the eye we show the linear fit to the data points. Figure reprinted from Ref. [241].

symmetry (see fig. 5.15) is realized in the eight materials studied and that a small change in the hopping parameters can push the system into a  $d_{xy}$  gap symmetric state [273]. In contrast to this study we find that only two out of the eight compounds exhibit  $s+d_{x^2-y^2}$  gap symmetry while the others converge to a  $d_{xy}$  gap solution. The two materials that show the exotic gap symmetry are  $\kappa$ -(ET) $_2$ Cu(NCS) $_2$  and  $\kappa$ -(ET) $_2$ Cu[N(CN) $_2$ ](CN) which are the ones that have the largest in-plane anisotropy  $t_2/t_4$ .

material	$t'/t$	$t_4/t_2$	$U_{\text{dim}}$ [eV]	$T_c^{\text{TPSC}}$ [K]	$T_c$ [K]
$\kappa$ -(ET) $_2$ Ag(CF $_3$ ) $_4$ (TCE)	0.449	0.362	0.336	32.5	2.6
$\kappa$ -(ET) $_2$ I $_3$	0.346	0.266	0.36	44.1	3.6
$\kappa$ -(ET) $_2$ Ag(CN) $_2$ I·H $_2$ O	0.473	0.305	0.37	31.3	5.0
$\kappa$ - $\alpha'_1$ -(ET) $_2$ Ag(CF $_3$ ) $_4$ (TCE)	0.495	0.362	0.332	27.1	9.5
$\kappa$ -(ET) $_2$ Cu(NCS) $_2$	0.69	0.171	0.38	15	10.4
$\kappa$ - $\alpha'_2$ -(ET) $_2$ Ag(CF $_3$ ) $_4$ (TCE)	0.495	0.369	0.33	26.2	11.1
$\kappa$ -(ET) $_2$ Cu[N(CN) $_2$ ](CN)	0.669	0.172	0.35	13.9	11.2
$\kappa$ -(ET) $_2$ Cu[N(CN) $_2$ ]Br	0.455	0.379	0.354	32.5	11.6

TABLE 5.1. Comparison of the superconducting critical temperatures  $T_c$  from TPSC and experiment for several organic charge transfer salts (see [273]). We find that the calculations within the dimer model do not reproduce the general trend of the experimental results but can be understood by means of geometric frustration (see fig. 5.14). The experimental critical temperatures are taken from [253–256]. Table reprinted from Ref. [241].

Nevertheless, it is important to note that this gap symmetry is only stable at low temperatures and large values of on-site interaction  $U_{\text{mol}}$  or else the systems converge towards the  $d_{xy}$  gap symmetry solution. In order to estimate the value of  $U_{\text{mol}}$  such that all eight organic superconductors show  $s+d_{x^2-y^2}$  gap symmetry we average the  $t_1$ ,  $t_2$  and  $t_3$  and study the dependence of the largest Eliashberg eigenvalue as a function of  $U_{\text{mol}}$  and the in-plane anisotropy  $t_4/t_2$ . The results of this analysis are shown in

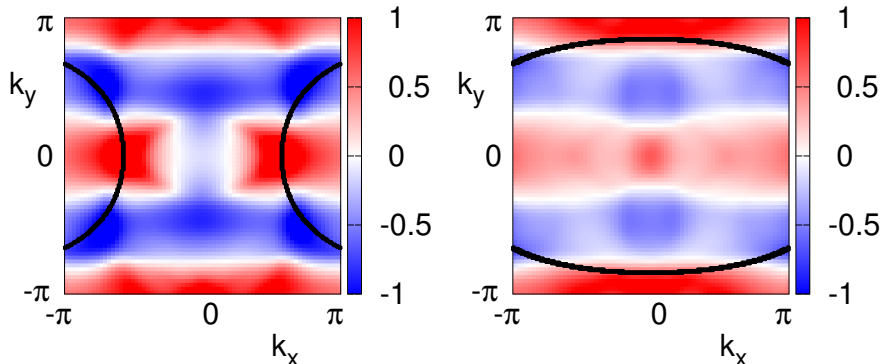


FIGURE 5.15.  $s_{\pm}+d_{x^2-y^2}$  superconducting gap  $\Delta(\vec{k}, i\omega_0)$  as obtained in the four band molecule model at low temperatures. This kind of symmetry was already observed in [273] where the calculations are performed in the framework of the spin fluctuation random phase approximation. The Fermi surface is again shown as black line. Figure reprinted from [241].

fig. 5.16. Thus, only if we choose  $U_{\text{mol}} \gtrsim 0.7\text{eV}$  we can stabilize the  $s+d_{x^2-y^2}$  solution for all eight compounds and we find that in-plane anisotropy  $t_4/t_2$  is a good way to further stabilize this solution.

Note that it is not possible to extract critical temperatures for the eight compounds since for reasonable values of  $U_{\text{mol}}$  we cannot access sufficiently low temperatures due to strong divergences in the spin susceptibility which make an accurate calculation impossible [241].

**5.5.4. Summary and Outlook.** As an application of the multi-site TPSC we studied superconducting critical temperatures of eight  $\kappa$ -(BEDT-TTF) $_2$ X organic superconductors by means of the linearized Eliashberg equation. Those complex materials can be modeled by the simple dimer model and a more complex molecule model.

We find that the dimer model cannot reproduce the right trends in the experimentally measured critical temperatures but only reflects the interplay between geometric frustration and enhanced spin fluctuations due to strong on-site repulsion.

Thus, we investigated the molecule model, where additional degrees of freedom such as the in-plane anisotropy are active. This model indeed exhibits the exotic  $s+d_{x^2-y^2}$  superconducting gap structure as already predicted in Ref. [273] but this solution is only stable for the two compounds with the largest in-plane anisotropy. Nevertheless, our calculations show that this solution can be stabilized for all eight materials if the on-site interaction  $U_{\text{mol}}$  is sufficiently large.

Moreover, our calculations support the idea that small variations of the crystal parameters by means of pressure, strain or endgroup disorder may allow for dynamical switching between the  $s+d_{x^2-y^2}$  and the  $d_{xy}$  gap symmetry.

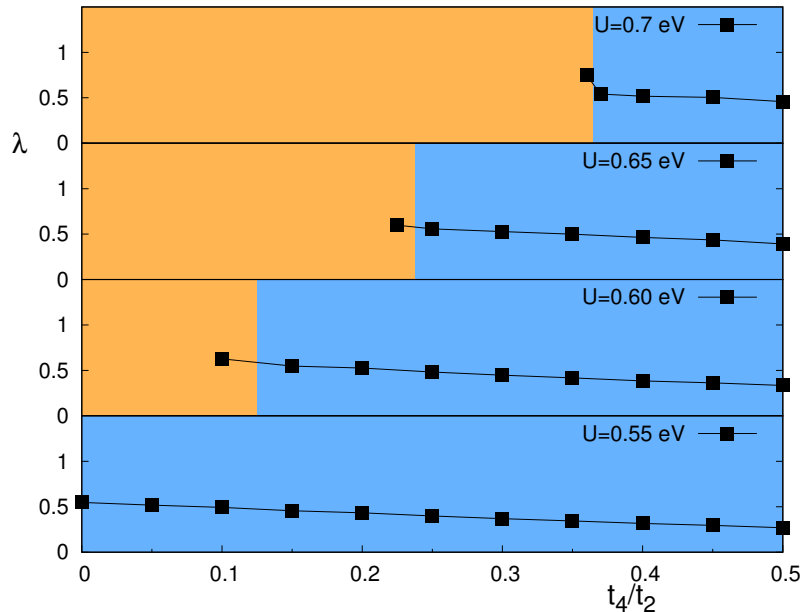


FIGURE 5.16. Largest eigenvalue of the linearized Eliashberg equation  $\lambda$  for  $U_{\text{mol}} = 0.55, 0.6, 0.65$  and  $0.7$  eV, where  $t_1, t_2$  and  $t_3$  averaged over the respective hoppings of the eight materials studied in Ref. [273]. We see an overall increase in  $\lambda$  by going to larger values of  $U_{\text{mol}}$  and an inset of extended  $s + d_{x^2-y^2}$  gap symmetry (orange background) at large in-plane anisotropy  $t_4/t_2$  while  $d_{xy}$  symmetry (blue background) is dominant otherwise. Figure reprinted from Ref. [241].

Finally, we remark that this study does not include effects from inter-site Coulomb repulsion. Extended model calculations that introduce this nearest neighbor Hubbard repulsion are able to see charge density wave phases close to the superconducting instabilities which means that this terms might be important to understand the experimental critical temperatures and give a more precise superconducting gap symmetry prediction [281–283].

## 5.6. Multi-orbital TPSC

**K. Zantout**, S. Backes, R. Valenti

Two-Particle Self-Consistent method for the multi-orbital Hubbard model  
arXiv: 2008.08098 (2020)  
[164]

The first extension of TPSC to multi-orbital problems was performed by Miyahara *et al.* in Ref. [284]. The approach developed in [164, 285] differs to the previously mentioned one in some details that will be commented on later. In the following derivation we follow the scheme presented in Refs. [164, 285] and supply additional steps and comments.

We assume a multi-orbital system that is described by the Hamiltonian

$$\begin{aligned}
 H = & \sum_{\alpha, \beta, i, j, \sigma} \left( t_{\alpha\beta}^{r_i - r_j} - \mu \delta_{i,j} \delta_{\alpha,\beta} \right) c_{\alpha,\sigma}^\dagger(r_i) c_{\beta,\sigma}(r_j) \\
 & + \frac{1}{2} \sum_{\alpha, \beta, i, \sigma} U_{\alpha\beta} n_{\alpha,\sigma}(r_i) n_{\beta,-\sigma}(r_i)
 \end{aligned}$$

$$\begin{aligned}
 & + \frac{1}{2} \sum_{\substack{\alpha, \beta, i, \sigma \\ \alpha \neq \beta}} (U_{\alpha\beta} - J_{\alpha\beta}) n_{\alpha, \sigma}(r_i) n_{\beta, \sigma}(r_i) \\
 & - \frac{1}{2} \sum_{\substack{\alpha, \beta, i, \sigma \\ \alpha \neq \beta}} J_{\alpha\beta} \left( c_{\alpha, \sigma}^\dagger(r_i) c_{\alpha, -\sigma}(r_i) c_{\beta, -\sigma}^\dagger(r_i) c_{\beta, \sigma}(r_i) \right. \\
 (5.297) \quad & \left. + c_{\alpha, \sigma}^\dagger(r_i) c_{\beta, -\sigma}(r_i) c_{\alpha, -\sigma}^\dagger(r_i) c_{\beta, \sigma}(r_i) \right),
 \end{aligned}$$

where  $t_{\alpha\beta}^{r_i - r_j}$  are all hopping matrix elements connecting orbitals  $\alpha$  and  $\beta$  that are related by lattice vectors  $r_i - r_j$ . We drop the spin index in the kinetic part of the Hamiltonian because we assume a paramagnetic state without breaking of time-reversal symmetry and spin rotational invariance. The matrix element  $U_{\alpha\beta}$  denotes the onsite orbital-dependent Hubbard interaction while  $J_{\alpha\beta}$  are the onsite inter-orbital Hund's couplings. An extensive discussion on the determination of the values of  $t$ ,  $U$  and  $J$  can be found in chap. 2 and 3. The operator  $c_{\alpha, \sigma}(r_i, \tau)$  destroys an electron with spin  $\sigma$  in the  $\alpha$ -orbital at unit cell position  $r_i$  and imaginary time  $\tau$  and  $c_{\beta, \sigma}^\dagger(r_j, \tau')$  creates an electron with spin  $\sigma$  in the  $\beta$ -orbital at unit cell position  $r_j$  and imaginary time  $\tau'$ . The density operator is defined as in eq. (5.111). Note that we dropped the time dependence of the Hamilton operator since it is not explicitly time dependent. An alternative formulation of the Hamiltonian in terms of spin matrices can be found in appendix C.2.

Since many steps in the multi-orbital TPSC derivation are the same as in the multi-site derivation that we presented in detail in sec. 5.1 and 5.4 we only give the final results if both can formally be deduced in the same way.

The strategy of both TPSC versions is exactly the same, i.e. first derive the Dyson equation by means of the equation of motion for the interaction Green's function. Then, express the implicitly defined self-energy in terms of generalized susceptibilities and derive the self-consistent Bethe-Salpeter equation for those susceptibilities. Finally, assume that the four-point interaction vertex is local and static in order to obtain approximate expressions for the susceptibilities and the self-energy equation of motion. By enforcing local spin and charge sum rules one can determine the four-point interaction vertex.

First, we work with the same longitudinal channel generalized partition function as in eq. (5.7),

$$\begin{aligned}
 Z[\phi] &= \text{tr} \left[ e^{-\beta H} T_\tau e^{-\sum_{\alpha, \beta, \sigma} \int d(1) \int d(2) c_{\alpha, \sigma}^\dagger(1) \phi_{\alpha\beta, \sigma}(1, 2) c_{\beta, \sigma}(2)} \right] \\
 &=: \left\langle T_\tau e^{-c_{\bar{\alpha}, \bar{\sigma}}^\dagger(\bar{1}) \phi_{\bar{\alpha}\bar{\beta}, \bar{\sigma}}(\bar{1}, \bar{2}) c_{\bar{\beta}, \bar{\sigma}}(\bar{2})} \right\rangle \\
 (5.298) \quad &=: \langle T_\tau S[\phi] \rangle,
 \end{aligned}$$

from which we can deduce the Green's function

$$(5.299) \quad G_{\alpha\beta, \sigma}(1, 2)_\phi := -\frac{\delta \ln(Z[\phi])}{\delta \phi_{\beta\alpha, \sigma}(2, 1)} = -\frac{\langle T_\tau S[\phi] c_{\alpha, \sigma}(1) c_{\beta, \sigma}^\dagger(2) \rangle}{\langle T_\tau S[\phi] \rangle}$$

via functional differentiation (see eq. (5.20)) and the generalized susceptibility

$$\begin{aligned}
 & -\frac{\delta G_{\alpha\beta, \sigma}(1, 2)_\phi}{\delta \phi_{\gamma\epsilon, \sigma'}(3, 4)} \\
 (5.300) \quad & = -\left\langle c_{\alpha, \sigma}(1) c_{\beta, \sigma}^\dagger(2) c_{\gamma, \sigma'}^\dagger(3) c_{\epsilon, \sigma'}(4) \right\rangle_\phi - G_{\alpha\beta, \sigma}(1, 2)_\phi G_{\epsilon\gamma, \sigma'}(4, 3)_\phi
 \end{aligned}$$

from functional differentiation of the Green's function  $G$  (see eq. (5.24)).

**5.6.1. Dyson equation.** In order to derive the Dyson equation (see eq. (5.49)) we need to evaluate

$$\begin{aligned}
 (5.301) \quad & \frac{\partial c_{\nu,\sigma'}(r_k, \tau)}{\partial \tau} = [H, c_{\nu,\sigma'}(r_k, \tau)] = [H(\tau), c_{\nu,\sigma'}(r_k, \tau)] \\
 & = \sum_{\alpha,\beta,i,j,\sigma} \left( t_{\alpha\beta}^{r_i-r_j} - \mu \delta_{i,j} \delta_{\alpha,\beta} \right) \left[ c_{\alpha,\sigma}^\dagger(r_i, \tau) c_{\beta,\sigma}(r_j, \tau), c_{\nu,\sigma'}(r_k, \tau) \right] \\
 & \quad + \frac{1}{2} \sum_{\alpha,\beta,i,\sigma} U_{\alpha\beta} \left[ n_{\alpha,\sigma}(r_i, \tau) n_{\beta,-\sigma}(r_i, \tau), c_{\nu,\sigma'}(r_k, \tau) \right] \\
 & \quad + \frac{1}{2} \sum_{\substack{\alpha,\beta,i,\sigma \\ \alpha \neq \beta}} (U_{\alpha\beta} - J_{\alpha\beta}) \left[ n_{\alpha,\sigma}(r_i, \tau) n_{\beta,\sigma}(r_i, \tau), c_{\nu,\sigma'}(r_k, \tau) \right] \\
 & \quad - \frac{1}{2} \sum_{\substack{\alpha,\beta,i,\sigma \\ \alpha \neq \beta}} J_{\alpha\beta} \left[ \left( c_{\alpha,\sigma}^\dagger(r_i, \tau) c_{\alpha,-\sigma}(r_i, \tau) c_{\beta,-\sigma}^\dagger(r_i, \tau) c_{\beta,\sigma}(r_i, \tau) + \right. \right. \\
 (5.302) \quad & \quad \left. \left. + c_{\alpha,\sigma}^\dagger(r_i, \tau) c_{\beta,-\sigma}(r_i, \tau) c_{\alpha,-\sigma}^\dagger(r_i, \tau) c_{\beta,\sigma}(r_i, \tau) \right), c_{\nu,\sigma'}(r_k, \tau) \right] \\
 & = \sum_{\alpha,\beta,i,j,\sigma} \left( t_{\alpha\beta}^{r_i-r_j} - \mu \delta_{i,j} \delta_{\alpha,\beta} \right) \left( c_{\alpha,\sigma}^\dagger(r_i, \tau) \left\{ c_{\beta,\sigma}(r_j, \tau), c_{\nu,\sigma'}(r_k, \tau) \right\} - \right. \\
 & \quad \left. - \left\{ c_{\alpha,\sigma}^\dagger(r_i, \tau), c_{\nu,\sigma'}(r_k, \tau) \right\} c_{\beta,\sigma}(r_j, \tau) \right) \\
 & \quad + \frac{1}{2} \sum_{\alpha,\beta,i,\sigma} U_{\alpha\beta} \left( n_{\alpha,\sigma}(r_i, \tau) \left[ n_{\beta,-\sigma}(r_i, \tau), c_{\nu,\sigma'}(r_k, \tau) \right] \right. \\
 & \quad \left. + \left[ n_{\alpha,\sigma}(r_i, \tau), c_{\nu,\sigma'}(r_k, \tau) \right] n_{\beta,-\sigma}(r_i, \tau) \right) \\
 & \quad + \frac{1}{2} \sum_{\substack{\alpha,\beta,i,\sigma \\ \alpha \neq \beta}} (U_{\alpha\beta} - J_{\alpha\beta}) \left( n_{\alpha,\sigma}(r_i, \tau) \left[ n_{\beta,\sigma}(r_i, \tau), c_{\nu,\sigma'}(r_k, \tau) \right] + \right. \\
 & \quad \left. + \left[ n_{\alpha,\sigma}(r_i, \tau), c_{\nu,\sigma'}(r_k, \tau) \right] n_{\beta,\sigma}(r_i, \tau) \right) \\
 & \quad - \frac{1}{2} \sum_{\substack{\alpha,\beta,i,\sigma \\ \alpha \neq \beta}} J_{\alpha\beta} \left( \left[ c_{\alpha,\sigma}^\dagger(r_i, \tau) c_{\alpha,-\sigma}(r_i, \tau) c_{\beta,-\sigma}^\dagger(r_i, \tau) c_{\beta,\sigma}(r_i, \tau), c_{\nu,\sigma'}(r_k, \tau) \right] + \right. \\
 (5.303) \quad & \quad \left. + \left[ c_{\alpha,\sigma}^\dagger(r_i, \tau) c_{\beta,-\sigma}(r_i, \tau) c_{\alpha,-\sigma}^\dagger(r_i, \tau) c_{\beta,\sigma}(r_i, \tau), c_{\nu,\sigma'}(r_k, \tau) \right] \right) \\
 & = - \sum_{\alpha,\beta,i,j,\sigma} \left( t_{\alpha\beta}^{r_i-r_j} - \mu \delta_{i,j} \delta_{\alpha,\beta} \right) \delta_{\alpha,\nu} \delta_{\sigma,\sigma'} \delta_{r_i,r_k} c_{\beta,\sigma}(r_j, \tau) - \\
 & \quad - \frac{1}{2} \sum_{\alpha,\beta,i,\sigma} U_{\alpha\beta} \left( n_{\alpha,\sigma}(r_i, \tau) \delta_{\nu,\beta} \delta_{\sigma',-\sigma} \delta_{r_i,r_k} c_{\beta,-\sigma}(r_i, \tau) + \right. \\
 & \quad \left. + \delta_{\alpha,\nu} \delta_{\sigma',\sigma} \delta_{r_i,r_k} c_{\alpha,\sigma}(r_i, \tau) n_{\beta,-\sigma}(r_i, \tau) \right) \\
 & \quad - \frac{1}{2} \sum_{\substack{\alpha,\beta,i,\sigma \\ \alpha \neq \beta}} (U_{\alpha\beta} - J_{\alpha\beta}) \left( n_{\alpha,\sigma}(r_i, \tau) \delta_{\nu,\beta} \delta_{\sigma',\sigma} \delta_{r_i,r_k} c_{\beta,\sigma}(r_i, \tau) + \right. \\
 & \quad \left. + \delta_{\alpha,\nu} \delta_{\sigma',\sigma} \delta_{r_i,r_k} c_{\alpha,\sigma}(r_i, \tau) n_{\beta,\sigma}(r_i, \tau) \right) \\
 & \quad - \frac{1}{2} \sum_{\substack{\alpha,\beta,i,\sigma \\ \alpha \neq \beta}} J_{\alpha\beta} \left( c_{\alpha,\sigma}^\dagger(r_i, \tau) c_{\alpha,-\sigma}(r_i, \tau) \left[ c_{\beta,-\sigma}^\dagger(r_i, \tau) c_{\beta,\sigma}(r_i, \tau), c_{\nu,\sigma'}(r_k, \tau) \right] + \right.
 \end{aligned}$$

$$\begin{aligned}
 & + \left[ c_{\alpha,\sigma}^\dagger(r_i, \tau) c_{\alpha,-\sigma}(r_i, \tau), c_{\nu,\sigma'}(r_k, \tau) \right] c_{\beta,-\sigma}^\dagger(r_i, \tau) c_{\beta,\sigma}(r_i, \tau) + \\
 & + c_{\alpha,\sigma}^\dagger(r_i, \tau) c_{\beta,-\sigma}(r_i, \tau) \left[ c_{\alpha,-\sigma}^\dagger(r_i, \tau) c_{\beta,\sigma}(r_i, \tau), c_{\nu,\sigma'}(r_k, \tau) \right] + \\
 (5.304) \quad & + \left[ c_{\alpha,\sigma}^\dagger(r_i, \tau) c_{\beta,-\sigma}(r_i, \tau), c_{\nu,\sigma'}(r_k, \tau) \right] c_{\alpha,-\sigma}^\dagger(r_i, \tau) c_{\beta,\sigma}(r_i, \tau) \\
 = & - \sum_{\beta,j} \left( t_{\nu\beta}^{r_k-r_j} - \mu \delta_{k,j} \delta_{\nu,\beta} \right) c_{\beta,\sigma'}(r_j, \tau) \\
 & - \frac{1}{2} \sum_{\alpha} U_{\alpha\beta} \left( n_{\alpha,-\sigma'}(r_k, \tau) c_{\nu,\sigma'}(r_k, \tau) + c_{\nu,\sigma'}(r_k, \tau) n_{\alpha,-\sigma'}(r_k, \tau) \right) \\
 & - \frac{1}{2} \sum_{\substack{\alpha \\ \alpha \neq \nu}} (U_{\alpha\nu} - J_{\alpha\nu}) \left( n_{\alpha,\sigma'}(r_k, \tau) c_{\nu,\sigma'}(r_k, \tau) + c_{\nu,\sigma'}(r_k, \tau) n_{\alpha,\sigma'}(r_k, \tau) \right) \\
 & + \frac{1}{2} \sum_{\substack{\alpha,\beta,i,\sigma \\ \alpha \neq \beta}} J_{\alpha\beta} \left( c_{\alpha,\sigma}^\dagger(r_i, \tau) c_{\alpha,-\sigma}(r_i, \tau) \delta_{\beta,\nu} \delta_{\sigma',-\sigma} \delta_{r_i,r_k} c_{\beta,\sigma}(r_i, \tau) + \right. \\
 & \quad + \delta_{\alpha,\nu} \delta_{\sigma',\sigma} \delta_{r_i,r_k} c_{\alpha,-\sigma}(r_i, \tau) c_{\beta,-\sigma}^\dagger(r_i, \tau) c_{\beta,\sigma}(r_i, \tau) + \\
 & \quad + c_{\alpha,\sigma}^\dagger(r_i, \tau) c_{\beta,-\sigma}(r_i, \tau) \delta_{\alpha,\nu} \delta_{\sigma',-\sigma} \delta_{r_i,r_k} c_{\beta,\sigma}(r_i, \tau) + \\
 & \quad \left. + \delta_{\alpha,\nu} \delta_{\sigma',\sigma} \delta_{r_i,r_k} c_{\beta,-\sigma}(r_i, \tau) c_{\alpha,-\sigma}^\dagger(r_i, \tau) c_{\beta,\sigma}(r_i, \tau) \right) \\
 = & - \sum_{\beta,j} \left( t_{\nu\beta}^{r_k-r_j} - \mu \delta_{k,j} \delta_{\nu,\beta} \right) c_{\beta,\sigma'}(r_j, \tau) \\
 & - \sum_{\alpha} U_{\alpha\beta} n_{\alpha,-\sigma'}(r_k, \tau) c_{\nu,\sigma'}(r_k, \tau) \\
 & - \sum_{\substack{\alpha \\ \alpha \neq \nu}} (U_{\alpha\nu} - J_{\alpha\nu}) n_{\alpha,\sigma'}(r_k, \tau) c_{\nu,\sigma'}(r_k, \tau) \\
 & + \frac{1}{2} \sum_{\substack{\alpha \\ \alpha \neq \nu}} J_{\alpha\nu} \left( c_{\alpha,-\sigma'}^\dagger(r_k, \tau) c_{\alpha,\sigma'}(r_k, \tau) c_{\nu,-\sigma'}(r_k, \tau) + \right. \\
 & \quad + c_{\nu,-\sigma'}(r_k, \tau) c_{\alpha,-\sigma'}^\dagger(r_k, \tau) c_{\alpha,\sigma'}(r_k, \tau) + \\
 & \quad + c_{\nu,-\sigma'}^\dagger(r_k, \tau) c_{\alpha,\sigma'}(r_k, \tau) c_{\alpha,-\sigma'}(r_k, \tau) + \\
 (5.305) \quad & \quad \left. + c_{\alpha,-\sigma'}(r_k, \tau) c_{\nu,-\sigma'}^\dagger(r_k, \tau) c_{\alpha,\sigma'}(r_k, \tau) \right) \\
 = & - \sum_{\beta,j} \left( t_{\nu\beta}^{r_k-r_j} - \mu \delta_{k,j} \delta_{\nu,\beta} \right) c_{\beta,\sigma'}(r_j, \tau) \\
 & - \sum_{\alpha} U_{\alpha\beta} n_{\alpha,-\sigma'}(r_k, \tau) c_{\nu,\sigma'}(r_k, \tau) \\
 & - \sum_{\substack{\alpha \\ \alpha \neq \nu}} (U_{\alpha\nu} - J_{\alpha\nu}) n_{\alpha,\sigma'}(r_k, \tau) c_{\nu,\sigma'}(r_k, \tau) \\
 & + \sum_{\substack{\alpha \\ \alpha \neq \nu}} J_{\alpha\nu} \left( c_{\alpha,-\sigma'}^\dagger(r_k, \tau) c_{\alpha,\sigma'}(r_k, \tau) c_{\nu,-\sigma'}(r_k, \tau) \right. \\
 (5.306) \quad & \quad \left. + c_{\nu,-\sigma'}^\dagger(r_k, \tau) c_{\alpha,\sigma'}(r_k, \tau) c_{\alpha,-\sigma'}(r_k, \tau) \right),
 \end{aligned}$$

where we have used the identities

$$(5.307) \quad [A, BC] = ABC - BCA = ABC + BAC - BAC - BCA$$

$$(5.308) \quad = \{A, B\}C - B\{A, C\}$$

$$(5.309) \quad [AB, C] = ABC - CAB = ABC - ACB + ACB - CAB$$

$$(5.310) \quad = A[B, C] + [A, C]B$$

$$(5.311) \quad [AB, C] = ABC - CAB = ABC + ACB - ACB - CAB$$

$$(5.312) \quad = A\{B, C\} - \{A, C\}B$$

and the fermionic commutation relations

$$(5.313) \quad [n_{\alpha,\sigma}(r_i), c_{\beta,\sigma'}(r_j)] \\ = [c_{\alpha,\sigma}^\dagger(r_i)c_{\alpha,\sigma}(r_i), c_{\beta,\sigma'}(r_j)]$$

$$(5.314) \quad = c_{\alpha,\sigma}^\dagger(r_i) \{c_{\alpha,\sigma}(r_i), c_{\beta,\sigma'}(r_j)\} - \{c_{\alpha,\sigma}^\dagger(r_i), c_{\beta,\sigma'}(r_j)\} c_{\alpha,\sigma}(r_i)$$

$$(5.315) \quad = c_{\alpha,\sigma}^\dagger(r_i) \cdot 0 - \delta_{\alpha,\beta} \delta_{\sigma,\sigma'} \delta_{r_i,r_j} c_{\alpha,\sigma}(r_i)$$

$$(5.316) \quad = -\delta_{\alpha,\beta} \delta_{\sigma,\sigma'} \delta_{r_i,r_j} c_{\alpha,\sigma}(r_i),$$

$$(5.317) \quad [c_{\alpha,\sigma}^\dagger(r_i)c_{\beta,\sigma'}(r_i), c_{\gamma,\sigma''}(r_j)] \\ = c_{\alpha,\sigma}^\dagger(r_i) \{c_{\beta,\sigma'}(r_i), c_{\gamma,\sigma''}(r_j)\} - \{c_{\alpha,\sigma}^\dagger(r_i), c_{\gamma,\sigma''}(r_j)\} c_{\beta,\sigma'}(r_i)$$

$$(5.318) \quad = c_{\alpha,\sigma}^\dagger(r_i) \cdot 0 - \delta_{\alpha,\gamma} \delta_{\sigma,\sigma''} \delta_{r_i,r_j} c_{\beta,\sigma'}(r_i)$$

$$(5.319) \quad = -\delta_{\alpha,\gamma} \delta_{\sigma,\sigma''} \delta_{r_i,r_j} c_{\beta,\sigma'}(r_i).$$

In the same fashion as for the multi-site case (see sec. 5.1.3) we obtain the imaginary-time derivative of the Green's function  $G$  but with the only difference that additional terms appear due to time-evolution of the annihilation operator  $c_{\nu,\sigma'}(r_k, \tau)$  (see eq. (5.306)). Thus, we obtain the similar result

$$(5.320) \quad \frac{\partial G_{\nu\xi,\sigma}(1,2)_\phi}{\partial \tau_1} = + \sum_{\beta} \left( t_{\nu\beta}^{r_1 - \bar{r}_3} - \mu \delta_{r_1, \bar{r}_3} \delta_{\nu,\beta} \right) \delta(\tau_1 - \bar{\tau}_3) G_{\beta\xi,\sigma}(\bar{3}, 2)_\phi \\ + \sum_{\alpha} U_{\alpha\nu} \left\langle n_{\alpha,-\sigma}(1^+) c_{\nu,\sigma}(1) c_{\xi,\sigma}^\dagger(2) \right\rangle_\phi \\ + \sum_{\substack{\alpha \\ \alpha \neq \nu}} (U_{\alpha\nu} - J_{\alpha\nu}) \left\langle n_{\alpha,\sigma}(1^+) c_{\nu,\sigma}(1) c_{\xi,\sigma}^\dagger(2) \right\rangle_\phi \\ - \sum_{\substack{\alpha \\ \alpha \neq \nu}} J_{\alpha\nu} \left( \left\langle c_{\alpha,-\sigma}^\dagger(1^+) c_{\alpha,\sigma}(1) c_{\nu,-\sigma}(1) c_{\xi,\sigma}^\dagger(2) \right\rangle_\phi \right. \\ \left. + \left\langle c_{\nu,-\sigma}^\dagger(1^{++}) c_{\alpha,\sigma}(1^+) c_{\alpha,-\sigma}(1) c_{\xi,\sigma}^\dagger(2) \right\rangle_\phi \right) \\ - \delta(1-2) \delta_{\nu,\xi} \\ - \phi_{\nu\bar{\beta},\sigma}(1, \bar{3}) G_{\bar{\beta}\xi,\sigma}(\bar{3}, 2)_\phi.$$

Again, we identify the non-interacting Green's function  $G^0$  in terms of its inverse

$$(5.321) \quad [(G^0)^{-1}]_{\nu\beta}(1, 2) = \delta'(\tau_1 - \tau_2) \delta_{r_1, r_2} \delta_{\nu,\beta} + \left( t_{\nu\beta}^{r_1 - r_2} - \mu \delta_{r_1, r_2} \delta_{\nu,\beta} \right) \delta(\tau_1 - \tau_2)$$

in the limit of no interactions and no external field.

Thus, we are able to rewrite the equation of motion (5.320) as

$$(5.322) \quad \left\{ [(G^0)^{-1}]_{\nu\bar{\beta}}(1, \bar{3}) - \phi_{\nu\bar{\beta}}(1, \bar{3}) - \sum_{\nu\bar{\beta},\sigma}(1, \bar{3})_\phi \right\} G_{\bar{\beta}\xi,\sigma}(\bar{3}, 2)_\phi = \delta(1-2) \delta_{\nu\xi},$$

where we implicitly defined the multi-orbital self-energy

$$\begin{aligned}
 \Sigma_{\nu\bar{\beta},\sigma}(1,\bar{3})_{\phi} G_{\bar{\beta}\xi,\sigma}(\bar{3},2)_{\phi} &= - \sum_{\alpha} U_{\alpha\nu} \left\langle n_{\alpha,-\sigma}(1^+) c_{\nu,\sigma}(1) c_{\xi,\sigma}^{\dagger}(2) \right\rangle_{\phi} \\
 &\quad - \sum_{\substack{\alpha \\ \alpha \neq \nu}} (U_{\alpha\nu} - J_{\alpha\nu}) \left\langle n_{\alpha,\sigma}(1^+) c_{\nu,\sigma}(1) c_{\xi,\sigma}^{\dagger}(2) \right\rangle_{\phi} \\
 &\quad + \sum_{\substack{\alpha \\ \alpha \neq \nu}} J_{\alpha\nu} \left( \left\langle c_{\alpha,-\sigma}^{\dagger}(1^+) c_{\alpha,\sigma}(1) c_{\nu,-\sigma}(1) c_{\xi,\sigma}^{\dagger}(2) \right\rangle_{\phi} \right. \\
 (5.323) \quad &\quad \left. + \left\langle c_{\nu,-\sigma}^{\dagger}(1^{++}) c_{\alpha,\sigma}(1^+) c_{\alpha,-\sigma}(1) c_{\xi,\sigma}^{\dagger}(2) \right\rangle_{\phi} \right).
 \end{aligned}$$

Rearranging equation (5.322) we obtain the Dyson equation

$$(5.324) \quad [G^{-1}]_{\nu\xi,\sigma}(1,2)_{\phi} = [(G^0)^{-1}]_{\nu\xi}(1,2) - \phi_{\nu\xi,\sigma}(1,2) - \Sigma_{\nu\xi,\sigma}(1,2)_{\phi}.$$

**5.6.2. A self-consistency equation for the generalized susceptibility.** To obtain the Bethe-Salpeter equation as in sec. 5.1.4 we identify the four-point correlation functions on the right-hand side of eq. (5.323) with the higher-order functional derivatives of the generalized partition function  $Z[\phi]$  (see eq. (5.300)). This yields

$$\begin{aligned}
 &\Sigma_{\alpha\bar{\beta},\sigma}(1,\bar{2})_{\phi} G_{\bar{\beta}\gamma,\sigma}(\bar{2},2)_{\phi} \\
 &= - \sum_{\beta} U_{\beta\alpha} \left( \frac{\delta G_{\alpha\gamma,\sigma}(1,2)}{\delta \phi_{\beta\beta,-\sigma}(1^{++},1^+)} - G_{\beta\beta,-\sigma}(1,1^+) G_{\alpha\gamma,\sigma}(1,2) \right) \\
 &\quad - \sum_{\substack{\beta \\ \beta \neq \alpha}} (U_{\beta\alpha} - J_{\beta\alpha}) \left( \frac{\delta G_{\alpha\gamma,\sigma}(1,2)}{\delta \phi_{\beta\beta,\sigma}(1^{++},1^+)} - G_{\beta\beta,\sigma}(1,1^+) G_{\alpha\gamma,\sigma}(1,2) \right) \\
 &\quad - \sum_{\substack{\beta \\ \beta \neq \alpha}} J_{\beta\alpha} \left[ \left( \frac{\delta G_{\beta\gamma,\sigma}(1,2)}{\delta \phi_{\beta\alpha,-\sigma}(1^+,1^{++})} - G_{\beta\gamma,\sigma}(1,2) G_{\alpha\beta,-\sigma}(1^+,1) \right) \right. \\
 (5.325) \quad &\quad \left. + \left( \frac{\delta G_{\beta\gamma,\sigma}(1^+,2)}{\delta \phi_{\alpha\beta,-\sigma}(1^{++},1)} - G_{\beta\gamma,\sigma}(1,2) G_{\beta\alpha,-\sigma}(1,1^+) \right) \right].
 \end{aligned}$$

In contrast to the multi-site expression (see eq. (5.51)) we deal here with more index combinations in  $\frac{\delta G}{\delta \phi}$ . Nevertheless, all those information are contained in the Bethe-Salpeter equation (see eq. (5.58) and fig. 5.1) that we derived in the multi-site case and which is derived analogously in the multi-orbital case.

$$\begin{aligned}
 \frac{\delta G_{\alpha\zeta,\sigma}(1,6)_{\phi}}{\delta \phi_{\nu\epsilon,\sigma'}(4,5)} &= G_{\alpha\nu,\sigma}(1,4)_{\phi} G_{\epsilon\zeta,\sigma}(5,6)_{\phi} \delta_{\sigma,\sigma'} \\
 (5.326) \quad &\quad + G_{\alpha\bar{\beta},\sigma}(1,\bar{3})_{\phi} \frac{\delta \Sigma_{\bar{\beta}\bar{\gamma},\sigma}(\bar{3},\bar{2})_{\phi}}{\delta G_{\bar{\rho}\bar{\lambda},\sigma''}(\bar{7},\bar{8})_{\phi}} \frac{\delta G_{\bar{\rho}\bar{\lambda},\sigma''}(\bar{7},\bar{8})_{\phi}}{\delta \phi_{\nu\epsilon,\sigma'}(4,5)} G_{\bar{\gamma}\zeta,\sigma}(\bar{2},6)_{\phi}.
 \end{aligned}$$

**5.6.3. Susceptibilities and sum rules.** While in the multi-site version of TPSC we only needed local spin and charge sum rules where all indices are the same (see eq. (5.251) and (5.252)) we will need more sum rules in the multi-orbital case because the interaction matrix elements are now also orbital dependent and contain additional terms like Hund's coupling.

In summary, we need the local spin sum rules

$$(5.327) \quad \frac{T}{N} \sum_{q, iq_m} \chi_{\alpha\alpha\alpha\alpha}^{sp}(q, iq_m) = 2 \langle n_{\alpha, \uparrow} \rangle - 2 \langle n_{\alpha, \uparrow} n_{\alpha, \downarrow} \rangle,$$

$$(5.328) \quad \frac{T}{N} \sum_{q, iq_m} \chi_{\alpha\alpha\beta\beta}^{sp}(q, iq_m) = 2 \langle n_{\alpha, \uparrow} n_{\beta, \uparrow} \rangle - 2 \langle n_{\alpha, \uparrow} n_{\beta, \downarrow} \rangle,$$

$$(5.329) \quad \frac{T}{N} \sum_{q, iq_m} \Re \chi_{\alpha\beta\alpha\beta}^{sp}(q, iq_m) = \langle n_{\alpha, \uparrow} \rangle + \langle n_{\beta, \uparrow} \rangle - 2 \langle n_{\alpha, \uparrow} n_{\beta, \downarrow} \rangle.$$

PROOF OF (5.327), (5.328) AND (5.329). While the first sum rule for all equal orbital indices can be derived in the same fashion as the multi-site version (see eq. (5.251)) the  $\alpha\alpha\beta\beta$ -sum rule follows analogously. To obtain the last sum rule we use eqs. (5.93), (5.98), (5.102), and (5.203). This leads to

$$(5.330) \quad \frac{T}{N} \sum_{q, iq_m} \Re \chi_{\alpha\beta\alpha\beta}^{sp}(q) = \frac{1}{2} \frac{T}{N} \sum_{q, iq_m} \left( \chi_{\alpha\beta\alpha\beta}^{sp} + \chi_{\beta\alpha\beta\alpha}^{sp} \right) (q)$$

$$(5.331) \quad = \frac{1}{2} \left( 2 \langle T_\tau c_{\alpha, \uparrow}^\dagger(1) c_{\beta, \downarrow}(1) c_{\beta, \downarrow}^\dagger(1^+) c_{\alpha, \uparrow}(1^+) \rangle \right. \\ \left. + 2 \langle T_\tau c_{\beta, \downarrow}^\dagger(1^+) c_{\alpha, \uparrow}(1^+) c_{\alpha, \uparrow}^\dagger(1) c_{\beta, \downarrow}(1) \rangle \right)$$

$$(5.332) \quad = \frac{1}{2} \left( 2 \langle n_{\alpha, \uparrow} \rangle - 2 \langle n_{\beta, \downarrow} n_{\alpha, \uparrow} \rangle + 2 \langle n_{\alpha, \uparrow} \rangle - 2 \langle n_{\alpha, \uparrow} n_{\beta, \downarrow} \rangle \right)$$

$$(5.333) \quad = \langle n_{\alpha, \uparrow} \rangle + \langle n_{\beta, \uparrow} \rangle - 2 \langle n_{\alpha, \uparrow} n_{\beta, \downarrow} \rangle.$$

□

The local charge sum rules are

$$(5.334) \quad \frac{T}{N} \sum_{q, iq_m} \chi_{\alpha\alpha\alpha\alpha}^{ch}(q, iq_m) = \langle n_\alpha \rangle + 2 \langle n_{\alpha, \uparrow} n_{\alpha, \downarrow} \rangle - \langle n_\alpha \rangle^2,$$

$$(5.335) \quad \frac{T}{N} \sum_{q, iq_m} \chi_{\alpha\alpha\beta\beta}^{ch}(q, iq_m) = 2 \langle n_{\alpha, \uparrow} n_{\beta, \uparrow} \rangle + 2 \langle n_{\alpha, \uparrow} n_{\beta, \downarrow} \rangle - \langle n_\alpha \rangle \langle n_\beta \rangle,$$

and

$$(5.336) \quad \frac{T}{N} \sum_{q, iq_m} \Re \chi_{\alpha\beta\alpha\beta}^{ch}(q, iq_m) \\ = \frac{1}{2} \langle n_\alpha + n_\beta \rangle - 4 \langle n_{\alpha, \uparrow} n_{\beta, \uparrow} \rangle + 2 \langle n_{\alpha, \uparrow} n_{\beta, \downarrow} \rangle - \langle n_{\beta\alpha} \rangle \langle n_{\alpha\beta} \rangle, \quad \alpha \neq \beta.$$

PROOF OF (5.334)-(5.336). The first sum rule (eq. (5.334)) is derived in the same way as the multi-site version (see eq. (5.117)) and similarly one can derive the second sum rule. The third sum rule (eq. (5.336)) is shown in a similar way like for the spin channel. One obtains

$$(5.337) \quad \frac{T}{N} \sum_{q, iq_m} \Re \chi_{\alpha\beta\alpha\beta}^{ch}(q, iq_m) \\ = \frac{1}{2} \left[ \langle (n_{\beta\alpha, \uparrow} + n_{\beta\alpha, \downarrow}) (n_{\alpha\beta, \uparrow} + n_{\alpha\beta, \downarrow}) \rangle \right. \\ \left. + \langle (n_{\alpha\beta, \uparrow} + n_{\alpha\beta, \downarrow}) (n_{\beta\alpha, \uparrow} + n_{\beta\alpha, \downarrow}) \rangle \right] - \langle n_{\beta\alpha} \rangle \langle n_{\alpha\beta} \rangle$$

$$(5.338) \quad = \frac{1}{2} \left[ \left\langle \left( c_{\alpha, \uparrow}^\dagger c_{\beta, \uparrow} + c_{\alpha, \downarrow}^\dagger c_{\beta, \downarrow} \right) \left( c_{\beta, \uparrow}^\dagger c_{\alpha, \uparrow} + c_{\beta, \downarrow}^\dagger c_{\alpha, \downarrow} \right) \right\rangle \right. \\ \left. + \left\langle \left( c_{\beta, \uparrow}^\dagger c_{\alpha, \uparrow} + c_{\beta, \downarrow}^\dagger c_{\alpha, \downarrow} \right) \left( c_{\alpha, \uparrow}^\dagger c_{\beta, \uparrow} + c_{\alpha, \downarrow}^\dagger c_{\beta, \downarrow} \right) \right\rangle \right] - \langle n_{\beta\alpha} \rangle \langle n_{\alpha\beta} \rangle$$

$$\begin{aligned}
 &= \frac{1}{2} [\langle n_{\alpha,\uparrow} (1 - n_{\beta,\uparrow}) \rangle + \langle n_{\alpha,\downarrow} (1 - n_{\beta,\downarrow}) \rangle \\
 &\quad + \langle n_{\beta,\uparrow} (1 - n_{\alpha,\uparrow}) \rangle + \langle n_{\beta,\downarrow} (1 - n_{\alpha,\downarrow}) \rangle] \\
 (5.339) \quad &+ 2 \langle c_{\alpha,\uparrow}^\dagger c_{\beta,\uparrow} c_{\beta,\downarrow}^\dagger c_{\alpha,\downarrow} \rangle - \langle n_{\beta\alpha} \rangle \langle n_{\alpha\beta} \rangle
 \end{aligned}$$

$$(5.340) \quad = \frac{1}{2} (n_\alpha + n_\beta) - 2 \langle n_{\alpha,\uparrow} n_{\beta,\uparrow} \rangle - 2 \langle c_{\alpha,\downarrow}^\dagger c_{\alpha,\uparrow} c_{\beta,\uparrow}^\dagger c_{\beta,\downarrow} \rangle - \langle n_{\beta\alpha} \rangle \langle n_{\alpha\beta} \rangle.$$

Here, we use our knowledge of the local spin sum rule (eq. (5.203) and (5.328)) to obtain

$$\begin{aligned}
 &\frac{T}{N} \sum_{q, iq_m} \Re \chi_{\alpha\beta\alpha\beta}^{ch}(q, iq_m) \\
 (5.341) \quad &= \frac{1}{2} (n_\alpha + n_\beta) - 2 \langle n_{\alpha,\uparrow} n_{\beta,\uparrow} \rangle - \chi_{\beta\beta\alpha\alpha}^{sp}(0, 0^+) - \langle n_{\beta\alpha} \rangle \langle n_{\alpha\beta} \rangle
 \end{aligned}$$

$$(5.342) \quad = \frac{1}{2} (n_\alpha + n_\beta) - 4 \langle n_{\alpha,\uparrow} n_{\beta,\uparrow} \rangle + 2 \langle n_{\alpha,\uparrow} n_{\beta,\downarrow} \rangle - \langle n_{\beta\alpha} \rangle \langle n_{\alpha\beta} \rangle.$$

□

**5.6.4. Self-energy in the longitudinal channel.** We start off with the implicit definition of the self-energy in eq. (5.325) and evaluate at  $\phi = 0$ ,

$$\begin{aligned}
 &\Sigma_{\alpha\bar{\beta},\sigma}(1, \bar{2}) G_{\bar{\beta}\gamma,\sigma}(\bar{2}, 2) \\
 &= - \sum_{\beta} U_{\beta\alpha} \left( \left. \frac{\delta G_{\alpha\gamma,\sigma}(1, 2)}{\delta \phi_{\beta\beta,-\sigma}(1^{++}, 1^+)} \right|_{\phi=0} - G_{\beta\beta,-\sigma}(1, 1^+) G_{\alpha\gamma,\sigma}(1, 2) \right) \\
 &\quad - \sum_{\substack{\beta \\ \beta \neq \alpha}} (U_{\beta\alpha} - J_{\beta\alpha}) \left( \left. \frac{\delta G_{\alpha\gamma,\sigma}(1, 2)}{\delta \phi_{\beta\beta,\sigma}(1^{++}, 1^+)} \right|_{\phi=0} - G_{\beta\beta,\sigma}(1, 1^+) G_{\alpha\gamma,\sigma}(1, 2) \right) \\
 &\quad - \sum_{\substack{\beta \\ \beta \neq \alpha}} J_{\beta\alpha} \left[ \left( \left. \frac{\delta G_{\beta\gamma,\sigma}(1, 2)}{\delta \phi_{\beta\alpha,-\sigma}(1^+, 1^{++})} \right|_{\phi=0} - G_{\beta\gamma,\sigma}(1, 2) G_{\alpha\beta,-\sigma}(1^+, 1) \right) \right. \\
 (5.343) \quad &\quad \left. + \left( \left. \frac{\delta G_{\beta\gamma,\sigma}(1^+, 2)}{\delta \phi_{\alpha\beta,-\sigma}(1^{++}, 1)} \right|_{\phi=0} - G_{\beta\gamma,\sigma}(1, 2) G_{\beta\alpha,-\sigma}(1, 1^+) \right) \right],
 \end{aligned}$$

and multiply with  $G_{\bar{\gamma}\nu,\sigma}^{-1}(\bar{2}, 5)$  and integrate over the internal degrees of freedom gives

$$\begin{aligned}
 &\Sigma_{\alpha\nu,\sigma}(1, 5) \\
 &= - \sum_{\beta} U_{\beta\alpha} \left[ -\frac{1}{4} \left( \chi_{\bar{\gamma}\alpha\beta\beta}^{ch}(1, \bar{2}; 1) - \chi_{\bar{\gamma}\alpha\beta\beta}^{sp}(1, \bar{2}; 1) \right) G_{\bar{\gamma}\nu,\sigma}^{-1}(\bar{2}, 5) - \langle n_{\beta,-\sigma}(1) \rangle \delta_{\alpha,\nu} \delta(1-5) \right] \\
 &\quad - \sum_{\substack{\beta \\ \beta \neq \alpha}} (U_{\beta\alpha} - J_{\beta\alpha}) \left[ -\frac{1}{4} \left( \chi_{\bar{\gamma}\alpha\beta\beta}^{ch}(1, \bar{2}; 1) + \chi_{\bar{\gamma}\alpha\beta\beta}^{sp}(1, \bar{2}; 1) \right) G_{\bar{\gamma}\nu,\sigma}^{-1}(\bar{2}, 5) - \langle n_{\beta,\sigma}(1) \rangle \delta_{\alpha,\nu} \delta(1-5) \right] \\
 &\quad - \sum_{\substack{\beta \\ \beta \neq \alpha}} J_{\beta\alpha} \left[ -\frac{1}{4} \left( \chi_{\bar{\gamma}\beta\alpha\beta}^{ch}(1, \bar{2}; 1) - \chi_{\bar{\gamma}\beta\alpha\beta}^{sp}(1, \bar{2}; 1) \right) G_{\bar{\gamma}\nu,\sigma}^{-1}(\bar{2}, 5) - \langle n_{\alpha\beta,-\sigma}(1) \rangle \delta_{\beta,\nu} \delta(1-5) \right. \\
 (5.344) \quad &\quad \left. + -\frac{1}{4} \left( \chi_{\bar{\gamma}\beta\beta\alpha}^{ch}(1, \bar{2}; 1) - \chi_{\bar{\gamma}\beta\beta\alpha}^{sp}(1, \bar{2}; 1) \right) G_{\bar{\gamma}\nu,\sigma}^{-1}(\bar{2}, 5) - \langle n_{\beta\alpha,-\sigma}(1) \rangle \delta_{\beta,\nu} \delta(1-5) \right],
 \end{aligned}$$

where we expressed the functional derivatives  $\frac{\delta G}{\delta \phi}$  in terms of spin and charge susceptibilities (see eq. (5.121) and (5.143)).

Next, we use the Bethe-Salpeter equation for the spin and charge susceptibility (eq. (5.129) and (5.152)) to expand

$$\begin{aligned}
 & \Sigma_{\alpha\nu,\sigma}(1, 5) \\
 = & \sum_{\beta} U_{\beta\alpha} \left[ \frac{1}{4} \left( G_{\alpha\bar{\beta}}(1, \bar{3}) \Gamma_{\bar{\epsilon}\beta\lambda\bar{\rho}}^{ch}(\bar{3}, \bar{9}; \bar{7}, \bar{8}) \chi_{\lambda\bar{\rho}\beta\beta}^{ch}(\bar{7}, \bar{8}; 1) G_{\bar{\epsilon}\bar{\gamma}}(\bar{9}, \bar{2}) \right. \right. \\
 & \quad \left. \left. + G_{\alpha\bar{\beta}}(1, \bar{3}) \Gamma_{\bar{\epsilon}\beta\lambda\bar{\rho}}^{sp}(\bar{3}, \bar{9}; \bar{7}, \bar{8}) \chi_{\lambda\bar{\rho}\beta\beta}^{sp}(\bar{7}, \bar{8}; 1) G_{\bar{\epsilon}\bar{\gamma}}(\bar{9}, \bar{2}) \right) G_{\bar{\gamma}\nu,\sigma}^{-1}(\bar{2}, 5) \right. \\
 & \quad \left. + \langle n_{\beta,-\sigma}(1) \rangle \delta_{\alpha,\nu} \delta(1-5) \right] \\
 + & \sum_{\substack{\beta \\ \beta \neq \alpha}} (U_{\beta\alpha} - J_{\beta\alpha}) \left[ \frac{1}{4} \left( G_{\alpha\bar{\beta}}(1, \bar{3}) \Gamma_{\bar{\epsilon}\beta\lambda\bar{\rho}}^{ch}(\bar{3}, \bar{9}; \bar{7}, \bar{8}) \chi_{\lambda\bar{\rho}\beta\beta}^{ch}(\bar{7}, \bar{8}; 1) G_{\bar{\epsilon}\bar{\gamma}}(\bar{9}, \bar{2}) \right. \right. \\
 & \quad \left. \left. - G_{\alpha\bar{\beta}}(1, \bar{3}) \Gamma_{\bar{\epsilon}\beta\lambda\bar{\rho}}^{sp}(\bar{3}, \bar{9}; \bar{7}, \bar{8}) \chi_{\lambda\bar{\rho}\beta\beta}^{sp}(\bar{7}, \bar{8}; 1) G_{\bar{\epsilon}\bar{\gamma}}(\bar{9}, \bar{2}) \right) G_{\bar{\gamma}\nu,\sigma}^{-1}(\bar{2}, 5) \right. \\
 & \quad \left. + (\langle n_{\beta,\sigma}(1) \rangle \delta_{\alpha\nu} - \langle n_{\alpha\nu,\sigma}(1) \rangle \delta_{\beta,\nu}) \delta(1-5) \right] \\
 + & \sum_{\substack{\beta \\ \beta \neq \alpha}} J_{\beta\alpha} \left[ \frac{1}{4} \left( G_{\beta\bar{\beta}}(1, \bar{3}) \Gamma_{\bar{\epsilon}\beta\lambda\bar{\rho}}^{ch}(\bar{3}, \bar{9}; \bar{7}, \bar{8}) \chi_{\lambda\bar{\rho}\alpha\beta}^{ch}(\bar{7}, \bar{8}; 1) G_{\bar{\epsilon}\bar{\gamma}}(\bar{9}, \bar{2}) \right. \right. \\
 & \quad \left. \left. + G_{\beta\bar{\beta}}(1, \bar{3}) \Gamma_{\bar{\epsilon}\beta\lambda\bar{\rho}}^{sp}(\bar{3}, \bar{9}; \bar{7}, \bar{8}) \chi_{\lambda\bar{\rho}\alpha\beta}^{sp}(\bar{7}, \bar{8}; 1) G_{\bar{\epsilon}\bar{\gamma}}(\bar{9}, \bar{2}) \right) G_{\bar{\gamma}\nu,\sigma}^{-1}(\bar{2}, 5) \right. \\
 & \quad \left. + \langle n_{\alpha\beta,-\sigma}(1) \rangle \delta_{\beta,\nu} \delta(1-5) \right. \\
 & \quad \left. + \frac{1}{4} \left( G_{\beta\bar{\beta}}(1, \bar{3}) \Gamma_{\bar{\epsilon}\beta\lambda\bar{\rho}}^{ch}(\bar{3}, \bar{9}; \bar{7}, \bar{8}) \chi_{\lambda\bar{\rho}\beta\alpha}^{ch}(\bar{7}, \bar{8}; 1) G_{\bar{\epsilon}\bar{\gamma}}(\bar{9}, \bar{2}) \right. \right. \\
 & \quad \left. \left. + G_{\beta\bar{\beta}}(1, \bar{3}) \Gamma_{\bar{\epsilon}\beta\lambda\bar{\rho}}^{sp}(\bar{3}, \bar{9}; \bar{7}, \bar{8}) \chi_{\lambda\bar{\rho}\beta\alpha}^{sp}(\bar{7}, \bar{8}; 1) G_{\bar{\epsilon}\bar{\gamma}}(\bar{9}, \bar{2}) \right) G_{\bar{\gamma}\nu,\sigma}^{-1}(\bar{2}, 5) \right. \\
 & \quad \left. + \langle n_{\beta\alpha,-\sigma}(1) \rangle \delta_{\beta,\nu} \delta(1-5) \right]. \tag{5.345}
 \end{aligned}$$

We can now get some  $\delta$  distributions from the product of the Green's functions with its inverse and reduce the expression to

$$\begin{aligned}
 & \Sigma_{\alpha\nu,\sigma}(1, 5) \\
 = & \sum_{\beta} U_{\beta\alpha} \left[ \frac{1}{4} \left( G_{\alpha\bar{\beta}}(1, \bar{3}) \Gamma_{\nu\beta\lambda\bar{\rho}}^{ch}(\bar{3}, 5; \bar{7}, \bar{8}) \chi_{\lambda\bar{\rho}\beta\beta}^{ch}(\bar{7}, \bar{8}; 1) \right. \right. \\
 & \quad \left. \left. + G_{\alpha\bar{\beta}}(1, \bar{3}) \Gamma_{\nu\beta\lambda\bar{\rho}}^{sp}(\bar{3}, 5; \bar{7}, \bar{8}) \chi_{\lambda\bar{\rho}\beta\beta}^{sp}(\bar{7}, \bar{8}; 1) \right) + \langle n_{\beta,-\sigma}(1) \rangle \delta_{\alpha,\nu} \delta(1-5) \right] \\
 + & \sum_{\substack{\beta \\ \beta \neq \alpha}} (U_{\beta\alpha} - J_{\beta\alpha}) \left[ \frac{1}{4} \left( G_{\alpha\bar{\beta}}(1, \bar{3}) \Gamma_{\nu\beta\lambda\bar{\rho}}^{ch}(\bar{3}, 5; \bar{7}, \bar{8}) \chi_{\lambda\bar{\rho}\beta\beta}^{ch}(\bar{7}, \bar{8}; 1) \right. \right. \\
 & \quad \left. \left. - G_{\alpha\bar{\beta}}(1, \bar{3}) \Gamma_{\nu\beta\lambda\bar{\rho}}^{sp}(\bar{3}, 5; \bar{7}, \bar{8}) \chi_{\lambda\bar{\rho}\beta\beta}^{sp}(\bar{7}, \bar{8}; 1) \right) + (\langle n_{\beta,\sigma}(1) \rangle \delta_{\alpha,\nu} - \langle n_{\alpha\nu,\sigma}(1) \rangle \delta_{\beta,\nu}) \delta(1-5) \right] \\
 + & \sum_{\substack{\beta \\ \beta \neq \alpha}} J_{\beta\alpha} \left[ \frac{1}{4} \left( G_{\beta\bar{\beta}}(1, \bar{3}) \Gamma_{\nu\beta\lambda\bar{\rho}}^{ch}(\bar{3}, 5; \bar{7}, \bar{8}) \chi_{\lambda\bar{\rho}\alpha\beta}^{ch}(\bar{7}, \bar{8}; 1) \right. \right. \\
 & \quad \left. \left. + G_{\beta\bar{\beta}}(1, \bar{3}) \Gamma_{\nu\beta\lambda\bar{\rho}}^{sp}(\bar{3}, 5; \bar{7}, \bar{8}) \chi_{\lambda\bar{\rho}\alpha\beta}^{sp}(\bar{7}, \bar{8}; 1) \right) + \langle n_{\alpha\beta,-\sigma}(1) \rangle \delta_{\beta,\nu} \delta(1-5) \right] \\
 + & \frac{1}{4} G_{\beta\bar{\beta}}(1, \bar{3}) \left( \Gamma_{\nu\beta\bar{\rho}\lambda}^{ch}(\bar{3}, 5; \bar{7}, \bar{8}) \chi_{\bar{\rho}\lambda\beta\alpha}^{ch}(\bar{7}, \bar{8}; 1) \right. \\
 & \quad \left. + \Gamma_{\nu\beta\bar{\rho}\lambda}^{sp}(\bar{3}, 5; \bar{7}, \bar{8}) \chi_{\bar{\rho}\lambda\beta\alpha}^{sp}(\bar{7}, \bar{8}; 1) \right)
 \end{aligned}$$

## 5.6. MULTI-ORBITAL TPSC

$$(5.346) \quad + \Gamma_{\nu\beta\bar{\rho}\bar{\lambda}}^{sp}(\bar{3}, 5; \bar{7}, \bar{8})\chi_{\bar{\rho}\bar{\lambda}\beta\alpha}^{sp}(\bar{7}, \bar{8}; 1) + \langle n_{\beta\alpha, -\sigma}(1) \rangle \delta_{\beta, \nu} \delta(1-5) \Big].$$

Reordering the equation and defining non-interacting vertices  $\Gamma^{sp,0}$  and  $\Gamma^{ch,0}$  leads to

$$\begin{aligned} & \Sigma_{\alpha\nu, \sigma}(1, 5) \\ = & \left[ \sum_{\beta} U_{\beta\alpha} \langle n_{\beta, -\sigma}(1) \rangle \delta_{\alpha, \nu} + \sum_{\beta \neq \alpha} (U_{\beta\alpha} - J_{\beta\alpha}) (\langle n_{\beta, \sigma}(1) \rangle \delta_{\alpha, \nu} - \langle n_{\alpha\nu, \sigma}(1) \rangle \delta_{\beta, \nu}) \right. \\ & \left. + J_{\nu\alpha} (\langle n_{\alpha\nu, -\sigma}(1) \rangle (1 - \delta_{\alpha, \nu}) + \langle n_{\nu\alpha, -\sigma}(1) \rangle (1 - \delta_{\alpha, \nu})) \right] \delta(1-5) \\ & + \frac{1}{4} G_{\bar{\gamma}\bar{\beta}}(1, \bar{3}) \left[ \begin{aligned} & U_{\alpha\alpha} \left( \Gamma^{ch}(\bar{3}, 5; \bar{7}, \bar{8})\chi^{ch}(\bar{7}, \bar{8}; 1) + \Gamma^{sp}(\bar{3}, 5; \bar{7}, \bar{8})\chi^{sp}(\bar{7}, \bar{8}; 1) \right)_{\nu\beta\zeta\zeta} \delta_{\alpha, \bar{\gamma}} \\ & + U_{\zeta\alpha} \left( \Gamma^{ch}(\bar{3}, 5; \bar{7}, \bar{8})\chi^{ch}(\bar{7}, \bar{8}; 1) + \Gamma^{sp}(\bar{3}, 5; \bar{7}, \bar{8})\chi^{sp}(\bar{7}, \bar{8}; 1) \right)_{\nu\beta\zeta\zeta} (1 - \delta_{\zeta, \alpha}) \delta_{\alpha, \bar{\gamma}} \\ & + (U_{\zeta\alpha} - J_{\zeta\alpha}) \left( \Gamma^{ch}(\bar{3}, 5; \bar{7}, \bar{8})\chi^{ch}(\bar{7}, \bar{8}; 1) - \Gamma^{sp}(\bar{3}, 5; \bar{7}, \bar{8})\chi^{sp}(\bar{7}, \bar{8}; 1) \right)_{\nu\beta\zeta\zeta} (1 - \delta_{\zeta, \alpha}) \delta_{\alpha, \bar{\gamma}} \\ & + J_{\bar{\gamma}\alpha} \left( \Gamma^{ch}(\bar{3}, 5; \bar{7}, \bar{8})\chi^{ch}(\bar{7}, \bar{8}; 1) + \Gamma^{sp}(\bar{3}, 5; \bar{7}, \bar{8})\chi^{sp}(\bar{7}, \bar{8}; 1) \right)_{\nu\bar{\beta}\alpha\bar{\gamma}} (1 - \delta_{\alpha, \bar{\gamma}}) \\ & + J_{\bar{\gamma}\alpha} \left( \Gamma^{ch}(\bar{3}, 5; \bar{7}, \bar{8})\chi^{ch}(\bar{7}, \bar{8}; 1) + \Gamma^{sp}(\bar{3}, 5; \bar{7}, \bar{8})\chi^{sp}(\bar{7}, \bar{8}; 1) \right)_{\nu\bar{\beta}\bar{\gamma}\alpha} (1 - \delta_{\alpha, \bar{\gamma}}) \end{aligned} \right] \\ =: & \left[ \sum_{\beta} U_{\beta\alpha} \langle n_{\beta, -\sigma}(1) \rangle \delta_{\alpha, \nu} + \sum_{\beta \neq \alpha} (U_{\beta\alpha} - J_{\beta\alpha}) (\langle n_{\beta, \sigma}(1) \rangle \delta_{\alpha, \nu} - \langle n_{\alpha\nu, \sigma}(1) \rangle \delta_{\beta, \nu}) \right. \\ & \left. + J_{\nu\alpha} (\langle n_{\alpha\nu, -\sigma}(1) \rangle (1 - \delta_{\alpha, \nu}) + \langle n_{\nu\alpha, -\sigma}(1) \rangle (1 - \delta_{\alpha, \nu})) \right] \delta(1-5) \\ (5.347) \quad & + \frac{1}{4} G_{\bar{\gamma}\bar{\beta}}(1, \bar{3}) \left( \Gamma^{ch}(\bar{3}, 5; \bar{7}, \bar{8})\chi^{ch}(\bar{7}, \bar{8}; 1)\Gamma^{ch,0} + \Gamma^{sp}(\bar{3}, 5; \bar{7}, \bar{8})\chi^{ch}(\bar{7}, \bar{8}; 1)\Gamma^{sp,0} \right)_{\nu\bar{\beta}\alpha\bar{\gamma}}, \end{aligned}$$

where we have defined

$$(5.348) \quad \Gamma_{\alpha\beta\gamma\delta}^{ch,0} = \begin{cases} U_{\alpha\alpha} & \alpha = \beta = \gamma = \delta \\ 2U_{\alpha\gamma} - J_{\alpha\gamma} & \alpha = \beta \neq \gamma = \delta \\ J_{\alpha\beta} & \alpha = \gamma \neq \beta = \delta \\ J_{\alpha\beta} & \alpha = \delta \neq \beta = \gamma \\ 0 & \text{else} \end{cases}$$

and

$$(5.349) \quad \Gamma_{\alpha\beta\gamma\delta}^{sp,0} = \begin{cases} U_{\alpha\alpha} & \alpha = \beta = \gamma = \delta \\ J_{\alpha\gamma} & \alpha = \beta \neq \gamma = \delta \\ J_{\alpha\beta} & \alpha = \gamma \neq \beta = \delta \\ J_{\alpha\beta} & \alpha = \delta \neq \beta = \gamma \\ 0 & \text{else} \end{cases}.$$

**5.6.5. Interaction vertices in RPA.** Comparing the interaction vertices  $\Gamma^{sp/ch,0}$  with the respective random phase approximation (RPA) expressions [286] (compare sec. 5.2) we see a difference in some matrix elements; namely,

$$(5.350) \quad \Gamma_{\alpha\beta\gamma\delta}^{ch,RPA} = \begin{cases} U_{\alpha\alpha} & \alpha = \beta = \gamma = \delta \\ 2U_{\alpha\gamma} - J_{\alpha\gamma} & \alpha = \beta \neq \gamma = \delta \\ -U_{\alpha\beta} + 2J_{\alpha\beta} & \alpha = \gamma \neq \beta = \delta \\ J_{\alpha\beta} & \alpha = \delta \neq \beta = \gamma \\ 0 & \text{else} \end{cases}$$

and

$$(5.351) \quad \Gamma_{\alpha\beta\gamma\delta}^{sp,RPA} = \begin{cases} U_{\alpha\alpha} & \alpha = \beta = \gamma = \delta \\ J_{\alpha\gamma} & \alpha = \beta \neq \gamma = \delta \\ U_{\alpha\beta} & \alpha = \gamma \neq \beta = \delta \\ J_{\alpha\beta} & \alpha = \delta \neq \beta = \gamma \\ 0 & \text{else} \end{cases}.$$

The origin of this difference is the fact that the RPA vertices are derived from eq. (5.347) by neglecting the spin and charge fluctuation contributions in terms of  $\Gamma^{sp/ch}\chi^{sp/ch}\Gamma^{sp/ch,0}$ . This results in the approximate expression

$$(5.352) \quad \Sigma_{\alpha\nu,\sigma}(1,5) \approx \left[ \sum_{\beta} U_{\beta\alpha} \langle n_{\beta,-\sigma}(1) \rangle \delta_{\alpha,\nu} + \sum_{\beta \neq \alpha} (U_{\beta\alpha} - J_{\beta\alpha}) (\langle n_{\beta,\sigma}(1) \rangle \delta_{\alpha,\nu} - \langle n_{\alpha\nu,\sigma}(1) \rangle \delta_{\beta,\nu}) + J_{\nu\alpha} (\langle n_{\alpha\nu,-\sigma}(1) \rangle (1 - \delta_{\alpha,\nu}) + \langle n_{\nu\alpha,-\sigma}(1) \rangle (1 - \delta_{\alpha,\nu})) \right] \delta(1-5),$$

which corresponds to the Hartree-Fock result.

Thus, we can calculate from eq. (5.153) the RPA two-particle irreducible spin vertex

$$(5.353) \quad \Gamma_{\nu\alpha\lambda\rho}^{sp,RPA}(1,5;7,8) = \sum_{\sigma} \sigma \frac{\delta \Sigma_{\alpha\nu,\sigma}(1,5)_{\phi}}{\delta G_{\rho\lambda,\downarrow}(7,8)_{\phi}} \Big|_{\phi=0}$$

$$(5.354) \quad = \delta(1-5) \left( \delta_{\alpha,\nu} \sum_{\beta} U_{\beta\alpha} \sum_{\sigma} \sigma \frac{\delta n_{\beta,-\sigma}(1)}{\delta G_{\rho\lambda,\downarrow}(7,8)} + \sum_{\beta \neq \alpha} (U_{\beta\alpha} - J_{\beta\alpha}) \sum_{\sigma} \sigma \frac{\delta [n_{\beta,\sigma}(1) \delta_{\alpha,\nu} - n_{\alpha\nu,\sigma}(1) \delta_{\beta,\nu}]}{\delta G_{\rho\lambda,\downarrow}(7,8)} + (1 - \delta_{\alpha,\nu}) J_{\nu\alpha} \sum_{\sigma} \sigma \frac{\delta [n_{\alpha\nu,-\sigma}(1) + n_{\nu\alpha,-\sigma}(1)]}{\delta G_{\rho\lambda,\downarrow}(7,8)} \right)$$

$$(5.355) \quad = \delta(1-5) \delta(1-7) \delta(1-8) \left( \delta_{\alpha,\nu} \sum_{\beta} U_{\beta\alpha} \delta_{\beta,\rho} \delta_{\beta,\lambda} + \sum_{\substack{\beta \\ \beta \neq \alpha}} (U_{\beta\alpha} - J_{\beta\alpha}) (-\delta_{\beta,\rho} \delta_{\beta,\lambda} \delta_{\alpha,\nu} + \delta_{\alpha,\rho} \delta_{\nu,\lambda} \delta_{\beta,\nu}) + (1 - \delta_{\alpha,\nu}) J_{\nu\alpha} (\delta_{\alpha,\rho} \delta_{\nu,\lambda} + \delta_{\nu,\rho} \delta_{\alpha,\lambda}) \right),$$

which corresponds to the previously mentioned vertex in eq. (5.351). One reproduces the RPA charge vertex in the same manner as presented for the spin vertex.

## 5.6. MULTI-ORBITAL TPSC

In summary, we see that although TPSC is similar in its functional form to the RPA expressions there are differences that stem from the quantum fluctuation contributions.

**5.6.6. TPSC approximation.** In the same fashion as we proceeded in the multi-site TPSC (see sec. 5.4) we approximate the Luttinger-Ward functional  $\Phi[G]$  in the multi-orbital case by

$$(5.356) \quad \Phi[G] = 0.5 \left[ G_{\bar{\alpha}\bar{\nu},\bar{\sigma}}(\bar{1}, \bar{1}^+) \Gamma_{\bar{\alpha}\bar{\nu}\xi\lambda}^{\bar{\sigma}\bar{\sigma}'} G_{\bar{\lambda}\bar{\xi},\bar{\sigma}'}(\bar{1}, \bar{1}^+) \right],$$

where  $\Gamma_{\bar{\alpha}\bar{\nu}\xi\lambda}^{\sigma-\sigma}$  and  $\Gamma_{\bar{\alpha}\bar{\nu}\xi\lambda}^{\sigma\sigma}$  are local and static constants that will be determined via the local spin and charge sum rules (see sec. 5.6.3). Analogously to the multi-site calculation we find that  $\frac{\delta\Phi[G]}{\delta G} = \Sigma$  leads to a static and local self-energy which we assume to be already absorbed in to the kinetic part of the Hamiltonian (see discussion in sec. 5.4). This ansatz for the Luttinger-Ward functional leads to static and local irreducible interaction vertices (by means of eq. (5.130))

$$(5.357) \quad \Gamma_{\gamma\beta\lambda\rho}^{ch}(1, 2; 3, 4) = \sum_{\sigma} \frac{\delta\Sigma_{\beta\gamma,\sigma}(1, 2)_{\phi}}{\delta G_{\rho\lambda,\uparrow}(3, 4)_{\phi}} \Big|_{\phi=0}$$

$$(5.358) \quad = \sum_{\sigma} \frac{\delta\Phi[G]}{\delta G_{\gamma\beta,\sigma}(2, 1)\delta G_{\rho\lambda,\uparrow}(3, 4)}$$

$$(5.359) \quad = \frac{1}{2} \sum_{\sigma} \frac{\delta}{\delta G_{\gamma\beta,\sigma}(2, 1)} \left[ \frac{\delta G_{\bar{\alpha}\bar{\nu},\bar{\sigma}}(\bar{1}, \bar{1}^+)}{\delta G_{\rho\lambda,\uparrow}(3, 4)} \Gamma_{\bar{\alpha}\bar{\nu}\xi\lambda}^{\bar{\sigma}\bar{\sigma}} G_{\bar{\lambda}\bar{\xi},\bar{\sigma}}(\bar{1}, \bar{1}^+) \right. \\ \left. + G_{\bar{\alpha}\bar{\nu},\bar{\sigma}}(\bar{1}, \bar{1}^+) \Gamma_{\bar{\alpha}\bar{\nu}\xi\lambda}^{\bar{\sigma}\bar{\sigma}} \frac{\delta G_{\bar{\lambda}\bar{\xi},\bar{\sigma}}(\bar{1}, \bar{1}^+)}{\delta G_{\rho\lambda,\uparrow}(3, 4)} \right. \\ \left. + \frac{\delta G_{\bar{\alpha}\bar{\nu},\bar{\sigma}}(\bar{1}, \bar{1}^+)}{\delta G_{\rho\lambda,\uparrow}(3, 4)} \Gamma_{\bar{\alpha}\bar{\nu}\xi\lambda}^{\bar{\sigma}-\bar{\sigma}} G_{\bar{\lambda}\bar{\xi},-\bar{\sigma}}(\bar{1}, \bar{1}^+) \right. \\ \left. + G_{\bar{\alpha}\bar{\nu},\bar{\sigma}}(\bar{1}, \bar{1}^+) \Gamma_{\bar{\alpha}\bar{\nu}\xi\lambda}^{\bar{\sigma}-\bar{\sigma}} \frac{\delta G_{\bar{\lambda}\bar{\xi},-\bar{\sigma}}(\bar{1}, \bar{1}^+)}{\delta G_{\rho\lambda,\uparrow}(3, 4)} \right]$$

$$(5.360) \quad = \frac{1}{2} \sum_{\sigma} \frac{\delta}{\delta G_{\gamma\beta,\sigma}(2, 1)} \left[ G_{\bar{\lambda}\bar{\xi},\uparrow}(3, 3^+) \Gamma_{\rho\lambda\xi\lambda}^{\uparrow\uparrow} \delta(3-4) + \right. \\ \left. + G_{\bar{\alpha}\bar{\nu},\uparrow}(3, 3^+) \Gamma_{\bar{\alpha}\bar{\nu}\lambda\rho}^{\uparrow\uparrow} \delta(3-4) \right. \\ \left. + \Gamma_{\rho\lambda\xi\lambda}^{\uparrow\downarrow} G_{\bar{\lambda}\bar{\xi},\downarrow}(3, 3^+) \delta(3-4) \right. \\ \left. + \Gamma_{\bar{\alpha}\bar{\nu}\lambda\rho}^{\uparrow\downarrow} G_{\bar{\alpha}\bar{\nu},\downarrow}(3, 3^+) \delta(3-4) \right]$$

$$(5.361) \quad = \frac{1}{2} \sum_{\sigma} \left[ \Gamma_{\rho\lambda\beta\gamma}^{\uparrow\uparrow} \delta(3-2)\delta(3^+-1)\delta(3-4)\delta_{\sigma,\uparrow} + \right. \\ \left. + \delta(2-3)\delta(1-3^+) \Gamma_{\gamma\beta\lambda\rho}^{\uparrow\uparrow} \delta(3-4)\delta_{\sigma,\uparrow} \right. \\ \left. + \Gamma_{\rho\lambda\beta\gamma}^{\uparrow\downarrow} \delta_{\sigma,\downarrow} \delta(3-4)\delta(2-3)\delta(1-3^+) + \right. \\ \left. + \delta(3-2)\delta(1-3^+)\delta(3-4)\delta_{\sigma,\downarrow} \Gamma_{\gamma\beta\lambda\rho}^{\uparrow\downarrow} \right]$$

$$(5.362) \quad = \frac{1}{2} \sum_{\sigma} \delta(3-4)\delta(2-3)\delta(1-3^+) (\Gamma_{\gamma\beta\lambda\rho}^{\sigma-\sigma} + \Gamma_{\gamma\beta\lambda\rho}^{\sigma\sigma})$$

$$(5.363) \quad = \delta(3-4)\delta(2-3)\delta(1-3^+) \Gamma_{\gamma\beta\lambda\rho}^{ch},$$

where we have used the crossing symmetry  $\Gamma_{\alpha\beta\gamma\delta} = \Gamma_{\delta\gamma\beta\alpha}$  (see sec. 5.1.8) and similarly we obtain from eq. (5.153),

$$(5.364) \quad \Gamma_{\gamma\beta\lambda\rho}^{sp}(1, 2; 3, 4) = \sum_{\sigma} \sigma \frac{\delta\Sigma_{\beta\gamma,\sigma}(1, 2)_{\phi}}{\delta G_{\rho\lambda,\downarrow}(3, 4)_{\phi}} \Big|_{\phi=0}$$

$$(5.365) \quad = \frac{1}{2} \sum_{\sigma} \delta(1-4)\delta(2-3)\delta(3^+-4)(\Gamma_{\gamma\beta\lambda\rho}^{\sigma-\sigma} - \Gamma_{\gamma\beta\lambda\rho}^{\sigma\sigma})$$

$$(5.366) \quad = \delta(1-4)\delta(2-3)\delta(3^+-4)\Gamma_{\gamma\beta\lambda\rho}^{sp}.$$

As presented in the multi-site TPSC section 5.4 we can now improve on the self-energy by inserting the non-interacting Green's function  $G^0$  and the local and static TPSC vertices  $\Gamma^{sp/ch}$  from eq. (5.363) and (5.366) into the equation of motion of the self-energy (eq. (5.347)). This corresponds to the original TPSC idea where the fluctuations feed back into the single-particle properties while one has to use the non-interacting Green's function  $G^0$  in order to be consistent with the assumption of static and non-local irreducible vertices  $\Gamma^{sp/ch}$  [163].

We end up with

$$(5.367) \quad \Sigma_{\alpha\nu,\sigma}(1, 5) = \left[ \sum_{\beta} U_{\beta\alpha} \langle n_{\beta,-\sigma}(1) \rangle \delta_{\alpha,\nu} + \sum_{\beta \neq \alpha} (U_{\beta\alpha} - J_{\beta\alpha}) (\langle n_{\beta,\sigma}(1) \rangle \delta_{\alpha,\nu} - \langle n_{\alpha\nu,\sigma}(1) \rangle \delta_{\beta,\nu}) + J_{\nu\alpha} (\langle n_{\alpha\nu,-\sigma}(1) \rangle (1 - \delta_{\alpha,\nu}) + \langle n_{\nu\alpha,-\sigma}(1) \rangle (1 - \delta_{\alpha,\nu})) \right] \delta(1-5) + \frac{1}{4} G_{\bar{\gamma}\bar{\beta}}^0(1, 5) \left( \Gamma^{ch} \chi^{ch}(5, 1) \Gamma^{ch,0} + \Gamma^{sp} \chi^{ch}(5, 1) \Gamma^{sp,0} \right)_{\nu\bar{\beta}\alpha\bar{\gamma}},$$

which leads to

$$(5.368) \quad \Sigma_{\alpha\nu,\sigma}(k, i\omega_n) = \sum_{\beta} U_{\beta\alpha} \langle n_{\beta,-\sigma} \rangle \delta_{\alpha,\nu} + \sum_{\beta \neq \alpha} (U_{\beta\alpha} - J_{\beta\alpha}) (\langle n_{\beta,\sigma} \rangle \delta_{\alpha,\nu} - \langle n_{\alpha\nu,\sigma} \rangle \delta_{\beta,\nu}) + J_{\nu\alpha} (\langle n_{\alpha\nu,-\sigma} \rangle (1 - \delta_{\alpha,\nu}) + \langle n_{\nu\alpha,-\sigma} \rangle (1 - \delta_{\alpha,\nu})) + \frac{T}{4N} \sum_{q, iq_m} \left[ \Gamma^{ch} \chi^{ch}(q, iq_m) \Gamma^{ch,0} + \Gamma^{sp} \chi^{sp}(q, iq_m) \Gamma^{sp,0} \right]_{\nu\bar{\beta}\alpha\bar{\gamma}} G_{\bar{\gamma}\bar{\beta}}^0(k+q, i\omega_{n+m}).$$

It is not a surprise that the TPSC vertices lead again to RPA-like spin and charge susceptibilities via the Bethe-Salpeter equations (5.129) and (5.152):

$$(5.369) \quad \chi_{\rho\lambda\nu\eta}^{sp}(1, 2) = -2G_{\lambda\eta}^0(1, 2)G_{\nu\rho}^0(2, 1) - G_{\lambda\bar{\gamma}}^0(1, 2)\Gamma_{\bar{\delta}\bar{\gamma}\bar{\alpha}\bar{\beta}}^{sp}\chi_{\bar{\alpha}\bar{\beta}\nu\eta}^{sp}(1, 2)G_{\bar{\delta}\rho}^0(2, 1)$$

$$(5.370) \quad = 2\chi_{\rho\lambda\nu\eta}^0(1, 2) - \Gamma_{\bar{\delta}\bar{\gamma}\bar{\alpha}\bar{\beta}}^{sp}\chi_{\bar{\alpha}\bar{\beta}\nu\eta}^{sp}(1, 2)G_{\lambda\bar{\gamma}}^0(1, 2)G_{\bar{\delta}\rho}^0(2, 1)$$

$$(5.371) \quad = 2\chi_{\rho\lambda\nu\eta}^0(1, 2)_{\phi} + \Gamma_{\bar{\delta}\bar{\gamma}\bar{\alpha}\bar{\beta}}^{sp}\chi_{\bar{\alpha}\bar{\beta}\nu\eta}^{sp}(1, 2)\chi_{\rho\lambda\bar{\delta}\bar{\gamma}}^0(1, 2)$$

$$(5.372) \quad 2\chi_{\rho\lambda\nu\eta}^0(1, 2)_{\phi} = \left( \delta_{\rho,\bar{\alpha}}\delta_{\lambda,\bar{\beta}} - \chi_{\rho\lambda\bar{\delta}\bar{\gamma}}^0(1, 2)_{\phi}\Gamma_{\bar{\delta}\bar{\gamma}\bar{\alpha}\bar{\beta}}^{sp} \right) \chi_{\bar{\alpha}\bar{\beta}\nu\eta}^{sp}(1, 2)$$

and by taking advantage of the usual tensor isomorphism (eq. (5.107)) we get

$$(5.373) \quad \chi_{\rho\lambda\nu\eta}^{sp}(q, iq_m) = [\mathbb{I} - \chi^0(q, iq_m)\Gamma_{sp}]_{\rho\lambda\bar{\alpha}\bar{\beta}}^{-1} 2\chi_{\bar{\alpha}\bar{\beta}\nu\eta}^0(q, iq_m).$$

Analogously, we determine the charge susceptibility

$$(5.374) \quad \chi_{\rho\lambda\nu\eta}^{ch}(q, iq_m) = [\mathbb{I} + \chi^0(q, iq_m)\Gamma_{ch}]_{\rho\lambda\bar{\alpha}\bar{\beta}}^{-1} 2\chi_{\bar{\alpha}\bar{\beta}\nu\eta}^0(q, iq_m).$$

**5.6.7. Ansatz equation for the spin vertex.** As was the case for the single-band and the multi-site TPSC we lack local spin sum rules to determine the spin vertex  $\Gamma^{sp}$ , namely:

We have  $N_{orb}$  many  $\alpha\alpha\alpha\alpha$ -local spin sum rules (eq. (5.327)),  $N_{orb}^2 - N_{orb}$  many  $\alpha\alpha\beta\beta$ -local spin sum rules (eq. (5.328)) and the same number for the  $\alpha\beta\alpha\beta$ -case (eq. (5.329)). This gives in total  $2N_{orb}^2 - N_{orb}$  equations, while those sum rules come along with equal spin and unequal spin double occupations, i.e.  $2N_{orb}^2 - N_{orb}$  unknowns, where we subtracted  $N_{orb}$  components due to the Pauli principle

$$(5.375) \quad \langle n_{\alpha,\uparrow} n_{\alpha,\uparrow} \rangle = \langle n_{\alpha,\uparrow} \rangle.$$

On top of that we have the irreducible spin vertex  $\Gamma^{sp}$  with its  $N_{orb}^2$  independent components<sup>17</sup>.

On taking stock we see that the set of equations is underdetermined with

$$(5.376) \quad (2N_{orb}^2 - N_{orb}) + N_{orb}^2 - (2N_{orb}^2 - N_{orb}) = N_{orb}^2$$

missing equations.

In order to supply those equations we proceed in the same way as in sec. 5.4.1 and start with the implicit equation for the self-energy (eq. (5.323)),

$$(5.377) \quad \begin{aligned} \Sigma_{\nu\bar{\beta},\sigma}(1,\bar{3})G_{\bar{\beta}\xi,\sigma}(\bar{3},2) = & - \sum_{\alpha} U_{\alpha\nu} \langle n_{\alpha,-\sigma}(1^+) c_{\nu,\sigma}(1) c_{\xi,\sigma}^{\dagger}(2) \rangle \\ & - \sum_{\substack{\alpha \\ \alpha \neq \nu}} (U_{\alpha\nu} - J_{\alpha\nu}) \langle n_{\alpha,\sigma}(1^+) c_{\nu,\sigma}(1) c_{\xi,\sigma}^{\dagger}(2) \rangle \\ & + \sum_{\substack{\alpha \\ \alpha \neq \nu}} J_{\alpha\nu} \left( \langle c_{\alpha,-\sigma}^{\dagger}(1^+) c_{\alpha,\sigma}(1) c_{\nu,-\sigma}(1) c_{\xi,\sigma}^{\dagger}(2) \rangle \right. \\ & \left. + \langle c_{\nu,-\sigma}^{\dagger}(1^{++}) c_{\alpha,\sigma}(1^+) c_{\alpha,-\sigma}(1) c_{\xi,\sigma}^{\dagger}(2) \rangle \right), \end{aligned}$$

and do a Hartree-Fock factorization for the right-hand side while writing prefactors  $A$ ,  $B$  in front of each term to recover the limit of equal imaginary time, orbital and position:

$$(5.378) \quad \begin{aligned} \Sigma_{\nu\bar{\beta},\sigma}(1,\bar{3})G_{\bar{\beta}\xi,\sigma}(\bar{3},2) \approx & A_{\nu}^{\sigma} \langle n_{\nu,-\sigma}(1) \rangle G_{\nu\xi,\sigma}(1,2) \\ & + \sum_{\substack{\alpha \\ \alpha \neq \nu, \sigma'}} B_{\alpha\nu}^{\sigma\sigma'} \langle n_{\alpha,\sigma'}(1) \rangle G_{\nu\xi,\sigma}(1,2) \\ & + \sum_{\substack{\alpha \\ \alpha \neq \nu}} J_{\alpha\nu} \left( \langle c_{\alpha,-\sigma}^{\dagger}(1^+) c_{\alpha,\sigma}(1) c_{\nu,-\sigma}(1) c_{\xi,\sigma}^{\dagger}(2) \rangle \right. \\ & \left. + \langle c_{\nu,-\sigma}^{\dagger}(1^{++}) c_{\alpha,\sigma}(1^+) c_{\alpha,-\sigma}(1) c_{\xi,\sigma}^{\dagger}(2) \rangle \right), \end{aligned}$$

where we defined

$$(5.379) \quad A_{\nu}^{\sigma} = U_{\nu\nu} \frac{\langle n_{\nu,\sigma} n_{\nu,-\sigma} \rangle}{\langle n_{\nu,\sigma} \rangle \langle n_{\nu,-\sigma} \rangle},$$

$$(5.380) \quad B_{\alpha\nu}^{\sigma\sigma} = (U_{\alpha\nu} - J_{\alpha\nu}) \frac{\langle n_{\alpha,\sigma} n_{\nu,\sigma} \rangle}{\langle n_{\alpha,\sigma} \rangle \langle n_{\nu,\sigma} \rangle}, \quad \alpha \neq \nu,$$

$$(5.381) \quad B_{\alpha\nu}^{\sigma-\sigma} = U_{\alpha\nu} \frac{\langle n_{\alpha,-\sigma} n_{\nu,\sigma} \rangle}{\langle n_{\alpha,-\sigma} \rangle \langle n_{\nu,\sigma} \rangle}, \quad \alpha \neq \nu.$$

<sup>17</sup>We assume that  $\Gamma^{sp}$  follows the same symmetry as  $\Gamma^{sp,0}$ . According to eq. (5.349) we need only to consider the elements  $\alpha\alpha\beta\beta$  since the other elements are either zero or renormalized in the same way as one of the  $\alpha\alpha\beta\beta$ -components.

Now we neglect<sup>18</sup> the off-diagonal orbital occupations  $\langle n_{\alpha\nu,\sigma} \rangle$  which means that a Hartree-Fock factorization of the equal imaginary time, position and orbital evaluation of the two remaining two-point functions in eq. (5.378) will vanish.

Multiplying eq. (5.378) with  $G_{\xi\gamma,\sigma}^{-1}(\bar{2}, 4)$  and integrating over all internal degrees of freedom leaves us with

$$(5.382) \quad \Sigma_{\nu\gamma,\sigma}(1, 4) = A_{\nu}^{\sigma} \langle n_{\nu,-\sigma}(1) \rangle \delta(1-4) \delta_{\nu,\gamma} + \sum_{\substack{\alpha \\ \alpha \neq \nu, \sigma'}} B_{\alpha\nu}^{\sigma\sigma'} \langle n_{\alpha,\sigma'}(1) \rangle \delta(1-4) \delta_{\nu,\gamma}.$$

From the definition of the spin vertex  $\Gamma^{sp}$  in eq. (5.153) we can calculate

$$(5.383) \quad \begin{aligned} & \Gamma_{\gamma\nu\lambda\rho}^{sp}(1, 4; 7, 8) \\ &= \sum_{\sigma} \sigma \frac{\delta \Sigma_{\nu\gamma,\sigma}(1, 4)_{\phi}}{\delta G_{\rho\lambda,\downarrow}(7, 8)_{\phi}} \Big|_{\phi=0} \end{aligned}$$

$$(5.384) \quad = \delta(1-4) \delta_{\nu,\gamma} \sum_{\sigma} \sigma \left( \frac{\delta A_{\nu}^{\sigma} \langle n_{\nu,-\sigma}(1) \rangle}{\delta G_{\rho\lambda,\downarrow}(7, 8)} + \sum_{\substack{\alpha \\ \alpha \neq \nu, \sigma'}} \frac{\delta B_{\alpha\nu}^{\sigma\sigma'} \langle n_{\alpha,\sigma'}(1) \rangle}{\delta G_{\rho\lambda,\downarrow}(7, 8)} \right).$$

By the same steps as in eq. (5.260) we obtain

$$(5.385) \quad \begin{aligned} & \Gamma_{\gamma\nu\lambda\rho}^{sp}(1, 4; 7, 8) \\ &= \delta(1-4) \delta(1-7) \delta(1^+ - 8) \delta_{\nu,\gamma} \delta_{\rho,\lambda} \left[ A_{\nu}^{\uparrow} \delta_{\nu,\rho} + (1 - \delta_{\nu,\rho}) \left( B_{\rho\nu}^{\downarrow\downarrow} - B_{\rho\nu}^{\uparrow\uparrow} \right) \right], \end{aligned}$$

where in the case of  $\alpha \neq \beta$  we set the values of  $\Gamma_{\alpha\beta\alpha\beta}^{sp}$ ,  $\Gamma_{\alpha\beta\beta\alpha}^{sp}$  equal to  $\Gamma_{\alpha\alpha\beta\beta}^{sp}$  as described previously in this section, which results in

$$(5.386) \quad \Gamma_{\alpha\beta\gamma\delta}^{sp} = \begin{cases} A_{\alpha}^{\uparrow} & \alpha = \beta = \gamma = \delta \\ B_{\alpha\gamma}^{\downarrow\downarrow} - B_{\alpha\gamma}^{\uparrow\uparrow} & \alpha = \beta \neq \gamma = \delta \\ \Gamma_{\alpha\alpha\beta\beta}^{sp} & \alpha = \gamma \neq \beta = \delta \\ \Gamma_{\alpha\alpha\beta\beta}^{sp} & \alpha = \delta \neq \beta = \gamma \\ 0 & \text{else} \end{cases}$$

The ansatz –like in the multi-site case– is not particle-hole symmetric and thus artificially breaks particle-hole symmetry if applied to a system that has this symmetry. In order to make our ansatz equations particle-hole symmetric we average between the ansatz in eq. (5.386) and the particle-hole transformed one. This yields

$$(5.387) \quad A_{\nu}^{\sigma} = U_{\nu\nu} \frac{1}{2} \left( \frac{\langle n_{\nu,\sigma} n_{\nu,-\sigma} \rangle}{\langle n_{\nu,\sigma} \rangle \langle n_{\nu,-\sigma} \rangle} + \frac{\langle (1 - n_{\nu,\sigma})(1 - n_{\nu,-\sigma}) \rangle}{\langle (1 - n_{\nu,\sigma}) \rangle \langle (1 - n_{\nu,-\sigma}) \rangle} \right)$$

$$(5.388) \quad B_{\alpha\nu}^{\sigma\sigma} \stackrel{\alpha \neq \nu}{=} (U_{\alpha\nu} - J_{\alpha\nu}) \frac{1}{2} \left( \frac{\langle n_{\alpha,\sigma} n_{\nu,\sigma} \rangle}{\langle n_{\alpha,\sigma} \rangle \langle n_{\nu,\sigma} \rangle} + \frac{\langle (1 - n_{\alpha,\sigma})(1 - n_{\nu,\sigma}) \rangle}{\langle (1 - n_{\alpha,\sigma}) \rangle \langle (1 - n_{\nu,\sigma}) \rangle} \right)$$

$$(5.389) \quad B_{\alpha\nu}^{\sigma-\sigma} \stackrel{\alpha \neq \nu}{=} U_{\alpha\nu} \frac{1}{2} \left( \frac{\langle n_{\alpha,\sigma} n_{\nu,-\sigma} \rangle}{\langle n_{\alpha,\sigma} \rangle \langle n_{\nu,-\sigma} \rangle} + \frac{\langle (1 - n_{\alpha,\sigma})(1 - n_{\nu,-\sigma}) \rangle}{\langle (1 - n_{\alpha,\sigma}) \rangle \langle (1 - n_{\nu,-\sigma}) \rangle} \right).$$

Alternatively, one can also keep the ansatz in eq. (5.381) and perform a particle-hole transformation when electron-doping a half-filled system as suggested in Ref. [163]. Nevertheless, we stick to the presented symmetric equations (5.387)-(5.389).

<sup>18</sup>We find for all cases studied in this thesis that this is a justified approximation since the corresponding on-site unequal orbital hopping matrix elements are much smaller than the diagonal components.

## 5.6. MULTI-ORBITAL TPSC

Note that the described ansatz does not work in the case where  $J = 0$  and  $U_{\alpha\beta} \neq 0$  because in this case we have only density-density interactions stemming from  $U_{\alpha\beta}$  which means that

$$(5.390) \quad \langle n_{\alpha,\uparrow} n_{\beta,\uparrow} \rangle \stackrel{J=0}{=} \langle n_{\alpha,\uparrow} n_{\beta,\downarrow} \rangle$$

and therefore  $\Gamma^{sp}$  reduces to the element  $\Gamma_{\alpha\alpha\alpha}^{sp}$  (see eq. (5.386)). Thus, the local spin sum rules for the  $\alpha\beta\alpha\beta$ -component (eq. (5.329)) which determine the value of  $\langle n_{\alpha,\uparrow} n_{\beta,\downarrow} \rangle$  can be evaluated by means of the Bethe-Salpeter equation (5.152) and result in

$$(5.391) \quad \begin{aligned} & \frac{T}{N} \sum_{q, iq_m} \chi_{\alpha\beta\alpha\beta}^{sp}(q, iq_m) \\ &= 2 \frac{T}{N} \left( \sum_{q, iq_m} \chi_{\alpha\beta\alpha\beta}^0(q, iq_m) + \chi_{\alpha\beta\nu\nu}^0(q, iq_m) \Gamma_{\nu\nu\nu\nu}^{sp} \chi_{\nu\nu\alpha\beta}^{sp}(q, iq_m) \right), \end{aligned}$$

which reduces to the local spin sum rule of the non-interacting spin susceptibility due to the negligible equal-site unequal-orbital hopping elements and therefore we end up with

$$(5.392) \quad \langle n_{\alpha,\uparrow} n_{\beta,\downarrow} \rangle = \langle n_{\alpha,\uparrow} \rangle \langle n_{\beta,\downarrow} \rangle = \langle n_{\alpha,\uparrow} n_{\beta,\uparrow} \rangle$$

which makes no sense if  $U_{\alpha\beta}$  is very large. In summary, we see that the ansatz for the spin vertex  $\Gamma^{sp}$  cannot be used in the case where  $J = 0$  since it produces non-interacting off-diagonal double occupations independent of the value of  $U_{\alpha\beta}$ .

**5.6.8. Numerical calculation of the irreducible vertices.** In the last section we have determined additional ansatz equations for  $\Gamma^{sp}$  in order to have enough equations to solve for  $\Gamma^{sp}$  and  $\langle n_{\alpha,\sigma} n_{\beta,\sigma'} \rangle$  by using the local spin sum rules (5.327), (5.328) and (5.329). Numerically, we use the multi root solvers from the GNU Scientific Library and in the case of the spin vertex and double occupations it is usually no problem to find a unique physical solution if one converges slowly from the limit of high temperatures and weak interaction strength.

On the other hand, we will see that the charge vertex component  $\Gamma_{\alpha\alpha\beta\beta}^{ch}$  tends to negative values (see chap. 6 for more details) which on the other hand leads to positive contribution in the high-frequency behavior of  $\text{Im}\Sigma(k, i\omega_n)$  (see eq. (5.368)) and this finally leads to negative spectral weight in  $A(k, \omega)$  (see eq. (4.245)). Those unphysical terms have to be avoided and this done by restricting the root search for  $\Gamma^{ch}$  to non-negative values. More details on this issue are postponed to chap 6.

With the spin and charge vertices at hand we can now proceed to the self-energy calculation and afterwards determine the full Green's function via the Dyson equation.

**5.6.9. Internal accuracy check.** In the same way that we derived an internal accuracy check for the multi-site TPSC in sec. 5.4.3 we derive here a similar expression for the multi-orbital TPSC.

By taking the equal imaginary time, position and orbital limit of eq. 5.323 we obtain

$$\begin{aligned} \Sigma_{\nu\bar{\beta},\sigma}(1, \bar{3}) G_{\bar{\beta}\nu,\sigma}(\bar{3}, 1^+) &= \sum_{\alpha} U_{\alpha\nu} \langle n_{\alpha,-\sigma}(1^+) n_{\nu,\sigma}(1) \rangle \\ &+ \sum_{\substack{\alpha \\ \alpha \neq \nu}} (U_{\alpha\nu} - J_{\alpha\nu}) \langle n_{\alpha,\sigma}(1^+) n_{\nu,\sigma}(1) \rangle \\ &+ \sum_{\substack{\alpha \\ \alpha \neq \nu}} J_{\alpha\nu} \left( \langle c_{\alpha,-\sigma}^\dagger(1^+) c_{\alpha,\sigma}(1) c_{\nu,-\sigma}(1) c_{\nu,\sigma}^\dagger(1^+) \rangle \right) \end{aligned}$$

$$(5.393) \quad + \left\langle c_{\nu,-\sigma}^\dagger(1^{++})c_{\alpha,\sigma}(1^+)c_{\alpha,-\sigma}(1)c_{\nu,\sigma}^\dagger(1^+) \right\rangle.$$

Via Fourier transformation and the definition of the spin susceptibility  $\chi^{sp,\pm}$  in eq. (5.203) we identify

$$(5.394) \quad \begin{aligned} & \lim_{\tau \nearrow 0} \frac{T}{N} \sum_{k, i\omega_n} e^{-i\omega_n \tau} \Sigma_{\nu\bar{\beta},\sigma}(k, i\omega_n) G_{\bar{\beta}\nu,\sigma}(k, i\omega_n) \\ &= \sum_{\alpha} U_{\alpha\nu} \langle n_{\alpha,-\sigma} n_{\nu,\sigma} \rangle + \sum_{\substack{\alpha \\ \alpha \neq \nu}} (U_{\alpha\nu} - J_{\alpha\nu}) \langle n_{\alpha,\sigma} n_{\nu,\sigma} \rangle \\ & - \frac{1}{2} \sum_{\substack{\alpha \\ \alpha \neq \nu}} J_{\alpha\nu} \left[ \frac{T}{N} \sum_{q, iq_m} \chi_{\alpha\alpha\nu\nu}^{sp}(q, iq_m) + \frac{T}{2N} \sum_{q, iq_m} \Re(\chi^{sp} - \chi^{ch})_{\nu\alpha\alpha\nu}(q, iq_m) \right]. \end{aligned}$$

This equation is fulfilled in the case where the full Green's function  $G$  is replaced by the non-interacting Green's function  $G^0$  as one can see from the proof in C.1.

Thus, we can use the sum rule for  $\text{tr}(\Sigma G^0)$  in eq. (5.394) to check the internal numerical accuracy in the program and the deviation to  $\text{tr}(\Sigma G)$  gives us a measure in how for the TPSC self-energy respects the consistency between the one- and two-particle level.

**5.6.10. Transversal particle-hole channel.** There is no easy way to include the transversal particle-hole channel as we did in the multi-site TPSC in sec. 5.1.9. The reason is that in the longitudinal particle-hole channel we are able to make use of the symmetry in  $\Gamma^{sp,0}$  (see eq. (5.349)), namely

$$(5.395) \quad \Gamma_{\alpha\alpha\beta\beta}^{sp,0} = \Gamma_{\alpha\beta\alpha\beta}^{sp,0} = \Gamma_{\alpha\beta\beta\alpha}^{sp,0}, \quad \alpha \neq \beta,$$

and state that the spin vertex  $\Gamma^{sp}$  retains this symmetry.

On the other hand, we find a more complex relation of the matrix elements of  $\Gamma^{sp,0}$  in the transversal channel (see appendix A) and since we do not have enough local spin sum rules to determine the vertices in eq. (5.395) independent from each other we need to find a different solution. There are three options of how one can proceed. First, one can construct a relation between the matrix elements similar to the one in eq. (5.395) but this makes the numerical search for  $\Gamma^{sp}$  harder due to the mixing of the different matrix components (see eq. (A.20)).

Second, one can also use double occupations from different methods as an external input which allows us to have enough local spin sum rules to determine the components  $\Gamma_{\alpha\alpha\beta\beta}^{sp}$ ,  $\Gamma_{\alpha\beta\alpha\beta}^{sp}$  and  $\Gamma_{\alpha\beta\beta\alpha}^{sp}$  independent of each other.

Third, in order to avoid additional complications from a first option and the possible error sources from the second one can also just ignore the contribution from the transversal particle-hole channel. This approach has the drawback that possible dominant contributions to the self-energy are neglected and that the crossing symmetry is not respected. On the other hand, we keep the simple form of the equations and keep many important mechanisms from the single-band TPSC such as the Kanamori-Brueckner screening.

For those reasons we present in this work only results where the transversal particle-hole channel is ignored but we underline once more that extensions are in principle possible and could result in further improvements on the method.

**5.6.11. Short summary on the applications of multi-orbital TPSC.** The first multi-orbital formulation of TPSC was provided by Miyahara *et al.* in 2013 [284] and was used to study unconventional superconductivity mediated by spin fluctuations.

## 5.7. DOUBLE COUNTING

---

Our multi-orbital TPSC scheme differs from this original one in the following aspects:

It restricts the charge vertex  $\Gamma^{ch}$  to non-negative values to ensure positivity of the spectral weight while in the original work in Ref. [284] one sets the negative contribution to the charge vertex  $\Gamma^{ch}$  to zero by hand.

Furthermore, we choose a symmetrized ansatz for  $\Gamma^{sp}$  (see eq. (5.386), (5.387), (5.388) and (5.389)) in contrast to the immediate result in eq. (5.381) that is used in Ref. [284]. Moreover, we derive a different set of local spin and charge sum rules and determine the bare vertices  $\Gamma^{ch/sp,0}$  from the Bethe-Salpeter equation (see eq. (5.348) and (5.349)) while in Ref. [284] the RPA result is used (see eq. (5.351)).

The TPSC scheme presented in this thesis was used to explain non-local correlation effects in iron-based superconductors [285, 287]. We discuss those results in more detail in chap. 7.

Later, a review article appeared as a pre-print where the important features of the method are presented [164]. In the same work TPSC and DMFT are applied to a toy model and compared to each other. This study is further extended in chap. 7.

### 5.7. Double counting

If we use TPSC on top of DFT, i.e. we take the localized Wannier states from DFT and put Hubbard interaction on those by means of TPSC, we need to correct for possible double counting errors as mentioned in chap. 3. In the same referenced chapter we pointed out that double counting schemes are always approximate or valid only in special limits.

Since we are mostly interested in non-local and dynamical correlation effects that go beyond DFT and we know that Hartree-Fock self-energy contributions are at least partly included in the low-energy model that we construct from DFT, we will subtract the Hartree-Fock contribution in all real materials calculations that are based on DFT. This leads to the self-energy

$$(5.396) \quad \Sigma_{\alpha\nu,\sigma} = \frac{1}{4} \left[ \Gamma^{ch} \chi^{ch} \Gamma^{ch,0} + \Gamma^{sp} \chi^{sp} \Gamma^{sp,0} \right]_{\nu\bar{\beta}\alpha\bar{\gamma}} * G_{\bar{\gamma}\bar{\beta}}^0.$$

This double counting was first suggested in Ref. [284].

**5.7.1. Flowchart of the multi-orbital TPSC.** For a better overview on the multi-orbital TPSC approach we give a flowchart of the method in fig. 5.17.

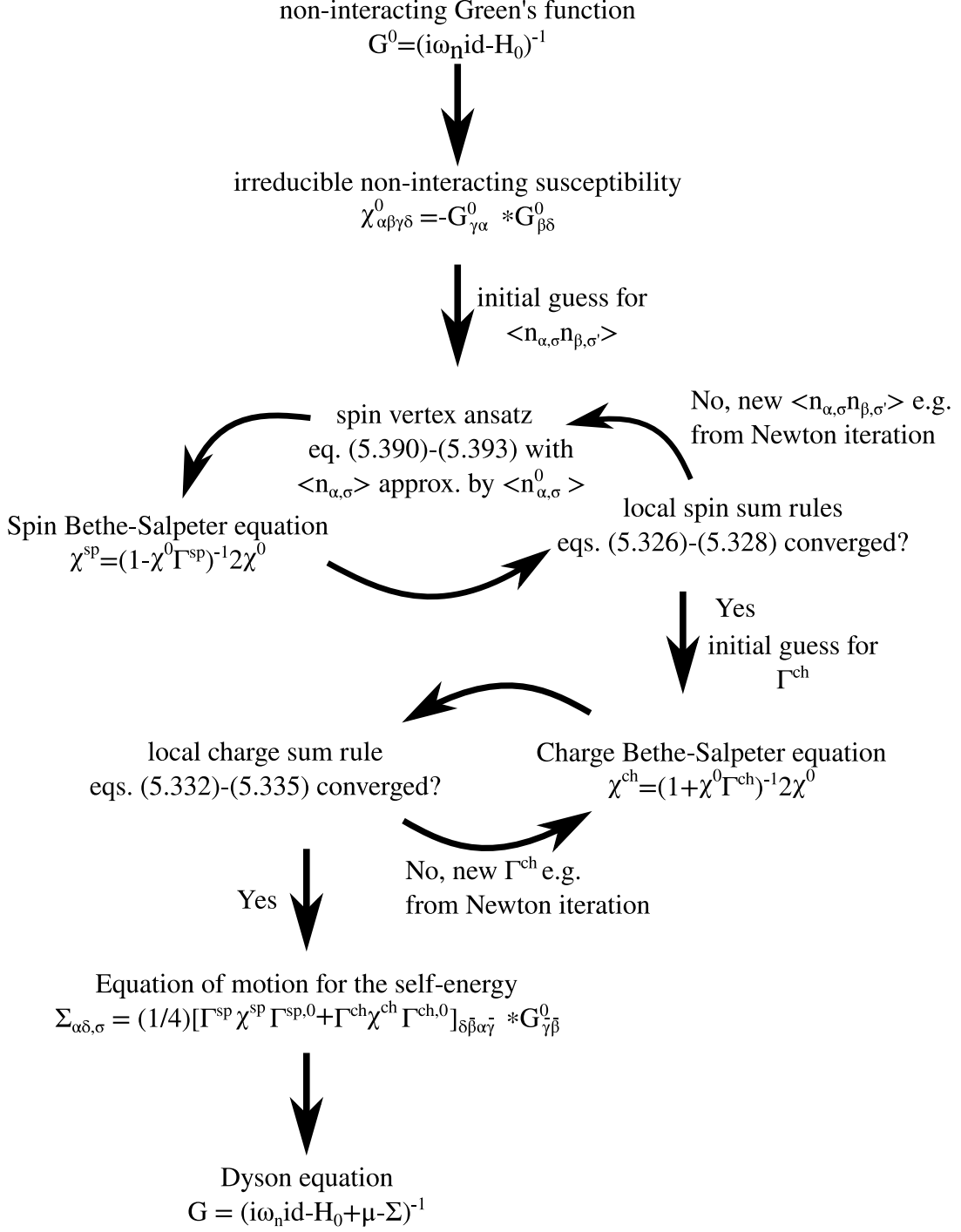


FIGURE 5.17. Multi-orbital TPSC flow diagram as described in sec. 5.6. After calculating the non-interacting Green's function in orbital-space and the irreducible susceptibility  $\chi^0$  one has to converge the spin and charge with respect to the local spin and charge sum rule and the Bethe-Salpeter equations. From those one is able to evaluate the self-energy and thus interacting Green's function via the Dyson equation. Note that  $id$  is the identity map in orbital-space which is equivalent to  $\mathbb{I}$ . Figure adapted from Ref. [164].

## Bechmarking the multi-orbital TPSC

**K. Zantout**, S. Backes, R. Valenti

Two-Particle Self-Consistent method for the multi-orbital Hubbard model

arXiv: 2008.08098 (2020)

[164]

The multi-orbital TPSC that we introduced in sec. 5.6 is different to the multi-site TPSC due to the effect of the inter-orbital interactions  $U_{\alpha\beta}$ ,  $J_{\alpha\beta}$ . For this reason it is important to study TPSC applied to a simple toy model and benchmark with different methods.

### 6.1. Model Hamiltonian

In this chapter we will consider a simple two-orbital Hubbard model on a square lattice with nearest neighbor hopping  $t$  only and Kanamori-Brueckner interaction [66], i.e.

$$(6.1) \quad U_{\alpha\beta} = \begin{cases} U & \alpha = \beta \\ U - 2J & \text{else} \end{cases},$$

$$(6.2) \quad J_{\alpha\beta} = J,$$

where  $U$ ,  $J$  are the bare interaction values and 0, 1 label the two orbitals (see fig. 6.1). We assume a temperature  $T/t = 0.5$  and a half-filled lattice if not stated differently.

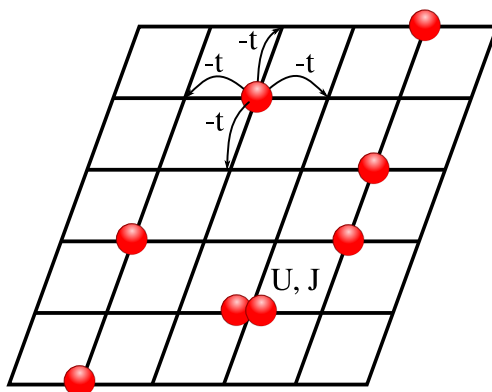


FIGURE 6.1. Simple toy model that is used to benchmark the multi-orbital TPSC approach. The red spheres represent electrons that can hop to neighboring sites with hopping amplitude  $t$ . In the case where two electrons are on the same site they feel orbital dependent interactions  $U$ ,  $J$ .

### 6.2. Double occupations and spin vertex

The first step within the TPSC routine consists of calculating the spin vertex  $\Gamma^{sp}$  and the double occupations  $\langle n_{\alpha,\sigma} n_{\beta,\sigma'} \rangle$ . In order to improve the assessment of the

TPSC results we also compare to DMFT results which represent the exact solution in infinite dimensions. Note that the DMFT calculations were carried out by Steffen Backes.

The double occupations for the simple toy model are show in fig. 6.2. DMFT and

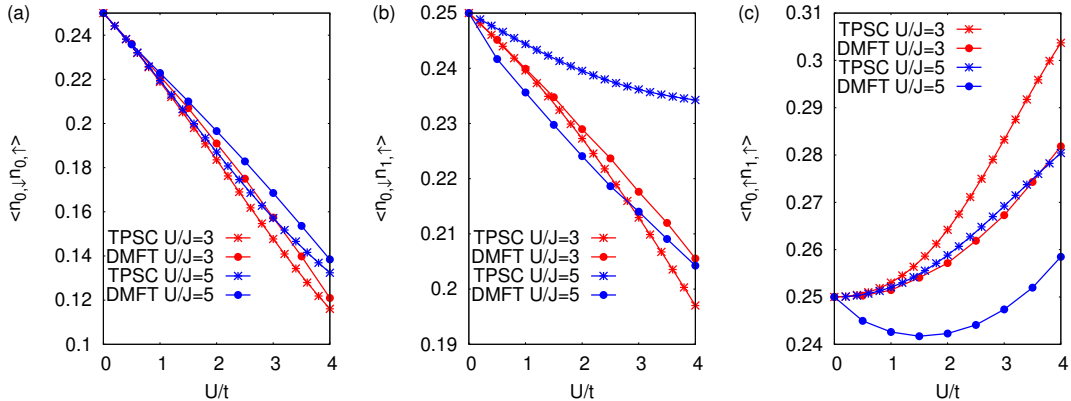


FIGURE 6.2. Double occupations  $\langle n_{\alpha,\sigma}n_{\beta,\sigma'} \rangle$  calculated from TPSC and DMFT. (a) The equal orbital double occupations from DMFT and TPSC agree well for all interaction strengths considered and show both a decay with increasing on-site interaction  $U/t$  while this effect is enhanced with increasing Hund's coupling  $J$ . (b) A similar behavior can be also seen for  $\langle n_{0,\uparrow}n_{1,\downarrow} \rangle$  while TPSC results exhibit a stronger dependence on  $U/J$  than DMFT. Moreover, TPSC predicts smaller double occupations  $\langle n_{0,\uparrow}n_{1,\downarrow} \rangle$  with increasing  $U/J$  ratio while DMFT predicts the opposite. Finally, in (c) we show the double occupation  $\langle n_{0,\uparrow}n_{1,\uparrow} \rangle$ . For those double occupations DMFT and TPSC follow the same trends except for small values of  $U/J$  where the DMFT double occupations make a small dip below the non-interacting value of 0.25. Fig. adapted from Ref. [164].

TPSC are in good agreement regarding the double occupations  $\langle n_{0,\uparrow}n_{0,\downarrow} \rangle$  for all values  $U/t = 0, \dots, 4$  and both ratios  $U/J = 3$  and  $U/J = 5$  (see (a)). Both methods predict a decay with increasing on-site interaction  $U/t$  and an enhancement of this effect with increasing Hund's coupling  $J$ . This behavior can be understood physically from the generic effect of the interactions  $U$  and  $J$  to energetically favor localized states over delocalized ones.

In (b) we observe a similar behavior of both methods for the double occupation  $\langle n_{0,\uparrow}n_{1,\downarrow} \rangle$ , namely functions that increase with  $U/t$  due to the inter-orbital repulsion  $U_{01} = U - 2J$ . But in contrast to (a) we find that TPSC results exhibit a stronger dependence on the  $U/J$  ratio; namely, TPSC predicts an inverse proportional dependence between the double occupation  $\langle n_{0,\uparrow}n_{1,\downarrow} \rangle$  and the  $U/J$  ratio while DMFT predicts both object to be proportional to each other. We assume that TPSC possibly overestimates the effects at low interaction strengths due to the Hartree-Fock decoupling that we performed to obtain an ansatz equation for the spin vertex  $\Gamma^{sp}$  (see sec. 5.4.1).

Finally, in (c) we present the double occupation  $\langle n_{0,\uparrow}n_{1,\uparrow} \rangle$  as a function of  $U/t$ . For those double occupations and for a large Hund's coupling  $U/J = 3$ , DMFT and TPSC predict increasing functions in dependence of the interaction strength  $U/t$  which we can understand from the Hund's coupling property to energetically favor high-spin states in different orbitals. On the contrary, DMFT exhibits a different behavior at small Hund's coupling  $U/J = 5$  and weak interaction  $U/t \lesssim 3$ : The double occupation

## 6.2. DOUBLE OCCUPATIONS AND SPIN VERTEX

$\langle n_{0,\uparrow} n_{1,\uparrow} \rangle$  drops below the non-interacting value of 0.25. We interpret this behavior to be due to the dominating inter-orbital repulsion  $U_{01}$  at low Hund's coupling  $J/U = 1/5$  which dominates over the effect of the Hund's coupling  $J$  to form a high-spin state. Only at larger interaction strengths  $U/t$  and therefore also at larger Hund's couplings  $J$  we see that the formation of high-spin states dominates over the mere repulsive effect of the inter-orbital repulsion  $U_{01}$ . Thus, we see similar trends for the double occupation  $\langle n_{0,\uparrow} n_{1,\uparrow} \rangle$  in (c) between DMFT and TPSC but with essential differences when it comes to additional effects at low interaction strength which might be due to the overestimation of correlation effects from the decoupling that we performed in sec. 5.4.1.

We draw now our attention to the spin vertex  $\Gamma^{sp}$  that is determined self-consistently from the local spin sum rules. The results are shown in fig. 6.3. First, we remark that

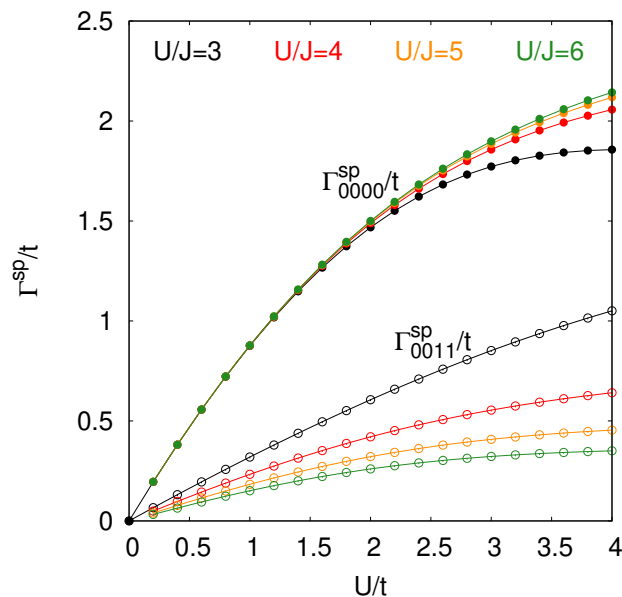


FIGURE 6.3. Matrix elements of the spin vertex  $\Gamma^{sp}$  as a function of  $U/t$ . We only show non-zero matrix elements and do not show  $\Gamma_{0101}^{sp} = \Gamma_{1010}^{sp} = \Gamma_{1001}^{sp} = \Gamma_{0110}^{sp}$  because they are equal to  $\Gamma_{1100}^{sp} = \Gamma_{0011}^{sp}$ . Similar to the single-band TPSC we observe Kanamori-Brueckner screening for larger values of  $U/t$ , i.e. the spin vertex converges toward a saturation value with increasing  $U/t$ . This behavior is observed for all values of  $U/J$  considered. Moreover, we see how larger Hund's couplings suppress the matrix elements  $\Gamma_{1111}^{sp} = \Gamma_{0000}^{sp}$  while it enhances the values of  $\Gamma_{1100}^{sp} = \Gamma_{0011}^{sp}$ . Fig. reprinted from Ref. [164].

in the range of weak to intermediate coupling strength it is always possible to solve the local spin sum rules (see eq. (5.327), (5.328) and (5.329)) for the double occupations  $\langle n_{\alpha,\uparrow} n_{\beta,\downarrow} \rangle$  and the spin vertex  $\Gamma^{sp}$ . Nevertheless, it is important to slowly converge the results from weak interaction strength and high temperatures.

Similar to the results from the single-orbital TPSC, we observe in fig. 6.3 Kanamori-Brueckner screening which means that the spin vertex does not increase boundlessly but reaches a saturation value as a function of  $U/t$ . The screening of the matrix element  $\Gamma_{0000}^{sp} = \Gamma_{1111}^{sp}$  is more pronounced in the case where the Hund's coupling is larger while the opposite effect is observed for  $\Gamma_{0011}^{sp} = \Gamma_{1100}^{sp}$ . This phenomenon can be traced back to the fact that larger Hund's couplings  $J/U$  favor states where the double

occupation of equal spins in different orbitals  $\langle n_{0,\uparrow} n_{1,\uparrow} \rangle$  while it suppresses double occupation of opposite spins in the same orbital  $\langle n_{0,\uparrow} n_{0,\downarrow} \rangle$  (see fig. 6.2). From this we can understand differently effective screenings via the ansatz equation for the spin vertex (see eqs. (5.386), (5.387), (5.388) and (5.389)),

$$(6.3) \quad \Gamma_{\alpha\beta\gamma\delta}^{sp} = \begin{cases} A_{\alpha}^{\uparrow} & \alpha = \beta = \gamma = \delta \\ B_{\alpha\gamma}^{\uparrow\downarrow} - B_{\alpha\gamma}^{\uparrow\uparrow} & \alpha = \beta \neq \gamma = \delta \\ \Gamma_{\alpha\alpha\beta\beta}^{sp} & \alpha = \gamma \neq \beta = \delta, \\ \Gamma_{\alpha\alpha\beta\beta}^{sp} & \alpha = \delta \neq \beta = \gamma \\ 0 & \text{else} \end{cases},$$

where we defined

$$(6.4) \quad A_{\nu}^{\sigma} = U_{\nu\nu} \frac{1}{2} \left( \frac{\langle n_{\nu,\sigma} n_{\nu,-\sigma} \rangle}{\langle n_{\nu,\sigma} \rangle \langle n_{\nu,-\sigma} \rangle} + \frac{\langle (1 - n_{\nu,\sigma})(1 - n_{\nu,-\sigma}) \rangle}{\langle (1 - n_{\nu,\sigma}) \rangle \langle (1 - n_{\nu,-\sigma}) \rangle} \right),$$

$$(6.5) \quad B_{\alpha\nu}^{\sigma\sigma} \stackrel{\alpha \neq \nu}{=} (U_{\alpha\nu} - J_{\alpha\nu}) \frac{1}{2} \left( \frac{\langle n_{\alpha,\sigma} n_{\nu,\sigma} \rangle}{\langle n_{\alpha,\sigma} \rangle \langle n_{\nu,\sigma} \rangle} + \frac{\langle (1 - n_{\alpha,\sigma})(1 - n_{\nu,\sigma}) \rangle}{\langle (1 - n_{\alpha,\sigma}) \rangle \langle (1 - n_{\nu,\sigma}) \rangle} \right),$$

$$(6.6) \quad B_{\alpha\nu}^{\sigma-\sigma} \stackrel{\alpha \neq \nu}{=} U_{\alpha\nu} \frac{1}{2} \left( \frac{\langle n_{\alpha,\sigma} n_{\nu,-\sigma} \rangle}{\langle n_{\alpha,\sigma} \rangle \langle n_{\nu,-\sigma} \rangle} + \frac{\langle (1 - n_{\alpha,\sigma})(1 - n_{\nu,-\sigma}) \rangle}{\langle (1 - n_{\alpha,\sigma}) \rangle \langle (1 - n_{\nu,-\sigma}) \rangle} \right).$$

Thus, the reduction/enhancement of the double occupations directly translates into an suppression/raise of the respective spin vertex matrix element.

### 6.3. Charge vertex

Next, we consider the charge vertex  $\Gamma^{ch}$  which is determined from the local charge sum rules (eqs. (5.334), (5.335) and (5.336)) and the double occupations  $\langle n_{\alpha,\sigma} n_{\beta,\sigma'} \rangle$ . In contrast to the spin vertex  $\Gamma^{sp}$ , it is much harder to determine the charge vertex  $\Gamma^{ch}$  due to the following reasons.

First, we consider the numerically unconstrained search for the charge vertex  $\Gamma^{ch}$  by finding a root of the local charge sum rules within the domain of real numbers for  $\Gamma^{ch}$ . The obtained results of this unrestricted search are the open symbols in fig. 6.4. Note that the open symbols are mostly overlapped by the same filled symbol that we will explain later. We observe that in the case large Hund's coupling  $J/U$  (see (a),(b)) the matrix elements  $\Gamma_{0101}^{ch} = \Gamma_{1010}^{ch}$  diverge as a function of  $U/t$  which makes the numerical treatment of the charge channel possibly unstable<sup>1</sup>. For such values of  $J/U$  one has to pay special attention to numerical errors and convergence issues.

If we take a look at lower  $J/U$  values (see (b)-(d)) we find that charge vertex component  $\Gamma_{0011}^{ch} = \Gamma_{1100}^{ch}$  assumes negative values which contributes negative spectral weight to the spectral function  $A(k, \omega)$ . In order to avoid those unphysical contributions to the spectral function we numerically restrict  $\Gamma^{ch}$  to non-negative values and determine  $\Gamma^{ch}$  as the matrix that minimizes the difference between the right-hand side and the left-hand side of the local charge sum rule equations (eqs. (5.334), (5.335) and (5.336)). The optimized values of this restricted charge vertex calculations are shown as filled symbols in fig. 6.4.

Throughout all calculations in fig. 6.4 we observe that this numerical restriction effects the charge vertex  $\Gamma^{ch}$  only if the interaction strength  $U/t$  is large and the Hund's coupling ratio  $J/U$  is small. In the other cases the unconstrained calculation of  $\Gamma^{ch}$  gives the same results as the constrained calculation<sup>2</sup>. Furthermore, we find that the

<sup>1</sup>In this particular case the numbers blow up to values of the order of  $10^{10}$ .

<sup>2</sup>The only exception to this statement is the point at  $U/t = 3.8, 4.0$  in fig. 6.4(a). But in this case the negative value is due to the divergence of  $\Gamma_{0101}^{ch}$ .

### 6.3. CHARGE VERTEX

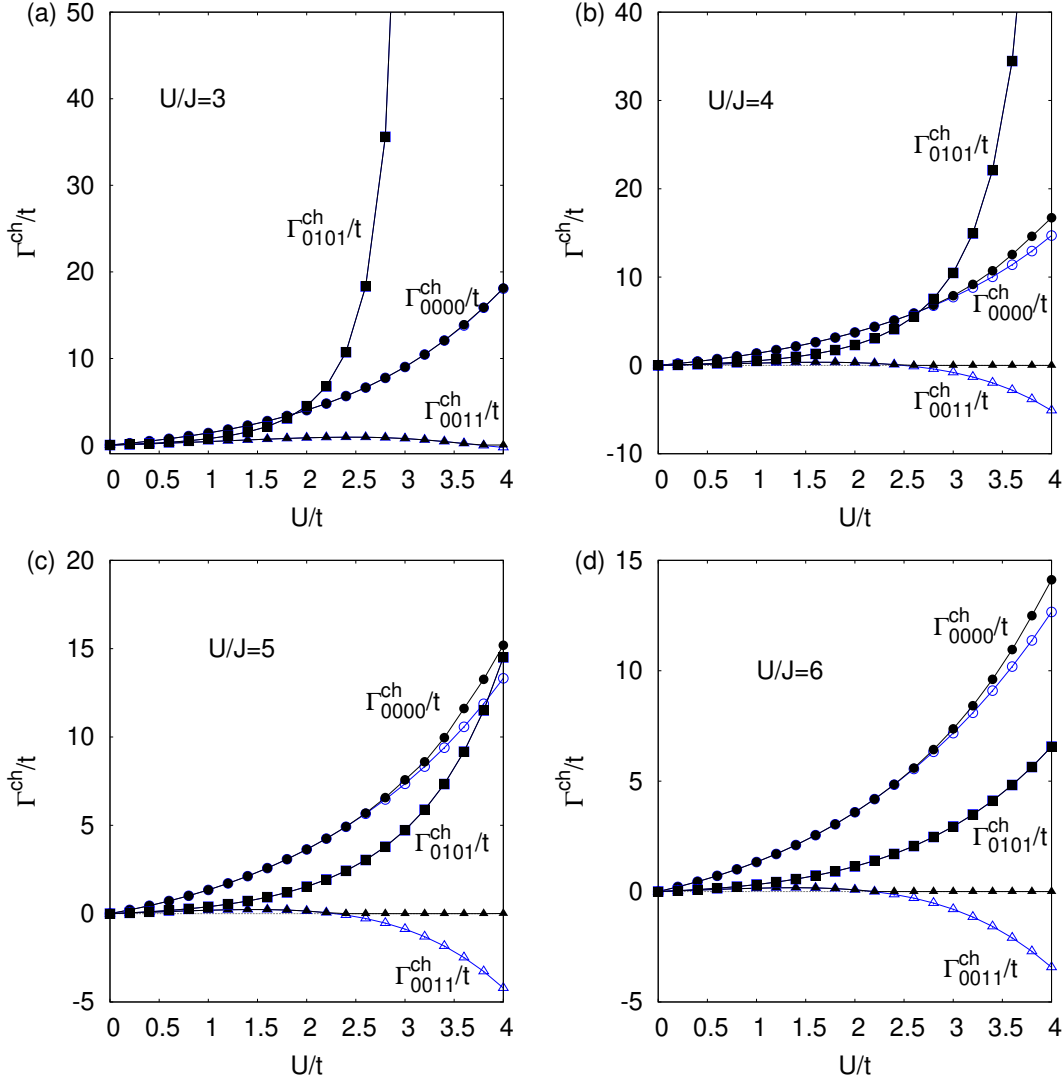


FIGURE 6.4. We present the components of the charge vertex  $\Gamma^{ch}$  as a function of  $U/t$  for different ratios of  $U/J$ . We do not show components that can be deduced by the ones shown in the figure, e.g.  $\Gamma_{0000}^{ch} = \Gamma_{1111}^{ch}$  and  $\Gamma_{1100}^{ch} = \Gamma_{0011}^{ch}$ . In (a) to (d) we show  $\Gamma^{ch}$  for  $U/J = 3, 4, 5, 6$  respectively. The open symbols that are mostly overlapping with their filled counterparts represent the solution for the charge vertex  $\Gamma^{ch}$  without numerical restriction of the values of  $\Gamma^{ch}$  while the filled symbols show the result when the matrix elements of  $\Gamma^{ch}$  are restricted to non-negative numbers. In (a) and (b) we see that in the case of large Hund's coupling  $J/U$  the matrix elements  $\Gamma_{0101}^{ch}$  diverge. In (b)-(d) we see that for small Hund's coupling the matrix element  $\Gamma_{0011}^{ch}$  assumes negative values. The general tendency of the charge vertex is similar to the results from the single-orbital TPSC with a diverging behavior as a function of  $U/t$  which leads to an overall suppression of charge fluctuations. Figure adapted from Ref. [164].

restriction mainly effects the value of  $\Gamma_{0011}^{ch} = \Gamma_{1100}^{ch}$  while minimally changing the other components of the charge vertex, namely  $\Gamma_{0101}^{ch}$  and  $\Gamma_{0000}^{ch}$ . Note that the authors in Ref. [284] also find that in the cases of small Hund's coupling ratio  $J/U$  the matrix element  $\Gamma_{0011}^{ch}$  is small compared to the other matrix elements which was their motivation to set this matrix element to zero.

Finally, we notice that the general trend of the charge vertex components is to diverge as a function of interaction strength  $U/t$ . The interpretation of this behavior can be adapted from the single-orbital case where this divergence leads to the destruction of charge fluctuations.

As we have seen previously the numerical restriction to non-negative matrix elements in the charge vertex  $\Gamma^{ch}$  leads necessarily to deviations in the local charge sum rules (see eqs. (5.334), (5.335), (5.336)). To quantify this source of error we take a look at the relative error of the local charge sum rules and compare this error from TPSC to the error from RPA since both methods treat fluctuation in a similar functional form (see eqs. (5.219), (5.220) and (5.267), (5.268)).

The relative error of the local charge sum rule is defined as the sum of differences between right-hand side and left-hand side of the equations (5.334), (5.335) and (5.336) divided by the respective right-hand sides. The result of this comparison between RPA and TPSC is shown in fig. 6.5.

In (a) we first present the scale of the charge sum rule error within TPSC. We observe no error for small interaction strengths  $U/t$  since the restricted and unconstrained calculation of the charge vertex  $\Gamma^{ch}$  arrive at the same (non-negative) result that obeys the local charge sum rules exactly.

On the one hand, we already see in fig. 6.4 that the charge vertex  $\Gamma_{0011}^{ch}$  converges to negative values if the onsite-repulsion  $U$  is large compared to the Hund's coupling  $J$ . Thus, we observe a jump in the charge sum rule error occurring at  $U/t \lesssim 2.5$  which goes to a value of up to 35% (red, orange and green curve). Moreover, we can recognize a different kind of error in the black curve which is due to the divergence of  $\Gamma_{0101}^{ch}$  (see fig. 6.4 (a)). As mentioned previously this blow up in numbers leads to numerical instabilities that cause a deviation in the local charge sum rules. For the toy model considered those error grow up to 50%.

A more detailed analysis of the local charge sum rule error reveals that the source is mainly the 0011-sum rule since the numerical restriction has its largest effect on the charge vertex component  $\Gamma_{0011}^{ch}$  (see also fig. 6.4). From this we can also understand why the jump in fig. 6.5 (a) happens at  $U/t \lesssim 2.5$  which is the region where the unrestricted calculation of  $\Gamma^{ch}$  leads to a sign change in  $\Gamma_{0011}^{ch}$  and restricted calculation will necessarily lead to a deviation in the local charge sum rule.

In addition to the above described error source we find a strong increase in the relative charge sum rule error for  $U/J = 3$  at  $U/t \gtrsim 3.8$  (see fig. 6.5 (a) black curve) which appears even in the unrestricted determination of  $\Gamma^{ch}$  (open symbols). The reason for those deviations is the diverging charge vertex component  $\Gamma_{0101}^{ch}$  (see fig. 6.4 (a)) which causes numerical instabilities that hinder an exact fulfillment of all local charge sum rules.

Note that those errors have to be interpreted in the right context: First, they only occur at small interaction strength  $U/t$  if  $U/J$  is large or at larger interaction strengths  $U/t$  if  $U/J$  is small. The typical case in realistic studies is the second case where additional hopping elements dampen the divergence of  $\Gamma_{0101}^{ch}$ . Second, we remind ourselves that in the self-energy expression (eq. (5.368)),

$$\begin{aligned} \Sigma_{\alpha\nu,\sigma}(k, i\omega_n) = & \sum_{\beta} U_{\beta\alpha} \langle n_{\beta,-\sigma} \rangle \delta_{\alpha,\nu} + \sum_{\beta \neq \alpha} (U_{\beta\alpha} - J_{\beta\alpha}) (\langle n_{\beta,\sigma} \rangle \delta_{\alpha,\nu} - \langle n_{\alpha\nu,\sigma} \rangle \delta_{\beta,\nu}) \\ & + J_{\nu\alpha} (\langle n_{\alpha\nu,-\sigma} \rangle (1 - \delta_{\alpha,\nu}) + \langle n_{\nu\alpha,-\sigma} \rangle (1 - \delta_{\alpha,\nu})) \end{aligned}$$

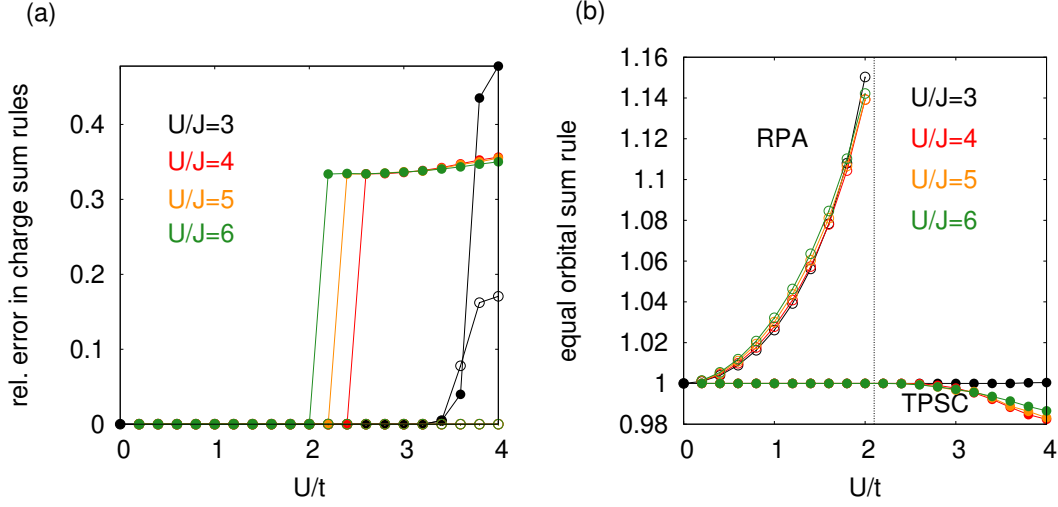


FIGURE 6.5. (a) The relative error in the charge sum rules for a restricted calculation of  $\Gamma^{ch}$  (filled symbols) is shown as function of the interaction strength  $U/t$ . For small values  $U/t \lesssim 2$  we observe that  $\Gamma^{ch}$  can be determined such that the local charge sum rules are fulfilled exactly. But when we have large onsite-repulsion  $U/t$  and small Hund's coupling ratio  $J/U$  we see that the error in the charge sum rules can grow up to 50%. On the other hand, we can also see a jump to an error of approximately 35% in the case where  $\Gamma_{0011}^{ch}$  changes sign (see fig. 6.4) which takes place at  $U/t \lesssim 2.5$ . (b) The value of the equal orbital sum rule (eq. (6.8)) is presented in dependence of  $U/t$  for different values of  $U/J$  and for RPA (open symbols) and TPSC (filled symbols). TPSC fulfills the equal orbital sum rule exactly except in the range of large interaction strength  $U/t$  where the numerical restriction of the charge vertex  $\Gamma^{ch}$  to non-negative values leads to small deviations of around 2%. The unrenormalized spin and charge vertices from RPA lead to violation the equal orbital sum rule already at small interaction values  $U/t$ . The quadratic increase in the error stops at the magnetic instability which occurs at  $U/t \approx 2.2$ . Figure adapted from Ref. [164].

$$(6.7) \quad + \frac{T}{4N} \sum_{q, iq_m} \left[ \Gamma^{ch} \chi^{ch}(q, iq_m) \Gamma^{ch,0} + \Gamma^{sp} \chi^{sp}(q, iq_m) \Gamma^{sp,0} \right]_{\nu\bar{\beta}\alpha\bar{\gamma}} G_{\bar{\gamma}\bar{\beta}}^0(k+q, i\omega_{n+m}),$$

it is the spin channel with the diverging spin susceptibility that gives the dominant contribution to the self-energy while the charge fluctuation play a secondary role. Thus, one can expect to obtain a self-energy that is still qualitatively and even quantitatively accurate even in the presence of those errors in the charge channel<sup>3</sup> as long as the original assumption of TPSC, namely that the spin and charge vertices  $\Gamma^{sp/ch}$  are constant, is still a good approximation.

In fig. 6.5 (b) we compare RPA and TPSC sum rule violations since both are functionally very similar but TPSC incorporates important vertex renormalizations that are not present in RPA (see eq. (5.351)). Notice that all local sum rules (eqs. (5.334), (5.335), (5.336), (5.327), (5.328) and (5.329)) contain double occupations that are – in general – different in TPSC and RPA. In order to compare both methods on equal footing we consider the sum of the local spin and charge sum rules in the case where all orbital

<sup>3</sup>We checked for instance the self-energy changes in LiFeAs (see chap. 7) are marginal if one removes the charge contribution in eq. (6.7).

indices are equal, i.e.

$$(6.8) \quad \frac{T}{N} \sum_{q, iq_n} \left( \chi^{sp} + \chi^{ch} \right)_{\alpha\alpha\alpha\alpha}(q, iq_n) = 2\langle n_\alpha \rangle - \langle n_\alpha \rangle^2 = 1,$$

where we have used that the toy model is at half filling and that both orbitals are degenerate, namely  $\langle n_0 \rangle = \langle n_1 \rangle = 1$ . We will call this sum rule the *equal orbital sum rule*.

While TPSC fulfills the equal orbital sum rule by construction up to the largest values of  $U/t$  considered if  $U/J = 3$  because in this domain we only have errors in the 0011-charge sum rule (see fig. 6.5 (b) black line). For interaction strengths  $U/t > 2.6$  and  $U/J > 3$  (see red, orange and green line) we observe a deviation of at most 2% which is due to the numerical restriction of  $\Gamma^{ch}$  to non-negative values. This leads to deviations not only in the 0011-local charge sum rule but also in the 0000-local charge sum rule<sup>4</sup> and therefore also in the equal orbital sum rule.

If we compare this small deviation of 2% to the deviations that grow up to 50% in the charge channel (see fig. 6.5 (a)), we realize once more that the largest source of errors is the numerical constraint on  $\Gamma_{0011}^{ch}$  that we need to ensure a physical spectral function  $A(k, \omega)$ . More importantly, we see that no renormalization of the spin and charge vertices  $\Gamma^{sp/ch}$  as in RPA leads to stronger violations of the orbital sum rule (see open symbols in fig. 6.5 (b)). The calculations in the figure were carried out until a maximum value of  $U/t \approx 2.2$  where one reaches the magnetic instability in RPA which does not occur in TPSC due to the renormalization of the spin vertex and in agreement with the Mermin-Wagner theorem. Moreover, one can deduce the quadratic deviation of RPA at low interaction strength  $U/t$  in the same fashion as for the single-orbital case (see Ref. [163]).

#### 6.4. Self-energy and quasi-particle properties

Finally, we take a look at the TPSC self-energy  $\Sigma$  and the quasi-particle properties that one can extract from it (see sec. 4.9).

In order to avoid additional sources of error we study here our model system at  $T/t = 0.03$  and slightly away from half filling, namely at  $n = 0.8$ . We checked that the two-particle consistency relation (see eq. (5.394)) is violated by at most 2.5% in the following calculations. The low temperature choice allows us to use the extrapolation formulas from appendix B.1.3 which are only valid at low temperatures while the small hole doping away from half filling helps us to avoid the strong anti-ferromagnetic fluctuations which cause the spin susceptibility to diverge at already small interaction strengths  $U/t$ . Thus, the combination of both parameter choices allows us obtain TPSC results at low temperatures for a interaction values that range from weak to intermediate coupling.

Before we show the TPSC results we introduce the local TPSC limit, where we replace the full momentum-dependent TPSC self-energy  $\Sigma(k, \omega)$  with its momentum average

$$(6.9) \quad \Sigma(k, i\omega_n) \rightarrow \frac{1}{N} \sum_k \Sigma(k, i\omega_n).$$

This construction will be needed later when we compare TPSC results to local DMFT results, where the DMFT calculation were all carried out by Steffen Backes.

In fig. 6.6 we present the TPSC self-energy  $\Sigma$  for  $U/t = 2.87$  and  $U/J = 4$  at the lowest Matsubara frequency  $i\omega_0$ . We observe in both the real and imaginary part of the self-energy a non-negligible momentum dependence that results in a variable effective

<sup>4</sup>Due to the matrix inversion in the TPSC expression for  $\chi^{sp/ch}$  (see eq. (5.268)) we have a contribution of the  $\Gamma_{0000}^{ch}$  and  $\Gamma_{0011}^{ch}$  matrix element to both the 0011- and 0000-local charge sum rule.

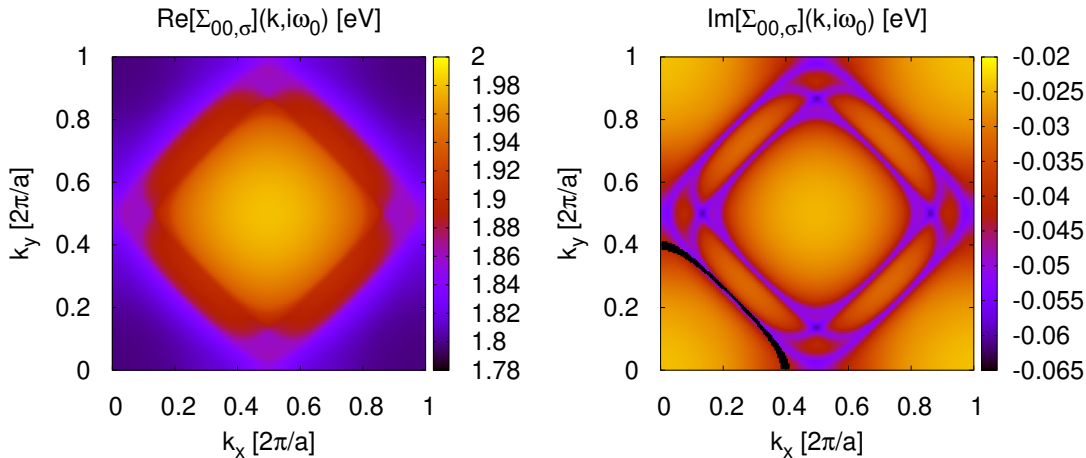


FIGURE 6.6. Momentum-dependent TPSC self-energy  $\Sigma$  for  $U/t = 2.87$  and  $U/J = 4$  at the lowest Matsubara frequency  $i\omega_0$ , filling  $n = 0.8$  and temperature  $T/t = 0.03$ . The black line in the lower quadrant is the Fermi surface which we only plot in this quadrant in order to make the full momentum dependence of the self-energy still visible. A strong momentum dependence is observed in both the real part and imaginary part.

mass renormalization and quasi-particle weight on the Fermi surface (black line right-hand side figure). For example, the renormalization effects close to the border  $k_x = 0$  and  $k_y = 0$  are smaller than the ones for states on the Fermi surface that are located at  $k_x = k_y$ . We will encounter the same momentum dependent effects later for LiFeAs (see chap. 7).

The DMFT self-energy is compared to TPSC by means of the local self-energy (see eq. (6.9)) and the resulting self-energies  $\Sigma_{00,\sigma}(i\omega_n)$  are shown in fig. 6.7. We observe a qualitative agreement of both methods, especially considering the low-frequency behavior of the imaginary part of the self-energy. Notice that the last agreement is of special value since the low-frequency behavior of the self-energy is directly related to the quasi-particle weights and lifetimes (see eq. (4.262) and (4.263)). Thus, we can expect a similar description of low-energy quasi-particle properties from both the local TPSC and DMFT approximation (see also fig. 6.8). Nevertheless, we already see an important difference between both methods, namely the high-frequency tail of the imaginary part of the self-energy. While in DMFT the high-frequency tail is correctly captured [288, 289] we already know from the single-band version that TPSC is not able to produce the correct high-frequency behavior [163]. The reason of the inadequate description within TPSC stems from the fundamental approximation that the spin and charge vertices  $\Gamma^{sp/ch}$  are frequency-independent. The local spin and charge sum rules that we used to determine those two vertices account for the fulfillment of the Pauli principle but in order to obtain the correct imaginary part of the self-energy for high frequency one needs a further frequency-dependent renormalization of the spin and charge vertices; namely, the vertices have to renormalize to the original bare vertices  $\Gamma^{sp/ch,0}$  [163]. This drawback from TPSC is also responsible why Hubbard bands cannot be obtained from TPSC [163].

Regarding the real part of the self-energy it is important to note that the dominant contribution in both DMFT and TPSC stems from the Hartree-Fock term which also

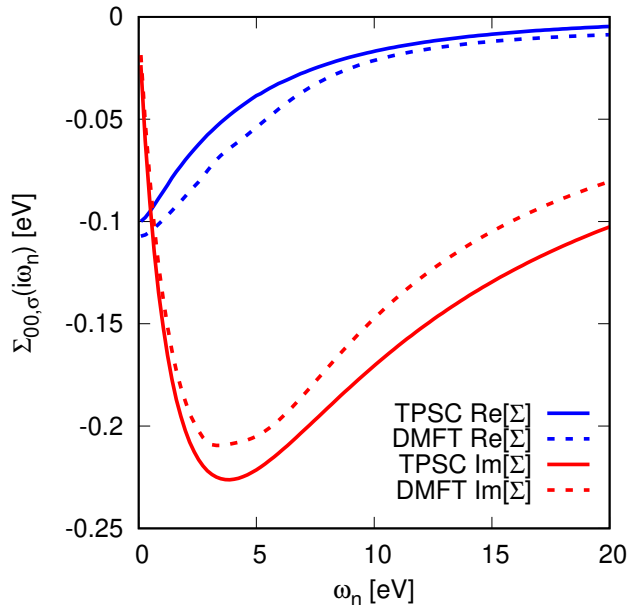


FIGURE 6.7. DMFT and local TPSC self-energy  $\Sigma_{\alpha\alpha,\sigma}(i\omega_n)$  for  $U/t = 2.5$  and  $U/J = 4$ , filling  $n = 0.8$  and temperature  $T/t = 0.03$ . Note that we subtracted the static Hartree-Fock term from both self-energies. We observe very good agreement in the low frequency behavior of the imaginary part while the high-frequency tail of TPSC is inadequate due to missing frequency-dependence of the spin and charge vertices  $\Gamma^{sp/ch}$ . The real part, that is mostly dominated by the Hartree-Fock term, does not have the problem of missing frequency renormalizations since the Hartree-Fock term is included in TPSC. Figure adapted from Ref. [164].

determines the high-frequency behavior. Comparing to this energy scale we also find a good agreement between the real parts of the self-energy in both methods.

Next, we compare the quasi-particle weight from DMFT and the local TPSC limit in fig. 6.8. As already visible from fig. 6.7 the quasi-particle weight  $Z$  takes similar values in DMFT and the local limit of TPSC. Both approximations predict a decay of quasi-particle weight  $Z$  as a function of increasing interaction strength  $U/t$  and Hund's coupling  $J/U$ .

In order to estimate the spin and charge channel contributions to the self-energy  $\Sigma$  we show in fig. 6.9 the spin and charge susceptibility components  $\chi_{0000}^{sp/ch}(q, 0)$  which are the dominant terms<sup>5</sup> in the self-energy equation (5.368). From the functional point of view both the spin and the charge susceptibility have a similar dependence on the momentum  $q$ . On the other hand, the spin susceptibility (a) is three orders of magnitude larger than the charge susceptibility which is a manifestation of the anti-ferromagnetic instability of the system. At the same time the strong suppression of the charge susceptibility (b) is directly related to the diminishing itinerant character of the charges. The large difference in the order of magnitude of both objects underlines again the importance of spin fluctuation for the low energy physics and thus the dominant contribution to the self-energy.

<sup>5</sup>In principle the 0011-component is also very large but since the  $q$ -dependence and the order of magnitude is very similar to the 0000-component we do not show this additional data.

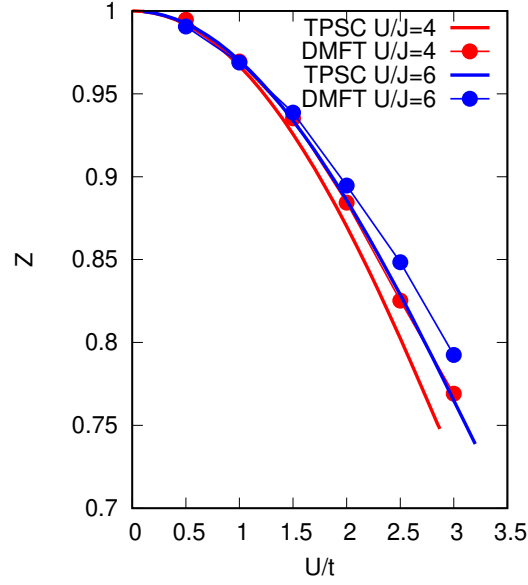


FIGURE 6.8. DMFT and local TPSC quasi-particle weight  $Z$  as a function of the interaction strength  $U/t$ . The filling is again  $n = 0.8$  and the temperature  $T/t = 0.03$ . Both methods describe a similar reduction of  $Z$  with increasing interaction strength  $U/t$  and Hund's coupling  $J/U$ . Figure reprinted from Ref. [164].

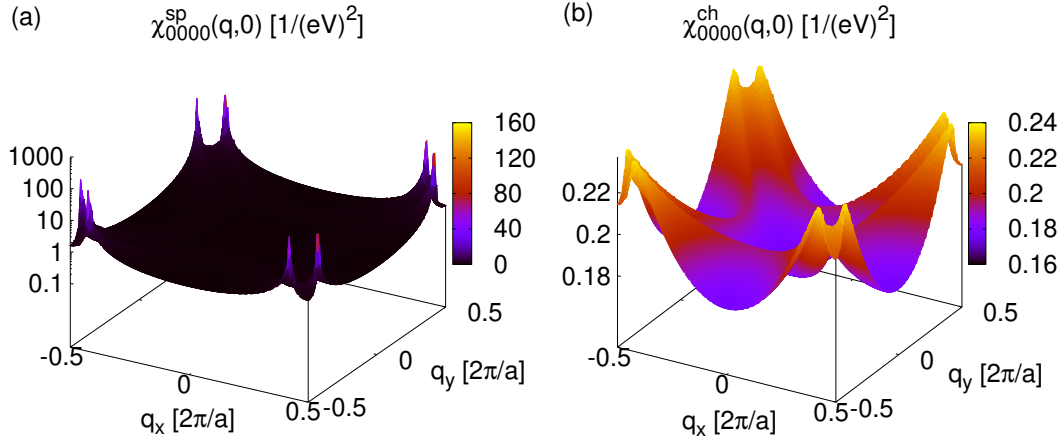


FIGURE 6.9. (a) Spin and (b) charge susceptibility components  $\chi_{0000}^{sp/ch}(q, 0)$  for  $U/t = 2.87$  and  $U/J = 4$ , filling  $n = 0.8$  and temperature  $T/t = 0.03$ . While both functions show a similar  $q$ -dependence in terms of peak position we see a large difference regarding the order of magnitude. The large spin susceptibility reveals large anti-ferromagnetic instabilities while the charge susceptibility reveals the tendency of charge localization.

## Nonlocal correlation effects in LiFeAs

**K. Zantout**, S. Backes, R. Valenti

Effect of non-local correlations on the electronic structure of LiFeAs  
 Phys. Rev. Lett. **123**, 256401 (2019)  
 [285]

In chap. 6 we studied multi-orbital TPSC results for a toy model and compared it to the local DMFT approximation. Among the different results we highlighted the significant non-locality of the self-energy (see fig. 6.6) which leads to momentum-dependent shifts of spectral weight and decrease of quasi-particle-lifetime. In this chapter we are going back to real materials and study this effect of non-locality on the electronic structure of LiFeAs.

### 7.1. Introduction

Since the discovery of iron-based superconductors in 2008 [290, 291] a lot of effort has been spent to investigate their electronic structure in the normal phase in order to understand the pairing mechanism in the superconducting phase [292–295].

The first attempts to describe the energy spectrum of iron-based superconductors in terms of *ab-initio* DFT calculations were successful regarding the qualitative shape of energy bands and Fermi surface [296–298] but for a more quantitative description of those materials it is important to incorporate the strong electron-electron interaction of the partially filled iron *3d*-states at the Fermi level. Those can lead to correlation effects such as large effective masses  $m^*/m$ , Fermi surface renormalization, finite quasi-particle lifetimes and precursor Hubbard satellites that are observed experimentally in some classes of iron-based superconductors [6, 299–311].

For this reason a combination of DFT and DMFT was applied to those materials, where DMFT was used to treat the local and orbital dependent correlation effects of the low-energy subspace. In many cases this framework was successfully applied and able to find many of the observations, such as orbital-dependent correlations, incoherent spectral weight distributions and Fermi surface renormalization [6, 8, 303–309, 311, 312].

While DMFT was successful in capturing important local correlation effects, it is – by construction – not able to resolve momentum-dependent correlation effects such as relative band shifts in opposite directions of, respectively, hole bands of the same orbital character centered at  $\Gamma$  and electron bands centered at the Brillouin zone edge M (the so-called “blue/red shift”) that is observed in many iron-based superconductors [7, 11, 313–315]. Moreover, there is also the possibility of momentum-dependent quasi-particle scattering rates [11, 12] that were observed in ARPES measurements of LiFeAs. Depending on the precise low energy spectrum of the iron-based superconductors one can construct different superconducting pairing scenarios [314, 316–318] which is an important motivation for better understanding the correlation effects in the family of iron-based superconductors.

Indeed, one finds many new developments that incorporate momentum-dependence in the self-energy for calculations of real materials [9, 10, 147, 148, 182, 183, 319–323], where the additional momentum-dependence can lead to bandwidth widening and

momentum-dependent shifts of energybands [9, 320, 321]. The cited approaches differ from each other in the way of how and which non-local contributions they take into account. For example, the GW+DMFT approach obtains the non-local self-energy effects mainly from charge fluctuations over the complete energy spectrum [307, 319] while the DGA method contains specific topologies of non-local diagrams in the self-energy expression [148].

Within the multi-orbital TPSC we can assess the contribution to local and non-local correlation effects that stem from the low-energy spin- and charge- fluctuations. This calculation helps to better estimate the different sources of non-locality in LiFeAs.

## 7.2. Experiment and Density Functional Theory

LiFeAs is an intrinsic<sup>1</sup> iron-based superconductor that does not develop a spin-density phase but a superconducting phase at  $T_c = 18K$  and ambient pressure [324]. Recent measurements and calculations also suggest LiFeAs as a candidate for quantum computing implementations due to its homogeneous stoichiometric composition and the charge neutral cleavage surface [325].

The crystal structure as obtained from X-ray diffraction is shown in fig. 7.1. It consists

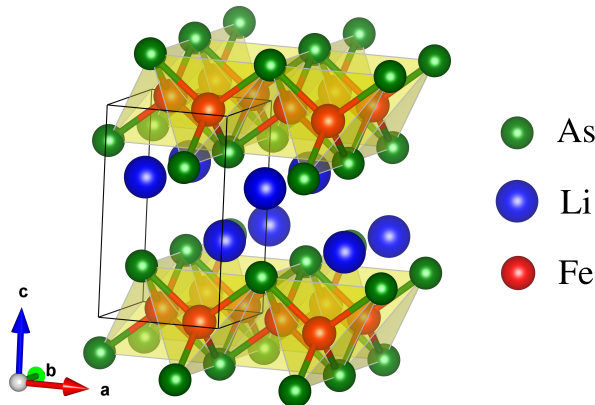


FIGURE 7.1. Crystal structure of LiFeAs according to Ref. [326]. We observe iron layers in a tetrahedral environment of arsenic. Those planes that are extended in the a-b plane are intercalated with a layer of Lithium. The unit cell is marked out by the transparent cuboid. Figure created with VESTA [327].

of iron-planes that are embedded in a tetrahedral As-environment with intercalated Li atoms that separate the FeAs-layers. LiFeAs belongs to the tetragonal  $P4/nmm$  space group and the precise structure data from Ref. [326] is shown in table 7.1 and 7.2.

space group	$a$ [Å]	$c$ [Å]
$P4/nmm$ (129)	3.7678	6.3151

TABLE 7.1. Lattice parameters of LiFeAs at 100K determined via Single Crystal X-Ray Diffractometry by Morozov *et al.* [326]. (see also fig. 7.1)

The ARPES measured electronic structure consists of two crossed quasi-circular electron pockets around M and a single hole-pocket centered at  $\Gamma$ . In addition one

<sup>1</sup>This means that undoped LiFeAs becomes superconducting at sufficiently low temperatures without the need of doping in contrast to many other FeAs-based superconductors [294, 324].

atom	Wyckoff position	x	y	z
Li	2c	0.250	0.250	0.655
Fe	2a	-0.250	0.250	0.000
As	2c	0.250	0.250	0.23626

TABLE 7.2. Internal positions of the atoms in LiFeAs according to the measured data of Morozov *et al.* [326] (see also fig. 7.1)

observes a flower-like shape of spectral weight directly around  $\Gamma$  which is assumed to play an important role for the superconductivity in this material [314, 326].

We start off with DFT, specifically the WIEN2k [328] implementation version 19.1, supplied by experimental structure data from Ref. [326]. The lattice parameters and atom positions for LiFeAs in the normal phase at 100K are given in table 7.1 and 7.2 respectively.

In order to assess the dependence of the electronic structure on the exchange correlation potential we apply here the LDA with WIEN2k convergence parameter  $RKmax = 9$  which is a measure for the size of the basis set [328] and 2000  $k$ -points. Those results can be directly compared to the GGA data that was used in [285] and where the calculations were converged with  $RKmax = 7$  and 1000  $k$ -points. We checked that both DFT settings yield the same low-energy spectrum apart from negligible differences of the order of at most  $\sim 10$ meV.

First, we take a look at the density of states from LDA (see fig. 7.2). It is obvious

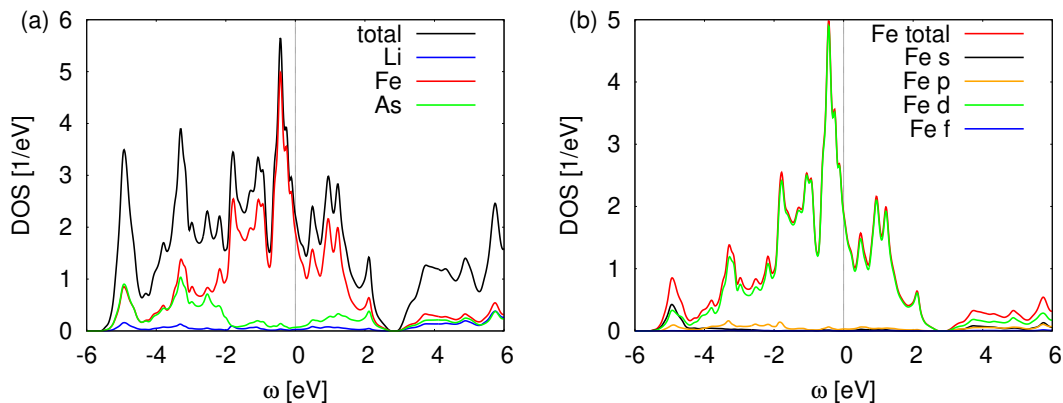


FIGURE 7.2. Density of states of LiFeAs from DFT. (a) DFT predicts dominant Fe contribution at Fermi level with small mixing of As states. Missing spectral weight is located in the interstitial region between the atoms. (b) The nature of the iron states close to the Fermi energy is mostly  $d$ -wave.

from (a) that the low energy spectrum is dominated by Fe states with small mixing of As. This is important for motivating a pure iron model as we will do in the course of this analysis. A closer inspection of the orbital character of those localized iron states (b) reveals a dominant  $d$ -wave nature. For this reason, we will aim at constructing a pure iron  $d$ -states low-energy model for LiFeAs. Note that those observation were already made and used to construct many different models also for other iron-based superconductors [295, 329].

Now, we consider the electronic bandstructure from DFT (see fig. 7.3). The spectrum is presented along the high-symmetry path  $\Gamma - X - M - \Gamma - Z - R - A - Z$  which corresponds to the relative coordinates  $(0, 0, 0) - (1/2, 0, 0) - (1/2, 1/2, 0) - (0, 0, 0) -$

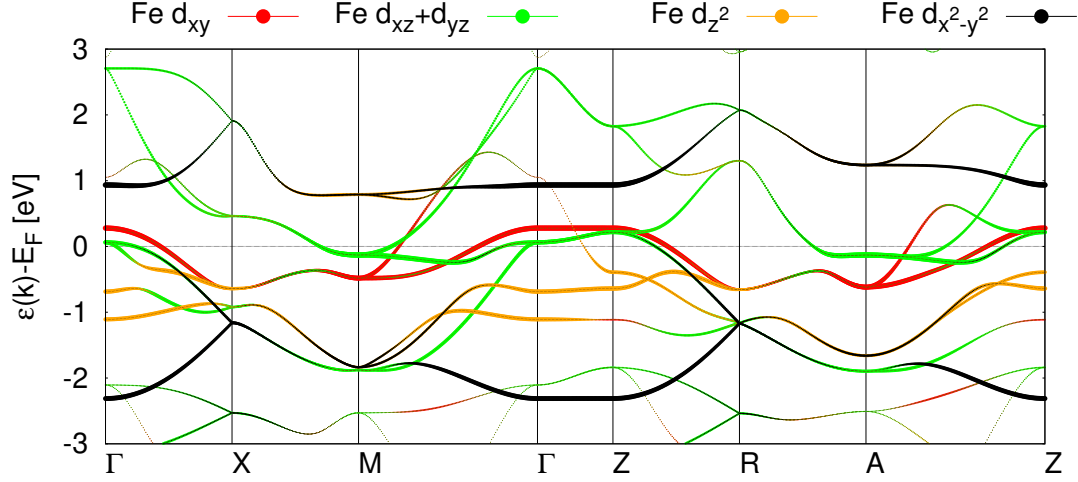


FIGURE 7.3. LDA bandstructure close to the Fermi energy along high-symmetry  $k$ -path. Three hole pockets are located around  $\Gamma$  with dominant  $d_{xy}$ - and  $d_{xz/yz}$ -character and two electron pockets around M with the same major band character. The similarity between the  $k_z = 0$ -dispersion ( $\Gamma - X - M - \Gamma$ ) and the  $k_z = \pi/c$ -bands ( $Z - R - A - Z$ ) is spoiled by one topological difference, namely the missing innermost hole pocket at  $k_z = \pi/c$ . Another difference in the bandstructure of those two planes is the strong widening of the outer electron pocket (see also fig. 7.4).

$(0, 0, 1/2) - (1/2, 0, 1/2) - (1/2, 1/2, 1/2) - (0, 0, 1/2)$  which corresponds effectively to the same high symmetry path in  $k_z = 0$  and  $k_z = \pi/c$ . From the tetrahedral crystal field splitting we expect three  $t_{2g}$  states,  $d_{xy}, d_{xz}$  and  $d_{yz}$ , that are energetically higher than the corresponding  $e_g$  states,  $d_{z^2}$  and  $d_{x^2-y^2}$ . This picture is also observed to high degree in the bandstructure of LiFeAs and can be used to construct further simplified models [295]. While the topology of the bands is very similar in both planes, namely we have hole pockets around  $\Gamma$  and two electron pockets around M with the same orbital character, the number of hole pockets is different. In the  $k_z = 0$ -plane we have three hole pockets while in the  $k_z = \pi/c$  we find only two and the innermost hole pocket is not present. Moreover, we see that the outer electron pocket is larger in size at  $k_z = \pi/c$  in comparison to the electron pocket at  $k_z = 0$ .

The two previously mentioned points suggest a three-dimensional modeling of LiFeAs but we will consider a two-dimensional model for the following reasons. First, the innermost hole pocket that disappears between  $k_z = 0$  and  $k_z = \pi/c$  is tiny and thus will carry only little weight in the electronic scattering processes that we will examine within TPSC. Second, the exact shape of the outer electron pocket might be important within TPSC since the change in size will lead to a shift of nesting vectors. Nevertheless, we expect only a small impact on the qualitative result of TPSC due to the similar topology. This assumption is supported by the toy model calculations performed in Ref. [287], where it was shown that a paramagnon-like self-energy like in TPSC and parabolic electron and hole pockets around M and  $\Gamma$  respectively are sufficient to predict the qualitative form of the self-energy  $\Sigma(k, 0)$ .

Notice that DFT predicts a band crossing between  $\Gamma$  and Z which is itself a discussed issue and object of current research [10]. We will not discuss this topic and restrict our calculations to the  $k_z = 0$ -plane.

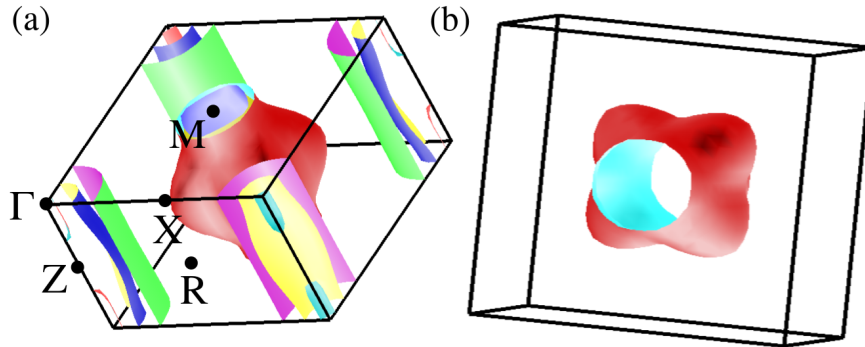


FIGURE 7.4. LDA Fermi surface of LiFeAs. (a) The electronic structure is quasi-two dimensional except for two features: The disappearance of the innermost hole pocket along  $\Gamma - Z$  and the increase in volume of the outer electron pocket at M. (b) In addition to the increase of size the outer electron pocket also deforms from a circular shape into a star shape. Figures created with xcrystden [330].

Before we move on and construct an effective Fe  $d-d$ -model for LiFeAs we show the DFT Fermi surface in fig. 7.4 as obtained from xcrystden [330]. As mentioned during the discussion of the bandstructure, the system is quasi two-dimensional except for the two features stemming from the outer electron and innermost hole pocket. In addition we observe in (b) that the outer electron pocket not only increases in size but also changes its shape from a circular form into a flower-like form<sup>2</sup>.

To obtain a low-energy iron  $d-d$ -model we use the Wannier projection implementation from Wien2Wannier [58, 59, 331]. We pick a  $k$ -resolution of  $15 \times 15 \times 4$ , where the low number of  $k_z$ -points is necessary to obtain a good agreement with the DFT bandstructure since in  $z$ -direction we find some hybridization of As  $p$ -orbitals with the Fe  $d$ -orbitals. Therefore, a low  $k_z$ -resolution can compensate for the exclusion of As states from the low-energy model and we still obtain an accurate model system for LiFeAs. The result of the Wannier projection is shown in fig. 7.5 and we find a precise description of the energy spectrum from  $-2\text{eV}$  to  $3\text{eV}$  in terms of a iron  $3d$  states. Notice that in the figure the blue data corresponding to the Wannier energy spectrum is mostly superimposed by red and green data that are described now.

A closer look at the structure of LiFeAs in fig. 7.1 reveals the existence of a glide plane in the FeAs layer, where the corresponding symmetry transformation consists of a translation of iron by  $(-1/2, 1/2, 0)$  and a successive reflection with respect to the  $a$ - $b$ -plane. Since we are restricting our calculations to inversion-symmetric structures without spin-orbit coupling we take advantage of this symmetry and unfold the two-iron Brillouin zone into a one-iron Brillouin zone. We follow here the scheme presented in Refs. [295, 332].

<sup>2</sup>Interestingly, the outer electron pocket assumes the same flower-like shape as observed for the spectral weight around  $\Gamma$  in ARPES [11, 12, 191, 314, 317, 326].

The unitary transformation that represents the glide symmetry is given by

$$(7.1) \quad U(k) = \frac{1}{\sqrt{2}} \begin{pmatrix} 1 & 0 & 0 & 0 & 0 & -z_k & 0 & 0 & 0 & 0 \\ 0 & 1 & 0 & 0 & 0 & 0 & -z_k & 0 & 0 & 0 \\ 0 & 0 & 1 & 0 & 0 & 0 & 0 & z_k & 0 & 0 \\ 0 & 0 & 0 & 1 & 0 & 0 & 0 & 0 & z_k & 0 \\ 0 & 0 & 0 & 0 & 1 & 0 & 0 & 0 & 0 & z_k \\ z_k^* & 0 & 0 & 0 & 0 & 1 & 0 & 0 & 0 & 0 \\ 0 & z_k^* & 0 & 0 & 0 & 0 & 1 & 0 & 0 & 0 \\ 0 & 0 & -z_k^* & 0 & 0 & 0 & 0 & 1 & 0 & 0 \\ 0 & 0 & 0 & -z_k^* & 0 & 0 & 0 & 0 & 1 & 0 \\ 0 & 0 & 0 & 0 & -z_k^* & 0 & 0 & 0 & 0 & 1 \end{pmatrix},$$

where  $z_k = e^{-2\pi k \cdot r}$  is a complex phase,  $r = (0.25, 0.75, 0)^T - (0.75, 0.25, 0)^T$  is the connection vector in relative coordinates between the two iron atoms within a unit cell and the orbital order is  $(d_{xy}, d_{xz}, d_{yz}, d_{x^2-y^2}, d_{z^2})$ .

In the ideal case of no hybridization between Fe and As states this transformation yields a block diagonal Hamiltonian

$$(7.2) \quad \tilde{H}(k) = UH(k)U^\dagger = \begin{pmatrix} H_{Fe1}(k) & 0_{5 \times 5} \\ 0_{5 \times 5} & H_{Fe2}(k) \end{pmatrix},$$

where the subscripts Fe1 and Fe2 denote the unfolding onto either of the two iron atoms in the unit cell. Notice that the unfolding is exact only in the  $k_z = 0$ -plane and else an approximation. The results of the Wannier projection and subsequent unfolding procedure are shown in fig. 7.5. We note that the unfolding reproduces the

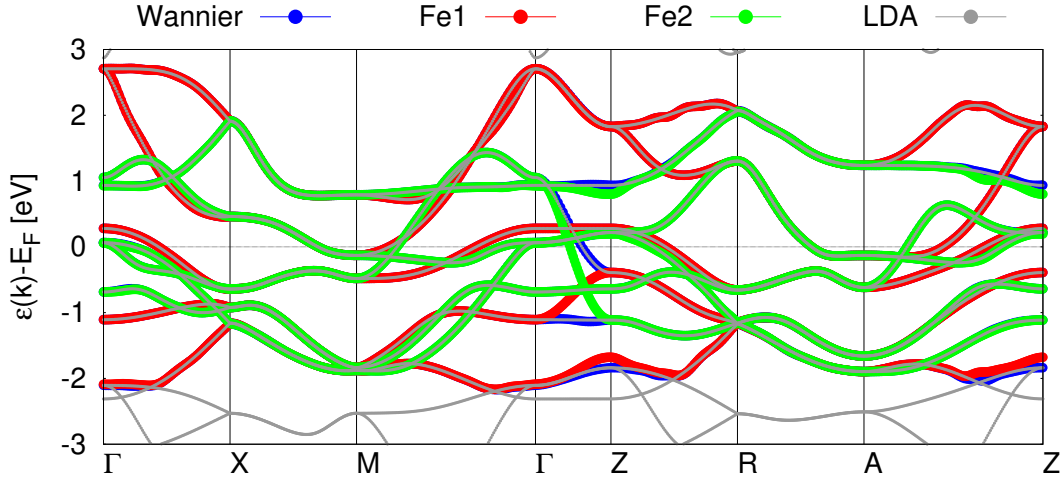


FIGURE 7.5. Wannier projection of the LDA bandstructure onto the Fe 3d-states. The obtained tight-binding model (blue) overlaps with the LDA calculation (gray). The unfolding procedure which takes advantage of a glide symmetry in the system allows to reduce the two-iron unit cell to two equivalent one-iron systems, namely Fe1 (red) and Fe2 (green). The folding is only approximate if  $k_z \neq 0$  which can be seen in the sections  $\Gamma - Z - R$  and  $A - Z$ .

LDA bandstructure  $k_z = 0$ -plane but shows some deviations at different  $k_z$ -values. Those differences appear for example in the sections  $\Gamma - Z - R$  and  $A - Z$ , where the unfolding is not exact.

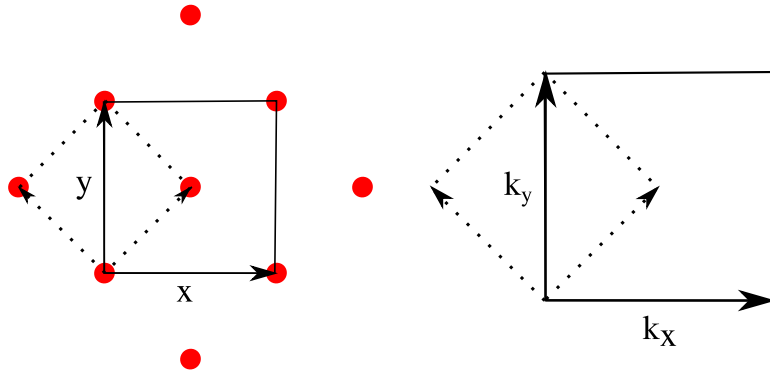


FIGURE 7.6. Change between two-iron unit cell (solid line) to one-iron unit cell (dotted lines) on the left. In reciprocal space this translates into the transformation on the right, namely also a rotation by  $45^\circ$  and scaling by a factor of  $\sqrt{2}$ .

In the following we will work within the Fe1-unfolded unit cell (see fig. 7.6). Thus, we need to rotate the  $k$ -points by  $45^\circ$  and scale the vectors by a factor of  $\sqrt{2}$  in order to relate back to the  $k$ -vectors of the two-iron Brillouin zone, i.e.

$$(7.3) \quad \begin{pmatrix} k_x \\ k_y \end{pmatrix} \rightarrow \begin{pmatrix} 1 & -1 \\ 1 & 1 \end{pmatrix} \begin{pmatrix} k_x \\ k_y \end{pmatrix}.$$

The transformation between the one-iron and two-iron unit cell is shown in fig. 7.6. Thus, one has to revert the rotation by  $45^\circ$  and scaling by  $\sqrt{2}$  to obtain the corresponding objects in the two-iron Brillouin zone. Additionally, the remaining parts that are not in the cut of the one-iron and two-iron Brillouin zone are folded back into the two-iron Brillouin zone. The electron occupation in the two-dimensional Fe1-model is six.

Next, we compute the interaction values  $U$ ,  $J$  from cRPA by means of the FHI-gap code [333]. Those calculations were carried out by Steffen Backes and the  $k$ -integration was converged on a  $8 \times 8 \times 5$  mesh [285].

The interaction parameters for the iron  $d$ - $d$ -model are given as

$$(7.4) \quad U = \begin{pmatrix} 3.40 & 1.94 & 2.03 & 2.39 & 2.39 \\ 1.94 & 2.54 & 2.13 & 1.89 & 1.89 \\ 2.03 & 2.13 & 2.66 & 1.98 & 1.98 \\ 2.39 & 1.89 & 1.98 & 2.75 & 2.02 \\ 2.39 & 1.89 & 1.98 & 2.02 & 2.75 \end{pmatrix} \text{ eV}$$

and

$$(7.5) \quad J = \begin{pmatrix} 0 & 0.49 & 0.51 & 0.34 & 0.34 \\ 0.49 & 0 & 0.23 & 0.39 & 0.39 \\ 0.51 & 0.23 & 0 & 0.41 & 0.41 \\ 0.34 & 0.39 & 0.41 & 0 & 0.41 \\ 0.34 & 0.39 & 0.41 & 0.41 & 0 \end{pmatrix} \text{ eV},$$

where the orbital basis is ordered as  $(d_{z^2}, d_{x^2-y^2}, d_{xy}, d_{xz}, d_{yz})$ . Notice that those values differ from the results in Ref. [71] which might be the result of a smaller  $k$ -mesh applied ( $4 \times 4 \times 4$ ) and the difference in the DFT basis choice. For more details on this issue we refer to the Supplemental Material in Ref. [285].

### 7.3. TPSC results

**7.3.1. Computational details.** Before we present the TPSC results for the electronic structure of LiFeAs, we mention the numerical parameters that were used to converge the calculations. For more details we refer to appendix B.

The momentum-space integration of the non-interacting susceptibility  $\chi^0(q, iq_m)$  (see eq. (5.92)) was performed by means of the adaptive cubature method with a three-point formula for triangles and an integration tolerance of  $10^{-6}$ . All other quantities and integrations are based on a  $100 \times 100$   $k$ -mesh.

We picked  $N_{\text{Mats}} = 416$  fermionic Matsubara frequencies and 277 bosonic Matsubara frequencies since all bosonic functions that we deal with decay faster than the fermionic ones. In both the fermionic and bosonic case we employed high-frequency corrections for  $\frac{1}{\omega^2}$ -tails that we obtained via fitting to the high-frequency tail. The temperature was slowly converged down to  $T = 0.015\text{eV} \approx 174\text{K}$  which corresponds to the lowest temperature before the development of peaks in the spin susceptibility is too far advanced to guarantee well-converged  $k$ -integration.

Steffen Backes employed the maximum entropy code from Ref. [334] to perform analytic continuation to obtain the spectral function  $A(k, \omega)$ . The Padé approximation was used for analytic continuation of the imaginary part of the self-energy  $\Sigma''(k, \omega)$  and the quasi-particle weight  $Z(k)$  was computed via linear extrapolation.

The charge sum rule violation was at most 6% but as discussed in chap. 6 this will only lead to a marginal influence on the self-energy since the spin-fluctuation are dominating for the set of parameters considered.

**7.3.2. Spectral function and Fermi surface.** We present the spectral function  $A(k, \omega)$  for LiFeAs along  $\Gamma$ -X-M- $\Gamma$  in the two-iron Brillouin zone in fig. 7.7. As expected from the effect of self-energies on a bandstructure we observe an overall decrease of the bandwidth. To accentuate the effect of the TPSC self-energy on the electronic structure which goes beyond this overall bandwidth renormalization, we overlay the data with the DFT bandstructure, that is scaled by a factor of two. This factor corresponds to the quasi-particle weight averaged over all momenta  $k$  and all orbitals. The introduction of correlation effects has two significant features. First, we find a downshift of the hole bands around the Fermi energy at  $\Gamma$ , whereas the electron pockets at M are slightly shifted up in energy. This effect is named the “red-blue shift” and is a common observation in iron-based superconductors where DFT predicts too large electron and hole pockets that need to be shifted into opposite directions (“red” and “blue”) in order to reconcile with experiment [7, 11, 313–315].

Notice that the shift of the outer electron pocket is also strongly  $k$ -dependent: While the shift of the electron pocket section crossing X-M is around 0.05eV we find that the section crossing M- $\Gamma$  is barely shifted. This behavior is more drastic for the hole pockets. For example, along  $\Gamma$ -X the middle hole pocket experiences a large energy shift which results in a shrinking to approximately 20% of its size compared to the renormalized DFT bandstructure. On the other hand, all other parts of the middle hole pocket on the Fermi surface shrink to 80-90% of their original size (compare  $\Gamma$ -M) which is about a factor of four smaller.

The inner hole pockets at  $\Gamma$  that are mainly composed  $d_{xz}/d_{yz}$  orbital character (see fig. 7.8 (a)), become very incoherent at the Fermi level due to scattering processes and thus leading to a significant reduction of quasi-particle lifetime. Combination of this incoherence and the previously mentioned momentum dependent shrinking of the hole pocket leads to incoherent spectral weight in a flower-like shape around  $\Gamma$  that is also observed in ARPES measurements [11, 12, 191, 314, 317]. Further, we see that the crest of the inner hole bands at  $\Gamma$  are shifted on top of the Fermi level and therefore

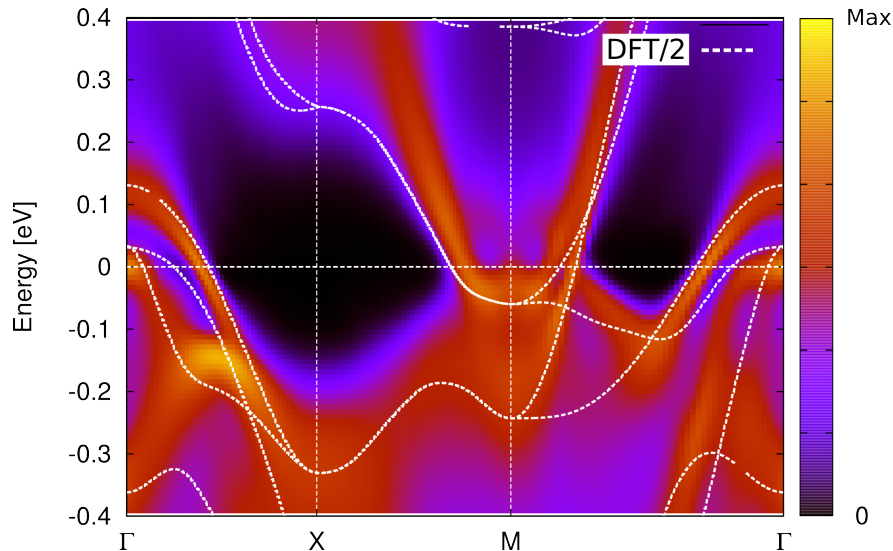


FIGURE 7.7. Spectral function  $A(k, \omega)$  of LiFeAs calculated from TPSC in the two-iron Brillouin zone at  $T = 0.015\text{eV}$ . In order to highlight the self-energy effects we also show the DFT bandstructure (GGA) rescaled by an average quasi-particle weight enhancement of approximately 2 (dotted lines). We observe an overall shrinking of the hole and electron pockets at  $\Gamma$  and  $M$  respectively originating from non-locality of the self-energy, the so-called “red-blue shift”. In addition we find that the two innermost hole pockets at  $\Gamma$  become incoherent due to finite lifetime effects stemming from the imaginary part of the self-energy. Figure reprinted from Ref. [285].

we assume that the inclusion of spin-orbit coupling, which is beyond the present multi-orbital TPSC approach, will lead to a splitting of the  $d_{xz/yz}$ -degenerate states around  $\Gamma$ , such that only one hole pocket consisting of incoherent spectral weight remains at  $\Gamma$ . This additional effect would further reconcile the DFT data with published ARPES measurements [11, 335] as well as de Haas-van Alphen (dHvA) experiments [336].

In order to understand why the TPSC self-energy is able to account for the “red-blue shift” we sketch the arguments developed in [287, 313]. Key ingredient is the inter-orbital repulsion that contributes to the real part of the self-energy via  $V = [\Gamma^{sp}\chi^{sp}\Gamma^{sp,0}]_{abab}$  in eq. (5.368). The vertex  $V$  is peaked at the anti-ferromagnetic instability vector  $k = \{(\pm\pi/a, 0), (0, \pm\pi/a)\}$  which corresponds to inter-band scattering processes related to this momentum-transfer at low energies. In the limit of zero temperature and by approximating the electronic structure to be composed only of a single hole band around  $\Gamma$  and a single electron band around  $M$  one can derive the opposite sign in the self-energy for hole and electron band [287, 313]. Thus, we find that spin fluctuations can indeed be an explanation for the observed “red-blue” shift. This result is further supported by similar findings from the fluctuation-exchange approximation and the RPA-self-energy formalism [287].

Now, we take a look at the Fermi surface properties in LiFeAs. We start off with the orbital-resolved Fermi surface obtained from DFT (GGA) (fig. 7.8 (a)) and distinguish three quasi-circular hole pockets around  $\Gamma$ , where the inner pockets have dominantly  $d_{xz}$  and  $d_{yz}$  orbital character (green and blue respectively), while the outer hole pocket is mainly composed of  $d_{xy}$  spectral weight (red). Moreover, we find two electron pockets with elliptical shape centered around  $M$  with dominantly  $d_{xy}$  orbital character on the outer orbit and  $d_{xz}$  and  $d_{yz}$  orbital character for the interior parts.

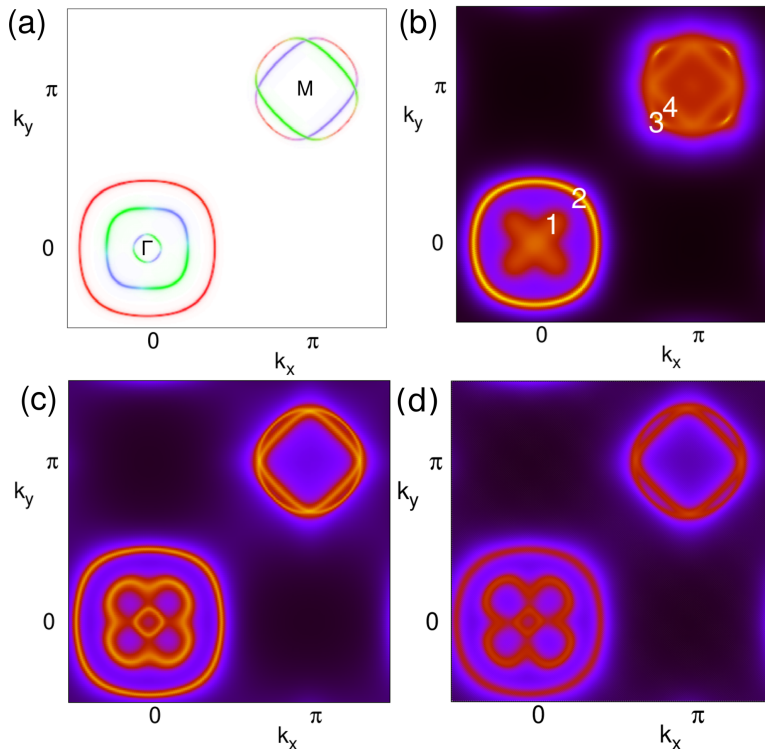


FIGURE 7.8. (a) Orbital-resolved Fermi surface obtained from DFT (GGA), where the dominant orbital characters are  $d_{xy}$  (red),  $d_{yz}$  (blue) and  $d_{xz}$  (green). We find three circular hole pockets centered around  $\Gamma$  and two electron pockets around  $M$  that resemble two ellipses. (b) Fermi surface from DFT+TPSC. Strong scattering processes lead to incoherence effects on the inner hole and electron pockets. Especially the two inner hole pockets become very incoherent and change from the circular form into a flower-like shaped region of incoherent spectral weight. (c) Fermi surface from DFT+“local TPSC”. In this local approximation of the TPSC self-energy we reproduce published DFT+DMFT result [6, 191] to a high degree. (d) DFT+DMFT Fermi surface for the same Fe  $d$ - $d$  model. We see a strong similarity to the DFT+“local TPSC” result in (c). Figure adapted from Ref. [285].

As we have already argued from the spectral function  $A(k, \omega)$  in fig. 7.7 we observe a shrinkage of all electron and hole pockets on the Fermi surface in DFT+TPSC (see fig. 7.8 (b)). Further, we find that the  $d_{xy}$ -components of the Fermi surface suffer less from scattering effects than the  $d_{xz}$ - and  $d_{yz}$ -components which results in sharper features. We will come back to this observation later.

Moreover, we find the flower-shaped incoherent spectral weight around  $\Gamma$  in agreement with experimental observations [11, 314, 336]. Those observations are in stark contrast to DFT+DMFT [6, 7] and GW [9] results. We ascribe those differences to the low-energy non-local spin fluctuations that are not included in DMFT and GW. In order to confirm this claim we have to relate the local DMFT to the non-local TPSC.

An interesting connection between TPSC and DMFT can be drawn if we consider the local limit of TPSC, where the momentum dependent TPSC self-energy  $\Sigma(k, \omega)$  is replaced by its local component  $\frac{1}{N} \sum_k \Sigma(k, \omega)$ . By this procedure we get a local self-energy which corresponds to a DMFT-like form. We call this approximation DFT+“local TPSC” and present the resulting Fermi surface in fig. 7.8 (c). The

DFT+“local TPSC” Fermi surface is indeed very close to the DFT+DMFT results in Ref. [6, 7] but those publications are based on a different double counting scheme, different interaction parameters and take the full LDA spectrum into account and are not projected onto an iron  $d$ - $d$ -model. Thus, Steffen Backes performed a DFT+DMFT calculation that incorporates exactly the same parameters and model assumptions as presented here, where the impurity model was solved by the continuous-time Quantum Monte-Carlo Solver in the segment picture as implemented in the ALPSCore package[331, 337].

The Fermi surface from this DFT+DMFT scheme is shown in fig. 7.8 (d) and the agreement to DFT+“local TPSC” becomes even better. Even the coherence of the inner hole states are restored in comparison to the DFT+TPSC results (see (b)) which shows that the momentum-dependence of the self-energy is not restricted to the real-part of the self-energy which causes the “red-blue shift” but extends also to the imaginary part. Another important aspect is that those Fermi surfaces are very close to initial DFT Fermi surface except for the non-trivial flower-like deformation of the middle hole pocket. We note that DFT+DMFT calculations with a different double counting scheme [8] are able to see a flower-like shape of spectral weight around  $\Gamma$  but the feature is not incoherent and there is also no “red-blue shift”.

In conclusion our results emphasize the importance of non-local correlation effects that stem from local Hubbard interaction in LiFeAs. Coming to our observation of a momentum- and orbital-dependent imaginary part of the self-energy, we notice that this behavior has been observed in recent ARPES experiments [11, 12], where the inner  $d_{xz}$  and  $d_{yz}$  derived hole Fermi surface has been found to be incoherent while the outer  $d_{xy}$  hole pocket shows Fermi liquid behavior.

**7.3.3. Quasi-particle scattering rate.** In this context we can analyze the energy dependence of the quasi-particle scattering rates, which contains information about Fermi liquid and non-Fermi liquid behavior.

We remind of the zero-temperature Fermi liquid result [30, 338] which states that close to the Fermi energy the quasi-particle scattering rate is given by

$$(7.6) \quad -Z(k)\text{Im}\Sigma(k, \omega) \approx c_0\omega^2.$$

One can extend [110, 126] this argument to finite temperatures and obtains

$$(7.7) \quad -Z(k)\text{Im}\Sigma(k, \omega) \approx c_0\omega^2 + c_1T^2.$$

In the original formulation of the Fermi Liquid result one has  $c_1 = c_0 + \pi^2$  but we will use a more general coefficient  $c_1$  since the multi-band structure might induce additional effects.

The TPSC quasi-particle scattering rates along the path  $\Gamma$ -M are shown in fig. 7.9 at the four points (see labels 1-4 in fig. 7.4(b)), where the spectral weight is maximal. The main orbital character on each point is: (1)  $d_{yz}$ , (2)  $d_{xy}$ , (3)  $d_{xy}$  and (4)  $d_{xz}$  (compare to fig. 7.4 (a)). In contrast to the quadratic energy dependence of the quasi-particle scattering rates with dominant  $d_{xy}$ -character, we find that the  $d_{xz/yz}$ -states exhibit linear quasi-particle scattering rates (red symbols). Comparing the actual values of the  $d_{xz/yz}$ -dominated states to measured data [11] we find that the TPSC numbers are even quantitatively in good agreement with experiment. Those curves are very flat and can be fitted to a linear function as shown in the fig. 7.9, where the fit is given by

$$(7.8) \quad (1): \tau(\omega) = 25\text{meV} - 0.09\omega,$$

$$(7.9) \quad (4): \tau(\omega) = 24\text{meV} - 0.091\omega.$$

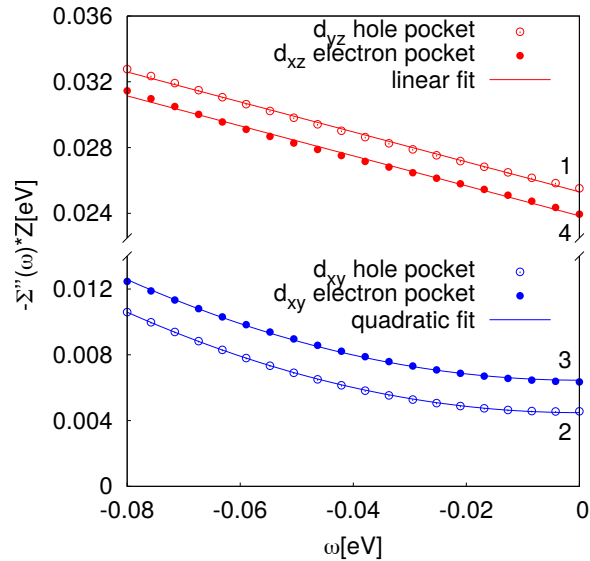


FIGURE 7.9. Quasi-particle scattering rate  $-Z(k)\Sigma''(k, \omega)$  along  $\Gamma$ -M as a function of the binding energy  $\omega$ . The  $k$ -points correspond to the maximal value of spectral weight and are labeled by 1-4 (see respective position in fig. 7.8(b)). We find that the quasi-particles with  $d_{xz/yz}$  character have scattering rates that are linear in energy while the electron pocket states exhibit a Fermi liquid behavior with quadratic scattering rates. Figure reprinted from Ref. [285].

On the other hand, we find that the  $d_{xy}$ -dominated quasi-particle scattering rates depend quadratically on the binding energy (blue symbols in fig. 7.9), which is a fingerprint of Fermi-liquid behavior and in agreement with ARPES measurements in Ref. [11]. The fitting curves applied in fig. 7.9 are

$$(7.10) \quad (2): \tau(\omega) = 4.5\text{meV} + \frac{0.95}{\text{eV}}\omega^2,$$

$$(7.11) \quad (3): \tau(\omega) = 6.5\text{meV} + \frac{0.96}{\text{eV}}\omega^2.$$

The quantitative match with the experimental data from Ref. [11] is not given for the  $d_{xy}$ -states—the measured values are a factor of 2-3 larger—which can perhaps be attributed to impurity scattering from the cleavage [11] or to the difference in temperature: The experiments were carried out at 25K while we performed the calculations at 174K. We expect that the lower temperatures enhance spin fluctuations and thus increase the overall value of scattering rates. Further, we expect that this effect is only restricted to  $d_{xy}$ -dominated orbitals as supported by measurements on  $\text{Ba}(\text{Fe}_{0.92}\text{Co}_{0.08})_2\text{As}_2$ , where the temperature dependence is only significant for the  $d_{xy}$ -dominated orbitals.

This comparison of scattering rates to experimental data suffers from another important issue regarding the different extraction schemes from ARPES, which lead to incommensurate experimental data [11, 12]. While both cited publications follow the same extraction scheme based on the energy- and momentum distribution curves, which directly connects to the imaginary part of the self-energy (see eq. (4.254)), they apply different models to obtain the scattering rates as fitting parameters to those models. We will not go into details about the different procedures but refer to Refs. [11, 12] and point out that this difficult technicality can yield significant results as is the case here.

$\alpha$	$d_{xy}$	$d_{xz}$	$d_{yz}$	$d_{x^2-y^2}$	$d_{z^2}$
$n_{\alpha}^{LDA}$	1.11	1.06	1.06	1.17	1.54
$n_{\alpha}^{TPSC}$	1.11	1.09	1.09	1.19	1.46

TABLE 7.3. Orbital-resolved occupations from DFT and DFT+TPSC. Notice that the LDA filling do not perfectly add up to 6 due to the finite temperature that is not included within LDA. We observe that the fillings barely change except for the  $d_{z^2}$ -filling which reduces due to the purely positive shift of the real part of the self-energy (see fig. 5(b) in [287]).

The data in fig. 7.9 suggests that the Fermi-/non-Fermi liquid distinction in LiFeAs can be based on the orbital character. To test this idea we also checked how the energy dependence changes with different  $k$ -points for the electron and hole pockets. We found that small translations along the tip of electron pocket (3) yields quasi-particle scattering rates that depend linearly on the binding energy, which could have been already expected from the incoherence of the quasi-particle weight away from the point (3) (see fig. 7.8(b)).

In conclusion we find that the quasi-particle scattering rates show an intricate momentum- and orbital-dependence containing both Fermi liquid and non-Fermi liquid features.

**7.3.4. Orbital fillings.** In this section we compare the DFT orbital fillings with the interacting fillings since this was an important approximation in the determination of  $\Gamma^{sp}$  (see sec. 5.6.7). There, we argued that we can approximate  $n_{\alpha}$  by its non-interacting value  $n_{\alpha}^{LDA}$  in the local spin and charge sum rules (see eqs. (5.327)-(5.329), (5.334), (5.335) and (5.336)) and the ansatz equation for  $\Gamma^{sp}$  (see eq. (5.386)) in order to avoid additional self-consistencies that would only introduce marginal effects but lead to additional iterations of the self-energy evaluations of eq. (5.368). The comparison is shown in table 7.3. We find that the fillings are indeed very close to the original non-interacting orbital occupations. The largest difference is in the  $d_{z^2}$ -component that is due to the strict positivity of the real part of self-energy over all  $k$ -points (comp. fig. 5(b) in Ref. [287]).

#### 7.4. Comparison of “local TPSC” and DMFT

Here, we resume our comparison of the “local TPSC” and DMFT that we started in the previous sections in terms Fermi surfaces (see fig. 7.8). For a more detailed estimation of both methods away from the Fermi energy we show in fig. 7.10 the spectral function obtained from “local TPSC”, DMFT and a renormalized DFT bandstructure. In contrast to the full TPSC results we observe that the “local TPSC” and DMFT spectral functions are very close to the renormalized DFT result, where the renormalization in DMFT (factor 2.1) is slightly larger than in “local TPSC” (factor 2). Only at larger binding energies we see that the imaginary part introduces additional features, where again the imaginary part of the self-energy is larger in DMFT than in “local TPSC”. Most importantly, both methods do not exhibit the “red-blue shift” that is needed to improve the agreement with experimental results.

Since the above presented comparisons rely on analytic continuation and are thus susceptible to the errors that come along with it, we will compare now the raw self-energies from both methods in fig. 7.11. Due to the constant spin and charge vertices in TPSC we cannot obtain the right self-energy high-frequency behavior in contrast to DMFT (see chap. 6 and [163]). This explains the larger deviations in fig. 7.11 at large Matsubara frequencies. The opposite is true for the low-frequency section of

#### 7.4. COMPARISON OF “LOCAL TPSC” AND DMFT

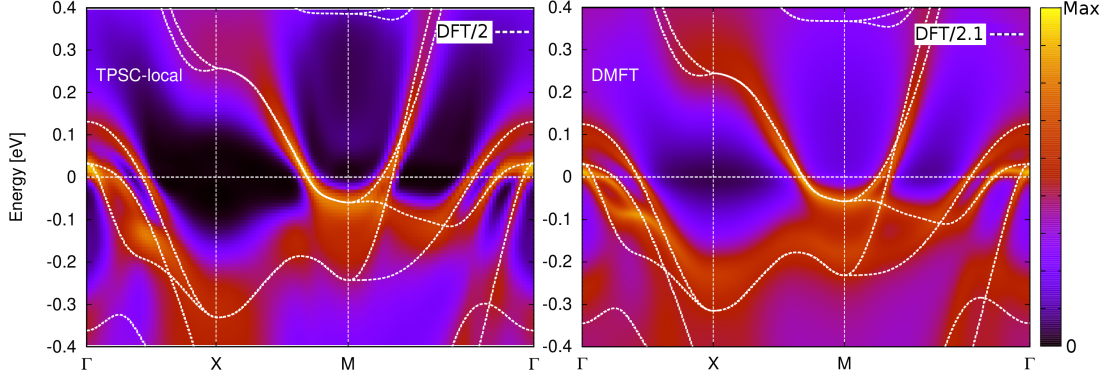


FIGURE 7.10. LiFeAs spectral functions for LiFeAs obtained from “local TPSC” (left) and DMFT (right). For comparison we also show the renormalized DFT bandstructure in both plots. The agreement of both methods is not only limited to the Fermi surface but also to the low-energy spectrum. Figure reprinted from Ref. [285].

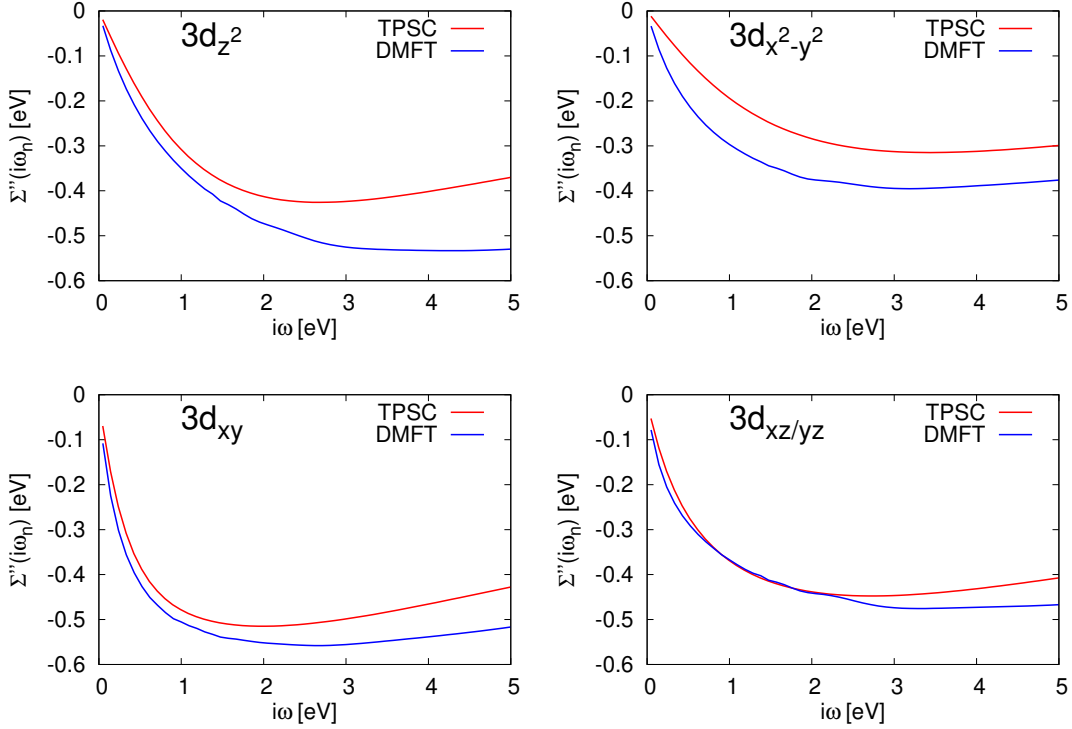


FIGURE 7.11. Imaginary part of the “local TPSC” (red) and DMFT (blue) self-energy. We observe a good agreement at small Matsubara frequencies (except for the  $d_{x^2-y^2}$  orbital). Since the low-frequency parts of the  $d_{xy}$ - and  $d_{xz/yz}$ -components of the self-energy are the largest contributors to the low-energy features of the spectrum, we can assume similar results from both methods. Figure reprinted from Ref. [285].

the self-energy, where large deviations only occur for the  $d_{x^2-y^2}$ -orbital. A remarkable difference in all orbital channels is the stronger quasi-particle renormalization in DMFT that can be seen from the steeper slope at low Matsubara frequencies. We have already

noticed this small difference in terms of the larger average effective mass (see fig. 7.10). Nevertheless, the overall similarity between both approaches suggests that some of the low-energy physics in LiFeAs are captured in a close way.

### 7.5. Conclusions

We applied the multi-orbital TPSC method to the correlated metal LiFeAs and found that non-local correlation effects are crucial for describing the low-energy spectral features.

While the local part of TPSC introduces an overall renormalization of a factor of two to the bandstructure, we find that the non-local part adds additional features such as momentum-dependent incoherence and momentum-dependent spectral weight shifts. Those effects result in the flower-like shape of incoherent spectral weight around  $\Gamma$  that is observed in ARPES experiments and a “red-blue shift” of the bandstructure that leads to an overall shrinking of all electron and hole pockets in agreement with ARPES and dHvA measurements [7, 11, 313–315].

Moreover, we found that the local TPSC limit exhibits strong similarity to DMFT results when it comes to spectral function and Fermi surface data in the low-energy region. It is important to notice that those local approaches are not able to capture the “red-blue shift” since one needs shifts in the positive energy direction at the M point and negative self-energy shifts at  $\Gamma$ .

This result is not only restricted to LiFeAs but can be extended to more representatives of iron-based superconductors which underlines the importance of non-local electronic correlation effects in this family of materials [287]. Similar studies on LiFeAs already suggested the importance of non-local correlations although they expect the non-locality to be originating from high-energy charge fluctuations [9, 10]. Nevertheless, our calculations and closely related approaches [287] suggest that the low-energy spin-fluctuations are at least an additional important ingredient. Moreover, our results predict the same Fermi-/non-Fermi liquid behavior of the Fermi surface states along  $\Gamma$ -M as extracted from ARPES by Brouet *et al.* [11].

In summary, our calculations underline the importance of non-local self-energy effects in LiFeAs that go beyond the DFT+DMFT description and show that the TPSC scheme is indeed able to improve the agreement between theory and experiment.

## Summary and Outlook

In this thesis, we presented the Two-Particle Self-Consistent approach as a method for describing moderately correlated electronic systems. Many phenomena such as unconventional superconductivity, the Mott metal-to-insulator transition or Pseudogap physics can be related to the emergent physics of interacting electrons.

In order to calculate properties of real materials we determine the electronic structure of those systems from *ab-initio* DFT as described in chap. 2. This method has proven several successes over the last decades and serves as a sensible starting point for many-body techniques that account for additional electronic effects beyond the independent electron picture.

Due to the intricate nature of many-body studies it is often impossible to work on the original system, where electrons are considered in continuum and interacting by means of the long-range Coulomb repulsion. In chap. 3 we presented the famous Hubbard model which is assumed to be a fundamental lattice model that incorporates the essential physics of interacting electrons. Moreover, we presented the cRPA scheme which allows to determine the effective Coulomb interaction parameters that enter the Hubbard model.

In chap. 4 we introduced the concept of Green's functions that stand in the center of the TPSC approximation. We not only summarized the different types of Green's functions but also explained how one can deduce physical observables from those abstract objects.

Next, we presented in chap. 5 the TPSC approach by first introducing the Kadanoff-Baym scheme upon which TPSC is based. An application of the multi-site TPSC was presented in terms of a study of superconducting properties of organic superconductors, where we were able to understand the superconducting critical temperatures obtained from the dimer model by means of a competition between geometric frustration and interaction induced spin fluctuations. Since the resulting critical temperatures did not follow the experimentally measured values or even trends we moved on to the more elaborate molecule model which in contrast also showed the exotic  $s+d_{x^2-y^2}$  gap symmetry as solution. Moreover, our study underlined the proximity of  $s+d_{x^2-y^2}$  and  $d_{xy}$  symmetry in the eight organic superconductors studied. Unfortunately, it was not possible to reach low enough temperatures in order to determine superconducting critical temperatures of those organic superconductors within the molecule model because of diverging antiferromagnetic correlation length which introduces numerical errors to our calculations.

Due to the novelty of the multi-orbital TPSC approach we dedicated chap. 6 to a thorough benchmark of the method and a detailed comparison to DMFT which represents the exact solution of the Hubbard in infinite dimensions. The major observations from this comparison are that TPSC and DMFT seem to produce the same local physics in the region of intermediate coupling but the TPSC ansatz for the irreducible spin vertex seems insufficient to capture certain aspects of multi-orbital interaction. This becomes obvious in the TPSC double occupations but possibly also in the tendency of negative charge vertices. Fortunately, those undesired features from TPSC can be circumvented

to some extent and there are promising improvements that have to be tested in future work.

After this toy model study we turned to a real material calculation in chap. 7, namely LiFeAs. This iron-based superconductor served as a perfect testing ground for the non-local dynamical multi-orbital TPSC approach since ARPES measurements suggest momentum-dependent correlation effects that cannot be reproduced within DFT+DMFT. Indeed, our DFT+TPSC study was able to produce the so-called “red-blue shift” which described the overestimation of the size of electron and hole pockets from DFT in many classes of iron-based superconductors. Additionally, we were able to reproduce the DMFT Fermi surface result by taking the local limit of TPSC and also certain aspects of quasi-particle lifetime measurements. The flower-like shape of spectral weight around the  $\Gamma$  point that is both observed in TPSC and ARPES measurements is crucial for certain strong coupling superconducting pairing mechanisms and thus TPSC supports the idea that momentum-dependent spin fluctuations might be important for fully understanding the low temperature physics of iron-based superconductors.

This last real material study demonstrates the non-trivial effects that can be generated by treating non-local and dynamical self-energy effects on equal footing. Nevertheless, we have to keep in mind that our toy model study revealed some non-negligible error sources within the method.

While the spin vertex ansatz in the single-band TPSC starts to fail only when antiferromagnetic correlations are too large we see that the multi-orbital ansatz ignores aspects of the Hund’s coupling for all interaction strengths. For this reason we plan to replace the TPSC spin vertex ansatz by directly taking double occupations from different methods such as DMFT. A similar procedure was already suggested in Ref. [207]. It is also interesting to check whether such an improved scheme could also fix the problem of negative charge vertices that appear in some interaction parameter regions.

Since TPSC is only valid in the weak to intermediate coupling regime one needs further extensions to incorporate the physics of strong coupling. The key for resolving Hubbard band features calls for dynamical and thus frequency-dependent spin and charge vertices [163].

Possible extensions are for example the TPSC+ approach that was recently developed for the single-band case [148]. This ansatz is capable of introducing dynamical vertex corrections that are not present in the original TPSC formulation. Another way to access the realm of intermediate-to-strong coupling is by combining TPSC and DMFT in a similar fashion as already suggested for GW+DMFT [182, 183], namely by taking the non-local self-energy from TPSC and the local part from DMFT. This new scheme would treat low-energy spin fluctuations that are not incorporated in the GW+DMFT approach.

Other combinations such as GW+TPSC are also interesting when high-energy charge fluctuations and low-energy spin fluctuations have to be taken account of.

Another yet open field of study is the inclusion of the transversal particle-hole channel that was left aside in this thesis due to the insufficient number of sum rules. This problem would be also solved if one takes the double occupations from a different many-body method.

So far, we only considered static screening of the Coulomb repulsion but as reported in [52, 68, 106] the inclusion of dynamical screening effects can lead to further important features of the spectral function.

Regarding the specific case of LiFeAs it would be also interesting to see how a three-dimensional calculation would influence the results in how far the TPSC could resolve the open problems that appear within DFT away from the  $k_z = 0$ -plane [10].

---

In conclusion, we have presented studies with the TPSC method which revealed that this many-body approach contains promising features regarding the description of interacting electrons in correlated materials. It is thus an auspicious path to follow in the future of method development; especially due to its efficient implementation possibilities.

## APPENDIX A

### Transversal particle-hole channel for multi-orbital TPSC

While we presented a detailed derivation of multi-orbital TPSC in the longitudinal particle-hole channel in sec. 5.6, we show in this appendix the TPSC equations in the transversal particle-hole channel.

The procedure is similar to the one presented for the multi-site case in sec. 5.1.9 and we introduce artificial fields

$$(A.1) \quad \Phi_{\alpha\beta} = \begin{pmatrix} 0 & \phi^-(1, 2) \\ \phi^+(1, 2) & 0 \end{pmatrix}$$

that appear in the grand canonical partition function

$$(A.2) \quad Z[\Phi] = \left\langle T_\tau e^{-c_{\bar{\alpha},\uparrow}^\dagger(\bar{1})\phi_{\bar{\alpha}\bar{\beta}}^-(\bar{1},\bar{2})c_{\bar{\beta},\downarrow}(\bar{2}) - c_{\bar{\alpha},\downarrow}^\dagger(\bar{1})\phi_{\bar{\alpha}\bar{\beta}}^+(\bar{1},\bar{2})c_{\bar{\beta},\uparrow}(\bar{2})} \right\rangle.$$

We define the spin-space Green's function

$$(A.3) \quad \mathbf{G}_{\alpha\beta}^{\sigma\sigma'}(1, 2)_\Phi := -\langle T_\tau c_{\alpha,\sigma}(1)c_{\beta,\sigma'}^\dagger(2) \rangle_\Phi.$$

which is generated via functional differentiation,

$$(A.4) \quad -\frac{\delta \ln Z[\Phi]}{\delta \Phi_{\beta\alpha}(2, 1)} = \begin{pmatrix} 0 & \mathbf{G}_{\alpha\beta}^{\uparrow\downarrow}(1, 2)_\Phi \\ \mathbf{G}_{\alpha\beta}^{\downarrow\uparrow}(1, 2)_\Phi & 0 \end{pmatrix},$$

with the previously defined matrix-valued derivative

$$(A.5) \quad \frac{\delta}{\delta \Phi_{\nu\epsilon}(4, 5)} := \begin{pmatrix} 0 & \frac{\delta}{\delta \phi_{\nu\epsilon}^+(4, 5)} \\ \frac{\delta}{\delta \phi_{\nu\epsilon}^-(4, 5)} & 0 \end{pmatrix}.$$

One derives the matrix Dyson equation

$$(A.6) \quad \mathbf{G}^{-1}(1, 2)_\Phi = (\mathbf{G}^0)^{-1}(1, 2) - \Sigma(1, 2)_\Phi - \Phi,$$

in the same manner as in sec. 5.1.9 and finds the self-energy equation

$$\begin{aligned} & \Sigma_{\alpha\bar{\lambda}}(1, \bar{3})_\Phi \mathbf{G}_{\bar{\lambda}\gamma}(\bar{3}, 2)_\Phi \\ &= -\sum_{\beta} U_{\beta\alpha} \begin{pmatrix} \langle T_\tau n_{\beta,\downarrow}(1)c_{\alpha,\uparrow}(1)c_{\gamma,\uparrow}^\dagger(2) \rangle_\Phi & \langle T_\tau n_{\beta,\downarrow}(1)c_{\alpha,\uparrow}(1)c_{\gamma,\downarrow}^\dagger(2) \rangle_\Phi \\ \langle T_\tau n_{\beta,\uparrow}(1)c_{\alpha,\downarrow}(1)c_{\gamma,\uparrow}^\dagger(2) \rangle_\Phi & \langle T_\tau n_{\beta,\uparrow}(1)c_{\alpha,\downarrow}(1)c_{\gamma,\downarrow}^\dagger(2) \rangle_\Phi \end{pmatrix} \\ & - \sum_{\substack{\beta \\ \beta \neq \alpha}} (U_{\beta\alpha} - J_{\beta\alpha}) \begin{pmatrix} \langle T_\tau n_{\beta,\uparrow}(1)c_{\alpha,\uparrow}(1)c_{\gamma,\uparrow}^\dagger(2) \rangle_\Phi & \langle T_\tau n_{\beta,\uparrow}(1)c_{\alpha,\uparrow}(1)c_{\gamma,\downarrow}^\dagger(2) \rangle_\Phi \\ \langle T_\tau n_{\beta,\downarrow}(1)c_{\alpha,\downarrow}(1)c_{\gamma,\uparrow}^\dagger(2) \rangle_\Phi & \langle T_\tau n_{\beta,\downarrow}(1)c_{\alpha,\downarrow}(1)c_{\gamma,\downarrow}^\dagger(2) \rangle_\Phi \end{pmatrix} \\ & + \sum_{\substack{\beta \\ \beta \neq \alpha}} J_{\beta\alpha} \begin{pmatrix} \langle T_\tau c_{\beta,\downarrow}^\dagger(1)c_{\beta,\uparrow}(1)c_{\alpha,\downarrow}(1)c_{\gamma,\uparrow}^\dagger(2) \rangle_\Phi & \langle T_\tau c_{\beta,\downarrow}^\dagger(1)c_{\beta,\uparrow}(1)c_{\alpha,\downarrow}(1)c_{\gamma,\downarrow}^\dagger(2) \rangle_\Phi \\ \langle c_{\beta,\uparrow}^\dagger(1)c_{\beta,\downarrow}(1)c_{\alpha,\uparrow}(1)c_{\gamma,\uparrow}^\dagger(2) \rangle_\Phi & \langle T_\tau c_{\beta,\uparrow}^\dagger(1)c_{\beta,\downarrow}(1)c_{\alpha,\uparrow}(1)c_{\gamma,\downarrow}^\dagger(2) \rangle_\Phi \end{pmatrix} \end{aligned}$$

(A.7)

$$+ \sum_{\substack{\beta \\ \beta \neq \gamma}} J_{\beta\alpha} \left( \begin{array}{c} \langle T_\tau c_{\alpha,\downarrow}^\dagger(1^{++}) c_{\beta,\uparrow}(1^+) c_{\beta,\downarrow}(1) c_{\gamma,\uparrow}^\dagger(2) \rangle_{\Phi} \\ \langle T_\tau c_{\alpha,\uparrow}^\dagger(1^{++}) c_{\beta,\downarrow}(1^+) c_{\beta,\uparrow}(1) c_{\gamma,\uparrow}^\dagger(2) \rangle_{\Phi} \end{array} \begin{array}{c} \langle T_\tau c_{\alpha,\downarrow}^\dagger(1^{++}) c_{\beta,\uparrow}(1^+) c_{\beta,\downarrow}(1) c_{\gamma,\downarrow}^\dagger(2) \rangle_{\Phi} \\ \langle T_\tau c_{\alpha,\uparrow}^\dagger(1^{++}) c_{\beta,\downarrow}(1^+) c_{\beta,\uparrow}(1) c_{\gamma,\downarrow}^\dagger(2) \rangle_{\Phi} \end{array} \right).$$

From the matrix equation

(A.8)
$$\mathbf{G}_{\alpha\bar{\beta}}(1, \bar{3}) (\mathbf{G}^{-1})_{\bar{\beta}\nu}(\bar{3}, 2) = \mathbf{I} \delta(1-2) \delta_{\alpha,\nu},$$

we derive via functional differentiation in the same way as in sec. 5.1.9 the two non-vanishing generalized susceptibilities

$$(A.9) \quad \frac{\delta \mathbf{G}_{\alpha\zeta}^{\downarrow\uparrow}(1, 6)_{\Phi}}{\delta \phi_{\nu\epsilon}^+(4, 5)} \Big|_{\Phi=0} = \mathbf{G}_{\alpha\nu}^{\downarrow\downarrow}(1, 4) \mathbf{G}_{\epsilon\zeta}^{\uparrow\uparrow}(5, 6) + \mathbf{G}_{\alpha\bar{\beta}}^{\downarrow\downarrow}(1, \bar{3}) \frac{\delta \Sigma_{\bar{\beta}\gamma}^{\downarrow\uparrow}(\bar{3}, \bar{2})_{\Phi}}{\delta \mathbf{G}_{\bar{\rho}\lambda}^{21}(\bar{7}, \bar{8})_{\Phi}} \frac{\delta \mathbf{G}_{\bar{\rho}\lambda}^{21}(\bar{7}, \bar{8})_{\Phi}}{\delta \phi_{\nu\epsilon}^+(4, 5)} \Big|_{\Phi=0} \mathbf{G}_{\gamma\zeta}^{\uparrow\uparrow}(\bar{2}, 6)$$

(A.10)
$$= - \left\langle T_\tau c_{\zeta,\uparrow}^\dagger(6) c_{\alpha,\downarrow}(1) c_{\nu,\downarrow}^\dagger(4) c_{\epsilon,\uparrow}(5) \right\rangle,$$

$$(A.11) \quad \frac{\delta \mathbf{G}_{\alpha\zeta}^{\uparrow\downarrow}(1, 6)_{\Phi}}{\delta \phi_{\nu\epsilon}^-(4, 5)} \Big|_{\Phi=0} = \mathbf{G}_{\alpha\nu}^{\uparrow\uparrow}(1, 4) \mathbf{G}_{\epsilon\zeta}^{\downarrow\downarrow}(5, 6) + \mathbf{G}_{\alpha\bar{\beta}}^{\uparrow\uparrow}(1, \bar{3}) \frac{\delta \Sigma_{\bar{\beta}\gamma}^{\uparrow\downarrow}(\bar{3}, \bar{2})_{\Phi}}{\delta \mathbf{G}_{\bar{\rho}\lambda}^{12}(\bar{7}, \bar{8})_{\Phi}} \frac{\delta \mathbf{G}_{\bar{\rho}\lambda}^{\uparrow\downarrow}(\bar{7}, \bar{8})_{\Phi}}{\delta \phi_{\nu\epsilon}^-(4, 5)} \Big|_{\Phi=0} \mathbf{G}_{\gamma\zeta}^{\downarrow\downarrow}(\bar{2}, 6)$$

(A.12)
$$= - \left\langle T_\tau c_{\zeta,\downarrow}^\dagger(6) c_{\alpha,\uparrow}(1) c_{\nu,\uparrow}^\dagger(4) c_{\epsilon,\downarrow}(5) \right\rangle.$$

### A.1. Self-energy and susceptibilities: Transverse channel

Starting from the implicit equation for the self-energy  $\Sigma$  (eq. (A.7)) we can see that the Hamiltonian is spin conserving and obtain in the limit  $\Phi = 0$  the expression

$$(A.13) \quad \begin{aligned} & \Sigma_{\alpha\bar{\beta}}(1, \bar{3}) \mathbf{G}_{\bar{\beta}\nu}(\bar{3}, 2) \\ &= - \sum_{\beta} U_{\beta\alpha} \begin{pmatrix} \langle T_\tau n_{\beta,\downarrow}(1) c_{\alpha,\uparrow}(1) c_{\nu,\uparrow}^\dagger(2) \rangle & 0 \\ 0 & \langle T_\tau n_{\beta,\uparrow}(1) c_{\alpha,\downarrow}(1) c_{\nu,\downarrow}^\dagger(2) \rangle \end{pmatrix} \\ & \quad - \sum_{\substack{\beta \\ \beta \neq \alpha}} (U_{\beta\alpha} - J_{\beta\alpha}) \begin{pmatrix} \langle T_\tau n_{\beta,\uparrow}(1) c_{\alpha,\uparrow}(1) c_{\nu,\uparrow}^\dagger(2) \rangle & 0 \\ 0 & \langle T_\tau n_{\beta,\downarrow}(1) c_{\alpha,\downarrow}(1) c_{\nu,\downarrow}^\dagger(2) \rangle \end{pmatrix} \\ & \quad + \sum_{\substack{\beta \\ \beta \neq \alpha}} J_{\beta\alpha} \begin{pmatrix} \langle T_\tau c_{\beta,\downarrow}^\dagger(1) c_{\beta,\uparrow}(1) c_{\alpha,\downarrow}(1) c_{\nu,\uparrow}^\dagger(2) \rangle & 0 \\ 0 & \langle T_\tau c_{\beta,\uparrow}^\dagger(1) c_{\beta,\downarrow}(1) c_{\alpha,\uparrow}(1) c_{\nu,\downarrow}^\dagger(2) \rangle \end{pmatrix} \\ & \quad + \sum_{\substack{\beta \\ \beta \neq \alpha}} J_{\beta\alpha} \begin{pmatrix} \langle T_\tau c_{\alpha,\downarrow}^\dagger(1) c_{\beta,\uparrow}(1) c_{\beta,\downarrow}(1) c_{\nu,\uparrow}^\dagger(2) \rangle & 0 \\ 0 & \langle T_\tau c_{\alpha,\uparrow}^\dagger(1) c_{\beta,\downarrow}(1) c_{\beta,\uparrow}(1) c_{\nu,\downarrow}^\dagger(2) \rangle \end{pmatrix}. \end{aligned}$$

From this we immediately see that the self-energy  $\Sigma$  and Green's function  $\mathbf{G}$  is diagonal in spin space. We use now our knowledge from the longitudinal channel to express the four-point expectation value that is scaled by  $U_{\beta\alpha} - J_{\beta\alpha}$  in eq. (A.13) in terms of the

spin and charge susceptibilities (see eq. (5.344)). Thus, by multiplying eq. (A.13) with  $(\mathbf{G}^{-1})_{\bar{\nu}\gamma}(\bar{3}, 2)$  and integrating over all internal degrees of freedom we find

$$\begin{aligned}
 & \Sigma_{\alpha\gamma}(1, 2) \\
 &= - \sum_{\beta} U_{\beta\alpha} \begin{pmatrix} \langle T_{\tau} n_{\beta,\downarrow}(1) c_{\alpha,\uparrow}(1) c_{\bar{\nu},\uparrow}^{\dagger}(\bar{3}) \rangle & 0 \\ 0 & \langle T_{\tau} n_{\beta,\uparrow}(1) c_{\alpha,\downarrow}(1) c_{\bar{\nu},\downarrow}^{\dagger}(\bar{3}) \rangle \end{pmatrix} (\mathbf{G}^{-1})_{\bar{\nu}\gamma}(\bar{3}, 2) \\
 & - \sum_{\substack{\beta \\ \beta \neq \alpha}} (U_{\beta\alpha} - J_{\beta\alpha}) \left[ -\frac{1}{4} \left( \chi_{\bar{\nu}\alpha\beta\beta}^{ch}(1, \bar{3}; 1) + \chi_{\bar{\nu}\alpha\beta\beta}^{sp}(1, \bar{3}; 1) \right) (\mathbf{G}^{-1})_{\bar{\nu}\gamma}(\bar{3}, 2) \right. \\
 & \quad \left. - \langle n_{\alpha,\sigma}(1) \rangle \delta_{\alpha,\gamma} \mathbf{I} \delta(1-2) \right] \\
 & + \sum_{\substack{\beta \\ \beta \neq \alpha}} J_{\beta\alpha} \begin{pmatrix} \langle T_{\tau} c_{\beta,\downarrow}^{\dagger}(1) c_{\beta,\uparrow}(1) c_{\alpha,\downarrow}(1) c_{\bar{\nu},\uparrow}^{\dagger}(\bar{3}) \rangle & 0 \\ 0 & \langle T_{\tau} c_{\beta,\uparrow}^{\dagger}(1) c_{\beta,\downarrow}(1) c_{\alpha,\uparrow}(1) c_{\bar{\nu},\downarrow}^{\dagger}(\bar{3}) \rangle \end{pmatrix} (\mathbf{G}^{-1})_{\bar{\nu}\gamma}(\bar{3}, 2) \\
 & (A.14) \\
 & + \sum_{\substack{\beta \\ \beta \neq \alpha}} J_{\beta\alpha} \begin{pmatrix} \langle T_{\tau} c_{\alpha,\downarrow}^{\dagger}(1) c_{\beta,\uparrow}(1) c_{\beta,\downarrow}(1) c_{\bar{\nu},\uparrow}^{\dagger}(\bar{3}) \rangle & 0 \\ 0 & \langle T_{\tau} c_{\alpha,\uparrow}^{\dagger}(1) c_{\beta,\downarrow}(1) c_{\beta,\uparrow}(1) c_{\bar{\nu},\downarrow}^{\dagger}(\bar{3}) \rangle \end{pmatrix} (\mathbf{G}^{-1})_{\bar{\nu}\gamma}(\bar{3}, 2),
 \end{aligned}$$

which can be represented in terms of generalized susceptibilities as

$$\begin{aligned}
 \Sigma_{\alpha\gamma}(1, 2) &= \left[ - \sum_{\beta} U_{\beta\alpha} \begin{pmatrix} \left. \frac{\delta \mathbf{G}_{\beta\bar{\nu}}^{\downarrow\uparrow}(1, \bar{3})_{\Phi}}{\delta \phi_{\beta\alpha}^{+}(1^{+}, 1)} \right|_{\Phi=0} & 0 \\ 0 & \left. \frac{\delta \mathbf{G}_{\beta\bar{\nu}}^{\uparrow\downarrow}(1, \bar{3})_{\Phi}}{\delta \phi_{\beta\alpha}^{-}(1^{+}, 1)} \right|_{\Phi=0} \end{pmatrix} \right. \\
 & - \sum_{\substack{\beta \\ \beta \neq \alpha}} J_{\beta\alpha} \begin{pmatrix} \left. \frac{\delta \mathbf{G}_{\alpha\bar{\nu}}^{\downarrow\uparrow}(1, \bar{3})_{\Phi}}{\delta \phi_{\beta\beta}^{+}(1^{+}, 1)} \right|_{\Phi=0} & 0 \\ 0 & \left. \frac{\delta \mathbf{G}_{\alpha\bar{\nu}}^{\uparrow\downarrow}(1, \bar{3})_{\Phi}}{\delta \phi_{\beta\beta}^{-}(1^{+}, 1)} \right|_{\Phi=0} \end{pmatrix} \\
 & - \sum_{\substack{\beta \\ \beta \neq \alpha}} J_{\beta\alpha} \begin{pmatrix} \left. \frac{\delta \mathbf{G}_{\beta\bar{\nu}}^{\downarrow\uparrow}(1, \bar{3})_{\Phi}}{\delta \phi_{\alpha\beta}^{+}(1^{+}, 1)} \right|_{\Phi=0} & 0 \\ 0 & \left. \frac{\delta \mathbf{G}_{\beta\bar{\nu}}^{\uparrow\downarrow}(1, \bar{3})_{\Phi}}{\delta \phi_{\alpha\beta}^{-}(1^{+}, 1)} \right|_{\Phi=0} \end{pmatrix} \left. \right] (\mathbf{G}^{-1})_{\bar{\nu}\gamma}(\bar{3}, 2) \\
 & - \sum_{\substack{\beta \\ \beta \neq \alpha}} (U_{\beta\alpha} - J_{\beta\alpha}) \left[ -\frac{1}{4} \left( \chi_{\bar{\nu}\alpha\beta\beta}^{ch}(1, \bar{3}; 1) + \chi_{\bar{\nu}\alpha\beta\beta}^{sp}(1, \bar{3}; 1) \right) (\mathbf{G}^{-1})_{\bar{\nu}\gamma}(\bar{3}, 2) \right. \\
 & \quad \left. - \langle n_{\alpha,\sigma}(1) \rangle \delta_{\alpha,\gamma} \mathbf{I} \delta(1-2) \right].
 \end{aligned}
 \tag{A.15}$$

Next, one can use the Bethe-Salpeter equations (eq. (A.9) and (A.11)) to further evaluate

$$\begin{aligned}
 \Sigma_{\alpha\gamma}^{\sigma\sigma}(1, 2) &= \sum_{\eta} U_{\eta\alpha} \mathbf{G}_{\eta\eta}^{-\sigma-\sigma}(1, 1^{+}) \mathbf{G}_{\alpha\bar{\nu}}^{\sigma\sigma}(1, \bar{3}) (\mathbf{G}^{-1})_{\bar{\nu}\gamma}^{\sigma\sigma}(\bar{3}, 2) \\
 & + \sum_{\eta} U_{\eta\alpha} \mathbf{G}_{\eta\bar{\beta}}^{-\sigma-\sigma}(1, \bar{9}) \left. \frac{\delta \Sigma_{\beta\bar{\gamma}}^{-\sigma\sigma}(\bar{9}, \bar{4})_{\Phi}}{\delta \mathbf{G}_{\bar{\rho}\bar{\lambda}}^{-\sigma\sigma}(\bar{7}, \bar{8})_{\Phi}} \frac{\delta \mathbf{G}_{\bar{\rho}\bar{\lambda}}^{-\sigma\sigma}(\bar{7}, \bar{8})_{\Phi}}{\delta \phi_{\eta\alpha}^{+}(1^{+}, 1)} \right|_{\Phi=0} \mathbf{G}_{\bar{\gamma}\bar{\nu}}^{\sigma\sigma}(\bar{4}, \bar{3}) (\mathbf{G}^{-1})_{\bar{\nu}\gamma}^{\sigma\sigma}(\bar{3}, 2)
 \end{aligned}$$

$$\begin{aligned}
 & - \sum_{\substack{\eta \\ \eta \neq \alpha}} (U_{\eta\alpha} - J_{\eta\alpha}) \left[ - \frac{1}{4} \left( \chi_{\bar{\gamma}\alpha\eta\eta}^{ch}(1, \bar{3}; 1) + \chi_{\bar{\gamma}\alpha\eta\eta}^{sp}(1, \bar{3}; 1) \right) (\mathbf{G}^{-1})_{\bar{\gamma}\gamma, \sigma}^{\sigma\sigma}(\bar{3}, 2) \right. \\
 & \quad \left. - \langle n_{\eta, \sigma}(1) \rangle \delta_{\alpha, \gamma} \delta(1-2) \right] \\
 & + \sum_{\substack{\eta \\ \eta \neq \alpha}} J_{\eta\alpha} \mathbf{G}_{\alpha\eta}^{-\sigma-\sigma}(1, 1^+) \mathbf{G}_{\eta\bar{\nu}}^{\sigma\sigma}(1, \bar{3}) (\mathbf{G}^{-1})_{\bar{\nu}\gamma}^{\sigma\sigma}(\bar{3}, 2) \\
 & + \sum_{\substack{\eta \\ \eta \neq \alpha}} J_{\eta\alpha} \mathbf{G}_{\alpha\bar{\beta}}^{-\sigma-\sigma}(1, \bar{9}) \frac{\delta \Sigma_{\bar{\beta}\bar{\gamma}}^{-\sigma\sigma}(\bar{9}, \bar{4})_{\Phi}}{\delta \mathbf{G}_{\bar{\rho}\bar{\lambda}}^{-\sigma\sigma}(\bar{7}, \bar{8})_{\Phi}} \frac{\delta \mathbf{G}_{\bar{\rho}\bar{\lambda}}^{-\sigma\sigma}(\bar{7}, \bar{8})_{\Phi}}{\delta \phi_{\eta\eta}^+(1^+, 1)} \Big|_{\Phi=0} \mathbf{G}_{\bar{\gamma}\bar{\nu}}^{\sigma\sigma}(\bar{4}, \bar{3}) (\mathbf{G}^{-1})_{\bar{\nu}\gamma}^{\sigma\sigma}(\bar{3}, 2) \\
 & + \sum_{\substack{\eta \\ \eta \neq \alpha}} J_{\eta\alpha} \mathbf{G}_{\eta\alpha}^{-\sigma-\sigma}(1, 1^+) \mathbf{G}_{\eta\bar{\nu}}^{\sigma\sigma}(1, \bar{3}) (\mathbf{G}^{-1})_{\bar{\nu}\gamma}^{\sigma\sigma}(\bar{3}, 2) \\
 & (A.16) \\
 & + \sum_{\substack{\eta \\ \eta \neq \alpha}} J_{\eta\alpha} \mathbf{G}_{\eta\bar{\beta}}^{-\sigma-\sigma}(1, \bar{9}) \frac{\delta \Sigma_{\bar{\beta}\bar{\gamma}}^{-\sigma\sigma}(\bar{9}, \bar{4})_{\Phi}}{\delta \mathbf{G}_{\bar{\rho}\bar{\lambda}}^{-\sigma\sigma}(\bar{7}, \bar{8})_{\Phi}} \frac{\delta \mathbf{G}_{\bar{\rho}\bar{\lambda}}^{-\sigma\sigma}(\bar{7}, \bar{8})_{\Phi}}{\delta \phi_{\alpha\eta}^+(1^+, 1)} \Big|_{\Phi=0} \mathbf{G}_{\bar{\gamma}\bar{\nu}}^{\sigma\sigma}(\bar{4}, \bar{3}) (\mathbf{G}^{-1})_{\bar{\nu}\gamma}^{\sigma\sigma}(\bar{3}, 2).
 \end{aligned}$$

We can now evaluate the matrix product with the inverse spin Green's function and get

$$\begin{aligned}
 \Sigma_{\alpha\gamma}^{\sigma\sigma}(1, 2) & = \sum_{\eta} U_{\eta\alpha} \mathbf{G}_{\eta\eta}^{-\sigma-\sigma}(1, 1^+) \delta_{\alpha, \gamma} \delta(1-2) \\
 & + \sum_{\eta} U_{\eta\alpha} \mathbf{G}_{\eta\bar{\beta}}^{-\sigma-\sigma}(1, \bar{9}) \frac{\delta \Sigma_{\bar{\beta}\bar{\gamma}}^{-\sigma\sigma}(\bar{9}, 2)_{\Phi}}{\delta \mathbf{G}_{\bar{\rho}\bar{\lambda}}^{-\sigma\sigma}(\bar{7}, \bar{8})_{\Phi}} \frac{\delta \mathbf{G}_{\bar{\rho}\bar{\lambda}}^{-\sigma\sigma}(\bar{7}, \bar{8})_{\Phi}}{\delta \phi_{\eta\alpha}^+(1^+, 1)} \Big|_{\Phi=0} \\
 & - \sum_{\substack{\eta \\ \eta \neq \alpha}} (U_{\eta\alpha} - J_{\eta\alpha}) \left[ - \frac{1}{4} \left( \chi_{\bar{\zeta}\alpha\eta\eta}^{ch}(1, \bar{3}; 1) + \chi_{\bar{\zeta}\alpha\eta\eta}^{sp}(1, \bar{3}; 1) \right) (\mathbf{G}^{-1})_{\bar{\zeta}\gamma, \sigma}^{\sigma\sigma}(\bar{3}, 2) \right. \\
 & \quad \left. - \langle n_{\eta, \sigma}(1) \rangle \delta_{\alpha, \gamma} \delta(1-2) \right] \\
 & + \sum_{\substack{\eta \\ \eta \neq \alpha}} J_{\eta\alpha} \mathbf{G}_{\alpha\eta}^{-\sigma-\sigma}(1, 1^+) \delta_{\eta, \gamma} \delta(1-2) \\
 & + \sum_{\substack{\eta \\ \eta \neq \alpha}} J_{\eta\alpha} \mathbf{G}_{\alpha\bar{\beta}}^{-\sigma-\sigma}(1, \bar{9}) \frac{\delta \Sigma_{\bar{\beta}\bar{\gamma}}^{-\sigma\sigma}(\bar{9}, 2)_{\Phi}}{\delta \mathbf{G}_{\bar{\rho}\bar{\lambda}}^{-\sigma\sigma}(\bar{7}, \bar{8})_{\Phi}} \frac{\delta \mathbf{G}_{\bar{\rho}\bar{\lambda}}^{-\sigma\sigma}(\bar{7}, \bar{8})_{\Phi}}{\delta \phi_{\eta\eta}^+(1^+, 1)} \Big|_{\Phi=0} \\
 & + \sum_{\substack{\eta \\ \eta \neq \alpha}} J_{\eta\alpha} \mathbf{G}_{\eta\alpha}^{-\sigma-\sigma}(1, 1^+) \delta_{\eta, \gamma} \delta(1-2) \\
 & (A.17) \\
 & + \sum_{\substack{\eta \\ \eta \neq \alpha}} J_{\eta\alpha} \mathbf{G}_{\eta\bar{\beta}}^{-\sigma-\sigma}(1, \bar{9}) \frac{\delta \Sigma_{\bar{\beta}\bar{\gamma}}^{-\sigma\sigma}(\bar{9}, 2)_{\Phi}}{\delta \mathbf{G}_{\bar{\rho}\bar{\lambda}}^{-\sigma\sigma}(\bar{7}, \bar{8})_{\Phi}} \frac{\delta \mathbf{G}_{\bar{\rho}\bar{\lambda}}^{-\sigma\sigma}(\bar{7}, \bar{8})_{\Phi}}{\delta \phi_{\alpha\eta}^+(1^+, 1)} \Big|_{\Phi=0}.
 \end{aligned}$$

We see now that the equation can be related to the spin susceptibilities via eq. (5.203) and we get

$$\begin{aligned}
\Sigma_{\alpha\gamma}(1, 2) &= \sum_{\eta} U_{\eta\alpha} \mathbf{G}_{\eta\eta}^{-\sigma-\sigma}(1, 1^+) \delta_{\alpha,\gamma} \delta(1-2) \\
&+ \sum_{\eta} \frac{U_{\eta\alpha}}{4} \mathbf{G}_{\eta\beta}^{-\sigma-\sigma}(1, \bar{9}) \Gamma_{\gamma\beta\lambda\bar{\rho}}^{sp}(\bar{9}, 2; \bar{7}, \bar{8}) 2\chi_{\lambda\bar{\rho}\alpha\eta}^{sp}(\bar{7}, \bar{8}; 1) \\
&+ \sum_{\substack{\eta \\ \eta \neq \alpha}} \frac{U_{\eta\alpha} - J_{\eta\alpha}}{4} \left[ G_{\alpha\beta}(1, \bar{3}) \left( \Gamma_{\gamma\beta\lambda\bar{\rho}}^{ch}(\bar{3}, 2; \bar{7}, \bar{8}) \chi_{\lambda\bar{\rho}\eta\eta}^{ch}(\bar{7}, \bar{8}; 1) \right. \right. \\
&\quad \left. \left. - \Gamma_{\gamma\beta\lambda\bar{\rho}}^{sp}(\bar{3}, 2; \bar{7}, \bar{8}) \chi_{\lambda\bar{\rho}\eta\eta}^{sp}(\bar{7}, \bar{8}; 1) \right) \right. \\
&\quad \left. + 4 \left( \langle n_{\eta,\sigma}(1) \rangle \delta_{\alpha,\gamma} - \langle n_{\alpha\gamma,\sigma}(1) \rangle \delta_{\eta,\gamma} \right) \delta(1-2) \right] \\
&+ \sum_{\substack{\eta \\ \eta \neq \alpha}} J_{\eta\alpha} \mathbf{G}_{\alpha\eta}^{-\sigma-\sigma}(1, 1^+) \delta_{\eta,\gamma} \delta(1-2) \\
&+ \sum_{\substack{\eta \\ \eta \neq \alpha}} \frac{J_{\eta\alpha}}{4} \mathbf{G}_{\alpha\beta}^{-\sigma-\sigma}(1, \bar{9}) \Gamma_{\gamma\beta\lambda\bar{\rho}}^{sp}(\bar{9}, 2; \bar{7}, \bar{8}) 2\chi_{\lambda\bar{\rho}\eta\eta}^{sp}(\bar{7}, \bar{8}; 1) \\
&+ \sum_{\substack{\eta \\ \eta \neq \alpha}} J_{\eta\alpha} \mathbf{G}_{\eta\alpha}^{-\sigma-\sigma}(1, 1^+) \delta_{\eta,\gamma} \delta(1-2) \\
\text{(A.18)} \quad &+ \sum_{\substack{\eta \\ \eta \neq \alpha}} \frac{J_{\eta\alpha}}{4} \mathbf{G}_{\eta\beta}^{-\sigma-\sigma}(1, \bar{9}) \Gamma_{\gamma\beta\lambda\bar{\rho}}^{sp}(\bar{9}, 2; \bar{7}, \bar{8}) 2\chi_{\lambda\bar{\rho}\eta\alpha}^{sp}(\bar{7}, \bar{8}; 1).
\end{aligned}$$

As expected we recover the same Hartree-Fock term as in the longitudinal channel (see eq. (5.347)) but a different second order part that can be regrouped to

$$\begin{aligned}
\Sigma_{\alpha\gamma}^{\sigma\sigma}(1, 2) &= \sum_{\eta} U_{\eta\alpha} \langle n_{\eta,-\sigma}(1) \rangle \delta_{\alpha,\gamma} \delta(1-2) \\
&+ \sum_{\eta \neq \alpha} (U_{\eta\alpha} - J_{\eta\alpha}) \left( \langle n_{\eta,\sigma}(1) \rangle \delta_{\alpha,\gamma} - \langle n_{\alpha\gamma,\sigma}(1) \rangle \delta_{\eta,\gamma} \right) \delta(1-2) \\
&+ \sum_{\eta \neq \alpha} J_{\eta\alpha} \left( \langle n_{\eta\alpha,-\sigma}(1) \rangle + \langle n_{\alpha\eta,-\sigma}(1) \rangle \right) \delta_{\eta,\gamma} \delta(1-2) \\
&+ \frac{1}{4} \Gamma_{\gamma\beta\lambda\bar{\rho}}^{sp}(\bar{9}, 2; \bar{7}, \bar{8}) \chi_{\lambda\bar{\rho}\eta\gamma}^{sp}(\bar{7}, \bar{8}; 1) \bar{\Gamma}_{\eta\gamma\alpha\bar{\epsilon}}^{sp,0} \mathbf{G}_{\bar{\epsilon}\beta}^{\sigma\sigma}(1, \bar{9}) \\
\text{(A.19)} \quad &+ \frac{1}{4} \Gamma_{\gamma\beta\lambda\bar{\rho}}^{ch}(\bar{9}, 2; \bar{7}, \bar{8}) \chi_{\lambda\bar{\rho}\eta\gamma}^{ch}(\bar{7}, \bar{8}; 1) \bar{\Gamma}_{\eta\gamma\alpha\bar{\epsilon}}^{ch,0} \mathbf{G}_{\bar{\epsilon}\beta}^{\sigma\sigma}(1, \bar{9}),
\end{aligned}$$

where we have defined unperturbed vertices

$$\text{(A.20)} \quad \bar{\Gamma}_{\alpha\beta\gamma\delta}^{sp,0} = \begin{cases} 2U_{\alpha\beta} & \alpha = \gamma, \beta = \delta \\ 3J_{\alpha\gamma} - U_{\alpha\gamma} & \alpha = \beta \neq \gamma = \delta \\ 2J_{\alpha\beta} & \alpha = \delta \neq \beta = \gamma \\ 0 & \text{else} \end{cases},$$

$$\text{(A.21)} \quad \bar{\Gamma}_{\alpha\beta\gamma\delta}^{ch,0} = \begin{cases} U_{\alpha\gamma} - J_{\alpha\gamma} & \alpha = \beta \neq \gamma = \delta \\ 0 & \text{else} \end{cases}.$$

## A.1. SELF-ENERGY AND SUSCEPTIBILITIES: TRANSVERSE CHANNEL

---

We see that the components of  $\bar{\Gamma}^{sp,0}$  are not as easily related to each other as was the case for the longitudinal counterpart  $\Gamma^{sp,0}$  (see eq. (5.349)). For this reason it is not possible to calculate the spin vertex as in the longitudinal channel (see also the discussion in sec. 5.6.10) from the local spin sum rules and the ansatz equation (5.386). Nevertheless, it is possible to construct the components of the spin vertex  $\Gamma^{sp}$  in the transversal channel from the bare spin vertex  $\bar{\Gamma}^{sp,0}$ . For example, under the assumption of Kanamori-Hubbard interaction interaction values  $U_{\alpha\beta}$ ,  $J_{\alpha\beta}$  we observe

$$(A.22) \quad \bar{\Gamma}_{\alpha\beta\alpha\beta}^{sp,0} = -\frac{4}{5}(5J - U) + \frac{6}{10}(2U)$$

$$(A.23) \quad \Rightarrow \bar{\Gamma}_{\alpha\beta\alpha\beta}^{sp} = -\frac{4}{5}\bar{\Gamma}_{\alpha\alpha\beta\beta}^{sp} + \frac{6}{10}\frac{1}{2}(\bar{\Gamma}_{\alpha\alpha\alpha\alpha}^{sp} + \bar{\Gamma}_{\beta\beta\beta\beta}^{sp}),$$

$$(A.24) \quad \bar{\Gamma}_{\alpha\beta\beta\alpha}^{sp,0} = \frac{2}{5}(5J - U) + \frac{1}{5}(2U)$$

$$(A.25) \quad \Rightarrow \bar{\Gamma}_{\alpha\beta\beta\alpha}^{sp} = \frac{2}{5}\bar{\Gamma}_{\alpha\alpha\beta\beta}^{sp} + \frac{1}{5}\frac{1}{2}(\bar{\Gamma}_{\alpha\alpha\alpha\alpha}^{sp} + \bar{\Gamma}_{\beta\beta\beta\beta}^{sp}).$$

## APPENDIX B

### Computational details

#### B.1. Matsubara functions

**B.1.1. Numerical implementation of the Matsubara sums.** In practical calculations one is limited to finite sums over Matsubara frequencies; let us assume that the number is  $N_{mats}$ . Nevertheless, it is possible to perform the sums with a small error by analytically calculating the tail contributions from the high frequency expansion:

$$\begin{aligned}
 (B.1) \quad & G_{\alpha\alpha,\sigma}(k, \tau) \\
 &= \frac{1}{\beta} \sum_{n=-\infty}^{\infty} G_{\alpha\alpha,\sigma}(k, i\omega_n) e^{-i\omega_n \tau} \\
 (B.2) \quad &= \frac{1}{\beta} \left( \sum_{n=-N_{mats}}^{N_{mats}} G_{\alpha\alpha,\sigma}(k, i\omega_n) e^{-i\omega_n \tau} + \sum_{n \notin [-N_{mats}, N_{mats}]} G_{\alpha\alpha,\sigma}(k, i\omega_n) e^{-i\omega_n \tau} \right) \\
 &\stackrel{(4.143)}{\approx} \frac{1}{\beta} \left[ \sum_{n=-N_{mats}}^{N_{mats}} G_{\alpha\alpha,\sigma}(k, i\omega_n) e^{-i\omega_n \tau} \right. \\
 (B.3) \quad &\left. + \sum_{n \notin [-N_{mats}, N_{mats}]} \left( \frac{1}{i\omega_n} + \frac{c_2(k)}{(i\omega_n)^2} + \frac{c_3(k)}{(i\omega_n)^3} + \frac{c_4(k)}{(i\omega_n)^4} \right) e^{-i\omega_n \tau} \right],
 \end{aligned}$$

where  $c_1(k), \dots, c_4(k)$  are real numbers that can be obtained by fitting the Green's function to the high frequency tail. The sum of those coefficients can be completed to  $n \in (\infty, \infty)$ ,

$$\begin{aligned}
 (B.4) \quad G_{\alpha\alpha,\sigma}(k, \tau) &\approx \frac{1}{\beta} \left[ \sum_{n=-N_{mats}}^{N_{mats}} \left( G_{\alpha\alpha,\sigma}(k, i\omega_n) - \left( \frac{1}{i\omega_n} + \frac{c_2(k)}{(i\omega_n)^2} + \frac{c_3(k)}{(i\omega_n)^3} + \frac{c_4(k)}{(i\omega_n)^4} \right) \right) e^{-i\omega_n \tau} \right. \\
 &\left. + \sum_{n=-\infty}^{\infty} \left( \frac{1}{i\omega_n} + \frac{c_2(k)}{(i\omega_n)^2} + \frac{c_3(k)}{(i\omega_n)^3} + \frac{c_4(k)}{(i\omega_n)^4} \right) e^{-i\omega_n \tau} \right].
 \end{aligned}$$

Analytical solutions for the infinite sums are available in terms of Euler polynomials that are implemented in symbolic manipulation programs such as Wolfram Mathematica or Maple. Those give in the limit of  $\lim_{\tau \rightarrow 0^-}$

$$\begin{aligned}
 (B.5) \quad & n_{\alpha,\sigma}(k) \\
 &\approx \frac{1}{2} - \frac{c_2(k)\tilde{\beta}}{4} + \frac{c_4(k)\tilde{\beta}^2}{48} + \frac{1}{\tilde{\beta}} \sum_{n=-N_{mats}}^{N_{mats}} \left( G_{\alpha\alpha,\sigma}(k, i\omega_n) + \frac{c_2(k)}{\omega_n^2} - \frac{c_4(k)}{\omega_n^4} \right).
 \end{aligned}$$

This result can now be inserted in the equation for the filling (eq. (4.241)).

The same strategy can be also used for calculating Matsubara sums of the local spin and charge sum rules. We first notice that symmetries of the irreducible susceptibility  $\chi^0$  (eq. (5.93) and (5.98)) allow us to rephrase the following expression for real-values

susceptibilities  $\chi$ :

$$(B.6) \quad \sum_{q, iq_m} \chi(q, iq_m) = \underbrace{\sum_q \chi(q, iq_0)}_{=:\chi^{loc}} + \sum_{q, m>0} \chi(q, iq_m) + \sum_{q, m<0} \chi(q, iq_m)$$

$$(B.7) \quad = \chi^{loc} + \sum_{q, m>0} \chi(q, iq_m) + \sum_{q, m<0} 2 [\mathbb{I} \pm \chi^0(q, iq_m)\Gamma]^{-1} \chi^0(q, iq_m)$$

$$(B.8) \quad = \chi^{loc} + \sum_{q, m>0} \chi(q, iq_m) + \sum_{q, m>0} 2 [\mathbb{I} \pm \chi^0(q, -iq_m)\Gamma]^{-1} \chi^0(q, -iq_m)$$

$$(B.9) \quad = \chi^{loc} + \sum_{q, m>0} \chi(q, iq_m) + \sum_{q, m>0} 2 [\mathbb{I} \pm (\chi^0)^\dagger(q, iq_m)\Gamma]^{-1} (\chi^0)^\dagger(q, iq_m)$$

$$(B.10) \quad = \chi^{loc} + \sum_{q, m>0} \chi(q, iq_m) + \sum_{q, m>0} 2 [\mathbb{I} \pm (\chi^0)^\dagger(-q, iq_m)\Gamma]^{-1} (\chi^0)^\dagger(-q, iq_m)$$

$$(B.11) \quad = \chi^{loc} + \sum_{q, m>0} \chi(q, iq_m) + \sum_{q, m>0} 2 [\mathbb{I} \pm (\chi^0)^*(q, iq_m)\Gamma]^{-1} (\chi^0)^*(q, iq_m)$$

$$(B.12) \quad = \chi^{loc} + 2 \sum_{q, m>0} \text{Re}\chi(q, iq_m).$$

Notice that we dropped the superscript for the susceptibilities since the procedure works for both the spin and the charge susceptibility.

Moreover, from the explicit form of irreducible susceptibility  $\chi^0$  with non-interacting Green's functions (see eq. (5.92)) we observe the high-frequency behavior

$$(B.13) \quad \sum_q \text{Re}\chi(q, iq_m) \sim \frac{d_2}{(iq_m)^2} + \frac{d_4}{(iq_m)^4} + \dots,$$

where we obtain the parameters  $d_2$ ,  $d_4$  by fitting to the tail of the momentum summed susceptibilities. By the same steps as performed for the Green's function  $G$  we obtain the formula

$$(B.14) \quad \sum_{q, iq_m} \chi(q, iq_m) \approx \chi^{loc} + 2 \left( -\frac{d_2(k)\tilde{\beta}^2}{24} + \frac{d_4(k)\tilde{\beta}^4}{1440} \right) + \sum_{m=1}^{N_{mats}} 2 \left( \sum_q \text{Re}\chi(q, iq_m) - \frac{d_2}{(iq_m)^2} - \frac{d_4}{(iq_m)^4} \right).$$

In contrast to the Green's function summation where the analytic correction of  $\frac{1}{2}$  is crucial to take into account since it stems from the limit  $\lim_{\tau \rightarrow 0^-}$  that cannot be taken account of numerically, the approximative formula for the susceptibility is only a way to save memory since the storage of the susceptibility scales like  $N \cdot N_{orb}^4$  for each bosonic Matsubara frequency.

**B.1.2. Matsubara sums of the form  $F(m) = \sum_n f(n)g(n+m)$ .** Many expressions that we use in this work to study the physics of correlated materials are convolutions in Matsubara frequency space (e.g. (5.396) and (5.290)). For this reason we consider here possible sources of error for sums of the form

$$(B.15) \quad F(m) = \sum_n f(n)g(n+m),$$

where  $n, m \in \mathbb{Z}$  are either fermionic or bosonic Matsubara indices. We start with a similar procedure as in the previous section B.1.1 by restricting the Matsubara sum to a finite number of frequencies,

$$(B.16) \quad F(m) \approx \sum_{n=-N_{mats}}^{N_{mats}} f(n)g(n+m).$$

Note that for our applications there is no need for analytical correction of the high-frequency tail since the convolutions considered are decaying fast enough to ensure convergence by a sufficient number of Matsubara frequencies. This is different if one considers to perform the Matsubara sum for  $\chi^0$  (eq. (5.72)) numerically [339] because the leading order  $O\left(\frac{1}{\omega_n \omega_{n+m}}\right)$  that appears in the sum decays too slowly.

We demonstrate that the shift in the factor  $g(n+m)$  leads to a problem if one carries the sum out in the interval  $[-N_{mats}, N_{mats}]$  for a particular choice of  $f, g$  shown in fig. B.1.

Assume we want to calculate  $F(0)$  by restricting the Matsubara sum to  $[-N_{mats}, N_{mats}]$ . In that case the sum is symmetric with respect to  $n=0$  and one neglects only the fast decaying high-frequency parts of both  $f$  and  $g$  (see fig. B.1)(a).

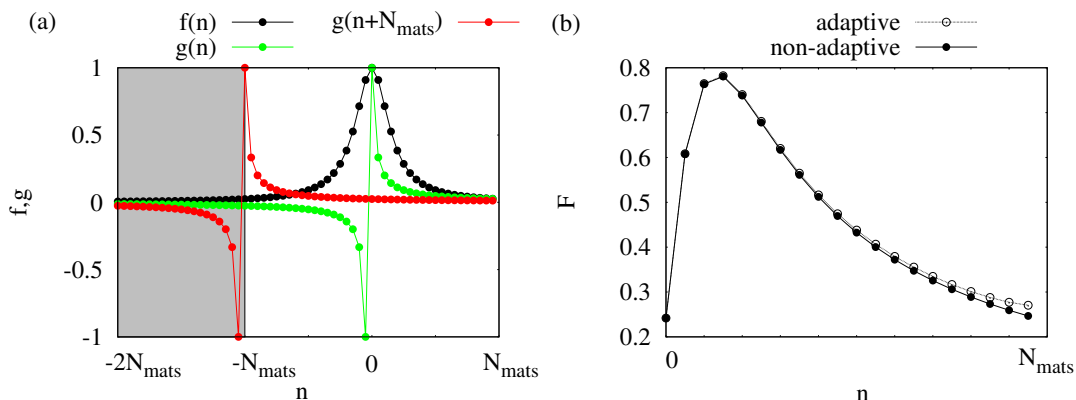


FIGURE B.1. Illustration of the Matsubara summation error that appears with rigid summation intervals. (a) In the convolution  $F = f * g$  we see that while  $f$  remains at a fixed position the key features of  $g$  are shifted out of the summation interval with increasing Matsubara index of  $F$ . The gray shaded area does not appear in the sum. (b) The effect of this incomplete summation becomes visible at large indices of  $n$  (empty symbols). An adaptive summation, i.e. summing over the interval  $[-N_{mats} - m, N_{mats}]$ , where  $m$  is the index of  $F$ , can fix the bending of the high-frequency tail of  $F$  (filled symbols).

On the other hand if one calculated  $F(N_{mats})$  we neglect the addends that would arise from the gray shaded area in fig. B.1(a) which results in the function  $F$  shown (b) with empty symbols. This effect can be compensated by summing over  $[-N_{mats} - m, N_{mats}]$ , i.e. depending on the Matsubara index of  $F$  we shift the lower bound in order to capture the tail in the shaded area of fig. B.1(a). The formula for  $F$  reads then

$$(B.17) \quad F(m) \approx \sum_{n=-N_{mats}-m}^{N_{mats}} f(n)g(n+m).$$

## B.1. MATSUBARA FUNCTIONS

---

The result of this adaptive summation is shown in (b) where the bending of the tail is compensated. This effect is especially important if one needs high-frequency extrapolation of  $F$  which necessitates precise values of the high-frequency values of  $F$ .

**B.1.3. Matsubara extrapolation.** In this section we present the numerical implementation for the quasi-particle weight (eq. (4.262))

$$(B.18) \quad Z_\alpha(k) \approx \left( 1 - \frac{\partial \text{Im}\Sigma_{\alpha\alpha}(k, i\omega_n)}{\partial \omega_n} \Big|_{\omega_n=0^+} \right)^{-1}$$

and the quasi-particle scattering rate (eq. (4.263))

$$(B.19) \quad \Gamma_\alpha(k, \omega) \approx -Z_\alpha(k) \text{Im}\Sigma_{\alpha\alpha}(k, i\omega_n \rightarrow 0).$$

From the Dyson equation (5.49) and the behavior of the Green's function under frequency inversion (eq. (4.136)) we can conclude that  $\Sigma_{\alpha\alpha}(k, i\omega_n)$  is anti-symmetric in Matsubara frequencies. Thus, we can use

$$(B.20) \quad \text{Im}\Sigma_{\alpha\alpha}(k, i\omega_n \rightarrow 0^+) \xrightarrow{T \rightarrow 0} 0$$

and a linear extrapolation to approximate

$$(B.21) \quad \frac{\partial \text{Im}\Sigma_{\alpha\alpha}(k, i\omega_n)}{\partial \omega_n} \Big|_{i\omega_n=0^+} \approx \frac{\text{Im}\Sigma_{\alpha\alpha}(k, i\omega_1) - \text{Im}\Sigma_{\alpha\alpha}(k, i\omega_n \rightarrow 0^+)}{\omega_1 - 0}$$

$$(B.22) \quad = \frac{\text{Im}\Sigma_{\alpha\alpha}(k, i\omega_1)}{\omega_1}.$$

A more elaborate approximation can be found by polynomial extrapolation that we explain in the following.

Consider the vectors

$$(B.23) \quad x := (\omega_0, \dots, \omega_5),$$

$$(B.24) \quad y := (\text{Im}\Sigma_{\alpha\alpha}(k, i\omega_0), \dots, \text{Im}\Sigma_{\alpha\alpha}(k, i\omega_5))^T$$

and the non-square matrix

$$(B.25) \quad A_{i,j} := x_i^j, \quad 1 \leq i \leq 6 \quad \text{and} \quad 1 \leq j \leq 5.$$

Next, we solve the linear equations

$$(B.26) \quad A\tilde{x} = y$$

that represent a polynomial fit of the real and imaginary part of the self-energy to the Matsubara frequencies<sup>1</sup>. Therefore, we get the improved approximations

$$(B.27) \quad \tilde{x}_0 \approx \text{Im}\Sigma_{\alpha\alpha}(k, i\omega_n \rightarrow 0^+),$$

$$(B.28) \quad \tilde{x}_1 \approx \frac{\partial \text{Im}\Sigma_{\alpha\alpha}(k, i\omega_n)}{\partial \omega_n} \Big|_{i\omega_n=0^+}.$$

---

<sup>1</sup>There are many numerical implementations for solving this. We made use of the householder QR decomposition as implemented in the eigen library.

## B.2. Non-convolutional $k$ -integration

We describe here the numerical two-dimensional  $k$ -space integration that we also implemented in [339]. For more details we refer to the mentioned reference whereupon this section is based.

Some of the TPSC internal  $k$ -summations (see e.g. eq. (4.240)) are not of convolutional type and are treated here separately. For the convolutional  $k$ -summation we refer to sec. B.3 where one takes advantage of Fast Fourier transformations.

Thus we restrict ourselves to summations of the type

$$(B.29) \quad \bar{f} = \frac{1}{N} \sum_k f(k)$$

in two dimensions.

We distinguish between three cases that are treated separately in the following three sections.

**B.2.1. Adaptive cubature.** First, we assume that  $f$  is given in a closed form which means that we have an analytic expression for the function  $f$  that we can evaluate  $f$  at arbitrary  $k$ -points. This allows us to make use of the adaptive cubature procedure following the description in [340, 341] and go into the limit of infinitely many unit cells, ie.

$$(B.30) \quad \bar{f} = \frac{1}{N} \sum_k f(k) \rightarrow \frac{1}{A_{BZ}} \int_{A_{BZ}} f(k) dk,$$

where  $A_{BZ}$  is the area of the first Brillouin zone.

This method is especially valuable if  $f$  exhibits rather flat behavior in many areas of  $k$ -space and strong  $k$  dependence in some regions; e.g. the non-interacting Green's function at low temperatures  $G^0$  changes drastically close to the Fermi energy (see eq. (4.235)) and is else flat as a function of  $k$ .

Note that since we work in relative coordinates  $k$ , the first Brillouin zone is always a square.

The adaptive cubature algorithm is given by the following steps:

- a) Divide  $A_{BZ}$  into  $n_0$  triangles and perform the following steps for each of the triangles  $\Delta_i$ ,  $i = 1, \dots, n_0$ . In the calculations presented in this work we pick  $n_0 = 17$ .
- b) Use the seven-point formula<sup>2</sup> to evaluate the integral over each triangle  $\Delta_i$  with  $i = 1, \dots, n_0$ , i.e.

$$(B.31) \quad \int_{\Delta_i} f(k_x, k_y) dk \approx |\Delta_i| \sum_{j=1}^7 w_j f(x_j, y_j),$$

where the nodes  $(x_i, y_i)$  and the respective weights  $w_i$  are shown in table B.1 and fig. B.2.

- c) Divide each triangle  $\Delta_i$  into four triangles (see fig. B.2) and integrate again over each new triangular region by means of eq. (B.31).
- d) Check convergence via

$$(B.32) \quad |I_{new} - I_{old}|/3. < \epsilon |I_{new} + 1|,$$

where  $I_{new}$  is the sum of the integrals over the four new triangles described in the previous step c) and  $I_{old}$  is the integral of the respective triangle  $\Delta_i$ . We take the convergence threshold  $\epsilon$  to be  $10^{-6}$ .

---

<sup>2</sup>Note that we used a less precise three-point formula in [245, 246, 285, 287, 339] due to the large numerical effort in multi-site and multi-orbital systems. The three-point formula takes only the blue nodes in fig. B.2 and with a weight of 1/3 for each node.

## B.2. NON-CONVOLUTIONAL K-INTEGRATION

If the convergence condition in eq. (B.32) is fulfilled return the value  $I_{new}$  and add it to the final result and else start from step a) with all four new triangles.

Note that one could use higher order integration formulas to improve the above mentioned algorithm but we checked that in all applications of this thesis the seven-point formula is sufficient. Finally, we want to point out that a precise calculation of  $\chi^0$  is important since the divergences in  $\chi^{sp}$  can be only described properly if  $\chi^0$  was determined with small numerical error (see eq. (5.267)).

$i$	$x_i$	$y_i$	$w_i$
1	0	0	3/60
2	0	1	
3	1	0	
4	0.5	0	8/60
5	0	0.5	
6	0.5	0.5	
7	1/3	1/3	27/60

TABLE B.1. Weights  $w_i$  and nodes  $(x_i, y_i)$  that are needed to evaluate the seven-point formula for integration over a triangular domain (see eq. (B.31)). The coordinates are given in so-called natural coordinates of the triangle (see fig. B.2)

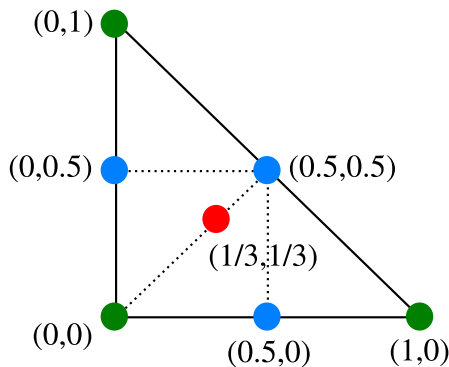


FIGURE B.2. Natural coordinates for a triangle that are used to designate the position of the nodes in the seven-point formula (eq. (B.31)) while the colors encode the respective weights as shown in tab. B.1. The dashed lines indicate the division of the triangle into four new triangles as needed in step c) of the adaptive cubature algorithm.

**B.2.2. Trapezoidal rule.** Here we assume that  $f$  is given only for finitely many  $k$ -points which in our case means that  $f$  is a function that was calculated numerically and we have no easy analytical expression that allows us to produce function values for arbitrary  $k$ -points.

This case covers summations where  $f$  is given for exactly  $N = \tilde{N}^2$   $k$ -points<sup>3</sup>. Therefore, we make use of the two-dimensional trapezoidal rule which corresponds to linear interpolation between the given  $N$  function value points of  $f$ . Obviously, one can think of more precise implementations such as spline interpolation or higher order integration formulas.

<sup>3</sup>Note that we assumed here that  $N$  is square which is true in all applications of this thesis since the number of unit cells in  $x$ -direction are assumed to be the same as in  $y$ -direction.

We assume that  $f$  is known on the nodes  $(x_i, y_j) \forall i, j \in \{1, \dots, \tilde{N}\}$  and that those points are homogeneously distributed over the first Brillouin zone in relative coordinates  $[0, 1] \times [0, 1]$ .

The two-dimensional trapezoidal rule can be understood as iterative application of the one-dimensional version. This yields

$$\begin{aligned}
 & \frac{1}{A_{BZ}} \int_{A_{BZ}} f(k) dk \\
 (B.33) \quad & \approx \frac{1}{\tilde{N}(y_{\tilde{N}} - y_1)} \int_{y_1}^{y_{\tilde{N}}} \left( \frac{1}{2} f(x_1, y) + \sum_{i=2}^{\tilde{N}-1} f(x_i, y) + \frac{1}{2} f(x_{\tilde{N}}, y) \right) dy \\
 & \approx \frac{1}{\tilde{N}^2} \left[ \frac{1}{4} \left( f(x_1, y_1) + f(x_1, y_{\tilde{N}}) + f(x_{\tilde{N}}, y_1) + f(x_{\tilde{N}}, y_{\tilde{N}}) \right) \right. \\
 & \quad + \frac{1}{2} \sum_{i=2}^{\tilde{N}-1} \left( f(x_1, y_i) + f(x_{\tilde{N}}, y_i) + f(x_i, y_1) + f(x_i, y_{\tilde{N}}) \right) \\
 (B.34) \quad & \left. + \sum_{i,j=2}^{\tilde{N}-1} f(x_i, y_j) \right].
 \end{aligned}$$

### B.3. The cross correlation theorem

In many equations that we encounter within TPSC (see eq. (5.396) and (5.290)) we have to evaluate expressions of the type

$$(B.35) \quad F(k) = \frac{1}{N} \sum_q f(k) g(k - q),$$

which represents a multi-dimensional convolution. Numerically one can perform this summation very efficiently by taking advantage of the circular convolution theorem,

$$(B.36) \quad F = \frac{1}{N^2} \mathfrak{F}^{-1} [[\mathfrak{F}f] \times [\mathfrak{F}g]],$$

where  $\mathfrak{F}$  denotes the discrete Fourier transform and  $\times$  is the array product of the vectors in  $k$ -space. To perform the discrete Fourier transformation –here exemplified for two dimensional functions– we interpret the functions  $f$  as array

$$\begin{aligned}
 f &= [f(0, 0), f(0, 1/N), \dots, f(0, 1 - 1/N), f(1/N, 0), \dots, f(1/N, 1 - 1/N), \dots \\
 (B.37) \quad & \dots, f(1 - 1/N, 1 - 1/N)]
 \end{aligned}$$

and similar for  $g$  and  $F$ . This represents all three functions as periodic discrete two-dimensional lattice functions.

By performing the discrete Fourier transforms in terms of fast Fourier transforms one can achieve a run time  $O(N \log N)$  that scales much better than the brute force  $O(N^2)$  version.

Similarly, the equations of type

$$(B.38) \quad F(k) = \frac{1}{N} \sum_q f(k) g(k + q)$$

can be dealt with in terms of the cross correlation theorem:

$$(B.39) \quad F = \frac{1}{N^2} \mathfrak{F}^{-1} [[\mathfrak{F}f^*]^* \times [\mathfrak{F}g]].$$

### B.4. Numerical instabilities at low temperatures

In this section we show why TPSC gets numerically unstable at low temperatures and in how far one can circumvent those restrictions.

**B.4.1. Adaptive  $k$ -meshes.** First, one has to deal with the divergence of the spin susceptibility  $\chi^{sp}$  (see fig. 6.9). This is due to the fact that at low temperatures the anti-ferromagnetic fluctuations will start to diverge at  $q$ -points where the nesting condition is fulfilled. Thus, one has to take care that enough  $q$ -points are used numerically to resolve the peak in the spin susceptibility.

In order to save memory we use an adaptive  $q$ -grid that is fine at low Matsubara frequencies<sup>4</sup>. Since the same argument applies to all Matsubara functions that we study, we apply the adaptive mesh to all Matsubara functions within TPSC.

The number of  $k_x$ - and  $k_y$ -points  $N_{k_x}(n)$ ,  $N_{k_y}(n)$  for a given Matsubara index  $n > 0$  is given by

$$(B.40) \quad N_{k_x}(n) = N_{k_y}(n) = \begin{cases} N_{max} & n < 6 \\ N_{max}/1.1^{n-6} & N_{max}/1.1^{n-6} > N_{min} \\ N_{min} & else \end{cases}$$

and analogously for a negative Matsubara index  $n^5$ . Note, that we keep a constant fine  $k$ -mesh of  $N_{max} \times N_{max}$  points for the first six Matsubara frequencies due to the extrapolation procedure described in sec. B.1.3. Otherwise, the number of  $k$ -points are slowly exponentially decreasing with Matsubara index  $n$  down to a minimal value  $N_{min}$ .

**B.4.2. Adaptive Matsubara frequencies.** The distance between Matsubara frequencies decreases with smaller temperature since

$$(B.41) \quad \omega_n = 2\pi(n+1)T \quad \text{and} \quad q_n = 2\pi nT.$$

This means that a constant number of Matsubara frequencies cannot resolve the same imaginary frequency window with decreasing temperatures.

This effect can be compensated by increasing the number of Matsubara frequencies  $N_{mats}$  inverse proportional to the temperature,

$$(B.42) \quad N_{mats}(T) = \begin{cases} N_0 T_0 / T & N_0 T_0 / T > 50 \\ 50 & else \end{cases},$$

where  $N_0$  is the number of Matsubara frequencies at  $T = T_0$  chosen such that the energy window sampled by the Matsubara frequencies  $[\omega_0, \dots, \omega_{N_0}]$  equals roughly the bandwidth of the non-interacting system.

In the case of bosonic Matsubara frequency functions we use only

$$(B.43) \quad (2/3)N_{mats}(T)$$

Matsubara frequencies since within TPSC those functions are faster decaying than the fermionic ones.

---

<sup>4</sup>Due to the  $1/iq_m$  decay of the susceptibilities (see eq. (5.92) and (5.267)) we know that the peak will be softened at larger Matsubara frequencies  $iq_m$ .

<sup>5</sup>In the case of bosonic frequencies one replaces  $n$  by  $-n$  and uses eq. (B.40) while in the fermionic case one has to replace  $n$  by  $-n-1$  because  $-i\omega_n = i\omega_{-n-1}$ .

**B.4.3. Non-interacting susceptibility  $\chi^0$ .** Note that the calculation of the non-interacting susceptibility  $\chi^0$  given by eq. (5.92),

$$(B.44) \quad \chi_{\eta\nu\zeta\lambda}^0(q, iq_m) = -\frac{1}{N} \sum_{k,b,c} a_b^\nu(k+q) a_b^{\lambda*}(k+q) a_c^\zeta(k) a_c^{\eta*}(k) \frac{f_{FD}(\xi_b(k+q)) - f_{FD}(\xi_c(k))}{-iq_m + \xi_b(k+q) - \xi_c(k)},$$

bears two numerical problems.

First, in the case where  $m = 0$  and energy degeneracy, i.e.

$$(B.45) \quad \xi_b(k+q) = \xi_c(k)$$

one has to apply L'Hôpital's rule and finds

$$(B.46) \quad \lim_{\xi_b(k+q) \rightarrow \xi_c(k)} \frac{f_{FD}(\xi_b(k+q)) - f_{FD}(\xi_c(k))}{\xi_b(k+q) - \xi_c(k)} = -\frac{1}{T} \frac{e^{\xi_c(k)/T}}{(1 + e^{\xi_c(k)/T})^2}.$$

Second, in the realm of very low temperatures the fraction on the right-hand side of eq. (B.46) will be a division of very large numbers which might result in an overflow error. In this cases it useful to check whether the exponential  $\xi_c(k)/T$  is larger than  $\sim 20$  and set the right-hand side to zero which is the limit of this expressions for very low temperatures.

## APPENDIX C

### Formal results

In this chapter we present some formal results that were used in the main text.

#### C.1. Proof of internal accuracy check

We start the proof of the internal multi-orbital accuracy check by evaluating the left-hand side of eq. (5.394).

PROOF OF (5.394).

$$\begin{aligned}
& \lim_{\tau \nearrow 0} \frac{T}{N} \sum_{k, i\omega_n} e^{-i\omega_n \tau} \Sigma_{\nu \bar{\beta}, \sigma}(k, i\omega_n) G_{\bar{\beta} \nu, \sigma}^0(k, i\omega_n) \\
&= \lim_{\tau \nearrow 0} \frac{T}{N} \sum_{k, i\omega_n} e^{-i\omega_n \tau} \left\{ \sum_{\eta} U_{\eta \nu} \langle n_{\eta, -\sigma} \rangle \delta_{\nu, \bar{\beta}} + \right. \\
&\quad + \sum_{\eta \neq \nu} (U_{\eta \nu} - J_{\eta \nu}) \left( \langle n_{\eta, \sigma} \rangle \delta_{\nu, \bar{\beta}} - \langle n_{\nu \bar{\beta}, \sigma} \rangle \delta_{\eta, \bar{\beta}} \right) \\
&\quad + J_{\bar{\beta} \nu} (\langle n_{\nu \bar{\beta}, -\sigma} \rangle + \langle n_{\bar{\beta} \nu, -\sigma} \rangle) (1 - \delta_{\nu, \bar{\beta}}) \\
&\quad + \left. \frac{T}{4N} \sum_{q, iq_m} \left[ \Gamma^{ch} \chi^{ch}(q, iq_m) \Gamma^{ch,0} + \Gamma^{sp} \chi^{sp}(q, iq_m) \Gamma^{sp,0} \right]_{\bar{\beta} \bar{\eta} \nu \bar{\gamma}} \times \right. \\
\text{(C.1)} \quad & \left. \times G_{\bar{\gamma} \bar{\eta}}^0(k + q, i\omega_{n+m}) \right\} G_{\bar{\beta} \nu, \sigma}^0(k, i\omega_n) \\
&= \sum_{\eta} U_{\eta \nu} \langle n_{\eta, -\sigma} \rangle \langle n_{\nu, \sigma} \rangle + \sum_{\eta \neq \nu} (U_{\eta \nu} - J_{\eta \nu}) (\langle n_{\eta, \sigma} \rangle \langle n_{\nu, \sigma} \rangle - \langle n_{\nu \eta, \sigma} \rangle \langle n_{\eta \nu, \sigma} \rangle) \\
&\quad + J_{\bar{\beta} \nu} (\langle n_{\nu \bar{\beta}, -\sigma} \rangle \langle n_{\bar{\beta} \nu, \sigma} \rangle + \langle n_{\bar{\beta} \nu, -\sigma} \rangle \langle n_{\bar{\beta} \nu, \sigma} \rangle) (1 - \delta_{\nu, \bar{\beta}}) \\
\text{(C.2)} \quad & - \frac{T}{4N} \sum_{q, iq_m} \left[ \chi^0 \Gamma^{ch} \chi^{ch} \Gamma^{ch,0} + \chi^0 \Gamma^{sp} \chi^{sp} \Gamma^{sp,0} \right]_{\nu \bar{\gamma} \nu \bar{\gamma}}(q, iq_m) \\
&= \sum_{\eta} U_{\eta \nu} \langle n_{\eta, -\sigma} \rangle \langle n_{\nu, \sigma} \rangle + \sum_{\eta \neq \nu} (U_{\eta \nu} - J_{\eta \nu}) (\langle n_{\eta, \sigma} \rangle \langle n_{\nu, \sigma} \rangle - \langle n_{\nu \eta, \sigma} \rangle \langle n_{\eta \nu, \sigma} \rangle) \\
&\quad + J_{\bar{\beta} \nu} (\langle n_{\nu \bar{\beta}, -\sigma} \rangle \langle n_{\bar{\beta} \nu, \sigma} \rangle + \langle n_{\bar{\beta} \nu, -\sigma} \rangle \langle n_{\bar{\beta} \nu, \sigma} \rangle) (1 - \delta_{\nu, \bar{\beta}}) \\
\text{(C.3)} \quad & - \frac{T}{4N} \sum_{q, iq_m} \left[ (2\chi^0 - \chi^{ch}) \Gamma^{ch,0} + (\chi^{sp} - 2\chi^0) \Gamma^{sp,0} \right]_{\nu \bar{\gamma} \nu \bar{\gamma}}(q, iq_m),
\end{aligned}$$

where we have used the definition of the non-interacting susceptibility  $\chi^0$  (eq. (5.72)) and the Bethe-Salpeter equation (5.372).

Following the definition of  $\Gamma^{sp/ch,0}$  (eqs. (5.348) and (5.349)) we will have three terms in each channel, namely

$$\text{(C.4)} \quad \chi_{\nu \bar{\gamma} \bar{\alpha} \bar{\beta}} \Gamma_{\bar{\alpha} \bar{\beta} \nu \bar{\gamma}} = \chi_{\nu \bar{\gamma} \nu \bar{\gamma}} \Gamma_{\nu \bar{\gamma} \nu \bar{\gamma}} (1 - \delta_{\nu, \bar{\gamma}}) + \chi_{\nu \bar{\gamma} \bar{\gamma} \nu} \Gamma_{\bar{\gamma} \nu \bar{\gamma} \nu} (1 - \delta_{\nu, \bar{\gamma}}) + \chi_{\nu \bar{\gamma} \bar{\gamma} \nu} \Gamma_{\bar{\gamma} \bar{\gamma} \nu \nu},$$

where we dropped the superscript for simplicity.

Using the local spin and charge sum rules (eqs. (5.327), (5.328), (5.329), (5.334), (5.335) and (5.336)) we can evaluate the  $q, iq_m$ -sum in eq. (C.3) and find

$$\begin{aligned}
 & \frac{T}{4N} \sum_{q, iq_m} \left[ (2\chi^0 - \chi^{ch}) \Gamma^{ch,0} + (\chi^{sp} - 2\chi^0) \Gamma^{sp,0} \right]_{\nu\bar{\gamma}\nu\bar{\gamma}}(q, iq_m) \\
 &= \frac{T}{4N} \sum_{q, iq_m} \left[ (2\chi^0 - \chi^{ch})_{\nu\bar{\gamma}\nu\bar{\gamma}} \Gamma_{\nu\bar{\gamma}\nu\bar{\gamma}}^{ch,0} + (\chi^{sp} - 2\chi^0)_{\nu\bar{\gamma}\nu\bar{\gamma}} \Gamma_{\nu\bar{\gamma}\nu\bar{\gamma}}^{sp,0} \right] (q, iq_m) (1 - \delta_{\nu, \bar{\gamma}}) + \\
 & \quad + \frac{T}{4N} \sum_{q, iq_m} \left[ (2\chi^0 - \chi^{ch})_{\nu\bar{\gamma}\gamma\nu} \Gamma_{\bar{\gamma}\nu\bar{\gamma}}^{ch,0} + (\chi^{sp} - 2\chi^0)_{\nu\bar{\gamma}\gamma\nu} \Gamma_{\bar{\gamma}\nu\bar{\gamma}}^{sp,0} \right] (q, iq_m) (1 - \delta_{\nu, \bar{\gamma}}) \\
 & \quad + \frac{T}{4N} \sum_{q, iq_m} \left[ (2\chi^0 - \chi^{ch})_{\nu\nu\bar{\gamma}\bar{\gamma}} \Gamma_{\bar{\gamma}\bar{\gamma}\nu\nu}^{ch,0} + (\chi^{sp} - 2\chi^0)_{\nu\nu\bar{\gamma}\bar{\gamma}} \Gamma_{\bar{\gamma}\bar{\gamma}\nu\nu}^{sp,0} \right] (q, iq_m) (1 - \delta_{\nu, \bar{\gamma}}) \\
 (C.5) \quad & \quad + \frac{T}{4N} \sum_{q, iq_m} \left[ (2\chi^0 - \chi^{ch})_{\nu\nu\nu\nu} \Gamma_{\nu\nu\nu\nu}^{ch,0} + (\chi^{sp} - 2\chi^0)_{\nu\nu\nu\nu} \Gamma_{\nu\nu\nu\nu}^{sp,0} \right] (q, iq_m) \\
 &= \frac{T}{4N} \sum_{q, iq_m} J_{\nu\bar{\gamma}} \left[ -\chi_{\nu\bar{\gamma}\nu\bar{\gamma}}^{ch} + \chi_{\nu\bar{\gamma}\nu\bar{\gamma}}^{sp} \right] (q, iq_m) (1 - \delta_{\nu, \bar{\gamma}}) + \\
 & \quad + \frac{T}{4N} \sum_{q, iq_m} J_{\nu\bar{\gamma}} \left[ -\chi_{\nu\bar{\gamma}\gamma\nu}^{ch} + \chi_{\nu\bar{\gamma}\gamma\nu}^{sp} \right] (q, iq_m) (1 - \delta_{\nu, \bar{\gamma}}) \\
 & \quad + \frac{T}{4N} \sum_{q, iq_m} \left[ 4(U_{\nu\bar{\gamma}} - J_{\nu\bar{\gamma}}) \chi_{\nu\nu\bar{\gamma}\bar{\gamma}}^0 - \chi_{\nu\nu\bar{\gamma}\bar{\gamma}}^{ch} \Gamma_{\bar{\gamma}\bar{\gamma}\nu\nu}^{ch,0} + \chi_{\nu\nu\bar{\gamma}\bar{\gamma}}^{sp} \Gamma_{\bar{\gamma}\bar{\gamma}\nu\nu}^{sp,0} \right] (q, iq_m) (1 - \delta_{\nu, \bar{\gamma}}) \\
 (C.6) \quad & \quad + \frac{T}{4N} \sum_{q, iq_m} U_{\nu\nu} \left[ -\chi_{\nu\nu\nu\nu}^{ch} + \chi_{\nu\nu\nu\nu}^{sp} \right] (q, iq_m) \\
 &= \frac{1}{4} J_{\nu\bar{\gamma}} \left[ 4(\langle n_{\bar{\gamma}, \sigma} n_{\nu, \sigma} \rangle - \langle n_{\bar{\gamma}, \sigma} n_{\nu, -\sigma} \rangle) + \langle n_{\bar{\gamma}\nu} \rangle \langle n_{\nu\bar{\gamma}} \rangle - \frac{1}{2} (\langle n_{\nu, \uparrow} \rangle - \langle n_{\bar{\gamma}, \downarrow} \rangle) \right] (1 - \delta_{\nu, \bar{\gamma}}) + \\
 & \quad + J_{\nu\bar{\gamma}} \frac{T}{4N} \sum_{q, iq_m} \left[ -\chi_{\nu\bar{\gamma}\gamma\nu}^{ch} + \chi_{\nu\bar{\gamma}\gamma\nu}^{sp} \right] (1 - \delta_{\nu, \bar{\gamma}}) \\
 & \quad + \frac{1}{4} \left[ -(2U_{\nu\bar{\gamma}} - J_{\nu\bar{\gamma}}) (2\langle n_{\bar{\gamma}, \sigma} n_{\nu, \sigma} \rangle + 2\langle n_{\bar{\gamma}, \sigma} n_{\nu, -\sigma} \rangle - \langle n_{\bar{\gamma}} \rangle \langle n_{\nu} \rangle) \right. \\
 & \quad \quad \left. + J_{\nu\bar{\gamma}} (2\langle n_{\bar{\gamma}, \sigma} n_{\nu, \sigma} \rangle - 2\langle n_{\bar{\gamma}, \sigma} n_{\nu, -\sigma} \rangle) \right] (1 - \delta_{\nu, \bar{\gamma}}) \\
 (C.7) \quad & \quad + \frac{1}{4} U_{\nu\nu} \left[ -4\langle n_{\nu, \sigma} n_{\nu, -\sigma} \rangle + \langle n_{\nu} \rangle^2 \right].
 \end{aligned}$$

Notice that the additional contribution in the  $\nu\bar{\gamma}\nu\bar{\gamma}$  contribution comes from the commutator when swapping  $\nu$  and  $\gamma$  to use the derived sum rules. Inserting this expression back into eq. (C.3) we obtain

$$\begin{aligned}
 & \lim_{\tau \nearrow 0} \frac{T}{N} \sum_{k, i\omega_n} e^{-i\omega_n \tau} \Sigma_{\nu\bar{\beta}, \sigma}(k, i\omega_n) G_{\bar{\beta}\nu, \sigma}^0(k, i\omega_n) \\
 &= \underbrace{\sum_{\eta} U_{\eta\nu} \langle n_{\eta, -\sigma} \rangle \langle n_{\nu, \sigma} \rangle}_{\eta \neq \nu} + \sum_{\eta \neq \nu} (U_{\eta\nu} - J_{\eta\nu}) \left( \underbrace{\langle n_{\eta, \sigma} \rangle \langle n_{\nu, \sigma} \rangle}_{\dots\dots\dots} - \underbrace{\langle n_{\nu\eta, \sigma} \rangle \langle n_{\eta\nu, \sigma} \rangle}_{\dots\dots\dots} \right)
 \end{aligned}$$

$$\begin{aligned}
 & + J_{\beta\nu} (\langle n_{\nu\bar{\beta},-\sigma} \rangle \langle n_{\bar{\beta}\nu,\sigma} \rangle + \langle n_{\bar{\beta}\nu,-\sigma} \rangle \langle n_{\nu\bar{\beta},\sigma} \rangle) (1 - \delta_{\nu,\bar{\beta}}) \\
 & - \frac{1}{4} J_{\nu\bar{\gamma}} \left[ 4 (\langle n_{\bar{\gamma},\sigma} n_{\nu,\sigma} \rangle - \langle n_{\bar{\gamma},\sigma} n_{\nu,-\sigma} \rangle) + \langle n_{\bar{\gamma}\nu} \rangle \langle n_{\nu\bar{\gamma}} \rangle - \frac{1}{2} (\langle n_{\nu,\uparrow} \rangle - \langle n_{\bar{\gamma},\downarrow} \rangle) \right] (1 - \delta_{\nu,\bar{\gamma}}) \\
 & - J_{\nu\bar{\gamma}} \frac{T}{4N} \sum_{q, iq_m} \left[ -\chi_{\nu\bar{\gamma}\bar{\gamma}\nu}^{ch} + \chi_{\nu\bar{\gamma}\bar{\gamma}\nu}^{sp} \right] (q, iq_m) (1 - \delta_{\nu,\bar{\gamma}}) \\
 & - \frac{1}{4} \left[ -U_{\nu\bar{\gamma}} \left( 2 \langle n_{\bar{\gamma},\sigma} n_{\nu,\sigma} \rangle + 2 \langle n_{\bar{\gamma},\sigma} n_{\nu,-\sigma} \rangle - \langle n_{\bar{\gamma}} \rangle \langle n_{\nu} \rangle \right) \right. \\
 & \quad \left. - (U_{\nu\bar{\gamma}} - J_{\nu\bar{\gamma}}) \left( 2 \langle n_{\bar{\gamma},\sigma} n_{\nu,\sigma} \rangle + 2 \langle n_{\bar{\gamma},\sigma} n_{\nu,-\sigma} \rangle - \langle n_{\bar{\gamma}} \rangle \langle n_{\nu} \rangle \right) \right. \\
 & \quad \left. + J_{\nu\bar{\gamma}} (2 \langle n_{\bar{\gamma},\sigma} n_{\nu,\sigma} \rangle - 2 \langle n_{\bar{\gamma},\sigma} n_{\nu,-\sigma} \rangle) \right] (1 - \delta_{\nu,\bar{\gamma}}) \\
 (C.8) \quad & - \frac{1}{4} U_{\nu\nu} \left[ -4 \langle n_{\nu,\sigma} n_{\nu,-\sigma} \rangle + \langle n_{\nu} \rangle^2 \right],
 \end{aligned}$$

where we marked the terms that cancel each other with different underline styles. Notice that the dashed underlined terms are zero for the reason that we have no inter-orbital on-site hopping terms. By grouping together the different double occupations we arrive at

$$\begin{aligned}
 & \lim_{\tau \searrow 0} \frac{T}{N} \sum_{k, i\omega_n} e^{-i\omega_n \tau} \Sigma_{\nu\bar{\beta},\sigma}(k, i\omega_n) G_{\bar{\beta}\nu,\sigma}(k, i\omega_n) \\
 & = \sum_{\alpha} U_{\alpha\nu} \langle n_{\alpha,-\sigma} n_{\nu,\sigma} \rangle + \sum_{\substack{\alpha \\ \alpha \neq \nu}} (U_{\alpha\nu} - J_{\alpha\nu}) \langle n_{\alpha,\sigma} n_{\nu,\sigma} \rangle + \frac{J_{\alpha\nu}}{8} (\langle n_{\nu,\uparrow} \rangle - \langle n_{\alpha,\downarrow} \rangle) \\
 (C.9) \quad & - \frac{1}{2} \sum_{\substack{\alpha \\ \alpha \neq \nu}} J_{\alpha\nu} \left( \frac{T}{N} \sum_{q, iq_m} \chi_{\alpha\alpha\nu\nu}^{sp}(q, iq_m) + \frac{T}{2N} \sum_{q, iq_m} (\chi^{sp} - \chi^{ch})_{\nu\alpha\alpha\nu}(q, iq_m) \right).
 \end{aligned}$$

□

## C.2. Multi-orbital Hamiltonian representation

In the literature one can find a different representation of the multi-orbital Hamiltonian  $H$  in eq. (5.297) that we use for the multi-orbital TPSC approach. In this appendix we prove that the Hamiltonian  $H$  used in the main part is equivalent to the Hamiltonian

$$\begin{aligned}
 H = & \sum_{\alpha,\beta,i,j,\sigma} \left( t_{\alpha\beta}^{r_i-r_j} - \mu \delta_{i,j} \delta_{\alpha,\beta} \right) c_{\alpha,\sigma}^\dagger(r_i) c_{\beta,\sigma}(r_j) \\
 & + \sum_{\alpha,i} U_{\alpha\alpha} n_{\alpha,\uparrow}(r_i) n_{\alpha,\downarrow}(r_i) \\
 & + \sum_{\substack{\alpha,\beta,i \\ \alpha > \beta}} \left( U_{\alpha\beta} - \frac{J_{\alpha\beta}}{2} \right) n_{\alpha}(r_i) n_{\beta}(r_i) \\
 & - 2 \sum_{\substack{\alpha,\beta,i \\ \alpha > \beta}} J_{\alpha\beta} \vec{S}_{\alpha}(r_i) \cdot \vec{S}_{\beta}(r_i) \\
 (C.10) \quad & + \sum_{\substack{\alpha,\beta,i \\ \alpha \neq \beta}} J_{\alpha\beta} c_{\alpha,\uparrow}^\dagger(r_i) c_{\alpha,\downarrow}^\dagger(r_i) c_{\beta,\downarrow}(r_i) c_{\beta,\uparrow}(r_i),
 \end{aligned}$$

where we define the spin matrices

$$(C.11) \quad S_\alpha(1) := S_{\alpha\alpha}(1)$$

according to the multi-site definition in eq. (5.132).

In order to express the Hamiltonian only in terms of creation and annihilation operators we do the following exercise.

$$(C.12) \quad \vec{S}_\alpha \cdot \vec{S}_\beta = (c_{\alpha,\uparrow}^\dagger \ c_{\alpha,\downarrow}^\dagger) \cdot \vec{\sigma} \cdot (c_{\alpha,\uparrow} \ c_{\alpha,\downarrow})^T (c_{\beta,\uparrow}^\dagger \ c_{\beta,\downarrow}^\dagger) \cdot \vec{\sigma} \cdot (c_{\beta,\uparrow} \ c_{\beta,\downarrow})^T$$

$$(C.13) \quad = (c_{\alpha,\uparrow}^\dagger \ c_{\alpha,\downarrow}^\dagger) \cdot \vec{\sigma} \cdot \begin{pmatrix} c_{\alpha,\uparrow} c_{\beta,\uparrow}^\dagger & c_{\alpha,\uparrow} c_{\beta,\downarrow}^\dagger \\ c_{\alpha,\downarrow} c_{\beta,\uparrow}^\dagger & c_{\alpha,\downarrow} c_{\beta,\downarrow}^\dagger \end{pmatrix} \cdot \vec{\sigma} \cdot (c_{\beta,\uparrow} \ c_{\beta,\downarrow})^T$$

$$(C.14) \quad = \frac{1}{2} (c_{\alpha,\uparrow}^\dagger \ c_{\alpha,\downarrow}^\dagger) \cdot \vec{\sigma} \cdot \begin{pmatrix} \begin{pmatrix} c_{\alpha,\uparrow} c_{\beta,\downarrow}^\dagger & c_{\alpha,\uparrow} c_{\beta,\uparrow}^\dagger \\ c_{\alpha,\downarrow} c_{\beta,\downarrow}^\dagger & c_{\alpha,\downarrow} c_{\beta,\uparrow}^\dagger \end{pmatrix} \\ i \begin{pmatrix} c_{\alpha,\uparrow} c_{\beta,\downarrow}^\dagger & -c_{\alpha,\uparrow} c_{\beta,\uparrow}^\dagger \\ c_{\alpha,\downarrow} c_{\beta,\downarrow}^\dagger & -c_{\alpha,\downarrow} c_{\beta,\uparrow}^\dagger \end{pmatrix} \\ \begin{pmatrix} c_{\alpha,\uparrow} c_{\beta,\uparrow}^\dagger & -c_{\alpha,\uparrow} c_{\beta,\downarrow}^\dagger \\ c_{\alpha,\downarrow} c_{\beta,\uparrow}^\dagger & -c_{\alpha,\downarrow} c_{\beta,\downarrow}^\dagger \end{pmatrix} \end{pmatrix} \cdot (c_{\beta,\uparrow} \ c_{\beta,\downarrow})^T$$

$$(C.15) \quad = \frac{1}{4} (c_{\alpha,\uparrow}^\dagger \ c_{\alpha,\downarrow}^\dagger) \cdot \left[ \begin{pmatrix} c_{\alpha,\downarrow} c_{\beta,\downarrow}^\dagger & c_{\alpha,\downarrow} c_{\beta,\uparrow}^\dagger \\ c_{\alpha,\uparrow} c_{\beta,\downarrow}^\dagger & c_{\alpha,\uparrow} c_{\beta,\uparrow}^\dagger \end{pmatrix} + \begin{pmatrix} c_{\alpha,\downarrow} c_{\beta,\downarrow}^\dagger & -c_{\alpha,\downarrow} c_{\beta,\uparrow}^\dagger \\ -c_{\alpha,\uparrow} c_{\beta,\downarrow}^\dagger & c_{\alpha,\uparrow} c_{\beta,\uparrow}^\dagger \end{pmatrix} + \begin{pmatrix} c_{\alpha,\uparrow} c_{\beta,\uparrow}^\dagger & -c_{\alpha,\uparrow} c_{\beta,\downarrow}^\dagger \\ -c_{\alpha,\downarrow} c_{\beta,\uparrow}^\dagger & c_{\alpha,\downarrow} c_{\beta,\downarrow}^\dagger \end{pmatrix} \right] \cdot (c_{\beta,\uparrow} \ c_{\beta,\downarrow})^T$$

$$(C.16) \quad = \frac{1}{4} (c_{\alpha,\uparrow}^\dagger \ c_{\alpha,\downarrow}^\dagger) \cdot \begin{pmatrix} 2c_{\alpha,\downarrow} c_{\beta,\downarrow}^\dagger + c_{\alpha,\uparrow} c_{\beta,\uparrow}^\dagger & -c_{\alpha,\uparrow} c_{\beta,\downarrow}^\dagger \\ -c_{\alpha,\downarrow} c_{\beta,\uparrow}^\dagger & 2c_{\alpha,\uparrow} c_{\beta,\uparrow}^\dagger + c_{\alpha,\downarrow} c_{\beta,\downarrow}^\dagger \end{pmatrix} \cdot (c_{\beta,\uparrow} \ c_{\beta,\downarrow})^T$$

$$(C.17) \quad = \frac{1}{4} (c_{\alpha,\uparrow}^\dagger \ c_{\alpha,\downarrow}^\dagger) \cdot \begin{pmatrix} 2c_{\alpha,\downarrow} c_{\beta,\downarrow}^\dagger c_{\beta,\uparrow} + c_{\alpha,\uparrow} c_{\beta,\uparrow}^\dagger c_{\beta,\uparrow} - c_{\alpha,\uparrow} c_{\beta,\downarrow}^\dagger c_{\beta,\downarrow} \\ -c_{\alpha,\downarrow} c_{\beta,\uparrow}^\dagger c_{\beta,\uparrow} + 2c_{\alpha,\uparrow} c_{\beta,\uparrow}^\dagger c_{\beta,\downarrow} + c_{\alpha,\downarrow} c_{\beta,\downarrow}^\dagger c_{\beta,\downarrow} \end{pmatrix}$$

$$(C.18) \quad = \frac{1}{4} \left( 2c_{\alpha,\uparrow}^\dagger c_{\alpha,\downarrow} c_{\beta,\downarrow}^\dagger c_{\beta,\uparrow} + c_{\alpha,\uparrow}^\dagger c_{\alpha,\uparrow} c_{\beta,\uparrow}^\dagger c_{\beta,\uparrow} - c_{\alpha,\uparrow}^\dagger c_{\alpha,\uparrow} c_{\beta,\downarrow}^\dagger c_{\beta,\downarrow} - c_{\alpha,\downarrow}^\dagger c_{\alpha,\downarrow} c_{\beta,\uparrow}^\dagger c_{\beta,\uparrow} + 2c_{\alpha,\downarrow}^\dagger c_{\alpha,\uparrow} c_{\beta,\uparrow}^\dagger c_{\beta,\downarrow} + c_{\alpha,\downarrow}^\dagger c_{\alpha,\downarrow} c_{\beta,\downarrow}^\dagger c_{\beta,\downarrow} \right)$$

$$(C.19) \quad = \frac{1}{4} \left( \sum_{\sigma} 2c_{\alpha,\sigma}^\dagger c_{\alpha,-\sigma} c_{\beta,-\sigma}^\dagger c_{\beta,\sigma} + \sum_{\sigma\sigma'} \sigma\sigma' n_{\alpha,\sigma} n_{\beta,\sigma'} \right),$$

which leads to the following representation of the Hamilton operator

$$\begin{aligned} H &= \sum_{\alpha,\beta,i,j,\sigma} \left( t_{\alpha\beta}^{r_i-r_j} - \mu\delta_{i,j}\delta_{\alpha,\beta} \right) c_{\alpha,\sigma}^\dagger(r_i) c_{\beta,\sigma}(r_j) \\ &+ \sum_{\alpha,i} U_{\alpha\alpha} n_{\alpha,\uparrow}(r_i) n_{\alpha,\downarrow}(r_i) \\ &+ \sum_{\substack{\alpha,\beta,i,\sigma \\ \alpha \neq \beta}} \frac{U_{\alpha\beta}}{2} n_{\alpha,\sigma}(r_i) n_{\beta,-\sigma}(r_i) \\ &+ \sum_{\substack{\alpha,\beta,i,\sigma \\ \alpha \neq \beta}} \left( \frac{U_{\alpha\beta}}{2} - \frac{J_{\alpha\beta}}{2} \right) n_{\alpha,\sigma}(r_i) n_{\beta,\sigma}(r_i) \end{aligned}$$

$$\begin{aligned}
 & - \sum_{\substack{\alpha, \beta, i, \sigma \\ \alpha \neq \beta}} \frac{J_{\alpha\beta}}{2} c_{\alpha, \sigma}^\dagger(r_i) c_{\alpha, -\sigma}(r_i) c_{\beta, -\sigma}^\dagger(r_i) c_{\beta, \sigma}(r_i) \\
 (C.20) \quad & - \sum_{\substack{\alpha, \beta, i, \sigma \\ \alpha \neq \beta}} \frac{J_{\alpha\beta}}{2} c_{\alpha, \sigma}^\dagger(r_i) c_{\beta, -\sigma}(r_i) c_{\alpha, -\sigma}^\dagger(r_i) c_{\beta, \sigma}(r_i) \\
 & = \sum_{\alpha, \beta, i, j, \sigma} \left( t_{\alpha\beta}^{r_i - r_j} - \mu \delta_{i,j} \delta_{\alpha,\beta} \right) c_{\alpha, \sigma}^\dagger(r_i) c_{\beta, \sigma}(r_j) \\
 & + \frac{1}{2} \sum_{\alpha, \beta, i, \sigma} U_{\alpha\beta} n_{\alpha, \sigma}(r_i) n_{\beta, -\sigma}(r_i) \\
 & + \frac{1}{2} \sum_{\substack{\alpha, \beta, i, \sigma \\ \alpha \neq \beta}} (U_{\alpha\beta} - J_{\alpha\beta}) n_{\alpha, \sigma}(r_i) n_{\beta, \sigma}(r_i) \\
 & - \frac{1}{2} \sum_{\substack{\alpha, \beta, i, \sigma \\ \alpha \neq \beta}} J_{\alpha\beta} \left( c_{\alpha, \sigma}^\dagger(r_i) c_{\alpha, -\sigma}(r_i) c_{\beta, -\sigma}^\dagger(r_i) c_{\beta, \sigma}(r_i) \right. \\
 (C.21) \quad & \left. + c_{\alpha, \sigma}^\dagger(r_i) c_{\beta, -\sigma}(r_i) c_{\alpha, -\sigma}^\dagger(r_i) c_{\beta, \sigma}(r_i) \right).
 \end{aligned}$$

## References

- [1] X. Blanc and M. Lewin. The Crystallization Conjecture: A Review. *EMS Surveys in Mathematical Sciences* 2, 2015.
- [2] M. Dumm, D. Faltermeier, N. Drichko, M. Dressel, C. Mézière, and P. Batail. Bandwidth-controlled Mott transition in  $\kappa$ -(BEDT-TTF)<sub>2</sub>Cu[N(CN)<sub>2</sub>]Br<sub>x</sub>Cl<sub>1-x</sub>: Optical studies of correlated carriers. *Phys. Rev. B* 79:195106, 2009.
- [3] L. Taillefer. Scattering and Pairing in Cuprate Superconductors. *Annual Review of Condensed Matter Physics* 1 (1):51–70, 2010.
- [4] A. Martinelli, F. Bernardini, and S. Massida. The phase diagrams of iron-based superconductors: Theory and experiments. *Comptes Rendus Physique* 17 (1):5–35, 2016.
- [5] R. Tazai, Y. Yamakawa, M. Tsuchiizu, and H. Kontani. *Prediction of d-wave bond-order and pseudogap in organic superconductor  $\kappa$ -(BEDT-TTF)<sub>2</sub>X: Similarities to cuprate superconductors*, 2020.
- [6] J. Ferber, K. Foyevtsova, R. Valentí, and H. O. Jeschke. LDA + DMFT study of the effects of correlation in LiFeAs. *Phys. Rev. B* 85:094505, 2012.
- [7] G. Lee, H. S. Ji, Y. Kim, C. Kim, K. Haule, G. Kotliar, B. Lee, S. Khim, K. H. Kim, K. S. Kim, K.-S. Kim, and J. H. Shim. Orbital Selective Fermi Surface Shifts and Mechanism of High  $T_c$  Superconductivity in Correlated AFeAs ( $A = \text{Li, Na}$ ). *Phys. Rev. Lett.* 109:177001, 2012.
- [8] R. Nourafkan, G. Kotliar, and A.-M. S. Tremblay. Correlation-Enhanced Odd-Parity Interorbital Singlet Pairing in the Iron-Pnictide Superconductor LiFeAs. *Phys. Rev. Lett.* 117:137001, 2016.
- [9] J. M. Tomczak, M. van Schilfgaarde, and G. Kotliar. Many-Body Effects in Iron Pnictides and Chalcogenides: Nonlocal Versus Dynamic Origin of Effective Masses. *Phys. Rev. Lett.* 109:237010, 2012.
- [10] M. Kim, H. Miao, S. Choi, M. Zingl, A. Georges, and G. Kotliar. *On the Spatial Locality of Electronic Correlations in LiFeAs*, 2020.
- [11] V. Brouet, D. LeBoeuf, P.-H. Lin, J. Mansart, A. Taleb-Ibrahimi, P. Le Fèvre, F. Bertran, A. Forget, and D. Colson. ARPES view of orbitally resolved quasiparticle lifetimes in iron pnictides. *Phys. Rev. B* 93:085137, 2016.
- [12] J. Fink, J. Nayak, E. D. L. Rienks, J. Bannies, S. Wurmehl, S. Aswartham, I. Morozov, R. Kappenberger, M. A. ElGhazali, L. Craco, H. Rosner, C. Felser, and B. Büchner. Evidence of hot and cold spots on the Fermi surface of LiFeAs. *Phys. Rev. B* 99:245156, 2019.
- [13] E. Engel and R. M. Dreizler. *Density Functional Theory: An Advanced Course*. Theoretical and Mathematical Physics. Springer Berlin Heidelberg, 2011.
- [14] S. Cottenier. *Density Functional Theory and the family of (L)APW-methods: a step-by-step introduction*, 2nd ed., 2013. (freely available at [http://www.wien2k.at/reg\\_user/textbooks](http://www.wien2k.at/reg_user/textbooks)).
- [15] P. Blanchard and E. Brüning. *Mathematical Methods in Physics*. Birkhäuser Basel, 2015.
- [16] R. M. Martin. *Electronic Structure: Basic Theory and Practical Methods*. Cambridge University Press, 2020.
- [17] M. Born and R. Oppenheimer. Zur Quantentheorie der Molekeln. *Annalen der Physik* 389 (20):457–484, 1927.
- [18] P. Hohenberg and W. Kohn. Inhomogeneous Electron Gas. *Phys. Rev.* 136:B864–B871, 1964.
- [19] E. H Lieb and B. Simon. The Thomas-Fermi theory of atoms, molecules and solids. *Advances in Mathematics* 23 (1):22–116, 1977.
- [20] V. L. Lignères and E. A. Carter. *An Introduction to Orbital-Free Density Functional Theory*. Edited by S. Yip. Springer Netherlands, Dordrecht, 2005.
- [21] R. G. Parr and W. Yang. *Density-Functional Theory of Atoms and Molecules*. Oxford University Press New York, 1989.
- [22] J. P. Perdew, A. Ruzsinszky, J. Tao, V. N. Staroverov, G. E. Scuseria, and G. I. Csonka. Prescription for the design and selection of density functional approximations: More constraint satisfaction with fewer fits. *The Journal of Chemical Physics* 123 (6):062201, 2005.
- [23] S. F. Sousa, P. A. Fernandes, and M. J. Ramos. General Performance of Density Functionals. *The Journal of Physical Chemistry A* 111 (42):10439–10452, 2007. PMID: 17718548.

- 
- [24] L. Goerigk and S. Grimme. Double-hybrid density functionals. *WIREs Computational Molecular Science* 4 (6):576–600, 2014.
- [25] R. Peverati and D. G. Truhlar. Quest for a universal density functional: the accuracy of density functionals across a broad spectrum of databases in chemistry and physics. *Philosophical Transactions of the Royal Society A: Mathematical, Physical and Engineering Sciences* 372 (2011):20120476, 2014.
- [26] V. I Anisimov, F Aryasetiawan, and A I Lichtenstein. First-principles calculations of the electronic structure and spectra of strongly correlated systems: the LDA+U method. *Journal of Physics: Condensed Matter* 9 (4):767–808, 1997.
- [27] M. Petersilka, U. J. Gossmann, and E. K. U. Gross. Excitation Energies from Time-Dependent Density-Functional Theory. *Phys. Rev. Lett.* 76:1212–1215, 1996.
- [28] R. M. Dreizler and E. K. U. Gross. *Density Functional Theory: An Approach to the Quantum Many-Body Problem*. Springer Berlin Heidelberg, 2012.
- [29] W. M. C. Foulkes, L. Mitas, R. J. Needs, and G. Rajagopal. Quantum Monte Carlo simulations of solids. *Rev. Mod. Phys.* 73:33–83, 2001.
- [30] A. L. Fetter and J. D. Walecka. *Quantum Theory of Many-particle Systems*. Dover Books on Physics. Dover Publications, 2003.
- [31] E. Runge and E. K. U. Gross. Density-Functional Theory for Time-Dependent Systems. *Phys. Rev. Lett.* 52:997–1000, 1984.
- [32] W. Kohn and L. J. Sham. Self-Consistent Equations Including Exchange and Correlation Effects. *Phys. Rev.* 140:A1133–A1138, 1965.
- [33] J. P. Perdew, R. G. Parr, M. Levy, and J. L. Balduz. Density-Functional Theory for Fractional Particle Number: Derivative Discontinuities of the Energy. *Phys. Rev. Lett.* 49:1691–1694, 1982.
- [34] C.-O. Almbladh and U. von Barth. Exact results for the charge and spin densities, exchange-correlation potentials, and density-functional eigenvalues. *Phys. Rev. B* 31:3231–3244, 1985.
- [35] U. Salzner and R. Baer. Koopmans’ springs to life. *The Journal of Chemical Physics* 131 (23):231101, 2009.
- [36] P. A. M. Dirac. Note on Exchange Phenomena in the Thomas Atom. *Mathematical Proceedings of the Cambridge Philosophical Society* 26 (3):376–385, 1930.
- [37] D. M. Ceperley and B. J. Alder. Ground State of the Electron Gas by a Stochastic Method. *Phys. Rev. Lett.* 45:566–569, 1980.
- [38] D. C. Langreth and M. J. Mehl. Beyond the local-density approximation in calculations of ground-state electronic properties. *Phys. Rev. B* 28:1809–1834, 1983.
- [39] J. P. Perdew, J. A. Chevary, S. H. Vosko, K. A. Jackson, M. R. Pederson, D. J. Singh, and C. Fiolhais. Atoms, molecules, solids, and surfaces: Applications of the generalized gradient approximation for exchange and correlation. *Phys. Rev. B* 46:6671–6687, 1992.
- [40] J. P. Perdew, K. Burke, and M. Ernzerhof. Generalized Gradient Approximation Made Simple. *Phys. Rev. Lett.* 77:3865–3868, 1996.
- [41] J. C. Slater. Atomic Shielding Constants. *Phys. Rev.* 36:57–64, 1930.
- [42] E. Clementi and D. L. Raimondi. Atomic Screening Constants from SCF Functions. *The Journal of Chemical Physics* 38 (11):2686–2689, 1963.
- [43] N. F. Mott. *Metal-insulator Transitions*. Taylor & Francis, 1974.
- [44] M. Imada, A. Fujimori, and Y. Tokura. Metal-insulator transitions. *Rev. Mod. Phys.* 70:1039–1263, 1998.
- [45] G. R. Stewart. Heavy-fermion systems. *Rev. Mod. Phys.* 56:755–787, 1984.
- [46] G. Zwirner. Quasi-particles in heavy fermion systems. *Advances in Physics* 41 (3):203–302, 1992.
- [47] P. Phillips. Mottness. *Annals of Physics* 321 (7):1634–1650, 2006. July 2006 Special Issue.
- [48] A. Alexandradinata, N. P. Armitage, A. Baydin, W. Bi, Y. Cao, H. J. Changlani, E. Chertkov, E. H. da Silva Neto, L. Delacretaz, I. E. Baggari, G. M. Ferguson, W. J. Gannon, S. A. A. Ghorashi, B. H. Goodge, O. Goulko, G. Grissonnanche, A. Hallas, I. M. Hayes, Y. He, E. W. Huang, A. Kogar, D. Kumah, J. Y. Lee, A. Legros, F. Mahmood, Y. Maximenko, N. Pellatz, H. Polshyn, T. Sarkar, A. Scheie, K. L. Seyler, Z. Shi, B. Skinner, L. Steinke, K. Thirunavukkuarasu, T. V. Trevisan, M. Vogl, P. A. Volkov, Y. Wang, Y. Wang, D. Wei, K. Wei, S. Yang, X. Zhang, Y.-H. Zhang, L. Zhao, and A. Zong. *The Future of the Correlated Electron Problem*, 2020.
- [49] P.-O. Löwdin. A Note on the Quantum-Mechanical Perturbation Theory. *The Journal of Chemical Physics* 19 (11):1396–1401, 1951.
- [50] P.-O. Löwdin. Quantum Theory of Many-Particle Systems. I. Physical Interpretations by Means of Density Matrices, Natural Spin-Orbitals, and Convergence Problems in the Method of Configurational Interaction. *Phys. Rev.* 97:1474–1489, 1955.

- [51] W. R. L. Lambrecht and O. K. Andersen. Minimal basis sets in the linear muffin-tin orbital method: Application to the diamond-structure crystals C, Si, and Ge. *Phys. Rev. B* 34:2439–2449, 1986.
- [52] P. Werner and M. Casula. Dynamical screening in correlated electron systems—from lattice models to realistic materials. *Journal of Physics: Condensed Matter* 28 (38):383001, 2016.
- [53] M. E. Fisher. The renormalization group in the theory of critical behavior. *Rev. Mod. Phys.* 46:597–616, 1974.
- [54] K. G. Wilson. The renormalization group: Critical phenomena and the Kondo problem. *Rev. Mod. Phys.* 47:773–840, 1975.
- [55] R. Shankar. Renormalization-group approach to interacting fermions. *Rev. Mod. Phys.* 66:129–192, 1994.
- [56] N. Marzari and D. Vanderbilt. Maximally localized generalized Wannier functions for composite energy bands. *Phys. Rev. B* 56:12847–12865, 1997.
- [57] I. Souza, N. Marzari, and D. Vanderbilt. Maximally localized Wannier functions for entangled energy bands. *Phys. Rev. B* 65:035109, 2001.
- [58] A. A. Mostofi, J. R. Yates, Y.-S. Lee, I. Souza, D. Vanderbilt, and N. Marzari. wannier90: A tool for obtaining maximally-localised Wannier functions. *Computer Physics Communications* 178 (9):685–699, 2008.
- [59] J. Kuneš, R. Arita, P. Wissgott, A. Toschi, H. Ikeda, and K. Held. Wien2wannier: From linearized augmented plane waves to maximally localized Wannier functions. *Computer Physics Communications* 181 (11):1888–1895, 2010.
- [60] E. Pavarini, E. Koch, D. Vollhardt, and A. Lichtenstein. *DMFT at 25: Infinite Dimensions. Modeling and Simulation*, vol. 4. Forschungszentrum Jülich Zentralbibliothek, Verlag. Autumn School on Correlated Electrons, Jülich (Germany), 15 Sep 2014 - 19 Sep 2014, Jülich, 2014.
- [61] E. Pavarini, E. Koch, and P. Coleman. *Many-Body Physics: From Kondo to Hubbard. Modeling and Simulation*, vol. 5. Forschungszentrum Jülich GmbH Zentralbibliothek, Verlag. Autumn School on Correlated Electrons, Jülich (Germany), 21 Sep 2015 - 25 Sep 2015, Jülich, 2015.
- [62] E. Pavarini, E. Koch, A. Lichtenstein, and D. (Eds.) Vollhardt. *The LDA+DMFT approach to strongly correlated materials*. Schriften des Forschungszentrums Jülich : Modeling and Simulation, vol. 1, 2011. Record converted from VDB: 12.11.2012.
- [63] E. Pavarini, E. Koch, F. Anders, and M. (Eds.) Jarrell. *Correlated electrons: from models to materials*. Schriften des Forschungszentrums Jülich. Reihe Modeling and simulation, vol. 2. Forschungszentrum Jülich GmbH, Jülich, 2012. Record converted from JUWEL: 18.07.2013.
- [64] M. C. Gutzwiller. Effect of Correlation on the Ferromagnetism of Transition Metals. *Phys. Rev. Lett.* 10:159–162, 1963.
- [65] J. Hubbard. Electron correlations in narrow energy bands. *Proceedings of the Royal Society of London. Series A. Mathematical and Physical Sciences* 276 (1365):238–257, 1963.
- [66] J. Kanamori. Electron Correlation and Ferromagnetism of Transition Metals. *Progress of Theoretical Physics* 30 (3):275–289, 1963.
- [67] M. Springer and F. Aryasetiawan. Frequency-dependent screened interaction in Ni within the random-phase approximation. *Phys. Rev. B* 57:4364–4368, 1998.
- [68] F. Aryasetiawan, M. Imada, A. Georges, G. Kotliar, S. Biermann, and A. I. Lichtenstein. Frequency-dependent local interactions and low-energy effective models from electronic structure calculations. *Phys. Rev. B* 70:195104, 2004.
- [69] F. Aryasetiawan, K. Karlsson, O. Jepsen, and U. Schönberger. Calculations of Hubbard  $U$  from first-principles. *Phys. Rev. B* 74:125106, 2006.
- [70] F. Aryasetiawan, J. M. Tomczak, T. Miyake, and R. Sakuma. Downfolded Self-Energy of Many-Electron Systems. *Phys. Rev. Lett.* 102:176402, 2009.
- [71] T. Miyake, F. Aryasetiawan, and M. Imada. Ab initio procedure for constructing effective models of correlated materials with entangled band structure. *Phys. Rev. B* 80:155134, 2009.
- [72] P. Fazekas. *Lecture Notes on Electron Correlation and Magnetism*. WORLD SCIENTIFIC, 1999.
- [73] P. Fulde. *Electron Correlations in Molecules and Solids*. Springer Series in Solid-State Sciences. Springer Berlin Heidelberg, 2012.
- [74] I. Ivantsov, A. Ferraz, and E. Kochetov. *Hubbard model vs. Kondo model: Strong coupling limit*, 2020.
- [75] R. A. Bari. Effects of Short-Range Interactions on Electron-Charge Ordering and Lattice Distortions in the Localized State. *Phys. Rev. B* 3:2662–2670, 1971.
- [76] J. E. Hirsch. Charge-Density-Wave to Spin-Density-Wave Transition in the Extended Hubbard Model. *Phys. Rev. Lett.* 53:2327–2330, 1984.
- [77] W. F. Brinkman and T. M. Rice. Application of Gutzwiller’s Variational Method to the Metal-Insulator Transition. *Phys. Rev. B* 2:4302–4304, 1970.

- 
- [78] E. H. Lieb and F. Y. Wu. Absence of Mott Transition in an Exact Solution of the Short-Range, One-Band Model in One Dimension. *Phys. Rev. Lett.* 20:1445–1448, 1968.
- [79] A. A. Ovchinnikov. Excitation Spectrum in the One-dimensional Hubbard Model. *JETP* 30 (6):1160, 1970.
- [80] C. F. Coll. Excitation spectrum of the one-dimensional Hubbard model. *Phys. Rev. B* 9:2150–2158, 1974.
- [81] F. Woynarovich. Excitations with complex wavenumbers in a Hubbard chain. I. States with one pair of complex wavenumbers. *Journal of Physics C: Solid State Physics* 15 (1):85–96, 1982.
- [82] F. H. L. Essler, V. E. Korepin, and K. Schoutens. Complete solution of the one-dimensional Hubbard model. *Phys. Rev. Lett.* 67:3848–3851, 1991.
- [83] E. H. Lieb. *XIth International Congress of Mathematical Physics*. Edited by D. Iagolnitzer. International Press, 1995.
- [84] F. H. L. Essler, H. Frahm, F. Göhmann, A. Klümper, and V. E. Korepin. *The One-Dimensional Hubbard Model*. Cambridge University Press, 2005.
- [85] A. Georges and G. Kotliar. Hubbard model in infinite dimensions. *Physical Review B* 45 (12):6479, 1992.
- [86] M. Jarrell. Hubbard model in infinite dimensions: A quantum Monte Carlo study. *Phys. Rev. Lett.* 69:168–171, 1992.
- [87] W. Metzner and D. Vollhardt. Correlated Lattice Fermions in  $d = \infty$  Dimensions. *Phys. Rev. Lett.* 62:324–327, 1989.
- [88] A. Georges, G. Kotliar, W. Krauth, and M. J. Rozenberg. Dynamical mean-field theory of strongly correlated fermion systems and the limit of infinite dimensions. *Rev. Mod. Phys.* 68:13–125, 1996.
- [89] H. Tasaki. The Hubbard Model: Introduction and Selected Rigorous Results. *arXiv e-prints:cond-mat/9512169*, 1995.
- [90] E. H. Lieb. Two theorems on the Hubbard model. *Phys. Rev. Lett.* 62:1201–1204, 1989.
- [91] N. D. Mermin and H. Wagner. Absence of Ferromagnetism or Antiferromagnetism in One- or Two-Dimensional Isotropic Heisenberg Models. *Phys. Rev. Lett.* 17:1133–1136, 1966.
- [92] M. B. Walker and Th. W. Ruijgrok. Absence of Magnetic Ordering in One and Two Dimensions in a Many-Band Model for Interacting Electrons in a Metal. *Phys. Rev.* 171:513–515, 1968.
- [93] D. K. Ghosh. Nonexistence of Magnetic Ordering in the One- and Two-Dimensional Hubbard Model. *Phys. Rev. Lett.* 27:1584–1587, 1971.
- [94] P. C. Hohenberg. Existence of Long-Range Order in One and Two Dimensions. *Phys. Rev.* 158:383–386, 1967.
- [95] T. Koma and H. Tasaki. Decay of superconducting and magnetic correlations in one- and two-dimensional Hubbard models. *Phys. Rev. Lett.* 68:3248–3251, 1992.
- [96] V. L. Berezinskiĭ. Destruction of Long-range Order in One-dimensional and Two-dimensional Systems having a Continuous Symmetry Group I. Classical Systems. *Soviet Journal of Experimental and Theoretical Physics* 32:493, 1971.
- [97] J M Kosterlitz and D J Thouless. Ordering, metastability and phase transitions in two-dimensional systems. *Journal of Physics C: Solid State Physics* 6 (7):1181–1203, 1973.
- [98] J. M. Kosterlitz. The critical properties of the two-dimensional xy model. *Journal of Physics C: Solid State Physics* 7 (6):1046–1060, 1974.
- [99] T. Yanagisawa. Kosterlitz–Thouless Transition in Two-Dimensional Hubbard Model Evidenced from Quantum Monte Carlo Calculations of Susceptibilities. *Journal of the Physical Society of Japan* 79 (6):063708, 2010.
- [100] A. K. McMahan, R. M. Martin, and S. Satpathy. Calculated effective Hamiltonian for  $\text{La}_2\text{CuO}_4$  and solution in the impurity Anderson approximation. *Phys. Rev. B* 38:6650–6666, 1988.
- [101] O. Gunnarsson, O. K. Andersen, O. Jepsen, and J. Zaanen. Density-functional calculation of the parameters in the Anderson model: Application to Mn in CdTe. *Phys. Rev. B* 39:1708–1722, 1989.
- [102] M. S. Hybertsen, M. Schlüter, and N. E. Christensen. Calculation of Coulomb-interaction parameters for  $\text{La}_2\text{CuO}_4$  using a constrained-density-functional approach. *Phys. Rev. B* 39:9028–9041, 1989.
- [103] O. Gunnarsson. Calculation of parameters in model Hamiltonians. *Phys. Rev. B* 41:514–518, 1990.
- [104] V. I. Anisimov and O. Gunnarsson. Density-functional calculation of effective Coulomb interactions in metals. *Phys. Rev. B* 43:7570–7574, 1991.
- [105] M. Cococcioni and S. de Gironcoli. Linear response approach to the calculation of the effective interaction parameters in the LDA + U method. *Phys. Rev. B* 71:035105, 2005.

- 
- [106] M. Casula, A. Rubtsov, and S. Biermann. Dynamical screening effects in correlated materials: Plasmon satellites and spectral weight transfers from a Green's function ansatz to extended dynamical mean field theory. *Phys. Rev. B* 85:035115, 2012.
- [107] J. Schwinger. On the Green's functions of quantized fields. I. *Proc. Natl. Acad. Sci.* 37 (7):452, 1951.
- [108] L. Hedin. New Method for Calculating the One-Particle Green's Function with Application to the Electron-Gas Problem. *Phys. Rev.* 139:A796–A823, 1965.
- [109] I. G. Lang and Y. A. Firsov. KINETIC THEORY OF SEMICONDUCTORS WITH LOW MOBILITY. *Sov. Phys. JETP* 16 (5):1301, 1963.
- [110] A.-M. S. Tremblay. *PHY-892 Problème à N-corps (notes de cours)*, 2014.
- [111] A. Avella and F. Mancini. *Strongly Correlated Systems: Numerical Methods*. Springer Series in Solid-State Sciences. Springer Berlin Heidelberg, 2013.
- [112] D. Sénéchal, A. M. Tremblay, and C. Bourbonnais. *Theoretical Methods for Strongly Correlated Electrons*. CRM Series in Mathematical Physics. Springer New York, 2006.
- [113] L. P. Kadanoff and G. Baym. *Quantum Statistical Mechanics: Green's Function Methods in Equilibrium and Nonequilibrium Problems*. Frontiers in Physics. A Lecture Note and Reprint Series. Benjamin, 1962.
- [114] P. C. Martin and J. Schwinger. Theory of Many-Particle Systems. I. *Phys. Rev.* 115:1342–1373, 1959.
- [115] G. Baym and L. P. Kadanoff. Conservation Laws and Correlation Functions. *Phys. Rev.* 124:287–299, 1961.
- [116] G. Baym. Self-Consistent Approximations in Many-Body Systems. *Phys. Rev.* 127:1391–1401, 1962.
- [117] J. M. Luttinger. Fermi Surface and Some Simple Equilibrium Properties of a System of Interacting Fermions. *Phys. Rev.* 119:1153–1163, 1960.
- [118] J. M. Luttinger and J. C. Ward. Ground-State Energy of a Many-Fermion System. II. *Phys. Rev.* 118:1417–1427, 1960.
- [119] M. Taylor. *Partial Differential Equations I*. 115. Springer-Verlag New York, 2nd ed., 2011.
- [120] G. Baym and N. D. Mermin. Determination of Thermodynamic Green's Functions. *Journal of Mathematical Physics* 2 (2):232–234, 1961.
- [121] M. R. Norman, H. Ding, H. Fretwell, M. Randeria, and J. C. Campuzano. Extraction of the electron self-energy from angle-resolved photoemission data: Application to  $\text{Bi}_2\text{Sr}_2\text{CaCu}_2\text{O}_{8+x}$ . *Phys. Rev. B* 60:7585–7590, 1999.
- [122] A. Damascelli. Probing the Electronic Structure of Complex Systems by ARPES. *Physica Scripta* 2004:61, 2004.
- [123] S. Hüfner, editor. *Very High Resolution Photoelectron Spectroscopy*. Lecture Notes in Physics, vol. 715. Springer-Verlag Berlin Heidelberg, 2007.
- [124] S. Hüfner. *Photoelectron Spectroscopy: Principles and Applications*. Advanced Texts in Physics. Springer Berlin Heidelberg, 2013.
- [125] A. A. Kordyuk. ARPES experiment in fermiology of quasi-2D metals (Review Article). *Low Temperature Physics* 40 (4):286–296, 2014.
- [126] A. V. Chubukov and D. L. Maslov. First-Matsubara-frequency rule in a Fermi liquid. I. Fermionic self-energy. *Phys. Rev. B* 86:155136, 2012.
- [127] A. V Ferris-Prabhu and D. H Withers. Numerical analytic continuation using Padé approximants. *Journal of Computational Physics* 13 (1):94–99, 1973.
- [128] K. S. D. Beach, R. J. Gooding, and F. Marsiglio. Reliable Padé analytical continuation method based on a high-accuracy symbolic computation algorithm. *Phys. Rev. B* 61:5147–5157, 2000.
- [129] S. F. Gull and J. Skilling. Maximum entropy method in image processing. *IEE Proceedings F (Communications, Radar and Signal Processing)* 131:646–659(13), 1984.
- [130] R. N. Silver, D. S. Sivia, and J. E. Gubernatis. Maximum-entropy method for analytic continuation of quantum Monte Carlo data. *Phys. Rev. B* 41:2380–2389, 1990.
- [131] J. E. Gubernatis, M. Jarrell, R. N. Silver, and D. S. Sivia. Quantum Monte Carlo simulations and maximum entropy: Dynamics from imaginary-time data. *Phys. Rev. B* 44:6011–6029, 1991.
- [132] F. Bao, Y. Tang, M. Summers, G. Zhang, C. Webster, V. Scarola, and T. A. Maier. Fast and efficient stochastic optimization for analytic continuation. *Phys. Rev. B* 94:125149, 2016.
- [133] G. J. Kraberger, R. Triebl, M. Zingl, and M. Aichhorn. Maximum entropy formalism for the analytic continuation of matrix-valued Green's functions. *Phys. Rev. B* 96:155128, 2017.
- [134] H Eschrig, R Richter, and B Velicky. A numerical method of analytical continuation of Green-function-like expressions. *Journal of Physics C: Solid State Physics* 19 (36):7173–7181, 1986.

- 
- [135] C. E. Creffield, E. G. Klepfish, E. R. Pike, and S. Sarkar. Spectral Weight Function for the Half-Filled Hubbard Model: A Singular Value Decomposition Approach. *Phys. Rev. Lett.* 75:517–520, 1995.
- [136] L.-F. Arsenault, R. Neuberger, L. A. Hannah, and A. J. Millis. Projected regression method for solving Fredholm integral equations arising in the analytic continuation problem of quantum physics. *Inverse Problems* 33 (11):115007, 2017.
- [137] J. Otsuki, M. Ohzeki, H. Shinaoka, and K. Yoshimi. Sparse modeling approach to analytical continuation of imaginary-time quantum Monte Carlo data. *Phys. Rev. E* 95:061302, 2017.
- [138] A. W. Sandvik. Stochastic method for analytic continuation of quantum Monte Carlo data. *Phys. Rev. B* 57:10287–10290, 1998.
- [139] A. S. Mishchenko, N. V. Prokof'ev, A. Sakamoto, and B. V. Svistunov. Diagrammatic quantum Monte Carlo study of the Fröhlich polaron. *Phys. Rev. B* 62:6317–6336, 2000.
- [140] K. S. D. Beach. Identifying the maximum entropy method as a special limit of stochastic analytic continuation. *arXiv e-prints:cond-mat/0403055*, 2004.
- [141] S. Fuchs, T. Pruschke, and M. Jarrell. Analytic continuation of quantum Monte Carlo data by stochastic analytical inference. *Phys. Rev. E* 81:056701, 2010.
- [142] A. W. Sandvik. Constrained sampling method for analytic continuation. *Phys. Rev. E* 94:063308, 2016.
- [143] M. Rumetshofer, D. Bauernfeind, and W. von der Linden. Bayesian parametric analytic continuation of Green's functions. *Phys. Rev. B* 100:075137, 2019.
- [144] H. Padé. Sur la représentation approchée d'une fonction par des fractions rationnelles. *Annales scientifiques de l'École Normale Supérieure* 3e série, 9:3–93, 1892.
- [145] J. Hubbard. Electron correlations in narrow energy bands. II. The degenerate band case. *Proceedings of the Royal Society of London. Series A. Mathematical and Physical Sciences* 277 (1369):237–259, 1964.
- [146] J. P. F. LeBlanc, A. E. Antipov, F. Becca, I. W. Bulik, G. K.-L. Chan, C.-M. Chung, Y. Deng, M. Ferrero, T. M. Henderson, C. A. Jiménez-Hoyos, E. Kozik, X.-W. Liu, A. J. Millis, N. V. Prokof'ev, M. Qin, G. E. Scuseria, H. Shi, B. V. Svistunov, L. F. Tocchio, I. S. Tupitsyn, S. R. White, S. Zhang, B.-X. Zheng, Z. Zhu, and E. Gull. Solutions of the Two-Dimensional Hubbard Model: Benchmarks and Results from a Wide Range of Numerical Algorithms. *Phys. Rev. X* 5:041041, 2015.
- [147] G. Rohringer, H. Hafermann, A. Toschi, A. A. Katanin, A. E. Antipov, M. I. Katsnelson, A. I. Lichtenstein, A. N. Rubtsov, and K. Held. Diagrammatic routes to nonlocal correlations beyond dynamical mean field theory. *Rev. Mod. Phys.* 90:025003, 2018.
- [148] T. Schäfer, N. Wentzell, F. Šimkovic IV, Y.-Y. He, C. Hille, M. Klett, C. J. Eckhardt, B. Arzhang, V. Harkov, F.-M. L. Régent, A. Kirsch, Y. Wang, A. J. Kim, E. Kozik, E. A. Stepanov, A. Kauch, S. Andergassen, P. Hansmann, D. Rohe, Y. M. Vilck, J. P. F. LeBlanc, S. Zhang, A. M. S. Tremblay, M. Ferrero, O. Parcollet, and A. Georges. *Tracking the Footprints of Spin Fluctuations: A Multi-Method, Multi-Messenger Study of the Two-Dimensional Hubbard Model*, 2020.
- [149] M. C. Gutzwiller. Effect of Correlation on the Ferromagnetism of Transition Metals. *Phys. Rev.* 134:A923–A941, 1964.
- [150] M. C. Gutzwiller. Correlation of Electrons in a Narrow  $s$  Band. *Phys. Rev.* 137:A1726–A1735, 1965.
- [151] T. Ogawa, K. Kanda, and T. Matsubara. Gutzwiller Approximation for Antiferromagnetism in Hubbard Model. *Progress of Theoretical Physics* 53 (3):614–633, 1975.
- [152] S. Arya, P. V. Sriluckshmy, S. R. Hassan, and A.-M. S. Tremblay. Antiferromagnetism in the Hubbard model on the honeycomb lattice: A two-particle self-consistent study. *Phys. Rev. B* 92:045111, 2015.
- [153] S. Moukouri, S. Allen, F. Lemay, B. Kyung, D. Poulin, Y. M. Vilck, and A.-M. S. Tremblay. Many-body theory versus simulations for the pseudogap in the Hubbard model. *Phys. Rev. B* 61:7887–7892, 2000.
- [154] S. Allen, A. M. S. Tremblay, and Y. M. Vilck. *Conserving Approximations vs. Two-Particle Self-Consistent Approach*. Edited by D. Sénéchal, A.-M. Tremblay, and C. Bourbonnais. Springer New York, New York, NY, 2004.
- [155] A.-M. S. Tremblay. *Two-Particle-Self-Consistent Approach for the Hubbard Model*. Edited by A. Avella and F. Mancini. Springer Berlin Heidelberg, Berlin, Heidelberg, 2012.
- [156] E. Koch. *Many-Body Methods for Real Materials*. Schriften des Forschungszentrums Jülich Modeling and Simulation, vol. 9. Edited by E. Pavarini and S. Zhang. Forschungszentrum Jülich GmbH Zentralbibliothek, Verlag. Autumn School on Correlated Electrons, Jülich (Germany), 16 Sep 2019 - 20 Sep 2019, Jülich, 2019.

- 
- [157] A. A. Abrikosov, L. P. Gorkov, I. E. Dzyaloshinski, and R. A. Silverman. *Methods of Quantum Field Theory in Statistical Physics*. Dover Books on Physics. Dover Publications, 2012.
- [158] G. Rohringer, A. Valli, and A. Toschi. Local electronic correlation at the two-particle level. *Phys. Rev. B* 86:125114, 2012.
- [159] G. Rohringer, *New routes towards a theoretical treatment of nonlocal electronic correlations*. Ph.D. Thesis, 2013.
- [160] O. Gunnarsson, T. Schäfer, J. P. F. LeBlanc, J. Merino, G. Sangiovanni, G. Rohringer, and A. Toschi. Parquet decomposition calculations of the electronic self-energy. *Phys. Rev. B* 93:245102, 2016.
- [161] S. Allen. *Two-particle self-consistent approximation, pseudogap and superconductivity in the attractive Hubbard model*, 2000.
- [162] S. Allen and A.-M. S. Tremblay. Nonperturbative approach to the attractive Hubbard model. *Phys. Rev. B* 64:075115, 2001.
- [163] Y.M. Vilk and A.-M.S. Tremblay. Non-Perturbative Many-Body Approach to the Hubbard Model and Single-Particle Pseudogap. *J. Phys. I France* 7 (11):1309–1368, 1997.
- [164] K. Zantout, S. Backes, and R. Valentí. *Two-Particle Self-Consistent method for the multi-orbital Hubbard model*, 2020.
- [165] T. Schäfer, G. Rohringer, O. Gunnarsson, S. Ciuchi, G. Sangiovanni, and A. Toschi. Divergent Precursors of the Mott-Hubbard Transition at the Two-Particle Level. *Phys. Rev. Lett.* 110:246405, 2013.
- [166] E. Kozik, M. Ferrero, and A. Georges. Nonexistence of the Luttinger-Ward Functional and Misleading Convergence of Skeleton Diagrammatic Series for Hubbard-Like Models. *Phys. Rev. Lett.* 114:156402, 2015.
- [167] J. Gukelberger, L. Huang, and P. Werner. On the dangers of partial diagrammatic summations: Benchmarks for the two-dimensional Hubbard model in the weak-coupling regime. *Phys. Rev. B* 91:235114, 2015.
- [168] N. E Bickers and D. J Scalapino. Conserving approximations for strongly fluctuating electron systems. I. Formalism and calculational approach. *Annals of Physics* 193 (1):206–251, 1989.
- [169] N. E. Bickers, D. J. Scalapino, and S. R. White. Conserving Approximations for Strongly Correlated Electron Systems: Bethe-Salpeter Equation and Dynamics for the Two-Dimensional Hubbard Model. *Phys. Rev. Lett.* 62:961–964, 1989.
- [170] N. E. Bickers and S. R. White. Conserving approximations for strongly fluctuating electron systems. II. Numerical results and parquet extension. *Phys. Rev. B* 43:8044–8064, 1991.
- [171] N. E. Bickers. PARQUET EQUATIONS FOR NUMERICAL SELF-CONSISTENT-FIELD THEORY. *International Journal of Modern Physics B* 05 (01n02):253–270, 1991.
- [172] S. Graser, T. Maier, P. Hirschfeld, and D. Scalapino. Near-degeneracy of several pairing channels in multiorbital models for the Fe pnictides. *New Journal of Physics* 11 (2):025016, 2009.
- [173] M. Altmeyer, D. Guterding, P. Hirschfeld, T. A Maier, R. Valentí, and D. J Scalapino. Role of vertex corrections in the matrix formulation of the random phase approximation for the multiorbital Hubbard model. *Physical Review B* 94 (21):214515, 2016.
- [174] F. Aryasetiawan and O. Gunnarsson. The GW method. *Reports on Progress in Physics* 61 (3):237–312, 1998.
- [175] W. G. Aulbur, L. Jönsson, and J. W. Wilkins. Quasiparticle Calculations in Solids, pages 1–218. 2000.
- [176] L. Reining. The GW approximation: content, successes and limitations. *WIREs Computational Molecular Science* 8 (3):e1344, 2018.
- [177] A. Georges and W. Krauth. Physical properties of the half-filled Hubbard model in infinite dimensions. *Phys. Rev. B* 48:7167–7182, 1993.
- [178] G. Kotliar, S. Y. Savrasov, K. Haule, V. S. Oudovenko, O. Parcollet, and C. A. Marianetti. Electronic structure calculations with dynamical mean-field theory. *Rev. Mod. Phys.* 78:865–951, 2006.
- [179] V I Anisimov, A I Poteryaev, M A Korotin, A O Anokhin, and G Kotliar. First-principles calculations of the electronic structure and spectra of strongly correlated systems: dynamical mean-field theory. *Journal of Physics: Condensed Matter* 9 (35):7359–7367, 1997.
- [180] A. I. Lichtenstein and M. I. Katsnelson. Ab initio calculations of quasiparticle band structure in correlated systems: LDA++ approach. *Phys. Rev. B* 57:6884–6895, 1998.
- [181] K Held, I. Nekrasov, G Keller, V Eyert, N Blümer, A. McMahan, R. Scalettar, T. Pruschke, V. Anisimov, and D. Vollhardt. Realistic investigations of correlated electron systems with LDA+DMFT. *physica status solidi (b)* 243 (11):2599–2631, 2006.

- 
- [182] S. Biermann, F. Aryasetiawan, and A. Georges. First-Principles Approach to the Electronic Structure of Strongly Correlated Systems: Combining the *GW* Approximation and Dynamical Mean-Field Theory. *Phys. Rev. Lett.* 90:086402, 2003.
- [183] S. Biermann. Dynamical screening effects in correlated electron materials - a progress report on combined many-body perturbation and dynamical mean field theory: *GW* + DMFT. *Journal of Physics: Condensed Matter* 26 (17):173202, 2014.
- [184] G. Kotliar, S. Y. Savrasov, G. Pálsson, and G. Biroli. Cellular Dynamical Mean Field Approach to Strongly Correlated Systems. *Phys. Rev. Lett.* 87:186401, 2001.
- [185] T. Maier, M. Jarrell, T. Pruschke, and M. H. Hettler. Quantum cluster theories. *Rev. Mod. Phys.* 77:1027–1080, 2005.
- [186] A.-M. S. Tremblay, B. Kyung, and D. Sénéchal. Pseudogap and high-temperature superconductivity from weak to strong coupling. Towards a quantitative theory (Review Article). *Low Temperature Physics* 32 (4):424–451, 2006.
- [187] H. Park, K. Haule, and G. Kotliar. Cluster Dynamical Mean Field Theory of the Mott Transition. *Phys. Rev. Lett.* 101:186403, 2008.
- [188] M. H. Hettler, A. N. Tahvildar-Zadeh, M. Jarrell, T. Pruschke, and H. R. Krishnamurthy. Nonlocal dynamical correlations of strongly interacting electron systems. *Phys. Rev. B* 58:R7475–R7479, 1998.
- [189] M. H. Hettler, M. Mukherjee, M. Jarrell, and H. R. Krishnamurthy. Dynamical cluster approximation: Nonlocal dynamics of correlated electron systems. *Phys. Rev. B* 61:12739–12756, 2000.
- [190] Maier, Th., Jarrell, M., Pruschke, Th., and Keller, J. A non-crossing approximation for the study of intersite correlations. *Eur. Phys. J. B* 13 (4):613–624, 2000.
- [191] H. Lee, K. Foyevtsova, J. Ferber, M. Aichhorn, H. O Jeschke, and R. Valenti. Dynamical cluster approximation within an augmented plane wave framework: Spectral properties of SrVO<sub>3</sub>. *Physical Review B* 85 (16):165103, 2012.
- [192] L. F Tocchio, H. Lee, H. O Jeschke, R. Valenti, and C. Gros. Mott correlated states in the underdoped two-dimensional Hubbard model: Variational Monte Carlo versus a dynamical cluster approximation. *Physical Review B* 87 (4):045111, 2013.
- [193] P. Staar, T. Maier, and T. C. Schulthess. Dynamical cluster approximation with continuous lattice self-energy. *Phys. Rev. B* 88:115101, 2013.
- [194] A. Toschi, A. A. Katanin, and K. Held. Dynamical vertex approximation: A step beyond dynamical mean-field theory. *Phys. Rev. B* 75:045118, 2007.
- [195] K. Held, A. A. Katanin, and A. Toschi. Dynamical Vertex Approximation: An Introduction. *Progress of Theoretical Physics Supplement* 176:117–133, 2008.
- [196] T. Ayrál and O. Parcollet. Mott physics and spin fluctuations: A unified framework. *Phys. Rev. B* 92:115109, 2015.
- [197] T. Ayrál and O. Parcollet. Mott physics and spin fluctuations: A functional viewpoint. *Phys. Rev. B* 93:235124, 2016.
- [198] T. Ayrál and O. Parcollet. Mott physics and collective modes: An atomic approximation of the four-particle irreducible functional. *Phys. Rev. B* 94:075159, 2016.
- [199] A. N. Rubtsov, M. I. Katsnelson, and A. Lichtenstein. Dual boson approach to collective excitations in correlated fermionic systems. *Annals of Physics* 327:1320–1335, 2012.
- [200] A. N. Rubtsov, M. I. Katsnelson, A. I. Lichtenstein, and A. Georges. Dual fermion approach to the two-dimensional Hubbard model: Antiferromagnetic fluctuations and Fermi arcs. *Phys. Rev. B* 79:045133, 2009.
- [201] Y. M. Vil'k, L. Chen, and A.-M. S. Tremblay. Theory of spin and charge fluctuations in the Hubbard model. *Phys. Rev. B* 49:13267–13270, 1994.
- [202] Y. M. Vil'k, L. Chen, and A.-M. S. Tremblay. Two-particle self-consistent theory for spin and charge fluctuations in the Hubbard model. *Physica C: Superconductivity* 235-240:2235–2236, 1994.
- [203] Y. M. Vil'k and A.-M. S. Tremblay. Destruction of the fermi liquid by spin fluctuations in two dimensions. *Journal of Physics and Chemistry of Solids* 56 (12):1769–1771, 1995. Proceedings of the Conference on Spectroscopies in Novel Superconductors.
- [204] Vil'k, Y. M. and S. Tremblay, A.-M. Destruction of Fermi-liquid quasiparticles in two dimensions by critical fluctuations. *Europhys. Lett.* 33 (2):159–164, 1996.
- [205] T. Schäfer, S. Ciuchi, M. Wallerberger, P. Thunström, O. Gunnarsson, G. Sangiovanni, G. Rohringer, and A. Toschi. Nonperturbative landscape of the Mott-Hubbard transition: Multiple divergence lines around the critical endpoint. *Phys. Rev. B* 94:235108, 2016.
- [206] V. Janiš and V. Pokorný. Critical metal-insulator transition and divergence in a two-particle irreducible vertex in disordered and interacting electron systems. *Phys. Rev. B* 90:045143, 2014.

- [207] B. Kyung, J.-S. Landry, and A.-M. S. Tremblay. Antiferromagnetic fluctuations and  $d$ -wave superconductivity in electron-doped high-temperature superconductors. *Phys. Rev. B* 68:174502, 2003.
- [208] K. S. Singwi, M. P. Tosi, R. H. Land, and A. Sjölander. Electron Correlations at Metallic Densities. *Phys. Rev.* 176:589–599, 1968.
- [209] S. Ichimaru. Strongly coupled plasmas: high-density classical plasmas and degenerate electron liquids. *Rev. Mod. Phys.* 54:1017–1059, 1982.
- [210] L. Chen, C. Bourbonnais, T. Li, and A.-M. S. Tremblay. Magnetic properties of the two-dimensional Hubbard model. *Phys. Rev. Lett.* 66:369–372, 1991.
- [211] T. Paiva, R. Scalettar, M. Randeria, and N. Trivedi. Fermions in 2D Optical Lattices: Temperature and Entropy Scales for Observing Antiferromagnetism and Superfluidity. *Phys. Rev. Lett.* 104:066406, 2010.
- [212] E. Khatami and M. Rigol. Thermodynamics of strongly interacting fermions in two-dimensional optical lattices. *Phys. Rev. A* 84:053611, 2011.
- [213] J. P. F. LeBlanc and E. Gull. Equation of state of the fermionic two-dimensional Hubbard model. *Phys. Rev. B* 88:155108, 2013.
- [214] F. Werner, O. Parcollet, A. Georges, and S. R. Hassan. Interaction-Induced Adiabatic Cooling and Antiferromagnetism of Cold Fermions in Optical Lattices. *Phys. Rev. Lett.* 95:056401, 2005.
- [215] A.-M. Daré, L. Raymond, G. Albinet, and A.-M. S. Tremblay. Interaction-induced adiabatic cooling for antiferromagnetism in optical lattices. *Phys. Rev. B* 76:064402, 2007.
- [216] E. V. Gorelik, I. Titvinidze, W. Hofstetter, M. Snoek, and N. Blümer. Néel Transition of Lattice Fermions in a Harmonic Trap: A Real-Space Dynamic Mean-Field Study. *Phys. Rev. Lett.* 105:065301, 2010.
- [217] A. F. Veilleux, A.-M. Daré, L. Chen, Y. M. Vilks, and A.-M. S. Tremblay. Magnetic and pair correlations of the Hubbard model with next-nearest-neighbor hopping. *Phys. Rev. B* 52:16255–16263, 1995.
- [218] H. Nelisse, C. Bourbonnais, H. Touchette, Y. M. Vilks, and A.-M. S. Tremblay. Spin susceptibility of interacting electrons in one dimension: Luttinger liquid and lattice effects. *Physics of Condensed Matter* 12:351–365, 1999.
- [219] Y. M. Vilks. Shadow features and shadow bands in the paramagnetic state of cuprate superconductors. *Phys. Rev. B* 55:3870–3875, 1997.
- [220] B. Kyung, V. Hankevych, A.-M. Daré, and A.-M. S. Tremblay. Pseudogap and Spin Fluctuations in the Normal State of the Electron-Doped Cuprates. *Phys. Rev. Lett.* 93:147004, 2004.
- [221] V. Hankevych, B. Kyung, A.-M. Daré, D. Sénéchal, and A.-M. S. Tremblay. Strong- and weak-coupling mechanisms for pseudogap in electron-doped cuprates. *Journal of Physics and Chemistry of Solids* 67 (1):189–192, 2006. Spectroscopies in Novel Superconductors 2004.
- [222] A.-M. Daré, Y. M. Vilks, and A. M. S. Tremblay. Crossover from two- to three-dimensional critical behavior for nearly antiferromagnetic itinerant electrons. *Phys. Rev. B* 53:14236–14251, 1996.
- [223] S. Roy and A.-M. S. Tremblay. Scaling and commensurate-incommensurate crossover for the  $d=2$ ,  $z=2$  quantum critical point of itinerant antiferromagnets. *EPL (Europhysics Letters)* 84 (3):37013, 2008.
- [224] D. Bergeron, D. Chowdhury, M. Punk, S. Sachdev, and A.-M. S. Tremblay. Breakdown of Fermi liquid behavior at the  $(\pi, \pi) = 2k_F$  spin-density wave quantum-critical point: The case of electron-doped cuprates. *Phys. Rev. B* 86:155123, 2012.
- [225] D. Bergeron, V. Hankevych, B. Kyung, and A.-M. S. Tremblay. Optical and dc conductivity of the two-dimensional Hubbard model in the pseudogap regime and across the antiferromagnetic quantum critical point including vertex corrections. *Phys. Rev. B* 84:085128, 2011.
- [226] V. Hankevych, B. Kyung, and A.-M. S. Tremblay. Weak ferromagnetism and other instabilities of the two-dimensional  $t - t'$  Hubbard model at van Hove fillings. *Phys. Rev. B* 68:214405, 2003.
- [227] S. R. Hassan, B. Davoudi, B. Kyung, and A.-M. S. Tremblay. Conditions for magnetically induced singlet  $d$ -wave superconductivity on the square lattice. *Phys. Rev. B* 77:094501, 2008.
- [228] J. Otsuki. Two-particle self-consistent approach to unconventional superconductivity. *Phys. Rev. B* 85:104513, 2012.
- [229] A.-M. Daré and G. Albinet. Magnetic properties of the three-dimensional Hubbard model at half filling. *Phys. Rev. B* 61:4567–4575, 2000.
- [230] Saikawa, T. and Ferraz, A. Remnant Fermi surface in a pseudogap regime of the two-dimensional Hubbard model at finite temperature. *Eur. Phys. J. B* 20 (1):65–74, 2001.
- [231] R. Arita, S. Onoda, K. Kuroki, and H. Aoki. Magnetic Properties of the Hubbard Model on Three-Dimensional Lattices: Fluctuation-Exchange and Two-Particle Self-Consistent Studies. *Journal of the Physical Society of Japan* 69 (3):785–795, 2000.

- 
- [232] B. Kyung, J. S. Landry, D. Poulin, and A.-M. S. Tremblay. Comment on “Absence of a Slater Transition in the Two-Dimensional Hubbard Model”. *Phys. Rev. Lett.* 90:099702, 2003.
- [233] B. Kyung. Spectral properties and pseudogaps in a model with d-wave pairing symmetry. *Phys. Rev. B* 63:014502, 2000.
- [234] B. Kyung, S. Allen, and A.-M. S. Tremblay. Pairing fluctuations and pseudogaps in the attractive Hubbard model. *Phys. Rev. B* 64:075116, 2001.
- [235] S. Verga, R. J. Gooding, and F. Marsiglio. Minimally self-consistent T-matrix approximation to describe the low-temperature properties of the Hubbard model in the atomic limit. *Phys. Rev. B* 71:155111, 2005.
- [236] B. Davoudi and A.-M. S. Tremblay. Nearest-neighbor repulsion and competing charge and spin order in the extended Hubbard model. *Phys. Rev. B* 74:035113, 2006.
- [237] B. Davoudi and A.-M. S. Tremblay. Non-perturbative treatment of charge and spin fluctuations in the two-dimensional extended Hubbard model: Extended two-particle self-consistent approach. *Phys. Rev. B* 76:085115, 2007.
- [238] B. Davoudi, S. R. Hassan, and A.-M. S. Tremblay. Competition between charge and spin order in the  $t-U-V$  extended Hubbard model on the triangular lattice. *Phys. Rev. B* 77:214408, 2008.
- [239] H. Aizawa, K. Kuroki, and J.-i. Yamada. Enhancement of electron correlation due to the molecular dimerization in organic superconductors  $\beta - (\text{BDA} - \text{TTP})_2X$  ( $X = \text{I}_3, \text{SbF}_6$ ). *Phys. Rev. B* 92:155108, 2015.
- [240] D. Ogura and K. Kuroki. Asymmetry of superconductivity in hole- and electron-doped cuprates: Explanation within two-particle self-consistent analysis for the three-band model. *Phys. Rev. B* 92:144511, 2015.
- [241] K. Zantout, M. Altmeyer, S. Backes, and R. Valentí. Superconductivity in correlated BEDT-TTF molecular conductors: Critical temperatures and gap symmetries. *Phys. Rev. B* 97:014530, 2018.
- [242] H. Aizawa and K. Kuroki. Microscopic theory of the superconducting gap in the quasi-one-dimensional organic conductor  $(\text{TMTSF})_2\text{ClO}_4$ : Model derivation and two-particle self-consistent analysis. *Phys. Rev. B* 97:104507, 2018.
- [243] K. Nishiguchi, S. Teranishi, and K. Kusakabe. Self-Doping Effect Arising from Electron Correlations in Multilayer Cuprates. *Journal of the Physical Society of Japan* 86 (8):084707, 2017.
- [244] K. Nishiguchi, S. Teranishi, K. Kusakabe, and H. Aoki. Superconductivity arising from layer differentiation in multilayer cuprates. *Phys. Rev. B* 98:174508, 2018.
- [245] J. M. Pizarro, S. Adler, K. Zantout, T. Mertz, P. Barone, R. Valentí, G. Sangiovanni, and T. O. Wehling. Deconfinement of Mott Localized Electrons into Topological and Spin-Orbit Coupled Dirac Fermions. *npj Quantum Mater.* 5:79, 2020.
- [246] T. Mertz, K. Zantout, and R. Valentí. Self-energy dispersion in the Hubbard model. *Phys. Rev. B* 98:235105, 2018.
- [247] Y. Shimizu, K. Miyagawa, K. Kanoda, M. Maesato, and G. Saito. Spin Liquid State in an Organic Mott Insulator with a Triangular Lattice. *Phys. Rev. Lett.* 91:107001, 2003.
- [248] B. J. Powell and R. H. McKenzie. Half-Filled Layered Organic Superconductors and the Resonating-Valence-Bond Theory of the Hubbard-Heisenberg Model. *Phys. Rev. Lett.* 94:047004, 2005.
- [249] N. Toyota, M. Lang, and J. Müller. *Low-Dimensional Molecular Metals*. Springer-Verlag Berlin Heidelberg, 2007.
- [250] F. Kawaga, K. Miyagawa, and K. Kanoda. Unconventional critical behaviour in a quasi-two-dimensional organic conductor. *Nature* 436:534–537, 2005.
- [251] B. Hartmann, J. Müller, and T. Sasaki. Mott metal-insulator transition induced by utilizing a glasslike structural ordering in low-dimensional molecular conductors. *Phys. Rev. B* 90:195150, 2014.
- [252] D. Guterding, R. Valentí, and H. O. Jeschke. Influence of molecular conformations on the electronic structure of organic charge transfer salt. *Phys. Rev. B* 92:081109(R), 2015.
- [253] R. Kato, H. Kobayashi, A. Kobayashi, S. Moriyama, Y. Nishio, K. Kajita, and W. Sasaki. A New Ambient-pressure Superconductor,  $\kappa$ -(BEDT-TTF) $_2\text{I}_3$ . *Chem. Lett.* 16:507, 1987.
- [254] H. Mori, I. Hirabayashi, S. Tanaka, T. Mori, and H. Inokuchi. A New Ambient-pressure Superconductor,  $\kappa$ -(BEDT-TTF) $_2\text{Ag}(\text{CN})_2\text{H}_2\text{O}$  ( $T_c = 5.0$  K). *Solid State Commun.* 76:35, 1990.
- [255] A. M. Kini, U. Geiser, H. H. Wang, K. D. Carlson, J. M. Williams, W. K. Kwok, K. G. Vandervoort, J. E. Thompson, D. L. Stupka, D. Jung, and M.-H. Whangbo. A new ambient-pressure organic superconductor,  $\kappa$ -(ET) $_2\text{Cu}[\text{N}(\text{CN})_2]\text{Br}$ , with the highest transition temperature yet observed (inductive onset  $T_c = 11.6$  K, resistive onset = 12.5 K). *Inorg. Chem.* 29:2555, 1990.
- [256] T. Hiramatsu, Y. Yoshida, G. Saito, A. Otsuka, H. Yamochi, M. Maesato, Y. Shimizu, H. Ito, and H. Kishida. Quantum spin liquid: design of a quantum spin liquid next to a superconducting state based on a dimer-type ET Mott insulator. *J. Mater. Chem. C* 3:1378, 2015.

- [257] H. Elsinger, J. Wosnitzer, S. Wanka, J. Hagel, D. Schweitzer, and W. Strunz.  $\kappa$ -(BEDT-TTF)<sub>2</sub>Cu[N(CN)<sub>2</sub>]Br: A Fully Gapped Strong-Coupling Superconductor. *Phys. Rev. Lett.* 84:6098, 2000.
- [258] J. Müller, M. Lang, R. Helfrich, F. Steglich, and T. Sasaki. High-resolution ac-calorimetry studies of the quasi-two-dimensional organic superconductor  $\kappa$ -(BEDT-TTF)<sub>2</sub>Cu(NCS)<sub>2</sub>. *Phys. Rev. B* 65:140509(R), 2002.
- [259] J. Wosnitzer, S. Wanka, J. Hagel, M. Reibelt, D. Schweitzer, and J. A. Schlueter. Thermodynamic properties of quasi-two-dimensional organic superconductors. *Synth. Met.* 133:201, 2003.
- [260] J. M. Schrama, E. Rzepniewski, R. S. Edwards, J. Singleton, A. Ardavan, M. Kurmoo, and P. Day. Millimeter-Wave Magneto-optical Determination of the Anisotropy of the Superconducting Order Parameter in the Molecular Superconductor  $\kappa$ -(BEDT-TTF)<sub>2</sub>Cu(NCS)<sub>2</sub>. *Phys. Rev. Lett.* 83:3041, 1999.
- [261] K. Izawa, H. Yamaguchi, T. Sasaki, and Y. Matsuda. Superconducting Gap Structure of  $\kappa$ -(BEDT-TTF)<sub>2</sub>Cu(NCS)<sub>2</sub> Probed by Thermal Conductivity Tensor. *Phys. Rev. Lett.* 88:027002, 2001.
- [262] T. Arai, K. Ichimura, K. Nomura, S. Takasaki, J. Yamada, S. Nakatsuji, and H. Anzai. Tunneling spectroscopy on the organic superconductor  $\kappa$ -(BEDT-TTF)<sub>2</sub>Cu(NCS)<sub>2</sub> using STM. *Phys. Rev. B* 63:104518, 2001.
- [263] O. J. Taylor, A. Carrington, and J. A. Schlueter. Specific-Heat Measurements of the Gap Structure of the Organic Superconductors  $\kappa$ -(ET)<sub>2</sub>Cu[N(CN)<sub>2</sub>]Br and  $\kappa$ -(ET)<sub>2</sub>Cu(NCS)<sub>2</sub>. *Phys. Rev. Lett.* 99:057001, 2007.
- [264] K. Ichimura, M. Takami, and K. Nomura. Direct Observation of *d*-Wave Superconducting Gap in  $\kappa$ -(ET)<sub>2</sub>Cu[N(CN)<sub>2</sub>]Br with Scanning Tunneling Microscopy. *J. Phys. Soc. Jpn.* 77:114707, 2008.
- [265] O. J. Taylor, A. Carrington, and J. A. Schlueter. Superconductor-insulator phase separation induced by rapid cooling of  $\kappa$ -(ET)<sub>2</sub>Cu[N(CN)<sub>2</sub>]Br. *Phys. Rev. B* 77:060503(R), 2008.
- [266] L. Malone, O. J. Taylor, J. A. Schlueter, and A. Carrington. Location of gap nodes in the organic superconductors  $\kappa$ -(ET)<sub>2</sub>Cu(NCS)<sub>2</sub> and  $\kappa$ -(ET)<sub>2</sub>Cu[N(CN)<sub>2</sub>]Br determined by magnetocalorimetry. *Phys. Rev. B* 82:014522, 2010.
- [267] S. Milbradt, A. A. Bardin, C. J. S. Truncik, W. A. Huttema, A. C. Jacko, P. L. Burn, S. C. Lo, B. J. Powell, and D. M. Broun. In-plane superfluid density and microwave conductivity of the organic superconductor  $\kappa$ -(ET)<sub>2</sub>Cu[N(CN)<sub>2</sub>]Br: Evidence for *d*-wave pairing and resilient quasiparticles. *Phys. Rev. B* 88:064501, 2013.
- [268] Y. Oka, H. Nobukane, N. Matsunaga, K. Nomura, K. Katono, K. Ichimura, and A. Kawamoto. Tunneling Spectroscopy in Organic Superconductor  $\kappa$ -(BEDT-TTF-d[3,3])<sub>2</sub>Cu[N(CN)<sub>2</sub>]Br. *J. Phys. Soc. Jpn.* 84:064713, 2015.
- [269] D. Guterding, S. Diehl, M. Altmeyer, T. Methfessel, U. Tutsch, H. Schubert, M. Lang, J. Müller, M. Huth, H. O. Jeschke, R. Valentí, M. Jourdan, and H.-J. Elmers. Evidence for eight node mixed-symmetry superconductivity in a correlated organic metal. *Phys. Rev. Lett.* 116:237001, 2016.
- [270] S. Kühlmorgen, R. Schönemann, E L Green, J Müller, and J Wosnitzer. Investigation of the superconducting gap structure in  $\kappa$ -(BEDT-TTF)<sub>2</sub>Cu(NCS)<sub>2</sub> and  $\kappa$ -(BEDT-TTF)<sub>2</sub>Cu[N(CN)<sub>2</sub>]Br by means of thermal-conductivity measurements. *Journal of Physics: Condensed Matter* 29 (40):405604, 2017.
- [271] R. H. McKenzie. Similarities Between Organic and Cuprate Superconductors. *Science* 278:820, 1997.
- [272] Y. Zhou, K. Kanoda, and T.-K. Ng. Quantum Spin Liquid States. *Rev. Mod. Phys.* 89 (025003), 2017.
- [273] D. Guterding, M. Altmeyer, H. O. Jeschke, and R. Valentí. Near-degeneracy of extended *s*+*d<sub>x<sup>2</sup>-y<sup>2</sup></sub>* and *d<sub>xy</sub>* order parameters in quasi-two-dimensional organic superconductors. *Phys. Rev. B* 94:024515, 2016.
- [274] A. A. Abrikosov, L. P. Gor'kov, and I. Dzyaloshinskii. *Quantum Field Theoretical Methods in Statistical Physics*. Pergamon Oxford, 1965.
- [275] Y. Yanase, T. Jujo, T. Nomura, H. Ikeda, T. Hotta, and K. Yamada. Theory of superconductivity in strongly correlated electron systems. *Physics Reports* 387 (1):1–149, 2003.
- [276] T. Takimoto, T. Hotta, and K. Ueda. Strong-coupling theory of superconductivity in a degenerate Hubbard model. *Phys. Rev. B* 69:104504, 2004.
- [277] R. V. Mises and H. Pollaczek-Geiringer. Praktische Verfahren der Gleichungsaufösung. *ZAMM - Journal of Applied Mathematics and Mechanics / Zeitschrift für Angewandte Mathematik und Mechanik* 9 (2):152–164, 1929.
- [278] D. J. Scalapino, E. Loh, and J. E. Hirsch. *d*-wave pairing near a spin-density-wave instability. *Phys. Rev. B* 34:8190–8192, 1986.

- 
- [279] B J Powell and R. H McKenzie. Strong electronic correlations in superconducting organic charge transfer salts. *Journal of Physics: Condensed Matter* 18 (45):R827, 2006.
- [280] J. Schmalian. Pairing due to Spin Fluctuations in Layered Organic Superconductors. *Phys. Rev. Lett.* 81:4232, 1998.
- [281] R. Kaneko, L. F. Tocchio, R. Valentí, and F. Becca. Charge orders in organic charge-transfer salts. *New J. Phys.* 19:103033, 2017.
- [282] A. Sekine, J. Nasu, and S. Ishihara. Polar charge fluctuation and superconductivity in organic conductors. *Phys. Rev. B* 87:085133, 2013.
- [283] H. Watanabe, H. Seo, and S. Yunoki. Phase Competition and Superconductivity in  $\kappa$ -(BEDT-TTF)<sub>2</sub>X: Importance of Intermolecular Coulomb Interactions. *J. Phys. Soc. Jpn.* 86:033703, 2017.
- [284] H. Miyahara, R. Arita, and H. Ikeda. Development of a two-particle self-consistent method for multiorbital systems and its application to unconventional superconductors. *Phys. Rev. B* 87:045113, 2013.
- [285] K. Zantout, S. Backes, and R. Valentí. Effect of Nonlocal Correlations on the Electronic Structure of LiFeAs. *Phys. Rev. Lett.* 123:256401, 2019.
- [286] M. Mochizuki, Y. Yanase, and M. Ogata. Ferromagnetic Fluctuation and Possible Triplet Superconductivity in Na<sub>x</sub>CoO<sub>2</sub> · yH<sub>2</sub>O: Fluctuation-Exchange Study of the Multiorbital Hubbard Model. *Phys. Rev. Lett.* 94:147005, 2005.
- [287] S. Bhattacharyya, K. Björnson, K. Zantout, D. Steffensen, L. Fanfarillo, A. Kreisel, R. Valentí, B. M. Andersen, and P. J. Hirschfeld. Nonlocal correlations in iron pnictides and chalcogenides. *Phys. Rev. B* 102:035109, 2020.
- [288] E. Gull, A. J. Millis, A. I. Lichtenstein, A. N. Rubtsov, M. Troyer, and P. Werner. Continuous-time Monte Carlo methods for quantum impurity models. *Rev. Mod. Phys.* 83:349–404, 2011.
- [289] X. Wang, H. T. Dang, and A. J. Millis. High-frequency asymptotic behavior of self-energies in quantum impurity models. *Phys. Rev. B* 84:073104, 2011.
- [290] Y. Kamihara, T. Watanabe, M. Hirano, and H. Hosono. Iron-based layered superconductor La[O(1-x)F(x)]FeAs (x = 0.05-0.12) with T(c) = 26 K. *Journal of the American Chemical Society* 130 (11):3296–3297, 2008.
- [291] M. Rotter, M. Tegel, and D. Johrendt. Superconductivity at 38 K in the Iron Arsenide (Ba<sub>1-x</sub>K<sub>x</sub>)Fe<sub>2</sub>As<sub>2</sub>. *Phys. Rev. Lett.* 101:107006, 2008.
- [292] A. V. Chubukov, D. V. Efremov, and I. Eremin. Magnetism, superconductivity, and pairing symmetry in iron-based superconductors. *Phys. Rev. B* 78:134512, 2008.
- [293] Z.-A. Ren and Z.-X. Zhao. Research and Prospects of Iron-Based Superconductors. *Advanced Materials* 21 (45):4584–4592, 2009.
- [294] A. A. Kordyuk. Iron-based superconductors: Magnetism, superconductivity, and electronic structure (Review Article). *Low Temperature Physics* 38 (9):888–899, 2012.
- [295] R. M Fernandes and A. V Chubukov. Low-energy microscopic models for iron-based superconductors: a review. *Reports on Progress in Physics* 80 (1):014503, 2016.
- [296] S. Lebegue. Electronic structure and properties of the Fermi surface of the superconductor LaOFeP. *Phys. Rev. B* 75:035110, 2007.
- [297] D. J. Singh and M.-H. Du. Density Functional Study of LaFeAsO<sub>1-x</sub>F<sub>x</sub>: A Low Carrier Density Superconductor Near Itinerant Magnetism. *Phys. Rev. Lett.* 100:237003, 2008.
- [298] I. I. Mazin, M. D. Johannes, L. Boeri, K. Koepernik, and D. J. Singh. Problems with reconciling density functional theory calculations with experiment in ferropnictides. *Phys. Rev. B* 78:085104, 2008.
- [299] C. Cao, P. J. Hirschfeld, and H.-P. Cheng. Proximity of antiferromagnetism and superconductivity in LaFeAsO<sub>1-x</sub>F<sub>x</sub>: Effective Hamiltonian from ab initio studies. *Phys. Rev. B* 77:220506(R), 2008.
- [300] Q. Si and E. Abrahams. Strong Correlations and Magnetic Frustration in the High T<sub>c</sub> Iron Pnictides. *Phys. Rev. Lett.* 101:076401, 2008.
- [301] M. M. Qazilbash, J. J. Hamlin, R. E. Baumbach, L. Zhang, D. J Singh, M. B. Maple, and D. N. Basov. Electronic correlations in the iron pnictides. *Nature Physics* 5 (9):647, 2009.
- [302] F. Rullier-Albenque, D. Colson, A. Forget, and H. Alloul. Hall Effect and Resistivity Study of the Magnetic Transition, Carrier Content, and Fermi-Liquid Behavior in Ba(Fe<sub>1-x</sub>Co<sub>x</sub>)<sub>2</sub>As<sub>2</sub>. *Phys. Rev. Lett.* 103:057001, 2009.
- [303] K Haule and G Kotliar. Coherence-incoherence crossover in the normal state of iron oxypnictides and importance of Hund’s rule coupling. *New Journal of Physics* 11 (2):025021, 2009.
- [304] M. Aichhorn, S. Biermann, T. Miyake, A. Georges, and M. Imada. Theoretical evidence for strong correlations and incoherent metallic state in FeSe. *Phys. Rev. B* 82:064504, 2010.
- [305] P. Hansmann, R. Arita, A. Toschi, S. Sakai, G. Sangiovanni, and K. Held. Dichotomy between Large Local and Small Ordered Magnetic Moments in Iron-Based Superconductors. *Phys. Rev. Lett.* 104:197002, 2010.

- [306] Z. P. Yin, K. Haule, and G. Kotliar. Kinetic frustration and the nature of the magnetic and paramagnetic states in iron pnictides and iron chalcogenides. *Nature Materials* 10:932–935, 2011.
- [307] P. Werner, M. Casula, T. Miyake, F. Aryasetiawan, A. J. Millis, and S. Biermann. Satellites and large doping and temperature dependence of electronic properties in hole-doped  $\text{BaFe}_2\text{As}_2$ . *Nature Physics* 8 (4):331, 2012.
- [308] J. Ferber, H. O. Jeschke, and R. Valentí. Fermi Surface Topology of  $\text{LaFePO}$  and  $\text{LiFeP}$ . *Phys. Rev. Lett.* 109:236403, 2012.
- [309] D. V. Evtushinsky, M. Aichhorn, Y. Sassa, Z.-H. Liu, J. Maletz, T. Wolf, A. N. Yaresko, S. Biermann, S. V. Borisenko, and B. Büchner. Direct observation of dispersive lower Hubbard band in iron-based superconductor  $\text{FeSe}$ . *arXiv preprint arXiv:1612.02313*, 2016.
- [310] E. Bascones, B. Valenzuela, and M. J. Calderón. Magnetic interactions in iron superconductors: A review. *Comptes Rendus Physique* 17 (1-2):36–59, 2016.
- [311] M. D. Watson, S. Backes, A. A. Haghighirad, M. Hoesch, T. K. Kim, A. I. Coldea, and R. Valentí. Formation of Hubbard-like bands as a fingerprint of strong electron-electron interactions in  $\text{FeSe}$ . *Phys. Rev. B* 95:081106(R), 2017.
- [312] H. Miao, Z. P. Yin, S. F. Wu, J. M. Li, J. Ma, B.-Q. Lv, X. P. Wang, T. Qian, P. Richard, L.-Y. Xing, X.-C. Wang, C. Q. Jin, K. Haule, G. Kotliar, and H. Ding. Orbital-differentiated coherence-incoherence crossover identified by photoemission spectroscopy in  $\text{LiFeAs}$ . *Phys. Rev. B* 94:201109(R), 2016.
- [313] L. Ortenzi, E. Cappelluti, L. Benfatto, and L. Pietronero. Fermi-Surface Shrinking and Interband Coupling in Iron-Based Pnictides. *Phys. Rev. Lett.* 103:046404, 2009.
- [314] S. V. Borisenko, V. B. Zabolotnyy, D. V. Evtushinsky, T. K. Kim, I. V. Morozov, A. N. Yaresko, A. A. Kordyuk, G. Behr, A. Vasiliev, R. Follath, and B. Büchner. Superconductivity without Nesting in  $\text{LiFeAs}$ . *Phys. Rev. Lett.* 105:067002, 2010.
- [315] Y. S. Kushnirenko, A. A. Kordyuk, A. V. Fedorov, E. Haubold, T. Wolf, B. Büchner, and S. V. Borisenko. Anomalous temperature evolution of the electronic structure of  $\text{FeSe}$ . *Phys. Rev. B* 96:100504(R), 2017.
- [316] Y. Wang, A. Kreisler, V. B. Zabolotnyy, S. V. Borisenko, B. Büchner, T. A. Maier, P. J. Hirschfeld, and D. J. Scalapino. Superconducting gap in  $\text{LiFeAs}$  from three-dimensional spin-fluctuation pairing calculations. *Phys. Rev. B* 88:174516, 2013.
- [317] H. Miao, T. Qian, X. Shi, P. Richard, T. K. Kim, M. Hoesch, L. Y. Xing, X.-C. Wang, C.-Q. Jin, J.-P. Hu, and H. Ding. Observation of strong electron pairing on bands without Fermi surfaces in  $\text{LiFe}(1-x)\text{Co}x\text{As}$ . *Nature communications* 6:6056, 2015.
- [318] D. Altenfeld, P. J. Hirschfeld, I. I. Mazin, and I. Eremin. Detecting sign-changing superconducting gap in  $\text{LiFeAs}$  using quasiparticle interference. *Phys. Rev. B* 97:054519, 2018.
- [319] J. M. Tomczak, M. Casula, T. Miyake, and S. Biermann. Asymmetry in band widening and quasiparticle lifetimes in  $\text{SrVO}_3$ : Competition between screened exchange and local correlations from combined *GW* and dynamical mean-field theory *GW* + DMFT. *Phys. Rev. B* 90:165138, 2014.
- [320] A. van Roekeghem, T. Ayrál, J. M. Tomczak, M. Casula, N. Xu, H. Ding, M. Ferrero, O. Parcollet, H. Jiang, and S. Biermann. Dynamical Correlations and Screened Exchange on the Experimental Bench: Spectral Properties of the Cobalt Pnictide  $\text{BaCo}_2\text{As}_2$ . *Phys. Rev. Lett.* 113:266403, 2014.
- [321] S. Li, N. Kaushal, Y. Wang, Y. Tang, G. Alvarez, A. Nocera, T. A. Maier, E. Dagotto, and S. Johnston. Nonlocal correlations in the orbital selective Mott phase of a one-dimensional multiorbital Hubbard model. *Phys. Rev. B* 94:235126, 2016.
- [322] P. Sémon, K. Haule, and G. Kotliar. Validity of the local approximation in iron pnictides and chalcogenides. *Phys. Rev. B* 95:195115, 2017.
- [323] J. Kaufmann, C. Eckhardt, M. Pickem, M. Kitatani, A. Kauch, and K. Held. *Self-consistent ab initio DGA approach*, 2020.
- [324] J. H. Tapp, Z. Tang, B. Lv, K. Sasmal, B. Lorenz, P. C. W. Chu, and A. M. Guloy.  $\text{LiFeAs}$ : An intrinsic  $\text{FeAs}$ -based superconductor with  $T_c = 18$  K. *Phys. Rev. B* 78:060505, 2008.
- [325] L. Kong, L. Cao, S. Zhu, M. Papaj, G. Dai, G. Li, P. Fan, W. Liu, F. Yang, X. Wang, S. Du, C. Jin, L. Fu, H.-J. Gao, and H. Ding. *Tunable vortex Majorana zero modes in  $\text{LiFeAs}$  superconductor*, 2020.
- [326] I. Morozov, A. Boltalin, O. Volkova, A. Vasiliev, O. Kataeva, U. Stockert, M. Abdel-Hafez, D. Bombor, A. Bachmann, L. Harnagea, M. Fuchs, H.-J. Grafe, G. Behr, R. Klingeler, S. Borisenko, C. Hess, S. Wurmehl, and B. Büchner. Single Crystal Growth and Characterization of Superconducting  $\text{LiFeAs}$ . *Crystal Growth & Design* 10 (10):4428–4432, 2010.
- [327] K. Momma and F. Izumi. *VESTA3* for three-dimensional visualization of crystal, volumetric and morphology data. *Journal of Applied Crystallography* 44 (6):1272–1276, 2011.

- 
- [328] P. Blaha, K Schwarz, G. K. H. Madsen, D Kvasnicka, and J Luitz. WIEN2k: An Augmented Plane Wave plus Local Orbitals Program for Calculating Crystal Properties. *Vienna University of Technology, Vienna*, 2001.
- [329] G A Ummarino, S. Galasso, and A Sanna. A phenomenological multiband Eliashberg model for LiFeAs. *Journal of Physics: Condensed Matter* 25 (20):205701, 2013.
- [330] A. Kokalj. XCrySDen—a new program for displaying crystalline structures and electron densities. *Journal of Molecular Graphics and Modelling* 17 (3):176–179, 1999.
- [331] A. A. Mostofi, J. R. Yates, G. Pizzi, Y.-S. Lee, I. Souza, D. Vanderbilt, and N. Marzari. An updated version of wannier90: A tool for obtaining maximally-localised Wannier functions. *Computer Physics Communications* 185 (8):2309–2310, 2014.
- [332] H. Eschrig and K. Koepf. Tight-binding models for the iron-based superconductors. *Phys. Rev. B* 80:104503, 2009.
- [333] H. Jiang, R. I. Gómez-Abal, X.-Z. Li, C. Meisenbichler, C. Ambrosch-Draxl, and M. Scheffler. FHI-gap: a GW code based on the All-electron augmented plane wave method. *Computer Phys. Commun.* 184:348, 2012.
- [334] R. Levy, J. P. F. LeBlanc, and E. Gull. Implementation of the maximum entropy method for analytic continuation. *Computer Physics Communications* 215:149–155, 2017.
- [335] Y S. Kushnirenko, D. V. Evtushinsky, T. K. Kim, I V. Morozov, S. Wurmehl, S Aswartham, A V. Chubukov, and S. V. Borisenko. Superconductivity-induced nematicity. *arXiv preprint arXiv:1810.04446*, 2018.
- [336] C. Putzke, A. I. Coldea, I. Guillaumon, D. Vignolles, A. McCollam, D. LeBoeuf, M. D. Watson, I. I. Mazin, S. Kasahara, T. Terashima, T. Shibauchi, Y. Matsuda, and A. Carrington. de Haas–van Alphen Study of the Fermi Surfaces of Superconducting LiFeP and LiFeAs. *Phys. Rev. Lett.* 108:047002, 2012.
- [337] A. Gaenko, A. E. Antipov, G. Carcassi, T. Chen, X. Chen, Q. Dong, L. Gamper, J. Gukelberger, R. Igarashi, S. Isakov, M. Könz, J. P. F. LeBlanc, R. Levy, P. N. Ma, J. E. Paki, H. Shinaoka, S. Todo, M. Troyer, and E. Gull. Updated core libraries of the ALPS project. *Computer Physics Communications* 213:235–251, 2017.
- [338] J. M. Luttinger. Analytic Properties of Single-Particle Propagators for Many-Fermion Systems. *Phys. Rev.* 121:942–949, 1961.
- [339] K. Zantout, *Unconventional superconductivity within the single-orbital Hubbard model beyond the Random Phase Approximation*. Master’s Thesis, 2016.
- [340] W. Vogt. *Adaptive Verfahren zur numerischen Quadratur und Kubatur*, 2006.
- [341] H. Büsing, *Multivariate numerische Integration und Anwendungen in der Peridynamik*. Master’s Thesis, 2008.

## Acknowledgements

This work would not have been possible without the support and guidance of many people that deserve to be mentioned here.

Foremost, I am thankful to Prof. Roser Valentí who guided me through the four years of my PhD work in her research group and gave me useful advice and many valuable opportunities for discussion. Those were important contributions to my understanding of the physics in the systems we studied. At this point I feel also indebted to mention her trust and encouragement that I experienced during my scientific work.

I am also very thankful to Prof. Eberhard Engel for being the second referee of this thesis.

I also express my gratitude towards Steffen Backes for his sincere and wholehearted support; not only as a collaborator and proofreader but also as a dear friend.

My special thanks go to my colleagues in Prof. Valentí's research group whose support was not only restricted to scientific discussion and collaboration but was also moral support: Michaela Altmeyer, Thomas Mertz, Aleksandar Razpopov, Sananda Biswas, Ying Li, Julian Stobbe, Aaram J. Kim, Dominik Lessnich, Steve Winter, Kira Riedl, Niclas Heinsdorf and Lucas Habeney.

Moreover, I am especially thankful for the support from Caroline Mohrs, Fabian Schubert, Arthur Scammel, Emanuele Varriale and Hendrik Wernecke.

Last but not least, I would like to thank all the scientists and students that I met and discussed with during my PhD studies like Shinibali Bhattacharyya, Peter J. Hirschfeld, Silke Biermann, Brian M. Andersen, Andreas Kreisel and many more.

## Curriculum Vitae

Karim Zantout

Institut für Theoretische Physik  
Goethe-Universität Frankfurt am Main  
Max-von-Laue-Straße 1  
60438 Frankfurt am Main  
Germany

email: [zantout@itp.uni-frankfurt.de](mailto:zantout@itp.uni-frankfurt.de)

URL: <https://itp.uni-frankfurt.de/~zantout/>



Born: December 3, 1991 in Beirut, Lebanon  
Nationality: German

### Education

- 2016-2020 PhD student in the group of Prof. Dr. Roser Valentí  
Institute for Theoretical Physics, Goethe University, Frankfurt
- 2016 Master of Science in Physics, Goethe University, Frankfurt
- Title of the Master thesis:  
*Unconventional superconductivity within the single-orbital Hubbard model beyond the Random Phase Approximation*
- 2014 Bachelor of Science in Physics, Goethe University, Frankfurt
- Title of the Bachelor thesis:  
*London-, Ginzburg-Landau- und Bardeen-Cooper-Schrieffer-Theorie für konventionelle Supraleiter*
- 2011 Abitur certificate (German high-school diploma)

## Awards and honors

- 2018      honorary certificate of the municipal foreign national representation of Frankfurt
- 2017      Philip-Siedler science award (Master thesis)
- 2014      Erasmus+ scholarship
- 2011-2016   scholarship of the Hans-Boeckler foundation

## Teaching

- winter term 2020      tutor “Programming for Physicists”
- summer term 2020      head tutor “Theoretical Quantum Mechanics I”
- winter term 2019      head tutor “Theoretical Solid State Theory I”
- summer term 2019      head tutor “Theoretical Solid State Theory II”
- winter term 2018      head tutor “Programming for Physicists”
- winter term 2016      tutor “Programming for Physicists”
- summer term 2016      tutor “Linear Algebra 2”
- winter term 2015      tutor “Theoretical Thermodynamics and Statistical Mechanics”
- summer term 2015      tutor “Analytical Mechanics”
- summer term 2014      tutor “Theoretical Quantum Mechanics I”
- winter term 2013      tutor “Mathematics for Physicists III”
- summer term 2013      tutor “Mathematics for Physicists II”

## Publications

- K. Zantout, S. Backes, R. Valenti,  
*Two-Particle Self-Consistent method for the multi-orbital Hubbard model*,  
arXiv:2008.08098 (2020)
- S. Bhattacharyya, K. Björnson, K. Zantout, D. Steffensen, L. Fanfarillo, A. Kreisel, R. Valenti, B. M. Andersen, P. J. Hirschfeld,  
*Non-local correlations in Iron Pnictides and Chalcogenides*,  
Phys. Rev. B **102**, 035109 (2020)
- J. M. Pizarro, S. Adler, K. Zantout, T. Mertz, P. Barone, R. Valenti, G. Sangiovanni, T. O. Wehling,

*Deconfinement of Mott Localized Electrons into Topological and Spin-Orbit Coupled Dirac Fermions,*  
npj Quantum Materials **5**, 79 (2020)

- K. Zantout, S. Backes, R. Valenti,  
*Effect of non-local correlations on the electronic structure of LiFeAs,*  
Phys. Rev. Lett. **123**, 256401 (2019)
- T. Mertz, K. Zantout, R. Valenti,  
*Statistical Analysis of the Chern Number in the Interacting Haldane-Hubbard Model,*  
Phys. Rev. B **100**, 125111 (2019)
- T. Mertz, K. Zantout, R. Valenti,  
*Self-Energy Dispersion in the Hubbard Model,*  
Phys. Rev. B **98**, 235105 (2018)
- K. Zantout, M. Altmeyer, S. Backes, R. Valenti,  
*Superconductivity in correlated BEDT-TTF molecular conductors: Critical temperatures and gap symmetries,*  
Phys. Rev. B **97**, 014530 (2018)